DTIC FILE COPY

LBL-24097

AFOSR-TR- 89-0195

(2)

LOW ENERGY X-RAY AND ELECTRON PHYSICS AND TECHNOLOGY FOR HIGH-TEMPERATURE PLASMA DIAGNOSTICS

AD-A206 486

Final ~~Annual~~ Scientific Report

for the period

01 October 1986 to 30 September 1987

AFOSR #ISSA-87-0019

BURTON L. HENKE

Principal Investigator

Center for X-Ray Optics
Lawrence Berkeley Laboratory
University of California
1 Cyclotron Road
Berkeley, California 94720

Prepared for the

Air Force Office of Scientific Research
Directorate of Physics
Bolling Air Force Base
Washington, D.C. 20332

October 1987

Approved for public release; distribution unlimited.

DTIC ELECTE FEB 16 1989 S D H

89 2 15 225

UNCLASSIFIED

ECURITY CLASSIFICATION OF THIS PAGE

REPORT DOCUMENTATION PAGE

1a. REPORT SECURITY CLASSIFICATION Unclassified	1b. RESTRICTIVE MARKINGS
2a. SECURITY CLASSIFICATION AUTHORITY	3. DISTRIBUTION/AVAILABILITY OF REPORT Approved for public release; Distribution unlimited
2b. DECLASSIFICATION/DOWNGRADING SCHEDULE	
4. PERFORMING ORGANIZATION REPORT NUMBER(S)	5. MONITORING ORGANIZATION REPORT NUMBER(S) AFOSR-TR- 89-0195
6a. NAME OF PERFORMING ORGANIZATION Lawrence Berkeley Laboratory University of California 6b. OFFICE SYMBOL (If applicable)	7a. NAME OF MONITORING ORGANIZATION AFOSR/NP
6c. ADDRESS (City, State and ZIP Code) Center for X-Ray Optics, LBL, MS: 80/101 1 Cyclotron Road Berkeley, CA 94720	7b. ADDRESS (City, State and ZIP Code) Building 410 Bolling AFB, Washington, D.C. 20332-6448
8a. NAME OF FUNDING/SPONSORING ORGANIZATION AFOSR 8b. OFFICE SYMBOL (If applicable) NP	9. PROCUREMENT INSTRUMENT IDENTIFICATION NUMBER AFOSR Grant #ISSA-87-0019
8c. ADDRESS (City, State and ZIP Code) Building 410 Bolling AFB, Washington, D.C. 20332-6448	10. SOURCE OF FUNDING NOS. PROGRAM ELEMENT NO. 61102F; PROJECT NO. 2301; TASK NO. A1; WORK UNIT NO.
11. TITLE (Include Security Classification) Low energy X-ray a Electron Physics & Technology for High-Temperature Plasma Diagnostics	
12. PERSONAL AUTHOR(S) Burton L. Henke	
13a. TYPE OF REPORT ~~Annual~~ Final	13b. TIME COVERED FROM 10/1/86 TO 9/30/87
14. DATE OF REPORT (Yr., Mo., Day) 01 October 1987	15. PAGE COUNT 262
16. SUPPLEMENTARY NOTATION	

17. COSATI CODES			18. SUBJECT TERMS (Continue on reverse if necessary and identify by block number)
FIELD	GROUP	SUB GR.	X-ray diagnostics, Fusion energy, X-ray laser, X-ray physics

19. ABSTRACT (Continue on reverse if necessary and identify by block number)

This longstanding AFOSR program and laborator (established in 1954 for low-energy x-ray physics and technology was transferred to the Lawrence Berkeley Laboratory's new Center for X-Ray Optics in December, 1984. Over the past three years, FY/85-87, it has expanded into a major program of the CXRO with the principal objective of supporting research and application programs at the new large x-ray source facilities, particularly the high temperature plasma and synchrotron radiation sources. These large national laboratory facilities have opened up for training a group of new young x-ray experimentalists. This program has been particularly addressed to the development of absolute x-ray diagnostics for the fusion energy and x-ray laser research and development, and to student training in experimental x-ray physics. This effort has also the supplemental support of the DOE lead national laboratories--Los Alamos National Laboratory, Lawrence Livermore National Laboratory, and the National Laser Users Facility at the University of Rochester.

20 DISTRIBUTION/AVAILABILITY OF ABSTRACT UNCLASSIFIED/UNLIMITED ☒ SAME AS RPT. ☒ DTIC USERS ☐	21 ABSTRACT SECURITY CLASSIFICATION Unclassified
22a. NAME OF RESPONSIBLE INDIVIDUAL HOWARD SCHLOSSBERG	22b TELEPHONE NUMBER (Include Area Code) (202) 767-4906 22c. OFFICE SYMBO NP

DD FORM 1473, 83 APR EDITION OF 1 JAN 73 IS OBSOLETE. UNCLASSIFIED

ANNUAL SCIENTIFIC REPORT

AFOSR #ISSA-87-0019

Low Energy X-Ray and Electron Physics and
Technology for High Temperature Plasma Diagnostics
01 October 1986 to 30 September 1987

Burton L. Henke
Principal Investigator

PROGRAM SUMMARY

This long-standing AFOSR program and laboratory (established in 1954) for low-energy x-ray physics and technology was transferred to the Lawrence Berkeley Laboratory's new Center for X-Ray Optics in December, 1984. Over the past three years, FY/85-87, it has expanded into a major program of the CXRO with the principal objective of supporting research and application programs at the new large x-ray source facilities, particularly the high temperature plasma and synchrotron radiation sources. These large national laboratory facilities have opened up important opportunities for advancing x-ray physics and technology and for training a group of new young x-ray experimentalists. This program has been particularly addressed to the development of absolute x-ray diagnostics for the fusion energy and x-ray laser research and development, and to student training in experimental x-ray physics. This effort has also the supplemental support of the DOE lead national laboratories--Los Alamos National Laboratory, Lawrence Livermore National Laboratory, and the National Laser Users Facility at the University of Rochester.

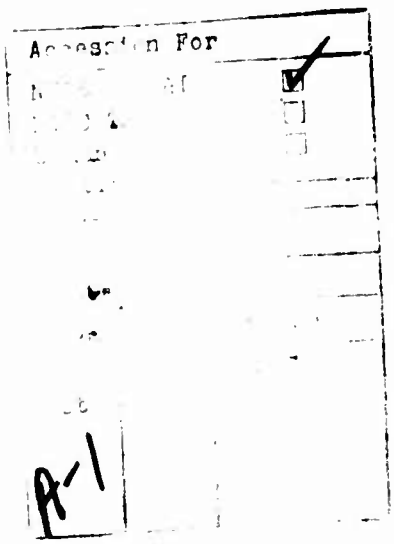
Our new LBL laboratory includes five specially designed spectrographic stations for the measurement of x-rays and the associated photoemissions in the 100-10,000 eV region, as described in Appendix 1. Reprints, preprints and technical notes on the recent work of this program, principally those on the development of absolute x-ray spectrometry, are presented in Appendix 2. A listing of research publications for the period 1975-1987 for this on-going program is presented in Appendix 3, and a listing of the citations to this work in the recent scientific literature (for the period 1980 to early 1987) is presented in Appendix 4.

Beginning in FY/88 the principal investigator for this program will be Eric Gullikson and the co-investigator (consultant and adviser) will be the present PI, Burton Henke. Eric Gullikson gained his initial training in this experimental x-ray physics laboratory under Professor Henke during his Junior and Senior years in an Honors program in physics at the University of Hawaii. He was then invited as a summer student assistant to help establish the first soft x-ray analysis facility at

the LLNL Plutonium Laboratory. He received his Ph.D in solid state experimental physics under Professor Schultz at UC-San Diego, and he has held a post-doctorate position at the Murray Hill AT&T Laboratories for the past two and a half years under Dr. Mills. Part of his research effort at AT&T has been on an investigation of the x-ray photon-counting efficiency of the rare gas solids and, in collaboration with this program, on a similar investigation of the absolute quantum efficiency in the 100-10,000 eV range of the "super photocathodes", solid Ar and Xe. Eric Gullikson was an invited speaker at the March 1986 New York APS meeting. He is now an LBL Staff Scientist on this program. His Curriculum Vitae is attached in Appendix 5.

With the continuity and on-going success of this program assured under Gullikson's leadership and Henke's advisory role, B.L. Henke will begin a phased retirement on October 1, 1987 and will begin writing a book on the "Basic Principles and Methods of Low-Energy X-Ray Physics and Technology" (which will be based in large part on his thirty-three years of AFOSR-supported research). The book will include an up-dated version of the x-ray photoabsorption and atomic scattering tables, which originally published from this project in 1982 (ADNDT, Vol. 27), along with the details of their application in absolute x-ray spectrometry. It is felt that such a book at this time will be particularly helpful to the many new young x-ray experimentalists now entering this rapidly expanding field of new applied x-ray physics.

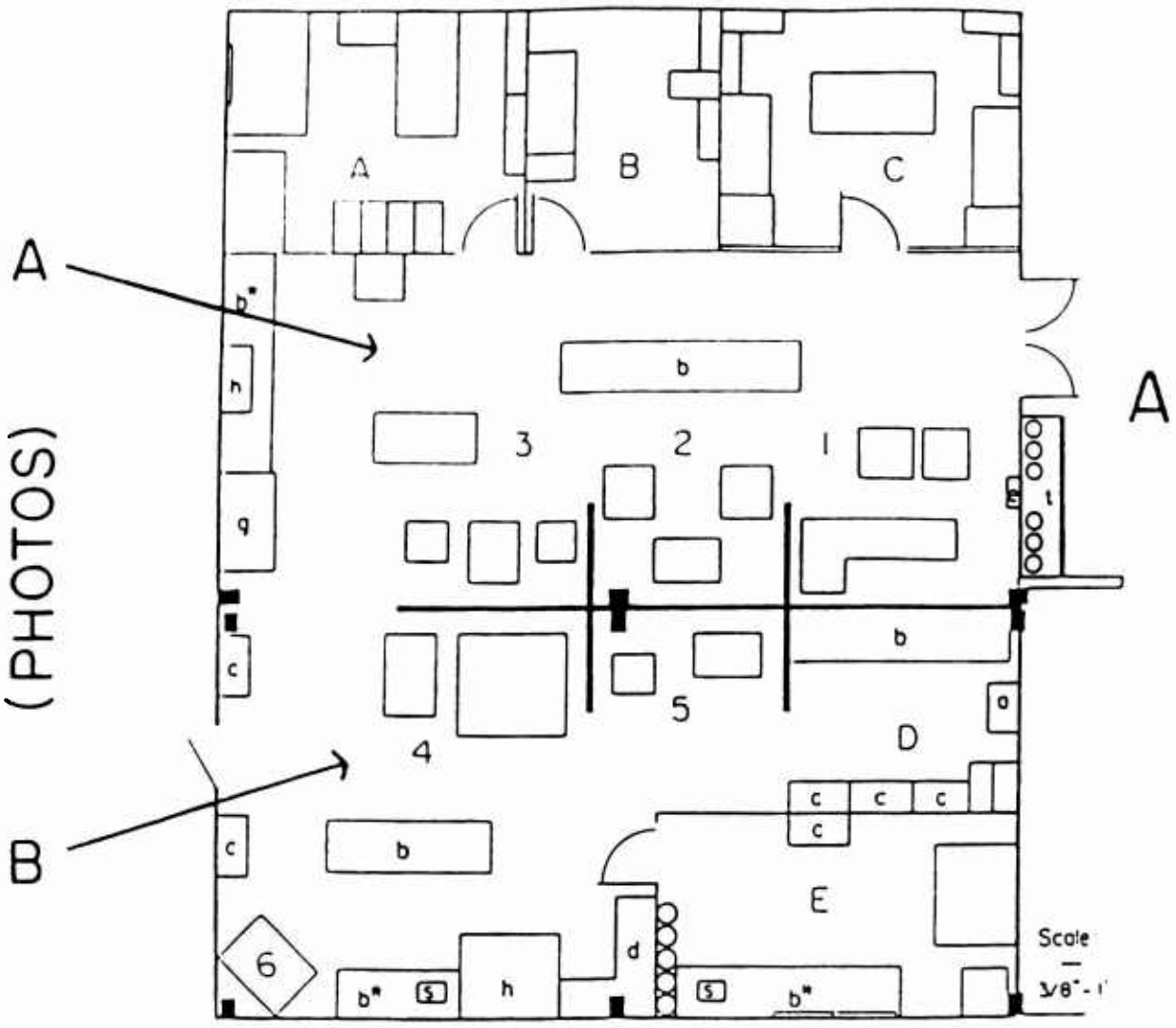




APPENDIX 1

LOW-ENERGY X-RAY PHYSICS LABORATORY
Center for X-Ray Optics
Lawrence Berkeley Laboratory

Low-Energy X-Ray Physics Laboratory
Center for X-Ray Optics
Lawrence Berkeley Laboratory



A Administrative; drafting, word processing, manuscript preparation, project library, catalogs, reprints.

B. Office--BLH

C PDP 1123 computer experimental data handling, plotting, library of data files, programs, conference.

D Electronics construction and maintenance, optical and electronic measurement instruments; supplies.

E. Construction of molecular multilayers for low-energy x-ray analyzers, thin film, high resolution photoresists.

B

---

1. Flat crystal scanning spectroscopy; multilayer characterization, absolute crystal reflectivity measurements; molecular and solid state spectroscopy.

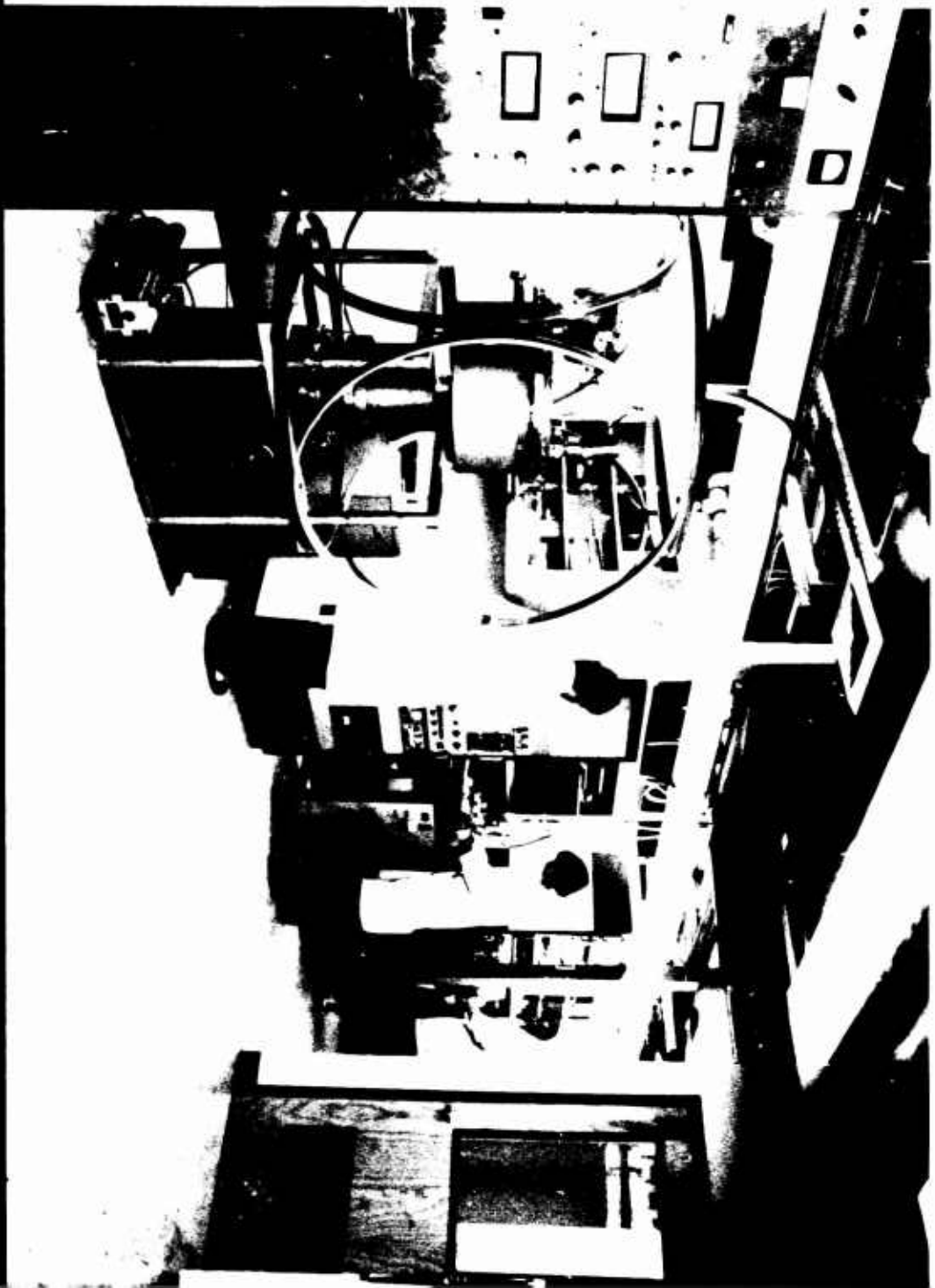
2. Fixed analyzer spectroscopy; absolute calibration of elliptical analyzers, mirror monochromators.

3. Curved crystal scanning, high sensitivity spectroscopy; evaluation of position sensitive detectors; "fast" spectroscopy for time-resolved measurements, radiation damage studies.

4. High sensitivity electron spectrograph (20", precision hemispherical analyzer); XPS, secondary electron energy distributions from x-ray photocathodes.

5. Absolute calibrated x-ray source facility (filtered fluorescent sources, photon-counting proportional counter monitor); photocathode quantum yield measurements; photoelectric detector and photographic film calibration.

6. Vacuum evaporation and sputtering, fabrication of thin films, x-ray mirrors, low/high density CsI photocathodes, etc.





APPENDIX 2 - REPORTS AND TECHNICAL NOTES DESCRIBING THE CURRENT WORK OF THIS PROGRAM

1. "Design and Characterization for Absolute X-Ray Spectrometry in the 100-10 000 eV Region," X-Ray Optics and Microanalysis, University of Western Ontario Press (1986).

2. "A Two-Channel, Elliptical Analyzer Spectrograph for Absolute Time-Resolving/Time-Integrating Spectrometry of Pulsed X-Ray Sources in the 100-10,000 eV Region" (w/ P.A. Jaanimagi), Rev. Sci. Instrum. (Aug. 1985), 1537-52.

3. Technical Notes: "Filter-Mirror Primary Monochromators"

4. "Characterization of Multilayer X-Ray Analyzers - Models and Measurements" (w/ J.Y. Uejio, H.T. Yamada, and R.E. Tackaberry), LBL-211003, Opt. Engin., Vol. 25, No. 8 (Aug. 1986), 937-947.

5. Technical Notes: "Low Energy X-Ray Multilayer Analyzers: Molecular and Sputtered/Evaporated"

6. Technical Notes: "High Energy X-Ray Response of Some Useful Crystal Analyzers"

7. Technical Notes: "The Characterization of Transmission Diffraction Gratings"

8. "Low-Energy X-Ray Response of Photographic Films: Part I. Mathematical Models" (w/ S.L. Kwok, J.Y. Uejio, H.T. Yamada and G.C. Young), J. Opt. Soc. Am. (Dec. 1984), 1-29.

9. "Low-Energy X-Ray Response of Photographic Films: Part II. Experimental Characterization" (w/ F.G. Fujiwara, M.A. Tester, C.H. Dittmore and M.A. Palmer), J. Opt. Soc. Am. (Dec. 1984), 1-29.

10. "High Energy X-Ray Response of Photographic Films. Models and Measurements" (w/ J.Y. Uejio, G.F. Stone, C.H. Dittmore, F.G. Fujiwara), LBL-21564, J. Opt. Soc. Am. (Aug. 1986), 818-827.

11. Technical Notes: "The Characterization of X-Ray Photocathodes"

12. Technical Notes: "Low-Energy Fluorescent X-Ray Spectroscopy for Materials Analysis"

13. "Temporal Dependence of the Mass-Ablation Rate in UV-Laser-Irradiated Spherical Targets," P.A. Jaanimagi (w/ J Delettrez, B.L. Henke, and M.C. Richardson), LBL-20787, Phys. Rev. A, Vol. 34, No. 2 (Aug. 1986), 1322-1327.

14. Technical Notes: "A Semi-Empirical Description of the Low-Energy X-Ray Interactions with Condensed Matter - Photoabsorption, Scattering, Specular and Bragg Reflection"

89 8 15 225

LBL-

1. DESIGN AND CHARACTERIZATION FOR ABSOLUTE X-RAY SPECTROMETRY IN THE 100-10 000 eV REGION

X-Ray Optics and Microanalysis
University of Western Ontario Press
(1987)

Burton L. Henke
Center for X-Ray Optics
University of California
Lawrence Berkeley Laboratory
1 Cyclotron Road
Berkeley, California 94720

ABSTRACT

Reviewed here are the design and characterization procedures used in our program for developing absolute x-ray spectrometry in the 100-10 000 eV region. Described are the selection and experimental calibration of the x-ray filters, mirror monochromators, crystal/multilayer analyzers, and the photographic (time integrating) and photoelectric (time resolving) position-sensitive detectors. Analytical response functions have been derived that characterize the energy dependence of the mirror and crystal/multilayer reflectivities and of the photographic film and photocathode sensitivities. These response functions permit rapid, small-computer reduction of the experimental spectra to absolute spectra (measured in photons per stearadian from the source for radiative transitions at indicated photon energies). Our x-ray spectrographic systems are being applied to the diagnostics of pulsed, high temperature plasma sources in laser fusion and x-ray laser research

I. INTRODUCTION

There is a considerable present need for the development of efficient absolute x-ray spectrometry for the characterization and application of the new high-intensity synchrotron and high-temperature plasma radiation sources. An example of a spectrographic system recently developed in this laboratory for time-integrated and time-resolved absolute spectrometry in the 100-10 000 eV region[1] is described in Fig. 1. Here the x radiation from a small source is line-imaged at a scatter aperture by reflection from an elliptically curved crystal/multilayer analyzer and then proceeds to form a normally incident spectrum along a detection

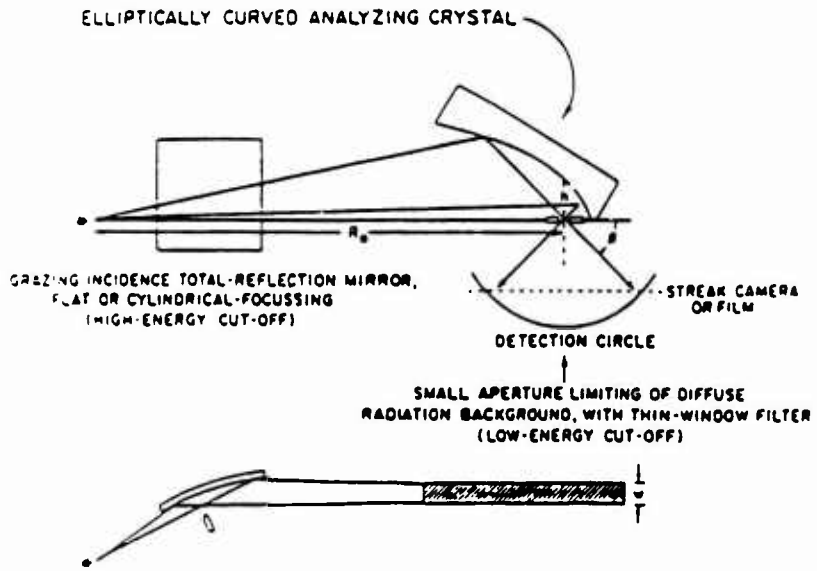


Fig. 1 The optical geometry of the elliptical analyzer x-ray spectrograph

circle. The Bragg angle range of the spectrum presented by the elliptical analyzer is about 20-70°. The usually intense high and low energy x-ray background radiation from the synchrotron and plasma sources is effectively reduced by the band-pass characteristic of a primary monochromator combination of a mirror and filter. To obtain the required time-integrated and time-resolved absolute spectrometry, twin

channels are employed using both position-sensitive photographic film and streak camera detection (illustrated in Fig. 2). This instrument is now being applied in laser fusion and x-ray laser research using the

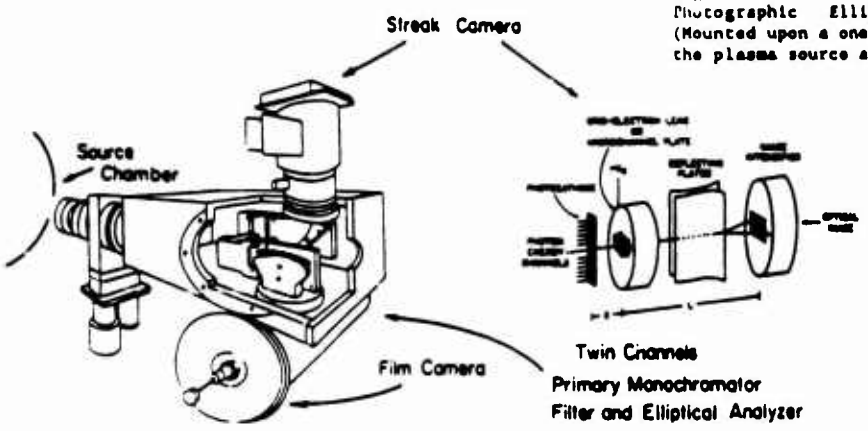


Fig 2. The two-channel, SPEAXS system - Streak and Photographic Elliptical Analyzer X-Ray Spectrograph (Mounted upon a one-meter target chamber with 120 cm between the plasma source and the scatter aperture.)

laser-produced plasma source of the OMEGA facility at the University of Rochester (utilizing 24 focussed UV laser beams of about 2000 joules total energy of 3510 A light within a 600 picosecond Gaussian pulse). Presented in Figs. 3 and 4 are examples of photographic and streak camera spectra obtained with this spectrograph on OMEGA.[2]

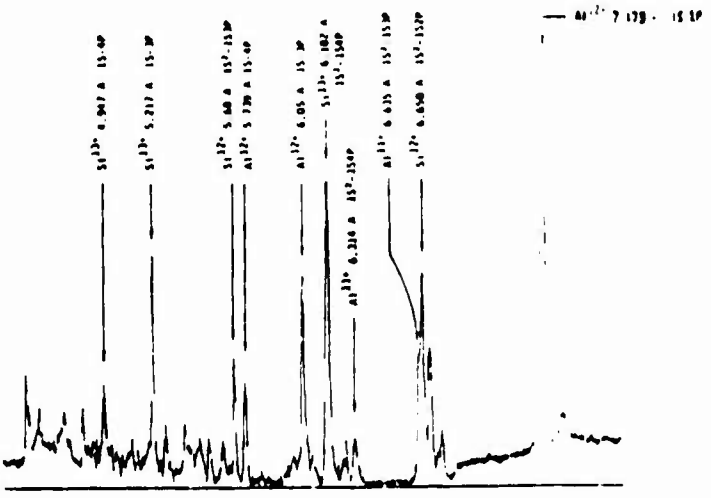


Fig. 3. Example of a photographically recorded spectrum with the SPEAXS system using the PET elliptical analyzer. Measured transitions are for the ionized species, Al^{11+}, Al^{12+}, Si^{12+} and Si^{13+} from a 200-μm-diameter glass microballoon coated with 1 μm of Al and excited by a 600-ps/200-J pulse of 351-nm light of the OMEGA facility. Exposure on RAR-2495 film.

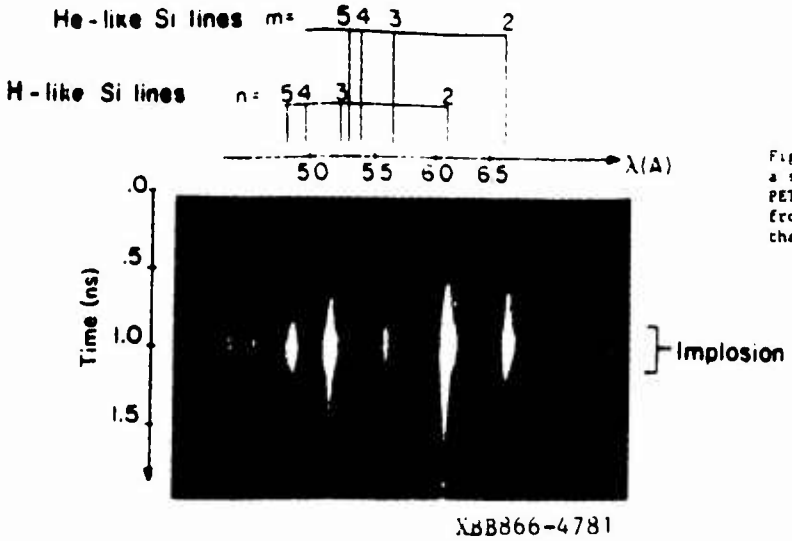


Fig 4 A photograph of the x-ray streak camera output for a spectrum presented to a CsI transmission photocathode by a PET elliptical analyzer. The spectrum was laser produced from a bare glass microballoon under excitation similar to that described in Fig. 3.

Illustrated in Fig. 5 is the relationship between a spectral line distribution of photons as measured at the detection circle and the absolute intensity, i_0, of the source. It may be readily derived[3] that i_0 is given by:

$$i_0 = N(L/FMR(d\chi/d\theta)) \qquad (1)$$

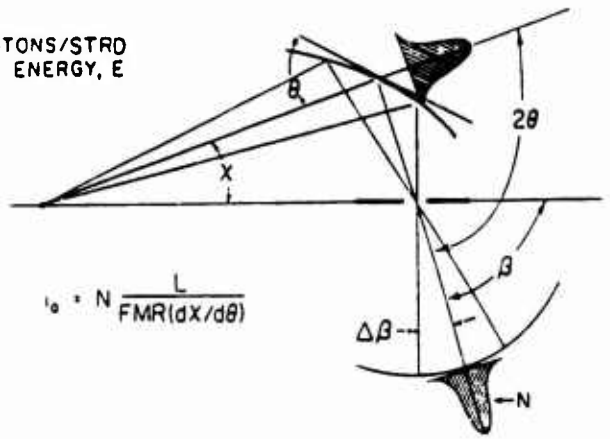


Fig 5. Relating the absolute source intensity, i_0 (photons/strd) to the total number of photons, N, within the measured diffraction profile at the detection circle. F is the filter transmission, M, the mirror reflectivity, R, the crystal/multilayer integrated reflectivity, and $(d\chi/d\theta)$ is the differential relation for the source emission angle and the Bragg reflection angle

where:

i_0 = photons/stearadian emitted at the source for a given radiati e transition and at the measured photon energy of the spectral line;

N = the total number of photons measured within the spectral line distribution per unit length of the spectral line (in the direction normal to the plane of Fig. 5).

L = the constant total geometric length of any reflected ray from the source to the detection circle (this invariance is a characteristic of the elliptical focussing geometry);

F = filter transmission;

M = mirror reflectivity;

R = the integrated reflectivity characteristic of the crystal/ multilayer reflection measured in $\Delta\theta$ Bragg angle units; and

$d\chi/d\theta$ = the ratio of the differential angular width, $d\chi$, of the radiation from the source to the associated differential angular width, $d\theta$, of the radiation that is Bragg reflected from the analyzer.

Note: The response function (1) applies generally for any cylindrical analyzer geometry, since $d\chi/d\theta$ can be given as an analytical expression characteristic of the particular cylindrical analyzer geometry that is generating the diffraction line profile, whether it be convex, concave (e.g. elliptical, as here) or flat.[3]

Efficient absolute x-ray spectrometry is achieved by applying the response relationships[1,3] to the measured spectrum (e.g. via a small computer associated with the spectrographic system) to immediately yield the absolute intensity spectrum of the source. The individual response functions for the primary mirror-filter monochromator, the crystal/ multilayer analyzer and for the position-sensitive detectors may be derived by fitting analytical energy-dependent model relations to calibrations measured at a few photon energies that are representative of the range of measurement.

In this paper we review our procedures for establishing the required absolute response functions and present typical results for applied x-ray spectroscopy in the 100-10,000 eV region. In the Bibliography are listed the recent reports of this laboratory (including those in preparation) which describe in detail these characterization procedures and which establish the co-authorship of students and research associates for each particular research effort.

II. SPECTROGRAPHIC RESPONSE CHARACTERIZATION

A. Crystals/Multilayers

For our crystal/multilayer characterizations we obtain absolute experimental spectra at several photon energies which include the small angle "total-reflection" region, the first order diffraction line and any higher orders that may be allowed. The measurement geometry is shown in Fig.6. A narrow beam of incident radiation of intensity, $I_0\cos\theta$, defined by a fine slit at a demountable x-ray tube window and by a razor blade placed near the analyzer, is reflected by the crystal/multilayer to a gas-flow proportional counter, where monochromatic characteristic line x radiation from the source is isolated by an appropriate filter and by pulse-height discrimination

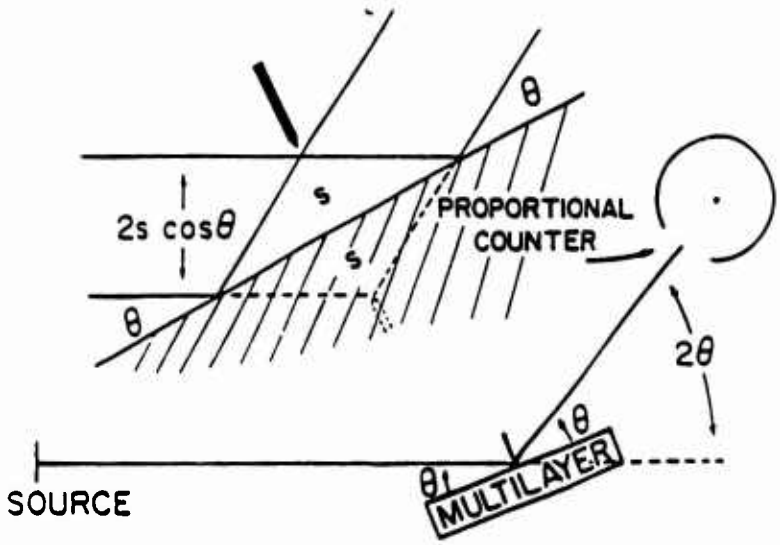


Fig. 6. Geometry for the measurement of crystal/multilayer reflectivity. The narrow incident x-ray beam intensity is $I_0 \cos\theta$ for reflection through the slit, while $I_0/2$ is the direct beam intensity that is measured at $\theta = 0$.

with the counter. (Any significant contamination background radiation will also appear in the measured spectrum and thereby the zero-angle incident beam can be corrected to yield the appropriate characteristic line intensity, $I_0/2$.)[4] The spectrum is step-scanned and appears first on a multichannel analyzer which permits reading out the critical angle for total reflection, θ_c, the integrated reflectivity, R, the

experimental FWHM, ω, and peak efficiency, P (defined in Fig. 7). As discussed in Ref. 4, the measured onset of the total reflection region signals an accurate goniometer zero-angle setting and the corresponding value of $I_0/2$. The critical angle for "total reflection," θ_c, can be used to yield an estimation of the analyzer's surface structure and refractive properties (optical constant, δ).

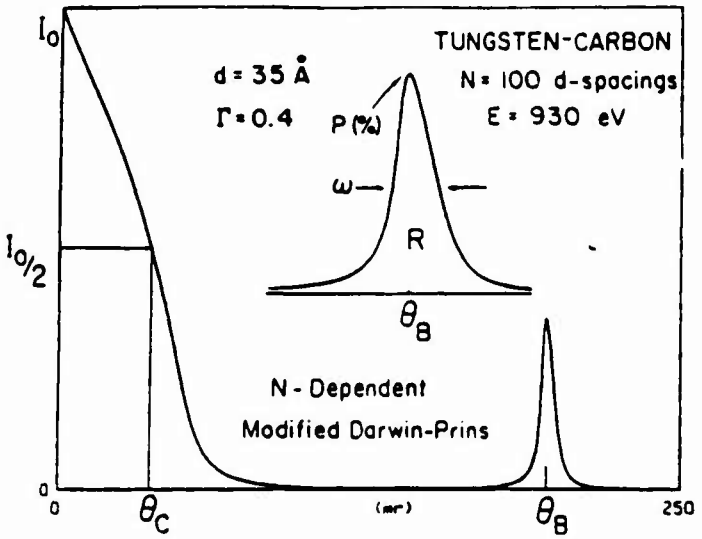


Fig. 7. Small-angle reflection and first order Bragg diffraction for a 100 layer tungsten-carbon multilayer. Tungsten thickness is 0.4 d (assumed sharp interfaces). Definition of the four experimental variables used to characterize the crystal/multilayer--the critical angle, θ_c, of reflection at $I_0/2$, the peak and integrated reflectivities, P and R, and the FWHM, ω.

We have recently developed a modification of the dynamical Darwin-Prins crystal reflectivity relation to extend its application for the low-energy x-ray region and for reflection by multilayer systems of a finite number of layers, N. Our analytical, modified Darwin-Prins model relation (MDP) can accurately predict the small-angle total reflection characteristic and all diffraction orders present for a given photon energy, and can allow the spectrum to be rapidly presented on a small computer screen and plotter (e.g. with the IBM PC equipped with a FORTRAN compiler). The derivation of this MDP analytical model is described in Refs. 4 and 5 and the resulting reflectivity equations are presented below.

As described in Fig. 8, the small fraction of the incident amplitude that is absorbed and reflected by a single layer of unit cells of the crystal, σ and s respectively, can be expressed in terms of the complex total scattering factor per unit cell, $F_0(= F_{01} + iF_{02})$, and the structure factor of the unit cell, $F(= F_1 + iF_2)$. F_0 is equal to F at its forward-angle scattering limit (setting $\theta = 0$ in F). In the

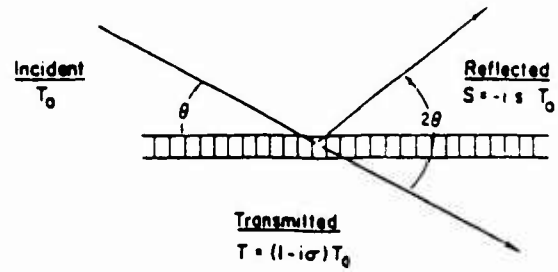


Fig. 6 In the Darwin-Prins dynamical model for crystal reflection, the reflection ratio for the semi-infinite crystal, S_0/T_0, is determined by a summing of all possible multiply reflected and transmitted components at periodically spaced elementary layers of unit cells. Defined here are the small fractional amplitudes that are absorbed and reflected by a plane of unit cells, σ and s respectively, which are related to the structure factor, F, and scattering factor F_0 per unit cell. F_0 is given by the forward-scattering value of F.

For m Unit Cells/Unit Area of Structure Factor, $F_1 + iF_2$, and of Total Scattering Factor, $F_{01} + iF_{02}$, Per Unit Cell

$$\sigma = -mr_0\lambda \frac{F_{01} + iF_{02}}{\sin\theta} \quad \text{and} \quad s = -mr_0\lambda \frac{F_1 + iF_2}{\sin\theta} P(2\theta)$$

$P(2\theta) = 1$ or $\cos 2\theta$ for the Two Polarized Components

Darwin-Prins reflectivity model for an ideal, semi-infinite crystal (with reflecting planes parallel to the surface) the ratio of the total amplitude that is dynamically reflected, S_0, to that incident, T_0, is given by the expression:

$$S_0/T_0 = \frac{-y}{(1-z) \pm \sqrt{(1-z)^2 - y^2}} \qquad (2)$$

where

$$y = \frac{FP(2\theta)}{F_0} \qquad (3)$$

and $$z = \frac{2\pi V}{r_0\lambda^2} \frac{\sin\theta\,[\sin\theta - (m\lambda/2d)]}{F_0} \qquad (4)$$

Here r_0 is the classical electron radius, λ the x-ray wavelength, d the unit cell thickness and crystal reflecting plane spacing, and V the unit cell volume. If the incident radiation is polarized (e.g. synchrotron

radiation) the appropriate value of S_0/T_0 is obtained by setting the polarization factor, $P(2\theta)$, equal to unity or cos 2θ (σ or π component) and the corresponding intensity ratio for this polarized component, I/I_0, is obtained by multiplying S_0/T_0 given by (2) by its complex conjugate. (Note: The choice of plus or minus sign in this expression is that which yields a value for I/I_0 that is less than unity.) For unpolarized incident x-radiation, the reflected intensity ratio is given by one-half of the sum of the two polarized components (with $P(2\theta)$ equal to unity and cos 2θ respectively).

In the definition of the parameter z, $m\lambda/2d$ equals sin θ_0, where θ_0 identifies an angular region for which S_0/T_0 has a significant value (i.e. for the small angle total reflection region $m = 0$, and for the first, second and third order diffractions, $m = 1,2,3\ldots$, as given by the Bragg equation). In our computer program, this order parameter m, is automatically taken as the integer that is nearest the value of $2d \sin\theta/\lambda$, thereby permitting a continuous plotting of the spectrum throughout the entire range of reflection angles, θ.

In our modified Darwin-Prins model we multiply the expression for S_0/T_0 in (2) for the semi-infinite crystal by a factor which then yields the amplitude, S_{0N}/T_0, reflected from a multilayer of a finite number of layers, N, given by:

$$S_{0N}/T = (S_0/T_0)\,\frac{1-x^{2N}}{1-(S_0/T_0)^2 x^{2N}} \qquad (5)$$

where

$$x = (-1)^m \exp(-\eta) \qquad (6)$$

and $$\eta = \pm \frac{r_0 \lambda d F_0}{V \sin\theta}\sqrt{y^2-(1-z)^2} \qquad (7)$$

(The plus or minus sign in η is chosen so that its real component is positive.)

It is important to note that in order to obtain this relatively simple analytical description for x-ray reflectivity, it was necessary to assume that the fractional amplitude that is absorbed within a unit cell layer, σ, is small as compared with unity. It can be easily shown[5] that this condition is fulfilled when d is sufficiently small that the angle for the first order reflection, θ_1, is greater than about three times the critical angle for total reflection from the analyzer, θ_c. ($\sigma = (\pi/2)(\theta_c/\sin\theta_1)^2$) This is usually not a serious limitation because for nearly all practical applications in spectroscopic analysis, $\theta_1 >> \theta_c$.

A more rigorous solution for the reflectivity of a multilayer consisting of N layer pairs of a heavy and light element (e.g. a sputtered tungsten-carbon multilayer) may be obtained by consecutively applying the E&M Fresnel reflection equation at each of the 2N interfaces, using as the material constants the refractive indices, $n(= 1 - \delta - i\beta)$ descriptive of each elementary layer, where:

$$\delta = \frac{r_o \lambda^2}{2\pi} n f_1 \qquad (8)$$

$$\beta = \frac{r_o \lambda^2}{2\pi} n f_2 \qquad (9)$$

Here n is the no. density and f_1 and f_2 are the atomic scattering factor components for the element (or compound) comprising each sub-layer. In Fig. 9 we have plotted the total reflection region and the first three orders of reflection for a tungsten-carbon multilayer (N = 30, 2d = 70 A and with the tungsten layer of 0.4 d thickness) comparing the optical E&M model[5] (OEM) (dashed line) and our modified Darwin-Prins model (MDP). As may be noted, the results are essentially identical.

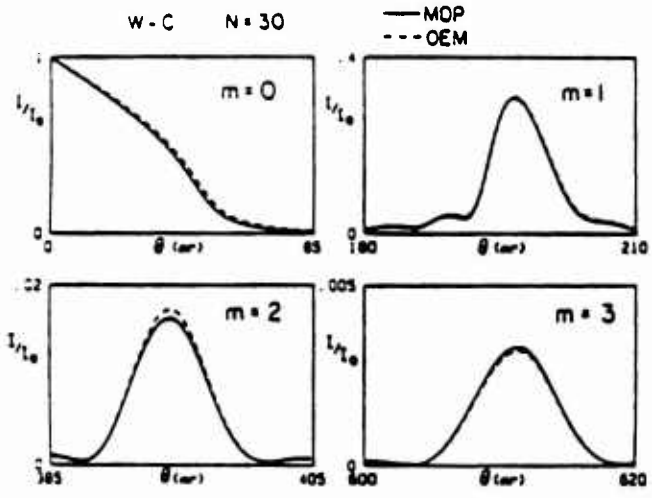


Fig. 9 Comparing the optical E&M (dashed line) and the MDP calculated spectra for a tungsten-carbon multilayer with 30 layers of the same photon energy as in Fig. 7

It was noted above that in order to calculate the crystal/multilayer reflectivity characteristics using the MDP model, we only need to specify the unit cell volume, V, and its complex structure factor, $F (= F_1 + iF_2)$. The total scattering factor per unit cell, $F_0(= F_{01} + iF_{02})$ is set equal to F with $\theta = 0$. For the crystallographic case in which the unit cell is comprised of a collection of n_p atoms of

type P, of atomic scattering factor f_p ($= f_{p1} + if_{p2}$), and located at position z_p from a plane of symmetry of the unit cell (z_p is perpendicular to the reflecting planes), the structure factor components are given by the relations:

$$F_1 = \sum_p x_p f_{p1} \cos\left(\frac{4\pi z_p \sin\theta'}{\lambda'}\right) \qquad (10)$$

$$F_2 = \sum_p x_p f_{p2} \cos\left(\frac{4\pi z_p \sin\theta'}{\lambda'}\right) \qquad (11)$$

In the case of a continuous high density distribution of two elements (or compounds) for the sputtered/evaporated multilayers, the structure factors are given as noted in Fig. 10 by:

$$F_1 = \frac{V}{d} \int_{-d/2}^{d/2} (nf_1 + n'f_1') \cos\left(\frac{4\pi z}{\lambda'} \sin\theta'\right) dz \qquad (12)$$

$$F_2 = \frac{V}{d} \int_{-d/2}^{d/2} (nf_2 + n'f_2') \cos\left(\frac{4\pi z}{\lambda'} \sin\theta'\right) dz \qquad (13)$$

Here n and n' are the no. densities of the two elements at position z within the assumed symmetric unit cell and m is the number of unit cells per unit area and is equal to (d/V), where V is the volume of the unit cell.

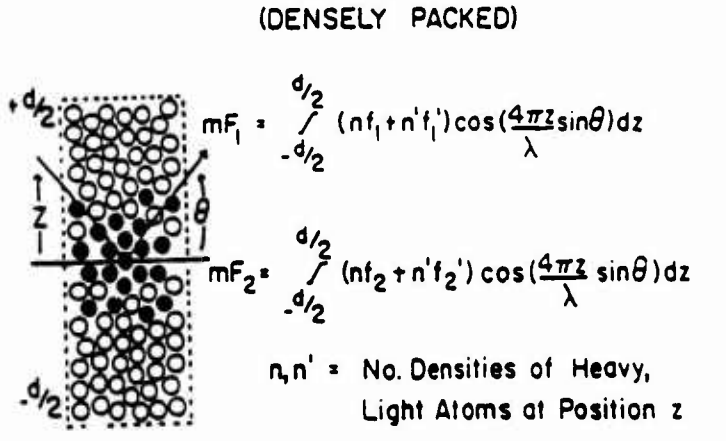


Fig. 10. Defining the structure factor components for the unit cell of a sputtered/evaporated multilayer. Model density distributions that are considered include sharp interface, a compound transition layer, a linearly varying density of each element through a transition layer and interface roughness.

Our MDP model predicts a refraction modified angle, θ', and wavelength, λ' within the crystal/multilayer, consistent with Snell's Law, and correspondingly it predicts a shift in the diffraction peak position from that angle given by the Bragg relation, $m\lambda = 2d \sin \theta_0$ by an amount given by $\delta/(\sin \theta_0 \cos \theta_0)$. The refractive index decrement, $\delta = r_0\lambda^2 F_{01}/2\pi V$ is explicitly independent of the structure factor, F, while the intensity of the diffracted line is strongly dependent upon the structure factor, $F_1 + iF_2$, as defined in (10) through (13) in terms of the angle, θ', and wavelength, λ', presented to each unit cell within the crystal/multilayer. It can be readily shown that the $\sin \theta'/\lambda'$ quantity in the structure factor relations can be expressed in the desired θ and λ variables by the relation:

$$\sin \theta'/\lambda' \approx (\sin\theta/\lambda)\sqrt{1 - \frac{2\delta}{\sin^2\theta}} \qquad (14)$$

(Note: This correction only applies for the calculation of the large angle Bragg diffractions for $m \geq 1$ and not for the "total reflection" region ($m = 0$).)

In Fig. 11 and in Table 1 we present a series of calculated integrated reflectivity curves, R vs E(eV), over the energy range 100-10 000 eV for those crystal/multilayer systems that are amenable to bending to the elliptical curvatures required for the spectrograph

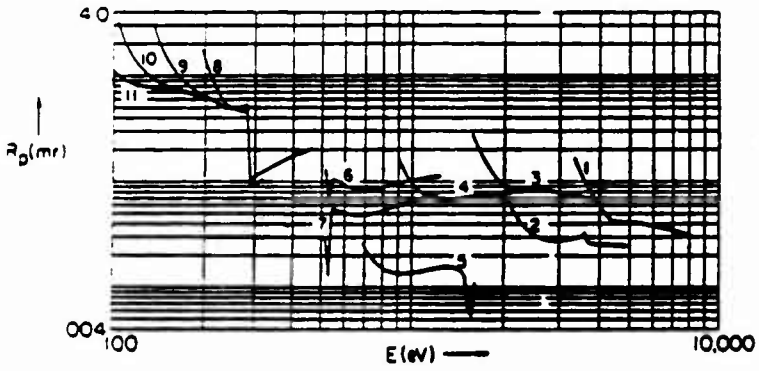


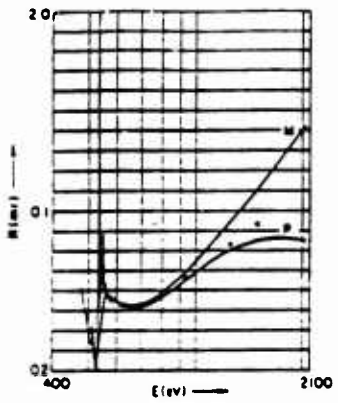
Fig. 11. Integrated reflectivity, R(mrad), vs photon energy, E(eV), for eleven crystal/multilayers that may be applied to cover the 100-10 000 eV region as elliptical analyzers and as listed in Table 1. The R plots have been calculated using the MDP model.

Table 1. Crystal/multilayers having integrated reflectivities as plotted in Fig. 11

No	Crystal name	Indices (hkl)	2D	Diffraction order	E (eV) limits 22.5°-(θ) – 67.5°	R (45°)* (mrad)
1	LiF	(200)	4.03	1	8046—3333	0.0433
2	Mica	(002)	19.84	3	4900—2029	0.0286
3	PET	(002)	8.74	1	3707—1535	0.0907
4	Gypsum	(020)	15.19	1	2134— 884	0.0711
5	Mica	(002)	19.84	1	1633— 676	0.0136
6	RAP	$(10\bar{1}0)$	26.12	1	1240— 514	0.0848
7	KAP	$(10\bar{1}0)$	26.63	1	1217— 504	0.0488
8	Laurate*		70.00	1	463— 192	0.4878
9	Stearate		100.00	1	324— 134	0.8262
10	Lignocerate		130.00	1	249— 103	0.9373
11	Melnsate		160.00	1	203— 84	0.8974

* Molecular multilayers of lead salts of straight-chain fatty acids.
* For Bragg angle, θ, equal to 45°

described in the Introduction. In Fig. 12 we compare the calculated and the experimental integrated reflectivity values for the potassium acid phthallate analyzer (KAP) using both the Darwin-Prins and the mosaic models.[5] Illustrated here is a measured sharp reflectivity "spike" at the oxygen-K absorption edge resulting from a condensed-matter molecular orbital resonance: a reminder that the atomic scattering description used here can apply only outside the absorption edge threshold regions where scattering may be considered "atomic-like" and unaffected by the chemical or solid state.



THEORETICAL
M··MOSAIC P··DARWIN-PRINS

EXPERIMENTAL
—— BLAKE, et al (1979)
• HENKE, et al (1980)

Fig. 12. The integrated reflectivity curves for the potassium acid phthalate (KAP) crystal calculated using the MDP and the Mosaic crystal models and compared with experimental measurement. These models, using the atomic scattering factors, cannot be applied near absorption thresholds where chemical and/or solid state effects may occur--e.g. the sharp, reflectivity "spike" appearing here near the Oxygen-K edge at 530 eV.

Finally, in Figs. 13 and 14, we present a comparison of the experimental and MDP model characterizations of two synthesized large d-spacing multilayers, a Langmuir-Blodgett lead stearate and a sputtered tungsten-carbon.[4] For our modeling of the W-C analyzer we assumed a linearly varying density in the tungsten-carbon transition layer (or equivalently, an interface roughness layer[5]).

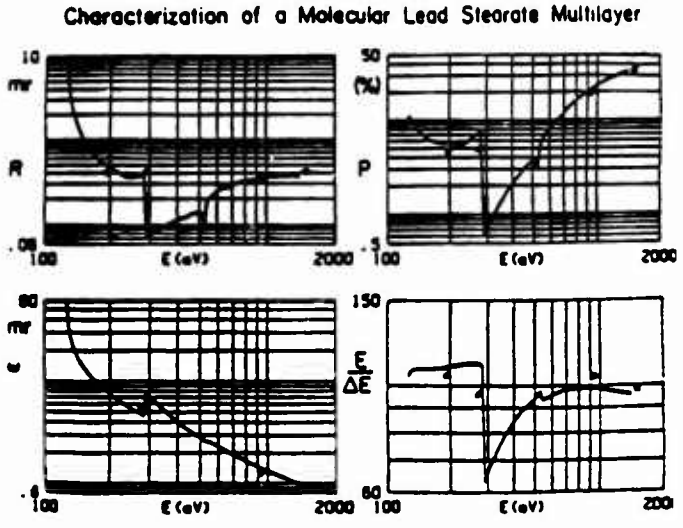


Fig. 13. The Langmuir-Blodgett Lead Stearate Multilayer - 2d = 99 A, N = 100. Comparison of the MDP model curves with experimental values for integrated reflectivity, R, peak efficiency, P, FWHM, ω, and resolving power, E/ΔE.

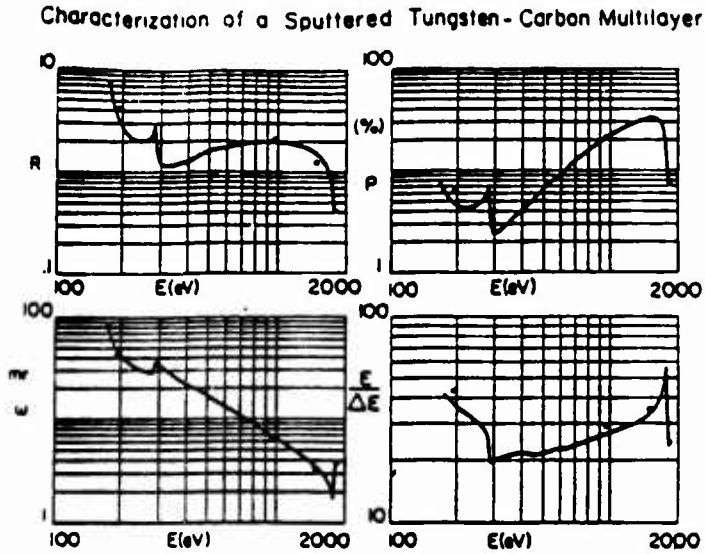


Fig. 14. The sputtered Tungsten-Carbon Multilayer. 2d = 75 A, N = 120. Model fit for 25 A tungsten and 17 A tungsten-carbon interface with an assumed linear variation of densities in the interface region. Comparison of MDP model curves with experimental values for integrated reflectivity, R, peak efficiency, P, FWHM, ω, and resolving power, E/ΔE.

Fig. 15 illustrates the complementary aspect of the sputtered/evaporated and the molecular Langmuir Blodgett analyzers. For the same d-spacing and for appropriate composition these analyzers have similar peak reflectivities, but the high-density sputtered/evaporated multilayer has the higher integrated reflectivity and correspondingly, lower resolving power.

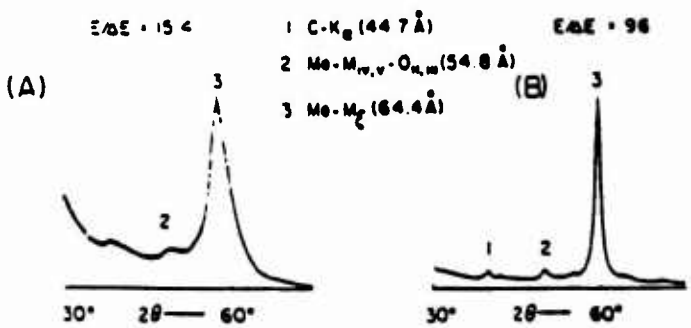


Fig. 15 Comparing spectra measured with the flat analyzers, (A) sputtered tungsten-carbon of 2d = 132 A and (B) Langmuir-Blodgett, lead lignocerate of 2d = 129 A. As suggested here by optimized measurements with sputtered and molecular multilayers of about the same 2d values, peak reflectivities are similar but the high density sputtered multilayers have appreciably higher integrated reflectivities and correspondingly lower resolving powers.

B. Mirrors and Filters

For optimized absolute x-ray spectrometry it is important to suppress the low and high energy background which may be particularly intense in the new large synchrotron and plasma sources. This "extra" radiation can thermally distort the analyzer and can appear in the measured spectrum as high-order diffracted or diffuse scattered background. As noted earlier, a primary monochromator combining the high-energy cut-off characteristic of a small-angle reflection and the low-energy cut-off characteristic of an absorption edge filter can provide an effective suppression of this "extra" radiation. The band-pass characteristic of a practical mirror-filter monochromator is presented in Fig. 16 for a 30 mrad reflection from an aluminized mirror and for transmission through a 300 $\mu g/cm^2$ copper foil.

The filter transmission, F, is readily calculated using the energy dependent mass absorption coefficient, μ, and the mass per unit area thickness, m, of the filter material, with the usual relation:

$$F = \exp(-\mu m) \qquad (15)$$

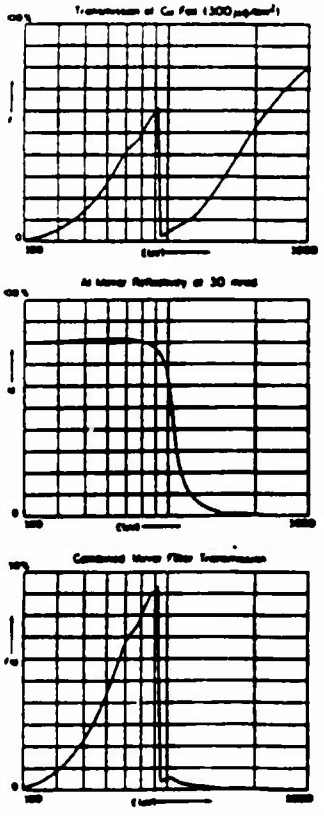


Fig. 16. The band-pass characteristic of the mirror-filter combination of a 30 mrad reflection from Aluminum and transmission through a 300 $\mu m/cm^2$ Copper foil.

It can be shown[5] that the Darwin-Prins relation for the semi-infinite crystal can accurately represent the Fresnel small-angle reflection characteristic, M, by setting the order parameter, m, in the variable, z, equal to zero. For the homogeneous mirror, the unit cell is simply described by a uniform distribution of a single element (or compound). Alternatively, the two intensity polarization components can be expressed by the following Fresnel relations for the relative intensities[7]:

For the incident E-vector perpendicular to the reflection plane,

$$I_s(\theta) = \frac{4\rho^2(\sin\theta - \rho)^2 + \gamma^2}{4\rho^2(\sin\theta + \rho)^2 + \gamma^2}. \qquad (16)$$

and for the polarization ratio,

$$\frac{I_s(\theta)}{I_s(\theta)} = \frac{4\rho^2(\rho - \cos\theta\cot\theta)^2 + \gamma^2}{4\rho^2(\rho + \cos\theta\cot\theta) + \gamma^2}. \qquad (17)$$

where the parameter, ρ, is given by:

$$\rho = (1/2)\{\sin^2\theta - \alpha + [(\sin^2\theta - \alpha)^2 + \gamma^2]^{1/2}\}. \qquad (18)$$

and $\alpha = 2\delta$ and $\gamma = 2\beta$
The optical constants, δ and β, are given in terms of the total scattering factor per unit volume, nF, by (8) and (9). (Again, these model calculations, using the atomic scattering factors, can be accurately applied only for photon energies outside the absorption threshold regions.)

Presented in Fig. 17 are comparisons of the Fresnel model prediction and the experimental measurement of the mirror reflectivity, M, for high quality surfaces of beryllium, aluminum and fused quartz[8] measured by the procedure outlined above (see Fig. 6).

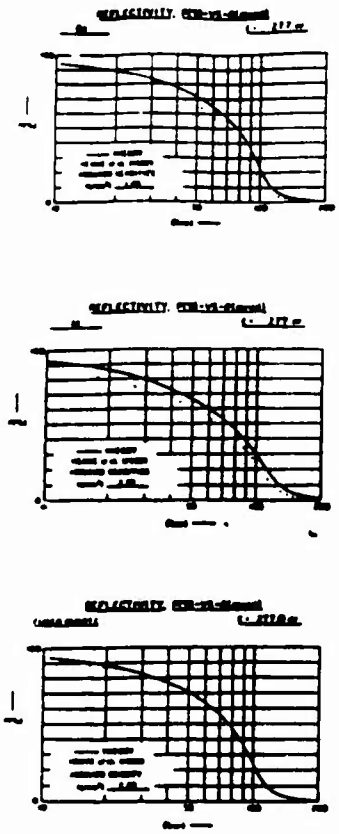


Fig. 17 Comparing Fresnel small-angle reflection curves with experimental measurement from high quality mirror surfaces of Beryllium, Aluminum and Fused Quartz.

C. Photographic Films

Described in Fig. 18 is our method for measuring the optical density, D, vs absolute exposure, I, response of a photographic film. A characteristic line spectrum from a filtered x-ray source is scanned along the detection circle of an elliptical analyzer by a proportional counter to yield the absolute peak intensity for each line in photons per μm^2-sec. Then a photographic camera is introduced with its 35 mm film transported along the same detection circle, and a series of exposures are taken at known exposure times. The film is processed by a controlled, standard procedure and microdensitometered spectra are obtained, as shown in Fig. 18. The slits on the proportional counter and on the microdensitometer are matched, and have widths that are small compared to the instrument-broadened diffraction lines. Plots of density, D, vs Exposure, I(photons/μm^2) for corresponding peaks yield the D-I calibration curves shown in Fig. 19 for recently collected data on the high energy x-ray films, Kodak SB-392 (single emulsion) and DEF (double emulsion). This procedure is operationally identical, but the reverse of that which is used to determine an absolute exposure from a measured density.

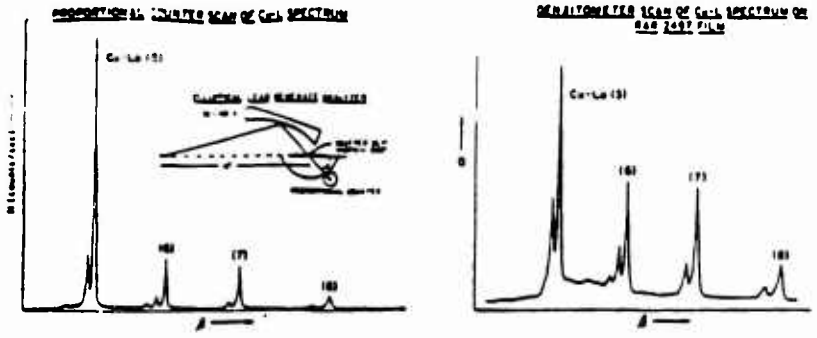


Fig. 18. Illustrating the method for photographic film calibration. An elliptical analyzer is used to place spectra of the desired photon energies along a detection circle. The absolute intensity spectrum is determined with a gas flow proportional counter with pulse height discrimination and a series of photographic exposures are then made. The photographic spectra are microdensitometered with a slit which matches that of the proportional counter and of width that is small as compared with that of the instrument-broadened diffraction lines. At corresponding line peaks, specular density values, D, are compared with absolute exposure values I(photons/μm^2) to yield the D-I calibration curves. This calibration procedure is operationally similar to that used (in reverse) for the determination of absolute exposures from microdensitometered spectra.

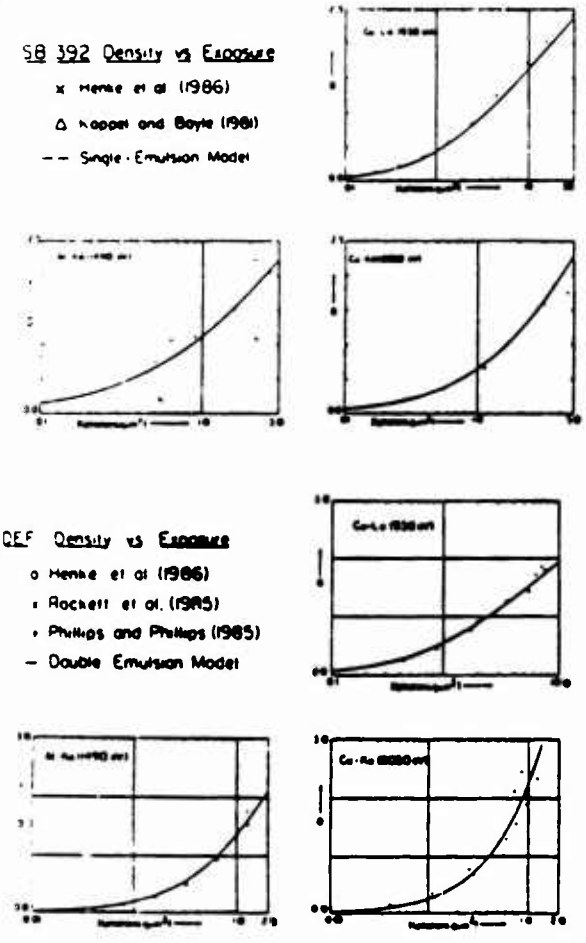


Fig. 19. Examples of Specular Density, D vs Exposure, I(photons/μm^2) curves for Kodak's single emulsion SB-392 and double-emulsion DEF x-ray films. These experimental data are compared with the predictions of our energy-dependent model response equations (21) and (22).

The smooth curves shown in Fig. 19 which fit the experimental data are D-I curves obtained from our analytical photographic film response model relations. The model relations are functions of the exposure, I(photons/μm^2), photon energy, E(eV) and the angle of incidence, θ, and require only two fitting parameters, a and b.[9,10,11]

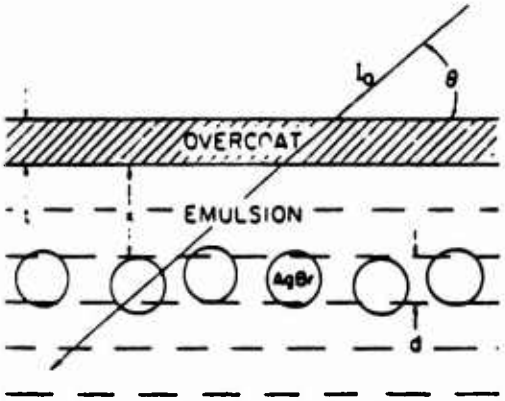
The general model description is shown in Fig. 20. The x radiation that reaches a layer of silver bromide grains at depth x (distributed within gelatin) is equal to that incident at angle θ, less the fraction absorbed by the protective supercoat and by the heterogeneous grain-gelatin emulsion above the layer. It follows that the probability for a photon absorption within a AgBr grain can be expressed as a function of the geometric grain cross section, σ, the grain diameter, d, the supercoat thickness, t, and the energy-dependent linear absorption coefficients, μ_1, μ_0 and μ', for AgBr, gelatin and the heterogeneous emulsion, respectively. It is further assumed for the 100-10 000 eV region of interest here that (1) the photon energies are sufficiently high that only one photon is required to render a grain developable and (2) that these energies are sufficiently low that the photoelectrons generated in the gelatin do not have sufficient range or energy to render additional unexposed grains developable. We list here the "universal" model relations that have been derived from such general model assumptions:[9,10,11]

For a monolayer of AgBr grains with no supercoat (designed for EUV and low energy x-rays as the Kodak 101):

$$D = a_1[1 - \exp(-b_1\beta_1 I)] \qquad (19)$$

For a thick emulsion (totally absorbing):

$$\propto D = a \ln(1 + b\beta I). \qquad (20)$$



PROBABILITY FOR ABSORPTION WITHIN AgBr GRAIN AT DEPTH, x

$$\sigma I\left[1 - \exp(-\mu_1 d)\right] \exp\left[\frac{-(\mu_0 t + \mu' x)}{\sin\theta}\right]$$

Fig. 20. The probability for a photon absorption within a AgBr grain of cross section, σ, at depth x within the emulsion and given here as a function of the grain diameter, d, the supercoat thickness, t, and the energy-dependent linear absorption coefficients, μ_0 of the supercoat, μ_1 of AgBr and μ' of the heterogeneous emulsion--for an exposure, I(photons per unit area) from direction, θ. Other model assumptions are (1) for the 100-10 000 eV photon energy region of interest here, only one photon absorption is required to render a grain developable and (2) the cross-section, σ, is independent of the photon energy.

For a thin partially absorbing emulsion of thickness T:

$$D = \alpha D = a \ln \frac{1 + b\beta I}{1 + b\beta I \exp(-\mu' T/\sin\theta)} . \qquad (21)$$

And, finally, for a double-emulsion film on a plastic base of thickness, t_b and linear absorption coefficient, μ_b:

$$\alpha D = a\ln\left(\left[\frac{1+b\beta I}{1+b\beta I\exp[(-\mu' T)/\sin\theta]}\right)\left(\frac{1+b\beta I\exp[(-\mu_b t_b-\mu' T)/\sin\theta]}{1+b\beta I\exp[(-\mu_b t_b-2\mu' T)/\sin\theta]}\right)\right] \qquad (22)$$

In these expressions the factors; β_1, α and β yield the dependence upon photon energy, E(eV) and the angle of incidence, θ, and are given in Refs. 9, 10 and 11.

Having determined the fitting parameters, a and b, by least squares fitting to D-I data at a few representative photon energies, the complete energy response may then be accurately predicted. These semi-empirical relations can then be used, for example, to derive the absolute film sensitivity curves as shown in Fig. 21. Here, sensitivity S is defined as the reciprocal of the exposure, I(photons/μm^2) which is required to produce a specular density, D, of 0.5.

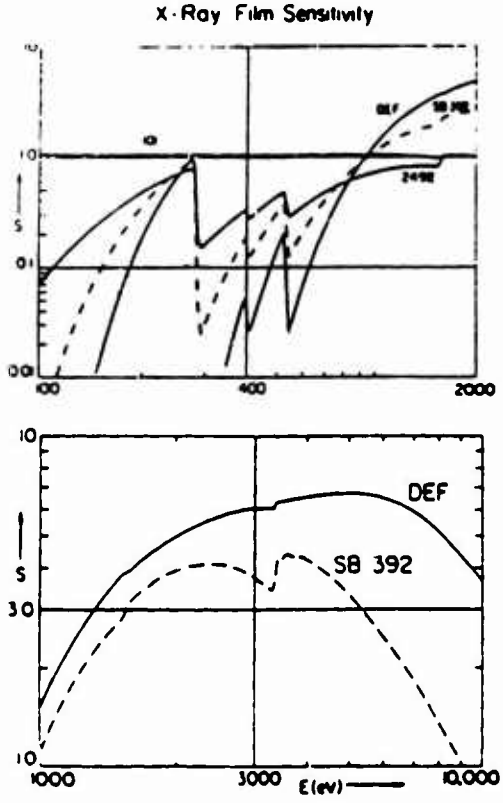


Fig. 21. Comparing the film sensitivities in the 100-10 000 eV region for the Kodak films. 101 (approximately a monolayer of AgBr grains without supercoat), the single emulsion films, RAR 2492 and SB 392 and the double emulsion film DEF. Here sensitivity, S, is defined as the reciprocal of the exposure, I(photons/μm^2) required to generate a specular density of 0.5.

D. Photocathodes

The position sensitive photoelectric detectors that are applied in x-ray spectroscopy include arrays of discrete x-ray diodes, x-ray streak cameras (as described above) and the multichannel plate amplifier detection systems, all of which utilize the basic photocathode element to convert the x-ray photon intensity to an electronic current by photoemission The energy distribution of the emitted electrons from either a front or back surface (transmission) photocathode is illustrated in Fig. 22. Typically most of the electrons are emitted as secondary electrons in the 0-10 eV region and only a few percent or less escape elastically through the photocathode surface as the original higher energy primary photoelectrons and Auger electrons. In the

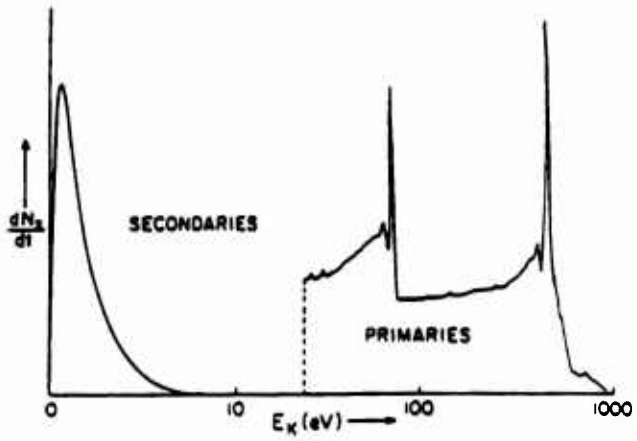
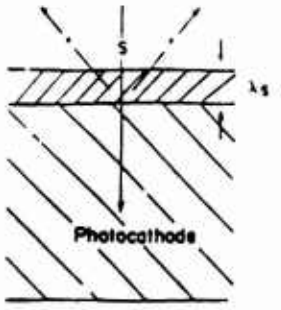


Fig. 22. Describing the electron energy distribution that is emitted from an x-ray photocathode. Only a small percentage of the electrons are emitted as elastically escaping high energy photoelectrons and Auger electrons. Most of the electron emission is within a secondary electron distribution in the 0-10 eV region and measured by the photocathode's characteristic quantum yield, Y (electrons/photon).

picosecond time-resolving detectors (e.g. the x-ray streak camera) the primaries are rejected and the higher energy secondaries arrive at the end of the streak camera sooner than the slower secondaries thereby setting a limit on the time resolution. For example, for the relatively sharp energy distribution width of about 1.5 eV characteristic of a CsI photocathode, and for the accelerating fields within the typical streak camera, an intrinsic time resolution of about two picoseconds may be expected. The total number of electrons within this secondary electron distribution is determined by the photocathode's quantum yield, Y, which is the number of electrons emitted per normally incident photon for the front surface photocathode. As suggested in Fig. 23 (for front surface operation), the photoemission yield for x-rays is characteristically low because most of the initial primary electrons and subsequently generated secondary electrons are deposited deeply within the photocathode, outside the escape depth region. The fraction of the incident intensity that is photoabsorbed within this escape depth is given by the linear



$Y_f \sim E\mu(E)\rho\lambda s$

E - photon energy

$\mu(E)\rho$ - linear x-ray absorption coef.

λ_s - secondary electron escape depth

Fig. 23. The energy dependent x-ray photocathode quantum yield, Y, is proportional to the fraction of the normally incident photons that are absorbed within the escape depth region (i.e. to the linear absorption coefficient, $\mu\rho$ times the escape depth, λ_s) and to the number of secondary electrons generated by a photon absorption (which is proportional to the photon energy, E, since the shape of the secondary electron energy distribution is independent of the photon energy).

absorption coefficient, $\mu\rho$ multiplied by the escape depth, λ_s. Because the shape of the secondary electron distribution is determined by the surface electronic state of the photocathode and does not depend upon the exciting photon's energy, E, it follows that the total number of emitted electrons should be proportional to E as well.[12] Therefore, in our modeling of the x-ray photocathode we establish the photon energy dependence of the quantum yield to be given by:

$$Y \sim E\mu(E)\rho\lambda_s \qquad (23)$$

In Ref. 12 we describe our method and instrumentation for the absolute measurement of photocathode quantum yields in the photon energy region of 100-10 000 eV. Examples of these measurements for the gold and cesium iodide photocathodes are presented here in Fig. 24. As can be seen by the superposition of $E\mu(E)$ curve on the plot of data, $E\mu(E)$ indeed follows the experimental photocathode energy dependence as suggested by (23). The considerably increased quantum yield of the cesium iodide photocathode (by a factor of about ten) is mostly the result of the larger escape depth λ_s which is determined by the longer mean free path of the secondary electrons within this insulator (electron-phonon interaction length) as compared to that for the metal photocathode (electron-electron interaction length).

III. X-RAY INTERACTION COEFFICIENTS

In Sec. II we have summarized our developments of efficient, analytic spectrographic response functions based upon the description of x-ray absorption, reflection and diffraction using the photon energy-dependent fundamental parameters, the atomic photoabsorption cross sections and the atomic scattering factors. We have demonstrated

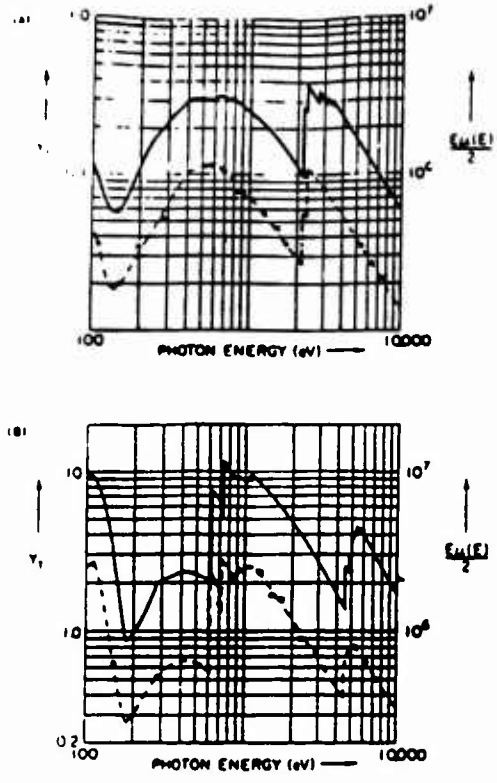


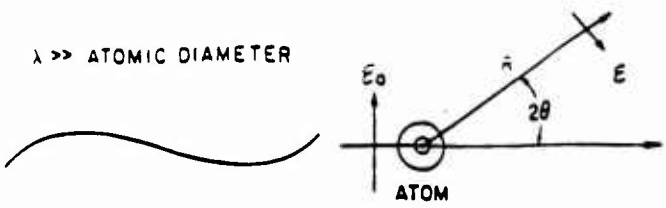
Fig. 24. Examples of measured photocathode front surface yield, Y (electrons/photon) vs photon energy, E(eV) for (A) a 300 A Au film and (B) a 3000 A cesium iodide film. The energy dependence expressed in Fig. 23 is demonstrated here by the superposition of the $E\mu(E)$ curves on these log-log plots. The considerably higher yields shown here for the CsI photocathode is predicted in our model by the fact that the escape depth for CsI (electron-phonon interaction length) is about ten times that of Au (electron-electron interaction length).

that our analytical modified Darwin-Prins (MDP) model for mirror and multilayer reflection is generally more efficient and yields results that are essentially identical to those obtained with the optical E&M model using the macroscopic material constants, δ and β. With either theoretical approach, the material properties can be derived from the atomic scattering factors for the photon energies outside the absorption threshold regions where the photon interactions within condensed matter may be considered to be with essentially free atoms. To facilitate accurate and detailed calculations of the model descriptions presented in Sec. II, we have established photoabsorption and atomic scattering factor tables for 94 elements within the 100-10 000 eV region.[13,14,15] A brief review of this work is presented here.

We define the atomic scattering factor, f ($= f_1 + if_2$) in Fig. 25 and have calculated the atomic scattering factors using the Kramers-Kronig dispersion relations based upon our compilations of experimental/theoretical photoabsorption cross sections. These relations are:

$$f_1 = Z + C\int_0^\infty \frac{\epsilon^2 \mu_a(\epsilon)\,d\epsilon}{E^2 - \epsilon^2} \qquad (24)$$

$$f_2 = (1/2)\pi C E \mu_a(E). \qquad (25)$$



SINGLE ELECTRON SCATTERING AMPLITUDE × ATOMIC SCATTERING FACTOR

$$\mathcal{E}(\theta,\lambda) = -\left[\mathcal{E}_0\left(\frac{r_0}{R}\right)P(2\theta)\right](f_1(\lambda)+if_2(\lambda))$$

Fig 25 Low-energy x-ray scattering by an atom. The amplitude scattered may be described by an atomic scattering function, $f_1 + if_2$, multiplied by the amplitude that would be scattered by a single Thomsonian electron in the same x-radiation field. Here r_0 is the classical electron radius; R the radial distance to the point of measurement, and $P(2\theta)$ is the polarization factor that is equal to unity or cos 2θ, depending upon whether the incident electric vector (of magnitude $\mathcal{E}_0$) is perpendicular or parallel to the plane of scattering. For the low-energy x-ray region for which the wavelengths are large compared with the atomic dimensions, the scattering of each atomic electron at any angle is with the same phase as for the forward direction. The atomic scattering factor is thus independent of the angle of scattering, 2θ.

where E is the photon energy, $C \doteq (\pi r_0 hc)^{-1}$, r_0 is the classical electron radius, h is Planck's constant, and c is the speed of light. The atomic absorption cross section, μ_a, is related to the mass absorption coefficient $\mu(cm^2/gm)$, by:

$$\mu_a = A\mu/N_0 \qquad (26)$$

where A is the atomic weight and N_0 is Avogadro's Number. In our numerical integrations for the values of f_1 in (24) it was considered sufficient to take the integration range on ϵ from 30 eV to 85 keV, using "state of the art" values for $\mu(E)$ to obtain the required μ_a values.

For the higher photon energies where the wavelength becomes comparable to the dimensions of the atom, the individual atomic electrons may not be scattering in phase, and the atomic scattering factor will be reduced by the effect of the interference of these electronic scattering components. For the forward scattering case (e.g. in small angle reflection), and within the entire 100-10 000 eV region of interest here, all atomic electrons are scattering essentially in phase and the atomic scattering factor, f_1, given by (24) needs no correction. However, it can be shown that for the larger angles of scattering the value of f_1 given by (24) should be corrected by replacing the atomic number, Z, by the angle-dependent form factor, f_0, for the given atom. (In Ref. 14 we list the sources for the tabulated form factors for all elements and various charge states.) Thus the atomic scattering factor for the larger angles of scattering (e.g. for Bragg diffraction) may be more accurately given as:

$$f = f_1' - \Delta f + if_2 \qquad (27)$$

where

$$\Delta f = Z - f_0. \qquad (28)$$

In Fig. 26 we have plotted the modulus, $\sqrt{(f_1^2 + f_2^2)}$, of the atomic scattering factor for neon (Z = 10) calculated as describe. above for the two scttering angles, 0° and 180°. Also plotted here are modulus values based upon nearly exact S-Matrix theoretical calculations (via a very expensive computer program) by Pratt, et al. As shown in Fig. 26, for most practical purposes the relatively simple Kramers-Kronig model and the simple form factor correction given above are sufficiently accurate.

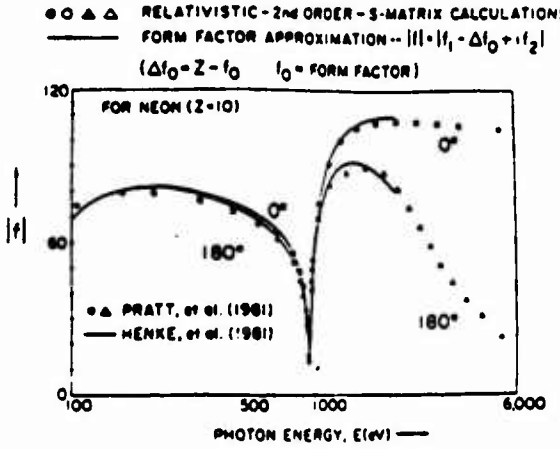


Fig. 26 Plots of the modulus of the atomic scattering factor, $\sqrt{f_1^2 + f_2^2}$, vs photon energy, E(eV) at 0° and 180° scattering angles for neon (Z = 10). Compared here are the atomic scattering factor modulus values calculated by the relatively simple Kramers-Kronig dispersion model and by the nearly exact (but expensive) 2nd order S-Matrix theoretical model. Also demonstrated here is the accuracy of the simple form factor correction that is applied in our calculation for large-angle scattering.

Finally, Fig. 27 (taken from our cross section tables[14]) presents plots of the atomic scattering factor components, f_1 and f_2, for Aluminum, illustrating in f_1 the strong anomolous dispersion throughout this photon energy region and in f_2 a comparison of our fit curve with data calculated directly from typical experimental measurements of μ using (25) and (26).

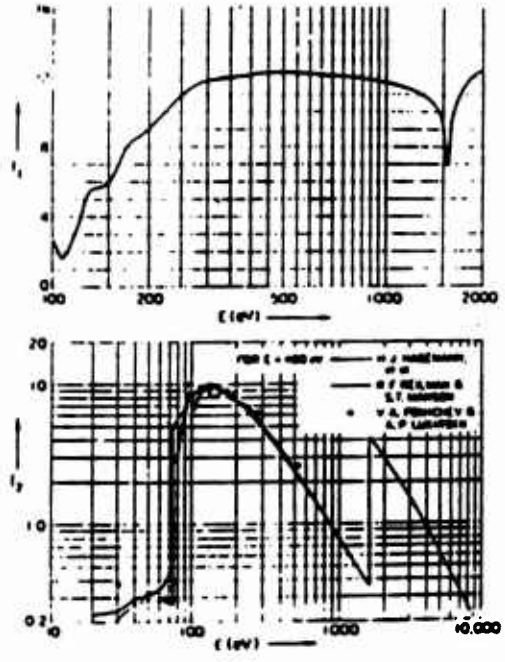


Fig. 27. Examples of plots of the atomic scattering factor components, f_1 and f_2 (for Aluminum) taken from Ref. 14. Illustrated here, in f_1, is the strong anomolous dispersion through this photon energy region, and in f_2, a comparison of our fit curve with present experimental photoabsorption data applying relations (25) and (26).

ACKNOWLEDGEMENTS

The author gratefully acknowledges the invaluable assistance of his many students and colleagues who have participated in the research efforts that have been reviewed here, and of Debra Nanod in the preparation of this manuscript. Our program on Low Energy X-Ray Physics and Technology is supported by a grant from the U.S. Air Force Office of Scientific Research, AFOSR-ISS4-85 and supplementally by contracts with the U.S. Department of Energy, CID#9501, Task I (via LANL and LLNL); CID#9501, Task II (via the National Lasers Users Facility), and DE-AC03-76SF00098 (via LBL).

BIBLIOGRAPHY

1. B.L. Henke and P.A. Jaanimagi, "A Two-Channel, Elliptical Analyzer Spectrograph for Absolute Time-Resolving/Time-Integrating Spectrometry of Pulsed X-Ray Sources in the 100-10,000 eV Region," Rev. Sci. Instrum. 56, 1537-1552, 1985.

2. P.A. Jaanimagi and B.L. Henke, "An Absolutely Calibrated Time-Resolving X-Ray Spectrometer," Proc. of Soc. of Photo-Opt. Instrum. Engin. (SPIE), San Diego, 1985.

3. B.L. Henke H. T. Yamada and T. J. Tanaka, "Pulsed Plasma Source Spectrometry in the 80-8000 eV X-Ray Region," Rev. Sci. Instrum. 54, 1311-1330, 1983.

4. B.L. Henke, J.Y. Uejio, H.T. Yamada, and R.E. Tackaberry, "The Characterization of Multilayer Analyzers - Models and Measurements," in press, Opt. Engin. (August 1986).

5. B.L. Henke, H.T. Yamada and J.Y. Uejio, "Reflectivity Characteristics of Multilayers and Crystal Analyzers for the 100-10,000 eV Region - Theory and Experiment" (in preparation).

6. H.T. Yamada and T.J. Tanaka, "A Computer Program for the Calculation of the X-Ray Reflectivity Characteristics of Sputtered or Evaporated Multilayers Using the Optical E&M Model," LBL-21909, 1986.

7. B.L. Henke, "Ultrasoft X-Ray Reflection, Refraction and Production of Photo-electrons (100-1000 eV Region)," Phys. Rev. A6, 94-104, 1972.

8. B.L. Henke, J. Kerner and D. Kania, "Reflectivity Characteristics of Low-Energy X-Ray Mirror Monochromators" (in preparation).

9. B.L. Henke, S. L. Kwock, J. Y. Uejio, H. T. Yamada and G. C. Young, "Low-Energy X-Ray Response of Photographic Films: Part I. Mathematical Models," J. Opt. Soc. Am. 1, 828-849, 1984.

10. B.L. Henke, F. G. Fujiwara, M. A. Tester, C. H. Dittmore and M. A. Palmer, "Low-Energy X-Ray Response of Photographic Films: Part II. Experimental Characterization," J. Opt. Soc. Am. 1, 818-827, 1984.

11. B.L. Henke, J.Y. Uejio, G.F. Stone, C.H. Dittmore, F.G. Fujiwara, "High Energy X-Ray Response of Photographic Films. Models and Measurements", (in press, J. Opt. Soc. 1, October 1986).

12. B.L.Henke, J. P. Knauer and K. Premaratne, "The Characterization of X-Ray Photocathodes in the 0.1-10 keV Photon Energy Region," J. Appl. Phys. 52, 1509-1520, 1981.

13. B.L. Henke, "Low Energy X-Ray Interactions: Photoionization, Scattering, Specular and Bragg Reflection," AIP Conf. Proc. 75, D. T. Attwood and B. L. Henke, Editors (Am. Instit. of Phys., New York), 146-155, 1981.

14. B.L. Henke, P. Lee, T.J. Tanaka, R.L. Shimabukuro, and B.K. Fujikawa, "Low Energy X-Ray Interaction Coefficients: Photoabsorption, Scattering and Reflection. E = 100-2000 eV, Z = 1-94," At. Data Nucl. Data Tables 27, 1-144, 1982.

15. B.L. Henke, H.T. Yamada and J.Y. Uejio, "Fine-Spaced Photoabsorption Cross-Sections and Atomic Scattering Factors for the 94 Elements in the 100-10,000 eV Photon Energy Region" (in preparation as 8" floppy disk, RT-11 format).

Two-channel, elliptical analyzer spectrograph for absolute, time-resolving time-integrating spectrometry of pulsed x-ray sources in the 100–10 000-eV region

B. L. Henke and P. A. Jaanimagi[a)]

Department of Physics and Astronomy, University of Hawaii, Honolulu, Hawaii 96822

(Received 11 December 1984; accepted for publication 18 April 1985)

A new spectrographic system has been developed and calibrated in this laboratory for the absolute spectrometry of high-intensity pulsed x-ray sources in the 100–10 000-eV region. This spectral region is analyzed with fixed elliptically curved crystals and molecular or sputtered-or-evaporated multilayers of 2d values in the 3–160-A range. Twin channels are utilized for simultaneous time-integrated photographic recording and for time-resolved x-ray streak camera recording. Absolute calibrations of the elliptical analyzers, of the photographic film, and of the gold and CsI transmission photocathodes have been made using monoenergetic, cw laboratory x-ray sources. The overall transmission characteristics of the spectrograph have also been determined. The instrument has been designed for mounting through a pneumatically controlled high-vacuum valve onto a 4-in. port of a 1-m-diameter source chamber and includes an appendage, high-vacuum, sputter-ion prepumping station. The initial dynamic testing and application of this new spectrographic system has been on the University of Rochester's LLE 24 laser beam OMEGA source facility.

INTRODUCTION

There is a considerable need at this time for absolute time-resolved/time-integrated spectrometry of high-intensity, pulsed x-ray sources in the 100–10 000-eV photon energy region. Typically these sources are the high-temperature plasmas as involved, for example, in fusion energy and x-ray laser research and in materials excited by the large synchrotron radiation facilities. The spatial extents of the sources to be measured (or imaged) usually subtend a relatively small angle at the spectrograph. The pulse structure to be analyzed requires time resolution in usually the picosecond to microsecond range. We describe here an instrument that can accomplish this type of spectrometry that has been constructed and cw-source calibrated in this laboratory and is now being applied to the diagnostics of laser-produced plasmas with the OMEGA facility at the Laboratory for Laser Energetics, University of Rochester.

In preparation for this type of x-ray spectrograph development we have recently completed some basic studies in low-energy x-ray spectrometry as reported in Refs. 1–9.

In Ref. 1 we discuss the geometrical and physical x-ray optics for fixed, Bragg reflecting analyzers for pulsed source spectroscopy. This study led to the choice of elliptically curved, fixed Bragg crystals or multilayers for the analyzing element (see Fig. 1). Some of the advantages of this type of dispersive geometry may be summarized as follows:

(a) With the source at one focal point for the given elliptical geometry, all reflected radiation passes through the second focal point where an effective scatter aperture may be located and at which is the geometric center for a normal-incidence detection circle along which photographic or electronic position-sensitive detection may be effectively applied.

(b) Small bandpass and/or low-energy cut-off filter foils may be mounted across this scatter aperture. High-energy cut-off mirror monochromators may be easily introduced between the elliptical analyzer and the source (as shown in Fig. 1).

(c) As described in Ref. 1, spectroscopy with spatial resolution for linear or two-dimensional source distributions may be accomplished by using slits or curved focusing mirror monochromators with the elliptical analyzers.

(d) This elliptical geometry yields a relatively simple analytical spectrometer transmission function for absolute photometric analysis along the detection circle (as discussed in Ref. 1).

In the design of the present instrument it was considered important to be able to measure simultaneously the spectrum of a subnanosecond source with time integration and with time resolution in the 10-ps range. To accomplish this, two identical elliptical analyzer channels were utilized, one

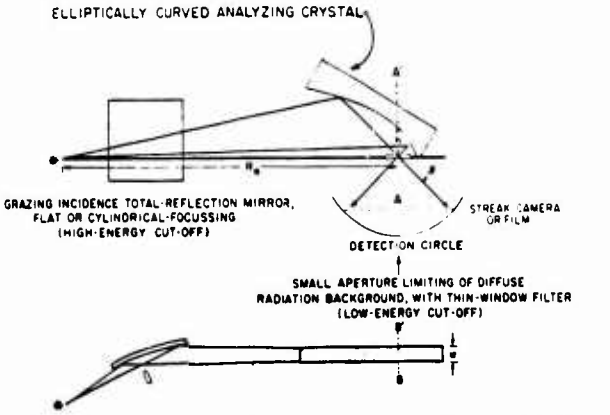


FIG. 1. The optical geometry of elliptical analyzer spectrograph. (The elliptical analyzer is mounted so as to permit small rotations about the *AA'* and *BB'* axes for alignment.)

 0034-6748/85/081537-16$01.30 © 1985 American Institute of Physics

to a photographic film camera and the other to a specially developed, long entrance slit x-ray streak camera. This streak camera/photographic camera elliptical analyzer x-ray spectrograph will be referred to as the SPEAXS system.

Presented in Sec. I is a description of the basic design features of this SPEAXS system along with that for the alignment procedure for application to the "point" laser-produced sources. In Sec. II we describe the response of the crystal/multilayer analyzers that we have chosen for the 100–10 000-eV region and that of the associated low- and high-energy cut-off characteristics of practical filters and mirror monochromators. In Sec. III we describe the photographic and streak camera detection that is applied with this SPEAXS system. And finally in Sec. IV we present some initial measurements on the OMEGA facility and discuss the combining of calibration data for the generation of an overall transmission function for the SPEAXS system as applied for absolute spectrometry.

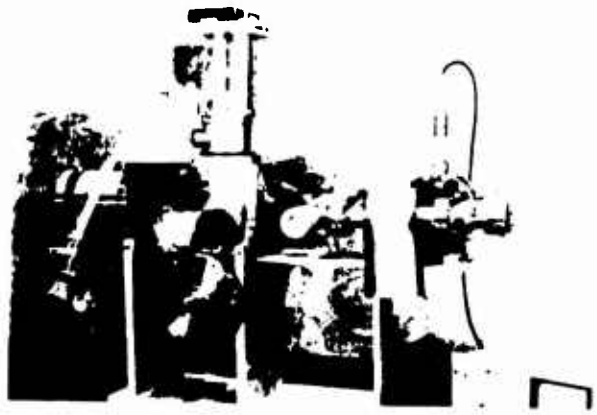


FIG. 3. The SPEAXS system with the x-ray streak camera in the up and the photographic camera in the down position. Also shown here is a pneumatically controlled 4-in. vacuum valve through which the system is bolted onto a 1-m-diameter target chamber, and the Vacion/molecular sieve appendage prepumping system.

I. DESIGN AND CONSTRUCTION OF THE SPEAXS SYSTEM

A drawing of the SPEAXS system is shown in Fig. 2. It has been designed to bolt onto a 4-in. port of the 1-m-diameter spherical source chamber of the OMEGA. The source-to-scatter aperture distance (between focal points of the elliptical analyzer) is 120 cm. The stainless-steel block housing is attached to the chamber through a pneumatically controlled 4-in vacuum valve and the system is prepumped to 10^{-6} Torr with a Vacion pump backed initially through a molecular sieve trap to a mechanical pump. The twin elliptical analyzer/mirror monochromator stations are mounted through a rear port and are adjustable through two side access ports. A photo of the assembled spectrograph and its appendage Vacion pump are shown in Fig. 3 with the streak camera mounted above and the photographic camera below the housing.

In order to allow a precise optical alignment of the elliptical analyzers, these along with their associated mirror monochromators are mounted on blocks that are attached to structures as shown in Figs. 4 and 5 which permit small rotations about two axes, one along the center line of the scatter aperture slit and the other perpendicular to the aperture plane and through its center (see axes *A-A'* and *B-B'* in Fig. 1). To achieve optical alignment with a small "point" target, an alignment telescope is precision fit to each elliptical analyzer block, in turn, with the optical axis of the telescope along the central ray to the source focal point of the ray system that illuminates the elliptical analyzer. The telescope-and-analyzer block is then rotated about the two axes to bring the image of an ambient-lighted point target to the middle of the telescope reticule as illustrated in Fig. 6. After this alignment, the rotatable crystal block mountings are clamped into fixed positions. When a mirror monochromator is attached to the elliptical analyzer block, with the desired angle of reflection fixed, the optical image that is centered within the alignment telescope field is formed directly by reflected rays presented by the monochromator mirror. (Aluminized optically reflecting test analyzers and mirrors are used in this alignment procedure.)

By placing a point source of visible light at the source position (or alternatively, an image of a point source with a ray system that proceeds to illuminate the total elliptical analyzer surface) the optical perfection of the mirror/analyzer system may be evaluated. With proper optical alignment, a sharp line image appears along the center line of the scatter aperture. A "knife edge" test of the uniformity of the optical reflection from the elliptically curved surface may be demonstrated by the uniformity of the illumination on a screen along the detection circle.



FIG. 2. Cut-away drawing illustrating the mounting of the two elliptical analyzer channels in the SPEAXS system. (1—x-ray streak camera; 2—elliptical analyzer channels; 3—photographic camera; 4—pneumatically controlled valve.)



FIG. 4. Showing the elliptical analyzer substrate and mirror monochromator as attached to the mounting block on the rotating table (with the *AA'* axis). The scatter aperture plate is mounted on the bottom of the circular table.



FIG. 5. Back view of rotating mount as shown in Fig. 4. Illustrated here is the rotational adjustment of the mounting block orientation about an axis perpendicular to that of the rotating table axis and through the center of the scatter aperture (the BB′ axis).

Finally, the geometrical and smoothness integrity of the crystal/multilayer analyzer surface and the absence of crystal defects may be tested by checking for waviness and variation of photographic density of the photographically recorded x-ray spectral lines on a film placed along the detection circle.

II. CRYSTAL/MULTILAYER ANALYZERS, MIRROR MONOCHROMATORS, AND FILTERS

Thin sections of crystals (0.5×4.0 in. and of 0.005--0.020 in. thickness) are cemented to standardized, elliptically curved substrates which are generated by a computer-controlled milling machine. The construction of the elliptical analyzers is described in detail in Ref. 1. The large 2d analyzers are deposited as molecular multilayers (lead salts of straight-chain fatty acids) and directly upon the curved substrates that have been clad with thin glass sections and as described in Refs. 1 and 2. In Table I we present a listing of crystals/multilayers that have been chosen for the present SPEAXS system and which are currently under evaluation by the authors for spectrometry in the 100–10 000-eV region. Given here are the 2d values, photon energy limits for Bragg angles of 22.5 to 67.5 deg and the calculated integrated reflectivity R_i (Darwin–Prins) at 45° Bragg angle. Our methods for the calculation and experimental measurements of the integrated reflectivities are discussed in Refs. 1, 3, and 4. In Fig. 7, we present the integrated reflectivities for the analyzers listed in Table I plotted for the appropriate photon energy segments through the entire 100–10 000-eV region in order to illustrate the "coverage" by this set of analyzers.

In Ref. 3 we have presented detailed reflectivity versus angle of grazing incidence and photon energy curves and tables for the mirror monochromator systems that are currently used in low-energy x-ray spectrometry. Two of these mirror monochromators have been applied in this SPEAXS system to effectively suppress the second- and higher-order diffracted background radiations. These are with a 30-mrad reflection from Al and with a 67.5-mrad reflection from Al_2O_3 having high-energy cut-off characteristics at about 1000 and 500 eV, respectively. The reflectivity versus photon energy curves for these mirror monochromators are shown in Fig. 8.

The low-energy background radiation that may be superimposed upon the higher-energy measured spectra can be excessive, first, because the sources of interest often have a relatively large component of low-energy x-rays and EUV and, second, because these longer wavelength radiations can strongly scatter and specularly reflect from the analyzer surface and effectively compete with the Bragg reflected spectral intensities. To suppress this low-energy background, a relatively thick filter with a strong transmission band for the particular spectral region being measured can often be effective (usually placed at the small scatter aperture). In Table II are listed some practical filter materials along with their mass thickness, $m(=1/2\mu)$ for which their transmission will be about 60% at a photon energy just below a given strong absorption edge (the high-energy limit of the particular transmission band). In Figs. 9 and 10 are plotted the transmission bands in the 100–10 000-eV region of interest here. [Filter mass thicknesses (Mg/cm^2) are used rather than linear thicknesses because these usually are more accurately measured and film density values are not required, which are usually not accurately definable for thin films.]

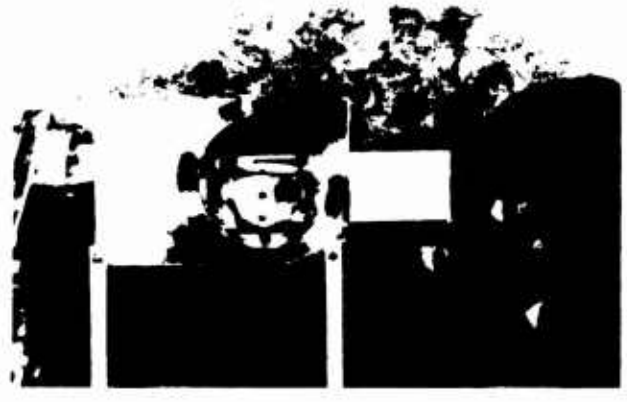


FIG. 6. Depicting the alignment procedure. A precision oriented alignment telescope is fastened to each mounting block in turn, rotating it about the two axes (*AA′* and *BB′*) until the image of the small target is on the center of the reticule. The mirror/analyzer mounting block is then fixed in this position by tightening its mounting bolts accessible through the side ports.

III. PHOTOGRAPHIC AND STREAK CAMERA DETECTION

Particularly in the fusion energy and present x-ray laser research, time-resolved x-ray diagnostics of high-temperature plasmas, is essential. For the application of the present SPEAXS system on the diagnostics of laser-produced plasmas (with subnanosecond pulses) the required time resolution in the 10-ps range has been achieved with a specially designed x-ray streak camera. In order to obtain an absolute calibration of the time-resolved streak spectrum, a simultaneous absolute time-integrated intensity value on the same spectrum is obtained by photographic recording with a parallel, identical elliptical analyzer channel.

In the present instrument an entrance aperture slit to each channel is applied which establishes a spectral line

TABLE I. Crystal multilayers for elliptical analyzers having integrated reflectivities as plotted in Fig. 7.

No.	Crystal name	Indices (hkl)	2D	Diffraction order	E (eV) limits $22.5° < \theta < 67.5°$	R (45°)[b] (mrad)
1	LiF	(200)	4.03	1	8046—3333	0.0433
2	Mica	(002)	19.84	3	4900—2029	0.0286
3	PET	(002)	8.74	1	3707—1535	0.0907
4	Gypsum	(020)	15.19	1	2134— 884	0.0711
5	Mica	(002)	19.84	1	1633— 676	0.0136
6	RAP	(1010)	26.12	1	1240— 514	0.0848
7	KAP	(1010)	26.63	1	1217— 504	0.0488
8	Laurate[a]		70.00	1	463— 192	0.4878
9	Stearate		100.00	1	324— 134	0.8262
10	Lignocerate		130.00	1	249— 103	0.9373
11	Melissate		160.00	1	203-- 84	0.8974

[a] Molecular multilayers of lead salts of straight-chain fatty acids.
[b] For Bragg angle, θ, equal to 45°.

length at the detection circle of 3 mm. The 1-mm width of the 40-mm streak camera slit (positioned along a chord of the detection circle) is aligned along the middle of this 3-mm-wide zone. Correspondingly, a photographic film placed on the detection circle measures spectra within this 3-mm-wide band, and a subsequent microdensitometer measurement may be with an effective 1-mm slit length scan averaged through the middle of the exposed 3-mm zone.

A 35-mm photographic film is mounted upon a semicircular film holder of a radius equal to 8.4 cm which may be advanced into this detection circle by means of a sliding/rotating vacuum feedthrough rod (see Fig. 2) permitting four exposures of the 3-mm spectral bands to be obtained on each 35-mm film strip. After making these exposures, the film holder cassette may be drawn back against the circular access plate that is sealed by an O-ring to the side of the camera housing. In this closed position, a light baffle may then be rotated into place over the cassette entrance slit and the side plate may then be removed along with the film holder within a light-tight enclosure which may be carried to a darkroom for processing.

The photographic camera and the streak camera can be set to have comparable sensitivities in the x-ray region as established by the choice of the photographic film and of the transmission photocathode material and thickness at the streak camera's entrance slit. Further adjustment of the sensitivity of the two channels is obtained by introducing matched filters of desired absorption thickness at the two scatter apertures as described earlier. Finally, to bring the exposure within the dynamic range of the photographic detection, the four exposures of the film strip may be with four thicknesses of additional calibrated filter material that are mounted as a wedge at the entrance slit of the translating film cassette.

After a standardized film processing, the properly exposed photographically recorded spectral line (or continuum) may be microdensitometered to yield a profile in photographic density, D. In Ref. 5 we have described an accurate method for analytically transforming this profile in photographic density, D, to a profile in absolute intensity at the detection circle, I (photons/μm^2) using a semiempirical photographic response function which relates the exposing intensity, I, to the measured density, D, for a given photon energy, E. This function may be combined with the transmission function of the elliptical analyzer channel via a microcomputer to yield an absolute source intensity plot (e.g., photons/steradian) versus photon energy, E, directly from the microdensitometer data as will be outlined in Sec. V.

Three practical photographic film types have been char-

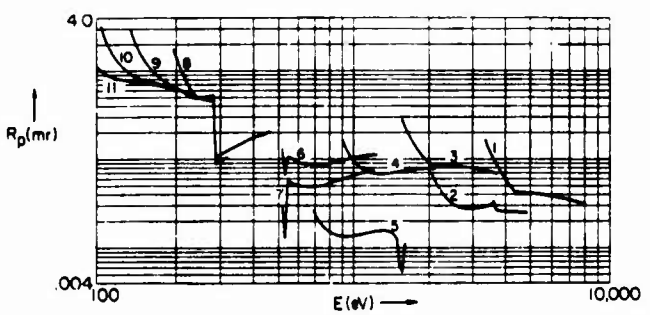


FIG. 7. Integrated reflectivity, R (mrad), vs photon energy, E (eV), for eleven crystal/multilayers that may be applied to cover the 100–10 000-eV region as elliptical analyzers and as listed in Table I. The R plots have been calculated using the Darwin–Prins model. (See Appendix B for detailed R vs E curves.)

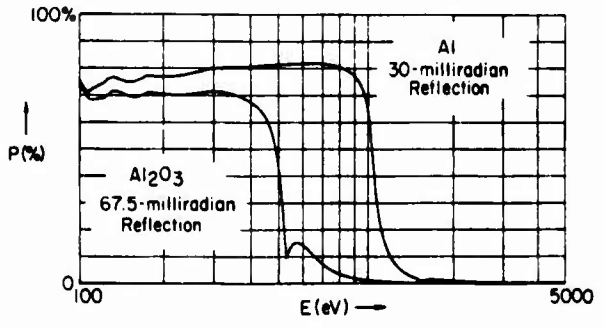


FIG. 8. Percent reflectivity, P (%), vs photon energy, E (eV), illustrating high-energy cut-off characteristics of a 67.5-mrad reflection from an Al_2O_3 mirror and of a 30-mrad reflection from an Al mirror. These monochromators effectively reduce the high-energy background above 500 and 1000 eV, respectively.

TABLE II. Mass thickness of filters with transmission band characteristics illustrated in Figs. 9 and 10.

No.	Filter	Edge (eV)	$1/2\mu$ ($\mu g/cm^2$)
1	Beryllium Be	Be-K (111)	81
2	Boron nitride BN	B-K (188)	68
3	Carbon C	C-K (284)	226
	Polypropylene $(CH_2 = CHCH_3)_x$	C-K (284)	256
	Formvar $C_5H_7O_2$	C-K (284)	156
	Mylar $C_{10}H_8O_4$	C-K (284)	152
	Kimfol $C_{16}H_{14}O_3$	C-K (284)	181
4	Boron nitride BN	N-K (400)	66
5	Aluminum oxide Al_2O_3	O-K (532)	126
	Silicon dioxide SiO_2	O-K (532)	116
	Polyformaldehyde $(CH_2O)_x$	O-K (532)	92
6	Iron Fe	Fe-L_3 (707)	234
7	Nickel Ni	Ni-L_3 (854)	279
8	Copper Cu	Cu-L_3 (933)	318
9	Magnesium Mg	Mg-K (1303)	1139
10	Aluminum Al	Al-K (1560)	1427
11	Silicon Si	Si-K (1840)	1680
12	Saran $(CH_2 = CCl_2)_x$	Cl-K (2820)	3151
13	Silver Ag	Ag-L_3 (3351)	1296
14	Tin Sn	Sn-L_3 (3929)	1669
15	Titanium Ti	Ti-K (4964)	6010
16	Chromium Cr	Cr-K (5989)	7924
17	Iron Fe	Fe-K (7111)	9804
18	Nickel Ni	Ni-K (8331)	11820
19	Copper Cu	Cu-K (8980)	13699

acterized in detail for absolute spectrometry in the 100–10 000-eV region with the SPEAXS system (see Ref. 5). Their sensitivities versus photon energy, E, are compared in Fig. 11.

The spectral range is covered with the x-ray streak camera by positioning the entrance slit along one of three chords on a detection circle (accomplished with straight through and a tilted mounting flange). The central axis of the streak camera passes through the focal point at the scatter aperture

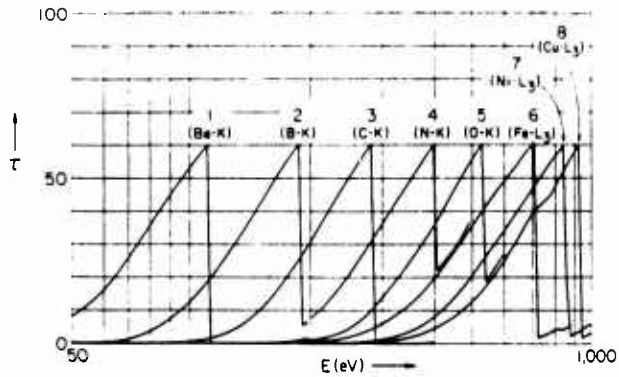


FIG. 9. Transmission bands of selected filters listed in Table II for the 100–1000 eV region. (See Appendix A for detailed transmission curves which indicate the effectiveness of the low-energy cut-off characteristics.)

center and may be mounted so as alternatively to make the angles, $-20°$, 0, and $+20°$ with the normal to the aperture plane. The minimum distance of the photocathode to the scatter aperture is 24 mm. Because of the large angular dispersion of Bragg reflecting analyzers and because of the mechanical and electrical problems associated with very close coupling of the entrance slit of the streak camera and the analyzer, it becomes of considerable advantage in crystal spectroscopy to employ streak cameras having relatively long entrance slits. For the SPEAXS system an x-ray streak camera has been specially developed that has an entrance slit of 1 by 40 mm with more than 300 spatially resolved elements along this slit. And it has the required 10-ps resolution. This was accomplished by a systematic series of experimental modifications of the basic structure of the RCA 73435 image tube as suggested by an associated series of measurements and precisely computed electron ray traces following each modification. This tube development is described in detail in the companion work of Ref. 6.

The transmission photocathodes that are used with this streak camera on the SPEAXS system are cesium iodide and gold for relatively high and low sensitivity applications, respectively. We have measured the absolute quantum efficiency for these photocathodes (secondary electrons emitted per incident photon) as described in Ref. 7 and examples of the yield versus photon energy curves for 1000-A CsI films and for 200-A gold films are presented in Figs. 12 and 13.

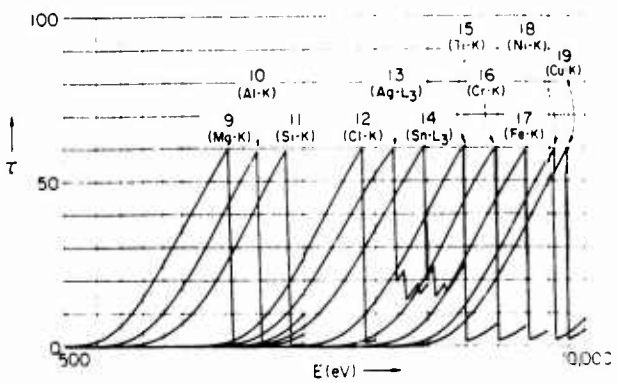


FIG. 10. Transmission bands for selected filters listed in Table II for the 500–10 000-eV region (see Appendix A).

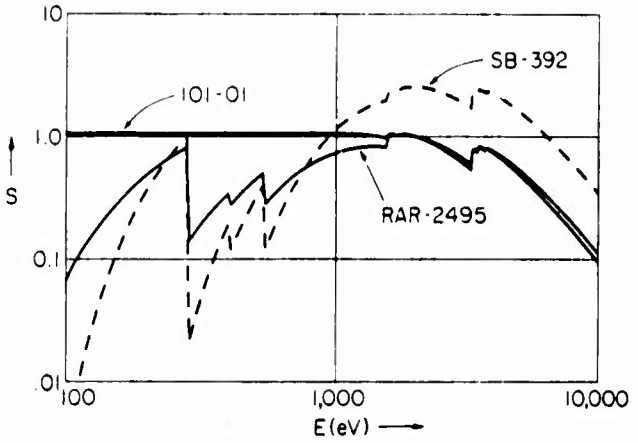


FIG. 11. Comparison of the sensitivities in the 100–10 000-eV region of three photographic film types suitable for absolute spectrometry with the SPEAXS system, Kodak's 101, RAR-2495 and SB-392 (35-mm) films. (See Ref. 5 for a description of their characterization.) Sensitivity is defined here as the reciprocal of the exposure, I (photons/μm^2), that is required to establish a specular density, D, equal to 0.5.

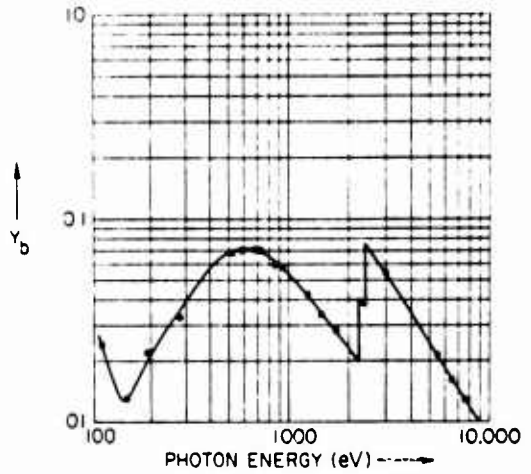


FIG. 13. Quantum yield, Y_b (secondary electrons per normally incident photon) for 200-A gold transmission photocathode (see Ref. 7).

IV. INITIAL RESULTS AND PROCEDURES FOR ABSOLUTE SPECTROMETRY

The initial dynamic tests of the SPEAXS system have been on microballoon targets irradiated by a six-beam ultraviolet laser pulse ($\lambda = 351$ nm) using the University of Rochester's Laboratory for Laser Energetics OMEGA facility. In Figs. 14 and 15 are shown examples of photographically recorded spectra using a 12.7 μm Be foil across the scatter aperture and with the LiF and PET analyzing crystals, respectively. Exposures were on Kodak's RAR 2495 (35 mm) film. The microdensitometry was with a 30×400-μm slit and with a multiscan integration of the optical density through the central one millimeter region of the exposed 3-mm band (as also measured by the streak camera's 1-mm slit).

The spectrum of Fig. 14 was generated by a 600-ps pulse of 200-J absorbed energy upon a bare glass microballoon of 200 μm diameter. The spectral lines measured here, using the LiF analyzer, are for highly ionized species of calcium (a minor element in the glass).

The spectrum of Fig. 15 was generated by a 600-ps pulse of 200-J absorbed energy upon a 200-μm-diameter glass microballoon that was coated with 1 μm of aluminum. The spectral lines measured here using the PET analyzer, are for highly ionized species of aluminum and silicon.

The intensities along the three millimeter length of the spectral lines as measured with the LiF analyzers were uniform. The measured intensities, however, symmetrically drop off in the first and third millimeter segments along the spectral line for the PET analyzer (and also for the RAP analyzers that have been applied for these initial tests). We believe that this nonuniformity has resulted from a slight curvature of the crystal surface in its short dimension. We hope to improve the flatness of the crystal mounting on the elliptical substrates by improving the mounting procedures over those as originally described in Ref. 1.

Presented in Fig. 16 is an example of the initial tests of the x-ray streak camera (a Polaroid photograph of the image intensifier output for a spectrum from a bare glass microballoon using a PET analyzing crystal and a CsI transmission photocathode). Having elliptically curved analyzers of improved quality, we may then proceed to measure accurate absolute photon energies and intensities of spectral lines and of continuum distributions.

The absolute photon energy E (eV), and wavelength λ (Å), may be determined from the measured angular position β, (see Fig. 1) along the detection circle for the elliptical analyzer by the following relation [from Eq. (6), Ref. 1]:

$$\lambda\,(\text{Å}) = \frac{2d}{m}\sin\left[\tan^{-1}\left(\frac{1-\epsilon\cos\beta}{c\sin\beta}\right)\right] = \frac{12\,398}{E\,(\text{eV})}.$$

Here m is the diffraction order and d is the effective atomic plane spacing of the analyze · (includes a refraction correction) and expressed in angstroms. The eccentricity parameter, ϵ, for the ellipticity of the analyzer has been given in Ref. 1 [Eq. (5)] by the relation

$$\epsilon = \sqrt{1+(h/R_0)^2} - h/R_0,$$

in which R_0 is the distance between the focal points (between

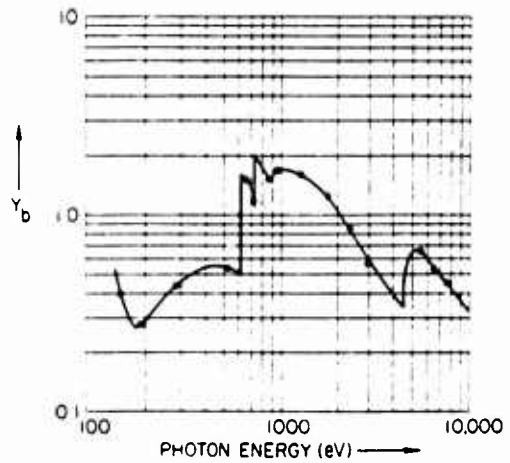


FIG. 12. The quantum yield, Y_b (secondary electrons emitted per normally incident photon), vs photon energy, E (eV), of a 1000-A cesium iodide transmission photocathode (evaporated under high vacuum. See Ref. 7).

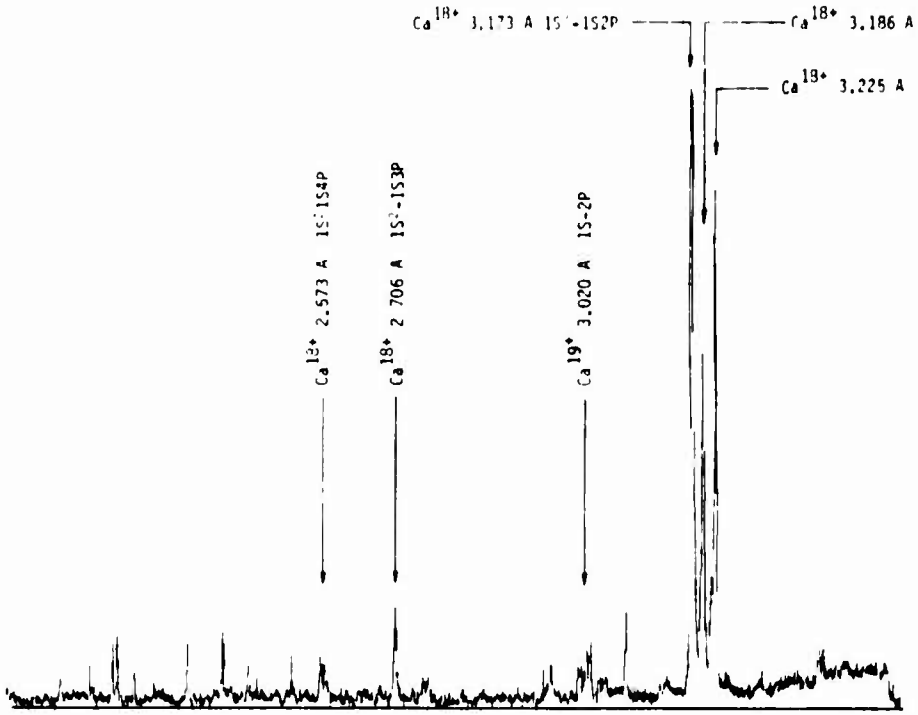


FIG. 14. Example of photographically recorded spectrum with the SPEAXS system using the LiF crystal elliptical analyzer. Measuring transitions for Ca^{18+} excited by a 600-ps/200-J pulse of 351-nm light of the OMEGA facility upon a 200-μm-diameter bare glass microballoon. Exposure on RAR-2495 film.

the source and the center of the scatter aperture) and h is the size parameter that measures the distance from the second focal point at the scatter aperture to the elliptical analyzer surface along the ray for $\beta = 90°$. (The elliptical geometry of the analyzer is completely characterized by the parameters R_0 and h which are equal to 120 and 5.08 cm, respectively, for the present SPEAXS system.)

The absolute source brightness for a characteristic line emission at photon energy E, may be determined as i_0 (photons-emitted-per-pulse/steradian) by the following relation [see Ref. 1, Eq. (14)]:

$$i_0 = NL/FMRW(d\chi/d\theta),$$

where N is the total number of photons measured at the detection circle or radius r, within a spectral line of length w. L is the constant total pathlength for all rays from the source point, off the analyzer, through the scatter aperture and then to the detection circle, and given by

$$L = \sqrt{R_0^2 + h^2} + h + r,$$

F is the filter transmission factor at photon energy E; M is the monochromator mirror reflectivity factor at photon energy E; R is the total integrated reflectivity factor of the crystal/multilayer analyzer at photon energy E; $(d\chi/d\theta)$ is the ratio of the differential angle $d\chi$, in the plane of reflection of the

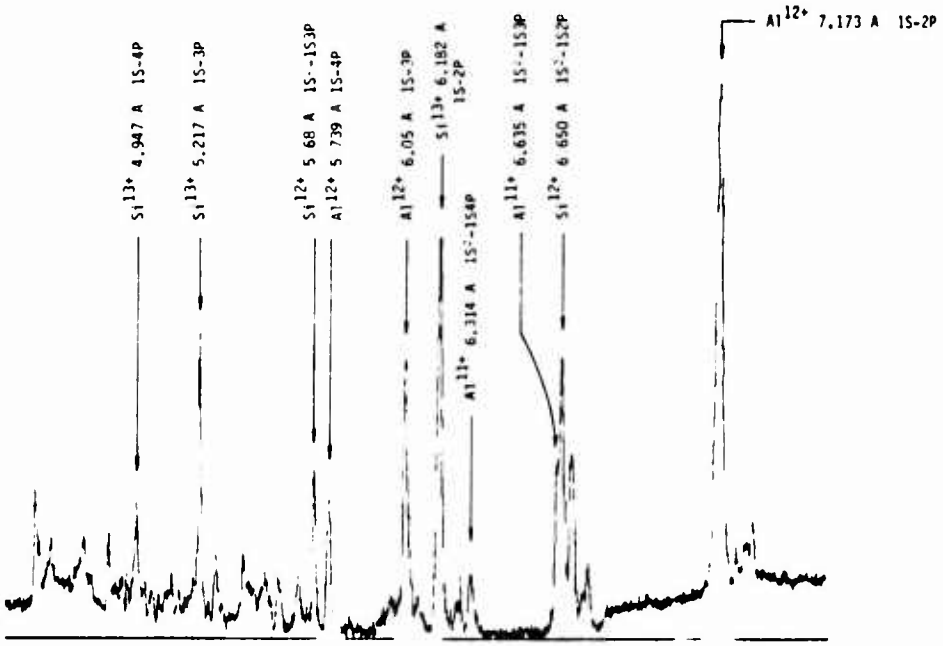


FIG. 15. Example of photographically recorded spectrum with the SPEAXS system using the PET elliptical analyzer. Measuring transitions for the ionized species, Al^{11+}, Al^{12+}, Si^{12+}, and Si^{13+} from a 200-μm-diameter glass microballoon coated with 1 μm of Al and excited by a 600-ps/200-J pulse of 351-nm light of the OMEGA facility. Exposure on RAR-2495 film.

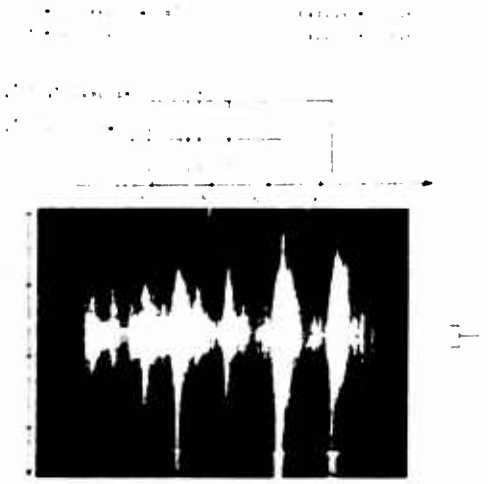


FIG. 16. A photograph of the x-ray streak camera output for a spectrum presented to a CsI transmission photocathode by a PET elliptical analyzer. The spectrum was laser produced from a bare glass microballon.

rays that originate at the source to the corresponding differential Bragg angle $d\theta$, of their reflection from the analyzer. It is given by the following relation [from Eq. (8) of Ref. 1]:

$$\frac{d\gamma}{d\theta} = \frac{\epsilon^2 - 1}{\epsilon(\epsilon - \cos\beta)},$$

N, for a given spectral line, may be determined by numerically integrating over the spectral line intensity distribution, I (photons/μm^2) vs E as derived from the measured photographic density D, vs line position β, using the photographic film response functions described in Ref. 5 (via a microcomputer connected to the microdensitometer).

The filter transmission F, mirror reflectivity M, and analyzer integrated reflectivity R, may be derived by calculations based upon the atomic photoionization cross sections and the associated complex atomic scattering factors. This procedure has been outlined in Ref. 3. We have presented recently in Ref. 4 the atomic photoionization and scattering factor tables for 94 elements which have been generated by fitting theoretical photoionization vs E curves to the "best available" experimental data for the 30–10 000-eV region and applying the quantum dispersion theory, with these data, to generate the corresponding atomic scattering factors. Also presented in Ref. 4 are the detailed calculations for mirror reflectivities and for crystal/multilayer integrated reflectivities, M and R, for materials that are important in currently applied x-ray diagnostics.

Presented in Appendix A are practical examples of filter transmission curves for the 100–10 000-eV region that have transmission bands which were described in Figs. 9 and 10.

We have found (see Ref. 8) that our theoretically calculated mirror reflectivity curves generally predict well the experimentally measured data only for mirror surfaces that have been obtained with "state of the art" smoothness. For the mirrors used in the SPEAXS system our calibration procedure is to normalize the theoretically calculated curves to reflectivity curves that we have measured experimentally (for effective averaging of the experimental data).

In Appendix B we present plots for the first and second diffraction orders for the integrated reflectivity, R, for the eleven crystal/multilayer analyzers that have been shown in Fig. 7 for the 100–10 000-eV region. Again, our calibration procedure for the crystal/multilayer analyzers involves fitting and averaging theoretical R vs E curves to directly measured integrated reflectivity data. We have found, as discussed in Ref. 9, that our closest fits with the experimental data are usually with the theoretical curves calculated with the Darwin–Prins model (as applied here for the R- curves shown in Fig. 7 and in Appendix B). Typical R (exp)/R (Darwin–Prins) normalizing ratios that have been determined for the elliptical analyzers calibrated for the present SPEAXS system are given in Table III.

In Appendix C we present a detailed table for the photographic specular density D vs the exposure I (photons/μm^2) and the photon energy E (eV) in the 100–10 000-eV region for normal incidence upon Kodak's RAR 2495 film. This film has been found to be particularly useful in the general appli-

TABLE III. Comparison of experimental and theoretical integrated reflectivity values—(a modified Darwin–Prins model has been applied for the theoretical calculations).

Analyzer	No. layers	2D	Photon energy	R_1 (mrad)	R_2 (mrad)	$R_1/R_2 \times 100$
LiF	—	4.03	4510.8	0.035	0.042	83
Mica-3rd order	—	19.84	2293.2	0.027	0.039	70
PET	—	8.74	2293.2	0.121	0.085	142
Gypsum	—	15.19	2622.4	0.055	0.055	99
Mica-1st order	—	19.84	929.7	0.020	0.013	147
RAP	—	26.12	676.8	0.088	0.085	104
KAP	—	26.63	676.8	0.052	0.049	106
Laurate	125	70.00	676.8	0.324	0.382	85
Myristate	200	80.00	192.6	0.940	0.990	95
Stearate	135	100.00	676.8	0.327	0.342	96
Behenate	150	120.00	277.0	0.425	0.532	80
Lignocerate	115	130.00	192.0	0.547	0.617	89
Melissate	100	160.00	277.0	0.359	0.522	69

cation of the SPEAXS system. It, along with other film types have been characterized as described in our recent works cited in Ref. 5.

We have outlined above our procedures for determining the number of photons-emitted-per-pulse/steradian, i_0, from a "point" source for a particular atomic transition (characteristic line). In Ref. 1 we have also presented a similar procedure for the determination of the photons-emitted-per-pulse/steradian-eV, S_0, for a continuum distribution [see Ref. 1, Eq. (15)]. Finally, in Ref. 1 we have described a procedure for the determination of the line shape parameters from the experimental spectral line distribution (a spectral line distribution of area under the line equal to the total number of photons, i_0, emitted-per-pulse/steradian for the given transition and as defined above). For this line shape analysis, a fold of Gaussian and Lorentzian shape functions (the Voigt function) was assumed for a sufficiently accurate fit of the experimental line profile (see Ref. 1, Sec. III).

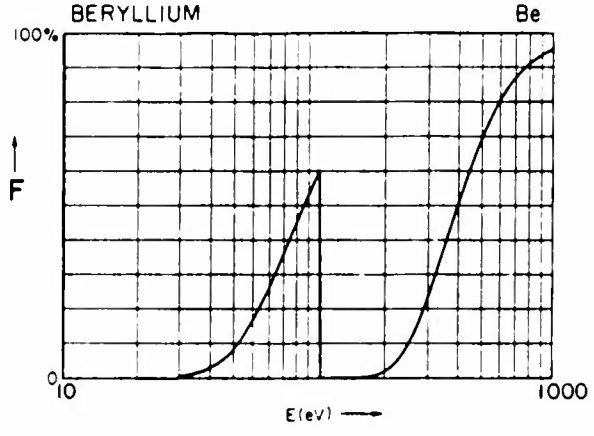
ACKNOWLEDGMENTS

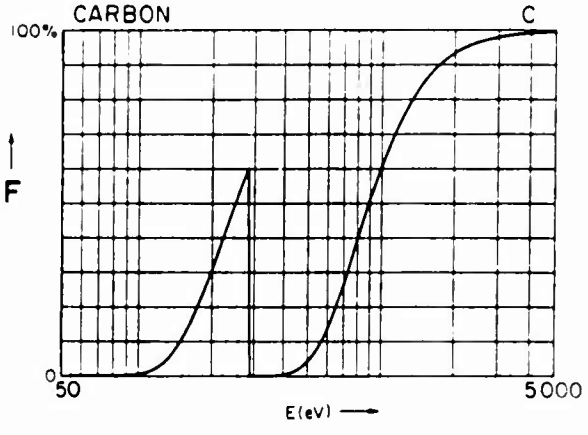
The authors gratefully acknowledge the invaluable assistance of the staff and students on this program, Priscilla Piano, Murray Tester, Ron Tackaberry, Cyril Lance, Siu Lung Kwok, Jeremy Uejio, and Gerald Young.

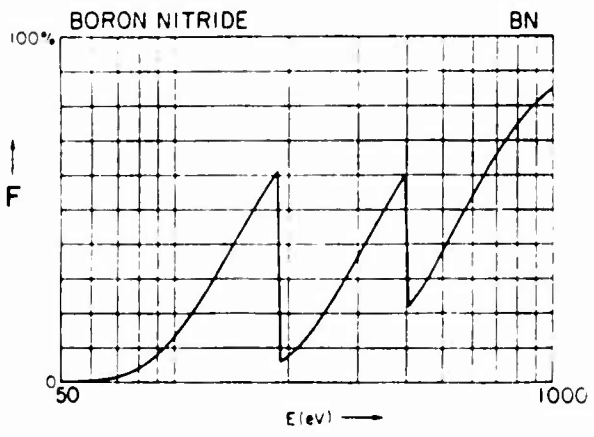
This project is part of an overall program on low-energy x-ray physics and technology now at the Center for X-Ray Optics—Lawrence Berkeley Laboratory, and supported by the Air Force Office of Scientific Research Grant No. 84-0001 and supplemented by the Department of Energy under Contract Nos. DE-AS08-83DP40181 (LANL/LLNL) and DE-AS08-82DP40175 (NLUF).

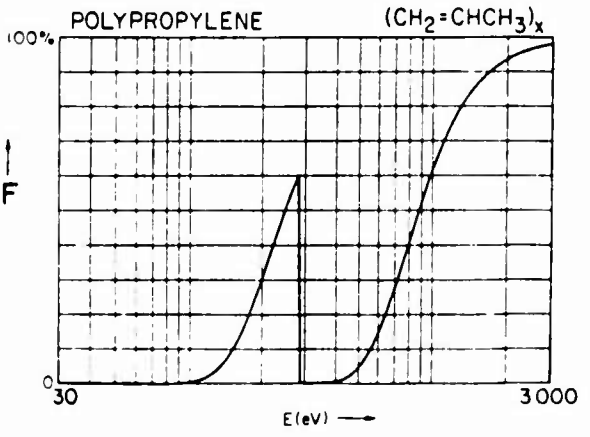
APPENDIX A

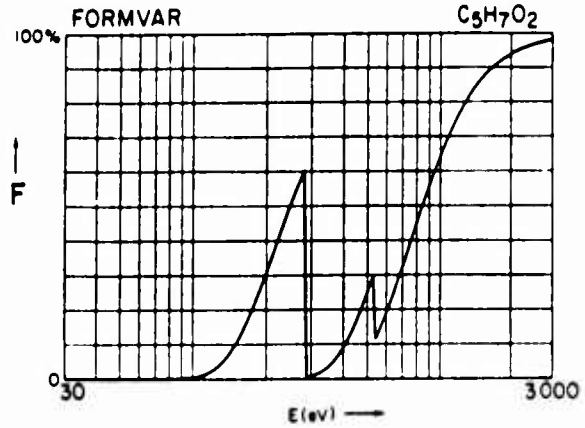
FIGS. A1–A25. Transmission band and low-energy cut-off characteristics of selected filters. [For the 100–10 000-eV region having filter thicknesses which yield transmission band peak values of about 60%. The corresponding mass thicknesses, $\rho\chi$ (μg/cm^2), are listed in Table II.]

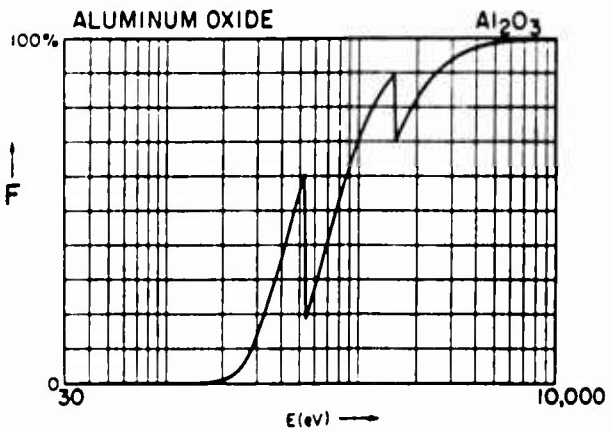


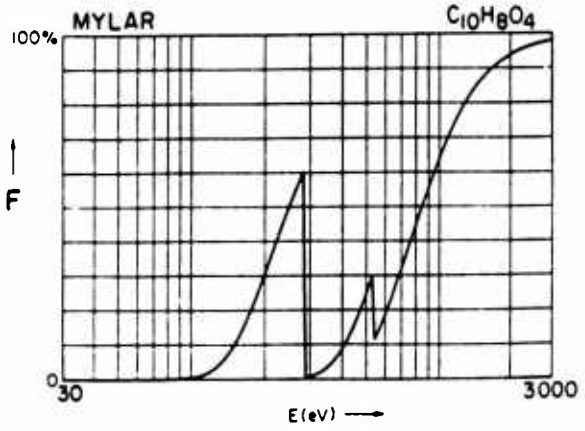


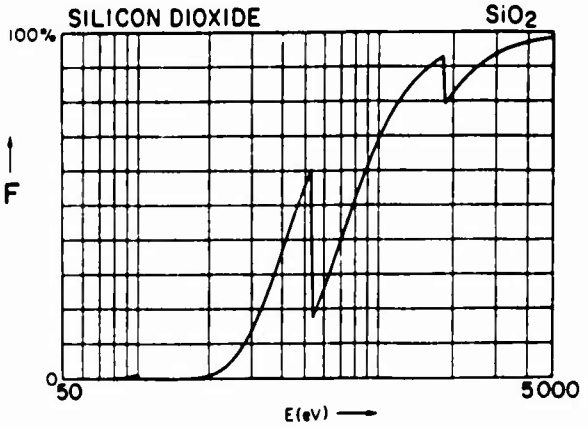


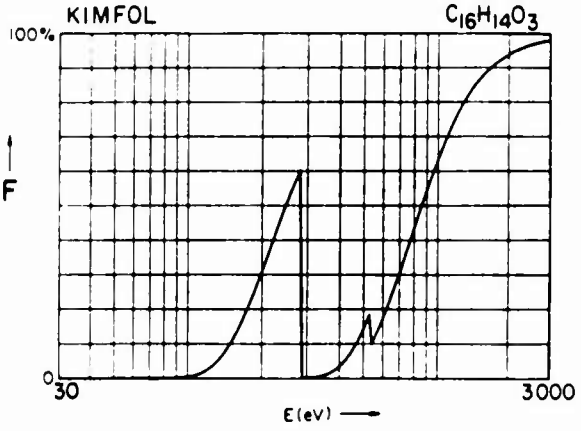


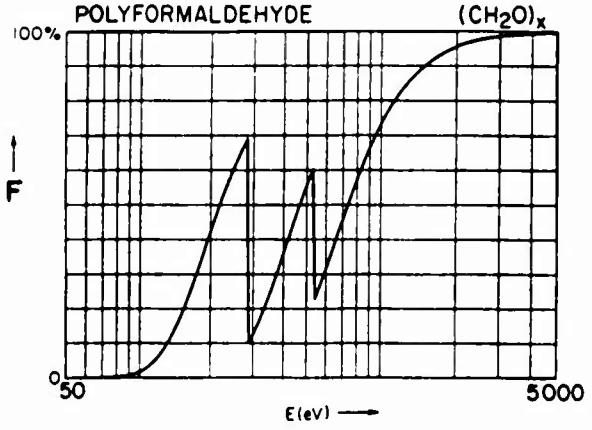

FORMVAR
$C_5H_7O_2$
100%
F
0
30
3000
E(eV)

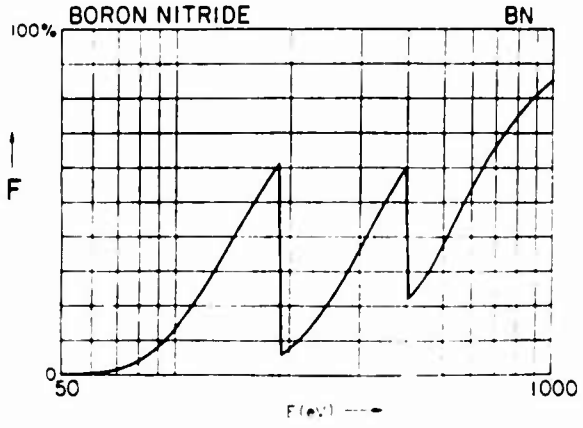

ALUMINUM OXIDE
Al_2O_3
100%
F
0
30
10,000
E(eV)

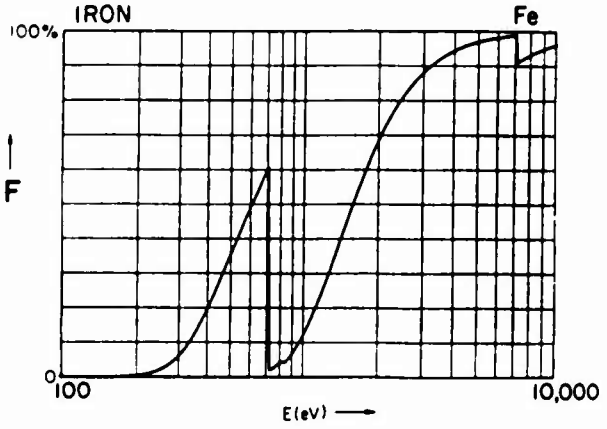

MYLAR
$C_{10}H_8O_4$
100%
F
0
30
3000
E(eV)

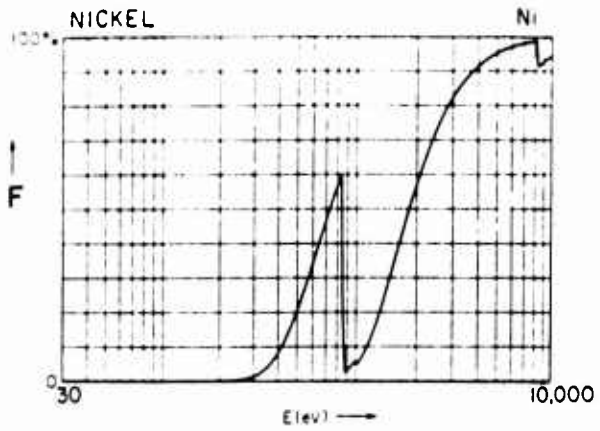

SILICON DIOXIDE
SiO_2
100%
F
0
50
5000
E(eV)

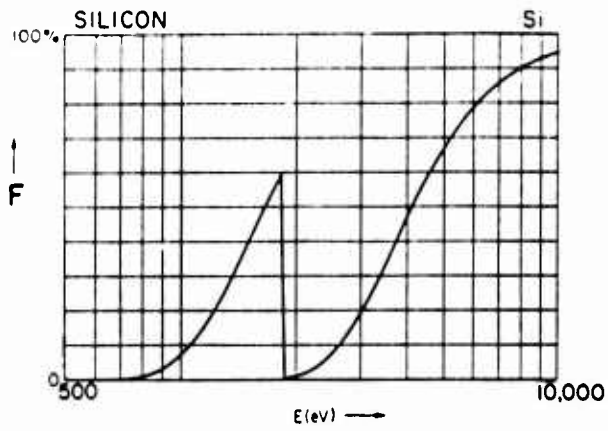

KIMFOL
$C_{16}H_{14}O_3$
100%
F
0
30
3000
E(eV)

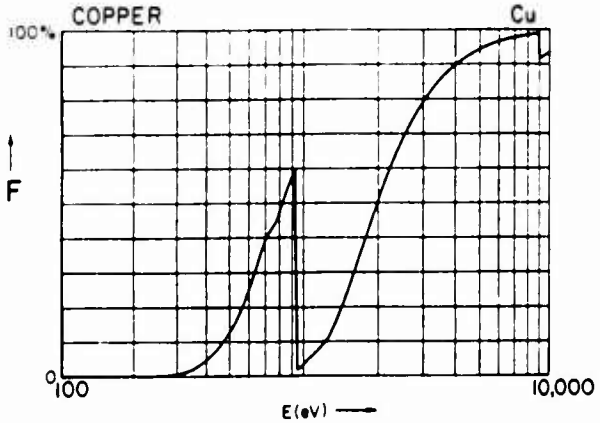

POLYFORMALDEHYDE
$(CH_2O)_x$
100%
F
0
50
5000
E(eV)

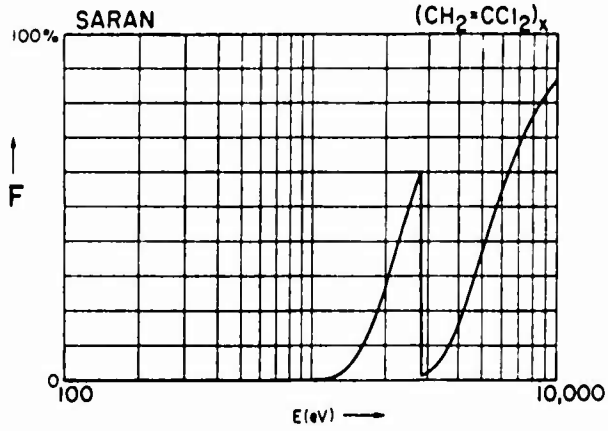

BORON NITRIDE
BN
100%
F
0
50
1000
E(eV)

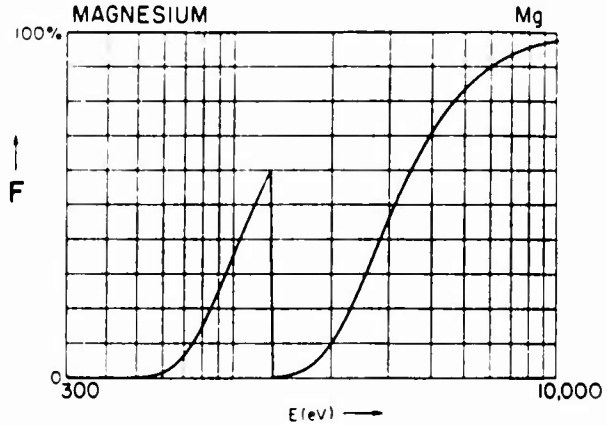

IRON
Fe
100%
F
0
100
10,000
E(eV)

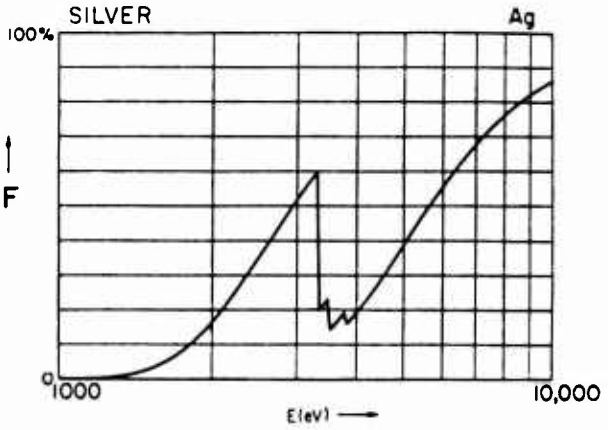

NICKEL
Ni
100%
F
0
30
10,000
E(eV)

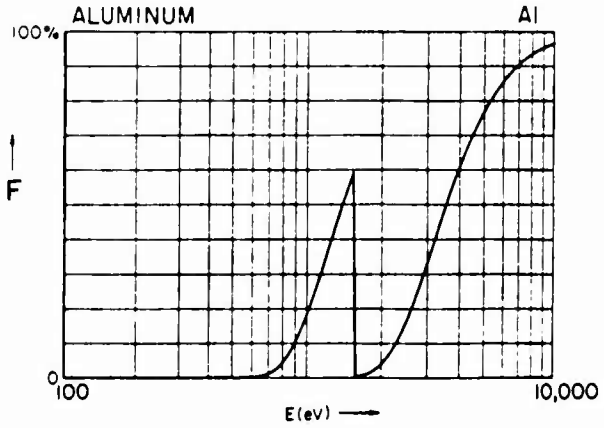

SILICON
Si
100%
F
0
500
10,000
E(eV)

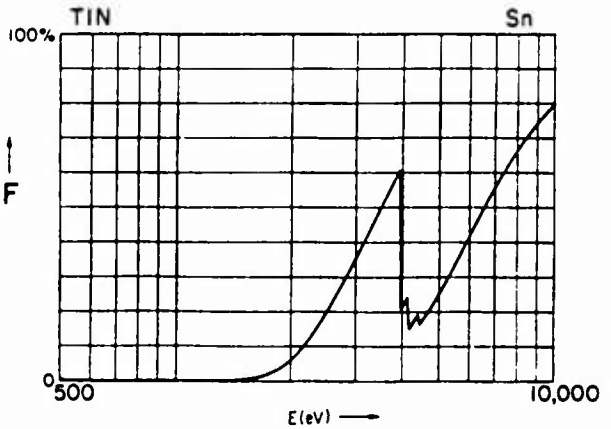

COPPER
Cu
100%
F
0
100
10,000
E(eV)

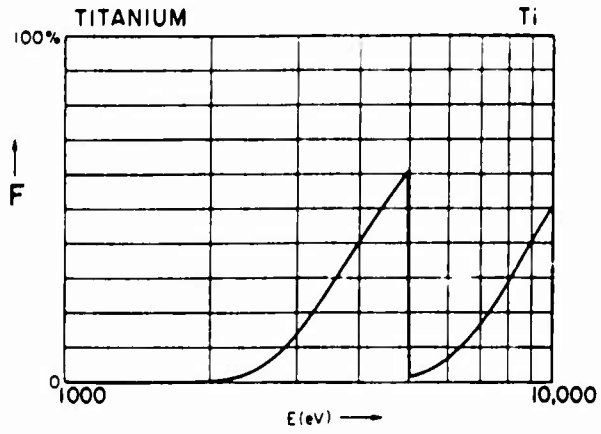

SARAN
$(CH_2{=}CCl_2)_x$
100%
F
0
100
10,000
E(eV)

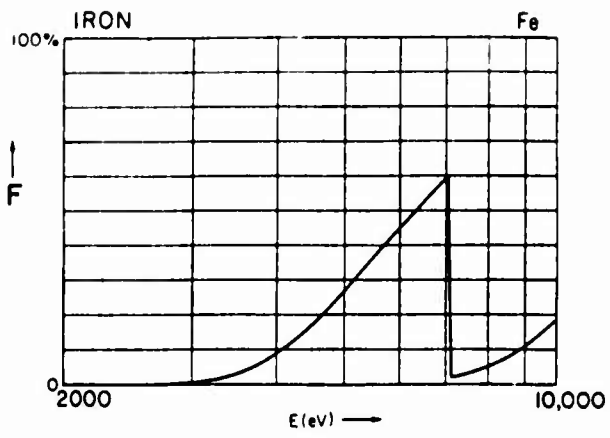

MAGNESIUM
Mg
100%
F
0
300
10,000
E(eV)

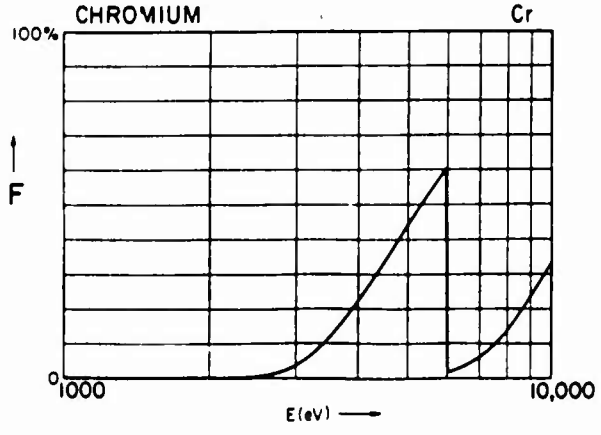

SILVER
Ag
100%
F
0
1000
10,000
E(eV)

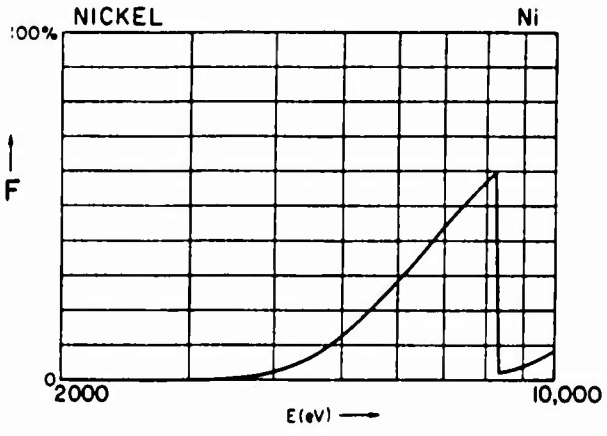

ALUMINUM
Al
100%
F
0
100
10,000
E(eV)

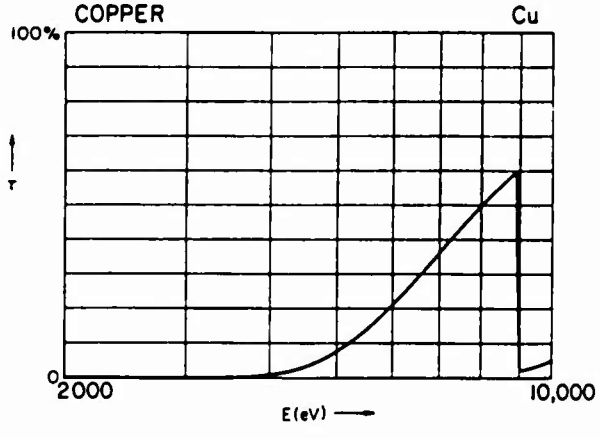

TIN
Sn
100%
F
0
500
10,000
E(eV)


TITANIUM
Ti
100%
F
0
1000
10,000
E(eV)


IRON
Fe
100%
F
0
2000
10,000
E(eV)

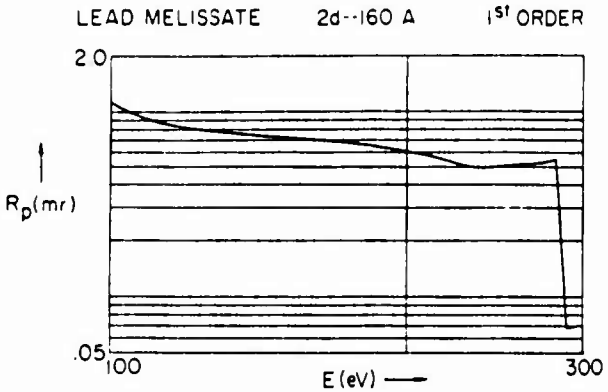

CHROMIUM
Cr
100%
F
0
1000
10,000
E(eV)

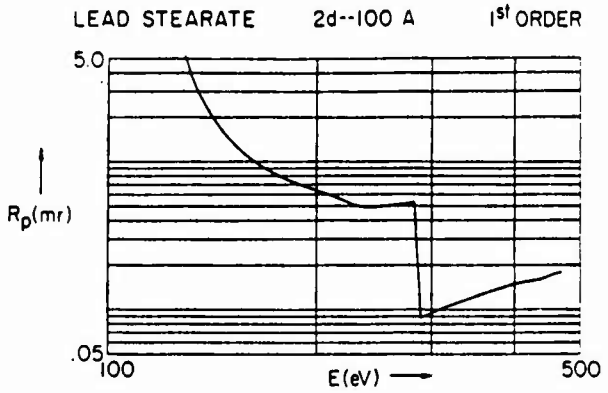

NICKEL
Ni
100%
F
0
2000
10,000
E(eV)

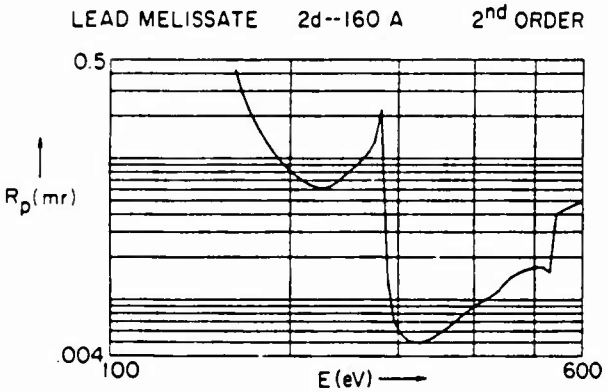

COPPER
Cu
100%
T
0
2000
10,000
E(eV)

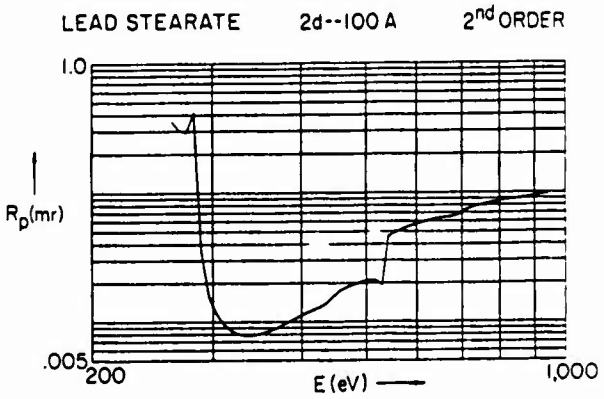
APPENDIX B

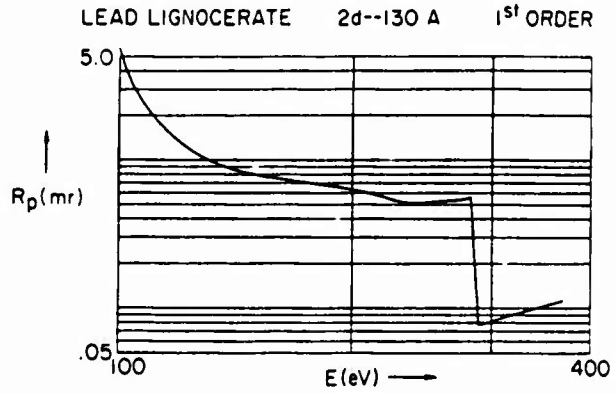
FIGS. B1–B20. Integrated reflectivity, R (Darwin–Prins), vs photon energy, E (eV), for first- and second-order diffraction from the eleven crystal/multilayer analyzers that have been listed in Table I and described in Fig. 7. These calculated values were for "thick" crystals (setting number of layers, N, equal to infinity).

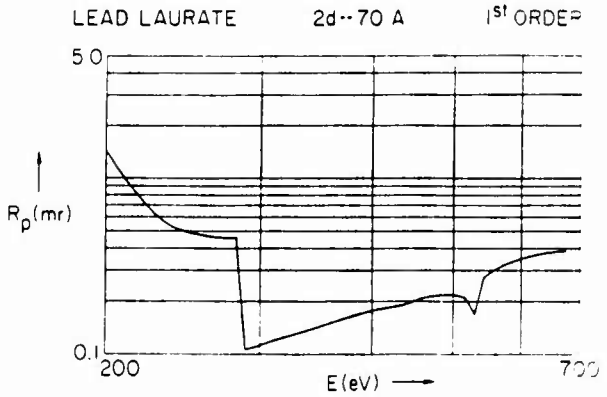


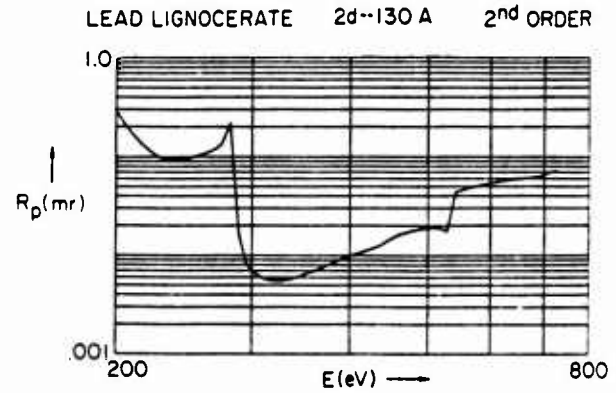


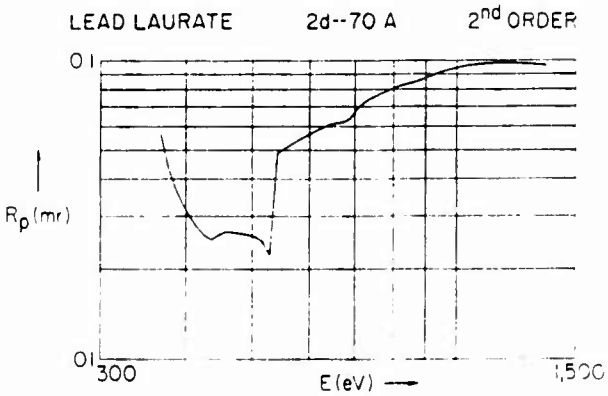


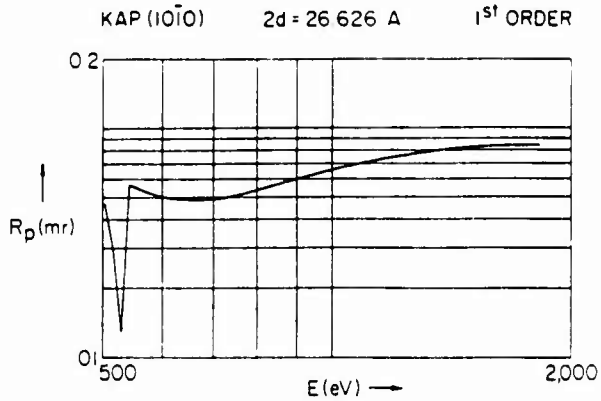


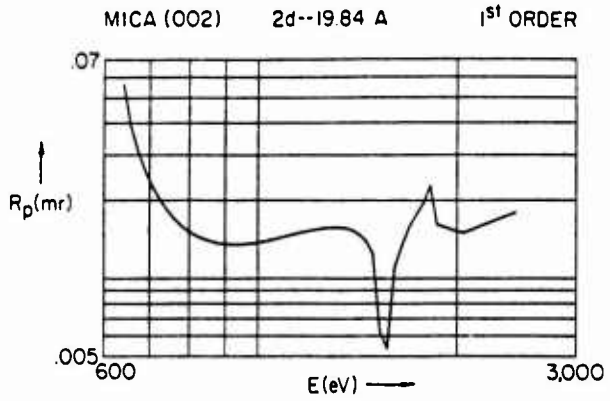


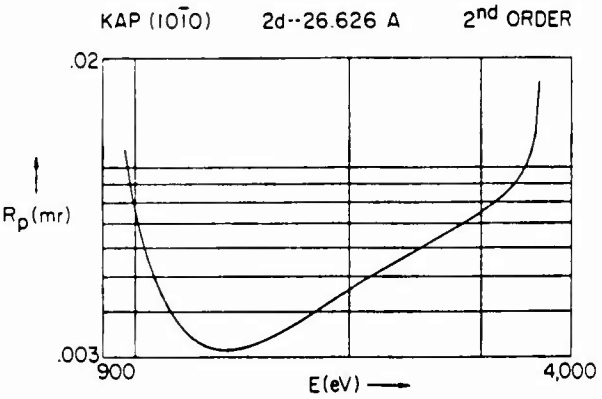


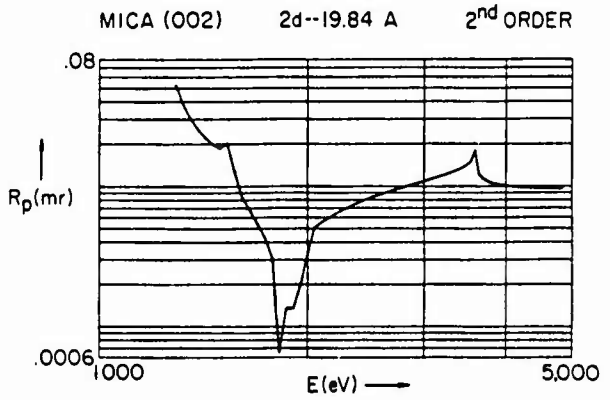


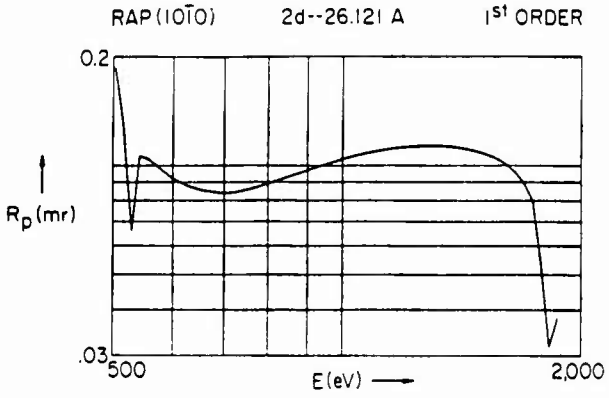


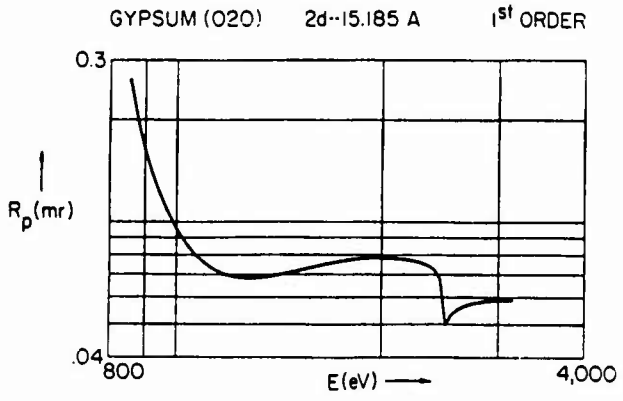

KAP (10$\bar{1}$0) 2d = 26.626 A 1st ORDER
0.2
0.1
R_p(mr)
500
2,000
E(eV)

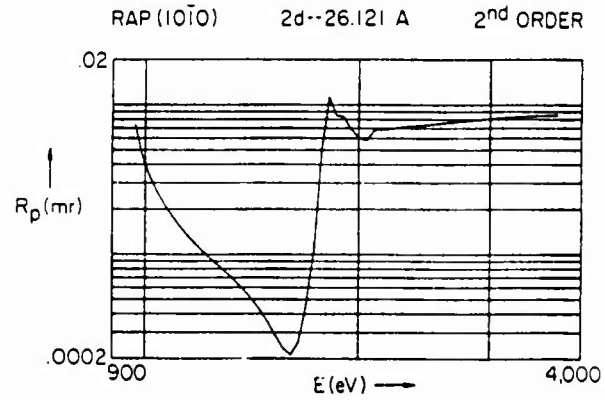

MICA (002) 2d--19.84 A 1st ORDER
.07
.005
R_p(mr)
600
3,000
E(eV)

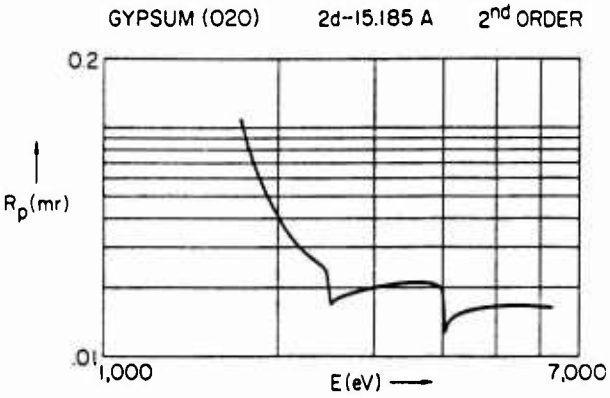

KAP (10$\bar{1}$0) 2d--26.626 A 2nd ORDER
.02
.003
R_p(mr)
900
4,000
E(eV)

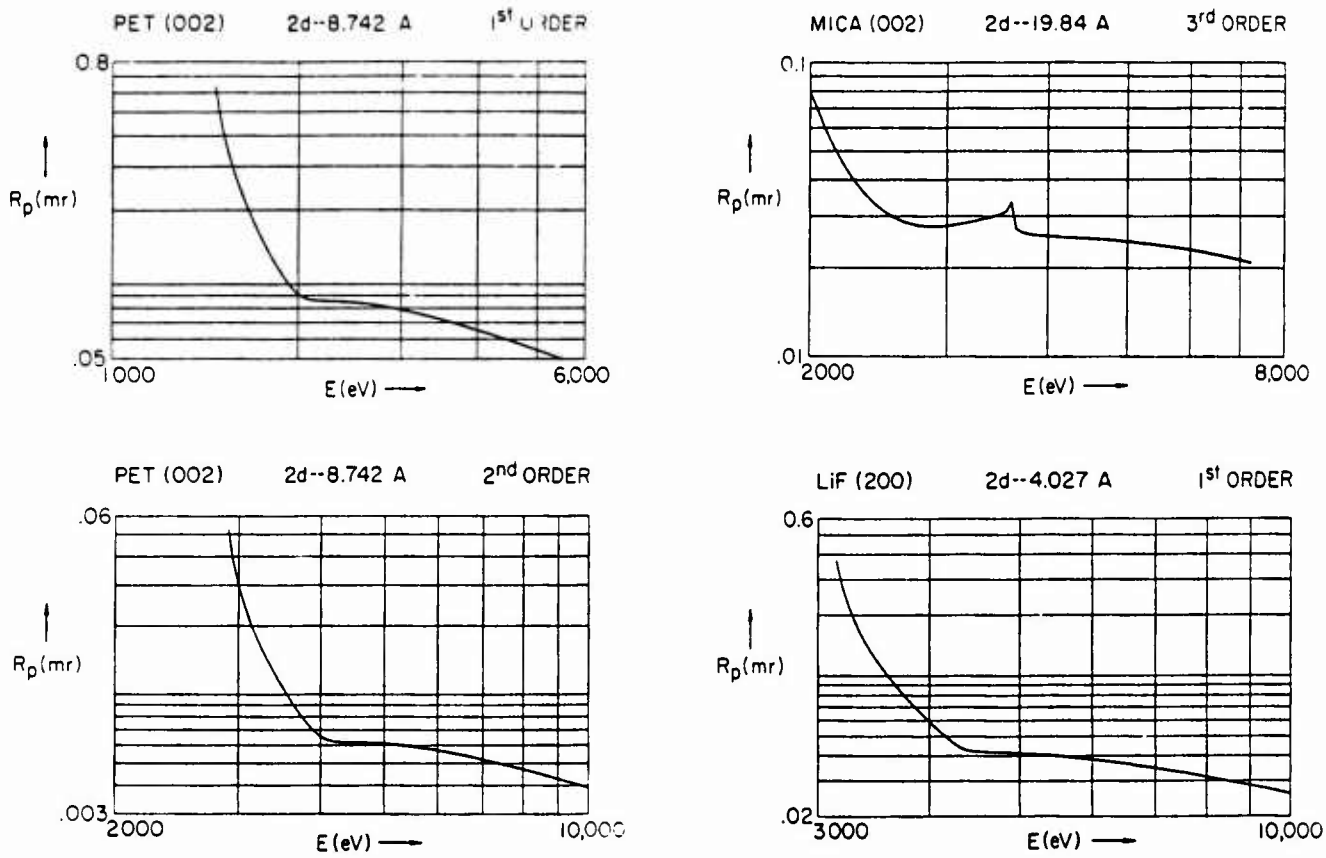

MICA (002) 2d--19.84 A 2nd ORDER
.08
.0006
R_p(mr)
1000
5,000
E(eV)


RAP (10$\bar{1}$0) 2d--26.121 A 1st ORDER
0.2
.03
R_p(mr)
500
2,000
E(eV)


GYPSUM (020) 2d--15.185 A 1st ORDER
0.3
.04
R_p(mr)
800
4,000
E(eV)


RAP (10$\bar{1}$0) 2d--26.121 A 2nd ORDER
.02
.0002
R_p(mr)
900
4,000
E(eV)


GYPSUM (020) 2d--15.185 A 2nd ORDER
0.2
.01
R_p(mr)
1,000
7,000
E(eV)



APPENDIX C

TABLE CI. A table of the exposures, I (photons/μm^2), for the RAR 2495 film at photon energies, E (eV), and wavelengths, λ (A) which yield specular photographic densities, D, in the range 0.2–2.0. These specular density values are as measured in the microdensitometry of photographic spectra when using the nominal 0.1 numerical aperture (nA) for both the illumination and the objective optics. (For the corresponding density values that apply with microdensitometry at other numerical apertures, see Ref. 5.)

2495 FILM--EXPOSURE, I(photons/μm^2)*

NET DENSITY,D
(SPECULAR-0.1×0.1 nA)

PHOTON ENERGY,E(eV)
WAVELENGTH,λ(A)

D

E(eV)	0.2	0.4	0.6	0.8	1.0	1.2	1.4	1.6	1.8	2.0	λ(A)
A											A
75	1.65 01	4.51 01	9.46 01	1.80 02	3.28 02	5.84 02	1.03 03	1.79 03	3.11 03	5.40 03	165.31
100	3.83 00	1.02 01	2.06 01	3.78 01	6.62 01	1.13 02	1.90 02	3.18 02	5.28 02	8.76 02	123.98
125	1.78 00	4.56 00	8.93 00	1.58 01	2.65 01	4.34 01	6.98 01	1.11 02	1.76 02	2.78 02	99.18
150	1.09 00	2.74 00	5.20 00	8.91 00	1.45 01	2.28 01	3.54 01	5.43 01	8.26 01	1.25 02	82.65
175	7.89-01	1.93 00	3.58 00	5.96 00	9.40 00	1.44 01	2.16 01	3.20 01	4.70 01	6.87 01	70.85
200	6.21-01	1.49 00	2.71 00	4.41 00	6.80 00	1.01 01	1.48 01	2.14 01	3.05 01	4.34 01	61.99
225	5.20-01	1.23 00	2.20 00	3.52 00	5.31 00	7.77 00	1.11 01	1.57 01	2.19 01	3.04 01	55.10
250	4.53-01	1.06 00	1.87 00	2.94 00	4.38 00	6.30 00	8.87 00	1.23 01	1.69 01	2.30 01	49.59
275	4.07-01	9.42-01	1.64 00	2.56 00	3.77 00	5.35 00	7.43 00	1.02 01	1.37 01	1.85 01	45.08
B											B
300	1.72 00	4.40 00	8.58 00	1.51 01	2.53 01	4.13 01	6.62 01	1.05 02	1.66 02	2.61 02	41.33
325	1.36 00	3.45 00	6.63 00	1.15 01	1.89 01	3.02 01	4.75 01	7.39 01	1.14 02	1.76 02	38.15
350	1.13 00	2.83 00	5.36 00	9.15 00	1.48 01	2.33 01	3.59 01	5.48 01	8.30 01	1.25 02	35.42
375	9.75-01	2.40 00	4.49 00	7.56 00	1.20 01	1.86 01	2.82 01	4.23 01	6.29 01	9.31 01	33.06
C											C
425	9.35-01	2.30 00	4.30 00	7.22 00	1.15 01	1.77 01	2.69 01	4.02 01	5.98 01	8.83 01	29.17
450	8.19-01	2.00 00	3.72 00	6.19 00	9.76 00	1.49 01	2.24 01	3.32 01	4.88 01	7.13 01	27.55
475	7.38-01	1.79 00	3.29 00	5.43 00	8.48 00	1.28 01	1.90 01	2.78 01	4.04 01	5.84 01	26.10
500	6.74-01	1.62 00	2.95 00	4.83 00	7.46 00	1.12 01	1.64 01	2.37 01	3.40 01	4.85 01	24.80

TABLE CI Cont'd.

E(eV)	0.2	0.4	0.6	0.8	1.0	1.2	1.4	1.6	1.8	2.0	λ(A)
D											D
550	9.92-01	2.45 00	4.61 00	7.78 00	1.25 01	1.94 01	2.95 01	4.45 01	6.66 01	9.92 01	22.54
600	8.29-01	2.02 00	3.73 00	6.20 00	9.74 00	1.48 01	2.21 01	3.27 01	4.78 01	6.95 01	20.66
650	7.17-01	1.72 00	3.14 00	5.13 00	7.92 00	1.18 01	1.74 01	2.51 01	3.60 01	5.13 01	19.07
700	6.38-01	1.52 00	2.72 00	4.39 00	6.68 00	9.83 00	1.42 01	2.01 01	2.83 01	3.97 01	17.71
750	5.85-01	1.37 00	2.44 00	3.87 00	5.80 00	8.41 00	1.19 01	1.67 01	2.30 01	3.16 01	16.53
800	5.45-01	1.27 00	2.22 00	3.48 00	5.14 00	7.34 00	1.02 01	1.41 01	1.92 01	2.59 01	15.50
850	5.14-01	1.18 00	2.05 00	3.17 00	4.63 00	6.52 00	8.97 00	1.22 01	1.63 01	2.17 01	14.59
900	4.91-01	1.12 00	1.92 00	2.94 00	4.24 00	5.90 00	8.03 00	1.07 01	1.42 01	1.87 01	13.78
950	4.73-01	1.07 00	1.81 00	2.75 00	3.93 00	5.42 00	7.29 00	9.64 00	1.26 01	1.63 01	13.05
1000	4.59-01	1.03 00	1.73 00	2.60 00	3.68 00	5.02 00	6.69 00	8.76 00	1.13 01	1.45 01	12.40
1100	4.40-01	9.71-01	1.61 00	2.39 00	3.33 00	4.47 00	5.85 00	7.53 00	9.58 00	1.21 01	11.27
1200	4.30-01	9.39-01	1.54 00	2.26 00	3.11 00	4.12 00	5.33 00	6.78 00	8.52 00	1.06 01	10.33
1300	4.27-01	9.24-01	1.51 00	2.18 00	2.98 00	3.92 00	5.03 00	6.34 00	7.90 00	9.77 00	9.54
1400	4.30-01	9.24-01	1.50 00	2.16 00	2.92 00	3.82 00	4.87 00	6.11 00	7.57 00	9.32 00	8.86
1500	4.37-01	9.37-01	1.51 00	2.17 00	2.93 00	3.80 00	4.83 00	6.03 00	7.45 00	9.15 00	8.27
E											E
1800	3.44-01	7.39-01	1.19 00	1.72 00	2.32 00	3.02 00	3.84 00	4.81 00	5.95 00	7.31 00	6.89
1900	3.49-01	7.47-01	1.20 00	1.72 00	2.33 00	3.03 00	3.84 00	4.79 00	5.92 00	7.26 00	6.53
2000	3.59-01	7.67-01	1.23 00	1.76 00	2.37 00	3.08 00	3.90 00	4.86 00	5.99 00	7.34 00	6.20
2100	3.70-01	7.88-01	1.26 00	1.80 00	2.43 00	3.14 00	3.97 00	4.94 00	6.09 00	7.46 00	5.90
2200	3.84-01	8.18-01	1.31 00	1.87 00	2.51 00	3.24 00	4.09 00	5.09 00	6.27 00	7.67 00	5.64
2300	4.01-01	8.52-01	1.36 00	1.94 00	2.60 00	3.36 00	4.24 00	5.28 00	6.49 00	7.95 00	5.39
2400	4.19-01	8.90-01	1.42 00	2.02 00	2.71 00	3.50 00	4.42 00	5.49 00	6.76 00	8.28 00	5.17
2500	4.40-01	9.33-01	1.49 00	2.12 00	2.84 00	3.66 00	4.62 00	5.74 00	7.07 00	8.66 00	4.96
3000	5.71-01	1.21 00	1.93 00	2.74 00	3.67 00	4.74 00	5.98 00	7.43 00	9.16 00	1.13 01	4.13
F											F
4000	4.97-01	1.05 00	1.68 00	2.39 00	3.19 00	4.12 00	5.20 00	6.46 00	7.96 00	9.78 00	3.10
5000	7.37-01	1.56 00	2.49 00	3.54 00	4.74 00	6.12 00	7.73 00	9.63 00	1.19 01	1.47 01	2.48
6000	1.09 00	2.30 00	3.67 00	5.22 00	7.00 00	9.05 00	1.14 01	1.43 01	1.77 01	2.18 01	2.07
7000	1.56 00	3.30 00	5.27 00	7.50 00	1.01 01	1.30 01	1.65 01	2.06 01	2.55 01	3.15 01	1.77
8000	2.17 00	4.59 00	7.33 00	1.04 01	1.40 01	1.81 01	2.29 01	2.87 01	3.56 01	4.41 01	1.55
9000	2.93 00	6.21 00	9.91 00	1.41 01	1.89 01	2.45 01	3.11 01	3.88 01	4.82 01	5.98 01	1.38
10000	3.86 00	8.18 00	1.31 01	1.86 01	2.50 01	3.23 01	4.10 01	5.13 01	6.37 01	7.90 01	1.24

* In our notation in this table, a number followed by a space and another number indicates that the first number is to be multiplied by 10 raised to the power of the second number; e.g., 1.27 -01 means 1.27×10^{-1}.
A - Br-M_4 edge; B - C-K edge; C - N-K, Ag-$M_{4,5}$ edges; D - O-K edge; E - Br-$L_{3,2}$ edge; F - Ag-$L_{3,2}$ edge.

[a] University of Rochester, Laboratory for Laser Energetics, 250 East River Road, Rochester, New York 14623.

[1] B. L. Henke, H. T. Yamada, and T. J. Tanaka, Rev. Sci. Instrum. **54**, 1311 (1983).

[2] B. L. Henke, N. S. Balakrishnan, and A. R. Bird, *Multilayer Analyzers for Low-Energy X-Ray Spectroscopy (100–500 eV): Part II. Construction and Characterization* (in preparation).

[3] B. L. Henke, *Low Energy X-Ray Interactions: Photoionization, Scattering, Specular and Bragg Reflection,* AIP Conference Proceedings No. 75, edited by D. T. Attwood and B. L. Henke (American Institute of Physics, New York, 1981), 85.

[4] B. L. Henke, P. Lee, T. J. Tanaka, R. L. Shimabukuro, and B. K. Fujikawa, *Atomic Data and Nuclear Data Tables 27* (Academic, New York, 1982), No. 1.

[5] B. L. Henke, S. L. Kwok, J. Y. Uejio, H. T. Yamada, and G. C. Young, J. Opt. Soc. Am. B **1**, 818 (1984); B. L. Henke, F. G. Fujiwara, M. A. Tester, C. H. Dittmore, and M. A. Palmer, J. Opt. Soc. Am. B **1**, 828 (1984).

[6] P. A. Jaanimagi and B. L. Henke, *Large Aperture Picosecond X-Ray Streak Camera* (to be published).

[7] B. L. Henke, J. P. Knauer, and K. Premaratne, J. Appl. Phys. **52**, 1509 (1981).

[8] B. L. Henke, F. G. Fujiwara, R. E. Tackaberry, and D. Kania, *Reflectivity Characteristics of Low-Energy Mirror Monochromators* (in preparation).

[9] B. L. Henke, H. T. Yamada, G. C. Young, S. L. Kwok, and J. Y. Uejio, Proceedings of the International Society for Optical Engineering (SPIE) Conference, San Diego, CA, Aug. 18–23, 1985.

3. TECHNICAL NOTES: FILTER-MIRROR PRIMARY MONOCHROMATORS

Associated with the absolute spectrometry of the large plasma and synchrotron x-radiation sources is the often difficult task of rejecting the intense longer and shorter wavelengths which can be strong sources of background scattered-and-fluorescent radiations and of high-order diffracted radiations. Illustrated in Fig. 1 is the generation of a transmission band for the rejection of such background radiations around the 500-1000 eV region by combining as a primary monochromator a 300 $\mu g/cm^2$ copper foil filter and a 30 milliradian reflection from an aluminized x-ray mirror. A copper foil of this thickness is self-supporting and is opaque to the intense uv and longer wavelength light also that is associated, for example, with the laser-produced and synchrotron radiation sources.

Fabrication of Low Energy X-Ray Filters

For the design and construction of light-opaque filters having transmission bands below 500 eV we have developed the following procedures:

(a) From our absorption tables we choose metallic elements which have a minimum in their absorption curves where a filter transmission band is required. Also the reflectivity and extinction coefficients for a thin film of this metal must be relatively high for the intense uv and longer wavelengths light of the source.

The metal film is deposited upon both sides of a Formvar-coated 30 $\mu g/cm^2$ carbon foil--very gently with a low power sputtering beam from a focussing Magnetron source (over a period of one to two hours). This slow sputtered deposition upon a rotating window mounted with a mirror-like, carbon foil produces a coating that is uniform, also mirror-like and with minimized and equalized stresses (as compared to those often obtained by deposition with evaporation sources). Our simple apparatus for fabricating these ultra-thin, self-supporting filter systems is shown in Fig. 2.

Shown in Fig. 3 is a the transmission curve of a filter that was designed and constructed as described above, to be about 59% transmissive at 200 eV and with transmission for the 351 nm uv light of OMEGA of 10^{-6}. For this filter 50 $\mu g/cm^2$ of molybdenum was deposited on each side of the 30 $\mu g/cm^2$ carbon foil.

In Table 1 is reproduced the sputtering rates of some useful filter materials.

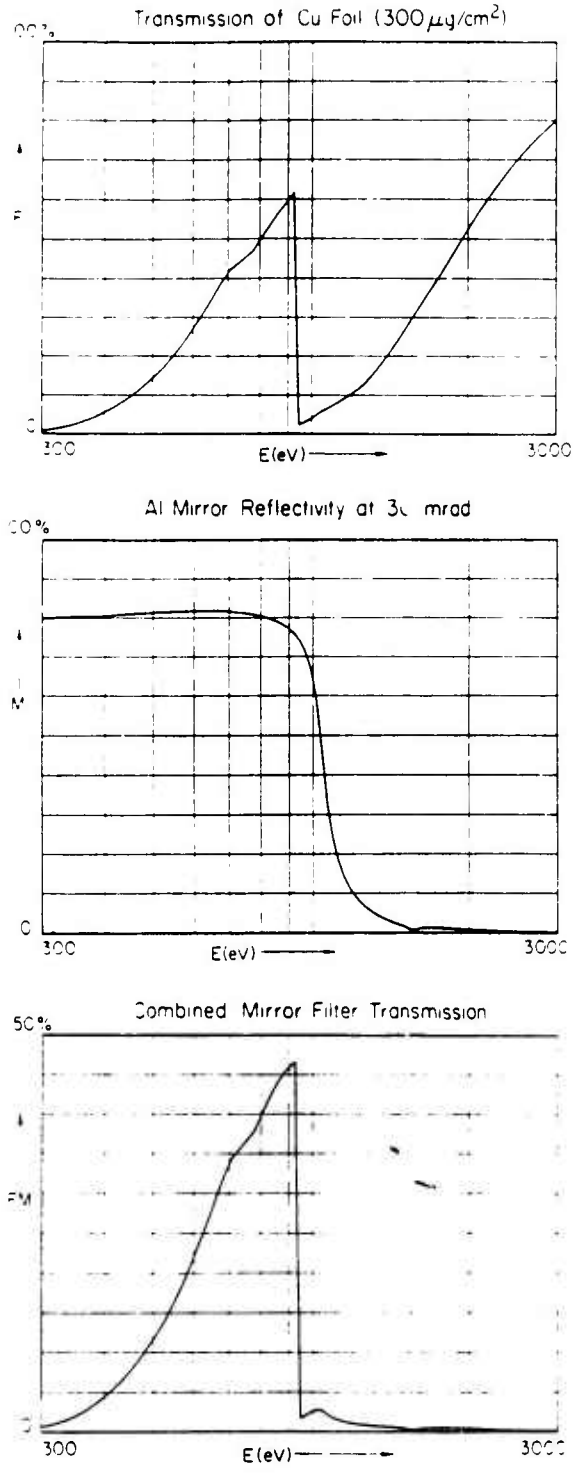
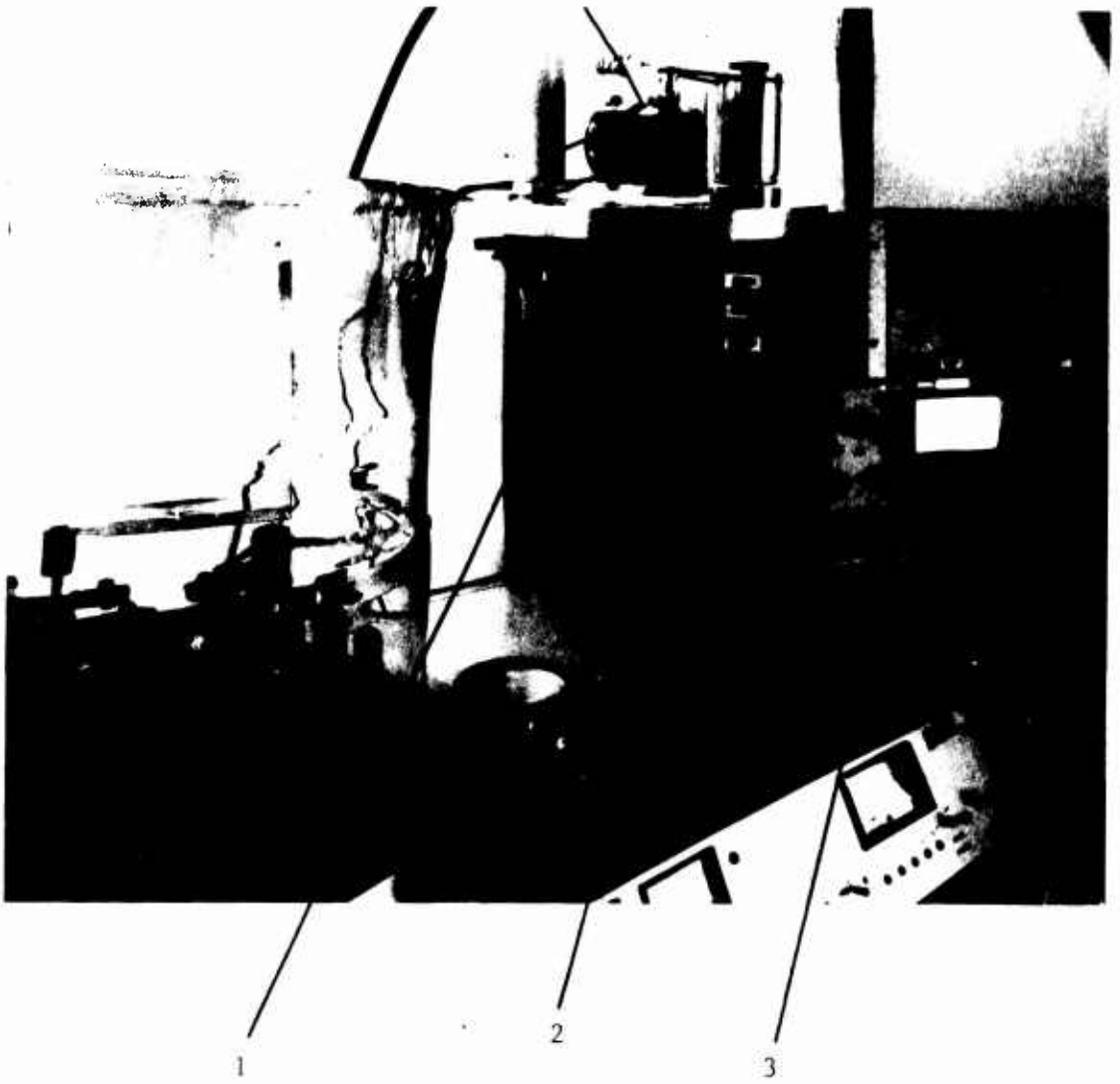


Figure 1. A filter-mirror primary monochromator for a transmission band around 800 eV.

Figure 2
Sputtering System
for the
Fabrication of Light-Opaque
Low Energy X-Ray Filters

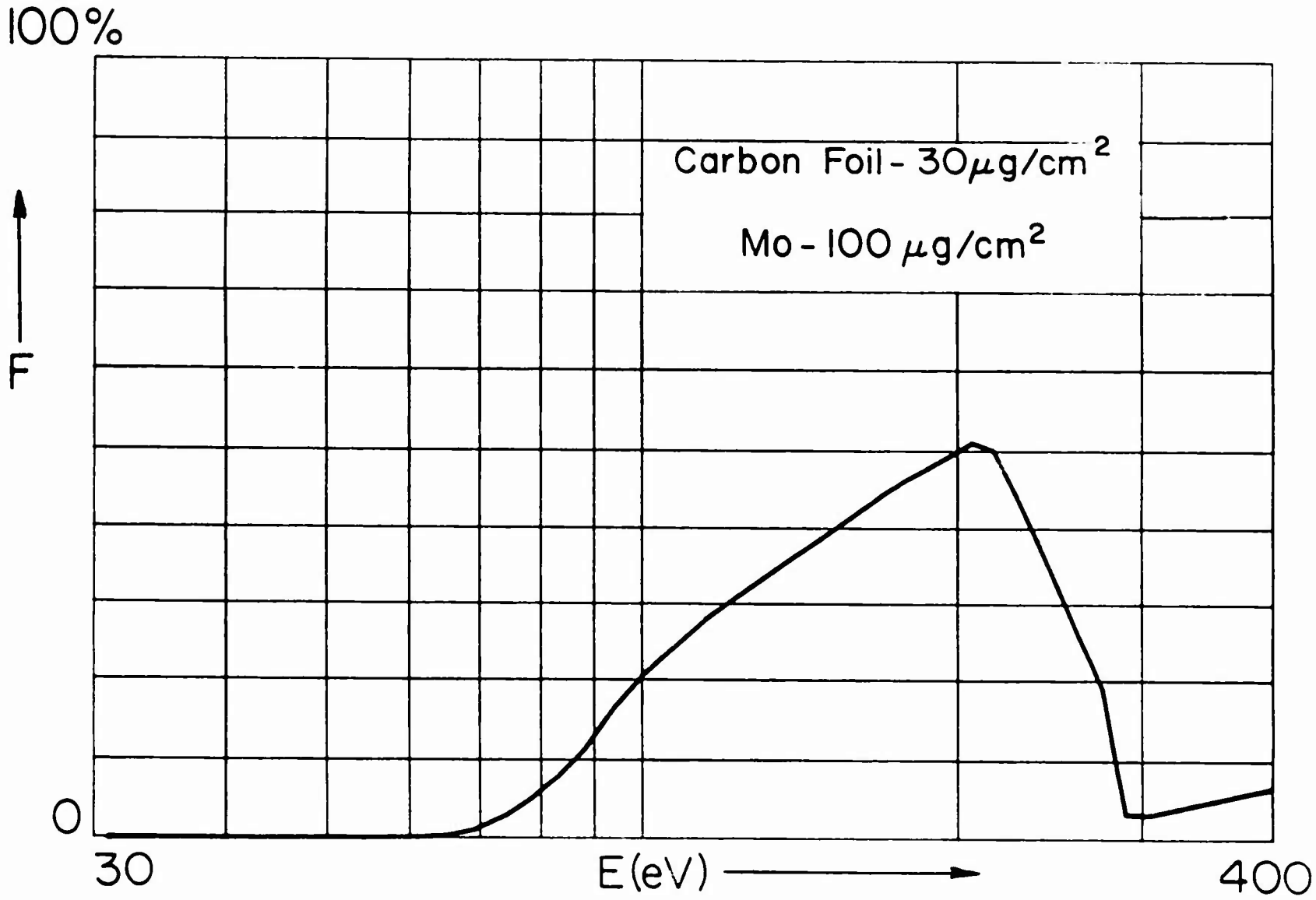


1 - Plasma Magnetron DC Sputter Source
2 - Rotating Filter-Window Assemblies
3 - Constant DC Power Supply and Baritron Pressure Gaging

A conventional, LN trapped, diffusion pump vacuum evaporation system is applied interchangeably for the sputter coating of thin x-ray filter systems. The bell jar is replaced by a glass cylinder on top of which is mounted a baseplate (sealed with an L-type Viton gasket) which supports the magnetron plasma source and a variable spead motor driven sample rotisserie. The high vacuum rotational feed-through is magnetic coupled.

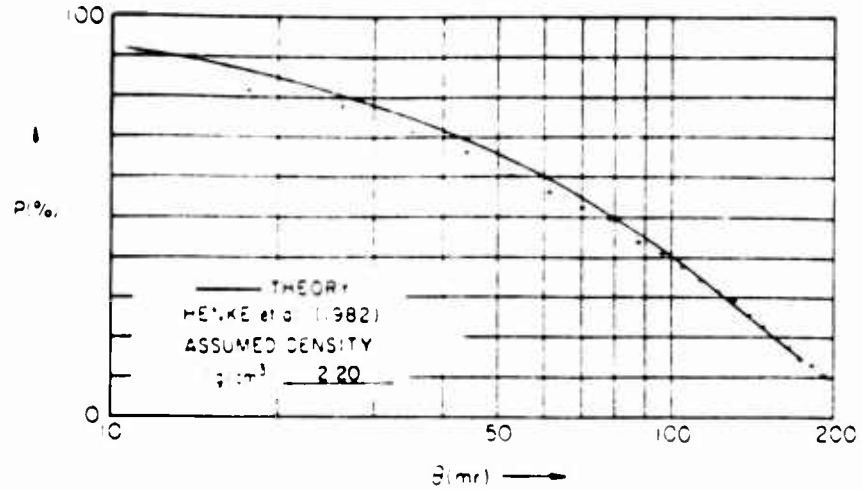
Figure 3

Transmission of Molybdenum - Coated Carbon Foil



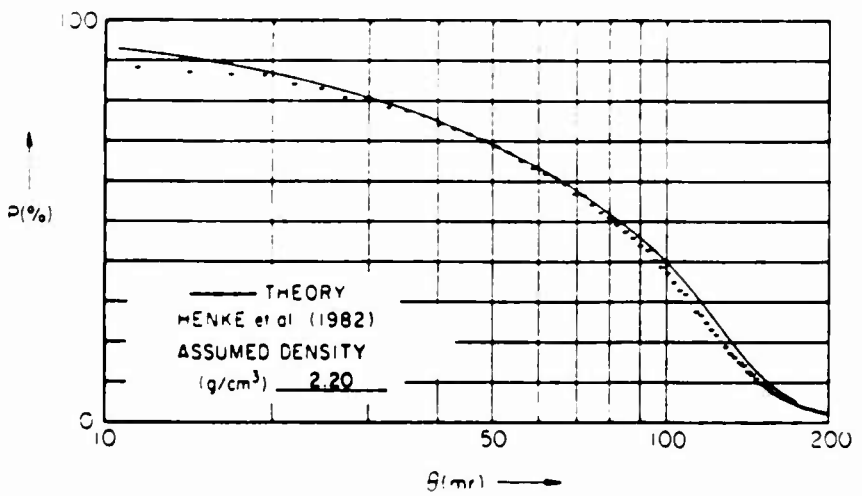
REFLECTIVITY, P(%)-VS-θ(mrad)

FUSED QUARTZ E = 108.5 eV



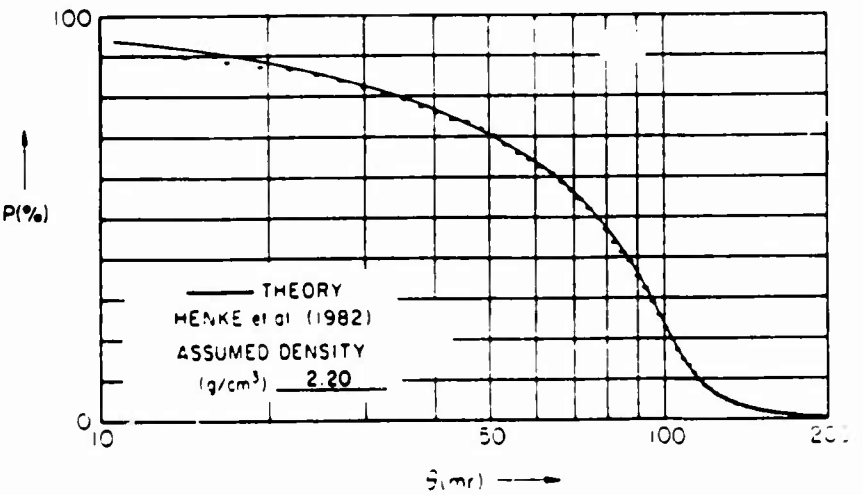
REFLECTIVITY, P(%)-VS-θ(mrad)

FUSED QUARTZ E = 192.6 eV



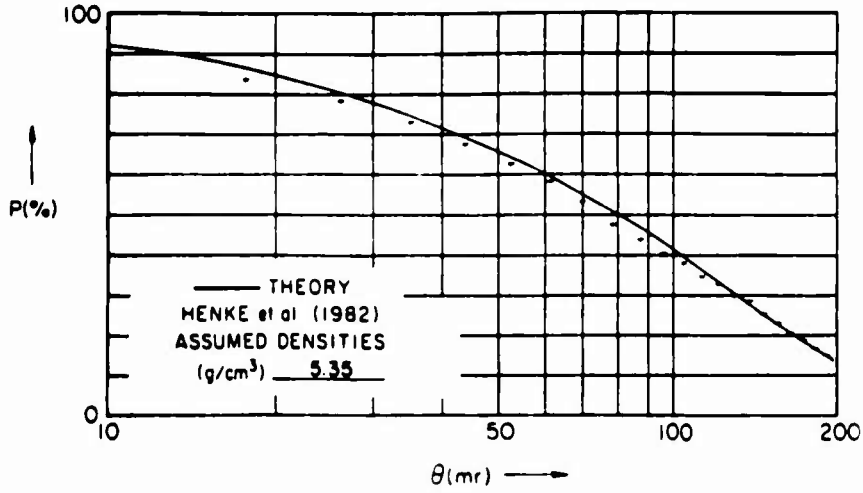
REFLECTIVITY, P(%)-VS-θ(mrad)

FUSED QUARTZ E = 277.0 eV



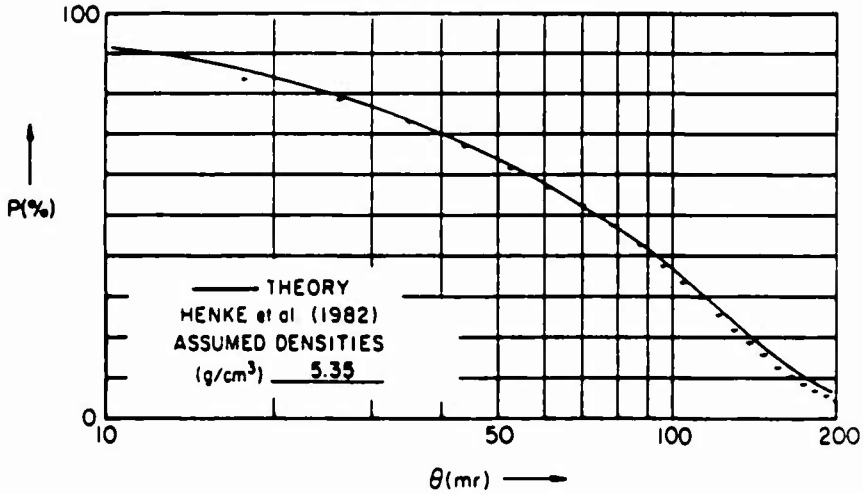
REFLECTIVITY, P(%)-VS-θ(mrad)

Ge — E = 108.5 eV



REFLECTIVITY, P(%)-VS-θ(mrad)

Ge — E = 192.6 eV



REFLECTIVITY, P(%)-VS-θ(mrad)

Ge — E = 277.0 eV

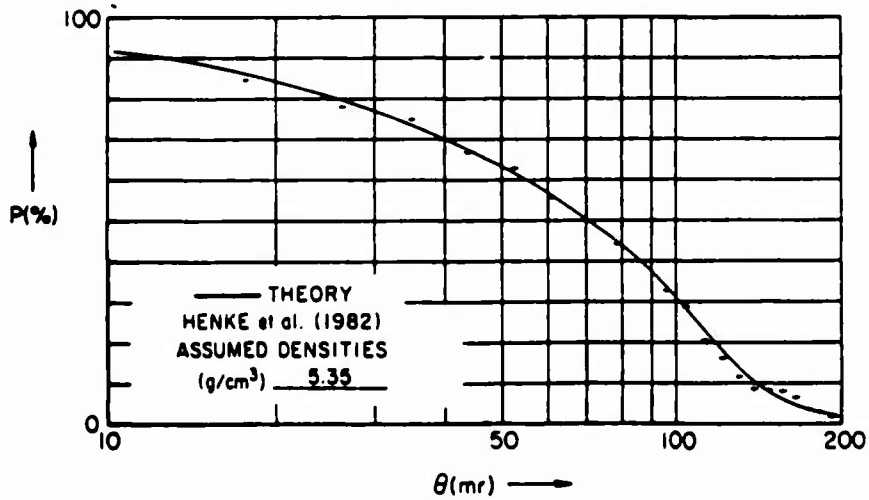


Table 1 (a) Sputtering Yields for Various Materials Bombarded by Ar^+ (Compiled by Maissel)**

Target	Bombarding energy, kV					
	0.2	0.6	1	2	5	10
Ag	1.6	3.4				8.8
Al	0.35	1.2				
Au	1.1	2.8				
Co	0.6	1.4				
	0.7	1.3				
Cu	1.1	2.3	3.2	4.3	5.5	6.6
Fe	0.5	1.3	1.4	2.0*	2.5*	
Ge	0.5	1.2	1.5	2.0	3.0	
Mo	0.4	0.9	1.1			2.2
Nb	0.25	0.65				
Ni	0.7	1.5	2.1			
Os	0.4	0.95				
Pd	1.0	2.4				
Pt	0.6	1.6				
Re	0.4	0.9				
Rh	0.55	1.5				
Si	0.2	0.5	0.6	0.9	1.4	
Ta	0.3	0.6				
Th	0.3	0.7				
Ti	0.2	0.6				
U	0.35	1.0				
W	0.3	0.6				
Zr	0.3	0.75				
GaSb (111)	0.4	0.9	1.2			
SiC		1.8				

*Type 304 stainless steel.

**L.I. Maissel, in "Physics of Thin Films" (G.Hass and R.E. Thun, eds.), Vol. 3, p. 61, Academic Press Inc., New York, 1966.

Characterization of X-Ray Mirrors

Several years ago we initiated an on-going investigation of the reflectivity characteristics of grazing incidence x-ray mirrors in collaboration with LANL and LLNL (Kania, Day and Kauffman). Generally, we find that state-of-the-art quality mirror surfaces reflected x-radiations of wavelengths not close to a mirror absorption edge wavelength according to the E&M Fresnel Eq. using optical constants derived from our calculated atomic scattering factors, f_1 and f_2. This reassuring predictability is illustrated in some examples of our measurements that are presented here at several photon energies of the percent reflectivity vs grazing incidence angle (milliradians) for three high optical quality mirror surfaces, fused quartz, aluminized fused quartz and germanium. We also found generally that with well characterized systems consisting of thin evaporated films (20 to 1000 A thickness) upon fused quartz, the measured reflectivity curves were closely predicted by a three-media solution of Maxwell's Eq. (vacuum-thin film-fused quartz substrate).

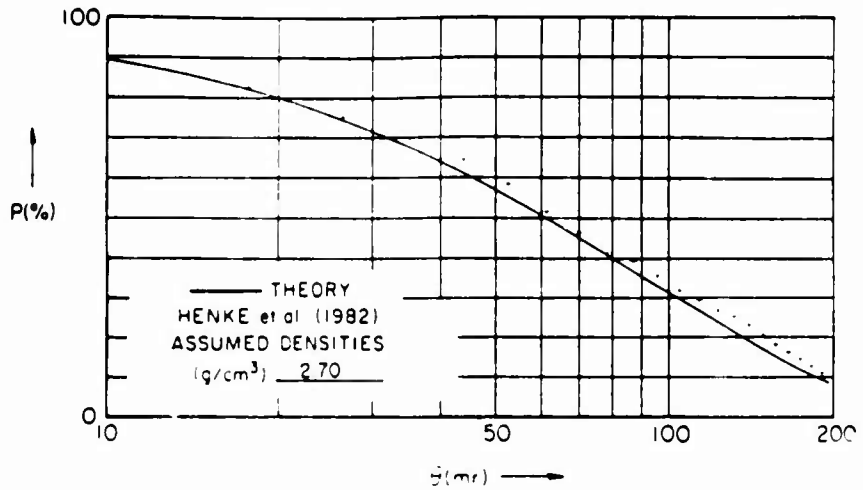
In order to derive an accurate semi-empirical analytical description for the reflectivity of a monochromator mirror that reflectivity should be measured at several photon energies in the region of application to determine if all are well fit by the Fresnel analytical equation. If at all but, say, at one photon energy are well fit by the Fresnel Eq., the atomic scattering factors, f_1 and f_2, at the photon energy of the poor fit curve may be adjusted. If a good fit is thus obtained for that curve as well we then have a basis for considering revising these particular atomic scattering factor values. This procedure is particularly important for photon energies very close to absorption thresholds where condensed matter effects often prevent the scattering from being "atomic-like".

In the event that the reflectivity curves cannot be closely fit by the Fresnel Eq. for any of the several photon energies, we then try to fit the several curves with a modified Fresnel Eq. that is based upon a simple modeling of surface roughness with one or two constant parameters determined empirically. Finally, if a surface film, e.g. an oxide layer, is suspected, a better semi-empirical analytical description may be found using a three-media E&M model solution for the reflectivity.

Because of the practical importance of mirrors in x-ray optics and spectrometry and because their modeling can yield valuable insights about interface structure and indeed about the accuracy of available optical constants and atomic scattering factors, we consider this on-going study of mirror reflectivity to be an important effort to continue.

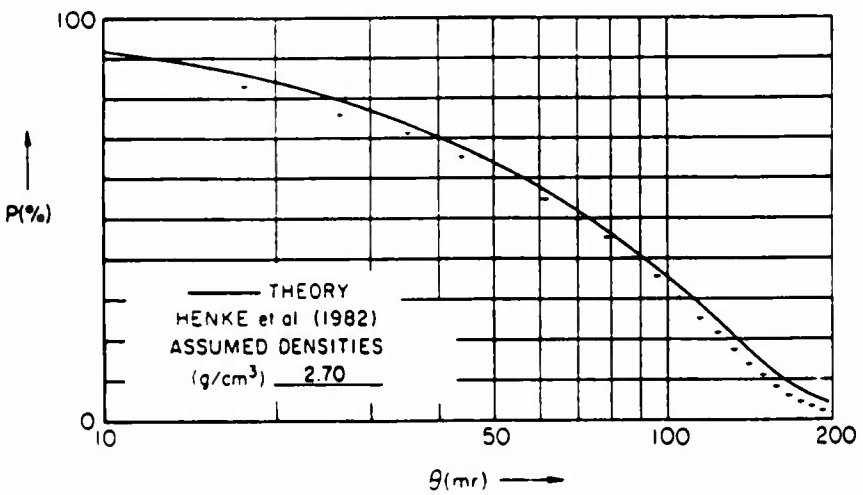
REFLECTIVITY, P(%)-VS-θ(mrad)

Al — E = 108.5 eV



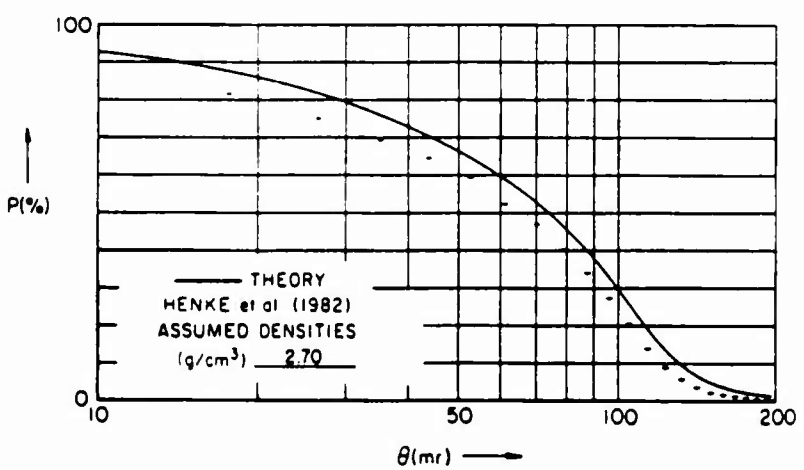
REFLECTIVITY, P(%)-VS-θ(mrad)

Al — E = 192.6 eV



REFLECTIVITY, P(%)-VS-θ(mrad)

Al — E = 277.0 eV



4.

Characterization of multilayer x-ray analyzers: models and measurements

B. L. Henke
J. Y. Uejio
H. T. Yamada
R. E. Tackaberry
University of California
Lawrence Berkeley Laboratory
Center for X-Ray Optics
Berkeley, California 94720

Abstract. A procedure is described for a detailed characterization of multilayer analyzers that can be effectively applied to their design, optimization, and application for absolute x-ray spectrometry in the 100 to 10,000 eV photon energy region. An accurate analytical model has been developed that is based upon a simple modification of the dynamical Darwin-Prins theory to extend its application to finite multilayer systems and to the low energy x-ray region. Its equivalence to the optical E&M solution of the Fresnel equations at each interface is demonstrated by detailed comparisons for the reflectivity of a multilayer throughout the angular range of incidence of 0° to 90°. A special spectrograph and an experimental method are described for the measurement of the absolute reflectivity characteristics of the multilayer. The experimental measurements at three photon energies in the 100 to 2000 eV region are fit by the analytical modified Darwin-Prins equation (MDP) for $I(\theta)$, generating a detailed characterization of two state-of-the-art multilayers: sputtered tungsten-carbon with $2d \sim 70$ Å and a molecular lead stearate with $2d \sim 100$ Å. The fitting parameters that are determined by this procedure are applied to help establish the structural characteristics of these multilayers.

Subject terms: x-ray multilayered optics; low energy x rays; x-ray spectroscopy; x-ray reflection, sputtered/evaporated multilayers; Langmuir-Blodgett multilayers.

Optical Engineering 25(8), 937-947 (August 1986).

CONTENTS

1. Introduction
2. An analytical description of multilayer reflectivity for the 100 to 10,000 eV region
3. Measurement of multilayer reflectivity
4. Fitting the modified Darwin-Prins (MDP) model to experimental measurements
   4.1. Characterization of a sputtered tungsten-carbon multilayer
   4.2. Characterization of a molecular (Langmuir-Blodgett) multilayer
   4.3. Reflectivity at small angles
5. Summary
6. Acknowledgments
7. Appendix: MDP finite multilayer model derivation
8. References

1. INTRODUCTION

X-ray physics and technology have been considerably advanced in the past decade, as demanded for the development and application of the new, high intensity x-ray generating sources of synchrotron and high temperature plasma radiations. These have important applications, for example, in the material sciences and in the research and development of fusion energy and now of x-ray lasers. Along with these developments has arisen a considerable need for accurate, absolute x-ray spectrometry.

Invited Paper XR-104 received Dec. 1, 1985; revised manuscript received March 19, 1986; accepted for publication March 19, 1986; received by Managing Editor March 21, 1986. This paper is a revision of Paper 563-30 which was presented at the SPIE conference on Applications of Thin-Film Multilayered Structures to Figured X-Ray Optics, Aug. 20-22, 1985, San Diego, Calif. The paper presented there appears (unrefereed) in SPIE Proceedings Vol. 563
© 1986 Society of Photo-Optical Instrumentation Engineers

For efficient x-ray analysis in the 100 to 10,000 eV region (1 to 100 Å range), an important class of analyzers may be applied that utilizes Bragg reflection from periodic layer structures that are parallel to the analyzer surface. These analyzers can be constructed in sufficiently thin sections to allow their effective application with curved, focusing optics. We define these analyzer systems generally to be *multilayers* of the natural or synthesized molecular types and of the synthesized *sputtered or evaporated* types. Examples of the molecular analyzers that we have used effectively in the 100 to 10,000 eV region (with 2d values of 3 to 160 Å) are LiF, PET, mica (at third and first orders), the acid phthalates, and the Langmuir-Blodgett multilayers.[1,2] The sputtered/evaporated types have been "tailored" in the 2d range of 20 to several hundred angstroms[3-5] of high and low Z layers chosen from a large group of possible combinations.[6] Compared to the high density, more rugged sputtered/evaporated multilayers of the same d-spacing, the Langmuir-Blodgett molecular analyzers generally have lower atomic densities, lower integrated reflectivities, similar peak reflectivities, and higher resolution. Both types have important application advantages in modern spectroscopy, and they are definitely complementary.

To efficiently design, optimize, and apply the multilayer analyzers for a given spectroscopic measurement, it is of considerable advantage to have a fast, flexible, and accurate mathematical model code that describes the important reflectivity characteristics and that can be accommodated on a small laboratory computer that may be associated with the spectrographic equipment. We have developed such a mathematical model for multilayer analyzers and apply it here to yield a detailed characterization of two state-of-the-art large-d-spacing analyzers: a sputtered tungsten-carbon analyzer ($2d \sim 70$ Å) and a molecular lead stearate analyzer ($2d \approx 100$ Å).

2. AN ANALYTICAL DESCRIPTION OF MULTILAYER REFLECTIVITY FOR THE 100 TO 10,000 eV REGION

We present here an analytical expression for the intensity I that is reflected from a system of N periodic layers for incident angles, θ, throughout the 0° to 90° range. It has been obtained by modifying the dynamical theory of Darwin-Prins (DP) (for reflection from an ideal crystal of an infinite number of layers) to obtain a description for N-layer finite crystal reflection for all angles of Bragg and total reflection and for the x-ray region of 100 to 10,000 eV. We intend this approach to complement that of the optical (E&M) boundary value solution at each interface of the Fresnel equations.[7,8] In the optical E&M wave solution (OEM), the layer pairs are defined by pairs of their refractive indices ($n = 1 - \delta - i\beta$). In our modified Darwin-Prins description (MDP) the reflecting layer systems are described as planes of unit cells of structure factor F ($= F_1 + iF_2$) and of average scattering factor $\bar{f}$ ($= \bar{f}_1 + i\bar{f}_2$). In Fig. 1 we present the DP expressions for the amplitudes reflected and transmitted at an elementary plane of unit cells in terms of the parameters s and σ, which have been related to $\bar{f}$ and F by using elementary physical optics (see, for example, Compton and Allison[9] and James[10]). In the DP description it is assumed that the fractional complex amplitude that is reflected, s, and the fractional complex amplitude that is absorbed, σ, by the unit cell plane are small compared to unity (as is generally required for the practical multilayer analyzer for which the effective number of interacting planes is large).

In the dynamical description of the propagation of waves through the multilayer, all possible multiple reflections within the layers must be taken into account in order to describe the net downward propagating wave amplitude, T, and the net upward propagating wave amplitude S. This accounting has been elegantly accomplished by Darwin in his solution of the self-consistent difference equations describing the process for any two adjacent layers within the semi-infinite multilayer.[9,10] This approach yields the analytical result for the ratio of the reflected to the incident amplitudes, S_0/T_0, at the surface of the semi-infinite multilayer, which is given by

$$\frac{S_0}{T_0} = \frac{-s}{(\sigma + \xi) \mp \sqrt{(\sigma + \xi)^2 - s^2}} \tag{1}$$

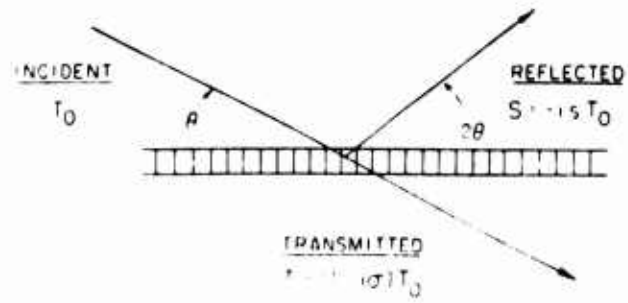
The third parameter, ξ, introduced in this result, is defined by

$$\xi = \frac{2\pi}{\lambda} d(\sin\theta - \sin\theta_0) . \tag{2}$$

where, as discussed below, $\sin\theta_0$ effectively defines a "region of interest" (given by the Bragg equation, $m\lambda = 2d\sin\theta_0$). Now, in this DP difference equation solution, it is established that the net downward propagating wave at the N*th* layer has an amplitude given simply by $T_0 x^N$, where x is defined by

$$x = (-1)^m \exp(-\eta) . \tag{3}$$

where $\eta = \mp\sqrt{s^2 - (\sigma + \xi)^2}$. The value of x is the result of the contributing effects of all possible multiple reflections within the semi-infinite multilayer. (In η, the sign + or − is chosen to have its real part be positive.) Using this result, we derive in Appendix A a modifying factor to be applied to the reflected amplitude ratio S_0/T_0, given in Eq. (1) for the semi-infinite multilayer, to obtain the required amplitude reflection



FOR m UNIT CELLS / UNIT AREA OF STRUCTURE FACTOR, $F_1 + iF_2$, AND OF AVERAGE SCATTERING FACTOR, $\bar{f}_1 + i\bar{f}_2$, PER UNIT CELL

$$-\sigma = mr_0\lambda\frac{\bar{f}_1 + i\bar{f}_2}{\sin\theta} \quad \text{AND} \quad -s = mr_0\lambda\frac{F_1 + iF_2}{\sin\theta}P(2\theta)$$

$P(2\theta) = 1$ OR $\cos 2\theta$ FOR THE TWO POLARIZED COMPONENTS

Fig. 1. Definition of the small absorption and reflection amplitude fractions σ and s at each plane of unit cells of the multilayer in terms of the average scattering factor $\bar{f}$ and the structure factor F for the unit cell, and their area density m.

ratio S_{0N}/T_0 for the finite multilayer of N layers. This is given by

$$\frac{S_{0N}}{T_0} = \frac{S_0}{T_0}\frac{1 - x^{2N}}{1 - (S_0/T_0)^2 x^{2N}} \tag{4}$$

Also derived in Appendix A is the amplitude ratio T_{0N}/T_0 that is transmitted through the N-layer system. This is given by

$$\frac{T_{0N}}{T_0} = \frac{[1 - (S_0/T_0)^2]x^N}{1 - (S_0/T_0)^2 x^{2N}} \tag{5}$$

In the usual way, the intensity ratio that is reflected or transmitted for unpolarized incident x-radiation is obtained by taking one-half of the sum of the moduli squared of the two polarization component amplitudes as obtained from Eqs. (4) and (5), by setting $P(2\theta)$ equal to unity and to $\cos 2\theta$.

As may be easily shown, the reflected intensity will be large only when the parameter ξ is small and, therefore, for the angular regions for which $\theta \approx \theta_0$ in this parameter ξ. θ_0 is defined by the Bragg relation

$$m\lambda = 2d\sin\theta_0 \tag{6}$$

($m = 0$ for the small-angle Fresnel-reflection region; $m = 1$ for the first-order diffraction line; $m = 2$ for the second-order diffraction line, etc.). To apply this intensity function continuously for the total angular range 0° to 90°, we automatically set m to be that integer that is nearest to the value of $(2d\sin\theta)/\lambda$ in our code.

By using a structure factor, F, and an average value of the atomic scattering factor, $\bar{f}$, calculated by relations given in the next section, we have applied this modified Darwin-Prins result (MDP) to calculate $I(\theta)$ for a sharply defined, pure tungsten-carbon (W-C) multilayer of d-spacing = 35 Å and $\Gamma = 0.4$ (Γ is the ratio of the heavy layer thickness to the total d thickness of the layer pair). A plot of $I(\theta)$ for the incident photons of Cu-L_α (930 eV / 13.3 Å) that includes the small angle Fresnel region and the first-order diffraction line is shown in Fig. 2 for a number of layer pairs, N, equal to 100. In

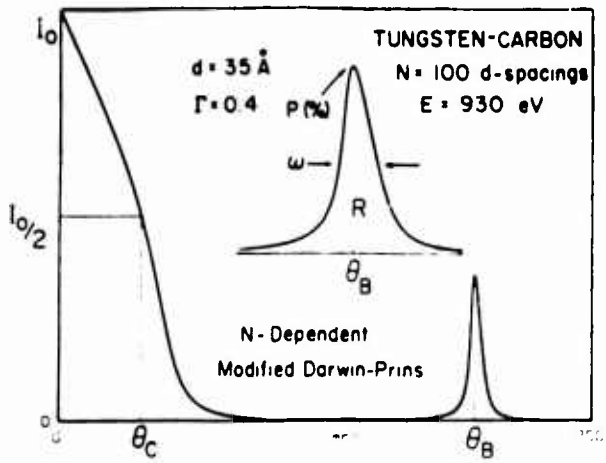


Fig. 2. An MDP calculated reflectivity curve for 930-eV photons upon a tungsten-carbon multilayer of 2d = 70 Å and with a sharply defined tungsten layer of thickness equal to Γd, with Γ = 0.4, N = 100. In the corresponding experimentally measured reflectivity curve, four characteristic values are determined for each photon energy: the total reflection cutoff angle θ_c (at $I_0/2$), the integrated reflectivity R, the peak reflectivity P, and the FWHM ω, at one or more diffraction orders.

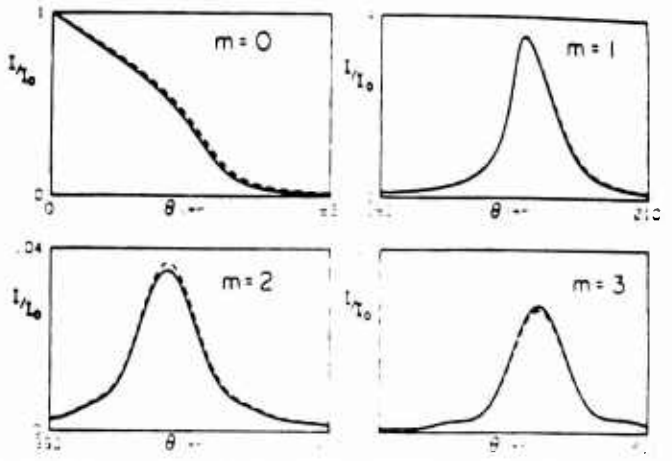


Fig. 3. Comparison of the MDP calculated reflectivity of the N = 100 multilayer described in Fig. 2 (solid lines) with that calculated by the optical E&M model (dashed lines) for the total reflection region (m = 0) and for the first three diffraction orders (m = 1, 2, 3).

Figs. 3 and 4 we compare, in detail, the total reflection region and the first-, second-, and third-order diffraction line intensities for this W-C multilayer, as calculated by this MDP model (solid lines), to those calculated by the optical E&M (OEM) model (dashed lines) for N = 100 and N = 30, respectively, to illustrate the equivalence of the two models in this low energy x-ray region. Similarly, we compare in Fig. 5 the intensities reflected by the multilayer of N = 100 at and near 90° (normal incidence).

3. MEASUREMENT OF MULTILAYER REFLECTIVITY

The detailed characteristics of the multilayer reflection as predicted in Fig. 2 are experimentally measured by a specially designed vacuum spectrograph that is schematically described in Fig. 6. A fine slit and filter are positioned at the isolation gate window of one of our demountable x-ray tubes[11] to provide a strong, characteristic line source in the 100 to 10,000 eV region. The multilayer is mounted with its surface on the axis of a precision θ-2θ goniometer. A sharply defined incident beam is restricted to a small sampled region of the multilayer by a razor blade edge placed close to its surface. The angular resolution of the measurement is set by the divergence of the incident beam and essentially by the slit width at the x-ray source that is 120 cm from the goniometer axis. It is typically set to an angular resolution width that is small compared to the diffraction line width of the multilayer analyzer. The reflected beam is measured by a subatmospheric, gas-flow-proportional counter. The counter has a window 10 cm from the goniometer axis; the width of the window is about one-third that of the multilayer analyzer. The counter also has a slit height that is large compared to that of the reflected beam. The effective incident beam is limited in width by the projection of the opening at the razor edge and is therefore proportional to $\cos\theta$, as noted in Fig. 6.

After the onset of the measured Fresnel-reflection region and at $\theta = 0$, there usually appears an inflection point in the intensity at $I_0/2$, as illustrated in Fig. 6 (and in the experimental plots of Fig. 13). This onset feature determines the incident intensity I_0 and the zero-angle position of the spectrograph.

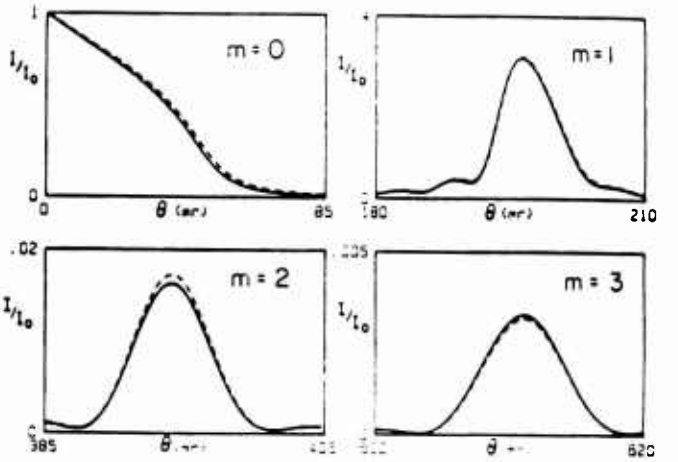


Fig. 4. Detailed calculation comparisons as for Fig. 3 but with N = 30.

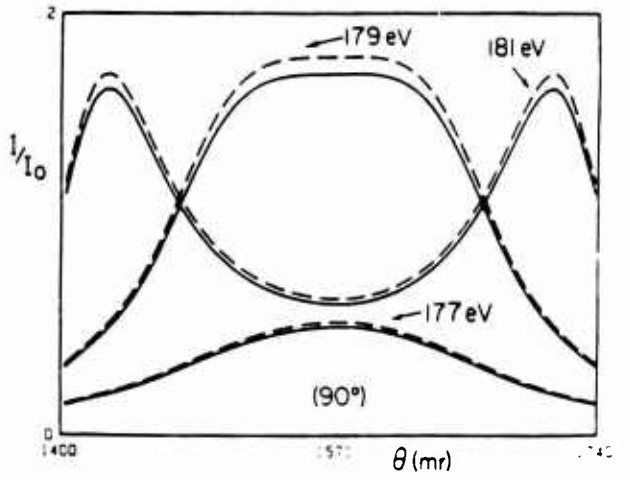


Fig. 5. Detailed calculation comparisons as described for the 100-layer system of Fig. 2 but in the region of normal incidence. Note the sensitive "tuning" by varying the photon energy ∓ 1% from that yielding the maximum normal incidence reflectivity (OEM-dashed lines).

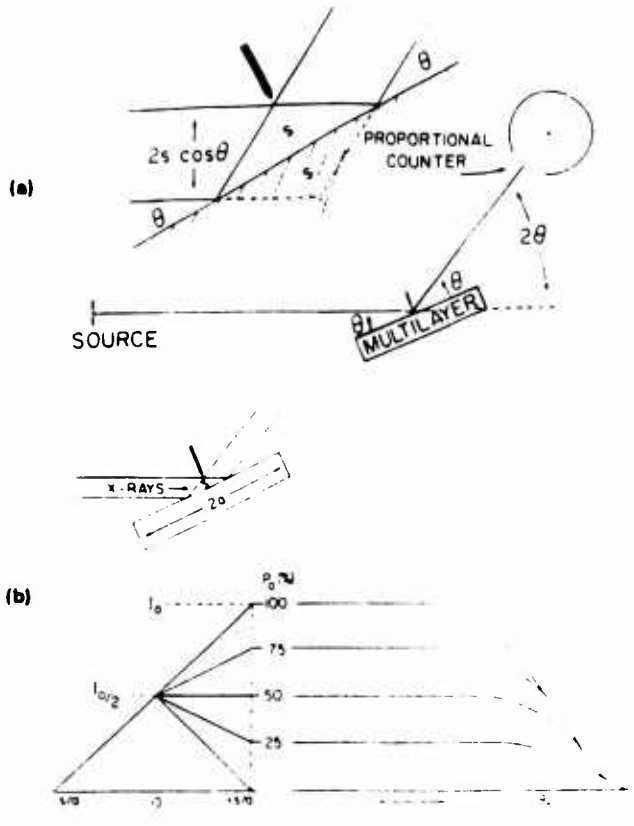


Fig. 6. (a) The spectrograph geometry used for the measurement of multilayer reflectivity in the region 0° to 70° and (b) the characteristic inflection point in the intensity distribution at $\theta = 0$ and at $I_0/2$ (thereby defining the zero angle position of the goniometer and incident intensity $I_0\cos\theta$). After the $I_0/2$ point, the contribution of the reflected intensity causes a change in slope, which is greater as the real mirror reflectivity P(%) for these small angles departs from 100%.

The angular full-width-at-half-maximum (FWHM) of the diffraction line profile (in θ) may be simply determined in terms of the experimentally measured width ω_x, the Gaussian instrumental width g, and the Lorentzian emission line width ϵ by the expression[12]

$$\omega = \omega_x\left[1 - \left(\frac{g}{\omega_x}\right)^2\right] - \epsilon \,, \tag{7}$$

where ϵ is given by

$$\epsilon = \frac{\Delta E}{E}\tan\theta_0 \,. \tag{8}$$

for which the x-ray source line of photon energy E has an effective energy width of ΔE.

The integrated reflectivity is determined by the total number of counts collected, N_x, as the diffraction line is scanned at an angular rate in θ of ω_θ by the relation[11]

$$R = \frac{\omega_\theta N_x}{I_0\cos\theta} \,. \tag{9}$$

The experimental peak reflectivity P_x is measured as the ratio of the intensity at the peak of the diffraction profile divided by the incident beam intensity $I_0\cos\theta$. Assuming the shape of the true diffraction profile is essentially the same as that of the experimentally measured profile, the area under the profile, R (integrated reflectivity), is equal to $K\omega P$ or $K\omega_x P_x$, where K is a shape factor. We may therefore obtain an estimate of true peak reflectivity, P, by the relation

$$P = \frac{P_x\omega_x}{\omega} \tag{10}$$

Note: It is required that the I_0 value used in these measurements be for only those incident photons of energy that are within the characteristic line being measured. Low energy background photons can usually be eliminated by an appropriate filter. The high energy photon background is effectively eliminated by the pulse height discrimination of the proportional counter. For our measurements, the Fresnel-reflection region through several orders of diffraction lines is measured at appropriate normalized x-ray intensities, recorded, and displayed with a multichannel analyzer (MCA). This spectrum, along with the associated pulse height spectrum for the detector, provides an accurate check on the possible presence of any significant background radiation that may need to be further eliminated literally or by correction. The MCA is programmed to permit an immediate determination for each diffraction line of its centroid position θ_x, FWHM ω_x, peak reflectivity P_x, and integrated reflectivity R. These data and the spectra are transferred from the MCA to a small computer for the final semiempirical characterization of the multilayer.

4. FITTING THE MDP MODEL TO EXPERIMENTAL MEASUREMENTS

To obtain an absolute, detailed characterization of a given multilayer using the MDP model, it is required to define for the unit cell its average scattering factor $\bar{f}$ and the structure factor F, thereby determining the σ and s material parameters of the MDP intensity relations. These may be determined by using an appropriate unit cell model and by requiring that the result, $I(\theta)$, precisely fit the experimental data for several photon energies at the characteristic values of R, P, and ω for several diffraction orders (defined in Fig. 2). We illustrate this procedure for the characterization of two types of multilayers, the sputtered tungsten-carbon (W-C) multilayer and the molecular Langmuir-Blodgett (LB) multilayer.

4.1. Characterization of a sputtered W-C multilayer

We shall assume that a transition layer of both tungsten and carbon atoms may exist between pure tungsten and pure carbon regions of the multilayer, as depicted in the unit cell model shown in Fig. 7. (Such a transition-layer model may be applied to account, for example, for an interface roughness[13] or a uniform distribution of W and C.) We shall assume here that this transition layer may be described as the chemically bonded compound WC, as suggested by Auger electron analyses of W-C multilayers.[14]

For such a uniform transition layer model, the mass per unit area for the light x-component (C), M_x, and the mass per unit area for the heavy y-component (W), M_y, that are originally deposited in the construction of each layer may be related to the mass densities ρ_x, ρ_y, and ρ_z and to the fractional thicknesses Γ_y and Γ_z for the y (W) and z (WC) components as follows:

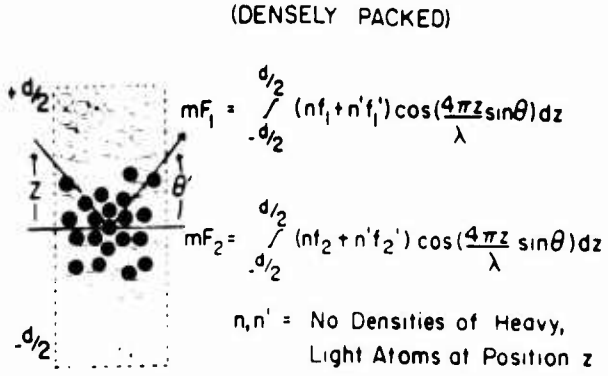


Fig. 7. The symmetric unit cell that has been chosen to model a two-element sputtered/evaporated, high-atomic density multilayer wth the possibility of having a transition layer interface structure. With N relatively large, the effects of fractional layers at the multilayer surfaces and of a substrate are usually negligible. Defined here are the general integrals for F_1 and F_2 for any symmetrical distribution of the heavy and light elements n(z) and n'(z), respectively.

$$M_x = (1 - \Gamma_y - \Gamma_z)\rho_x d + \Gamma_z \rho_z d \left(\frac{A_x}{A_z}\right) , \tag{11}$$

$$M_y = \Gamma_y \rho_y d + \Gamma_z \rho_z d \left(\frac{A_y}{A_z}\right) , \tag{12}$$

where d is the thickness of the layered system and A_x, A_y, and A_z are the atomic or molecular weights. And for the generalized symmetric description shown in Fig. 7, $(1 - \Gamma_y - \Gamma_z)d$, $\Gamma_y d$, and $\Gamma_z d$ are the total thicknesses of the carbon, tungsten, and tungsten carbide layers, respectively. We estimate the mass densities ρ_x (for amorphous carbon), ρ_y(tungsten), and ρ_z (tungsten carbide) to be 2.0, 19.3, and 15.6 $g \cdot cm^{-3}$, respectively.

For this WC transition layer model, as suggested in the relations presented in Eq. (11), accurately known values of M_x and M_y, along with those for the d-spacing and the mass densities ρ_x, ρ_y, and ρ_z, will allow the determination of the structural parameters Γ_y and Γ_z. [$\Gamma_x = 1 - (\Gamma_y + \Gamma_z)$.] These, in turn, may be applied to determine the average scattering factor $m\bar{f}$ and the structure factor mF per unit area of the unit cell layer depicted in Fig. 1 and therefore to determine the essential optical parameters, σ and s. Usually, however, the amounts of the light and heavy elements that are deposited per unit area, M_x and M_y, are not accurately known, and, as described below, these values or their equivalent parameters Γ_y and Γ_z are determined by fitting the model reflectivity relations to measured reflectivity data.

The structure factor mF per unit area of the unit cell layer ($F = F_1 + iF_2$) is defined by the following integral (derived from the general integrals presented in Fig. 7):

$$mF_i = 2n_y f_{iy} \int_0^{\frac{\Gamma_y d}{2}} \cos\left(\frac{4\pi z \sin\theta'}{\lambda'}\right) dz + 2n_z f_{iz} \int_{\frac{\Gamma_y d}{2}}^{\left(\frac{\Gamma_y + \Gamma_z}{2}\right)d} \cos\left(\frac{4\pi z \sin\theta'}{\lambda'}\right) dz + 2n_x f_{ix} \int_{\left(\frac{\Gamma_y + \Gamma_z}{2}\right)d}^{\frac{d}{2}} \cos\left(\frac{4\pi z \sin\theta'}{\lambda'}\right) dz , \tag{13}$$

letting i = 1 or 2 for the real and imaginary components. Here m is the number of unit cells per unit area, as applied in defining σ and s in Fig. 1.

The average scattering factor $m\bar{f}$ per unit area of the unit cell layer is equal to that value of mF for forward scattering for which all atoms are scattering in phase and their scattering amplitudes add directly. Thus $m\bar{f} = mF$ for $\theta = 0$, and we obtain from Eq. (13)

$$m\bar{f}_1 = n_x f_{1x} \Gamma_x d + n_y f_{1y} \Gamma_y d + n_z f_{1z} \Gamma_z d . \tag{14}$$

$$m\bar{f}_2 = n_x f_{2x} \Gamma_x d + n_y f_{2y} \Gamma_y d + n_z f_{2z} \Gamma_z d . \tag{15}$$

Here n_x, n_y, and n_z are the number of atoms or molecules per unit volume of atomic or molecular scattering factors $f_{1x} + if_{2x}$, $f_{1y} + if_{2y}$, and $f_{1z} + if_{2z}$, respectively ($n_x = N_0\rho_x/A_x$, $n_y = N_0\rho_y/A_y$, and $n_z = N_0\rho_z/A_z$, where N_0 is Avogadro's number and A_x, A_y, and A_z are the atomic or molecular weights).

Inside the multilayer, as a result of *refraction*, the angle of incidence and the wavelength at a unit cell plane must be the refraction-modified values θ' and λ'. The angle of refraction θ' and the modified wavelength λ' that must be used in the description of the wave interference within the multilayer are given by Snell's law, $\cos\theta/\cos\theta' = 1 - \delta = \lambda/\lambda'$. We use here only the real part of the refractive index, $1 - \delta$, because it can be shown that for x-ray refraction effects the first-order terms in β cancel. In the model description of multilayers in the low energy x-ray region where refraction effects become significant, we replace the ratio $(\sin\theta)/\lambda$ that appears in the structure factor F by $(\sin\theta')/\lambda'$ [in the cosine function of Eq. (13)]. In terms of θ and λ, we may easily obtain from Snell's law the relation

$$\frac{\sin\theta'}{\lambda'} = \frac{\sin\theta}{\lambda}\sqrt{1 - \frac{2\delta - \delta^2}{\sin^2\theta}} , \tag{16}$$

where $\delta = (r_0\lambda^2 m/2\pi d)\,\bar{f}_1$. Equation (13) is integrated to yield

$$\begin{aligned} mF_i = {} & \frac{n_y d f_{iy}}{\kappa} \sin(\kappa\Gamma_y) \\ & + \frac{n_z d f_{iz}}{\kappa} \{\sin[\kappa(\Gamma_y + \Gamma_z)] - \sin(\kappa\Gamma_y)\} \\ & + \frac{n_x d f_{ix}}{\kappa} \{\sin\kappa - \sin[\kappa(\Gamma_y + \Gamma_z)]\} , \end{aligned} \tag{17}$$

where $\kappa = (2\pi d \sin\theta')/\lambda'$ and where i = 1 or 2 for the real and imaginary components.

Note: Because multilayer analyzers normally have a relatively large number of layers, N, to produce the desired resolution, it is usually sufficiently precise to model the analyzer by N layers of symmetric unit cells, as defined in Fig. 7. The

reflection effects of fractional layers at the boundaries and of a substrate can usually be considered negligible.

We fit our analytical model to the experimental integrated reflectivities at three photon energies and at the first three diffraction orders, if present, by varying Γ_y and Γ_z. These fits are verified by comparing the calculated and the experimental secondary values of ω and P for the several diffraction orders. As noted above, M_x and M_y values are uniquely determined by the values of Γ_y, Γ_z, and d (given ρ_x, ρ_y, and ρ_z). The absolute value of the d-spacing is obtained from the measured d_x values defined by the Bragg equation ($m\lambda = 2d_x \sin\theta$) using Eq. (16) to obtain the relation

$$d_x = d\sqrt{1 - \frac{2\delta - \delta^2}{\sin^2\theta}} \approx d\left(1 - \frac{\delta}{\sin^2\theta} \cdots\right) \qquad (18)$$

Here again we need use only the real part of the complex refractive index, $1 - \delta$, because it may be shown that the terms involving β become negligibly small for the x-ray region of interest here. To calculate the absolute d-spacing, we simply linearly extrapolate a plot of the measured values of d_x versus $\csc^2\theta$, using the relation from Eq. (18), $d_x = d - \delta d \csc^2\theta$. An example of such a least squares fitting and extrapolation is shown in Fig. 8.

For a determination of the atomic scattering factors, we have recently developed state-of-the-art tables of f_1 and f_2 for $Z = 1$ to 94 and for photon energies 100 to 2000 eV.[15] These tables have been established by numerically calculating atomic scattering factors using the Kramers-Kronig dispersion relations with our compilation of the available photoabsorption data above 30 eV. By use of the numerical procedures and the photoabsorption data base from Ref. 15, these scattering factor tables have recently been extended to 10,000 eV.[16] These *atomic* scattering factors can be used to predict precisely the multilayer reflection characteristics, but only for photon energies outside the regions near the absorption thresholds and above about 100 eV, where the atoms within the solid can be expected to respond in an "atomic-like" manner. Near the thresholds one may expect the photoabsorption to be strongly affected by molecular orbital resonances, EXAFS, etc. An example of a dramatic threshold effect is the appearance of a strong and sharp reflectivity spike near the O-K_α edge (23.3 Å) for the potassium acid phthalate (KAP) analyzer.[17] Multilayer reflectivity at absorption edges should be determined by experimental measurement. Nevertheless, for the large extended regions in the 100 to 10,000 eV range, between absorption edges where the multilayer analyzers are normally applied, the atomic scattering description applied here should yield fairly accurate predictions.

Note: For only the low energy x-ray region (for which the wavelengths are large compared to the dimensions of the atomic electron "cloud" around the nuclei), these atomic scattering factors may be considered angle-independent. For the wave reflection description within the multilayer for which the incident photon energies are higher (> 1000 eV) and/or for the large angles of reflection, a simple form-factor correction should be added to f_1 for these atomic scattering factors appearing in the structure factor F. (A simple correction is described in Ref. 15.) Specifically, in the Darwin-Prins reflectivity expression, Eq. (1), the atomic scattering factors f_1 in the forward-scattering parameter σ are for zero-angle scattering and require no form-factor correction, but the atomic scattering factors f_1 in the parameter s, describing scattering in the 2θ reflection direction, must be form-factor corrected. This correction is not included in the optical E&M (OEM) model because in this description it is assumed that the wavelengths are large compared to atomic dimensions.

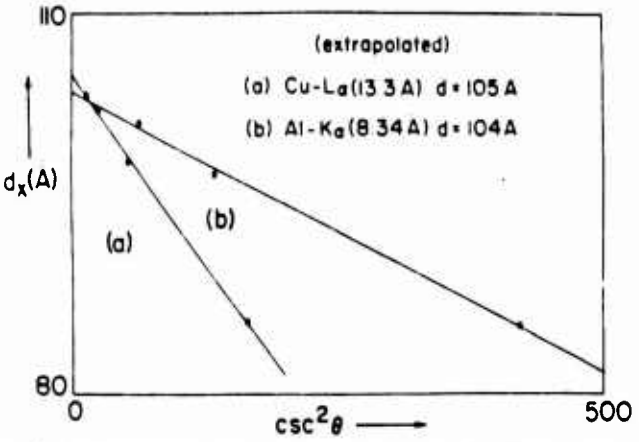


Fig. 8. Determination of the absolute d-spacing for a W-C multilayer (N = 100) by an extrapolation of the d_x versus $\csc^2\theta$ plot for several diffraction orders m of the refraction relation $d_x = d - \delta d \csc^2\theta$ [$d_x = m\lambda/2(\sin\theta)$]. The experimental values for the average optical constant δ for this multilayer as determined from the slopes of these linear plots are 1.12×10^{-3} and 4.24×10^{-4} for the wavelengths 13.3 Å and 8.34 Å, respectively.

With standard fitting procedures, using experimental values for the integrated reflectivities for the multilayer at several photon energies and, if present, at several diffraction orders, along with the model relations Eqs. (11), (12), (14), (15), and (17), one may determine the mass per unit area values, M_x and M_y, and, correspondingly, the fractional thicknesses Γ_y and Γ_z. The $I(\theta)$ function thus determined may then be tested by comparing the predicted results with those measured for the Fresnel-reflection characteristics and for the diffraction line profiles (P and ω).

In Table I and the plots of Fig. 9 we present the results of such a model fit for a typical sputtered tungsten-carbon multilayer.* The present accuracy of the fitting by the MDP analytical function $I(\theta)$ is indicated by the experimental points shown in the characterization plots of Fig. 9.

In Table II are presented the measured values of the integrated reflectivities at the several photon energies and diffraction orders, along with their ratios to the present fit values. Also presented, for comparison, are their ratios to fit values determined by assuming sharp tungsten-carbon interfaces with no transition layers present. We suggest that a transition layer can account for the relative measured intensities for the several diffraction orders that are not predictable by a simple W-C model.

4.2. Characterization of a molecular (LB) multilayer

In Fig. 10 we define the structure factor F for a symmetric unit cell of a molecular multilayer. The scattering factor for this unit cell, $\bar{f}$ $(= \bar{f}_1 + i\bar{f}_2)$, is given by the relations

*LSM 83-021 constructed by T. Barbee for the P-14 X-Ray Diagnostics Group, Los Alamos National Laboratory. LANL-P14 have also kindly loaned to us for this evaluation a W-C multilayer of the same d-spacing, #OVLA 070B-2, constructed by Energy Conversion Devices Inc. These multilayers have essentially the same reflectivity characteristics.

TABLE I. Characterization of a Sputtered Tungsten-Carbon Multilayer

2d = [illegible] Å N = 100 layers
Mass area-layer, W_A = 0.46 μg/cm² W_B = 3.55 μg/cm²
Γ_A = 0.41 Γ_B = 0.19 Γ_2 = 0.40

E(eV)	θ_C(mr)	θ_B(mr)	R(mr)	P(%)	ω(mr)	ΔE(eV)	E/ΔE	N(Å)
167.2	92.2	1570.6	27.84	3.84	270.52			74.1
171.7	89.1	1342.8	15.03	6.12	104.08	4.15	41	72.2
183.3	82.2	1148.0	8.28	6.57	83.47	4.39	42	67.6
192.6	78.4	1052.4	6.71	5.04	44.04	4.84	40	64.4
212.2	72.3	908.4	2.53	5.41	31.39	5.69	37	58.4
277.0	52.8	646.9	2.51	7.13	26.29	9.64	29	44.8
311.7	54.7	569.5	1.10	2.99	26.29	13.77	23	39.8
392.4	53.6	445.4	1.26	4.90	19.87	16.34	24	31.6
395.3	53.4	441.9	1.27	4.96	19.68	16.44	24	31.4
452.2	50.4	384.1	1.48	6.54	17.40	19.47	23	27.4
511.3	49.4	338.6	1.65	8.61	15.07	21.88	23	24.2
524.9	49.0	329.7	1.72	9.09	14.64	22.46	23	23.6
556.3	48.3	310.7	1.79	10.21	13.63	23.61	24	22.3
572.8	47.8	301.6	1.81	10.75	13.12	24.16	24	21.6
637.4	45.5	270.6	1.94	12.73	11.91	27.36	23	19.5
676.8	45.1	254.7	2.04	14.46	11.09	28.84	23	18.3
705.0	44.4	244.4	2.08	15.45	10.62	30.03	23	17.6
776.2	43.0	221.6	2.19	18.26	9.53	32.81	24	16.0
851.5	41.4	202.0	2.26	21.15	8.58	35.66	24	14.6
929.7	39.7	184.9	2.30	23.98	7.78	38.70	24	13.3
1011.7	37.9	169.8	2.32	26.77	7.09	41.83	24	12.3
1041.0	37.2	164.9	2.32	27.74	6.86	42.93	24	11.9
1188.0	34.1	144.4	2.26	32.07	5.89	48.15	25	10.4
1253.6	32.7	136.7	2.22	33.68	5.52	50.33	25	9.89
1486.7	28.0	115.0	1.91	37.65	4.30	55.38	27	8.34
1740.0	20.7	97.8	1.31	29.96	2.47	43.97	40	7.13

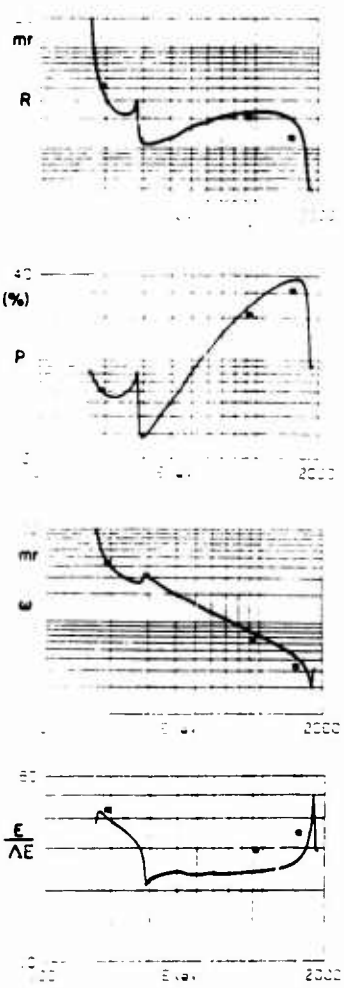


Fig. 9. Plots of the integrated reflectivity R (mrad), the peak reflectivity P (%), the FWHM values ω (mrad), and the resolving power E/ΔE for the sputtered W-C multilayer as characterized in Table I. Presented here are the experimental determinations of the parameters at three x-ray lines: (1) Mo-M_ζ (192.6 eV/64.4 Å), (2) Cu-L_α (930 eV/13.3 Å), and (3) Al-K_α (1487 eV/8.34 Å).

$$\bar{f}_1 = \sum n_q f_{1q} \,, \qquad \bar{f}_2 = \sum n_q f_{2q} \,. \tag{19}$$

where n_q is the number of atoms of type q in the unit cell having the atomic scattering factor $f_{1q} + if_{2q}$.

For the $m\bar{f}$ and mF values needed to obtain σ and s (see Fig. 1), we may use $m = 1/A_0$, where A_0 is the cross-sectional area of the molecular unit cell.

Figure 11 shows the molecular structure and the unit cell for the lead salt of the straight-chain fatty acids that are used in our construction of molecular analyzers of the Langmuir-Blodgett type. The general formula for the 20 molecules that can be used to generate Langmuir-Blodgett multilayers is $[CH_3(CH_2)_nCOO]_2Pb$. The d-spacing in the LB multilayer is approximately given by $2.50(n + 4)$ Å.[18] We have constructed multilayers in the range $n = 10$ to 28 with 2d values of 70 to 160 Å.

To fit the MDP analytical description to the experimental LB multilayer reflectivity, we may adjust $\bar{f}$ and F by slightly varying the area density $m (= 1/A_0$, where A_0 is the molecular cross section), and the fraction α of the fatty acid molecules that have chemically combined with the lead ions to form the lead salt. It is easily shown that the latter adjustment is obtained by simply multiplying the scattering factor f_{Pb} for the lead atom by α where it appears in the calculation for $\bar{f}$ and F ($\alpha \approx 1$ and $A_0 \approx 20.5$ Å^2, nominally). Again, the parameters A_0 and α are varied to obtain the "best fit" of the MDP results for the integrated reflectivities R at the first three diffraction orders (when present) and at several photon energies.

TABLE II. Absolute Experimental Integrated Reflectivity Values at Several Diffraction Orders and Photon Energies—Comparisons to Corresponding Fit Values by the Transition Layer (W-WC-C) and the Pure (W-C) Models

Photon energy (eV)	Diffraction order	R (exp) (mrad)	R (exp) / R(W-WC-C)	R (exp) / R (W-C)
192.6	1	4 40	1.13	1.10
929.7	1	2 04	0 386	0.873
929.7	2	0 0196	0 927	0.291
929.7	3	0 0137	1.13	0.360
1486.7	1	1 258	0 659	0.653
1486.7	2	0 016	0.773	0.265
1486.7	3	0 0!0	0 926	0.264

In Table III and the associated Fig. 12 we present a detailed characterization of a state-of-the-art lead stearate analyzer.*

*Pb-Str (6-5-85 F3) constructed in this laboratory (see Refs. 11 and 19).

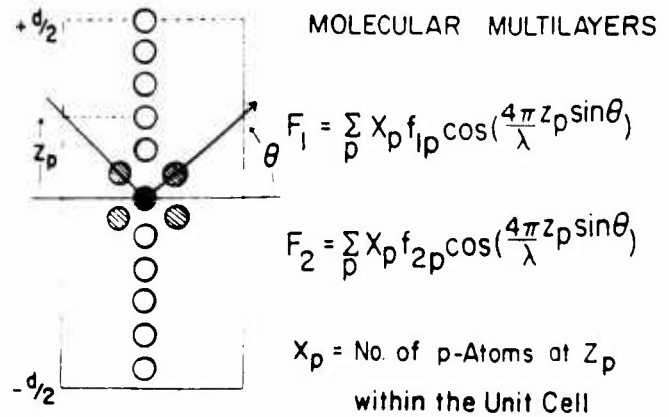


Fig. 10. Definition of the molecular structure factor components F_1 and F_2 for a symmetric unit cell of a molecular multilayer.

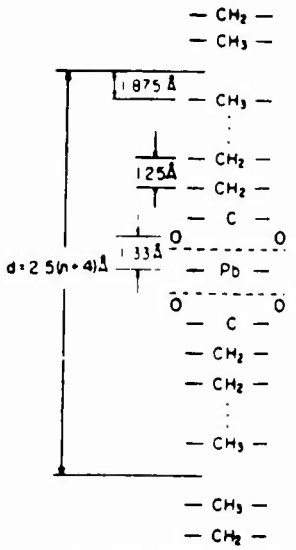


Fig. 11. Unit cell structure for the lead salt of the straight-chain fatty stearic acid that comprises a molecular Langmuir-Blodgett multilayer. Given this structure, the average atomic scattering factor f and the structure factor F are determined.

Also shown in these plots are the experimental measurements for R, P, ω, and $E/\Delta E$ at the four photon energies 192.6 eV, 277 eV, 930 eV, and 1487 eV.

4.3. Reflectivity at small angles

To calculate the reflectivity at small angles, as noted earlier, we apply our MDP calculation for the region approaching $\theta = 0$ by setting $m[= 2d(\sin\theta_0)/\lambda]$ equal to zero. For this small-angle region of essentially only forward scattering, the values of $\bar{f}$ and F approach the same value, and the DP parameters σ and s become essentially equal in this Fresnel-reflection region. In this region the Darwin-Prins model and our modified Darwin-Prins model can be easily shown to yield the Fresnel-reflection equation depending only upon the optical constants δ and β, provided we make the substitutions for the average atomic scattering factor terms $\bar{f}_1$ and $\bar{f}_2$, using the relations

$$\delta = \frac{r_0 \lambda^2 m}{2\pi d} \bar{f}_1 \ , \qquad \beta = \frac{r_0 \lambda^2 m}{2\pi d} \bar{f}_2 \ , \tag{20}$$

where r_0 is the classical electron radius. These indeed are the usual equations that relate the macroscopic optical constants δ and β to the atomic scattering parameters (e.g., see Refs. 9, 10, 15, and 19).

Even at larger angles than those usually associated with a "total reflection" region, the Fresnel equation predicts a reflection tail that can be shown in this limit to become

$$I(\text{Fresnel}) \approx \frac{\delta^2 + \beta^2}{4\sin^4\theta} \quad \text{for } \theta >> \sqrt{2\delta} \ . \tag{21}$$

In practice, this tail can be measured directly in the absence of any significant Bragg reflected lines. When the amplitude of a Bragg reflection is imposed, a distortion of this tail occurs, as is illustrated in the measured spectra shown in Fig. 13 for two cases, with a first-order diffracted line near and removed from the region of total reflection. As may be noted, the principal effect upon the shape of the diffraction line as it approaches the total reflection region is to distort the low angle side of the diffraction profile. It is for this reason that we have chosen as our definition for the measurement of the integrated reflectivity R and of the FWHM ω_x to measure only the area from the peak position on the large-angle side (a range of $3\omega_x$) and the associated one-half width, which values are then doubled to define R and ω_x. By this procedure, these values are different from those determined from the total profile only in the angles of Bragg diffraction near the total reflection region. We believe this procedure improves the definition of R and ω for the small-angle region and also improves the speed of their computation.

It should be noted here that generally, for an optimized spectral measurement, a multilayer should be chosen with a 2d value that places the spectrum at large Bragg angles. It is for these angles that the effect of the Fresnel-reflection tail (combined effect for all wavelengths present) is minimized and maximum peak-to-background ratios are obtained. Also, for the larger angles of Bragg diffraction, the spectral resolution is less affected by the instrumental resolution, which is usually fixed by sensitivity requirements and is angle-independent. The dispersion and the natural analyzer FWHM increase with the angle of diffraction.

The background enhancement at small angles is generally greater for the sputtered/evaporated multilayers than for the molecular multilayers because of their appreciably higher density and correspondingly higher δ and β values. This is illustrated in the measured spectra of Fig. 14 for the M-series of molybdenum (the principal line, M_ζ, is at 64.4 Å/192.6 eV). These spectra are measured with multilayers of the same 2d values (≈130 Å) of sputtered tungsten-carbon and of the molecular lead lignocerate. Both were of effectively infinite thickness for this wavelength region. Comparative spectra like those shown in Fig. 14 usually demonstrate that the molecular multilayers of the same 2d value have similar absolute peak reflectivities, higher resolving power, and appreciably lower integrated reflectivities than do the higher density, sputtered/evaporated multilayer systems.

5. SUMMARY

A simple and accurate analytical model for the multilayer analyzer has been developed that can be effectively applied for

TABLE III. Characterization of a Molecular Lead Stearate Multilayer

$2d = 99$ Å, $N = 100$ layers
$A_0 = 20.4$ Å^2, $\gamma = 0.8$

E(eV)	θ_c(mr)	θ_B(mr)	R(mr)	P(%)	ω(mr)	ΔE(eV)	E/ΔE	λ(Å)
125.3	141.8	1570.4	22.02	11.38	188.61			98.9
132.8	131.4	1233.6	2.83	9.41	26.47	1.23	108	93.4
148.7	120.9	1002.2	1.11	6.82	14.44	1.37	108	83.4
151.1	119.0	977.8	1.02	6.61	13.69	1.39	108	82.1
171.7	104.4	817.7	0.62	5.64	9.83	1.58	109	72.2
183.3	97.3	752.3	0.53	5.49	8.59	1.68	109	67.6
192.6	92.2	707.9	0.48	5.50	7.83	1.76	109	64.4
212.2	82.2	631.0	0.41	5.56	6.63	1.93	110	58.4
277.0	45.7	466.9	0.38	7.38	4.57	2.51	110	44.8
311.7	31.7	413.2	0.08	0.86	6.37	4.53	69	39.8
392.4	36.2	325.7	0.11	1.97	4.05	4.71	83	31.6
395.3	36.2	323.2	0.12	2.01	4.00	4.72	84	31.4
452.2	34.8	281.6	0.13	2.94	3.22	5.04	90	27.4
511.3	32.9	248.3	0.13	3.73	2.68	5.40	95	24.2
524.9	32.1	241.8	0.12	3.49	2.57	5.46	96	23.6
556.3	30.0	227.9	0.21	6.12	2.48	5.84	94	22.3
572.8	29.9	221.3	0.22	6.93	2.38	6.07	94	21.6
637.4	28.7	198.6	0.27	9.70	2.08	6.60	97	19.5
676.8	27.7	186.9	0.28	11.02	1.93	6.92	98	18.3
705.0	26.8	179.4	0.29	12.06	1.85	7.19	98	17.6
776.2	25.4	162.8	0.32	15.31	1.67	7.89	98	16.0
851.5	23.8	148.3	0.34	18.12	1.51	8.63	99	14.6
929.7	22.2	135.7	0.35	20.91	1.39	9.44	99	13.3
1011.7	20.8	124.7	0.36	23.87	1.28	10.34	98	12.3
1041.0	20.4	121.2	0.37	24.83	1.25	10.66	98	11.9
1188.0	18.2	106.1	0.37	29.01	1.10	12.31	97	10.4
1253.6	17.3	100.5	0.37	30.53	1.05	13.04	96	9.89
1486.7	14.8	84.7	0.35	34.99	0.90	15.68	95	8.34

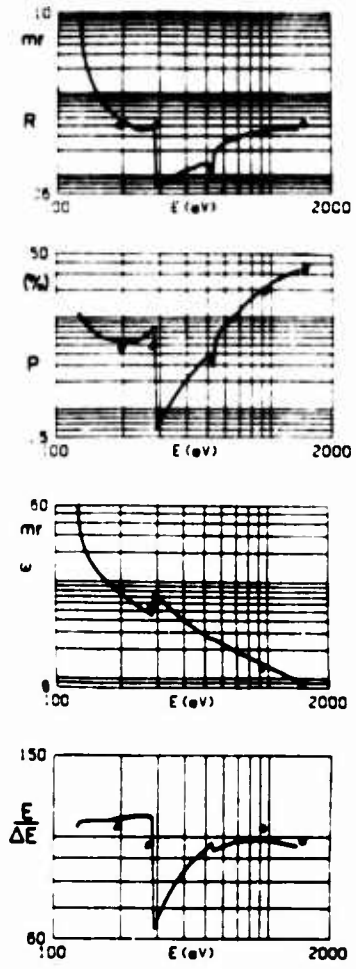


Fig. 12. Plots for the integrated reflectivity R (mrad), peak reflectivity P (%), FWHM values ω (mrad), and resolving power E/ΔE for the lead stearate molecular multilayer characterized in Table III. Experimentally determined points are indicated here as for Fig. 9, including one at C-K$_\alpha$ (44.7 Å/280 eV).

the design, optimization, and application of multilayers in absolute x-ray spectrometry. It may be applied (1) for finite systems of N layers and (2) for the low energy as well as the conventional x-ray region (100 to 10,000 eV). The structural detail of the multilayer is defined by a unit cell that in turn allows a determination by simple mathematical formulae of the model parameters, which are the average scattering factor $\bar{f}$ and the structure factor F. These parameters and m, the area density of the unit cells, are the only material parameters that are required for the MDP description.

By fitting the MDP model to the experimental measurements, as described here, we are able (1) to obtain a detailed analytical characterization of a given multilayer analyzer as based upon measurements at only a few photon energies and (2) to gain some important insights as to the structure of the multilayer.

We are looking forward to improving the overall accuracy of the characterization procedures described here as we obtain multilayers of higher perfection and more accurate photoabsorption data, which are needed for the determination of the atomic scattering factors.

6. ACKNOWLEDGMENTS

The authors gratefully acknowledge the important assistance of other members of this Low Energy X-Ray Physics and Technology Project: Robert Ehrlich, Debra Nanod, and Laureen Sasaki; we also thank Mary Hockaday (of the P14 group, Los Alamos National Laboratory) for her helpful suggestions in preparation of this report. This program is supported by a grant from the Air Force Office of Scientific Research (AFOSR-No. 84-0001) and by contracts with the Department of Energy (SAN # CID #9501, Task I) via LANL and LLNL (No. DE-AC03-76SF0098) via LBL.

7. APPENDIX: MDP FINITE MULTILAYER MODEL DERIVATION

The Darwin-Prins (DP) solution for the ratio of the amplitude reflected to that incident, S_0/T_0, at the vacuum interface of a semi-infinite multilayer also established that the phase and effective attenuation of the net amplitude for a wave propagating into the semi-infinite crystal through N layers may simply be expressed as $T_0 x^N$, x being given by the relation $x = (-1)^m \exp(-\eta)$, where $\eta = \mp \sqrt{s^2 - (\sigma + \xi)^2}$ and is the result of the effects of all possible multiple reflections and transmissions occurring within the semi-infinite multilayer. (The + or − sign for η is chosen by the requirement that its real part be positive.)

The amplitude reflection ratio at the N*th* layer, corresponding again to a boundary at an infinitely deep crystal, must also be S_0/T_0, and therefore the upward propagating wave amplitude at the N*th* layer must be $S_0 x^N$, as depicted in Fig. A1(a). To obtain the reflection ratio for a finite multilayer of N layers, we need to eliminate the boundary condition of an

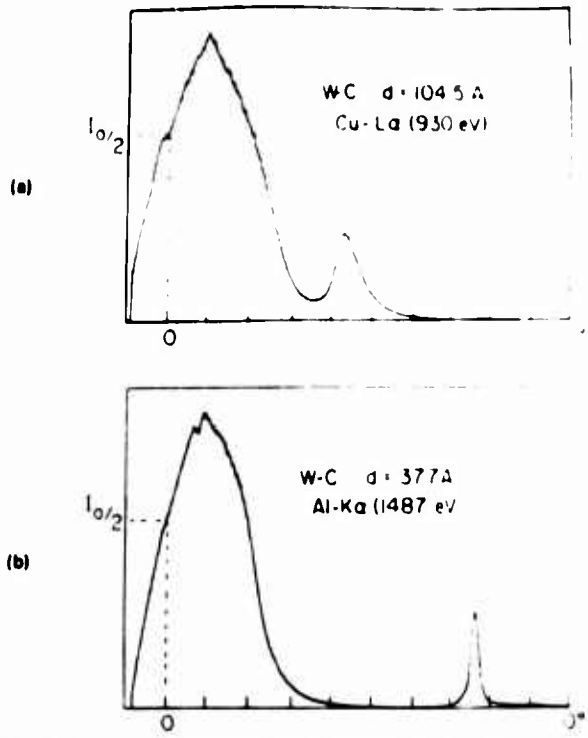


Fig. 13. Low angle distortion of a spectral line that appears in the small-angle reflection region. Experimental spectra from W-C multilayers: (a) 2d ~ 200 Å at Cu-L_α (13.3 Å/930 eV) and (b) 2d ~ 70 Å at Al-K_α (8.34 Å/1487 eV).

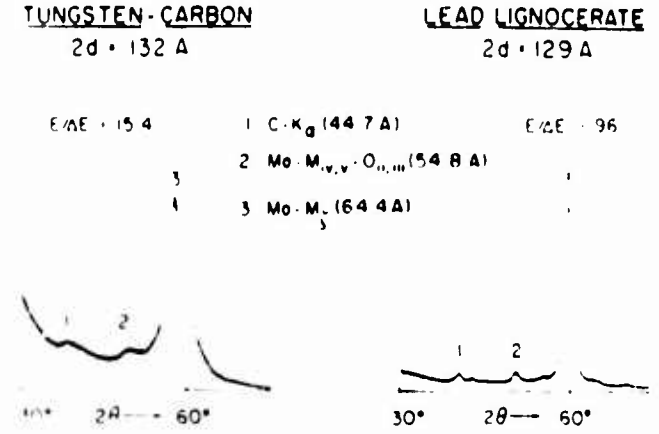


Fig. 14. Comparison of the experimental spectra for the molybdenum-M series lines measured with a sputtered W-C multilayer and with a molecular lead lignocerate multilayer, each of 2d ~ 130 Å.

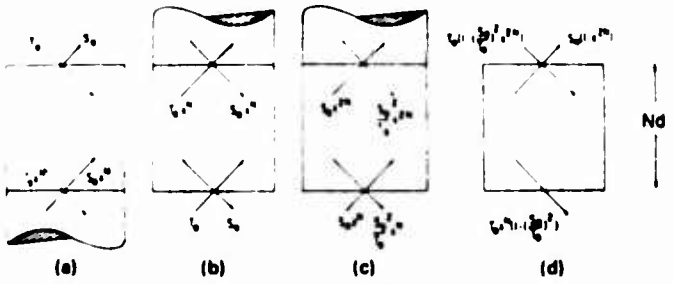


Fig. A1. Illustration of the superposition of particular solutions given for a semi-infinite crystal by the Darwin-Prins model, which yields the solution for the finite, N-layer crystal (the modified Darwin-Prins solution).

effect of the wave interaction of the infinite multilayer below the N*th* layer. Let us reverse the roles of downward and upward waves in Fig. A1(a) by inverting the reflection geometry of (a), as shown in (b). Now by multiplying each boundary wave amplitude indicated in (b) by the same constant factor, $S_0 x^N / T_0$, we obtain another consistent set of values for the boundary wave amplitudes, as depicted in (c), with an incident wave from below of amplitude $S_0 x^N$ and equal to that in (a).

We now subtract, by a superposition, the two boundary wave solutions depicted in (a) and (c), obtaining the boundary amplitudes indicated in (d) and, with the net upward propagating wave at the lower boundary equal to zero, the required boundary condition for the finite crystal of N layers.

Finally, by dividing each amplitude in (d) by the incident amplitude $T_0[1 - (S_0/T_0)^2 x^{2N}]$, we obtain the amplitude ratio for finite multilayer reflection and for finite multilayer transmission, as was given in Eqs. (4) and (5), viz.,

$$\frac{S_{0N}}{T_0} = \frac{S_0}{T_0} \frac{1 - x^{2N}}{1 - (S_0/T_0)^2 x^{2N}} ,$$

$$\frac{T_{0N}}{T_0} = \frac{[1 - (S_0/T_0)^2] x^N}{1 - (S_0/T_0)^2 x^{2N}}$$

These analytical results combined with Eq. (1) are accurate and adaptable, have an appreciably higher computational speed and ease of programming than do the usual optical E&M (OEM) methods, and may be applied with a small laboratory computer having complex number arithmetic capability.

The equivalence of the MDP and the OEM models for low energy x rays has been demonstrated here by detailed comparison plots (shown in Figs. 3 to 5). In recent reports by Lee[20] and by Perkins and Knight,[21] the equivalence of the DP difference equation and the OEM approaches has been demonstrated by a formal rewriting of the latter into closed form. We are pleased to note that coincident with our presentation of the above derivation of the MDP results, Eqs. (4) and (5), Spiller and Rosenbluth[22] have presented their derivation of the same relations as developed from the OEM solution [see their Eqs. (A13) and (A14)].

This MDP phenomenological description that we have presented here can effectively provide the basis for a better understanding of the physical nature of multilayer reflection.

Finally, as noted earlier, we believe that our MDP model is more accurate at the higher photon energies (> 1000 eV) than the OEM model, which does not include the angle dependence of the scattered wave amplitudes, which may be large for the shorter x-ray wavelengths. As discussed earlier, it is straightforward to distinguish between forward and 2θ scattering in the MDP solution by inserting angle-dependent atomic scattering factors using a simple form-factor correction.[15]

8. REFERENCES

1. B. L. Henke, H. T. Yamada, and T. J. Tanaka, "Pulsed plasma source spectrometry in the 80–8000-eV x-ray region," Rev. Sci. Instrum. 54, 1311-1330 (1983).
2. B. L. Henke and P. A. Jaanimagi, "Two-channel, elliptical analyzer spectrograph for absolute, time-resolving time-integrating spectrometry of pulsed x-ray sources in the 100–10000-eV region," Rev. Sci. Instrum. 56, 1537-1552 (1985).

3 J. W. Barbee, Jr., S. Mrowka, and M. C. Hettrick, "Molybdenum/silicon multilayer mirrors for the extreme ultraviolet," Appl. Opt. 24, 883–886 (1985).
4 J. Spiller, in *AIP Conf. Proc. No. 75 on Low-Energy X-Ray Diagnostics* (Monterey, Calif.), D. T. Attwood and B. L. Henke, eds., p. 124, American Institute of Physics, New York (1965).
5 J. Contardi, S. S. Chao, J. Keem, and J. Tyler, "Detection of nitrogen with a layered structure analyzer in a wavelength dispersive x-ray microanalyzer," Scanning Electron Microscopy 1984 II, 575–582 (1984).
6 A. E. Rosenbluth, "Reflecting properties of x-ray multilayer devices," Ph.D. thesis, U. Rochester (1982).
7 J. H. Underwood and J. W. Barbee, Jr., "Layered synthetic microstructures as Bragg diffractors for x rays and extreme ultraviolet: theory," Appl. Opt. 20, 3027–3034 (1981).
8 J. H. Underwood and J. W. Barbee, Jr., in *AIP Conf. Proc. No. 75 on Low-Energy X-Ray Diagnostics* (Monterey, Calif.), D. T. Attwood and B. L. Henke, eds., p. 170, American Institute of Physics, New York (1965).
9 H. A. Compton and S. K. Allison, *X-Rays in Theory and Experiment*, 2nd edition, Van Nostrand, New York (1935).
10 R. W. James, *The Optical Principles of Diffraction of X-Rays*, Cornell University Press, Ithaca, N.Y. (1965).
11 B. L. Henke and M. A. Tester, "Techniques of low-energy x-ray spectroscopy," Adv. X-Ray Anal. 18, 76 (1975).
12 B. L. Henke, R. C. C. Perera, E. M. Gullikson, and M. L. Schattenburg, "High-efficiency low-energy x-ray spectroscopy in the 100–500-eV region," J. Appl. Phys. 49, 480–494 (1978).
13 L. A. Smirnov, L. D. Sotnikova, B. S. Anokhin, and B. Z. Tatbin, "Total external reflection of x-rays from rough surfaces," Opt. Spectrosc. 46, 329–332 (1979).
14 K. D. Rachocki, D. R. Brown, R. W. Springer, and P. N. Arendt, "Auger and depth profile analysis of synthetic crystals for dispersion of soft x-rays," Applications of Surface Sci. 18, 165–181 (1984).
15 B. L. Henke, P. Lee, T. J. Tanaka, R. L. Shimabukuro, and B. K. Fujikawa, Atomic Data and Nuclear Data Tables 27, No. 1 (1982).
16 J. M. Auerbach and K. G. Tirsell, "Software for reflectivity calculation of x-ray mirrors," LCRL Report No. 91230 (1984).
17 D. M. Barrus, R. L. Blake, H. Felthauser, E. E. Fenimore, and A. J. Burek, in *AIP Conf. Proc. No. 75 on Low-Energy X-Ray Diagnostics* (Monterey, Calif.), D. T. Attwood and B. L. Henke, eds., p. 115, American Institute of Physics, New York (1965).
18 B. L. Henke, in *AIP Conf. Proc. No. 75 on Low-Energy X-Ray Diagnostics* (Monterey, Calif.), D. T. Attwood and B. L. Henke, eds., p. 85, American Institute of Physics, New York (1965).
19 B. L. Henke, in *AIP Conf. Proc. No. 75 on Low-Energy X-Ray Diagnostics* (Monterey, Calif.), D. T. Attwood and B. L. Henke, eds., p. 146, American Institute of Physics, New York (1965).
20 P. Lee, "X-ray diffraction in multilayers," Opt. Commun. 37, 159–164 (1981).
21 R. T. Perkins and T. V. Knight, "An exact solution of Darwin's difference equations," Acta Cryst. A40, 617 (1984).
22 J. Spiller and A. L. Rosenbluth, "Determination of thickness errors and boundary roughness from the measured performance of a multilayer coating," in *Applications of Thin-Film Multilayered Structures to Figured X-Ray Optics*, G. F. Marshall, ed., Proc. SPIE 563, 221 (1985).



Burton L. Henke received the A.B. degree from Miami University (Ohio) in 1944, and the M.S. and Ph.D. degrees in physics from the California Institute of Technology in 1946 and 1953, respectively.

From 1949 to 1967 he was a faculty member in the Department of Physics at Pomona College (Professor of Physics from 1958 to 1967), and from 1967 to 1984 he was Professor of Physics at the University of Hawaii.

Since January 1985 he has been a Senior Staff Scientist with the Lawrence Berkeley Laboratory, University of California, where his chief research interests are the physics of low-energy x rays and electrons. He has also served as a consultant in x-ray physics to government and industry.

Dr. Henke is a member of the American Physical Society (elected as a Fellow in 1969), American Astronomical Society, American Association of Physics Teachers, and American Association of University Professors. He was a Guggenheim Fellow in 1956, received the Wig Distinguished Professor Award in 1960, and received a Merit Award with Distinction for Research and Teaching from the University of Hawaii in 1982.



Jeremy Y. Uejio received the B.S. degree from the University of Hawaii in 1984 and is currently working toward an M.S. degree in computing science at the University of California at Davis.



Hubert T. Yamada received the B.S. degree in physics from the University of Hawaii in 1983 and the M.S. degree in physics from the California Institute of Technology in 1985. He is currently a graduate student at the University of California at Berkeley working toward a Ph.D. in physics.



Ron E. Tackaberry is a graduate of the Naval Nuclear Engineering School. He is currently pursuing a B.S. degree at San Francisco State University.

5. TECHNICAL NOTES: LOW ENERGY X-RAY MULTILAYER ANALYZERS: MOLECULAR AND SPUTTERED/EVAPORATED

For efficient x-ray analysis above about 500 eV one generally applies the grown or natural crystals (6). For the lower photon energies, one can apply at large diffraction angles, the constructed multilayers of the molecular or sputtered/evaporated types, and at the small diffraction angles reflection or transmission gratings (7). In these notes, we outline some of the important characteristics of the molecular and sputtered/evaporated multilayers that we are currently investigating.

Molecular Multilayers

For many years we have been developing relatively high resolution molecular multilayers of the Langmuir-Blodgett type. These are constructed by the repeated dipping of a substrate in and out of a water surface on which is deposited a monomolecular layer system (usually a barium or lead salt of a straight-chain fatty acid). Our dipping tank is described in Fig. 1 and the process for generating one of the usual types of molecular multilayers is described in Fig. 2. In this way, very regular periodic structures are formed consisting of thin, high electron density double-atomic-layers of cations, e.g. barium or lead, separated by a low density carbon chain matrix. Using a series of straight-chain fatty acids we have successfully generated this type of multilayer with 2d-spacings in the 70-160 A range.

The energy response of these molecular multilayers can be accurately predicted by our Modified Darwin-Prins (MDP) model (4) using a single fitting parameter that allows a small adjustment for the area density of the multilayers. The very good fits between the MDP analytical description and our experimental measurements are illustrated in the plots of Fig. 3 for the integrated reflectivity, R, the peak reflectivity, P, the FWHM, ω(mr), and the resolving power, $E/\Delta E$, for a lead stearate multilayer. Once the analytical characterization of the multilayer has been established in this way, it is often useful to apply it for the plotting of the analyzer's energy response (at a fixed Bragg angle) to a flat-continuum radiation. This is shown in Fig. 4 for the lead stearate analyzer at θ = 40 degrees with a first order peak at 194.4 eV and with no significant second-order radiation.

In Figs. 5 and 6 we present our modified Darwin-Prins (MDP) plots comparing the integrated and peak reflectivities for three stearate multilayers using Ba, Hg and Pb as the cations.

In order to fit our MDP analytical characterizations to the measured reflectivities of the sputtered multilayer systems, we have found that a two-parameter adjustment is usually required. These parameters establish the thickness of the heavy element layer and the thickness of a linear transition region which accounts for penetration

of the heavy element into the light element layer and vice versa. Such a fit is illustrated in Fig. 7 for a vanadium-carbon sputtered multilayer of 2d-spacing similar to that of the molecular lead stearate described above. For comparison with the lead stearate, a flat-continuum response of the sputtered multilayer is shown in Fig. 8 for a fixed Bragg angle of θ = 40 degrees. Finally, Figs. 9 and 10 show the flat-continuum response of a real and typical tungsten-carbon multilayer at a smaller fixed Bragg angle of 22.5 degrees for the first four diffraction orders. Illustrated here is the significant low energy specularly reflected component resulting from an application of the high density sputtered multilayers at the smaller angles.

Figure 1. MOLECULAR MULTILAYER DIPPING TANK

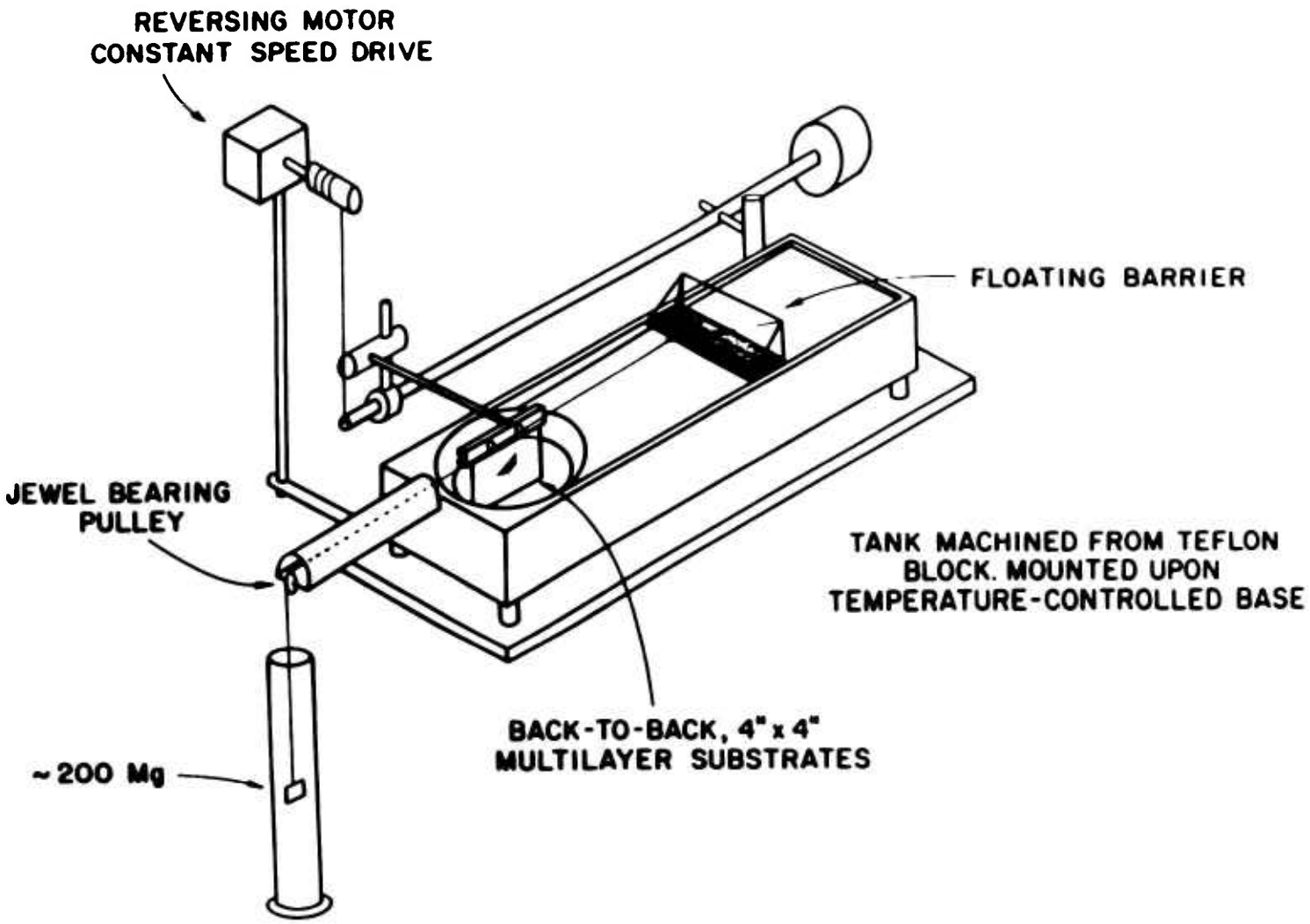


Figure 2.

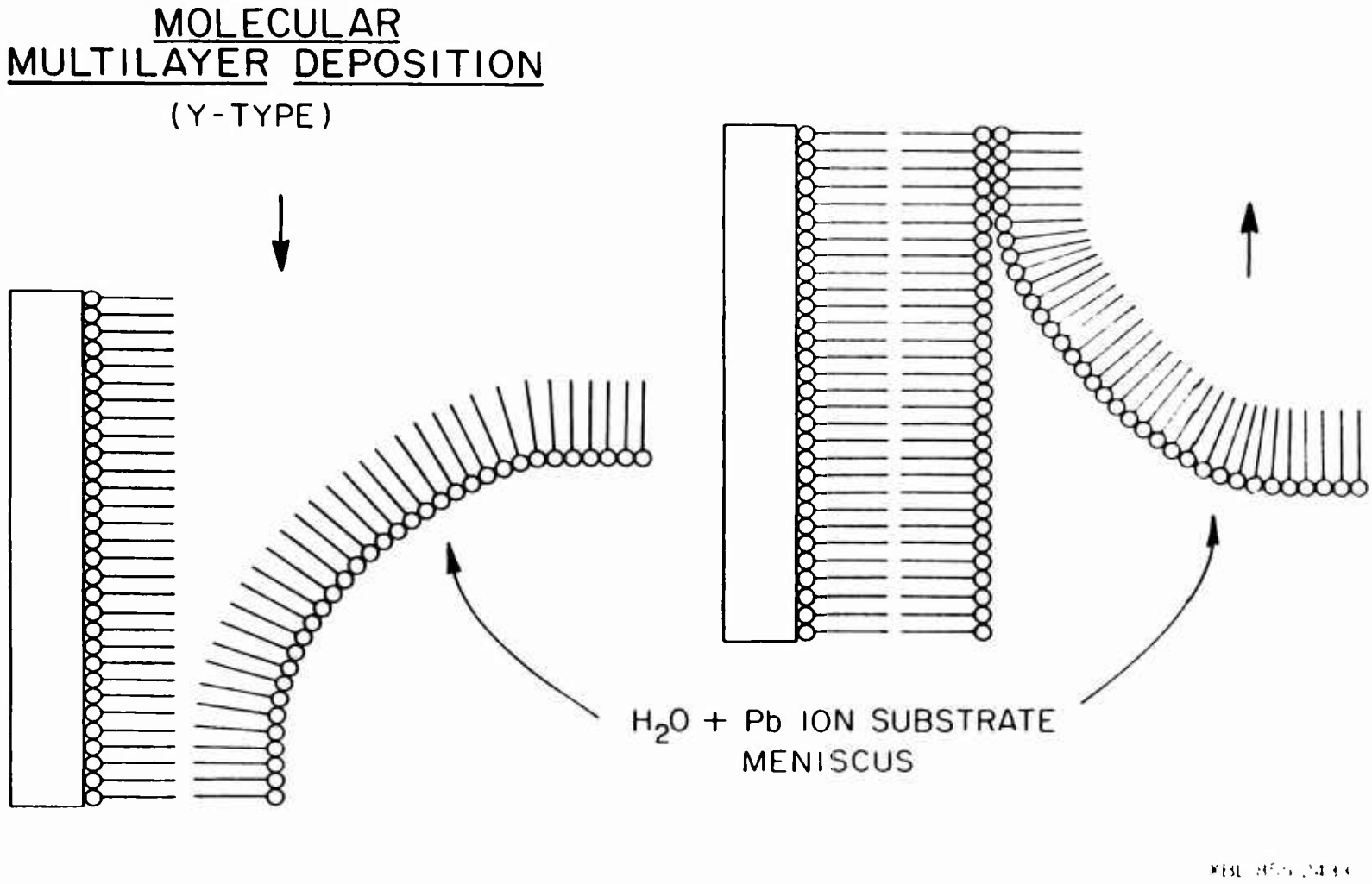
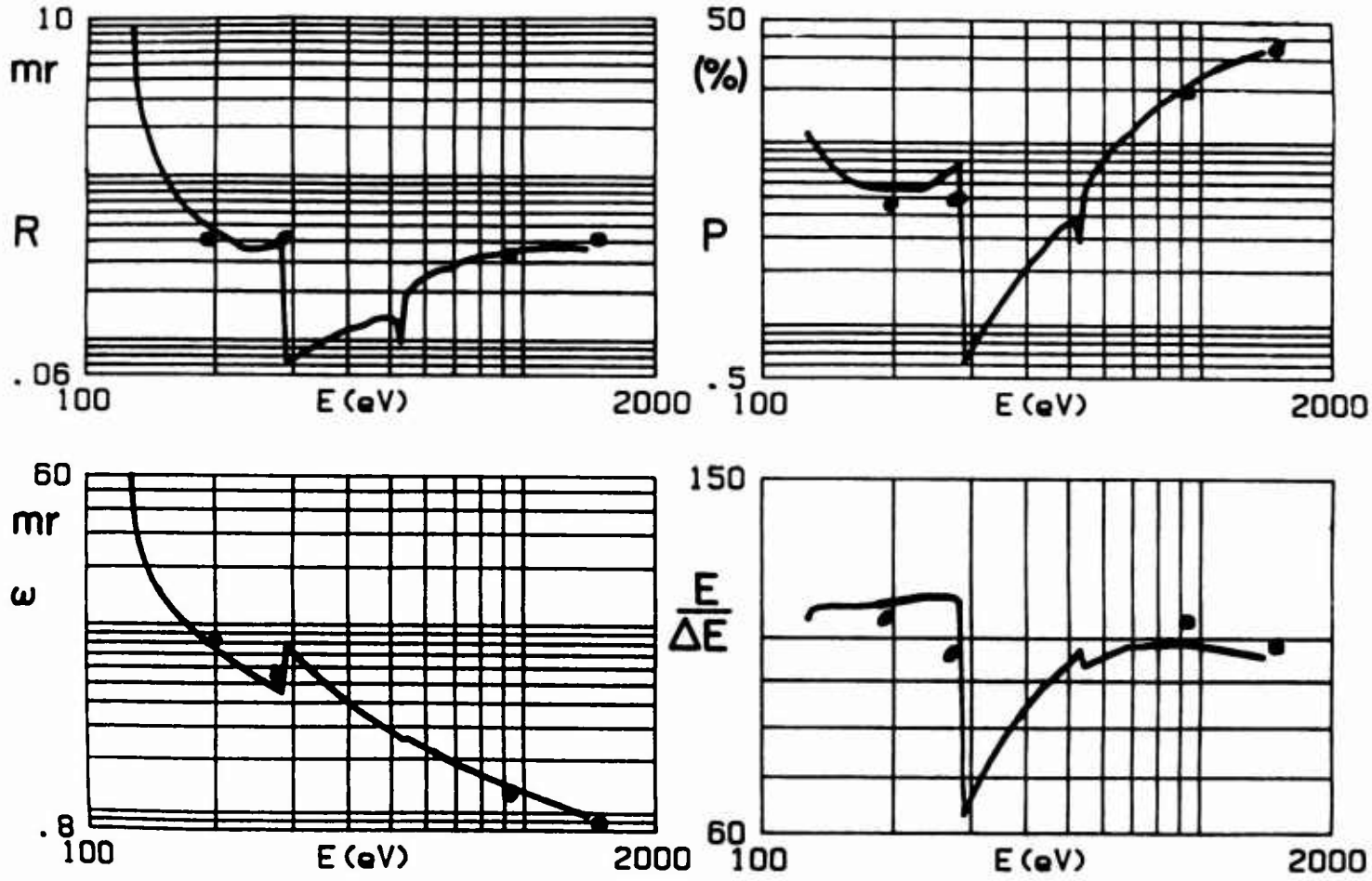

MOLECULAR
MULTILAYER DEPOSITION
(Y-TYPE)
H_2O + Pb ION SUBSTRATE
MENISCUS

Figure 3. Characterization of a Molecular Lead Stearate Multilayer



XBL 867-2662

Figure 4. Flat-Continuum Response of Lead Stearate (2d = 100 A)

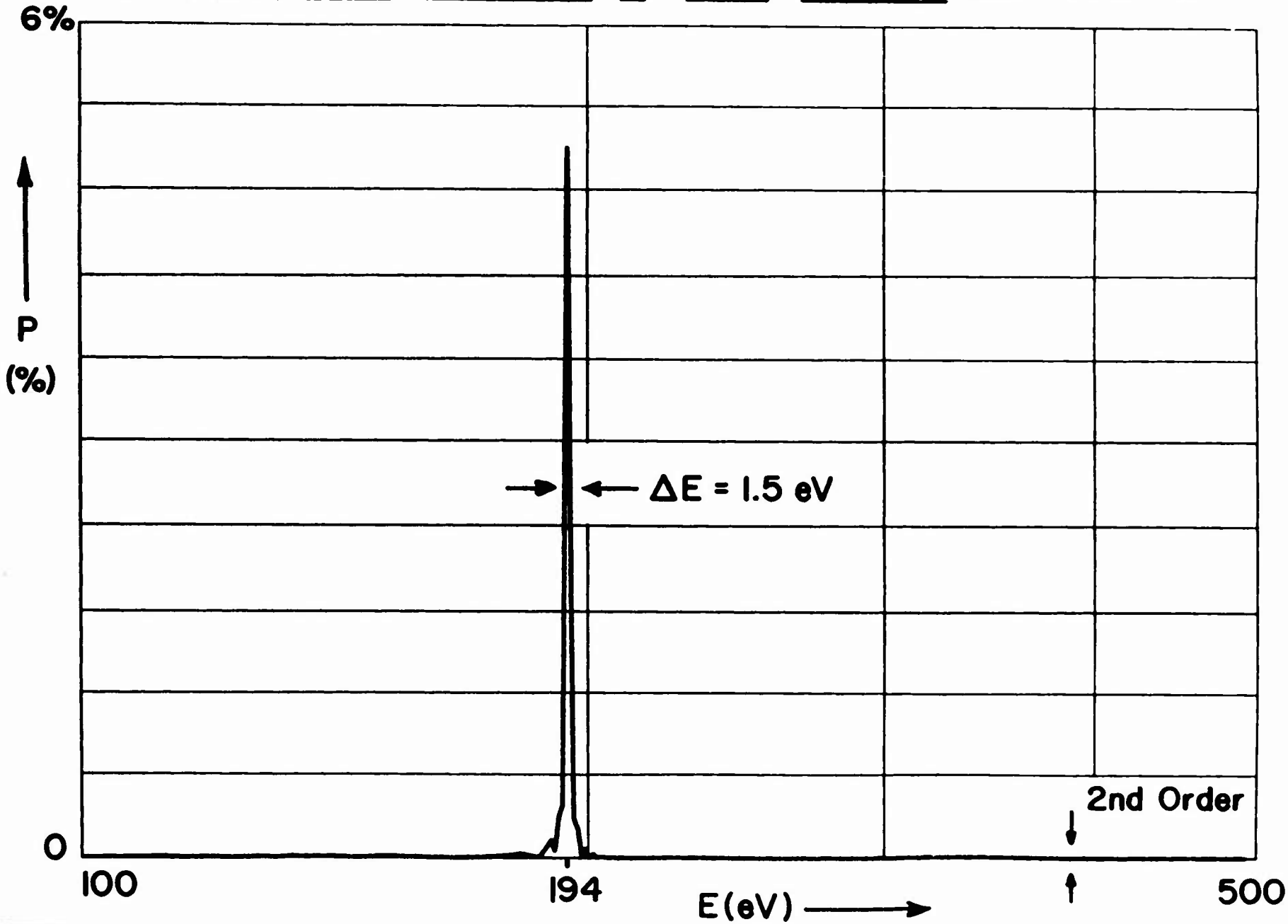


Figure 5. Integrated Reflectivity for Three Stearate Multilayer Crystals

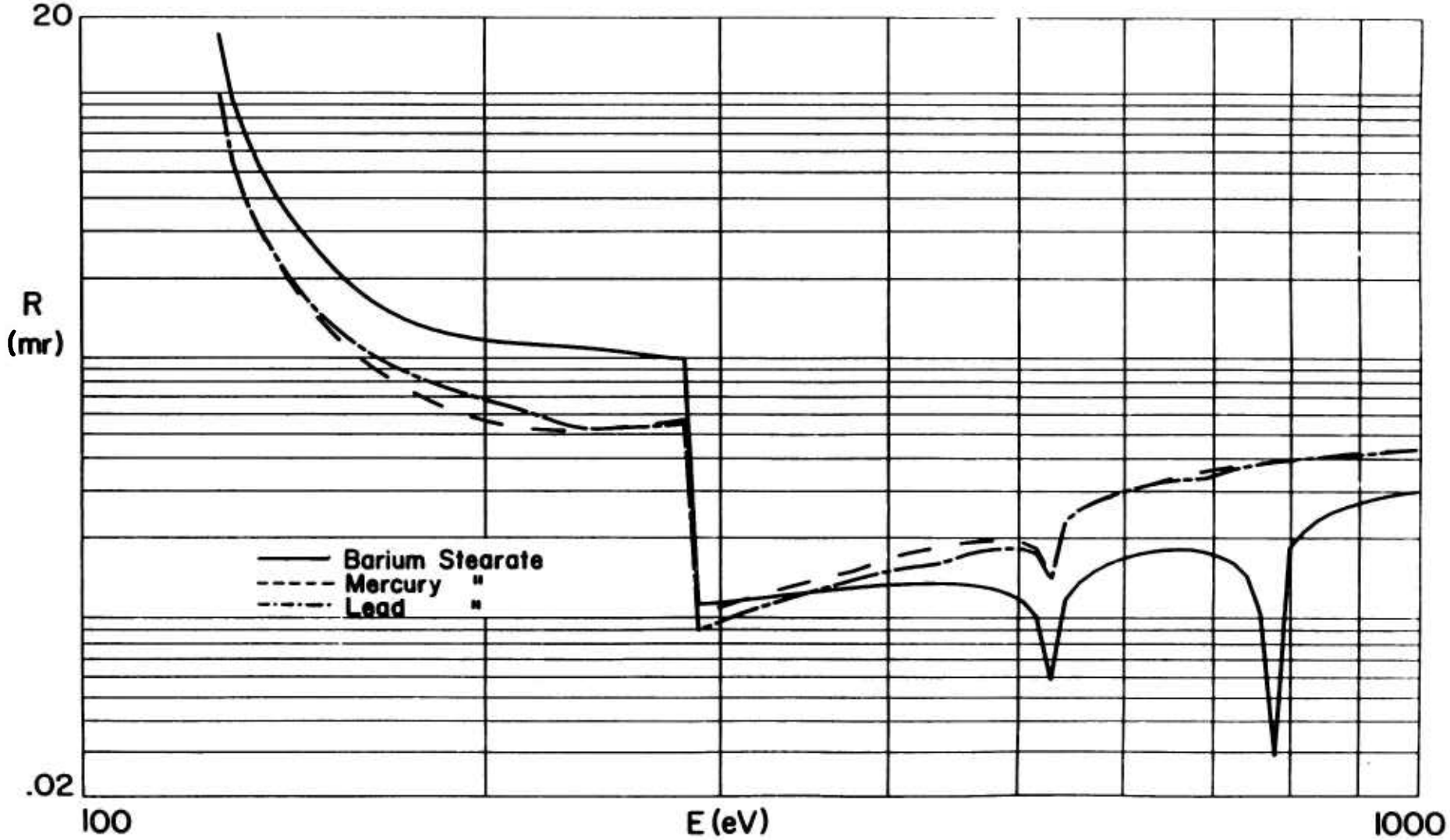


Figure 6. Peak Reflectivity for Three Stearate Multilayer Crystals

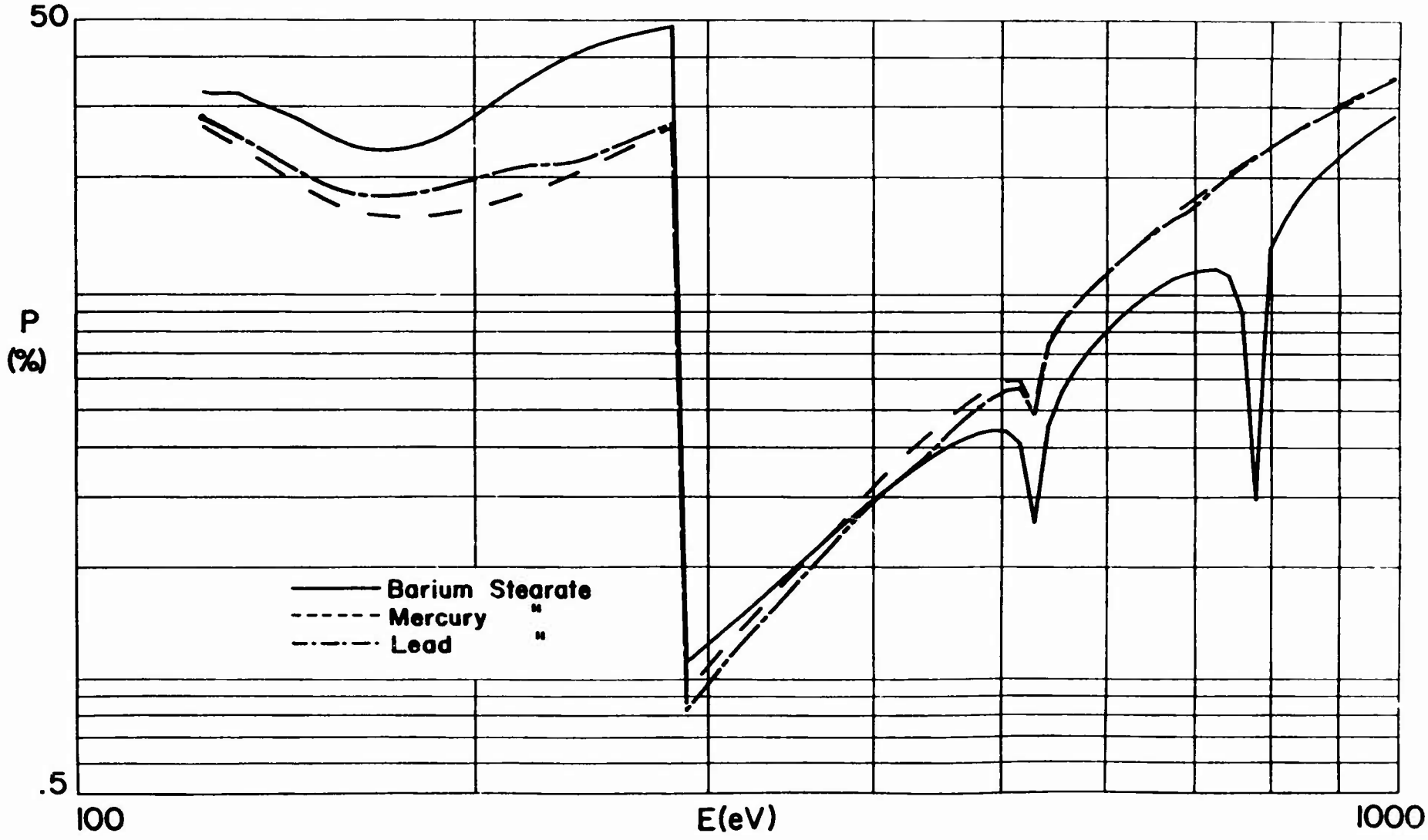


Figure 7.

Characterization of a Sputtered Vanadium/Carbon Multilayer

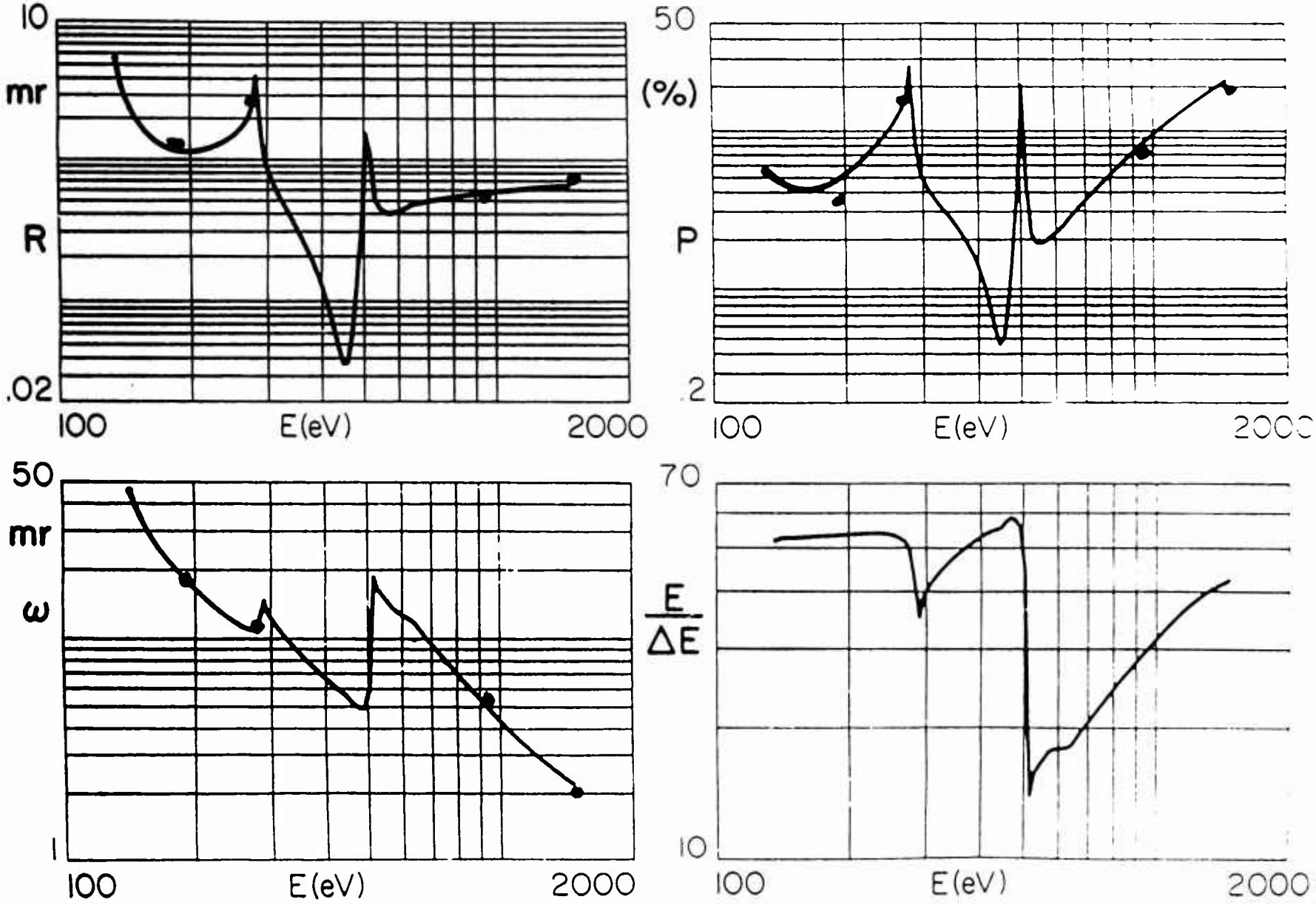


Figure 8.

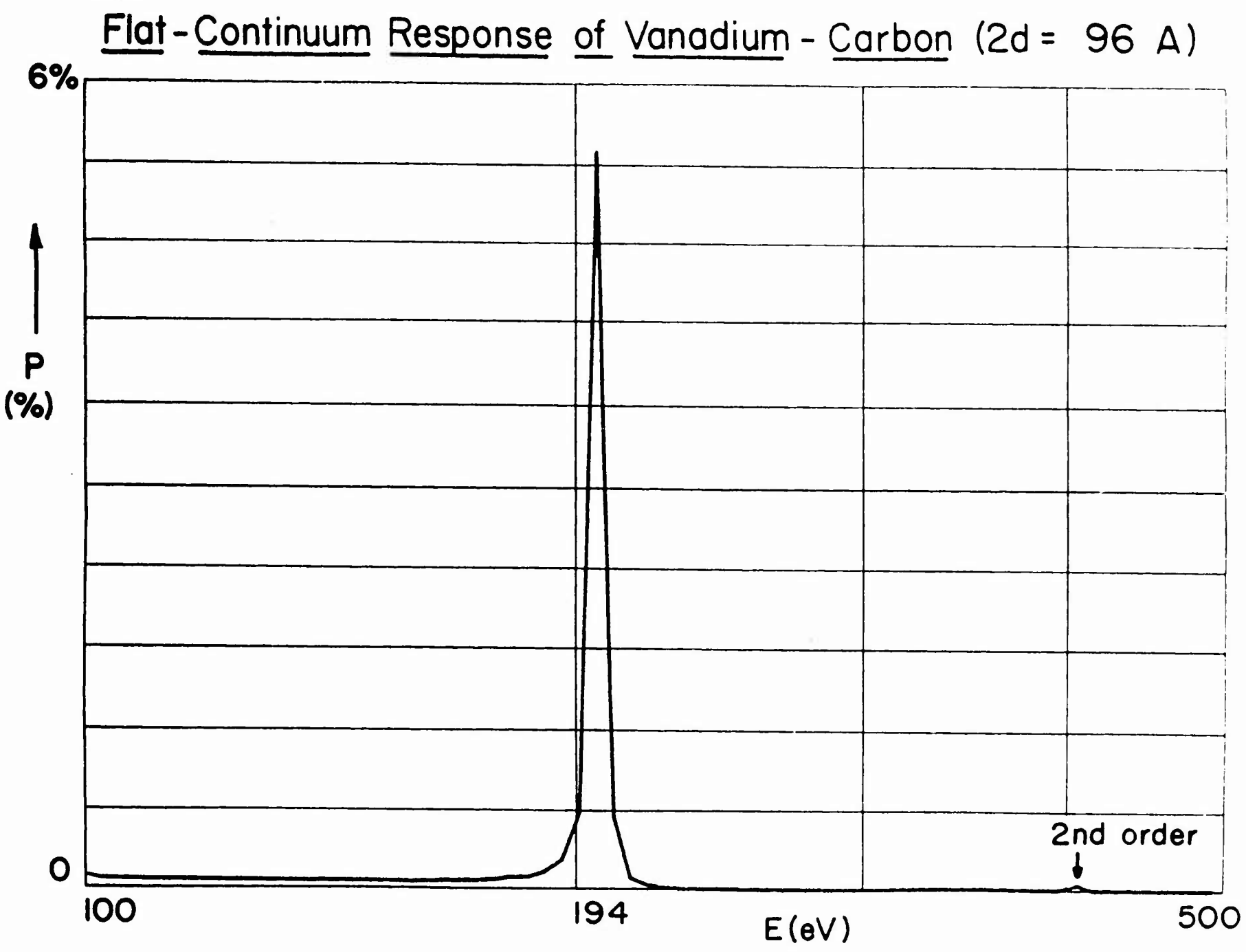

Flat - Continuum Response of Vanadium - Carbon (2d = 96 A)
6%
P
(%)
0
100
194
E(eV)
500
2nd order

Figure 9.

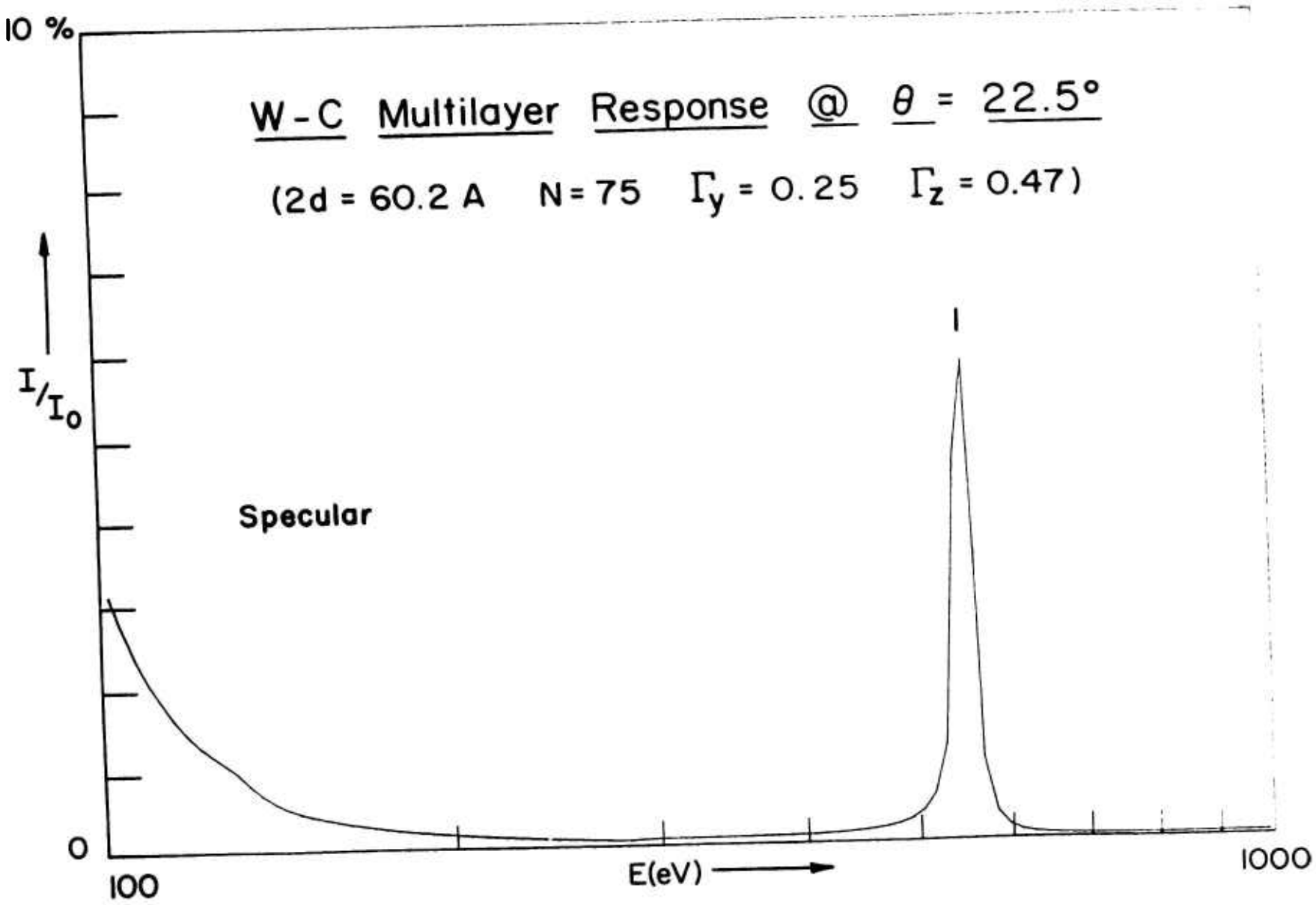
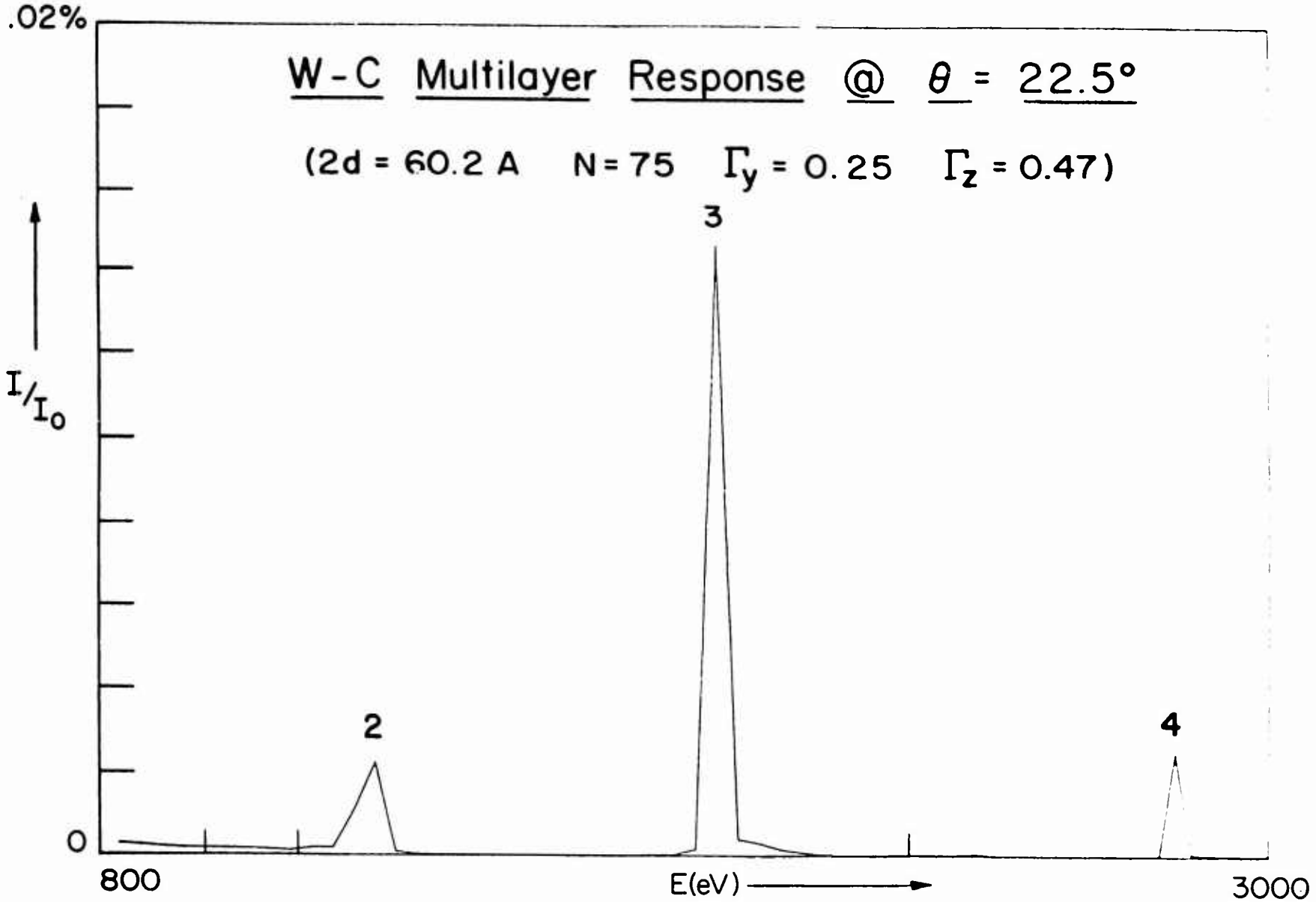

10 %
W-C Multilayer Response @ θ = 22.5°
(2d = 60.2 A N = 75 Γy = 0.25 Γz = 0.47)
I/I0
Specular
1
0
100
E(eV)
1000

Figure 10.


.02%
W-C Multilayer Response @ θ = 22.5°
(2d = 60.2 A N = 75 Γy = 0.25 Γz = 0.47)
I/I0
0
2
3
4
800
E(eV)
3000

6. TECHNICAL NOTES

The High Energy X-Ray Response of Some Useful Crystal Analyzers

The crystal analyzers that are applied in the SPEAXS system are characterized on our LBL calibration facility at several photon energies. We fit to these experimentally derived data appropriate theoretical analytical reflectivity functions which then yield absolute reflectivity characteristics for the entire photon energy region of application. Theoretical crystal reflectivity tables and curves are not only useful as an interpolational basis but can also provide important insights as to relative reflection efficiencies, existence and effect of absorption edges, and generally, the appropriateness of a given crystal analyzer for analysis within a particular photon energy region.

Presented here are tabulated and plotted values for the integrated reflectivity, R, the peak percent reflectivity, P, the FWHM, ω, and the resolving power, $E/\Delta E$ for some natural crystals that may be cleaved or cut with the desired reflecting planes parallel to the surface of a thin bendable section. The crystals that are characterized are:

Crystal (Plane)	2d(A)	Diffraction Orders
Silicon-Si (422)	2.218	1
Germanium-Ge (422)	2.310	1
Lithium Fluoride-LiF (220)	2.848	1
Silicon-Si (220)	3.840	1,2
Florite-CaF_2 (220)	3.862	1,2
Germanium-Ge (220)	4.000	1,2
Lithium Floride-LiF (200)	4.026	1,2
Florite-CaF_2 (111)	6.308	1,2,3
Germanium-Ge (111)	6.532	1,3
Graphite-C (002)	6.696	1,2,3
Petaerythritol-Pet (002)	8.742	1,2,3,4,5
Mica (002)	20.000	1,2,3,4,5
Rubidium Acid Phthalate-RAP (001)	26.140	1,2,3,4,5
Potassium Acid Pthalate-KAP (001)	26.620	1,2,3,4,5
Thallium Acid Pthalate-TAP (001)	26.620	1,2,3,4,5

These crystals may be described by symmetrical unit cells of volume, V, spacing, d, and of structure factor, $F_1 + F_2$. For symmetric unit cells,

The specific crystal planes being used are normally specified by their Miller indices (hkl). When these indices and the crystal coordinates are known, the volume of the unit cell, V, is given by:

$$V = abc\sqrt{1 + 2\cos\alpha\cos\beta\cos\gamma - \cos^2\alpha - \cos^2\beta - \cos^2\gamma}$$

and d may be found from:

$$\begin{aligned}(V/d)^2 = {} & h^2b^2c^2\sin^2\alpha + k^2a^2c^2\sin^2\beta + l^2a^2b^2\sin^2\gamma \\ & + 2hk\,(abc^2)\,(\cos\alpha\cos\beta - \cos\gamma) \\ & + 2kl\,(a^2bc)\,(\cos\beta\cos\gamma - \cos\alpha) \\ & + 2lh\,(ab^2c)\,(\cos\gamma\cos\alpha - \cos\beta)\end{aligned}$$

z/d is given by:

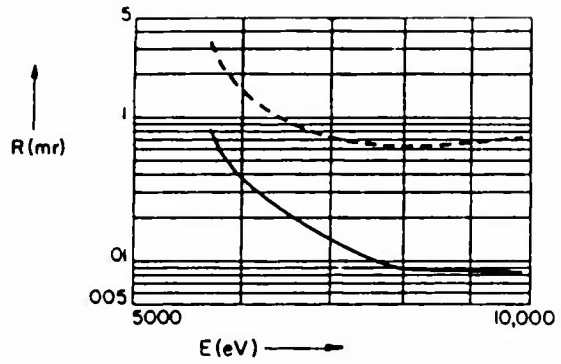
$$z/d = hx' + ky' + mz'$$

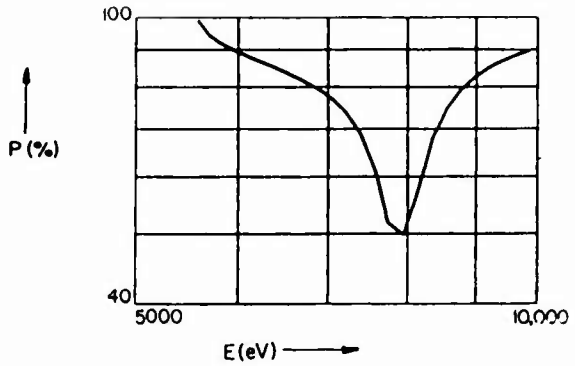
A constant may be added in order to make the z/d positions symmetrical about z = 0. Note: For crystals with a hexagonal unit cell, often four-component Miller indices are used; this notation may be converted to normal Miller indices by neglecting the third component.

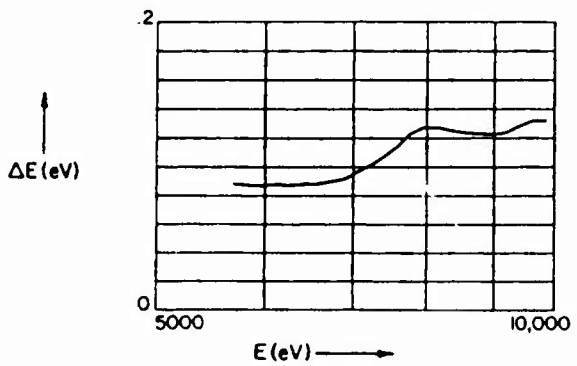
Silicon
Si

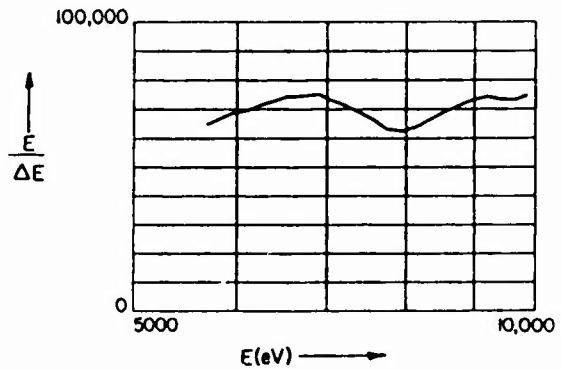
2d = 2.218Å
(422) m = 1

E(eV)	θ_c(mr)	θ_B(mr)	R_p(mr)	R_m(mr)	P(%)	ω(mr)	ΔE(eV)	E/ΔE	λ(Å)
5592.0	5.7	1571.0	2.90100		99.0	1.960			2.217
5899.0	5.4	1247.0	0.04503	0.1815	91.0	0.044	0.088	67400.	2.102
6930.0	4.6	939.0	0.01482	0.0739	79.0	0.018	0.093	74400.	1.789
7478.0	4.2	845.0	0.01067	0.0649	66.0	0.017	0.110	67700.	1.658
8048.0	3.9	768.0	0.00877	0.0628	51.0	0.016	0.129	62400.	1.541
8639.0	3.7	704.0	0.00855	0.0644	77.0	0.012	0.123	70200.	1.435
9886.0	3.2	601.0	0.00834	0.0736	90.0	0.009	0.135	73300.	1.254





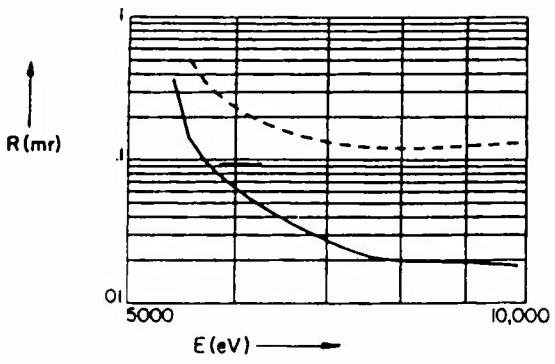


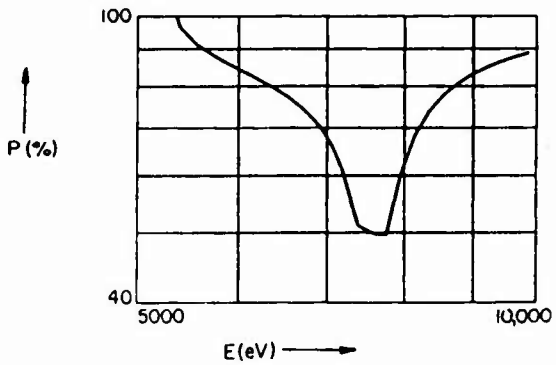


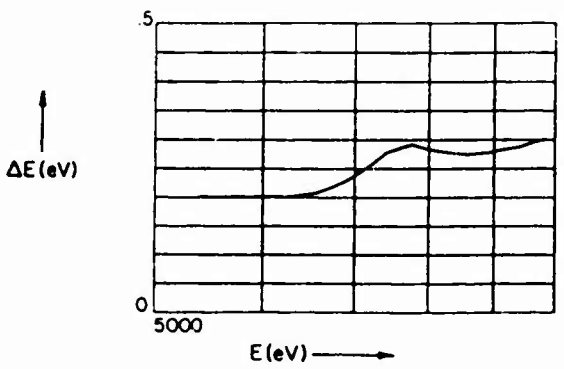
Germanium
Ge

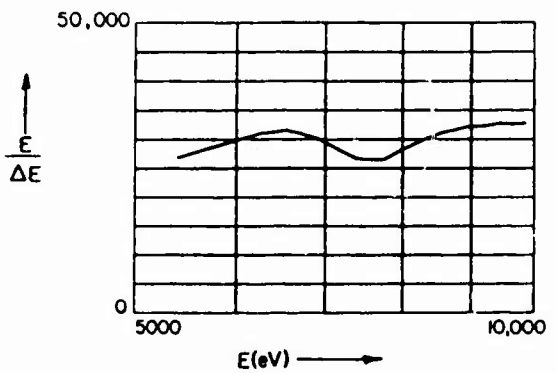
2d - 2.310Å
(422) m - 1

E(eV)	θ_c(mr)	θ_β(mr)	R_p(mr)	R_m(mr)	P(%)	ω(mr)	ΔE(eV)	E/ΔE	λ(Å)
5368.7	8.2	1571.0	4.4970		99.0	3.190			2.309
5414.7	8.1	1440.0	0.2993	1.069	96.0	0.284	0.20	26900.	2.290
5898.8	7.5	1144.0	0.0714	0.260	86.0	0.075	0.20	29400.	2.102
6930.3	6.4	886.0	0.0285	0.135	70.0	0.041	0.23	29900.	1.789
7478.1	5.9	801.0	0.0216	0.123	50.0	0.039	0.28	26400.	1.658
8047.8	5.5	730.0	0.0197	0.120	65.0	0.032	0.28	28500.	1.541
8638.9	5.1	671.0	0.0193	0.123	79.0	0.025	0.27	31400.	1.435
9886.4	4.4	574.0	0.0181	0.131	89.0	0.020	0.30	32700.	1.254





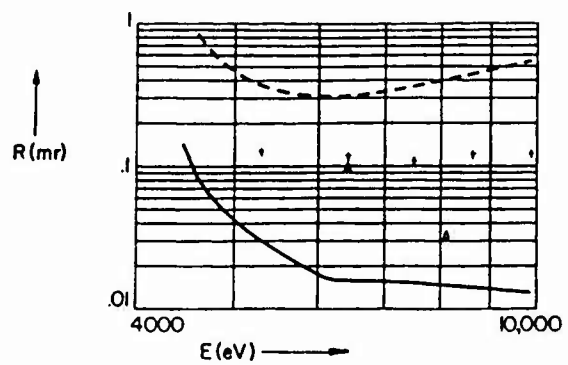


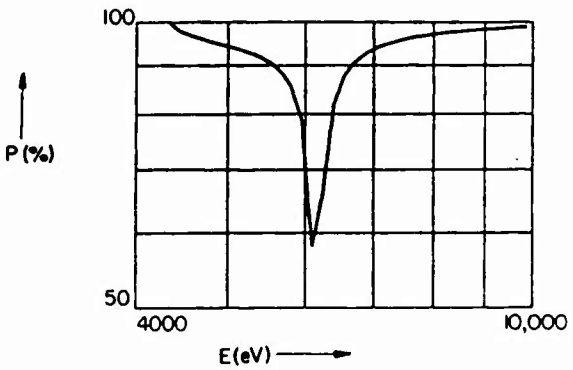


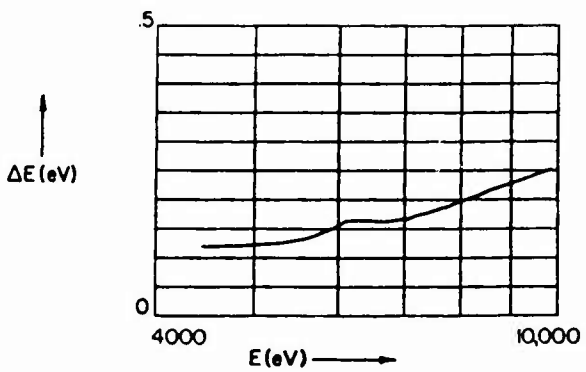
Lithium Floride
LiF

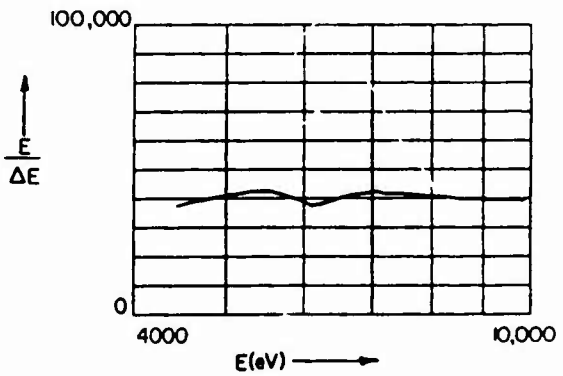
2d = 2.848Å
(220) m = 1

E(eV)	θ_c(mr)	θ_B(mr)	R_p(n)	R_m(mr)	P(%)	ω(mr)	ΔE(eV)	E/ΔE	λ(Å)
4353.0	7.5	1571.0	3.9780		99.0	2.710			2.848
4466.0	7.3	1346.0	0.1312	1.312	98.0	0.116	0.12	37500.	2.776
4511.0	7.2	1306.0	0.1086	1.088	97.0	0.097	0.12	37900.	2.748
4952.0	6.6	1074.0	0.0449	0.484	94.0	0.045	0.12	40900.	2.504
5415.0	6.0	934.0	0.0274	0.353	92.0	0.032	0.13	42600.	2.290
5899.0	5.5	830.0	0.0188	0.313	82.0	0.028	0.15	39500.	2.102
6930.0	4.7	679.0	0.0156	0.330	93.0	0.019	0.17	41800.	1.789
7478.0	4.3	621.0	0.0152	0.361	96.0	0.017	0.18	41300.	1.658
8048.0	4.0	572.0	0.0148	0.400	97.0	0.016	0.20	40400.	1.541
8639.0	3.7	528.0	0.0142	0.444	98.0	0.015	0.22	39600.	1.435
9886.0	3.3	456.0	0.0129	0.547	99.0	0.013	0.25	39000.	1.254





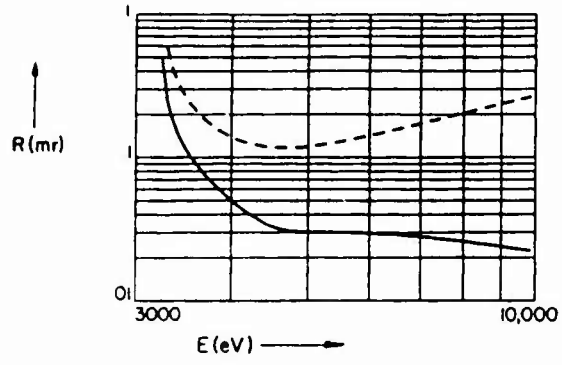


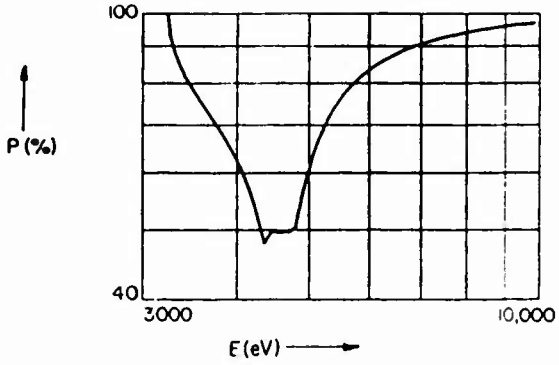


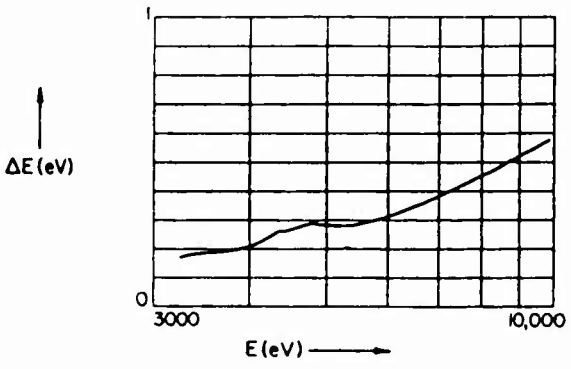
Silicon
Si

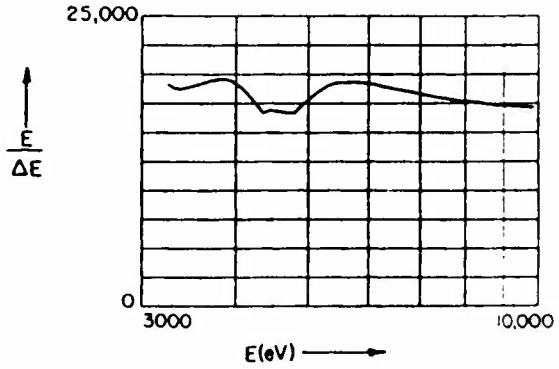
2d = 3.840Å
(220) m = 1

E(eV)	θ_c(mr)	θ_B(mr)	R_p(mr)	R_m(mr)	P(%)	ω(mr)	ΔE(eV)	E/ΔE	λ(Å)
3229.0	9.4	1571.0	5.5960		99.00	3.890			3.840
3692.0	8.4	1065.0	0.0764	0.186	72.00	0.093	0.19	19400.	3.358
4466.0	7.0	808.0	0.0336	0.118	50.00	0.062	0.26	16900.	2.776
4511.0	7.0	798.0	0.0328	0.117	50.00	0.061	0.27	16800.	2.748
4952.0	6.4	710.0	0.0302	0.118	59.00	0.049	0.28	17600.	2.504
5415.0	5.8	639.0	0.0300	0.127	74.00	0.039	0.28	19200.	2.290
5899.0	5.4	579.0	0.0296	0.139	82.00	0.034	0.31	19300.	2.102
6930.0	4.6	485.0	0.0280	0.171	90.00	0.029	0.38	18300.	1.789
7478.0	4.2	446.0	0.0269	0.188	93.00	0.027	0.42	18000.	1.658
8048.0	3.9	413.0	0.0258	0.206	94.00	0.025	0.46	17700.	1.541
8639.0	3.7	383.0	0.0246	0.225	95.00	0.023	0.50	17400.	1.435
9886.0	3.2	333.0	0.0222	0.265	97.00	0.020	0.58	17100.	1.254





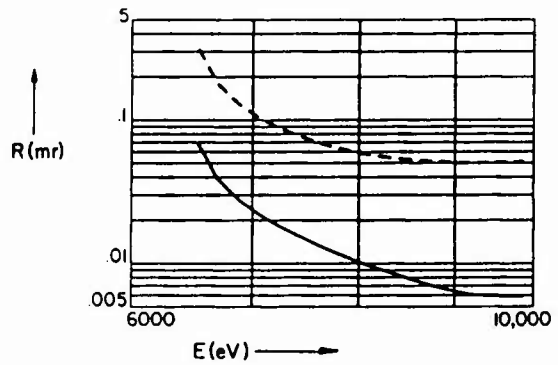


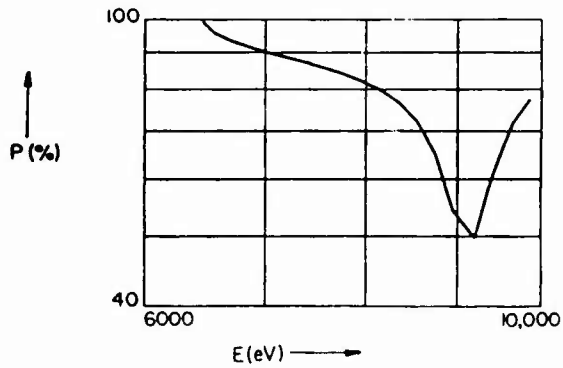


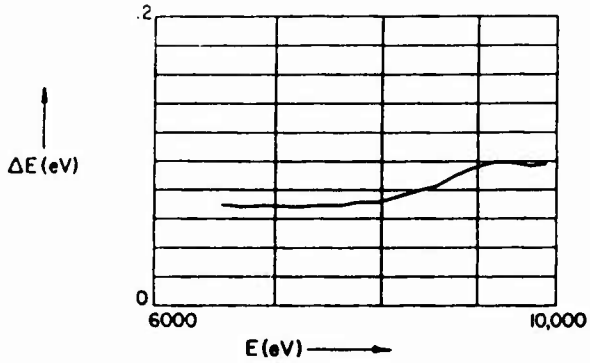
Silicon
Si

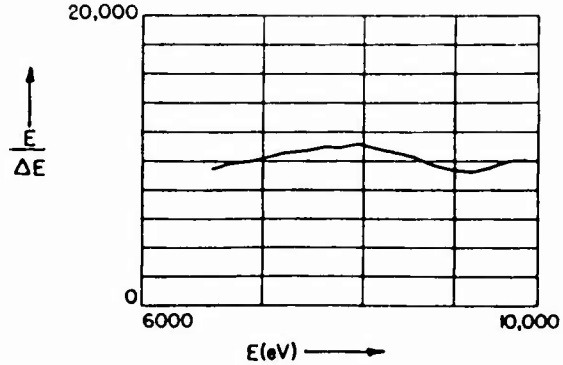
2d = 3.840Å
(220) m = 2

E(eV)	θ_c(mr)	θ_B(mr)	R_p(mr)	R_m(mr)	P(%)	ω(mr)	ΔE(eV)	E/ΔE	λ(Å)
6457.0	4.9	1571.0	2.2920		99.0	1.4700			1.920
6930.0	4.6	1199.0	0.0258	0.1207	91.0	0.0255	0.069	101000.	1.789
7478.0	4.2	1042.0	0.0147	0.0742	86.0	0.0160	0.070	107000.	1.658
8048.0	3.9	931.0	0.0100	0.0581	81.0	0.0123	0.074	109000.	1.541
8639.0	3.7	844.0	0.0073	0.0518	69.0	0.0113	0.087	99900.	1.435
9886.0	3.2	712.0	0.0059	0.0513	78.0	0.0083	0.096	103000.	1.254





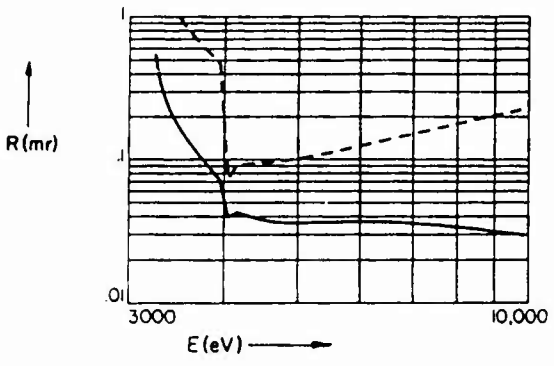


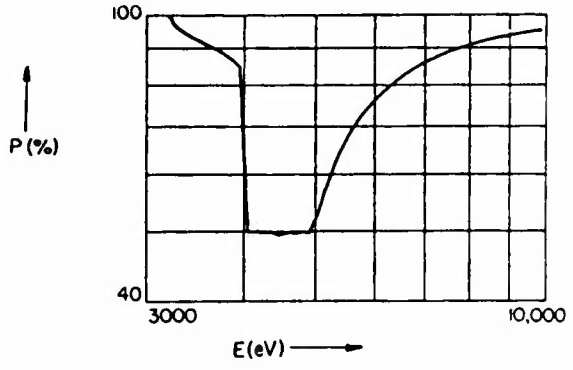


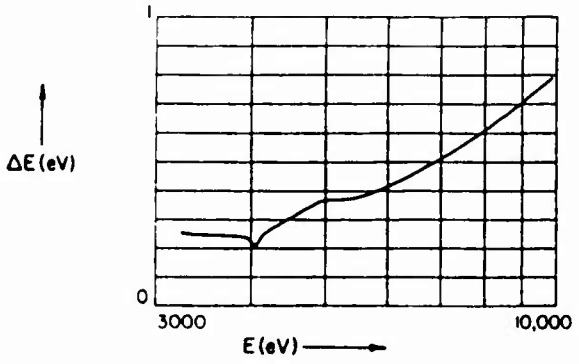
Florite
CaF_2

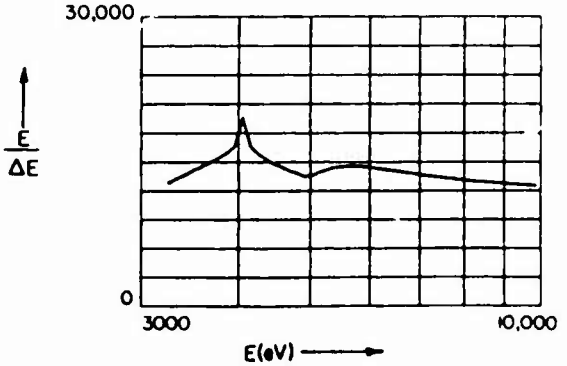
2d = 3.862Å
(220) m = 1

E(eV)	θ_c(mr)	θ_B(mr)	R_p(mr)	R_m(mr)	P(%)	ω(mr)	ΔE(eV)	E/ΔE	λ(Å)
3209.8	11.1	1571.0	6.3510		100.0	4.370			3.863
3691.7	9.6	1054.0	0.1112	0.682	89.0	0.117	0.24	15100.	3.358
4466.3	7.7	802.0	0.0381	0.095	49.0	0.070	0.30	14800.	2.776
4510.8	7.6	792.0	0.0376	0.095	50.0	0.069	0.31	14600.	2.749
4952.2	7.1	705.0	0.0361	0.101	49.0	0.064	0.37	13300.	2.504
5414.7	6.6	635.0	0.0366	0.110	65.0	0.051	0.37	14500.	2.290
5898.8	6.1	575.0	0.0369	0.122	75.0	0.045	0.41	14500.	2.102
6930.3	5.2	482.0	0.0359	0.150	86.0	0.038	0.50	13700.	1.789
7478.1	4.9	444.0	0.0349	0.165	89.0	0.036	0.56	13400.	1.658
8047.8	4.5	410.0	0.0337	0.180	91.0	0.033	0.62	13100.	1.541
8638.9	4.2	381.0	0.0323	0.195	93.0	0.031	0.67	12800.	1.435
9886.4	3.7	331.0	0.0295	0.227	95.0	0.028	0.79	12500.	1.254





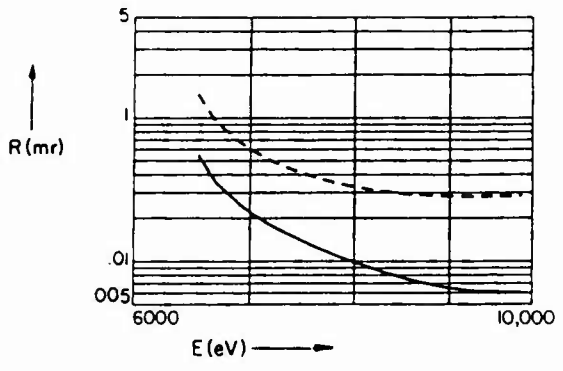


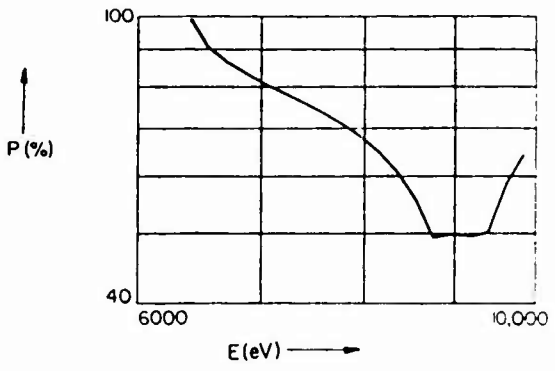


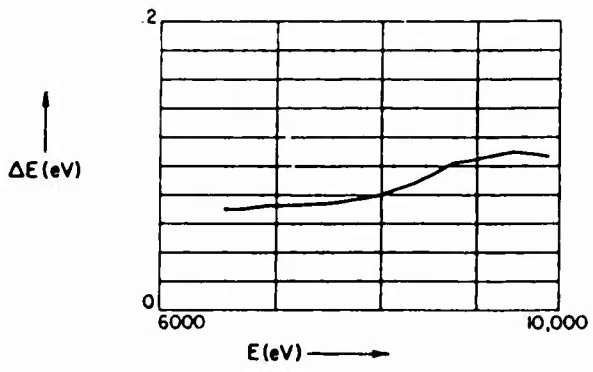
Florite
CaF_2

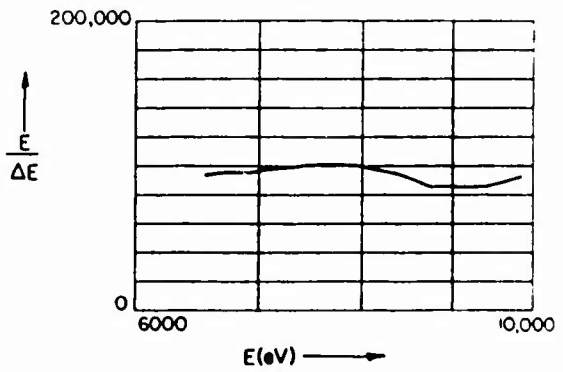
2d = 3.862Å
(220) m = 2

E(eV)	θ_c(mr)	θ_B(mr)	R_p(mr)	R_m(mr)	P(%)	ω(mr)	ΔE(eV)	E/ΔE	λ(Å)
6419.5	5.6	1571.0	2.3530		99.0	1.470			1.931
6930.3	5.2	1184.0	0.0238	0.0650	82.0	0.026	0.07	96400.	1.789
7478.1	4.9	1032.0	0 0139	0.0410	75.0	0.016	0.07	102000.	1.658
8047.8	4.5	923.0	0.0096	0.0324	67.0	0.013	0.08	99100.	1.541
8638.9	4.2	838.0	0.0073	0.0290	53.0	0.013	0.10	87500.	1.435
9286.4	3.7	707.0	0.0060	0.0286	65.0	0.009	0.11	92400.	1.254





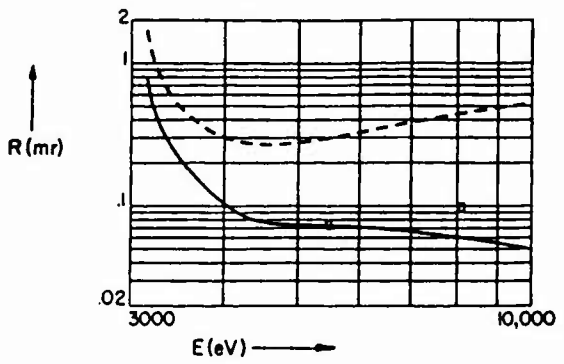


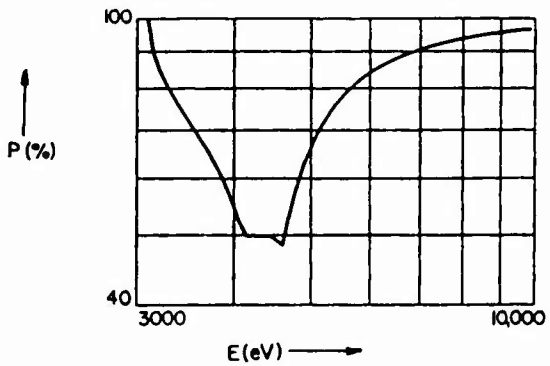


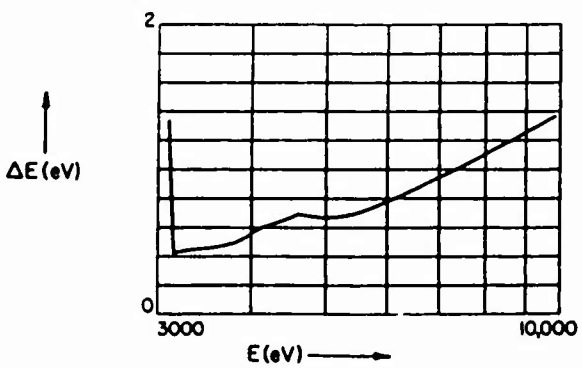
Germanium
Ge

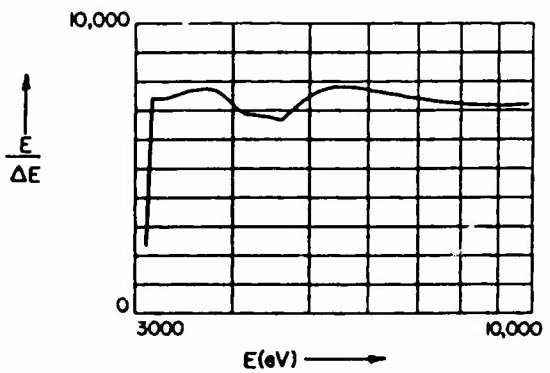
2d = 4.000Å
(220) m = 1

E(eV)	θ_c(mr)	θ_B(mr)	R_p(mr)	R_m(mr)	P(%)	ω(mr)	ΔE(eV)	E/ΔE	λ(Å)
3099.7	13.4	1571.0	9.0260		99.0	6.260			4.000
3691.7	11.6	997.0	0.1508	0.374	66.0	0.199	0.5	7750.	3.358
4466.3	9.8	767.0	0.0771	0.269	50.0	0.143	0.7	6760.	2.776
4510.8	9.7	758.0	0.0763	0.269	50.0	0.140	0.7	6740.	2.749
4952.2	8.9	676.0	0.0735	0.275	65.0	0.108	0.7	7420.	2.504
5414.7	8.1	610.0	0.0728	0.295	76.0	0.090	0.7	7800.	2.290
5898.8	7.5	553.0	0.0714	0.321	83.0	0.080	0.8	7740.	2.102
6930.3	6.4	464.0	0.0665	0.380	90.0	0.067	0.9	7420.	1.789
7478.1	5.9	427.0	0.0634	0.411	92.0	0.062	1.0	7310.	1.658
8047.8	5.5	395.0	0.0602	0.441	94.0	0.058	1.1	7220.	1.541
8638.9	5.1	367.0	0.0569	0.470	95.0	0.054	1.2	7180.	1.435
9886.4	4.4	319.0	0.0501	0.517	97.0	0.046	1.4	7220.	1.254





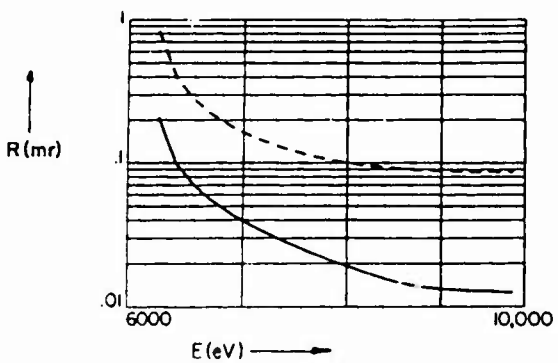


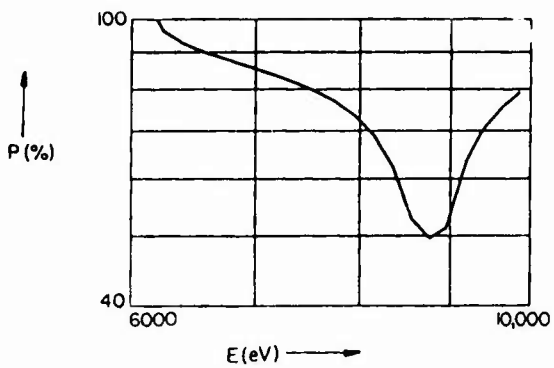


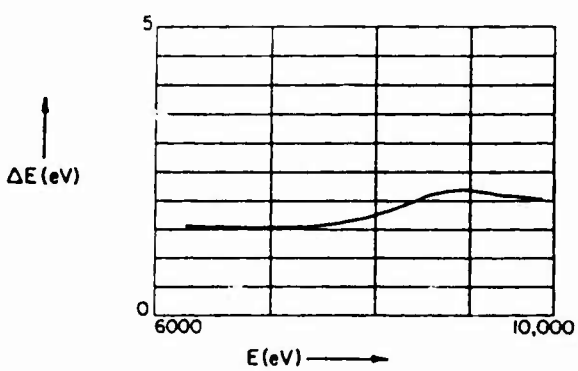
Germanium
Ge

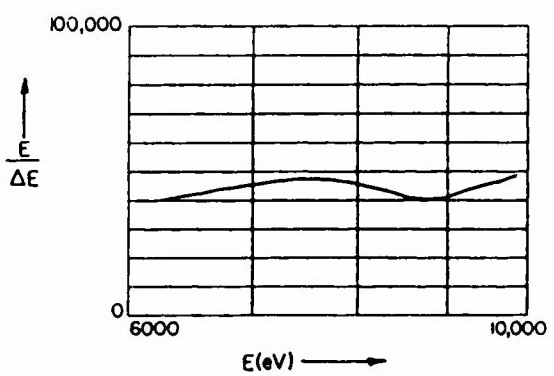
2d = 4.000Å
(220) m = 2

E(eV)	θ_c(mr)	θ_B(mr)	R_p(mr)	R_m(mr)	P(%)	ω(mr)	ΔE(eV)	E/ΔE	λ(Å)
6199.3	7.1	1571.0	3.533		99.0	2.380			2.000
6930.3	6.4	1107.0	0.042	0.1725	86.0	0.045	0.15	45000.	1.789
7478.1	5.9	977.0	0.027	0.1200	80.0	0.031	0.16	47300.	1.658
8047.8	5.5	879.0	0.019	0.0988	71.0	0.027	0.18	45400.	1.541
8638.9	5.1	800.0	0.014	0.0900	48.0	0.026	0.22	39900.	1.435
9886.4	4.4	678.0	0.013	0.0861	80.0	0.016	0.20	48800.	1.254





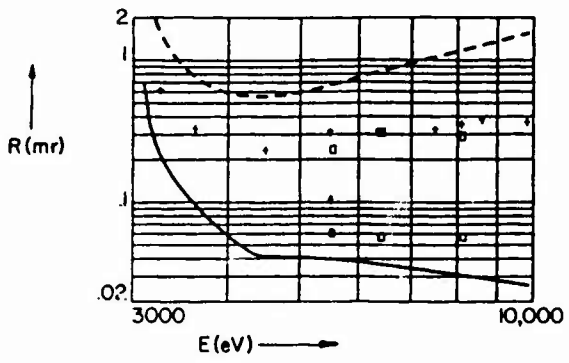


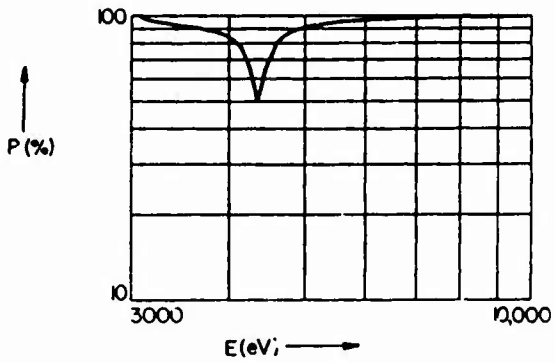


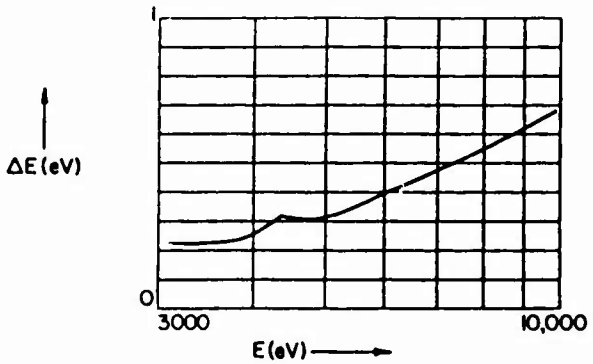
Lithium Floride
LiF

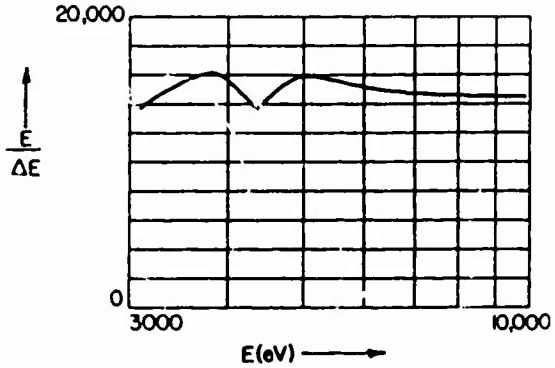
2d = 4.026Å
(200) m = 1

E(eV)	θ_c(mr)	θ_B(mr)	R_p(mr)	R_m(mr)	P(%)	ω(mr)	ΔE(eV)	E/ΔE	λ(Å)
3079.0	10.6	1571.0	6.0270		100.0	4.150			4.027
3692.0	8.8	986.0	0.0859	0.708	90.0	0.094	0.23	16000.	3.358
4466.0	7.3	761.0	0.0416	0.555	68.0	0.067	0.31	14300.	2.776
4511.0	7.2	751.0	0.0414	0.557	74.0	0.064	0.31	14500.	2.748
4952.0	6.6	671.0	0.0408	0.593	91.0	0.050	0.31	15800.	2.504
5415.0	6.0	605.0	0.0397	0.657	95.0	0.044	0.34	15700.	2.290
5899.0	5.5	549.0	0.0382	0.739	96.0	0.040	0.39	15300.	2.102
6930.0	4.7	460.0	0.0345	0.937	98.0	0.034	0.47	14700.	1.789
7478.0	4.3	424.0	0.0326	1.047	99.0	0.031	0.51	14600.	1.658
8048.0	4.0	393.0	0.0308	1.165	99.0	0.028	0.55	14600.	1.541
8639.0	3.7	364.0	0.0291	1.289	99.0	0.026	0.59	14500.	1.435
9886.0	3.3	317.0	0.0259	1.556	99.0	0.023	0.68	14500.	1.254





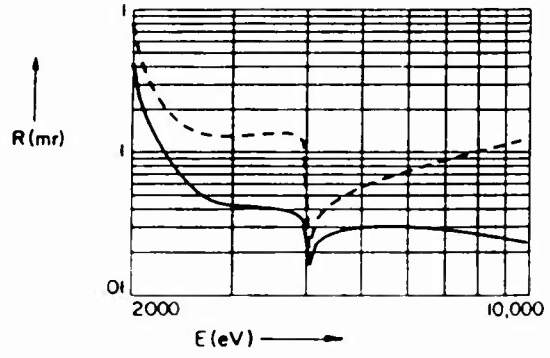


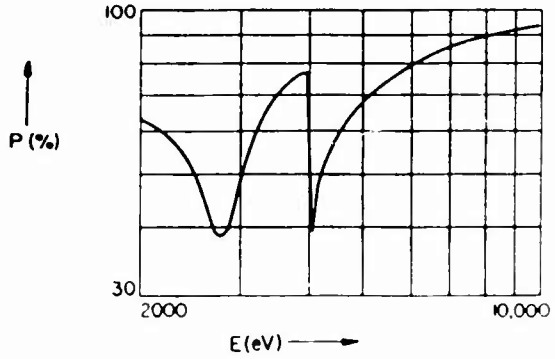


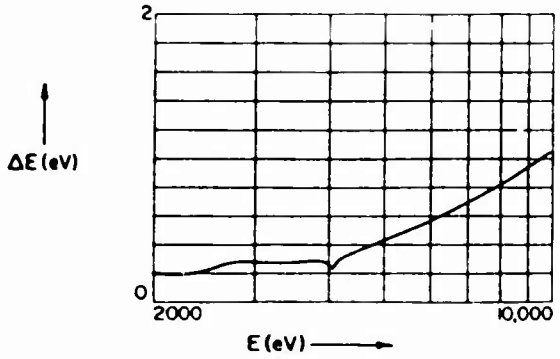
Flourite
CaF_2

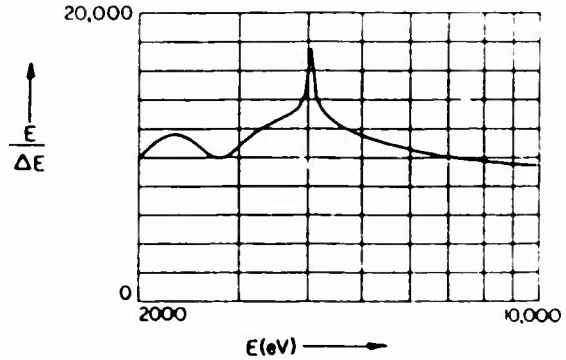
2d = 6.308Å
(111) m = 1

E(eV)	θ_c(mr)	θ_B(mr)	R_p(mr)	R_m(mr)	P(%)	ω(mr)	ΔE(eV)	E/ΔE	λ(Å)
1965.8	17.0	1571.0	11.7600		63 0	17.000			6.307
2042.4	16.4	1296.0	0.2578	0.502	62.0	0.344	0.20	10300.	6.070
2165.9	15.5	1138.0	0.1377	0.274	60.0	0.193	0.19	11200.	5.724
2293.2	14.7	1030.0	0.0944	0.198	57.0	0.144	0.20	11600.	5.407
2622.4	12.9	847.0	0.0526	0.137	43.0	0.109	0.25	10400.	4.728
2984.3	11.3	719.0	0.0425	0.128	48.0	0.082	0.28	10700.	4.154
3691.7	9.0	562.0	0.0388	0.136	75.0	0.049	0.28	13000.	3.358
4466.3	7.3	456.0	0.0274	0.045	58.0	0.039	0.36	12500.	2.776
4510.8	7.3	451.0	0.0277	0.047	59.0	0.039	0.36	12400	2.749
4952.2	6.7	408.0	0.0297	0.056	67.0	0.037	0.43	11600.	2.504
5414.7	6.2	372.0	0.0302	0.065	74.0	0.035	0.49	11100.	2.290
5898.8	5.7	340.0	0.0301	0.072	79.0	0.033	0.55	10600.	2.102
6930.3	4.9	288.0	0.0286	0.087	85.0	0.029	0.69	10100.	1.789
7478.1	4.6	266.0	0.0276	0.094	88.0	0.028	0.76	9860.	1.658
8047.8	4.3	247.0	0.0265	0.101	90.0	0.026	0.83	9700.	1.541
8638.9	4.0	230.0	0.0253	0.109	91.0	0.024	0.90	9590.	1.435
9886.4	3.5	200.0	0.0231	0.123	94.0	0.022	1.05	9410.	1.254





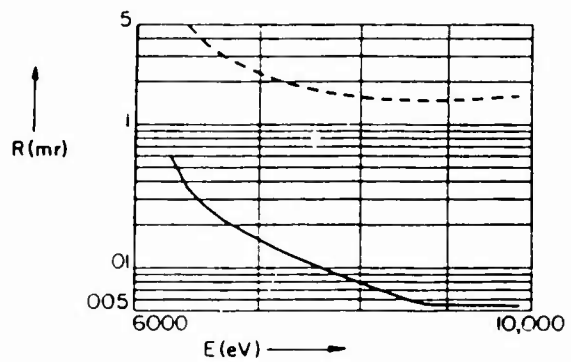


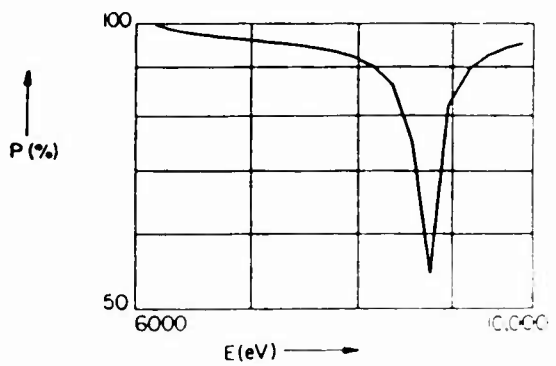


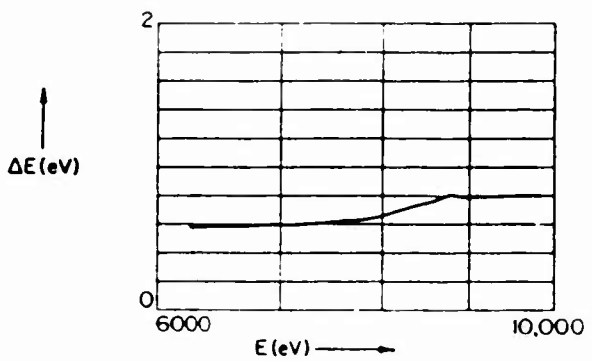
Lithium Floride
LiF

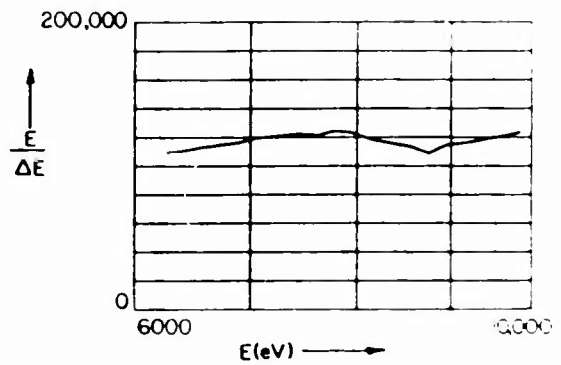
2d = 4.026Å
(200) m = 2

E(eV)	θ_c(mr)	θ_B(mr)	R_p(mr)	R_m(mr)	P(%)	ω(mr)	ΔE(eV)	E/ΔE	λ(Å)
6158.0	5.3	1571.0	2.25400		100.0	1.4700			2.013
6930.0	4.7	1094.0	0.01674	0.240	96.0	0.0165	0.059	118000.	1.789
7478.0	4.3	967.0	0.01072	0.177	95.0	0.0119	0.061	122000.	1.658
8048.0	4.0	871.0	0.00759	0.153	91.0	0.0098	0.067	121000.	1.541
8639.0	3.7	794.0	0.00570	0.147	58.0	0.0094	0.080	109000.	1.435
9886.0	3.3	672.0	0.00538	0.160	95.0	0.0066	0.081	121000.	1.254



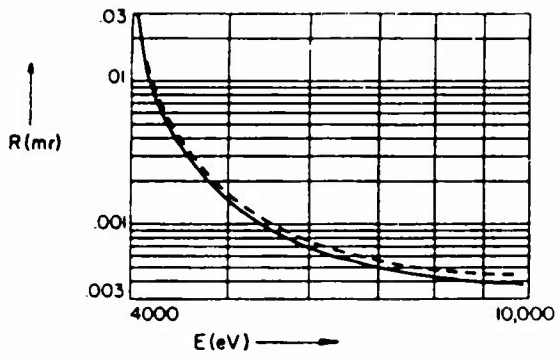


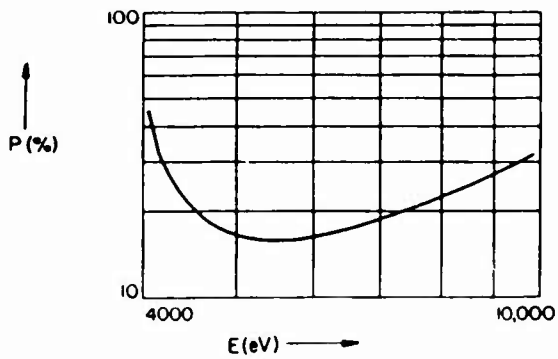


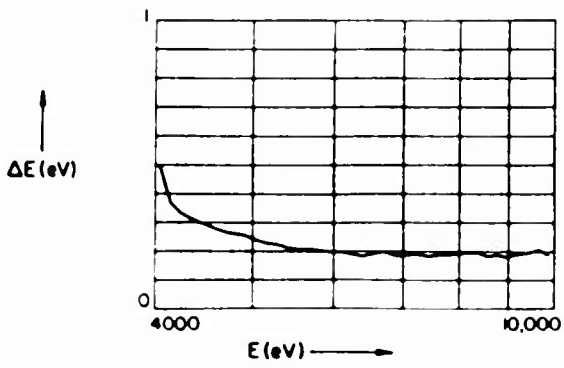


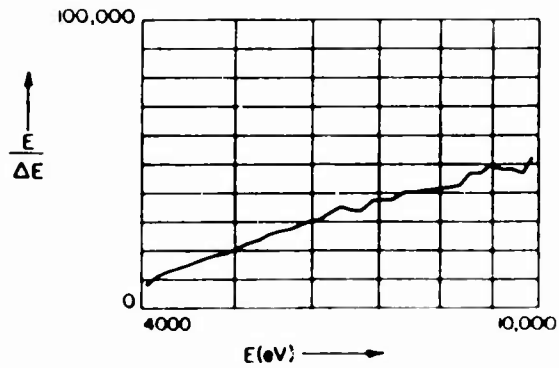
Florite CaF_2 — 2d = 6.308Å (111) — m = 2

E(eV)	θ_c(mr)	θ_B(mr)	R_p(mr)	R_m(mr)	P(%)	ω(mr)	ΔE(eV)	E/ΔE	λ(Å)
3931.2	8.4	1571.0	4.36300		68.0	5.9800			3.154
4466.3	7.3	1076.0	0.00368	0.00414	21.0	0.0125	0.030	148000.	2.776
4510.8	7.3	1058.0	0.00331	0.00371	20.0	0.0116	0.029	154000.	2.749
4952.2	6.7	917.0	0.00154	0.00172	17.0	0.0064	0.024	203000.	2.504
5414.7	6.2	813.0	0.00097	0.00108	16.0	0.0042	0.021	253000.	2.290
5898.8	5.7	729.0	0.00072	0.00080	16.0	0.0031	0.021	288000.	2.102
6930.3	4.9	603.0	0.00051	0.00057	18.0	0.0020	0.020	350000.	1.789
7478.1	4.6	554.0	0.00046	0.00051	20.0	0.0015	0.018	415000.	1.658
8047.8	4.3	510.0	0.00042	0.00048	23.0	0.0013	0.019	427000.	1.541
8638.9	4.0	472.0	0.00040	0.00046	25.0	0.0011	0.019	463000.	1.435
9886.4	3.5	409.0	0.00038	0.00044	32.0	0.0009	0.020	485000.	1.254





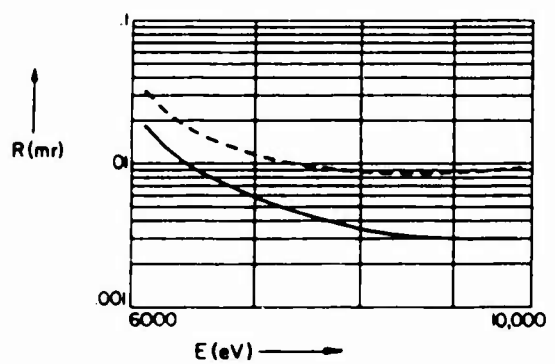


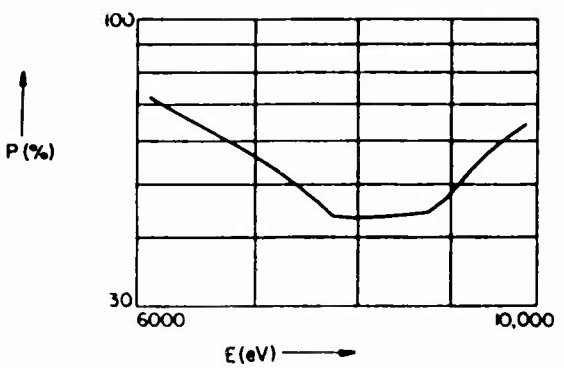


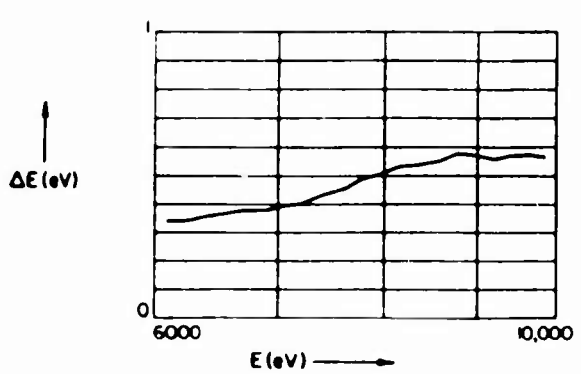
Florite
CaF_2

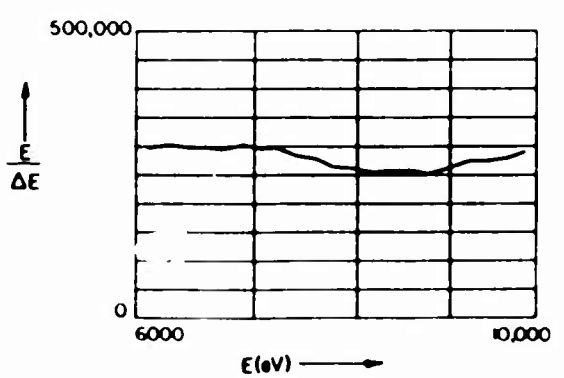
2d - 6.308Å
(111) m - 3

E(eV)	θ_c(mr)	θ_B(mr)	R_p(mr)	R_m(mr)	P(%)	ω(mr)	ΔE(eV)	E/ΔE	λ(Å)
5896.6	5.8	1571.0	2.2570		77.0	2.3200			2.103
5898.8	5.7	1544.0	0.1936	0.3385	77.0	0.2070	0.033	180000.	2.102
6930.3	4.9	1018.0	0.0061	0.0119	57.0	0.0092	0.039	176000.	1.789
7478.1	4.6	908.0	0.0043	0.0096	48.0	0.0078	0.046	164000.	1.658
8047.8	4.3	822.0	0.0034	0.0087	44.0	0.0068	0.051	158000.	1.541
8638.9	4.0	751.0	0.0031	0.0086	44.0	0.0060	0.056	155000.	1.435
9886.4	3.5	639.0	0.0030	0.0093	65.0	0.0043	0.057	173000.	1.254





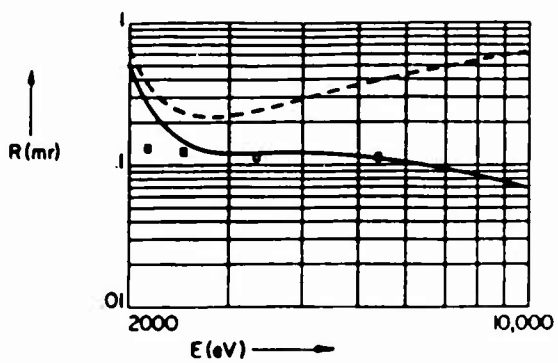


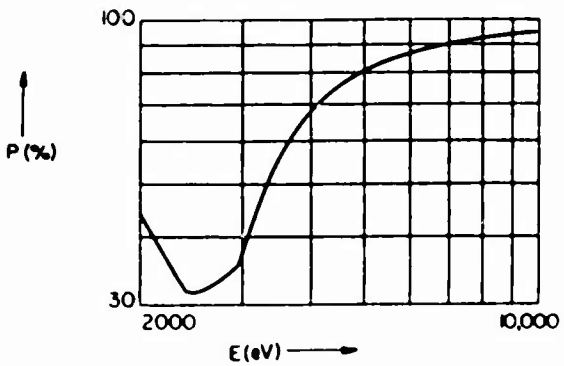


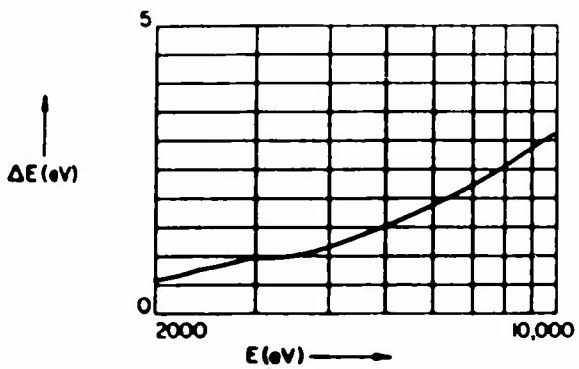
Germanium
Ge

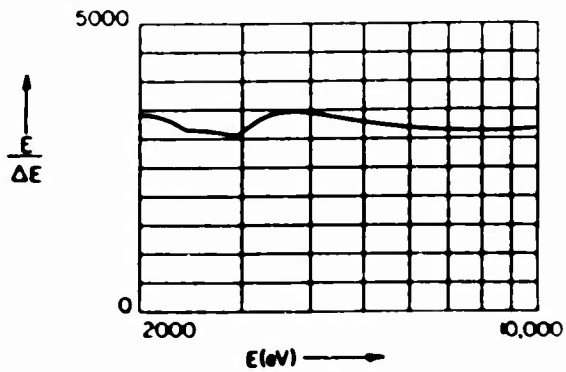
2d = 6.532Å
(111) m = 1

E(eV)	θ_c(mr)	θ_B(mr)	R_p(mr)	R_m(mr)	P(%)	ω(mr)	ΔE(eV)	E/ΔE	λ(Å)
1898.4	17.2	1571.0	14.3300		48.0	25.000			6.531
2042.4	17.0	1193.0	0.4035	0.541	42.0	0.741	0.6	3400.	6.070
2165.9	16.6	1069.0	0.2623	0.363	38.0	0.541	0.6	3360.	5.724
2293.2	16.2	975.0	0.1967	0.285	34.0	0.452	0.7	3270.	5.407
2622.4	15.1	809.0	0.1321	0.222	32.0	0.336	0.8	3120.	4.728
2984.3	13.8	690.0	0.1196	0.221	37.0	0.267	1.0	3090.	4.154
3691.7	11.6	540.0	0.1220	0.265	61.0	0.173	1.1	3460.	3.358
4466.3	9.8	439.0	0.1195	0.324	75.0	0.140	1.3	3370.	2.776
4510.8	9.7	434.0	0.1191	0.327	76.0	0.138	1.3	3360.	2.749
4952.2	8.9	393.0	0.1152	0.359	80.0	0.126	1.5	3290.	2.504
5414.7	8.1	358.0	0.1104	0.391	84.0	0.116	1.7	3240.	2.290
5898.8	7.5	328.0	0.1051	0.423	86.0	0.106	1.8	3190.	2.102
6930.3	6.4	277.0	0.0941	0.486	90.0	0.091	2.2	3140.	1.789
7478.1	5.9	257.0	0.0888	0.517	91.0	0.084	2.4	3130.	1.658
8047.8	5.5	238.0	0.0836	0.547	92.0	0.078	2.6	3120.	1.541
8638.9	5.1	222.0	0.0785	0.576	93.0	0.072	2.8	3130.	1.435
9886.4	4.4	193.0	0.0687	0.622	95.0	0.062	3.1	3170.	1.254





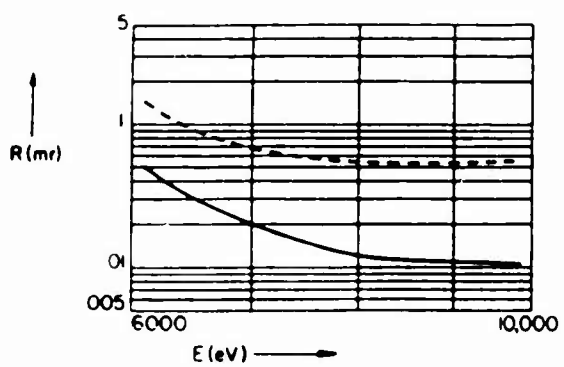


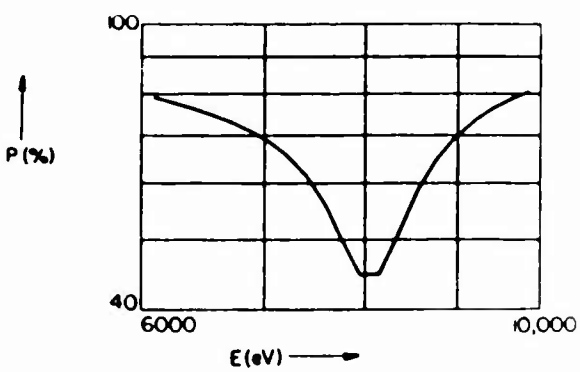


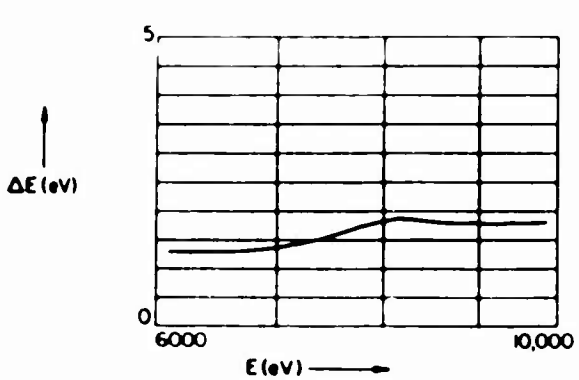
Germanium
Ge

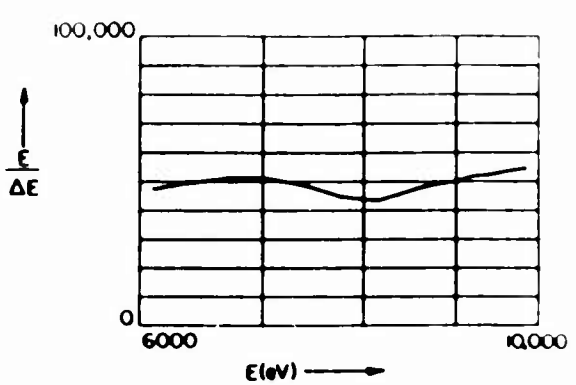
2d - 6.532Å
(111) m - 3

E(eV)	θ_c(mr)	θ_B(mr)	R_p(mr)	R_m(mr)	P(%)	ω(mr)	ΔE(eV)	E/ΔE	λ(Å)
5694.5	7.7	1571.0	0.7040		82.0	5.910			2.177
5898.8	7.5	1307.0	0.0761	0.2177	81.0	0.082	0.13	45300.	2.102
6930.3	6.4	964.0	0.0210	0.0697	70.0	0.028	0.14	51100.	1.789
7478.1	5.9	866.0	0.0149	0.0582	59.0	0.025	0.16	47500.	1.658
8047.8	5.5	786.0	0.0119	0.0539	45.0	0.023	0.18	43900.	1.541
8638.9	5.1	720.0	0.0111	0.0531	61.0	0.018	0.18	47700.	1.435
9886.4	4.4	614.0	0.0105	0.0551	81.0	0.013	0.18	55000.	1.254





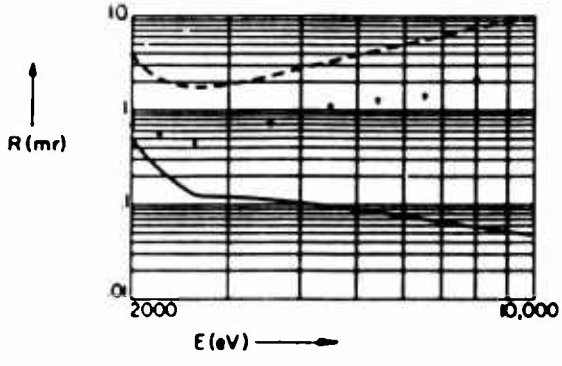


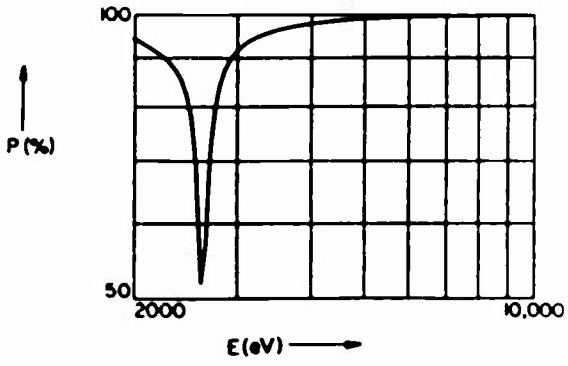


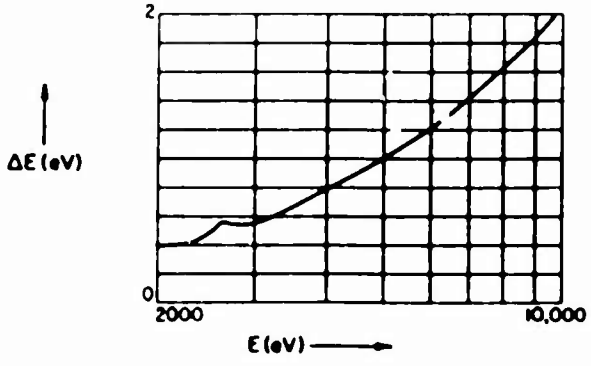
Graphite
C

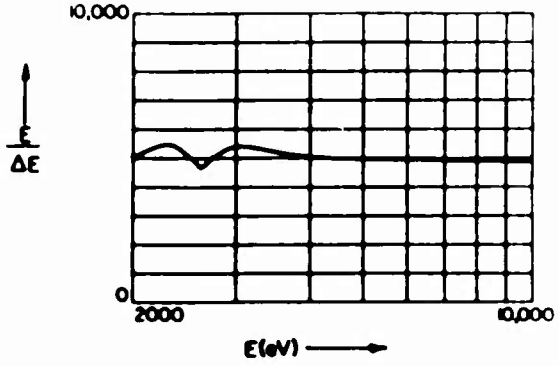
2d - 6.696Å
(002) m - 1

E(eV)	θ_c(mr)	θ_B(mr)	R_p(mr)	R_m(mr)	P(%)	ω(mr)	ΔE(eV)	E/ΔE	λ(Å)
1851.7	17.0	1571.0	10.3600		100.0	7.090			6.696
2042.4	15.4	1135.0	0.4291	3.34	94.0	0.420	0.40	5120.	6.070
2165.9	14.6	1026.0	0.2915	2.45	92.0	0.307	0.40	5360.	5.724
2293.2	13.7	940.0	0.2154	2.04	89.0	0.250	0.42	5480.	5.407
2622.4	12.0	784.0	0.1251	1.75	50.0	0.215	0.57	4640.	4.728
2984.3	10.5	669.0	0.1202	1.88	91.0	0.147	0.55	5400.	4.154
3691.7	8.5	525.0	0.1097	2.48	97.0	0.113	0.72	5130.	3.358
4466.3	7.0	428.0	0.0963	3.29	99.0	0.091	0.89	5000.	2.776
4510.8	6.9	423.0	0.0956	3.34	99.0	0.090	0.90	4990.	2.749
4952.2	6.3	383.0	0.0887	3.83	99.0	0.081	1.00	4970.	2.504
5414.7	5.8	349.0	0.0823	4.36	99.0	0.073	1.09	4960.	2.290
5898.8	5.3	319.0	0.0764	4.92	99.0	0.067	1.19	4940.	2.102
6930.3	4.5	270.0	0.0661	6.15	100.0	0.056	1.41	4920.	1.789
7478.1	4.2	250.0	0.0616	6.82	100.0	0.052	1.52	4910.	1.658
8047.8	3.9	232.0	0.0575	7.54	100.0	0.048	1.64	4900.	1.541
8638.9	3.6	216.0	0.0538	8.30	100.0	0.045	1.77	4890.	1.435
9886.4	3.2	188.0	0.0473	9.97	100.0	0.039	2.03	4860.	1.254





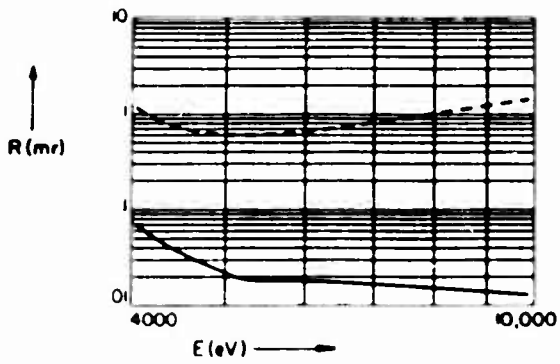


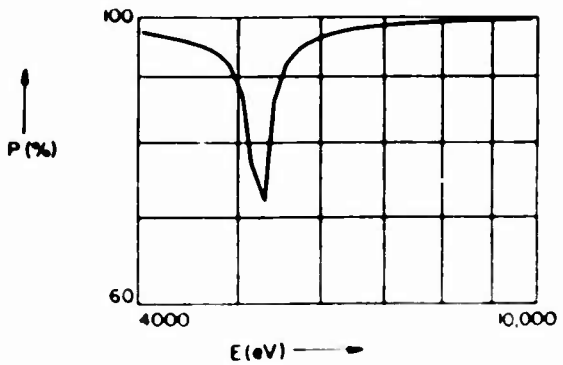


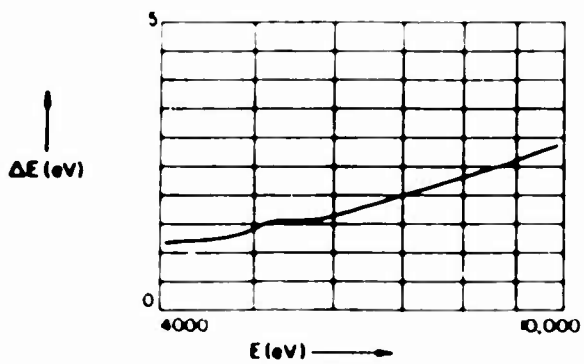
Graphite
C

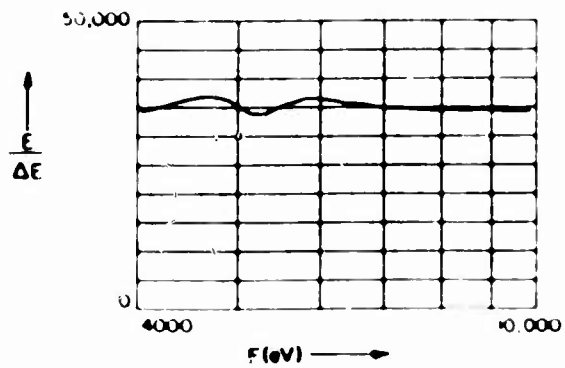
2d = 6.696Å
(002) m = 2

E(eV)	θ_c(mr)	θ_B(mr)	R_p(mr)	R_m(mr)	P(%)	ω(mr)	ΔE(eV)	E/ΔE	λ(Å)
3703.3	8.5	1571.0	3.9200		100.0	2.710			3.348
4466.3	7.0	978.0	0.0372	0.732	96.0	0.041	0.12	36500.	2.776
4510.8	6.9	963.0	0.0353	0.711	95.0	0.039	0.12	36500.	2.749
4952.2	6.3	845.0	0.0229	0.610	91.0	0.032	0.14	35500.	2.504
5414.7	5.8	753.0	0.0182	0.605	87.0	0.027	0.16	34600.	2.290
5898.8	5.3	679.0	0.0180	0.648	96.0	0.022	0.16	36600.	2.102
6930.3	4.5	564.0	0.0168	0.811	98.0	0.018	0.20	35100.	1.789
7478.1	4.2	518.0	0.0160	0.917	99.0	0.016	0.21	34800.	1.658
8047.8	3.9	478.0	0.0152	1.035	99.0	0.015	0.23	34500.	1.541
8638.9	3.6	443.0	0.0144	1.164	99.0	0.014	0.25	34500.	1.435
9886.4	3.2	384.0	0.0130	1.452	100.0	0.012	0.29	34200.	1.254





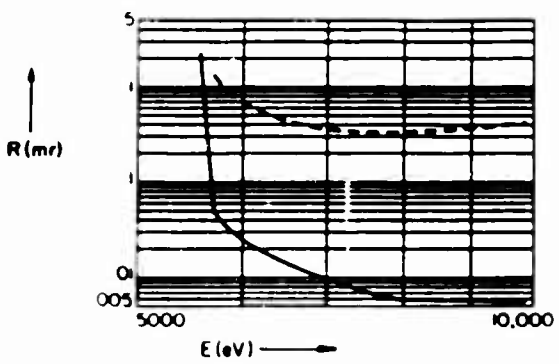


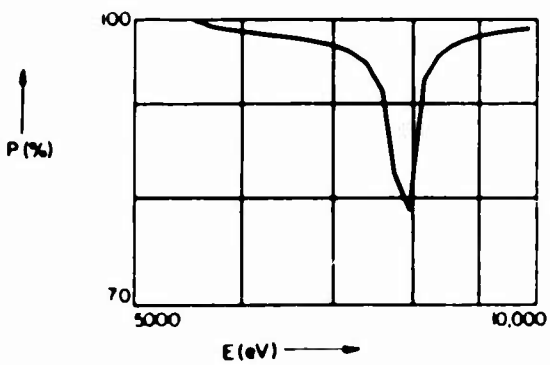


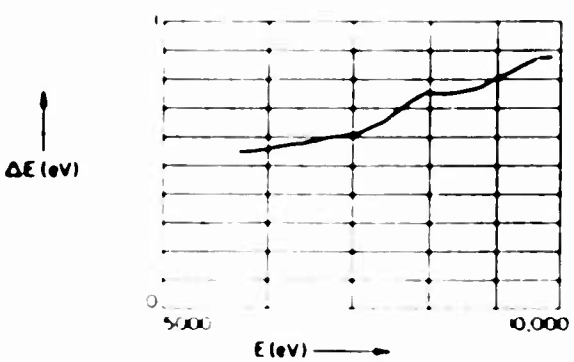
Graphite
C

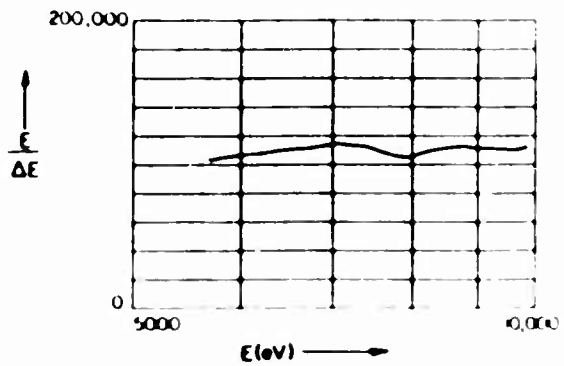
2d = 6.696Å
(002) m = 3

E(eV)	θ_c(mr)	θ_B(mr)	R_p(mr)	R_m(mr)	P(%)	ω(mr)	ΔE(eV)	E/ΔE	λ(Å)
5554.9	5.6	1571.0	2.21000		100.0	1.4500			2.232
5898.8	5.3	1228.0	0.02937	0.798	99.0	0.0265	0.056	106000.	2.102
6930.3	4.5	930.0	0.01015	0.363	97.0	0.0119	0.061	113000.	1.789
7478.1	4.2	837.0	0.00721	0.331	94.0	0.0101	0.068	110000.	1.658
8047.8	3.9	762.0	0.00588	0.331	89.0	0.0089	0.075	107000.	1.541
8638.9	3.6	698.0	0.00582	0.350	97.0	0.0075	0.077	112000.	1.435
9886.4	3.2	597.0	0.00554	0.421	99.0	0.0061	0.089	111000.	1.254





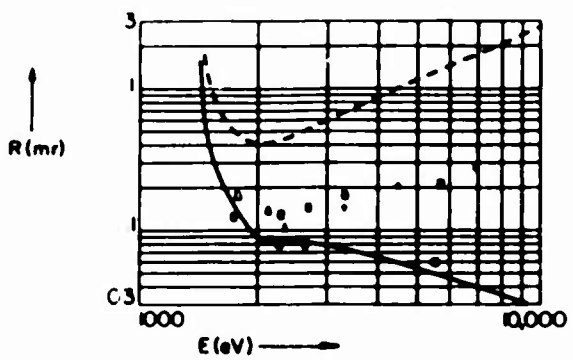


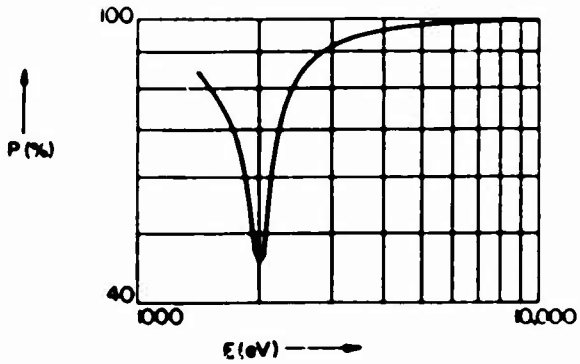


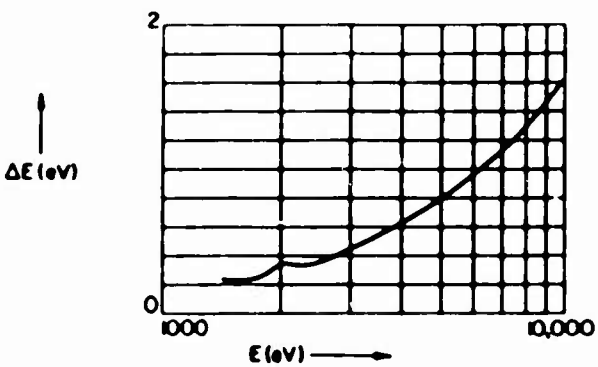
Pentaerythritol -- PET
$C(CH_2OH)_4$

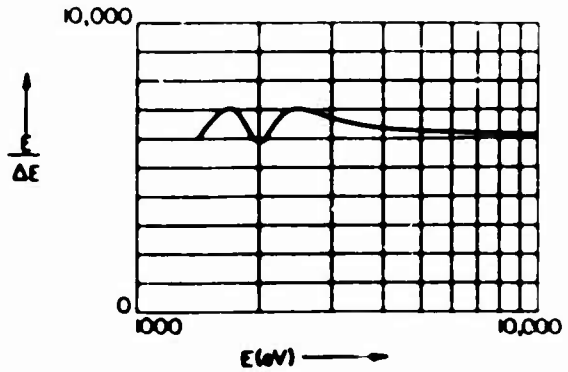
2d - 8.742Å
(002) m - 1

E(eV)	θ_c(mr)	θ_B(mr)	R_p(mr)	R_m(mr)	P(%)	ω(mr)	ΔE(eV)	E/ΔE	λ(Å)
1418.4	18.0	1571.0	14.2500		84.0	14.000			8.741
1486.7	17.2	1267.0	0.4647	1.304	81.0	0.497	0.23	6410.	8.339
1740.0	14.7	953.0	0.1494	0.500	70.0	0.201	0.25	7000.	7.125
2042.4	12.6	768.0	0.0872	0.410	46.0	0.164	0.35	5870.	6.070
2165.9	11.9	714.0	0.0845	0.416	64.0	0.135	0.34	6440.	5.724
2293.2	11.2	667.0	0.0840	0.433	75.0	0.115	0.33	6840.	5.407
2622.4	9.8	572.0	0.0822	0.500	86.0	0.092	0.38	6970.	4.728
2984.3	8.6	495.0	0.0780	0.592	91.0	0.081	0.44	6710.	4.154
3691.7	7.0	394.0	0.0684	0.785	95.0	0.065	0.58	6410.	3.358
4466.3	5.7	323.0	0.0591	1.007	97.0	0.053	0.71	6300.	2.776
4510.8	5.7	320.0	0.0586	1.020	97.0	0.053	0.72	6300.	2.749
4952.2	5.2	290.0	0.0542	1.148	98.0	0.048	0.79	6270.	2.504
5414.7	4.7	265.0	0.0501	1.283	98.0	0.044	0.87	6240.	2.290
5898.8	4.3	243.0	0.0464	1.427	99.0	0.040	0.95	6230.	2.102
6930.3	3.7	206.0	0.0400	1.739	99.0	0.034	1.12	6200.	1.789
7478.1	3.4	191.0	0.0372	1.909	99.0	0.031	1.21	6190.	1.658
8047.8	3.2	177.0	0.0347	2.089	99.0	0.029	1.30	6170.	1.541
8638.9	3.0	165.0	0.0324	2.280	99.0	0.027	1.40	6150.	1.435
9886.4	2.6	144.0	0.0285	2.694	100.0	0.024	1.61	6140.	1.254



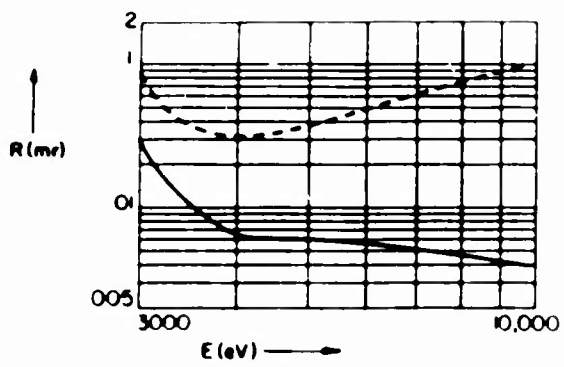


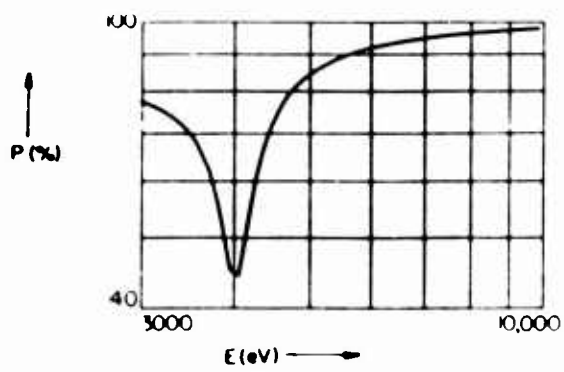


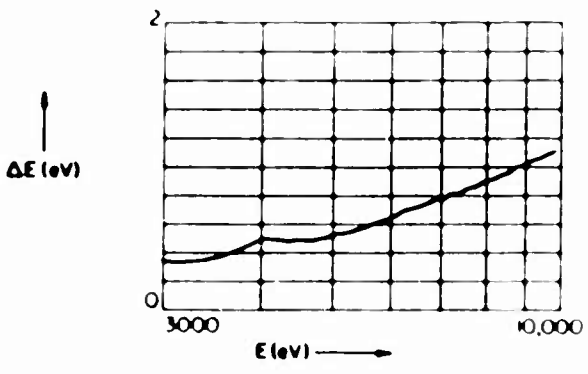


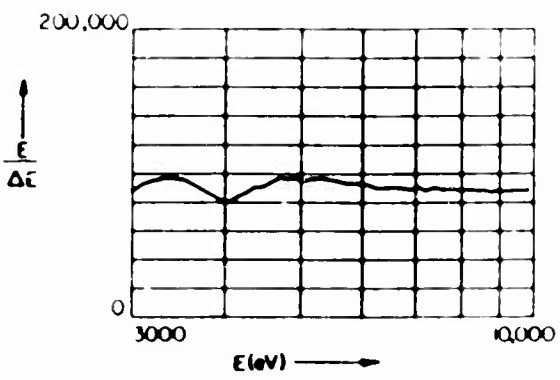
Pentaerythritol -- PET $C(CH_2OH)_4$ 2d - 8.742Å (002) m - 2

E(eV)	θ_c(mr)	θ_B(mr)	R_p(mr)	R_m(mr)	P(%)	ω(mr)	ΔE(eV)	$E/\Delta E$	λ(Å)
2836.6	9.1	1571.0	4.61300		78.0	5.2300			4.371
2984.3	8.6	1255.0	0.03137	0.0911	77.0	0.0346	0.034	88500.	4.154
3691.7	7.0	876.0	0.00823	0.0332	62.0	0.0132	0.041	90700.	3.358
4466.3	5.7	688.0	0.00605	0.0330	72.0	0.0089	0.049	92000.	2.776
4510.8	5.7	680.0	0.00605	0.0333	74.0	0.0086	0.048	93600.	2.749
4952.2	5.2	610.0	0.00600	0.0371	84.0	0.0073	0.052	96100.	2.504
5414.7	4.7	551.0	0.00585	0.0420	89.0	0.0064	0.056	96400.	2.290
5898.8	4.3	502.0	0.00564	0.0477	91.0	0.0058	0.063	93900.	2.102
6930.3	3.7	422.0	0.00514	0.0609	95.0	0.0049	0.076	90700.	1.789
7478.1	3.4	389.0	0.00487	0.0681	96.0	0.0046	0.084	89300.	1.658
8047.8	3.2	360.0	0.00461	0.0759	96.0	0.0043	0.091	88400.	1.541
8638.9	3.0	335.0	0.00435	0.0840	97.0	0.0039	0.097	89000.	1.435
9886.4	2.6	291.0	0.00389	0.1017	98.0	0.0034	0.113	87400.	1.254





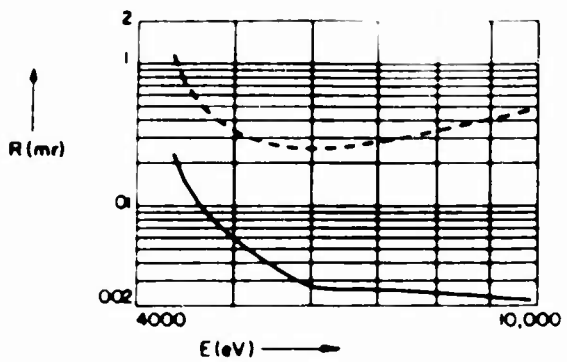


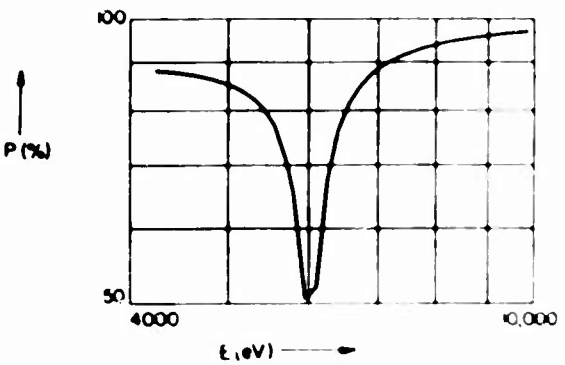


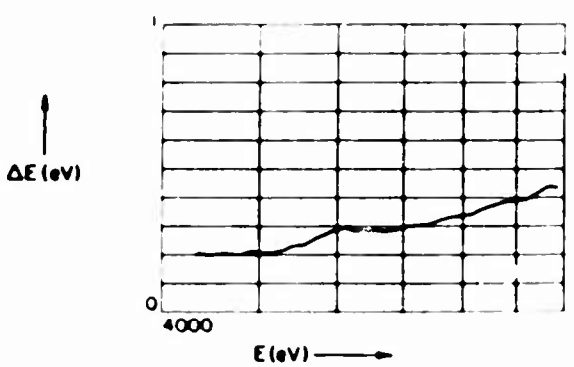
Pentaerythritol -- PET
$C(CH_2OH)_4$

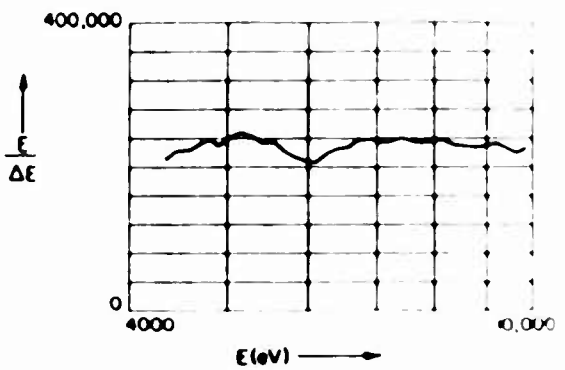
2d = 8.742Å
(002) n = 3

E(eV)	θ_c(mr)	θ_B(mr)	R_p(mr)	R_m(mr)	P(%)	ω(mr)	ΔE(eV)	E/ΔE	λ(Å)
4254.9	6.0	1571.0	3.26500		88.00	3.3000			2.914
4466.3	5.7	1262.0	0.01446	0.0724	88.00	0.0142	0.020	221000.	2.776
4510.8	5.7	1232.0	0.01286	0.0647	88.00	0.0128	0.020	223000.	2.749
4952.2	5.2	1034.0	0.00630	0.0351	86.00	0.0071	0.021	235000.	2.504
5414.7	4.7	904.0	0.00400	0.0273	80.00	0.0055	0.023	232000.	2.290
5898.8	4.3	806.0	0.00285	0.0252	56.00	0.0048	0.027	216000.	2.102
6930.3	3.7	661.0	0.00259	0.0278	88.00	0.0033	0.029	237000.	1.789
7478.1	3.4	605.0	0.00254	0.0307	92.00	0.0029	0.031	242000.	1.658
8047.8	3.2	557.0	0.00247	0.0343	94.00	0.0026	0.034	238000.	1.541
8638.9	3.0	515.0	0.00237	0.0384	95.00	0.0024	0.037	232000	1.435
9886.4	2.6	445.0	0.00217	0.0477	97.00	0.0021	0.043	232000	1.254



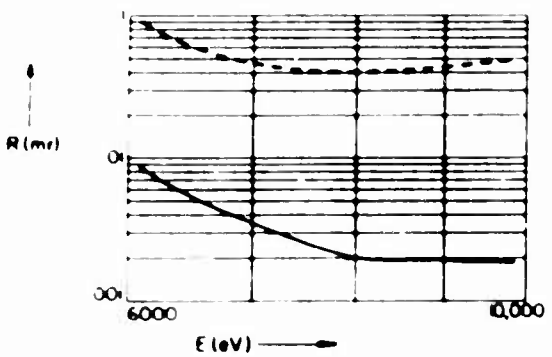


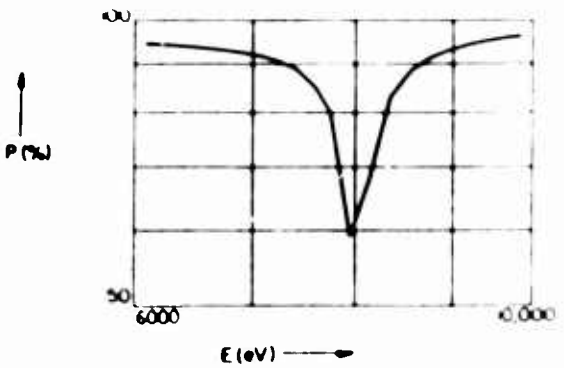


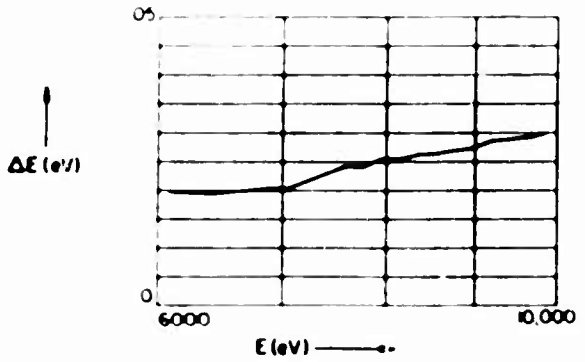


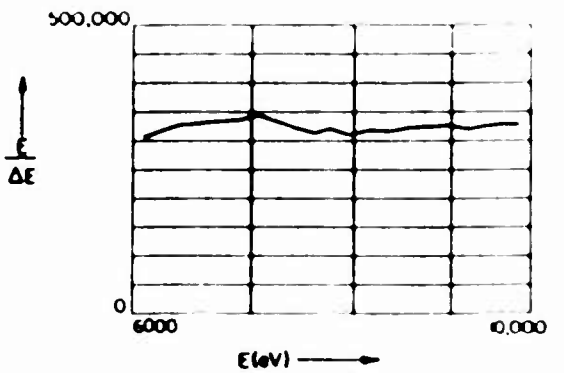
Pentaerythritol -- PET $C(CH_2OH)_4$ — 2d = 8.742Å (002) — m = 4

E(eV)	θ_c(mr)	θ_B(mr)	R_p(mr)	R_m(mr)	P(%)	ω(mr)	ΔE(eV)	E/ΔE	λ(Å)
5673.1	4.5	1571.0	2.66900		95.0	2.3600			2.185
5898.8	4.3	1293 0	0.01262	0.1307	95.0	0.0116	0.019	304000.	2.102
6930 3	3.7	959.0	0.00368	0.0477	92.0	0.0043	0.021	332000.	1.789
7478.1	3 4	861.0	0.00257	0.0419	88.0	0.0035	0.022	337000.	1.658
8047.8	3 2	782 0	0 00197	0.0408	49.0	0.0033	0.027	303000.	1.541
8638 9	3 0	716 0	0 00193	0 0423	90 0	0.0026	0.026	332000	1.435
9886 4	2 6	611 0	0 00187	0 0498	96 0	0.0021	0.030	327000	1 254





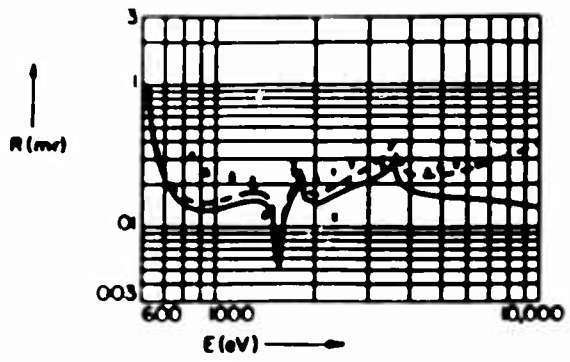


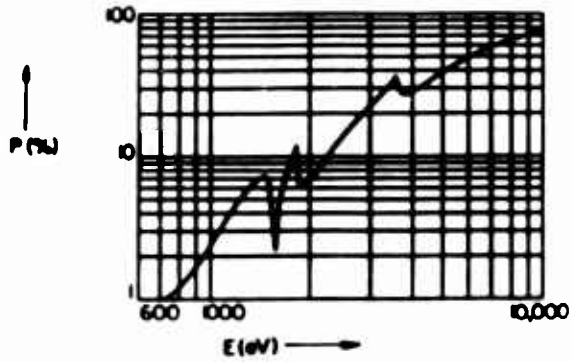


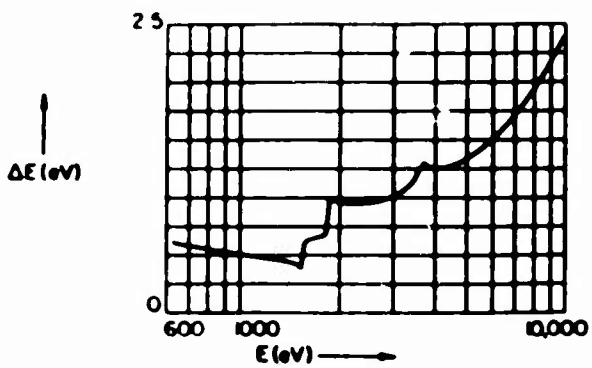
Mica
$K_2O*3Al_2O_3*6SiO_2*2H_2O$

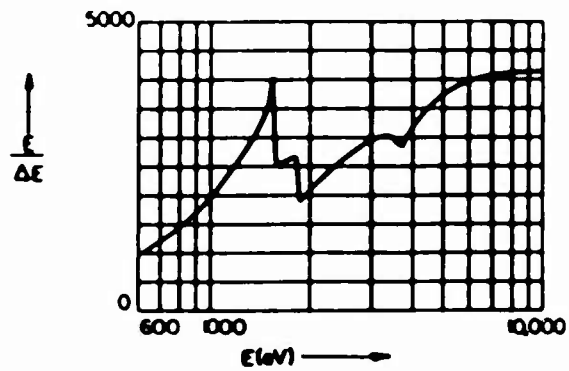
2d = 20.000Å
(002) n = 1

E(eV)	θ_c(mr)	θ_B(mr)	R_p(mr)	R_m(mr)	P(%)	ω(mr)	ΔE(eV)	E/ΔE	λ(Å)
620.4	38.0	1571.0	0.6215		0.9	62.000			19.980
637.4	38.2	1340.0	0.0522	0.0586	0.9	4.040	0.6	1050.	19.450
676.8	38.2	1160.0	0.0270	0.0303	1.0	1.980	0.6	1160.	18.320
705.0	37.8	1076.0	0.0210	0.0236	1.0	1.530	0.6	1220.	17.590
776.2	36.5	926.0	0.0151	0.0170	1.1	0.959	0.6	1390.	15.970
851.5	34.9	817.0	0.0134	0.0151	1.4	0.672	0.5	1580.	14.560
929.7	33.0	731.0	0.0130	0.0147	1.9	0.503	0.5	1780.	13.340
1012.0	31.1	660.0	0.0134	0.0152	2.5	0.388	0.5	2000.	12.250
1041.0	30.4	639.0	0.0136	0.0155	2.8	0.356	0.5	2090.	11.910
1188.0	27.3	550.0	0.0148	0.0170	4.4	0.243	0.5	2520.	10.440
1254.0	26.0	518.0	0.0152	0.0174	5.3	0.210	0.5	2720.	9.890
1487.0	22.0	431.0	0.0126	0.0146	7.1	0.130	0.4	3550.	8.339
1740.0	18.4	365.0	0.0176	0.0203	8.8	0.145	0.7	2630.	7.125
2042.0	15.7	309.0	0.0145	0.0166	7.1	0.149	1.0	2140.	6.070
2166.0	15.1	291.0	0.0154	0.0178	8.6	0.131	0.9	2280.	5.724
2293.0	14.4	274.0	0.0164	0.0191	10.0	0.116	0.9	2420.	5.407
2622.0	12.9	239.0	0.0186	0.0222	15.0	0.090	1.0	2710.	4.728
2984.0	11.4	210.0	0.0210	0.0261	22.0	0.072	1.0	2940.	4.154
3692.0	9.2	169.0	0.0216	0.0278	28.0	0.060	1.3	2820	3.358
4466.0	7.7	139.0	0.0169	0.0227	33.0	0.040	1.3	3500	2.776
4511.0	7.7	138.0	0.0169	0.0228	33.0	0.040	1.3	3520	2.748
4952.0	7.0	126.0	0.0164	0.0232	38.0	0.034	1.3	3720	2.504
5415.0	6.4	115.0	0.0162	0.0241	43.0	0.030	1.4	3860	2.290
5899.0	5.9	105.0	0.0159	0.0252	48.0	0.027	1.5	3960.	2.102
6930.0	5.0	89.7	0.0154	0.0282	58.0	0.022	1.7	4070	1.789







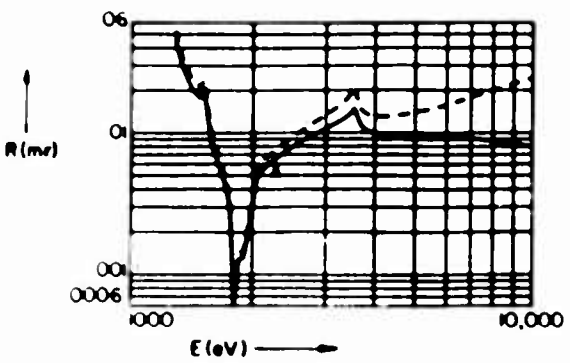


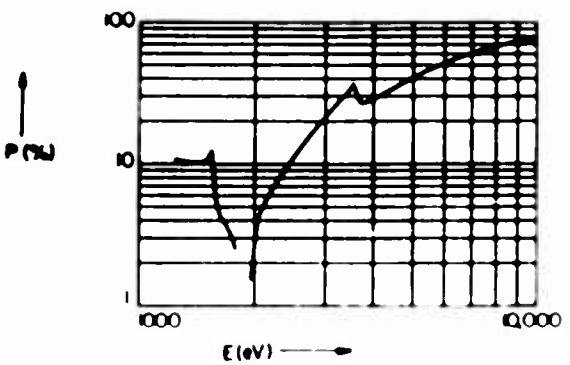
Mica

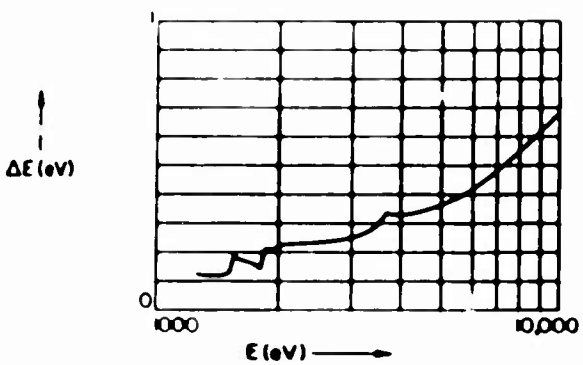
$K_2O*3Al_2O_3*6SiO_2*2H_2O$

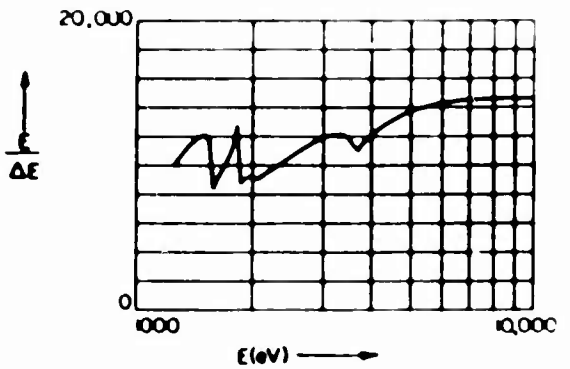
2d = 20.000Å
(002) m = 2

E(eV)	θ_c(mr)	θ_B(mr)	R_p(mr)	R_m(mr)	P(%)	ω(mr)	ΔE(eV)	E/ΔE	λ(Å)
1240.0	26.3	1571.0	2.35500		11.0	20.000			10.000
1254.0	26.0	1422.0	0.09601	0.1120	11.0	0.663	0.12	10000	9.890
1487.0	22.0	986.0	0.01778	0.0213	11.0	0.125	0.12	12100	8.339
1740.0	18.4	793.0	0.00390	0.0044	3.0	0.094	0.16	10800	7.125
2042.0	15.7	652.0	0.00489	0.0056	4.2	0.085	0.23	9010	6.070
2166.0	15.1	609.0	0.00593	0.0068	5.8	0.074	0.23	9440	5.724
2293.0	14.4	571.0	0.00682	0.0079	7.7	0.065	0.23	9910	5.407
2622.0	12.9	492.0	0.00878	0.0104	13.0	0.049	0.24	11100	4.728
2984.0	11.4	428.0	0.01066	0.0132	21.0	0.038	0.25	11900	4.154
3692.0	9.2	343.0	0.01132	0.0147	27.0	0.033	0.34	10900	3.358
4466.0	7.7	281.0	0.00960	0.0132	34.0	0.022	0.34	13100	2.775
4511.0	7.7	278.0	0.00959	0.0132	35.0	0.022	0.34	13100	2.748
4952.0	7.0	253.0	0.00951	0.0138	40.0	0.019	0.36	13700	2.504
5415.0	6.4	231.0	0.00946	0.0146	46.0	0.017	0.39	14000	2.290
5899.0	5.9	212.0	0.00938	0.0156	51.0	0.015	0.41	14300	2.102
6930.0	5.0	180.0	0.00911	0.0177	60.0	0.013	0.48	14500	1.789
7478.0	4.6	167.0	0.00892	0.0189	64.0	0.012	0.51	14500	1.658
8048.0	4.3	155.0	0.00870	0.0202	68.0	0.011	0.55	14600	1.541
8639.0	4.0	144.0	0.00846	0.0215	72.0	0.010	0.59	14600	1.435
9886.0	3.5	126.0	0.00793	0.0243	77.0	0.009	0.68	14600	1.254





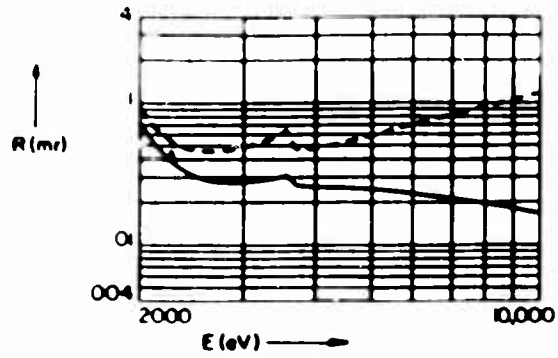


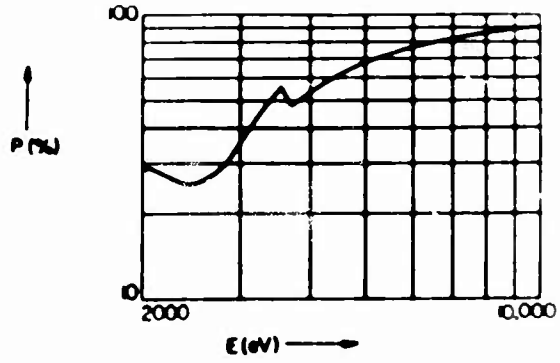


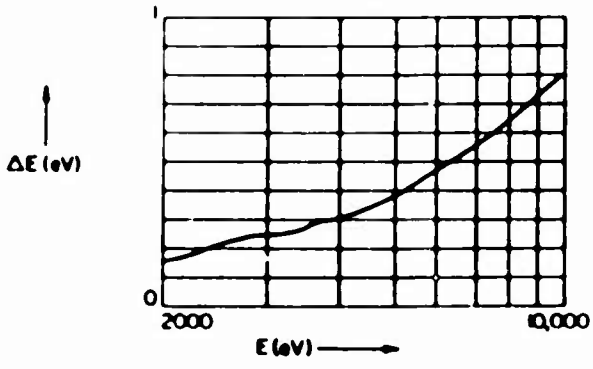
Mica
$K_2O*3Al_2O_3*6SiO_2*2H_2O$

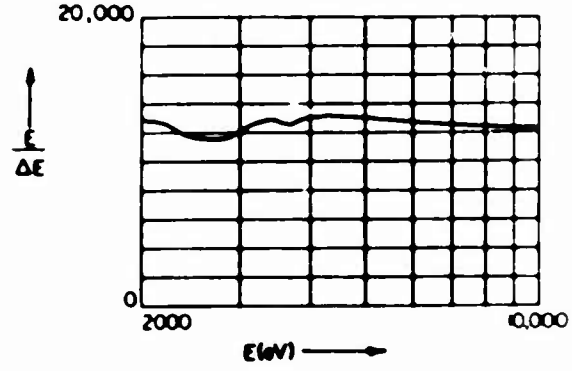
2d = 20.000Å
(002) m = 3

E(eV)	θ_c(mr)	θ_B(mr)	R_p(mr)	R_m(mr)	P(%)	ω(mr)	ΔE(eV)	E/ΔE	λ(Å)
1859.0	15 9	1571.0	4.5690		27.0	15.000			6.669
2042 0	15 7	1144 0	0 0645	0.0831	29.0	0.172	0.2	12800.	6.070
2166 0	15.1	1032.0	0.0466	0.0622	28.0	0.132	0.2	12700.	5.724
2293 0	14 4	945.0	0 0374	0 0524	26.0	0.113	0.2	12300.	5.407
2622 0	12 9	788 0	0 0284	0 0453	26 0	0.087	0.2	11500.	4.728
2984 0	11 4	673 0	0 0276	0 0485	35.0	0.066	0.2	12000.	4.154
3692 0	9 2	528 0	0 0265	0 0476	48 0	0 047	0.3	12500	3 358
4466 0	7	429 0	0 0252	0 0527	61 0	0.035	0.3	13100	2 776
4511 0	7	425 0	0 0251	0 0532	62 0	0.035	0.3	13100	2 748
4952 0	7 0	385 0	0 0247	0 0581	67 0	0.031	0.4	13000	2 504
5415 0	6 4	351 0	0 0240	0 0635	72 0	0 028	0 4	12900	2 290
5899 0	5 9	321 0	0 0232	0 0692	76 0	0 026	0 5	12800	2 102
6930 0	5 0	272 0	0 0214	0 0814	82 0	0 022	0.6	12500	1 789
7478 0	4 6	251 0	0 0204	0 0879	84 0	0 021	0.6	12500	1 658
8048 0	4 3	233 0	0 0194	0 0946	86 0	0 019	0.6	12400	1 541
8639 0	4 0	217 0	0 0185	0 1016	88 0	0 018	0 7	12400	1 435
9886 0	3 5	189 0	0 0167	0 1163	91 0	0 016	0 8	12300	1 254









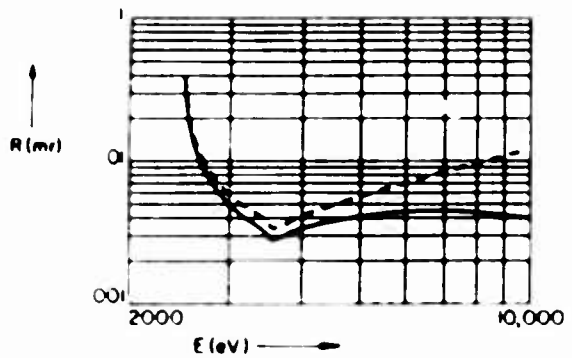
Mica

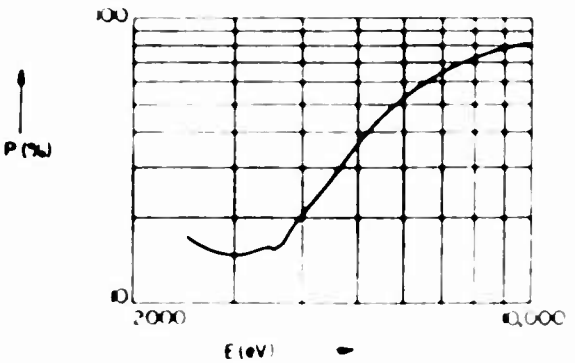
$K_2O*3Al_2O_3*6SiO_2*2H_2O$

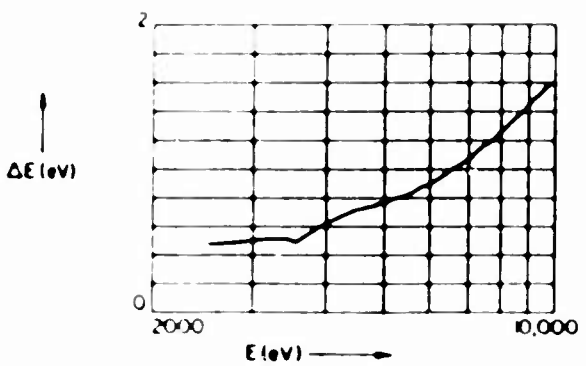
2d = 20.000Å

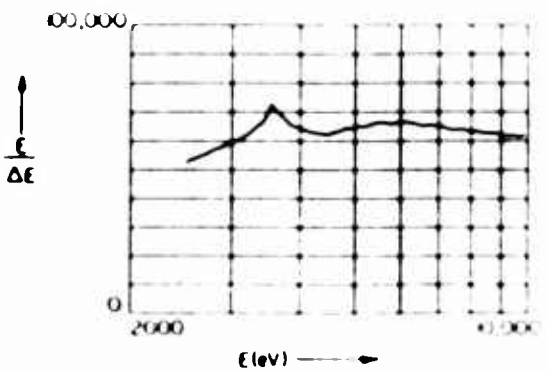
(002) m = 4

E(eV)	θ_c(mr)	θ_B(mr)	R_p(mr)	R_m(mr)	P(%)	ω(mr)	ΔE(eV)	E/ΔE	λ(Å)
2479.0	13.5	1571.0	1.53800		17.0	7.9500			5.002
2622.0	12.9	1238.0	0.01174	0.01335	16.0	0.0533	0.05	54300.	4.728
2984.0	11.4	980.0	0.00505	0.00590	15.0	0.0252	0.05	59200.	4.154
3692.0	9.2	736.0	0.00289	0.00338	16.0	0.0131	0.05	69100.	3.358
4466.0	7.7	588.0	0.00378	0.00488	27.0	0.0106	0.07	62900	2.776
4511.0	7.7	582.0	0.00382	0.00495	28.0	0.0105	0.07	62700	2.748
4952.0	7.1	524.0	0.00409	0.00561	36.0	0.0089	0.08	64700	2.504
5415.0	6.4	476.0	0.00430	0.00628	44.0	0.0078	0.08	65700	2.290
5899.0	5.9	434.0	0.00443	0.00697	52.0	0.0070	0.09	65800	2.102
6930.0	5.0	366.0	0.00450	0.00836	64.0	0.0059	0.11	65200	1.789
7478.0	4.6	338.0	0.00445	0.00906	69.0	0.0055	0.12	64100	1.658
8048.0	4.3	313.0	0.00437	0.00978	73.0	0.0052	0.13	62800	1.541
8639.0	4.0	291.0	0.00426	0.01050	77.0	0.0048	0.14	62800	1.435
9886.0	3.5	253.0	0.00400	0.01199	82.0	0.0042	0.16	61600	1.254





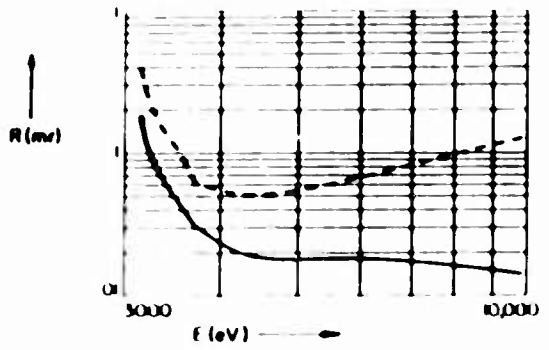


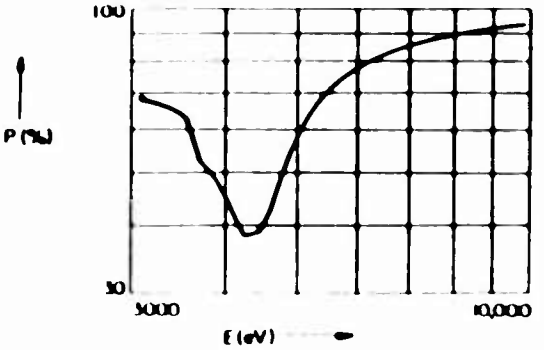


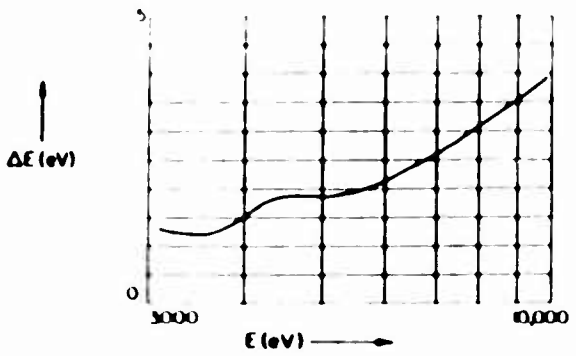
Mica
$K_2O*3Al_2O_3*6SiO_2*2H_2O$

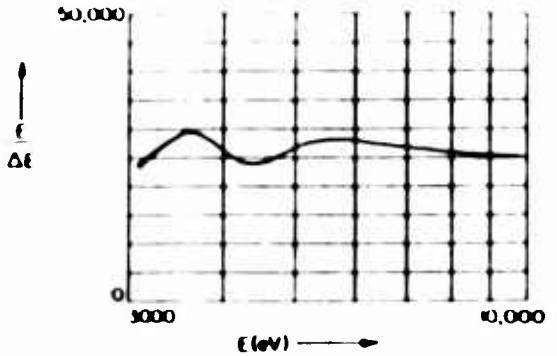
2d - 20.000Å
(002) n - 5

E(eV)	θ_c(mr)	θ_B(mr)	R_p(mr)	R_m(mr)	P(%)	ω(mr)	ΔE(eV)	E/ΔE	λ(Å)
3098.0	11.0	1571.0	8.1150		68.0	11.000			4.002
3692.0	9.2	996.0	0.0320	0.0638	52.0	0.053	0.13	29300.	3.358
4466.0	7.7	767.0	0.0186	0.0517	39.0	0.040	0.19	23800.	2.776
4511.0	7.7	757.0	0.0184	0.0518	39.0	0.040	0.19	23800.	2.748
4952.0	7.0	676.0	0.0180	0.0546	57.0	0.030	0.19	26500.	2.504
5415.0	6.4	609.0	0.0182	0.0599	69.0	0.025	0.19	28000.	2.290
5899.0	5.9	553.0	0.0182	0.0665	77.0	0.022	0.21	28000.	2.102
6930.0	5.0	464.0	0.0175	0.0821	85.0	0.019	0.26	26900.	1.789
7478.0	4.6	427.0	0.0169	0.0907	88.0	0.017	0.28	26300.	1.658
8048.0	4.3	395.0	0.0162	0.0995	90.0	0.016	0.31	25900.	1.541
8639.0	4.0	367.0	0.0155	0.1087	91.0	0.015	0.34	25600.	1.435
9886.0	3.5	319.0	0.0141	0.1278	94.0	0.013	0.39	25100.	1.254





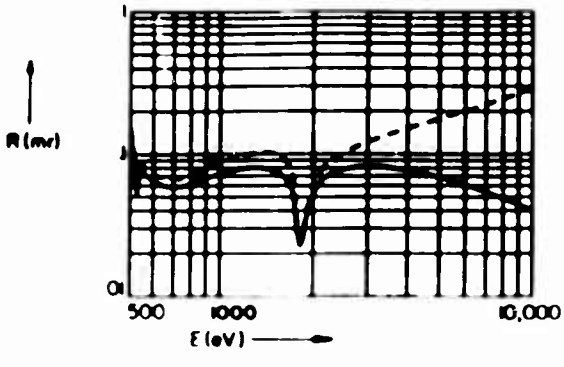


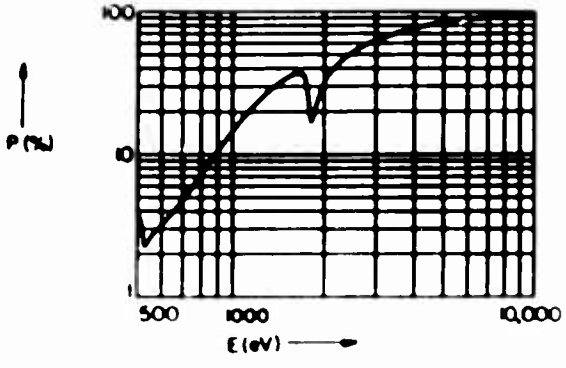


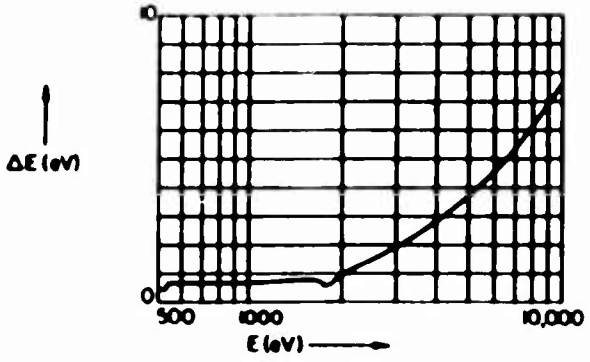
Rubidium Acid Phthalate -- RAP
$C_6H_4(COOH)(COO)Rb$

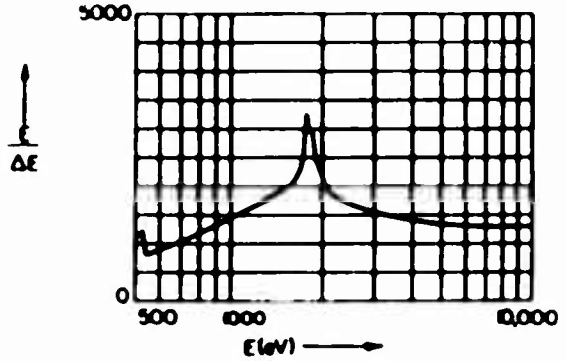
2d = 26.140Å
(001) n = 1

E(eV)	θ_c(mr)	θ_B(mr)	R_p(mr)	R_m(mr)	P(%)	ω(mr)	ΔE(eV)	E/ΔE	λ(Å)
475.0	40.2	1571.0	3 0570		4.5	61.00			26.100
511 3	37 9	1192.0	0 1108	0 1243	3 6	2 20	0.4	1140.	24.248
524 9	36.0	1131 0	0 0736	0 0825	2 9	1 78	0 4	1190	23.620
556 3	31.1	1023 0	0 0748	0 0835	2 7	1 9[illegible]	0 7	824	22 287
572 8	31 7	978 0	0 0704	0 0787	2 9	1 74	0 7	851	21 645
637 4	32 1	841 0	0 0610	0 0686	3 7	1 18	0 7	949	19 451
676 8	31 8	778 0	0 0591	0 0669	4 4	0 97	0 7	1010	18 319
705 0	31 2	739 0	0 0586	0 0665	4 8	0 87	0 7	1050	17 586
776 2	30 0	659 0	0 0609	0 0697	6 6	0 67	0 7	1150	15 973
851 5	28 5	592 0	0 0652	0 0754	8 9	0 53	0 7	1260	14 560
929 7	26 9	536 0	0 0694	0 0813	12 0	0 44	0 7	1370	13 336
1011 7	25 3	489 0	0 0736	0 0874	15 0	0 36	0 7	1470	12 255
1041 0	24 8	474 0	0 0748	0 0893	16 0	0 34	0 7	1510	11 910
1188 0	22 2	411 0	0 0791	0 0976	23 0	0 26	0 7	1660	10 436
1253 6	21 2	389 0	0 0799	0 1002	26 0	0 24	0 7	1720	9 890
1486 7	18 0	325 0	0 0765	0 1015	34 0	0 17	0 8	1930	8 339
1740 0	15 2	277 0	0 0697	0 0659	35 0	0 11	0 7	2550	7 125
2042 4	12 5	235 0	0 0587	0 0680	35 0	0 12	1 0	2010	6 070
2165 9	11 9	221 0	0 0676	0 0800	40 0	0 12	1 2	1850	5 724
2293 2	11 5	209 0	0 0731	0 0896	45 0	0 12	1 3	1770	5 407
2622 4	10 3	182 0	0 0796	0 1068	55 0	0 11	1 6	1650	4 728
2984 3	9 2	160 0	0 0814	0 1209	63 0	0 10	1 9	1560	4 154
3691 7	7 6	129 0	0 0788	0 1430	73 0	0 09	2 6	1440	3 358
4466 3	6 3	107 0	0 0729	0 1638	80 0	0 08	3 3	1370	2 776
4510 8	6 2	106 0	0 0726	0 1649	81 0	0 08	3 3	1370	2 749
4952 2	5 7	96 1	0 0690	0 1759	84 0	0 07	3 7	1350	2 504
5414 7	5 2	87 8	0 0653	0 1871	86 0	0 07	4 1	1330	2 290





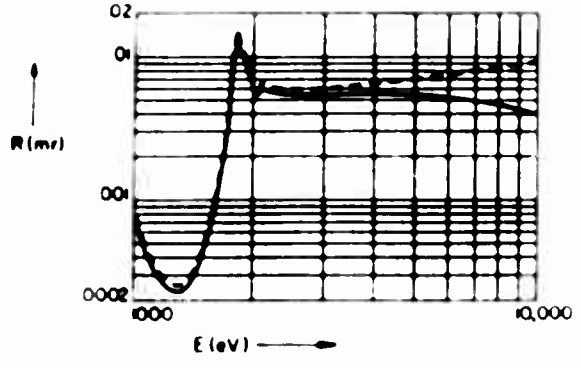


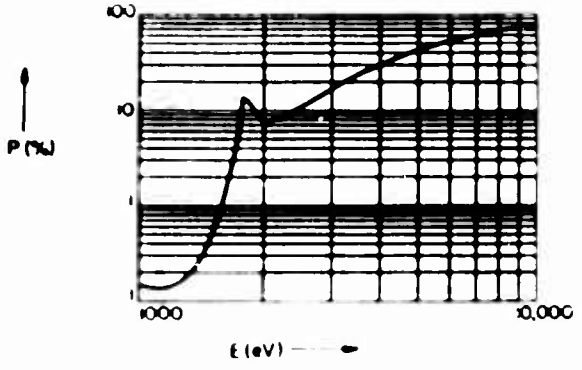


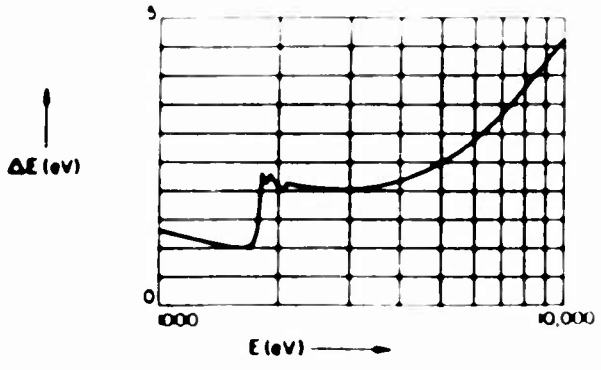
Rubidium Acid Phthalate -- RAP
$C_6H_4(COOH)(COO)Rb$

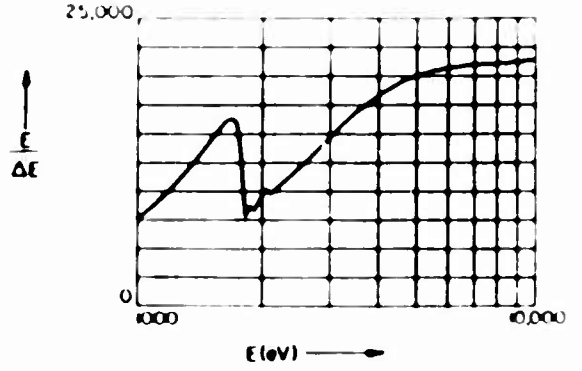
2d = 26.140Å
(001) n = 2

E(eV)	θ_c(mr)	θ_B(mr)	R_p(mr)	R_m(mr)	P(%)	ω(mr)	ΔE(eV)	E/ΔE	λ(Å)
949.2	26.5	1571.0	0.04317		0.2	24.000			13.062
1011.7	25.3	1217.0	0.00072	0.00080	0.1	0.350	0.13	7750.	12.255
1041.0	24.8	1148.0	0.00054	0.00061	0.1	0.274	0.13	8100.	11.910
1188.0	22.2	926.0	0.00026	0.00029	0.1	0.133	0.12	10000.	10.436
1253.6	21.2	859.0	0.00023	0.00026	0.2	0.106	0.11	10900.	9.890
1486.7	18.0	692.0	0.00038	0.00043	0.5	0.058	0.10	14300	8.339
1740.0	15.2	577.0	0.00359	0.00415	6.4	0.041	0.11	15800	7.125
2042.4	12.5	483.0	0.00545	0.00594	7.3	0.052	0.20	10200	6.070
2165.9	11.9	454.0	0.00582	0.00635	8.4	0.048	0.21	10200	5.724
2293.2	11.5	427.0	0.00560	0.00611	9.3	0.041	0.21	11000	5.407
2622.4	10.3	370.0	0.00546	0.00599	13.0	0.030	0.20	12800	4.728
2984.3	9.2	324.0	0.00546	0.00607	17.0	0.023	0.20	14700	4.154
3691.7	7.6	260.0	0.00552	0.00638	26.0	0.015	0.21	17500	3.358
4466.3	6.3	214.0	0.00551	0.00678	37.0	0.011	0.23	19400	2.776
4510.8	6.2	212.0	0.00550	0.00680	37.0	0.011	0.23	19400	2.749
4952.2	5.7	193.0	0.00545	0.00704	43.0	0.010	0.25	20000	2.504
5414.7	5.2	176.0	0.00536	0.00728	48.0	0.009	0.26	20400	2.290
5898.8	4.8	162.0	0.00525	0.00752	53.0	0.008	0.29	20600	2.102
6930.3	4.1	137.0	0.00496	0.00804	61.0	0.007	0.33	20900	1.789
7478.1	3.8	127.0	0.00479	0.00829	65.0	0.006	0.36	21000	1.658
8047.8	3.5	118.0	0.00460	0.00855	68.0	0.006	0.38	21100	1.541
8638.9	3.3	110.0	0.00442	0.00880	71.0	0.005	0.41	21200	1.435
9886.4	2.8	96.2	0.00403	0.00924	76.0	0.005	0.46	21400	1.254





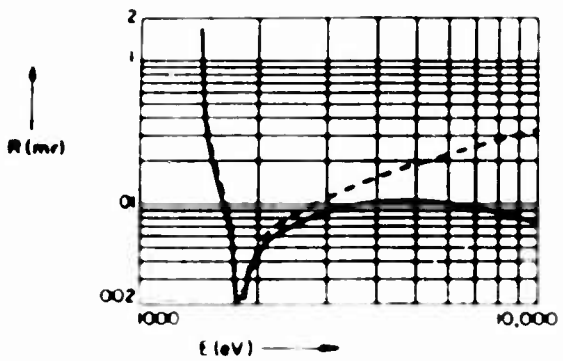


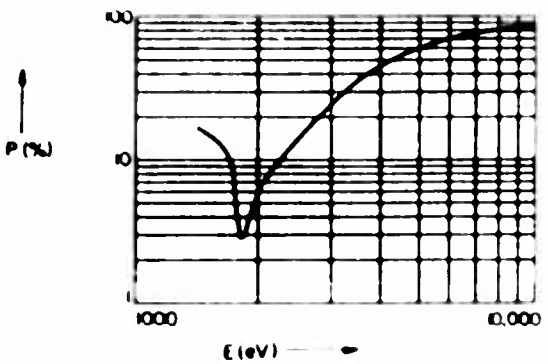


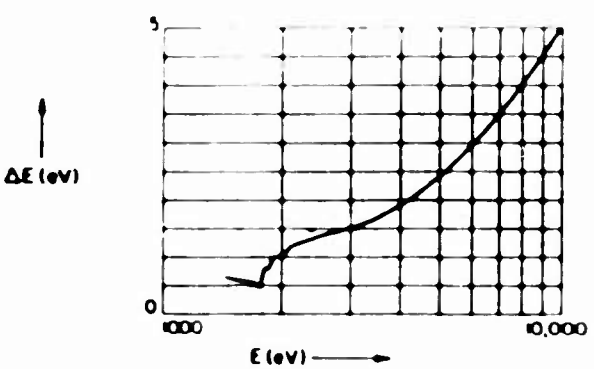
Rubidium Acid Phthalate -- RAP
$C_6H_4(COOH)(COO)Rb$

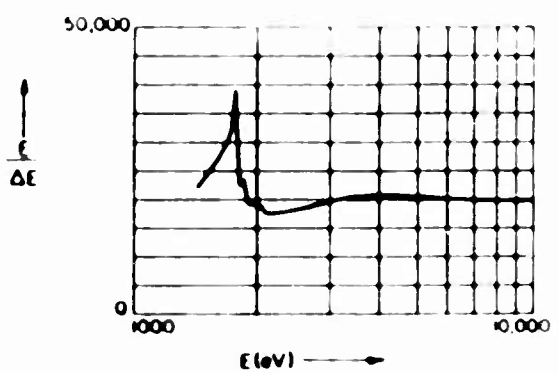
2d = 26.140Å
(001) m = 3

E(eV)	θ_c(mr)	θ_B(mr)	R_p(mr)	R_m(mr)	P(%)	ω(mr)	ΔE(eV)	E/ΔE	λ(Å)
1423.4	18.8	1571.0	2.37600		17.0	13.000			8.710
1486.7	18.0	1278.0	0.02880	0.0343	15.0	0.138	0.06	24000	8.339
1740.0	15.2	958.0	0.00505	0.0060	8.6	0.043	0.05	32900	7.125
2042.4	12.5	771.0	0.00508	0.0057	7.0	0.052	0.11	18700	6.070
2165.9	11.9	717.0	0.00590	0.0067	8.6	0.049	0.12	17600	5.724
2293.2	11.3	670.0	0.00648	0.0075	11.0	0.044	0.13	17900	5.407
2622.4	10.3	574.0	0.00770	0.0092	16.0	0.035	0.14	18600	4.728
2984.3	9.2	497.0	0.00880	0.0110	24.0	0.028	0.15	19700	4.154
3691.7	7.6	396.0	0.01013	0.0141	40.0	0.020	0.18	20700	3.358
4466.3	6.3	324.0	0.01060	0.0171	53.0	0.016	0.21	20800	2.776
4510.8	6.2	321.0	0.01060	0.0173	54.0	0.016	0.22	20800	2.749
4952.2	5.7	292.0	0.01056	0.0189	60.0	0.015	0.24	20600	2.504
5414.7	5.2	266.0	0.01040	0.0204	65.0	0.013	0.27	20400	2.290
5898.8	4.8	244.0	0.01014	0.0220	70.0	0.012	0.29	20300	2.102
6930.3	4.1	207.0	0.00946	0.0251	77.0	0.011	0.35	20000	1.789
7478.1	3.8	192.0	0.00907	0.0266	79.0	0.010	0.37	19900	1.658
8047.8	3.5	178.0	0.00867	0.0282	82.0	0.009	0.42	19800	1.541
8638.4	3.3	166.0	0.00828	0.0297	84.0	0.008	0.44	19800	1.435
9886.6	2.8	144.0	0.00750	0.0328	87.0	0.007	0.50	19800	1.254







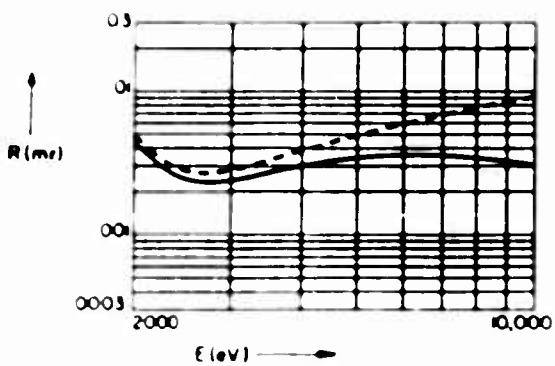


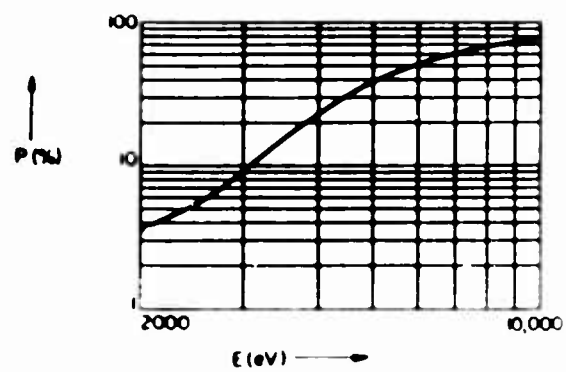
Rubidium Acid Phthalate -- RAP

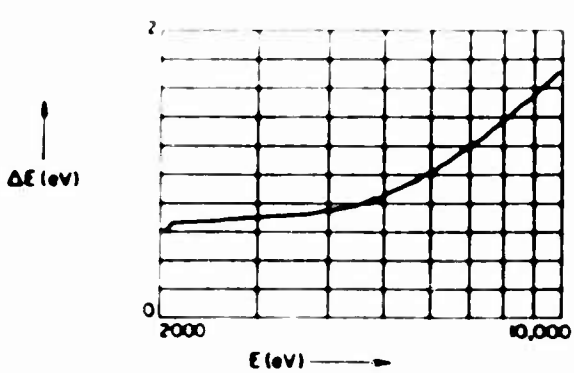
$C_6H_4(COOH)(COO)Rb$

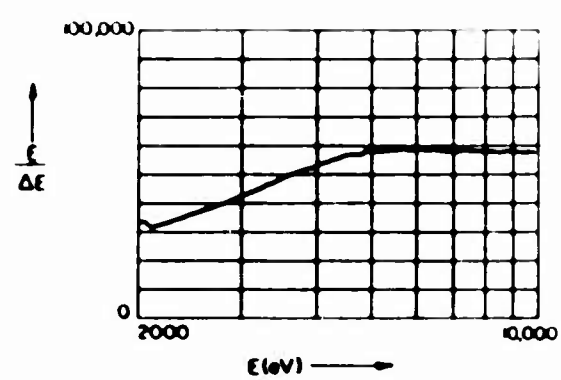
2d = 26.140Å
(001) n = 4

E(eV)	θ_c(mr)	θ_B(mr)	R_p(mr)	R_m(mr)	P(%)	ω(mr)	ΔE(eV)	E/ΔE	λ(Å)
1897.7	12.6	1571.0	0.31050		2.6	11.0000			6.533
2042.4	12.5	1192.0	0.00416	0.00466	3.9	0.0749	0.06	33600	6.070
2165.9	11.9	1068.0	0.00327	0.00367	4.2	0.0559	0.07	32500	5.724
2293.2	11.5	975.0	0.00277	0.00313	4.6	0.0429	0.07	34400	5.407
2622.4	10.3	809.0	0.00233	0.00269	6.2	0.0274	0.07	38300	4.728
2984.3	9.2	689.0	0.00238	0.00281	9.1	0.0194	0.07	42400	4.154
3691.2	7.6	540.0	0.00283	0.00351	18.0	0.0118	0.07	50800	3.358
4466.3	6.3	439.0	0.00327	0.00438	31.0	0.0083	0.08	56500	2.776
4510.8	6.2	434.0	0.00329	0.00443	31.0	0.0082	0.08	56600	2.749
4952.2	5.7	393.0	0.00344	0.00490	38.0	0.0071	0.09	58200	2.504
5414.7	5.2	358.0	0.00353	0.00537	45.0	0.0063	0.09	59000	2.290
5898.8	4.8	328.0	0.00359	0.00585	51.0	0.0058	0.10	58800	2.102
6930.3	4.1	277.0	0.00356	0.00679	61.0	0.0049	0.12	58600	1.789
7478.1	3.8	257.0	0.00350	0.00726	65.0	0.0045	0.13	58300	1.658
8047.8	3.5	238.0	0.00341	0.00773	69.0	0.0042	0.14	58200	1.541
8638.9	3.3	221.0	0.00331	0.00819	72.0	0.0039	0.15	57900	1.435
9886.4	2.8	193.0	0.00309	0.00911	77.0	0.0034	0.17	57300	1.254





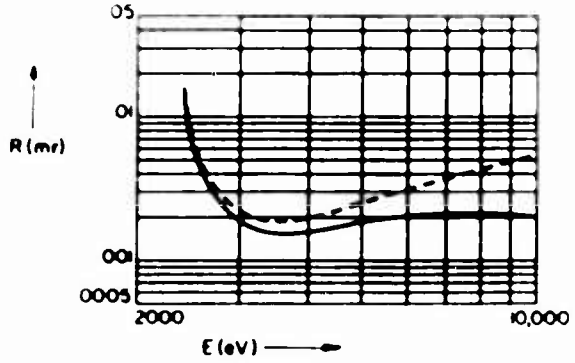


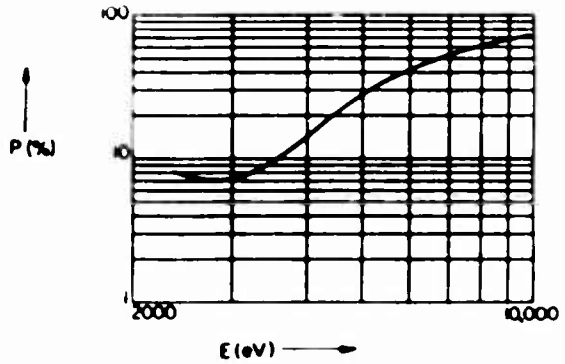


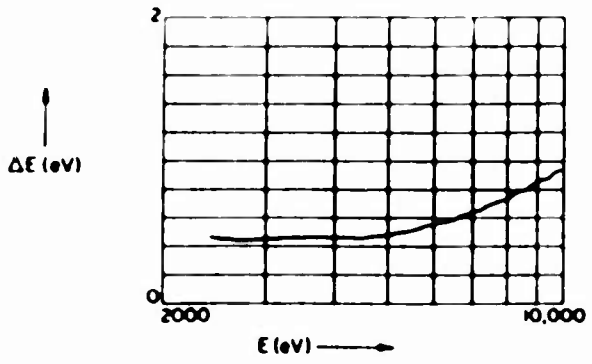
Rubidium Acid Phthalate -- RAP
$C_6H_4(COOH)(COO)Rb$

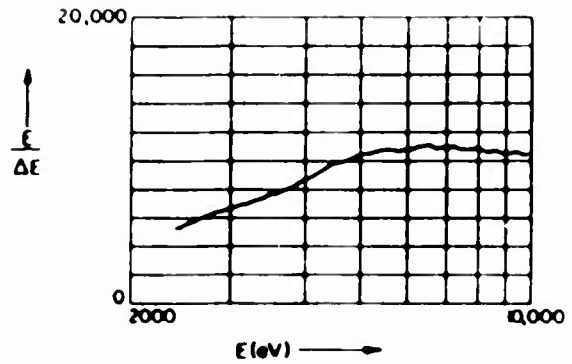
2d = 26.140Å
(001) n = 5

E(eV)	θ_c(mr)	θ_B(mr)	R_p(mr)	R_m(mr)	P(%)	ω(mr)	ΔE(eV)	E/ΔE	λ(Å)
2372.1	11.2	1571.0	0.7931		8.1	8.9300			5.227
2622.4	10.3	1130.0	0.0036	0.0041	7.2	0.0360	0.045	58900.	4.728
2984.3	9.2	919.0	0.0019	0.0023	7.2	0.0196	0.045	66800.	4.154
3691.7	7.6	698.0	0.0015	0.0019	11.0	0.0104	0.046	80400.	3.358
4466.3	6.3	560.0	0.0017	0.0022	20.0	0.0066	0.047	95600.	2.776
4510.8	6.2	554.0	0.0017	0.0022	21.0	0.0064	0.047	96900.	2.749
4952.2	5.7	500.0	0.0018	0.0025	27.0	0.0052	0.048	104000.	2.504
5414.7	5.2	453.0	0.0019	0.0028	34.0	0.0045	0.050	108000.	2.290
5898.8	4.8	414.0	0.0020	0.0030	40.0	0.0040	0.054	109000.	2.102
6930.3	4.1	349.0	0.0021	0.0037	52.0	0.0033	0.062	111000	1.789
7478.1	3.8	323.0	0.0021	0.0040	57.0	0.0031	0.070	107000	1.658
8047.8	3.5	299.0	0.0021	0.0043	62.0	0.0029	0.075	107000	1.541
8638.9	3.3	278.0	0.0021	0.0046	66.0	0.0027	0.082	105000	1.435
9886.4	2.8	242.0	0.0020	0.0053	73.0	0.0024	0.095	104000	1.254





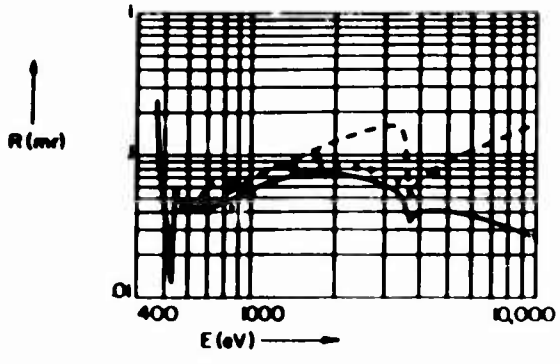


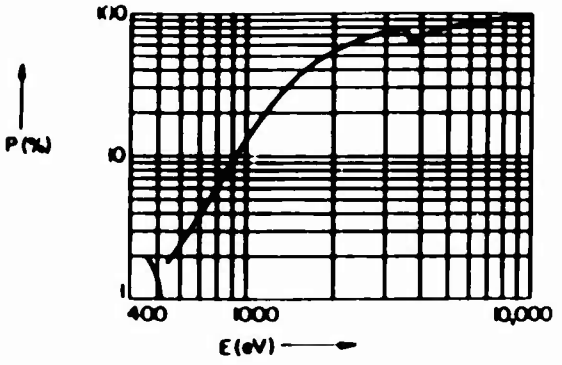


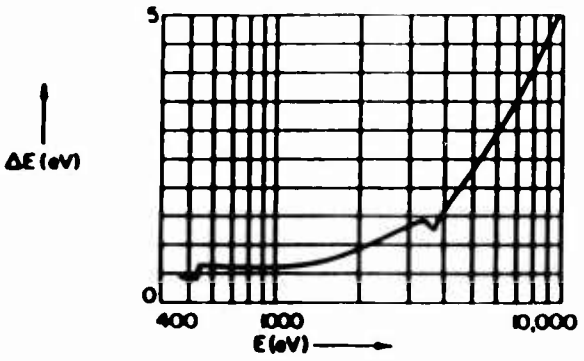
Potasium Acid Phthalate -- KAP
$C_6H_4(COOH)(COO)K$

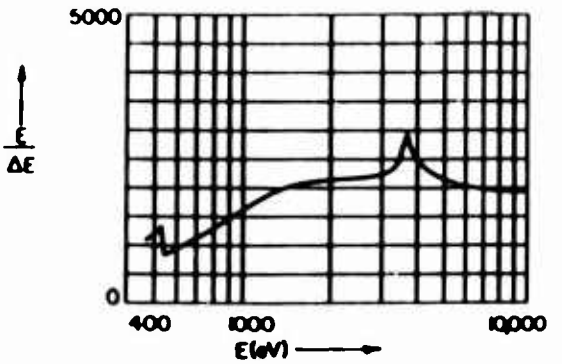
2d = 26.620Å
(001) n = 1

E(eV)	θ_c(mr)	θ_B(mr)	R_p(mr)	R_m(mr)	P(%)	ω(mr)	ΔE(eV)	E/ΔE	λ(Å)
466 2	39 5	1571 0	1 2730		1.9	60.00			26.590
511 3	36.9	1148 0	0 0299	0 0334	1 2	1.78	0 41	1250.	24.250
524 9	35 0	1093 0	0 0162	0 0181	0 8	1.48	0 40	1310.	23.620
556 3	29 8	994 0	0 0496	0 0551	2 0	1.79	0.65	861.	22.290
572 8	30 5	951 0	0 0470	0 0523	2 1	1 57	0 64	894.	21.640
637 4	31 2	821 0	0 0431	0 0482	2 9	1 06	0 63	1010.	19.450
676 8	31 0	760 0	0 0427	0 0480	3 5	0 87	0 62	1090.	18.320
705 0	30 5	723 0	0 0430	0 0484	3 9	0 78	0 62	1130.	17.590
776 2	29 3	644 0	0 0456	0 0518	5 5	0 60	0 62	1260	15.970
851 5	27 9	580 0	0 0497	0 0570	7 7	0 47	0 61	1390	14.560
929 7	26 4	525 0	0 0538	0 0625	10 0	0 38	0 61	1520	13.340
1012 0	24 8	479 0	0 0580	0 0682	13 0	0 32	0 62	1640	12.250
1041 0	24 2	465 0	0 0594	0 0702	15 0	0 30	0 62	1680	11.910
1188 0	21 8	403 0	0 0655	0 0803	21 0	0 23	0 64	1850.	10.440
1254 0	20 8	381 0	0 0676	0 0845	25 0	0 21	0 66	1910.	9.890
1487 0	17 8	319 0	0 0728	0 0985	35 0	0 16	0 73	2050.	8.339
1740 0	15 3	271 0	0 0758	0 1120	46 0	0 13	0 82	2110.	7 125
2042 0	13 0	230 0	0 0734	0 1263	56 0	0 11	0 95	2150	6.070
2166 0	12 3	217 0	0 0727	0 1312	59 0	0 10	1 00	2160.	5.724
2293 0	11 6	205 0	0 0714	0 1365	62 0	0 10	1 06	2170.	5.407
2622 0	10 1	179 0	0 0673	0 1487	69 0	0 08	1 20	2190.	4 728
2984 0	8 9	157 0	0 0618	0 1581	74 0	0 07	1.33	2240	4 154
3692 0	7 1	127 0	0 0333	0 0489	62 0	0 04	1 24	2970.	3 358
4466 0	5 9	105 0	0 0412	0 0797	75 0	0 05	1 97	2270.	2 776
4511 0	5 9	104 0	0 0412	0 0807	76 0	0 05	2 00	2260	2 748
4952 0	5 4	94 3	0 0407	0 0898	80 0	0 04	2.30	2160.	2.504







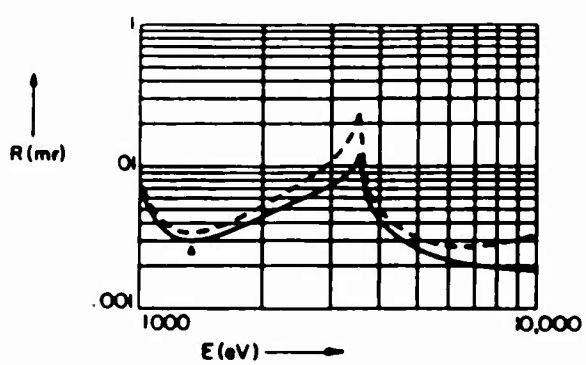


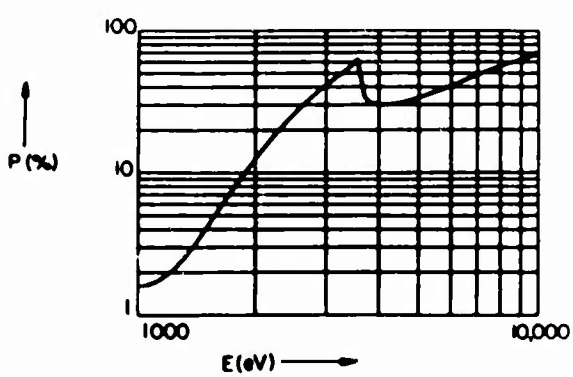
Potasium Acid Phthalate -- KAP

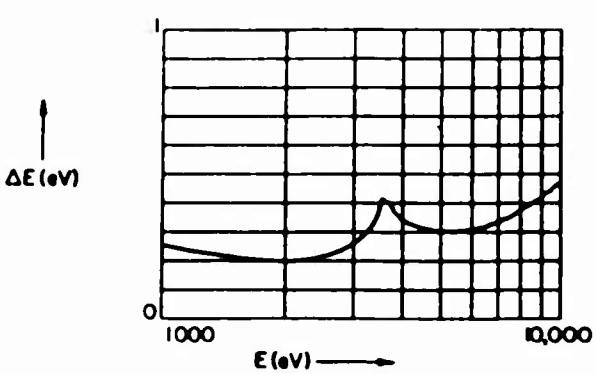
$C_6H_4(COOH)(COO)K$

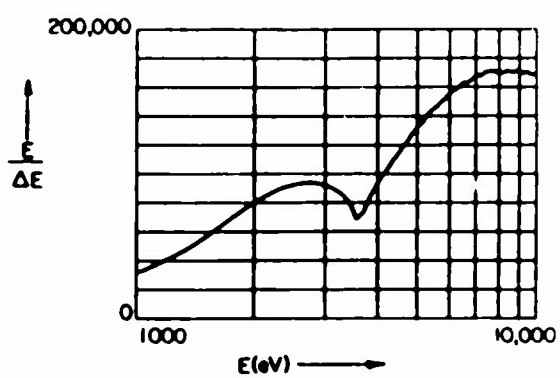
2d = 26.620Å
(001) m = 2

E(eV)	θ_c(mr)	θ_B(mr)	R_p(mr)	R_m(mr)	P(%)	ω(mr)	ΔE(eV)	E/ΔE	λ(Å)
931.5	26.3	1571.0	0.43270		1.6	24.000			13.310
1012.0	24.8	1170.0	0.00660	0.00742	1.6	0.296	0.13	7990.	12.250
1041.0	24.2	1108.0	0.00541	0.00609	1.6	0.240	0.12	8350.	11.910
1188.0	21.8	901.0	0.00334	0.00377	1.9	0.124	0.12	10200	10.440
1254.0	20.8	838.0	0.00309	0.00351	2.2	0.101	0.11	11000	9.890
1487.0	17.8	677.0	0.00313	0.00359	3.9	0.058	0.11	13900	8.339
1740.0	15.3	565.0	0.00370	0.00431	7.4	0.037	0.10	17100	7.125
2042.0	13.0	474.0	0.00454	0.00545	14.0	0.025	0.10	20400	6.070
2166.0	12.3	445.0	0.00491	0.00600	17.0	0.022	0.10	21400	5.724
2293.0	11.6	418.0	0.00527	0.00657	20.0	0.020	0.10	22200	5.407
2622.0	10.1	363.0	0.00618	0.00824	30.0	0.016	0.11	23300	4.728
2984.0	8.9	318.0	0.00727	0.01073	41.0	0.014	0.13	23100	4.154
3692.0	7.1	255.0	0.00652	0.00799	34.0	0.015	0.20	18000	3.358
4466.0	5.9	210.0	0.00316	0.00374	31.0	0.008	0.16	28400	2.776
4511.0	5.9	208.0	0.00309	0.00367	31.0	0.007	0.16	29000.	2.748
4952.0	5.4	189.0	0.00265	0.00318	33.0	0.006	0.15	32600.	2.504
5415.0	4.9	173.0	0.00238	0.00291	36.0	0.005	0.15	35800.	2.290
5899.0	4.5	159.0	0.00221	0.00277	40.0	0.004	0.15	38500	2.102
6930.0	3.8	135.0	0.00202	0.00272	48.0	0.003	0.17	41800.	1.789
7478.0	3.6	125.0	0.00197	0.00277	52.0	0.003	0.18	42600	1.658
8048.0	3.3	116.0	0.00193	0.00287	56.0	0.003	0.19	42500.	1.541
8639.0	3.1	108.0	0.00189	0.00299	60.0	0.003	0.20	42900.	1.435
9886.0	2.7	94.4	0.00183	0.00331	68.0	0.002	0.23	42300.	1.254



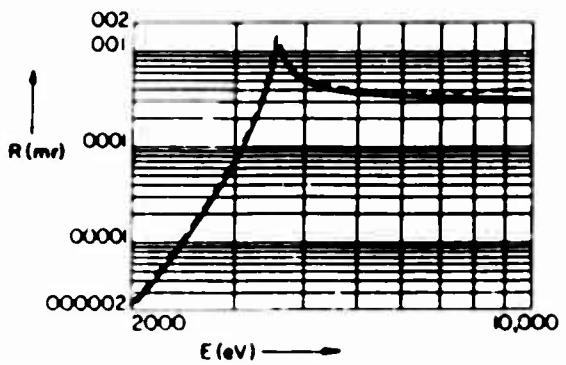


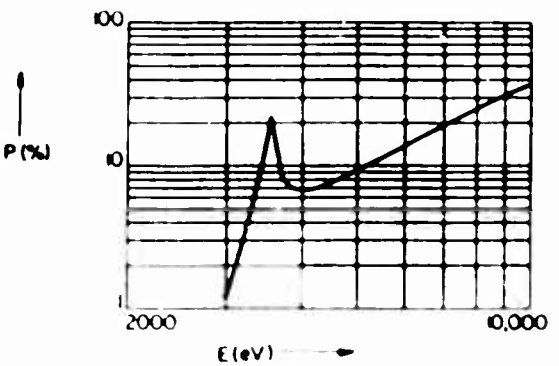


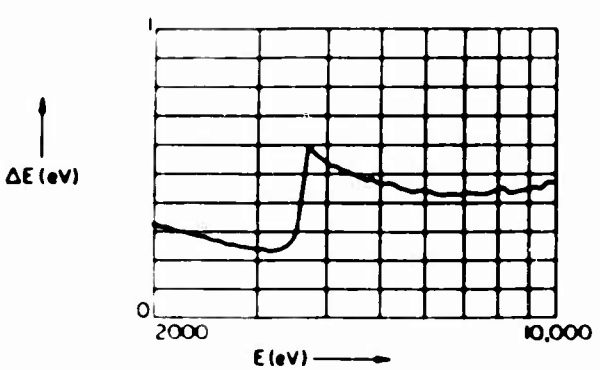


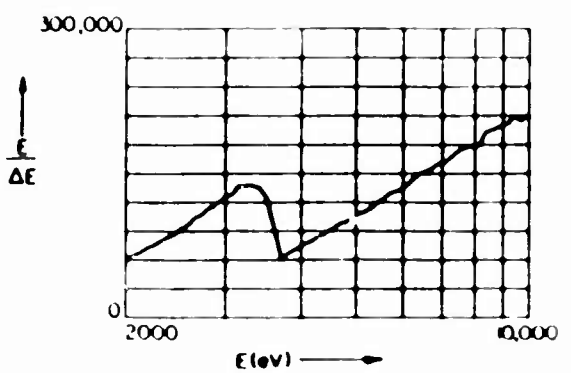
Potasium Acid Phthalate -- KAP — 2d = 26.620Å
$C_6H_4(COOH)(COO)K$ — (001) m = 3

E(eV)	θ_c(mr)	θ_B(mr)	R_p(mr)	R_m(mr)	P(%)	ω(mr)	ΔE(eV)	E/ΔE	λ(Å)
1397.0	18.8	1571.0	0.002190		0.02	11.0000			8.875
1487.0	17.8	1222.0	0.000012	0.000014	0.01	0 0761	0.041	36100.	8.339
1740.0	15.3	932.0	0 000002	0.000003	0.01	0 0283	0.037	47600	7.125
2042.0	13.0	753.0	0.000002	0.000002	0 01	0 0147	0.032	63700.	6.070
2166.0	12.3	701.0	0 000004	0.000004	0 02	0.0119	0.031	70800.	5.724
2293 0	11 6	655 0	0 000006	0.000006	0 04	0 0098	0.029	78600.	5.407
2622 0	10.1	562 0	0.000019	0.000021	0 21	0 0063	0.026	101000.	4.728
2984.0	8 9	487 0	0.000067	0.000075	1 12	0 0042	0.024	126000.	4.154
3692.0	7.1	388.0	0 000803	0.000887	8.50	0 0067	0.060	61200.	3 358
4466 0	5 9	318.0	0 000397	0.000434	7 54	0 0037	0 050	89100	2 776
4511 0	5.9	315.0	0 000392	0.000430	7 67	0 0036	0.049	91800	2 748
4952 0	5 4	286.0	0 000366	0 000402	9 16	0 0028	0.047	106000	2 504
5415 0	4 9	261 0	0 000352	0.000389	11 00	0 0022	0.045	119000	2 290
5899.0	4.5	239.0	0 000344	0.000383	13 00	0 0018	0 044	135000	2 102
6930.0	3.8	203.0	0.000336	0.000383	19 00	0 0012	0 042	164000.	1.789
7478.0	3.6	188.0	0.000335	0.000386	22 00	0 0011	0.044	170000	1 658
8048.0	3 3	175.0	0 000334	0 000391	26 00	0 0009	0 043	188000	1.541
8639.0	3.1	162.0	0.000331	0.000398	29 00	0 0008	0 045	193000.	1 435
9886.0	2.7	142.0	0 000325	0.000414	37 00	0 0007	0 046	213000.	1.254



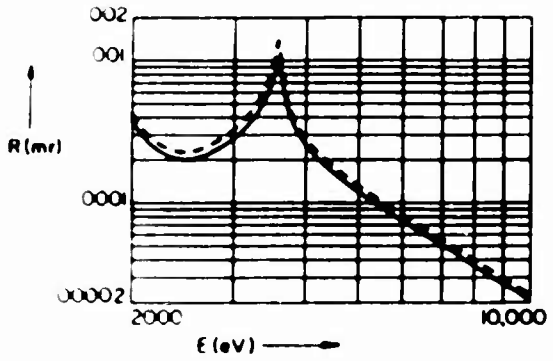


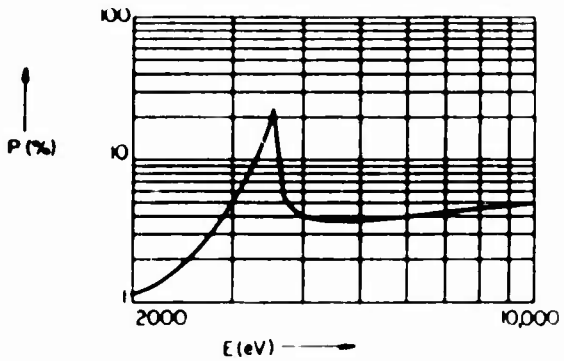


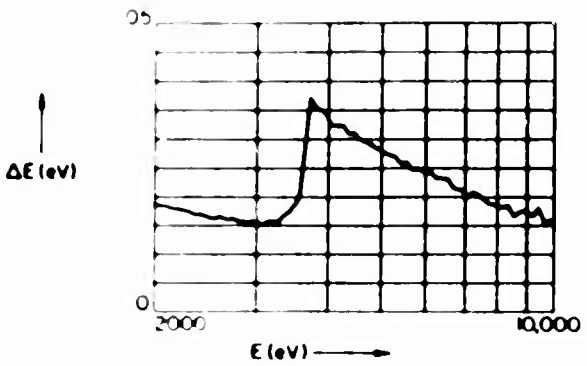


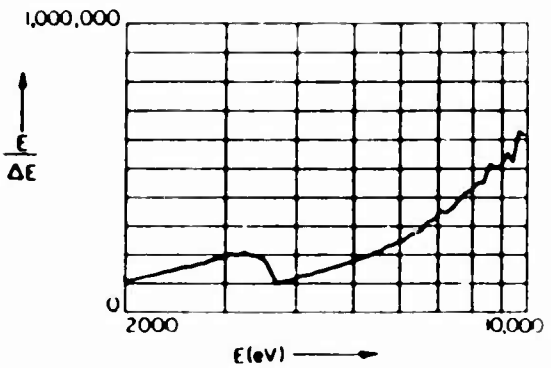
Potasium Acid Phthalate -- KAP 2d = 26.620Å
$C_6H_4(COOH)(COO)K$ (001) m = 4

E(eV)	θ_c(mr)	θ_B(mr)	R_p(mr)	R_m(mr)	P(%)	ω(mr)	ΔE(eV)	E/ΔE	λ(Å)
1863.0	14.3	1571.0	0.077790		1.08	6.4900			6.657
2042.0	13.0	1148.0	0.000326	0.000366	1.16	0.0200	0.018	111000.	6.070
2166.0	12.3	1035.0	0.000248	0.000279	1.28	0.0137	0.018	123000.	5.724
2293.0	11.6	948.0	0.000214	0.000241	1.46	0.0105	0.017	133000.	5.407
2622.0	10.1	790.0	0.000208	0.000237	2.42	0.0062	0.016	163000.	4.728
2984.0	8.9	674.0	0.000281	0.000324	4.89	0.0043	0.016	186000	4.154
3692.0	7.1	529.0	0.000476	0.000535	5.75	0.0059	0.037	99000	3.358
4466.0	5.9	440.0	0.000164	0.000181	3.70	0.0031	0.031	147000.	2.776
4511.0	5.9	423.0	0.000158	0.000176	3.69	0.0030	0.030	151000	2.748
4952.0	5.4	386.0	0.000121	0.000133	3.71	0.0023	0.028	177000	2.504
5415.0	4.9	351.0	0.000095	0.000105	3.81	0.0017	0.026	212000	2.290
5899.0	4.5	321.0	0.000077	0.000085	3.95	0.0014	0.024	243000	2.102
6930.0	3.8	272.0	0.000051	0.000057	4.25	0.0008	0.021	334000	1.789
7478.0	3.6	252.0	0.000043	0.000047	4.40	0.0007	0.020	375000	1.658
8048.0	3.3	234.0	0.000036	0.000039	4.53	0.0006	0.019	420000	1.541
8639.0	3.1	217.0	0.000030	0.000033	4.66	0.0004	0.018	494000	1.435
9886.0	2.7	190.0	0.000021	0.000023	4.88	0.0003	0.016	613000	1.254







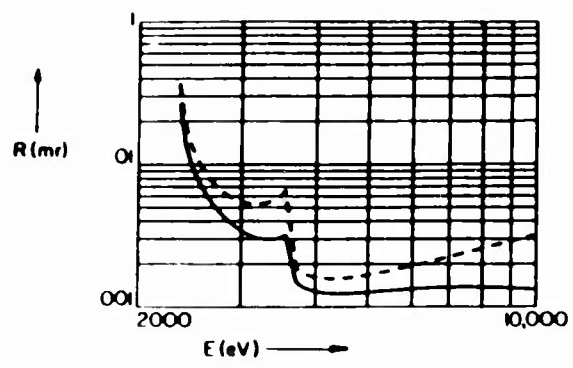


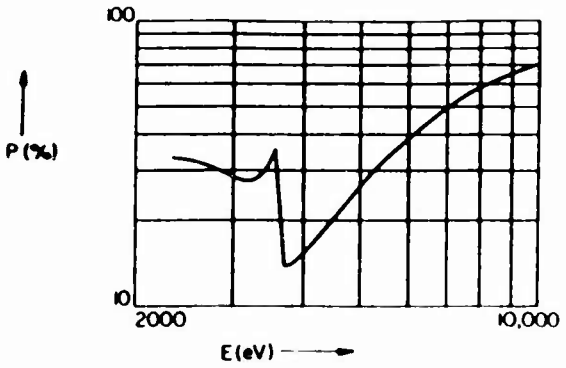
Potasium Acid Phthalate -- KAP

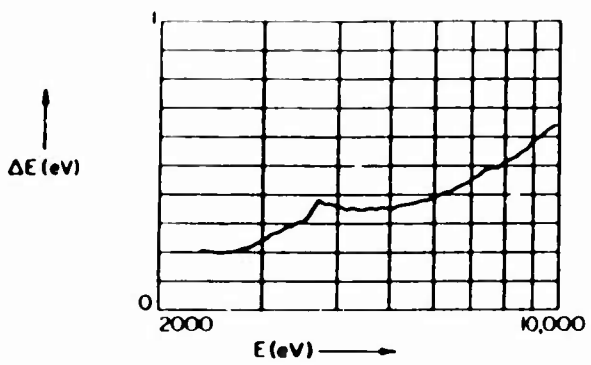
$C_6H_4(COOH)(COO)K$

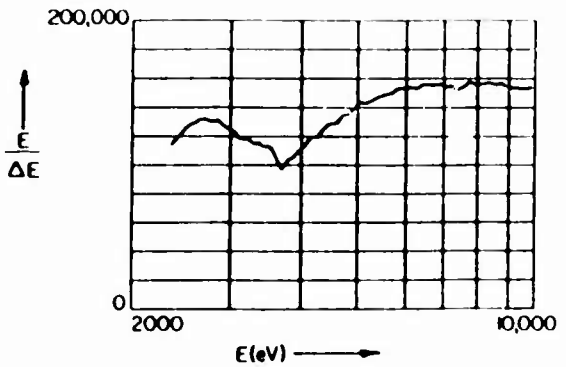
2d = 26.620Å
(001) m = 5

E(eV)	θ_c(mr)	θ_B(mr)	R_p(mr)	R_m(mr)	P(%)	ω(mr)	ΔE(eV)	E/ΔE	λ(Å)
2328.0	11.4	1571.0	2.07900		33.0	5.7700			5.325
2622.0	10.1	1092.0	0.00592	0.00829	32.0	0.0148	0.020	130000.	4.728
2984.0	8.9	895.0	0.00347	0.00551	29.0	0.0102	0.024	122000.	4.154
3692.0	7.1	682.0	0.00152	0.00191	14.0	0.0083	0.038	97400.	3.358
4466.0	5.9	548.0	0.00125	0.00159	20.0	0.0048	0.035	128000.	2.776
4511.0	5.9	542.0	0.00125	0.00160	21.0	0.0047	0.035	130000.	2.748
4952.0	5.4	489.0	0.00127	0.00168	26.0	0.0038	0.035	141000.	2.504
5415.0	4.9	444.0	0.00130	0.00179	32.0	0.0032	0.036	149000.	2.290
5899.0	4.5	406.0	0.00134	0.00193	38.0	0.0028	0.039	152000.	2.102
6930.0	3.8	343.0	0.00138	0.00224	49.0	0.0023	0.045	155000.	1.789
7478.0	3.6	317.0	0.00138	0.00242	54.0	0.0021	0.048	155000.	1.658
8048.0	3.3	294.0	0.00138	0.00261	59.0	0.0019	0.051	158000	1.541
8639.0	3.1	273.0	0.00137	0.00280	63.0	0.0018	0.055	157000.	1.435
9886.0	2.7	238.0	0.00132	0.00322	70.0	0.0015	0.063	156000.	1.254







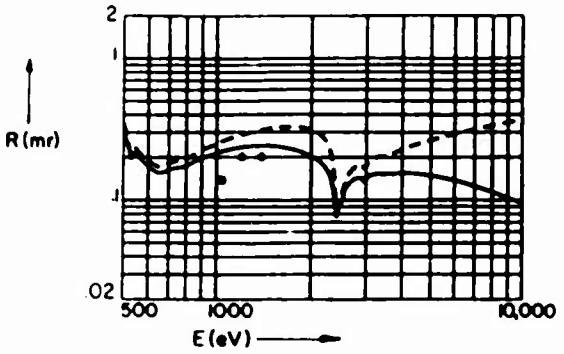


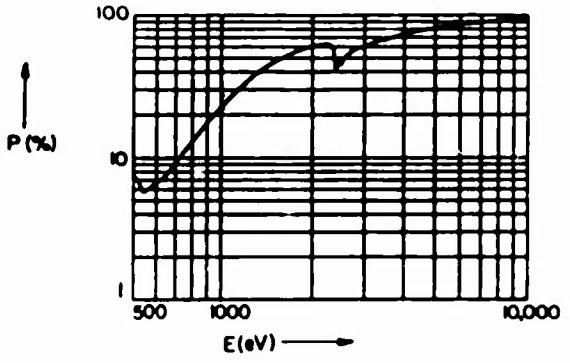
Thallium Acid Phthalate -- TAP

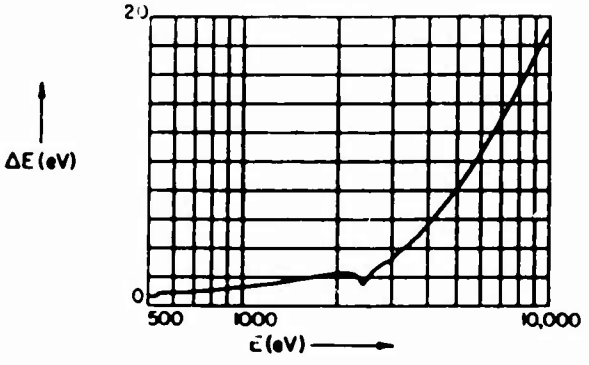
$C_6H_4(COOH)(COO)Tl$

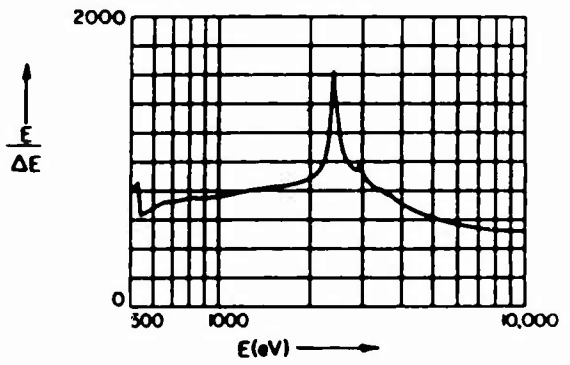
2d = 26.620Å
(001) m = 1

E(eV)	θ_c(mr)	θ_B(mr)	R_p(mr)	R_m(mr)	P(%)	ω(mr)	ΔE(eV)	E/ΔE	λ(Å)
466.2	34.4	1571.0	6.425		8.3	69.00			26.590
511.3	31.8	1148.0	0.276	0.305	7.1	2.71	0.62	818.	24.250
524.9	30.2	1093.0	0.221	0.244	6.7	2.31	0.63	837.	23.620
556.3	27.5	994.0	0.203	0.224	5.9	2.39	0.87	642.	22.290
572.8	28.0	951.0	0.189	0.209	6.2	2.14	0.87	656.	21.640
637.4	28.1	821.0	0.156	0.173	7.3	1.51	0.90	711.	19.450
676.8	27.2	760.0	0.159	0.176	8.4	1.32	0.94	723.	18.320
705.0	27.0	723.0	0.164	0.183	9.4	1.22	0.98	721.	17.590
736.2	26.5	644.0	0.172	0.193	12.0	1.01	1.05	743.	15.970
851.5	25.4	580.0	0.187	0.212	15.0	0.88	1.14	746.	14.560
929.7	24.6	525.0	0.203	0.233	19.0	0.77	1.24	751.	13.340
1012.0	23.6	479.0	0.217	0.253	23.0	0.68	1.33	760.	12.250
1041.0	23.3	465.0	0.221	0.260	25.0	0.66	1.36	764.	11.910
1188.0	21.6	403.0	0.236	0.288	33.0	0.54	1.50	790.	10.440
1254.0	20.8	381.0	0.239	0.298	36.0	0.50	1.57	800.	9.890
1487.0	18.4	319.0	0.239	0.320	46.0	0.40	1.81	824.	8.339
1740.0	16.1	271.0	0.227	0.327	55.0	0.33	2.06	843.	7.125
2042.0	13.8	230.0	0.198	0.306	61.0	0.26	2.28	896.	6.070
2166.0	12.9	217.0	0.179	0.279	62.0	0.23	2.28	952.	5.724
2293.0	12.0	205.0	0.145	0.221	62.0	0.19	2.09	1100	5.407
2622.0	9.0	179.0	0.130	0.152	52.0	0.17	2.50	1050	4.728
2984.0	8.2	157.0	0.126	0.150	57.0	0.15	2.91	1030.	4.154
3692.0	7.6	127.0	0.153	0.214	70.0	0.17	4.84	763.	3.358
4466.0	6.7	105.0	0.154	0.248	78.0	0.16	6.82	655.	2.776
4511.0	6.6	104.0	0.153	0.250	78.0	0.16	6.93	651	2.748
4952.0	6.1	94.3	0.149	0.264	81.0	0.15	8.03	616.	2.504





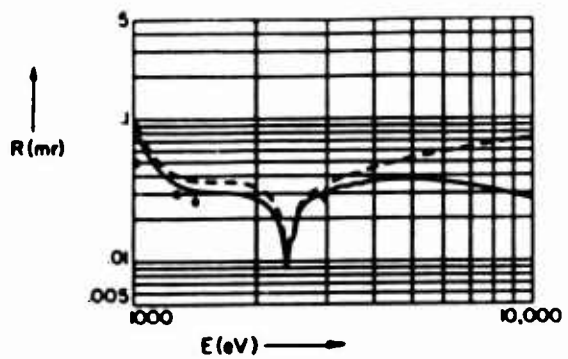


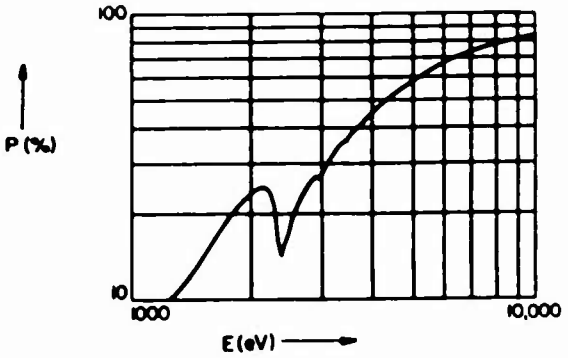


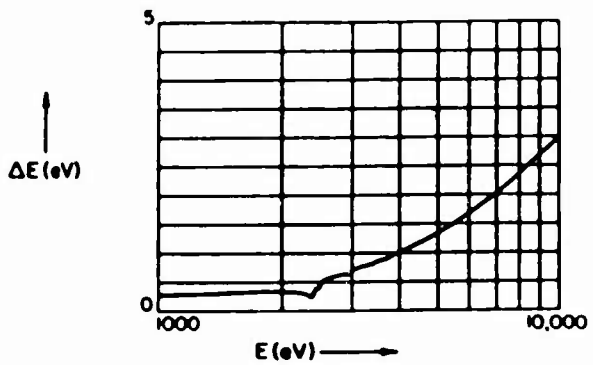
Thallium Acid Phthalate -- TAP
$C_6H_4(COOH)(COO)Tl$

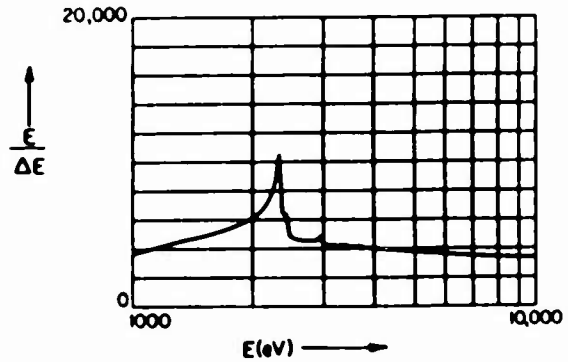
2d = 26.620Å
(001) n = 2

E(eV)	θ_c(mr)	θ_B(mr)	R_p(mr)	R_m(mr)	P(%)	ω(mr)	ΔE(eV)	E/ΔE	λ(Å)
931.6	24.5	1571.0	3.8650		11.0	32.000			13.310
1012.0	23.6	1170.0	0.0865	0.0969	9.6	0.642	0.3	3680.	12.250
1041.0	23.3	1108.0	0.0703	0.0789	9.4	0.534	0.3	3760.	11.910
1188.0	21.6	901.0	0.0399	0.0454	9.4	0.303	0.3	4170.	10.440
1254.0	20.8	838.0	0.0354	0.0406	10.0	0.256	0.3	4330.	9.890
1487.0	18.4	677.0	0.0307	0.0360	13.0	0.167	0.3	4810.	8.339
1740.0	16.1	565.0	0.0299	0.0357	19.0	0.119	0.3	5330.	7.125
2042.0	13.8	474.0	0.0263	0.0318	24.0	0.082	0.3	6280.	6.070
2166.0	12.9	445.0	0.0225	0.0271	25.0	0.068	0.3	6990.	5.724
2293.0	12.0	418.0	0.0153	0.0179	22.0	0.052	0.3	8550.	5.407
2622.0	9.0	363.0	0.0256	0.0280	21.0	0.083	0.6	4570.	4.728
2984.0	8.2	318.0	0.0256	0.0282	25.0	0.071	0.6	4630.	4.154
3692.0	7.6	255.0	0.0345	0.0414	40.0	0.063	0.9	4140.	3.358
4466.0	6.7	210.0	0.0374	0.0493	52.0	0.055	1.2	3850.	2.776
4511.0	6.6	208.0	0.0374	0.0497	52.0	0.055	1.2	3850.	2.748
4952.0	6.1	189.0	0.0374	0.0527	58.0	0.051	1.3	3750.	2.504
5415.0	5.7	173.0	0.0369	0.0555	63.0	0.048	1.5	3670.	2.290
5899.0	5.3	159.0	0.0361	0.0581	66.0	0.045	1.6	3590.	2.102
6930.0	4.5	135.0	0.0340	0.0629	73.0	0.039	2.0	3470.	1.789
7478.0	4.2	125.0	0.0327	0.0651	76.0	0.037	2.2	3430.	1.658
8048.0	3.9	116.0	0.0313	0.0671	78.0	0.034	2.4	3390.	1.541
8639.0	3.7	108.0	0.0300	0.0690	80.0	0.032	2.6	3370.	1.435
9886.0	3.2	94.4	0.0271	0.0719	83.0	0.028	3.0	3350.	1.254









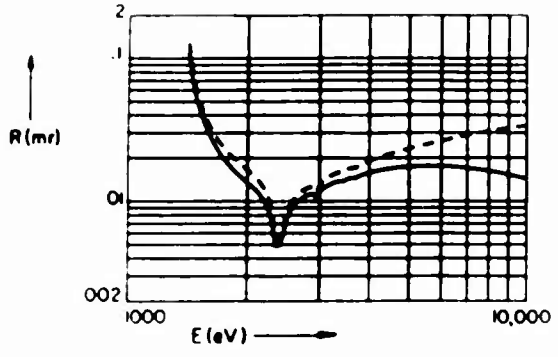
Thallium Acid Phthalate -- TAP

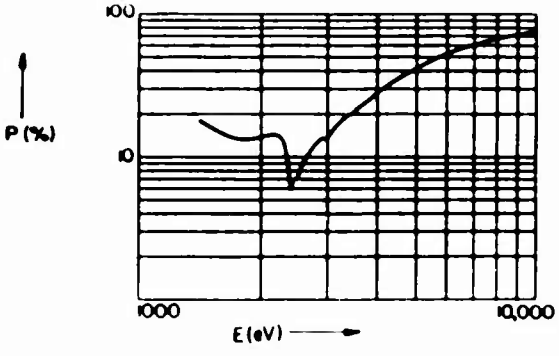
$C_6H_4(COOH)(COO)Tl$

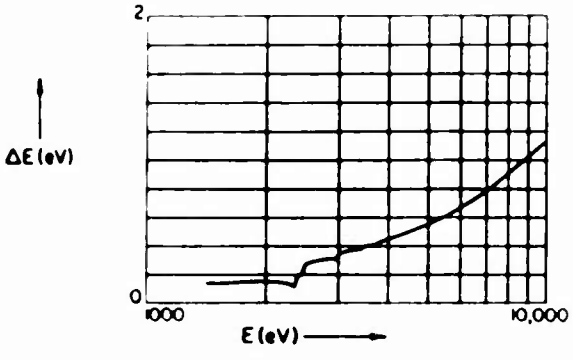
2d = 26.620Å

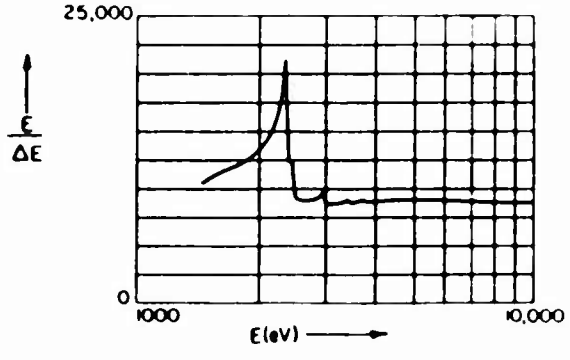
(001) n = 3

E(eV)	θ_c(mr)	θ_B(mr)	R_p(mr)	R_m(mr)	P(%)	ω(mr)	ΔE(eV)	E/ΔE	λ(Å)
1397.0	19.3	1571.0	3.6010		18.0	18.000			8.874
1487.0	18.4	1222.0	0.0547	0.0637	16.0	0.252	0.14	10900.	8.339
1740.0	16.1	932.0	0.0201	0.0240	13.0	0.112	0.14	12000.	7.125
2042.0	13.8	753.0	0.0127	0.0155	14.0	0.068	0.15	13700.	6.070
2166.0	12.9	701.0	0.0106	0.0130	14.0	0.056	0.14	15100.	5.724
2293.0	12.0	655.0	0.0075	0.0089	13.0	0.043	0.13	17900.	5.407
2622.0	9.0	562.0	0.0096	0.0107	9.6	0.070	0.29	8970	4.728
2984.0	8.2	487.0	0.0099	0.0111	12.0	0.058	0.33	9070	4.154
3692.0	7.6	388.0	0.0146	0.0172	24.0	0.046	0.41	8980	3.358
4466.0	6.7	318.0	0.0168	0.0212	35.0	0.037	0.50	8990	2.776
4511.0	6.6	315.0	0.0169	0.0214	36.0	0.036	0.50	9000	2.748
4952.0	6.1	286.0	0.0173	0.0230	41.0	0.033	0.55	9030	2.504
5415.0	5.7	261.0	0.0175	0.0246	47.0	0.030	0.60	9020	2.290
5899.0	5.3	239.0	0.0175	0.0260	52.0	0.027	0.66	8990	2.102
6930.0	4.5	203.0	0.0170	0.0286	60.0	0.023	0.78	8890	1.789
7478.0	4.2	188.0	0.0165	0.0298	64.0	0.022	0.84	8850	1.658
8048.0	3.9	175.0	0.0160	0.0309	67.0	0.020	0.91	8820	1.541
8639.0	3.7	162.0	0.0155	0.0319	70.0	0.019	0.98	8790	1.435
9886.0	3.2	142.0	0.0143	0.0335	75.0	0.016	1.12	8800	1.254







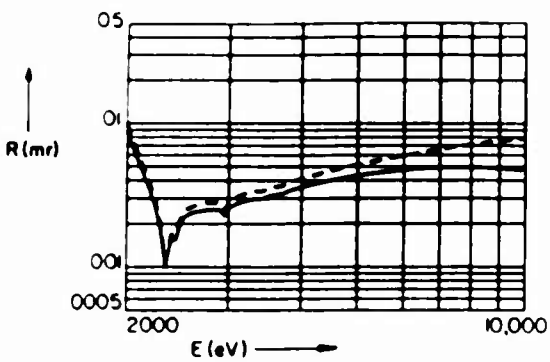


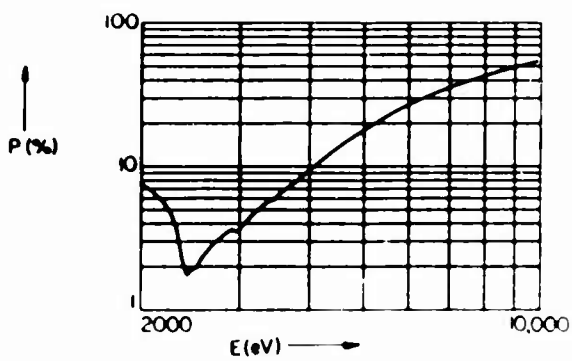
Thallium Acid Phthalate -- TAP

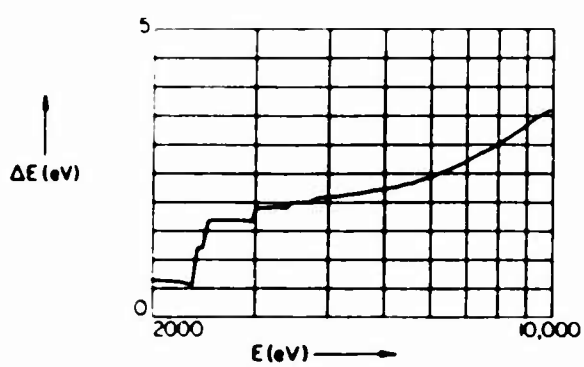
$C_6H_4(COOH)(COO)Tl$

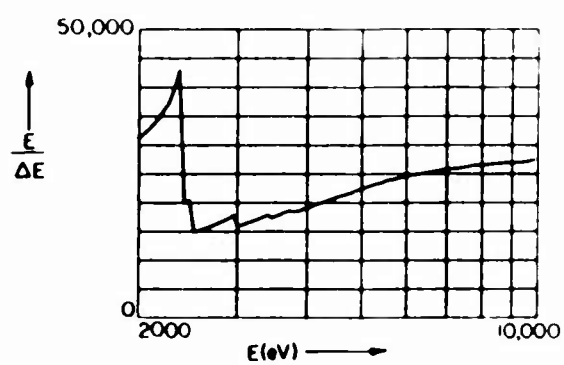
2d = 26.620Å
(001) n = 4

E(eV)	θ_C(mr)	θ_B(mr)	R_p(mr)	R_m(mr)	P(%)	ω(mr)	ΔE(eV)	$E/\Delta E$	λ(Å)
1863.0	15.1	1571.0	1.16300		9.10	11.000			6.656
2042.0	13.8	1148.0	0.00683	0.00778	7.10	0.069	0.06	32100	6.070
2166.0	12.9	1035.0	0.00386	0.00440	5.77	0.048	0.06	34900	5.724
2293.0	12.0	948.0	0.00191	0.00215	3.86	0.036	0.06	39300	5.407
2622.0	9.0	790.0	0.00238	0.00265	2.59	0.065	0.17	15600	4.728
2984.0	8.2	674.0	0.00219	0.00243	3.11	0.050	0.19	16100	4.154
3692.0	7.6	529.0	0.00322	0.00366	7.34	0.032	0.20	18500	3.358
4466.0	6.7	430.0	0.00399	0.00464	13.00	0.022	0.21	20800	2.776
4811.0	6.6	426.0	0.00402	0.00468	14.00	0.022	0.22	20900	2.648
4952.0	6.1	386.0	0.00430	0.00511	18.00	0.018	0.22	22300	2.504
5415.0	5.7	351.0	0.00453	0.00550	22.00	0.016	0.23	23400	2.290
5899.0	5.3	321.0	0.00470	0.00587	26.00	0.014	0.24	24400	2.102
6930.0	4.5	272.0	0.00489	0.00654	35.00	0.011	0.27	25700	1.789
7478.0	4.2	252.0	0.00491	0.00684	39.00	0.010	0.29	26200	1.658
8048.0	3.9	234.0	0.00490	0.00712	44.00	0.009	0.30	26500	1.541
8639.0	3.7	217.0	0.00485	0.00737	47.00	0.008	0.32	26800	1.435
9886.0	3.2	190.0	0.00466	0.00778	54.00	0.007	0.36	27300	1.254







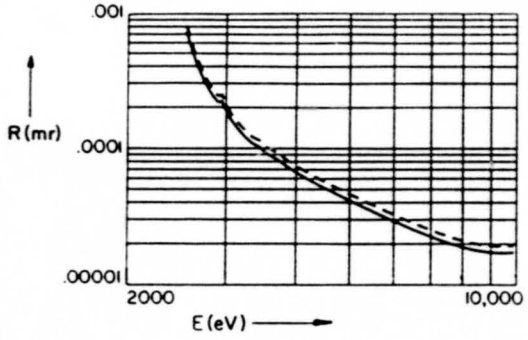


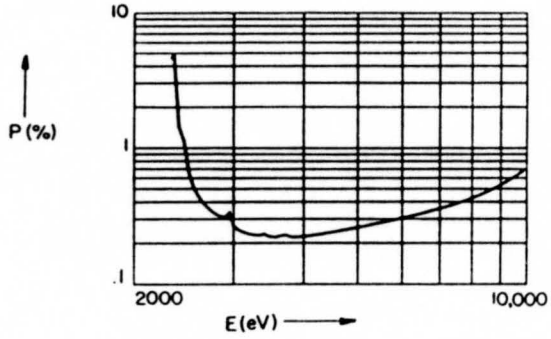
Thallium Acid Phthalate -- TAP

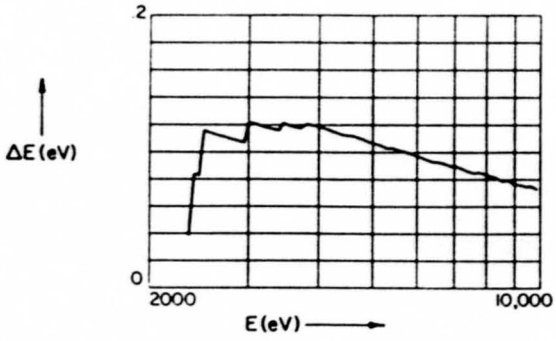
$C_6H_4(COOH)(COO)Tl$

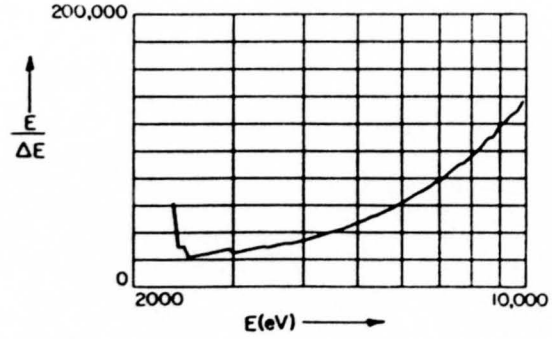
2d = 26.620Å
(001) m = 5

E(eV)	θ_c(mr)	θ_B(mr)	R_p(mr)	R_m(mr)	P(%)	ω(mr)	ΔE(eV)	E/ΔE	λ(Å)
2328.0	11.7	1571.0	0.405900		4.5	8.1100			5.325
2622.0	9.0	1092.0	0.000484	0.000541	0.4	0.0828	0.113	23300.	4.728
2984.0	8.2	895.0	0.000228	0.000254	0.3	0.0511	0.122	24400.	4.154
3692.0	7.6	682.0	0.000083	0.000092	0.2	0.0259	0.118	31400.	3.358
4466.0	6.7	548.0	0.000052	0.000058	0.2	0.0154	0.112	39700.	2.776
4511.0	6.6	542.0	0.000051	0.000057	0.2	0.0150	0.112	40300.	2.748
4952.0	6.1	489.0	0.000042	0.000047	0.3	0.0115	0.107	46300.	2.504
5415.0	5.7	445.0	0.000035	0.000039	0.3	0.0090	0.103	52700.	2.290
5899.0	5.3	406.0	0.000030	0.000034	0.3	0.0071	0.097	60600.	2.102
6930.0	4.5	343.0	0.000023	0.000025	0.4	0.0046	0.089	78200.	1.789
7478.0	4.2	317.0	0.000020	0.000023	0.4	0.0037	0.085	87900.	1.658
8048.0	3.9	294.0	0.000019	0.000021	0.4	0.0031	0.083	97500.	1.541
8639.0	3.7	273.0	0.000018	0.000020	0.5	0.0026	0.079	109000.	1.435
9886.0	3.2	238.0	0.000017	0.000019	0.7	0.0018	0.073	136000.	1.254









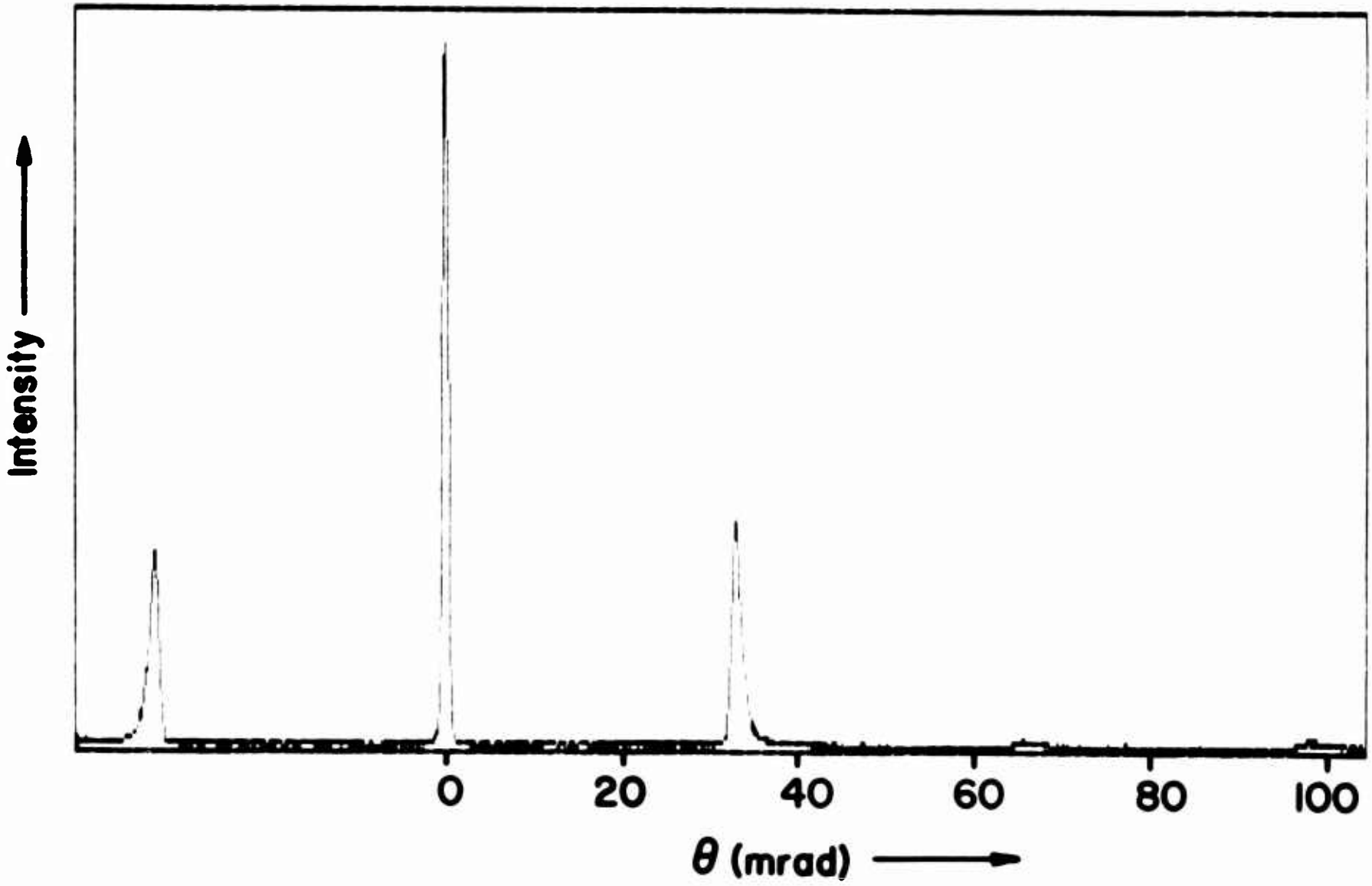
7. TECHNICAL NOTES: THE CHARACTERIZATION OF TRANSMISSION DIFFRACTION GRATINGS

We have recently initiated a collaborative effort with LLNL and LANL on the absolute characterization of x-ray transmission gratings as those which have been originally developed with microlithography thechniques by the MIT group. Examples of the B-Kα (67.6 A, 183.3 eV) spectra are shown here. These are measured using nearly parallel incident radiation and an appropriately fine slit on the proportional counter to limit the collimination error to a magnitude approximately matching that of the emission line width and grating diffraction width. The spectra are step-scanned and are recorded with a multichannel analyzer (MCA). By the same procedures we have developed in our absolute characterizations of crystal/multilayer analyzers (4), we measure for each diffraction order the FWHM and the line heights and areas relative to these values for the zero order line. The measurement is made absolute by also measuring the ratio of the total intensity within the zero order line to that incident within the illuminated area of the grating.

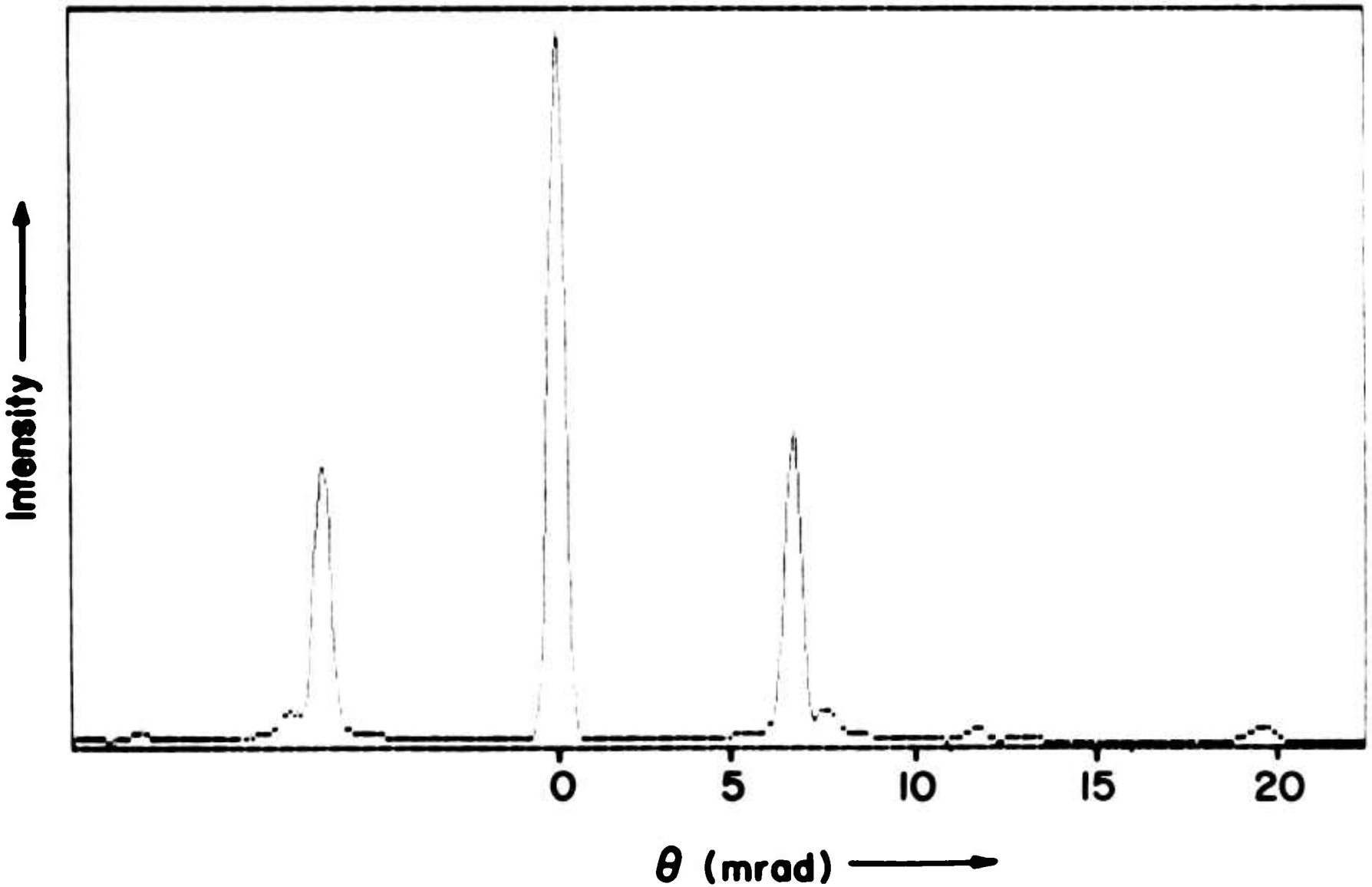
The line widths are the result of an intensity fold of the collimination width, the emission line width and the grating diffraction width. By a similar unfolding procedure as applied in our crystal/multilayer characterizations, we determine the characteristic diffraction width (FWHM) parameters at several photon energies.

With measurements, as shown here, at several photon energies along with the usual analytical theoretical intensity equations for transparent-bar gratings, we plan to derive semi-empirical analytical descriptions that accurately characterize the energy dependence of the real transmission gratings for absolute spectrometry.

B-Kα (67.6 A, 183.3 eV) Transmission Grating Spectra



Cu-Lα (13.3 A, 929.7 eV) Transmission Grating Spectra

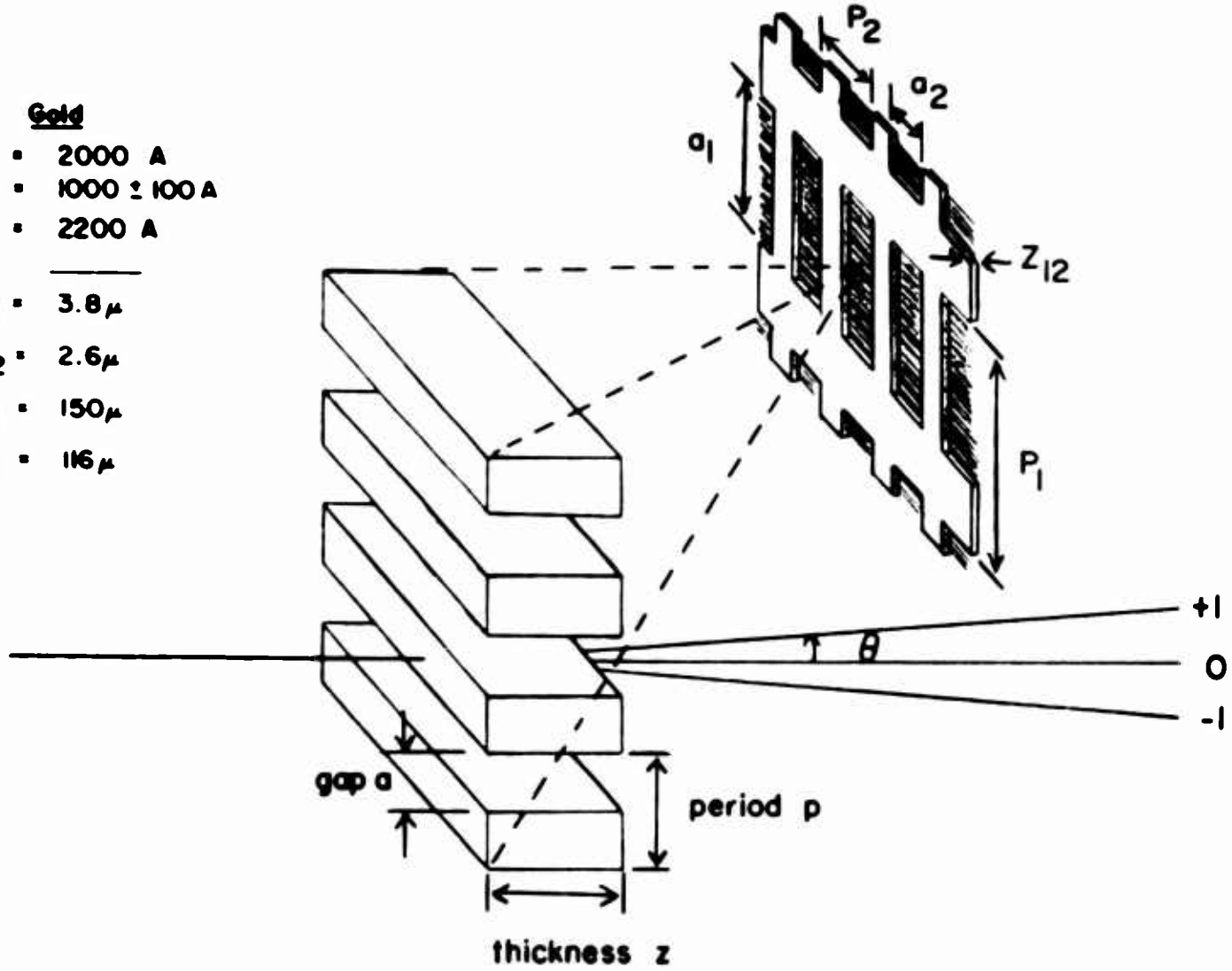


Transmission Grating Geometry

Gold

P = 2000 A
a = 1000 ± 100 A
z = 2200 A

P_2 = 3.8 μ
a_2 = 2.6 μ
P_1 = 150 μ
a_1 = 116 μ



8 Low-energy x-ray response of photographic films. I. Mathematical models

B. L. Henke, S. L. Kwok, J. Y. Uejio, H. T. Yamada, and G. C. Young

University of Hawaii, Honolulu, Hawaii 96822

Received February 27, 1984; accepted July 2, 1984

Relatively simple mathematical models are developed to determine the optical density as a function of the x-ray intensity, its angle of incidence, and its photon energy in the 100–10,000-eV region for monolayer and emulsion types of photographic films. Semiempirical relations are applied to characterize a monolayer film (Kodak 101-07) and an emulsion-type film (Kodak RAR 2497); these relations fit calibration data at nine photon energies well within typical experimental error.

1. INTRODUCTION

Photographic film is used extensively as the time-integrating, position-sensitive detector for x-ray spectrometry of pulsed, high-temperature plasma sources.[1] These sources include the inertially and magnetically confined plasmas studied in fusion-energy research and other areas, such as the Z pinch, the exploding wire, and the imploding linear plasma sources. Photographic detection is often chosen for the fixed-analyzer spectroscopy of such sources because of its relatively high sensitivity, wide latitude of response, and simplicity of implementation as compared with the alternative position-sensitive electronic-detection array systems.

For the diagnostics of high-temperature plasma sources there is considerable need for well-calibrated absolute spectrometry. The spectral analysis that is required demands a precise knowledge of peak and integrated intensities and shapes of spectral lines and of the intensity distributions in continua. Such information can be deduced from the measured optical density versus position along the film and its quantitative relationship to the incident intensity for a given photographic emulsion of appropriate sensitivity and resolution.

Because the optical density is a function not only of the intensity of the x radiation but also of its angle of incidence and of its photon energy, it is important to supplement experimental calibration with theoretical modeling. Semiempirical, universal mathematical relations may then be established that yield detailed photometric information (including the effects of x-ray absorption-edge structure) based on a minimum set of experimental data. An optimum design for the experimental calibration may be effectively guided by these model relations.

In Part I of this series of papers we develop relatively simple mathematical models for the photographic response of monolayer and of thick- and thin-emulsion films for the low-energy x-ray region of 100–10,000 eV. These are derived, in the description of the basic photographic-exposure process, in order to define the appropriate experimental parameters and finally to establish universal, semiempirical relations that can assist in efficient quantitative spectroscopic x-ray analysis. Their validity is established by applying them to the description of two examples of photographic films: Kodak 101-07, a monolayer, and Kodak RAR 2497, an emulsion-type system.

2. SIMPLE MODELS FOR THE PHOTOGRAPHIC X-RAY RESPONSE

A. Monolayer Model

Figure 1 depicts a photographic film for which the sensitive region is a monolayer of densely packed AgBr grains with a packing density of M_0 (AgBr grains per unit area). A scanning-electron-microscope (SEM) photograph of this type of film (Kodak 101-07) is shown in Fig. 2. As is suggested by this photograph, the grains may be considered to be nearly spherical, with a mean diameter of about 1 μm.

We would like to model this monolayer film as a thin slab of average thickness t_1, which, for practical films, such as the Kodak 101, may be somewhat larger than a single grain diameter. Such a thin-slab geometry introduces a total photon absorption proportional to $\sin\theta$, the dependence of which, as described below, is demonstrated by experimental measurement.

The probability that a AgBr grain will absorb a photon under an exposing radiation intensity I (photons per square micrometer) of photon energy E (electron volts) and at an angle of incidence θ is simply the total number of photons absorbed per unit area within the slab divided by the number of grains per unit area M_0, viz.,

$$\frac{I \sin\theta \left[1 - \exp\left(-\mu_1 \frac{t_1}{\sin\theta}\right)\right]}{M_0},$$

where μ_1 is the linear x-ray absorption coefficient of AgBr (which parameter introduces the only dependence on photon energy E). For the low-energy x-ray region of interest here (100–10,000 eV), it may be assumed that the absorption of a single photon is sufficient to render the AgBr grain developable, and therefore any additional absorption events within that grain cannot contribute to its effective exposure process.[2] We may therefore write the differential equation that determines the increase in the number of grains per unit area dM

Reprinted from Journal of the Optical Society of America B, Vol. 1, p. 818, December 1984
Copyright © 1984 by the Optical Society of America and reprinted by permission of the copyright owner.

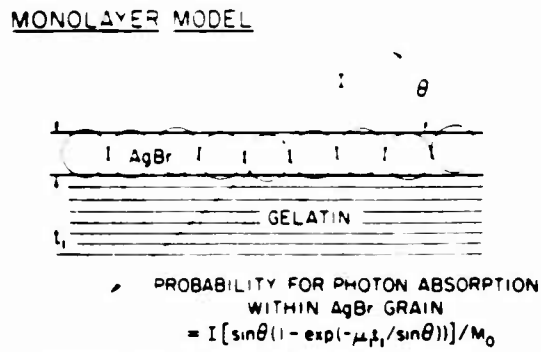


Fig. 1. Monolayer model for an effective film thickness t_1 of M_0, densely packed nearly spherical AgBr grains per unit area, and of linear x-ray absorption coefficient equal to μ_1 (for AgBr).



Fig. 2. SEM photograph of the Kodak 101-07 film showing nearly spherical AgBr grains of about 1-μm average diameter.

that have been rendered developable when the radiation intensity is increased by an amount dI; we do this by equating dM to the number of grains within the layer that have not yet been rendered developable, viz., $M_0 - M$, multiplied by the probability of a photon's being absorbed within a given grain for an increment of intensity dI. Hence

$$dM = (M_0 - M)\left\{\frac{\sin\theta\left[1-\exp\left(-\mu_1\frac{t_1}{\sin\theta}\right)\right]}{M_0}\right\}dI. \quad (1)$$

This may be integrated immediately to yield the number of grains per unit area M rendered developable under a total exposure of incident beam of intensity I photons per unit area at incident angle θ; we obtain

$$M = M_0\left(1-\exp\left\{-\sigma\sin\theta\left[1-\exp\left(-\mu_1\frac{t_1}{\sin\theta}\right)\right]I\right\}\right). \quad (2)$$

Here, we have substituted for $(M_0)^{-1}$ in the argument of the exponential an effective average cross-sectional area of the AgBr grain, σ.

In the development process, the exposed grain is reduced chemically to a cluster of silver usually of somewhat increased cross-sectional area, which we shall define here as S. This silver cluster strongly absorbs and scatters the light beam, as can be measured in a densitometer for the exposed-grain density.

In microdensitometry, as required for the quantitative analysis of spectroscopic line images, a relatively small-angle cone of illuminating light is focused and transmitted at a small, optically defined slit-region area of the film; the transmitted beam is received by a nearly matched, small-angle acceptance aperture of an objective lens, imaged at a fixed slit, and then delivered to a photocell. We designate i_0 as the measured photocell current for the transmitted rays that pass through an unexposed section of the film and i as that for the same small-angle light-cone system passing through a similar section of an exposed region of the film having M silver-cluster grains per unit area. We may relate the fraction transmitted, τ (i.e., i/i_0), to the grain density M by using the fraction of the area that is blocked by the silver grains MS, obtaining

$$\tau = i/i_0 = 1 - MS. \quad (3)$$

Rather than by using the transmission τ, this measurement is conventionally expressed by using an alternative variable, the optical density D, which is defined as the logarithm of the reciprocal of the transmission τ. Thus

$$D = \log_{10}(1/\tau) = -\log_{10}(1 - MS)$$

and

$$D = -\log_{10}\left[1 - M_0 S \times\left(1-\exp\left\{-\sigma\sin\theta\left[1-\exp\left(-\frac{\mu_1 t_1}{\sin\theta}\right)\right]I\right\}\right)\right]. \quad (4)$$

For relatively low spectroscopic exposures on the monolayer films, the value of MS will be small compared to unity. Then Eq. (4) may be simplified to obtain

$$D = \frac{M_0 S}{2.30}\left(1-\exp\{-\sigma\sin\theta[1-\exp(-\mu_1 t_1/\sin\theta)]I\}\right). \quad (5)$$

In the density measurement defined here by using illumination and objective lenses of small and nearly matched numerical apertures, D is essentially the *specular density*. This optical density may be related to the smaller value, the *diffuse density*, which is measured when all the forward-scattered light in the transmitted beam is included in the measurement. The relationship between specular and diffuse density will be discussed in Part II[3] of this research.

As noted above, the practical monolayer film may be effectively thicker than the individual grain diameter, and, in the light-scattering geometry of the developed film, there may be a superposition of the scattering clusters. A more detailed analysis than that given for the derivation of Eq. (4) is then required. Nevertheless, a modified result must again be simply a function of the universal variable $\beta_1 I$. The same approach for the derivation of a universal relation for D is described in more detail in the thick-emulsion analysis that is presented below. Thus an important implication of this analysis in deriving Eq. (4) is that the monolayer film density D is a function of the single variable $\beta_1 I$, where β_1 introduces the total dependence on the photon energy E and on the in-

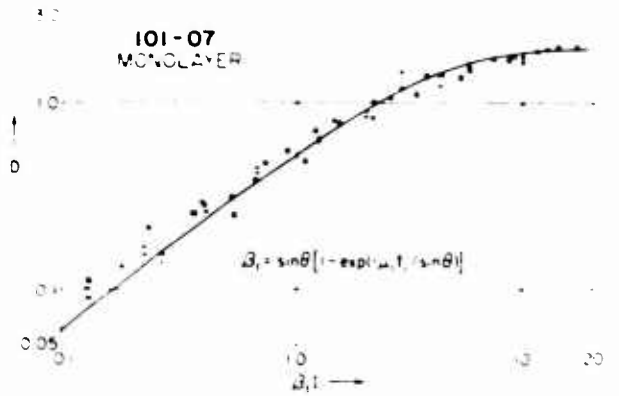


Fig. 3. The universal plot of D versus $\beta_1 I$ for the Kodak 101-07 monolayer using D-versus-I calibration data as measured at eight photon energies in the 100–1500-eV region. The smooth curve is from fitting the semiempirical Eq. (7), derived here from the monolayer film. The photon-energy dependence is introduced by the scaling factor β_1.

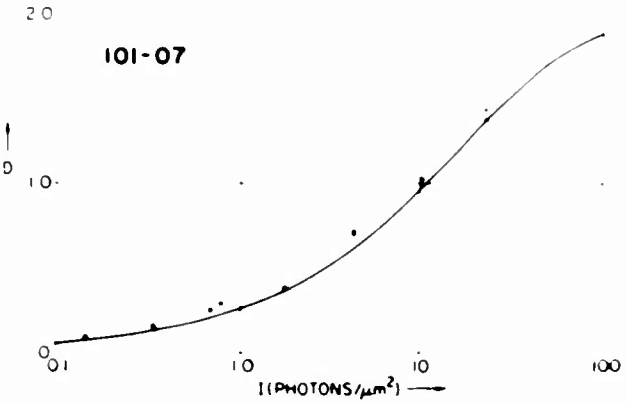


Fig. 4. Comparing the experimental D-versus-log-I calibration data for the Kodak 101-07 film at the C-Kα (277-eV) photon energy with the averaged, semiempirical universal response predicted by Eq. (7).

cidence angle θ and is defined by

$$\beta_1 = \sin\theta \left[1 - \exp\left(\frac{-\mu_1 t_1}{\sin\theta}\right)\right]. \tag{6}$$

To test this universal-model relationship for the monolayer film, we have plotted (Fig. 3) for Kodak 101-07 film the specular densities (which have been measured as described in Part II[3]) for normal-incidence exposures and for eight photon energies in the 100–1500-eV region. This plot is presented as density D versus the universal variable $[1 - \exp(-\mu_1 t_1)]/I$. The value of the effective layer thickness t_1 was chosen so that the data for the entire range of photon energies best fitted a single universal curve. These data for Kodak 101-07 film yielded an empirical value for t_1 of 2 μm. An efficient, two-parameter empirical equation, suggested by this model [see Eq. (5)], has been found to be

$$D = a_1[1 - \exp(-b_1\beta_1 I)] \tag{7}$$

For the Kodak 101-07 monolayer film, the constants a_1 and b_1 have been determined by least-squares fitting of this D versus-$\beta_1 I$ data for photon energies in the 100–1500-eV region to be 1.96 and 0.313 μm^2, respectively. This empirically fitted curve is also plotted in Fig. 3. In Fig. 4 a comparison of the measured data and of the semiempirical curve is presented for D versus log I for the Kodak 101-07 film at the photon energy of 277 eV. Also, as described in Part II,[3] the optical film density D was measured with an essentially constant incident intensity at a range of incidence angles θ of 5–90°. In Fig. 5, the optical density D for a constant incident intensity is presented for two ranges of exposure along with that angular dependence predicted by the semiempirical model relation [Eqs. (6) and (7)] for this monolayer film. Note that, in the relation for density D given in Eq. (7), the intensity I should be multiplied by a factor of $[1 - F(\theta)]$ to account for the reduction in exposure at very small angles of incidence ($\theta < 5°$). $F(\theta)$ is the fraction of the incident radiation intensity that is low-angle scattered and/or totally reflected outward from the monolayer surface and therefore not allowed to be photoelectrically absorbed within the AgBr grains.

The prediction accuracy of this simple model relation, using empirically determined values of t_1 and of a_1 and b_1, seems to be well within the experimental errors associated with the D-versus-I measurements. It may seem, at first glance, that the scatter of the points on the universal curves as in Fig. 3 may be somewhat excessive, particularly in the region of low densities associated with low measurement statistics. Most of the variations from the universal curves reflect the fact that we are comparing here the measurements on many different film samples and at many different photon energies. Most of this error is attributed to the error in the measurement of the absolute intensity I (photons per square micrometer) and to a variation of the optical density with development conditions. The effect of development is expressed here entirely through the developed silver-grain-cluster cross section S [to which the constant a_1 is proportional, according to Eq. (5)].

Finally, we may solve for the exposing intensity I (photons per square micrometer) in Eq. (7) to obtain

$$I = (1/b_1\beta_1) \ln[a_1/(a_1 - D)] \tag{8}$$

By using the values of $\mu_1(E)$ calculated from the absorption data for Ag and Br given by Henke *et al.*,[4] we have plotted in Fig. 6 the intensity I (photons per square micrometer) as a function of the photon energy E (electron volts) in the 100–10,000-eV region for normal-incidence exposures that result in optical densities D equal to 0.5 and 1.0 for the Kodak 101-07 monolayer film. (The reciprocal of these intensities for a given density value is conventionally defined as the *film sensitivity*.)

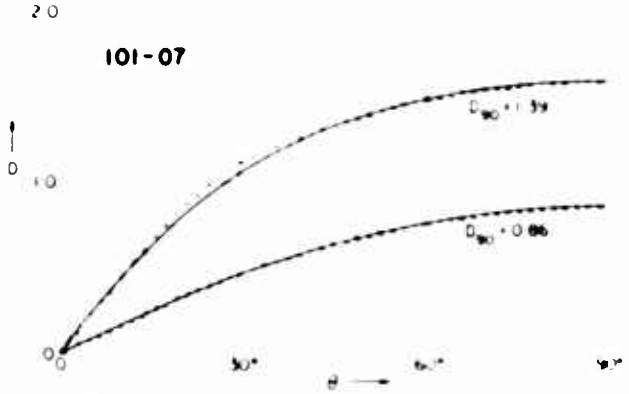


Fig. 5. Comparing D versus θ plots (at constant I and measured as described in Part II[3]) with those obtained from the universal response function given by Eq. (7).

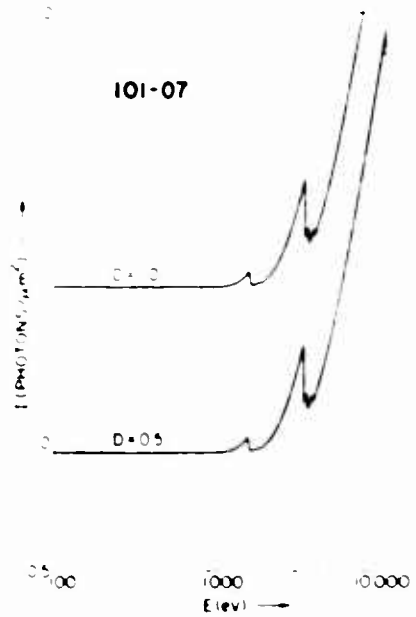


Fig. 6. The intensity I (photons per square micrometer) required to establish a spectral density of 0.5 and of 1.0 in the Kodak 101-07 monolayer film. These I versus E plots were derived using the semiempirical relation given in Eq. (8) and illustrate the flat, high-sensitivity response for the 100–1000-eV region and the reduced sensitivity along with the absorption-edge structure (Br-L and Ag-L) in the 1000–10 000-eV region.

B. Thick-Emulsion Model

We now consider the more complicated problem: establishing an optical-density relation for a thick emulsion in which the photons are completely absorbed within a heterogeneous system of AgBr grains imbedded in gelatin. The total volume fraction V of the AgBr is relatively small (typically $<20\%$). The thick-emulsion film will usually have a protective overcoat of thickness t, which we assume here to be gelatinlike. We consider (as for the monolayer-film analysis above) the AgBr grains to be approximately spherical with a cross section equal to σ and with an effective absorbing thickness equal to d.

In Fig. 7, a monolayer section is depicted within this emulsion with low-density packing and with gelatin that is assumed to be only between the grains. The probability that an incident photon will be absorbed within an individual AgBr grain in this monolayer section at depth x within the emulsion may be written as

$$I\{\sigma[1-\exp(-\mu_1 d)]\exp(-\mu' x/\sin\theta)\exp(-\mu_0 t/\sin\theta)\} = \gamma I,$$

which is the product of the number of incident photons per unit area I, the AgBr-grain cross section σ, the probability that a photon reaching the AgBr grain is absorbed within that grain, the transmission fraction through the emulsion of thickness x, and the transmission fraction through the overcoat of thickness t for a beam at incidence angle θ. (μ_0 and μ_1 are the linear absorption coefficients of the gelatin and of the AgBr, respectively, and μ' is the heterogeneous linear absorption coefficient for the emulsion.) By defining the quantity in this probability expression within the braces as γ, we may write the differential equation for the additional number of grains rendered developable as a result of an additional increment of incident exposure intensity dI [similarly as for Eq. (1) above] as

$$dM = (M_0 - M)\gamma dI,$$

where again the quantity $(M_0 - M)$ is the number of grains not yet rendered developable by at least one photon absorption. After integrating, we obtain, for the total exposing intensity of I at θ incidence with the film surface, the relation for the number of grains rendered developable within the monolayer section at depth x:

$$M = M_0[1-\exp(-\gamma I)]. \tag{9}$$

On development, the exposed grains are reduced to silver clusters of average cross section S. The fraction τ of a light beam that is transmitted through this monolayer section can be written, as described in Section 2.A, as

$$\begin{aligned}\tau_n &= 1 - MS = 1 - M_0 S[1-\exp(-\gamma I)] \\ &= 1 - M_0 S\{1-\exp[-\sigma\beta I\exp(-\mu' x/\sin\theta)]\},\end{aligned}$$

with

$$\beta = [1-\exp(-\mu_1 d)]\exp(-\mu_0 t/\sin\theta). \tag{10}$$

This is the transmission for a narrow cone system of light through the nth monolayer section of thickness d and at a depth x equal to nd.

We assume, as a first consideration, that the total optical transmission for the thick emulsion may be given simply by the product of the monolayer-section transmissions. This assumption is valid only for relatively small values of MS and of d, so that the probability for shadowing (one grain blocking another in the light beam) is negligible. Then the total transmission is simply

$$\begin{aligned}\tau &= \prod_0^{\infty}\tau_n = \prod_0^{\infty}(1 - M_0 S\{1 \\ &\quad - \exp[-\sigma\beta I\exp(-\mu' nd/\sin\theta)]\}).\end{aligned} \tag{11}$$

Since the optical density D is defined as $\log_{10}(1/\tau)$, we may then write

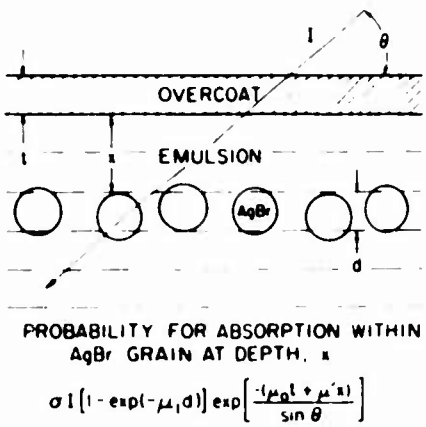


Fig. 7. Emulsion-film model for an overcoat of thickness t and a heterogeneous emulsion consisting of V volume fraction of AgBr spherical grains distributed within a $(1-V)$ volume fraction of gelatin. Noted here is the probability for photon absorption of an AgBr grain within an assumed monolayer section of average, effective absorption thickness d at a depth x within the emulsion.

$$D = -\log_{10}\left[\prod_0^{\infty}(\tau_n)\right] = -(1/2.30)\sum_0^{\infty}\ln(1 - M_0S\{1 - \exp[-\sigma\beta I\exp(-\mu' nd/\sin\theta)]\}). \quad (12)$$

With the assumption that MS is small, this expression for D may then be approximated simply as

$$D = (1/2.30)\sum_0^{\infty} M_0S\{1 - \exp[-\sigma\beta I\exp(-\mu' nd/\sin\theta)]\}. \quad (13)$$

It is useful here to re-express Eq. (13) as an integral, replacing M_0 by N_0dx, with N_0 equal to the number of AgBr grains per unit volume (and therefore equal to M_0/d), and nd by x. We may then write for the optical density

$$D = (1/2.30)\int_0^{\infty} N_0S\{1 - \exp[-\sigma\beta I\exp(-\mu' x/\sin\theta)]\}dx. \quad (14)$$

This integral may be evaluated easily as a converging-series solution. It is considered here, however, that the assumptions made in its derivation (low AgBr-grain density and exposures) are too restrictive for many practical applications of photographic measurement. A more detailed (but more complicated) expression for the transmission through a dense, heterogeneous system of light-absorbing silver-grain clusters could be derived. Nevertheless, for this more precise description, the resulting transmission in any event must also be a function of the intrinsic exposed AgBr-grain density N at depth x and consequently of the variable

$$z = \sigma\beta I\exp(-\mu' x/\sin\theta),$$

which determines the number of grains rendered developable within a differential monolayer section of the emulsion. Here, β is defined by Eq. (10). With no assumptions about the details of the light-absorption process within the thick emulsion, we may write a general expression for the optical density:

$$D = \int_0^{\infty} F(z)dx, \quad (15)$$

where $F(z)$ is a function that may be determined empirically, for example, from D-versus-I data for photons of such energy as to be completely absorbed within the given emulsion's total thickness. $F(z)$ has a constant saturation value for large z (at small penetration depths with large exposure I) [$N_0S/2.30$ in Eq. (14)]. $F(z)$ approaches zero value as z becomes small (for small exposure I and/or at large depth x). By differentiating the variable z, we have

$$dz = -(\mu'/\sin\theta)\sigma\beta I\exp(-\mu' x/\sin\theta)dx = -(\mu'/\sin\theta)z\,dx,$$

and we may therefore rewrite Eq. (14) completely in the dimensionless variable z as

$$D = \left(\frac{\sin\theta}{\mu'}\right)\int_0^{\sigma\beta I}\frac{F(z)}{z}dz. \quad (16)$$

We conclude, therefore, that the integral must simply be a function of the integration limit $\sigma\beta I$, and we may write for D versus I the universal relation of the form

$$D = \left(\frac{\sin\theta}{\mu'}\right)\phi(\beta I). \quad (17)$$

We note that the factor $(\sin\theta/\mu')$ is a mean penetration depth in the x direction of the incident beam inside the emulsion, and, for a given exposure I, the function $\phi(\beta I)$ yields the optical density D per unit mean penetration depth.

Now for the low-energy x radiations of particular interest here, this penetration depth will approach effectively the thickness of the surface monolayer section (see Fig. 7). For such a surface exposure, the transmission factor $\exp(-\mu' x/\sin\theta)$ is not involved, and we consider the contribution to the density D for this surface region to be an amount equal to $d_0\phi(\beta I)$, where d_0 will be an empirically determined parameter that measures the effective surface monolayer depth. We add this limiting surface-layer contribution to D in Eq. (17) to obtain finally for the optical-density contributions for both surface and volume generation of the optical density

$$D = \left(\frac{\sin\theta}{\mu'} + d_0\right)\phi(\beta I). \quad (18)$$

Equation (18) may then be written as a function of the universal variables αD and βI, viz.,

$$\left(\frac{\mu'/\sin\theta}{1 + \mu' d_0/\sin\theta}\right)D = \alpha D = \phi(\beta I) \quad (19)$$

(thus defining the universal variables that establish the scaling for D and I as the photon energy and the angle of incidence of the exposing radiation are varied).

The heterogeneous absorption coefficient μ' may be appreciably different from that which is calculated as $\bar{\mu}$ for a homogeneous absorbing system with the same volume fractions of AgBr and of gelatin. We have derived an expression for the linear heterogeneous absorption coefficient in Appendix A; the expression may be written as follows:

$$\mu' = \mu_0 - (1/d)(\ln\{1 - V\{1 - \exp[-(\mu_1 - \mu_0)d]\}). \quad (20)$$

For the same volume fraction V for AgBr, and hence $(1 - V)$ for the gelatin, the linear homogeneous absorption coefficients $\bar{\mu}$ may be given by

$$\bar{\mu} = (1 - V)\mu_0 + V\mu_1. \quad (21)$$

It may be noted that Eq. (21), given for the heterogeneous linear coefficient in Eq. (20), does reduce to Eq. (20) for the homogeneous coefficient $\bar{\mu}$ for small values of the grain size d.

In Fig. 8 we have plotted for comparison the linear absorption coefficients μ' and $\bar{\mu}$, given by Eqs. (20) and (21), for Kodak RAR 2497 film, assuming a value for d equal to 0.3 μm.

In order to illustrate the accuracy of prediction of a universal curve as defined by Eq. (19) and of the associated description for the heterogeneous absorption coefficient given in Eq. (20), we have plotted in Fig. 9 the variables $\mu' D/(1 + \mu' d_0)$ and $[1 - \exp(-\mu_1 d)]\exp(-\mu_0 t)I$ using D-versus-I data for the Kodak RAR 2497 film measured at $\theta = 90°$ (and as described in Part II[3]). These data have been measured at eight photon energies in the 100–1500-eV region for which we can assume complete absorption within this emulsion. The overcoat thickness t, the mean grain size d, the volume fraction V, and the surface-layer thickness d_0 were chosen so as to yield a minimum variation from a universal curve for the entire photon-energy range (see Section 3). The values so determined for t, d, d_0, and V were 0.3, 0.3, and 0.6 μm, and

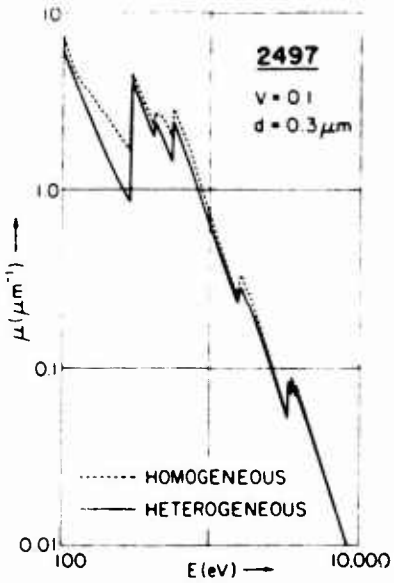


Fig. 8. Comparison of the linear absorption coefficient as calculated for the heterogeneous RAR 2497 emulsion-film system with an amorphous system of the same volume fraction of AgBr (see Appendix A). Note the appreciable differences in the low-energy x-ray region.

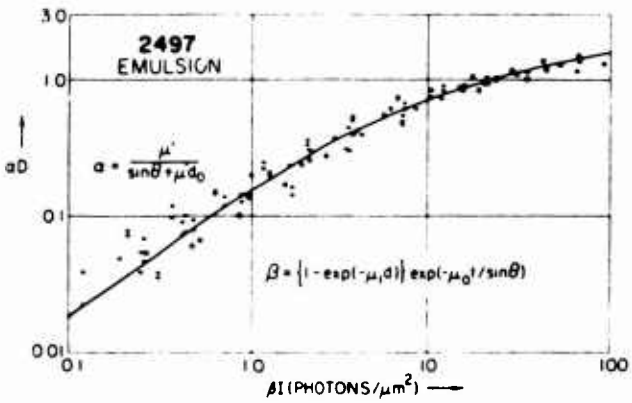


Fig. 9. The universal plot of αD versus βI for the Kodak RAR 2497 emulsion film using D-versus-I calibration data as measured at eight photon energies in the 100–1500-eV region. The smooth curve is obtained by fitting to these points the semiempirical Eq. (26) derived here for the emulsion-type film. The photon-energy dependence is introduced through the scaling factors α and β.

0.1, respectively. Again we consider the departures from a universal curve among these data points as plotted here to be well within experimental error.

We have also plotted in Fig. 9 a semiempirical equation for the universal curve, the derivation of which is described below.

Early in the exposure process, the first layers that are encountered within the emulsion may become saturated, i.e., all the AgBr grains within these layers are rendered developable. As the exposure increases, the depth x_s of this saturation region increases. The corresponding growth in optical density is depicted in Fig. 10 along with a plot of $F(z)$, which is defined in Eq. (15), where $z = \sigma\beta I \exp(-\mu' x/\sin\theta)$. For sufficiently large values of z and, correspondingly, for sufficiently small values of penetration depth x, and/or for large values of I, $F(z)$ is equal to a constant saturation value F_s. For relatively low densities of AgBr grains within the emulsion, this saturation value is simply $N_0 S/2.30$, as suggested in Eq. (14). $F(z)$ may then be interpreted as the optical-absorption cross section per unit volume of developed silver-grain clusters for an exposure that initiates saturation. For small z, $F(z)$ approaches zero value. We shall define by z_s that value of z for which $F(z)$ reaches its constant saturation value, defined here as F_s (within, say, a few percent). The corresponding saturation depth x_s may then be related to z_s by

$$z_s = \sigma\beta I \exp(-\mu' x_s/\sin\theta),$$
$$x_s = (\sin\theta/\mu') \ln(\sigma\beta I/z_s). \tag{22}$$

We may now write Eq. (15) as follows:

$$D = \int_0^{x_s} F(z)dx + \int_{x_s}^{\infty} F(z)dx$$
$$= F_s x_s + (\sin\theta/\mu') \int_0^{x_s} (F(z)/z)dz,$$

and, by using Eqs. (22), (16), and (17), we obtain

$$D = (\sin\theta/\mu')[F_s \ln(\sigma\beta I/z_s) + \phi(z_s)]. \tag{23}$$

By including the parameter d_0 to account for the surface-layer exposure [as described for Eq. (18)], we may rewrite Eq. (23) as

$$D = \left(\frac{\sin\theta}{\mu'} + d_0\right)[F_s \ln(\sigma\beta I) + \text{constant}]. \tag{24}$$

We therefore predict that, after an initial exposure that will initiate the onset of saturation in the first layers, the optical density D should vary linearly with the logarithm of the exposure I. This is indeed what is usually observed, as is illustrated, for example, in the D-versus-log-I plot for the Kodak RAR 2497 film presented in Fig. 11. This strong linearity in D-versus-log-I is illustrated more generally for the thick-emulsion films in the experimental data, which are presented in Figs. 4–7 of Part II[3] of this research.

Equation (24) may be written as a universal semiempirical equation of the form

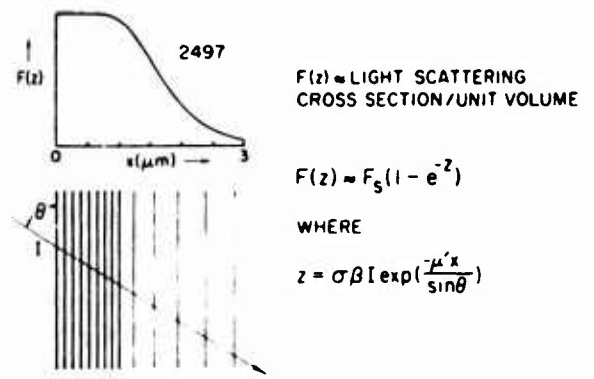


Fig. 10. Plotted here is the approximate function $F(z)$ for the light-scattering cross section per unit volume associated with the developed silver-grain clusters and resulting from an intermediate exposure I (calculated for the RAR 2497 film). An exposure was chosen so as to render all grains developable within the first half-thickness of the emulsion. As the exposure I increases, this saturation region increases in depth s, and, according to this model, this process accounts for the linear relationship between D and log I after the onset of the saturation process.

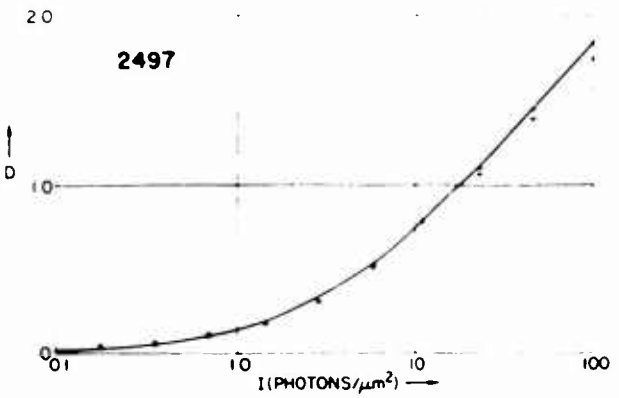


Fig. 11. Comparing the D-versus-log-I calibration data for the RAR 2497 film at the O-Kα (525-eV) photon energy with the averaged universal response function given by the semiempirical Eq. (26).

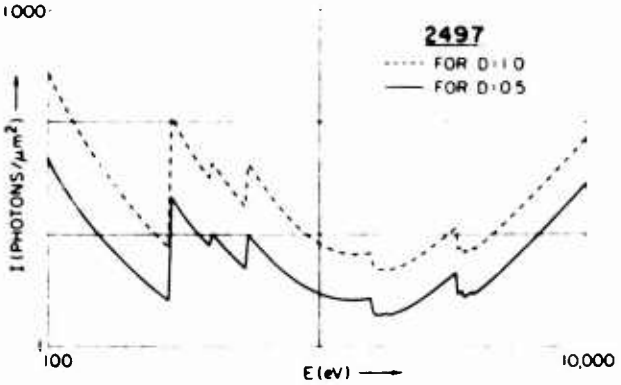


Fig. 12. The intensity I (photons per square micrometer) required to establish a specular density of 0.5 and of 1.0 in the RAR 2497 emulsion film.

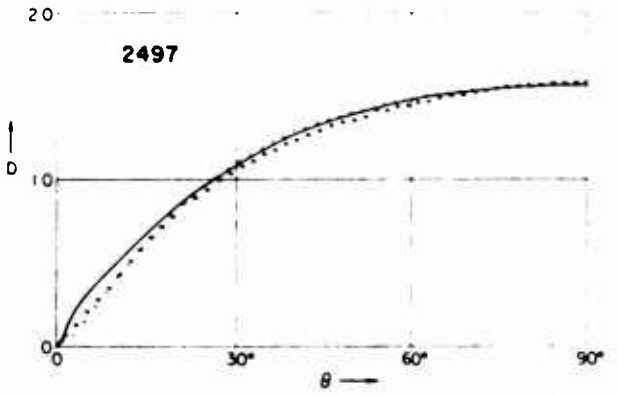


Fig. 13. Comparison of experimentally measured D-versus-θ plots [measured as described in Part II[3] for constant incident intensity I and energy Al-Kα (1487-eV)] with those predicted by the semiempirical, universal response function given in Eq. (28) for the RAR 2497 film.

$$\left[\frac{\mu'/\sin\theta}{1+(\mu' d_0/\sin\theta)}\right] D = \alpha D = a \ln(b\beta I). \tag{25}$$

However, for exposure I below that which may induce saturation, it is expected that D is directly proportional to I. This may be deduced, for example, by integrating Eq. (14) after expanding the exponential for small values of its argument $[\sigma\beta I \exp(-\mu' x/\sin\theta)]$, obtaining

$$D \approx \left(\frac{\sin\theta}{\mu'}\right)\frac{N_0 S}{2.30}\sigma\beta I$$

for small I. In order to require that our model relation for the optical density D increase initially as I in the toe region of the D-versus-I response, we make a simple addition to the argument of the logarithmic term in Eq. (25) to obtain, finally, the semiempirical relation for D versus I:

$$\alpha D = a \ln(1 + b\beta I). \tag{26}$$

For the Kodak RAR 2497 film, the constants a and b have been determined by least-squares fitting of the αD-versus-βI data, as plotted in Fig. 9, yielding the values of 0.414 μm^{-1} and 0.454 μm^2, respectively. This least-squares-fit function has been plotted as the universal curve in Fig. 9, and it has been applied to yield the D-versus-log-I curve presented in Fig. 11, as an example, at the particular photon energy of 525 eV.

C. Thin-Emulsion Model

For the thick-emulsion model described above it was assumed that all the incident photons were absorbed in the overcoating and in the emulsion layers. For the thin-emulsion model it is required that the predicted contribution to the optical density for emulsion depths greater than the value T (the actual emulsion thickness) be subtracted from the density D, as predicted for the thick emulsion as given by Eq. (18).

For the thin-emulsion case, therefore, we rewrite Eq. (16) (after including the surface-exposure correction parameter d_0) as

$$D = \left(\frac{\sin\theta}{\mu'} + d_0\right)\int_{\beta I \exp(-\mu' T/\sin\theta)}^{\beta I} (F(z)/z)\,dz,$$

yielding for emulsion thickness T a predicted universal relation

$$\alpha D = \int_{\beta I \exp(-\mu' T/\sin\theta)}^{\beta I} \frac{F(z)\,dz}{z} = \phi(\beta I) - \phi[\beta I \exp(-\mu' T/\sin\theta)]. \tag{27}$$

Correspondingly, we may rewrite Eq. (26) for the thin-emulsion case as

$$\alpha D = a \ln\left[\frac{1 + b\beta I}{1 + b\beta I \exp(-\mu' T/\sin\theta)}\right]. \tag{28}$$

Note that we have assumed here that the universal function [and its semiempirical description given in Eq. (28) defined through the parameters a and b] is established by using calibration data for which the emulsion is thick, i.e., for photons that are completely absorbed within the emulsion.

The photographic-response function presented in Eq. (28) is applicable in the photon-energy region for which the primary assumption made in its derivation obtains, viz., that each AgBr grain will be rendered developable by a single photon absorption within the grain. It has been thus assumed that the effective cross section for photon excitation σ is constant, i.e., that σ is independent of the photon energy. For photons of energy above about 10 keV it is expected that the photoelectrons that are generated within the emulsion in the vicinity of a given AgBr grain may have sufficient range to contribute, along with the direct photon absorption, to the excitation cross section of that AgBr grain. The effective cross section σ may then be energy dependent at the higher photon energies, re-

quiring that the relatively simple analysis presented here be modified for $E > 10$ keV.[2]

In Fig. 12, we have applied Eq. (28) to predict for this 100–10,000-eV region the number of photons per square micrometer required to yield optical specular densities of 0.5 and 1.0 for normal incidence upon the Kodak RAR 2497 film.

In many practical spectrographic measurements, the x-ray intensity is not incident at 90° upon the film. Nevertheless, the density–exposure–photon-energy characterizations presented in Figs. 11 and 12 can be presented for angles of incidence other than 90° through the θ dependence of Eq. (28). The optical density D has been measured (as described in Part II[3]) for θ values in the 5–90° range for essentially constant incident intensity I and for several photon energies. As is suggested in Fig. 13, the θ dependence as predicted by Eq. (28) for a photon energy of 1487 eV is demonstrated to be well within the limits of the experimental errors for the Kodak RAR 2497 film.

3. SUMMARY AND APPLICATION

In this section, we summarize the results of the foregoing analysis of the low-energy x-ray response of photographic films. These are expressed as semiempirical equations that relate the specular optical density D, the incident intensity I (photons per square micrometer), the angle of incidence θ, and the photon energy E (electron volts) (through the linear absorption coefficients μ_0 for gelatin, μ_1 for AgBr, and μ' for the heterogeneous emulsion mixture).

The monolayer is defined as a densely packed layer of AgBr grains of effective thickness t_1, having

$$D = a_1[1 - \exp(-b_1\beta_1 I)]$$

or

$$I = 1/(b_1\beta_1)\ln\left(\frac{a_1}{a_1 - D}\right),$$

in which

$$\beta_1 = \sin\theta[1 - \exp(-\mu_1 t_1/\sin\theta)]$$

(a_1 varies approximately as S/d^2 and b_1 as d^2).

The thick emulsion is defined as completely absorbing with an effective AgBr-grain thickness d, AgBr volume fraction V, and with a gelatinlike overcoat of thickness t. For the thick emulsion

$$\alpha D = a\ln(1 + b\beta I)$$

or

$$\beta I = (1/b)[\exp(\alpha D/a) - 1],$$

in which

$$\beta = [1 - \exp(-\mu_1 d)]\exp(-\mu_0 t/\sin\theta),$$
$$\alpha = \mu'/(\sin\theta + \mu' d_0),$$

where

$$\mu' = \mu_0 - (1/d)\ln(1 - V[1 - \exp[-(\mu_1 - \mu_0)d]])$$

and d_0 is an effective emulsion-surface-layer thickness (a varies approximately as S/d^3 and b as d^2).

The thin-emulsion definition is the same as that for the thick-emulsion case for the lower-energy photons but is modified to account for the incomplete absorption of higher-energy photons within a finite emulsion thickness T. Here,

$$\alpha D = a\ln\left[\frac{1 + b\beta I}{1 + b\beta I\exp(-\mu' T/\sin\theta)}\right]$$

or

$$\beta I = (1/b)\frac{\exp(\alpha D/a) - 1}{1 - \exp(-\mu' T/\sin\theta)\exp(\alpha D/a)}.$$

In order to apply photographic materials efficiently as absolute x-ray detectors, it is helpful to have at least approximate information about the film's physical and chemical structure, particularly the volume fraction V, the emulsion thickness T, the overcoat thickness t, and the constituency of the overcoating material if it is not gelatin. Ideally, these parameters would be supplied by the film manufacturers. Unfortunately, at this time these data were not shared with the user. Many of the larger laboratories do have the facilities to measure these parameters directly, but it would seem important to avoid such an expenditure of additional time and effort.

Alternatively, if these film characteristics are not available from the manufacturer or by independent analytical means, their effective values may be determined by more-extensive calibration measurements of D versus I at additional photon energies. This has been the approach adopted in this research.

For the monolayer film, this procedure is not so difficult. A minimum of two photon energies is required for which D-versus-I data are chosen so that the absorption within AgBr is appreciably different. Because it is predicted that D is a function of the single universal variable $\beta_1 I$, the ratio of the I values for the two photon energies that yield the same D values is a constant and equal to the corresponding ratio of the β_1 values. The average value for this ratio r may then be applied to determine the effective AgBr-monolayer thickness t_1. Thus

$$r = \frac{1 - \exp[-\mu_1(E')t_1]}{1 - \exp[-\mu_1(E'')t_1]},$$

in which E' and E'' are the two photon energies for which the two D-versus-I curves are measured. This expression may be solved numerically for the value of t_1. With this parameter determined, the universal curve $D = \phi(\beta_1 I)$ is established, and a least-squares fitting to this curve, based on D-versus-I data at the different photon energies, may then be applied to determine the parameters a_1 and b_1. These define the semiempirical equation given above, which relates I (photons per square micrometer) to the values of D, θ, and photon energy E. This equation permits a straightforward microcomputer analysis of the densitometer data to yield an absolute spectrum in I.

In order to characterize similarly an overcoated thick-emulsion film, at least three D-versus-I sets of data are required at appreciably different photon energies for which complete absorption within the film is obtained. This is because two parameters, d and t, are required to define β; V and d_0 also need to be determined to define the scaling factor α.

Finally, for the thin-emulsion-type film, the thickness parameter T is determined by using at least one more D-versus-I data set at a higher photon energy of a radiation that is appreciably transmitted through the emulsion.

We have found that, by using a small computer-plotter system, a graphic, iterative determination of the film structure parameters was usually rapid and efficient with an accuracy commensurate with that of the experimental calibration data. Log–log plots of αD versus $\mathcal{I}I$ were generated in order (1) to obtain values of t and d that establish a set of $\mathcal{I}$ values for a series of photon energies that translate the corresponding αD-versus-$\mathcal{I}I$ curves along the log $\mathcal{I}I$ axis to form a parallel set and (2) to vary d_0 and V parameters to establish the values of α for the different photon energies so that the set of parallel curves can then be reduced to a single universal curve by shifting along the log αD axis. Examples of such universal curves for the monolayer film Kodak 101-07 and the thick-emulsion film Kodak RAR 2497 were presented in Figs. 3 and 9. These curves were then least-squares fitted to yield the complete semiempirical equations, as based on the normal-incidence D-versus-I data that yield the parameters a and b, which define the complete θ-dependent semiempirical relations described above.

In Part II of this research,[3] the calibration and the characterization of five films considered to be appropriate for absolute low-energy x-ray spectroscopic analysis are described. These calibrations are shown to be well described by the semiempirical equations that have been developed here.

APPENDIX A: LINEAR ABSORPTION COEFFICIENT μ' FOR HETEROGENEOUS MATERIALS

In our analysis of the number of AgBr grains that are rendered developable at emulsion depth x [derivation for Eq. (9)], it was necessary to introduce a transmission factor $\exp(-\mu' x/\sin\theta)$, in which μ' is the effective linear absorption coefficient for the heterogeneous system of finite-size AgBr grains embedded within a gelatin matrix. For AgBr-grain sizes that are small compared with the reciprocal linear absorption coefficient of AgBr, the heterogeneous coefficient will approach the homogeneous absorption coefficient $\bar{\mu}$, as given by

$$\bar{\mu} = (1 - V)\mu_0 + V\mu_1, \tag{A1}$$

where μ_0 and μ_1 are the linear absorption coefficients for gelatin and for AgBr, respectively, and V is the volume fraction for the AgBr component.

In Fig. 14, we present a SEM photo of the cross section of the SB-392 film (described in Part II[3]) that illustrates the heterogeneity of the photographic emulsions.

In order to determine μ', we shall again assume that it is sufficiently accurate to model this heterogeneous system as a system of s layers of thickness d equal to the effective grain size, with the grains ordered completely within each layer (absorbing as equivalent, aligned cubes). This geometry is depicted in Fig. 15. We define the x-ray transmission factor τ for the heterogeneous absorber (an averaged value for a large number of incident photons) as follows:

$$\tau = \sum_{0}^{s} p_n \tau_n = \exp(-\mu' x), \tag{A2}$$

where n is the number of AgBr-grain encounters for a given photon passing through the s layers ranging from zero to s as possible values (for n), p_n is the probability of having n encounters, and τ_n is the associated transmission factor for a photon passing through nd thickness of AgBr, multiplied by

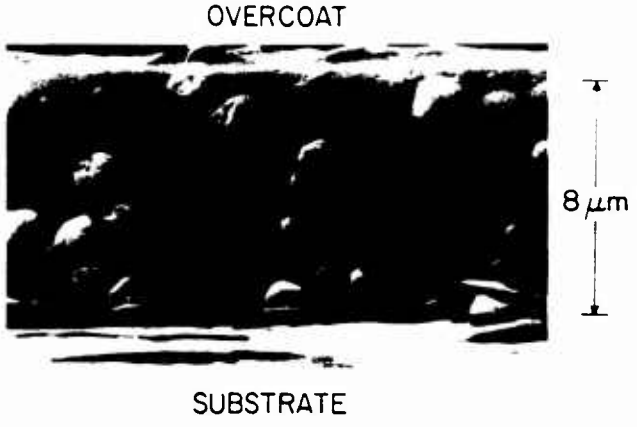


Fig. 14. A SEM photograph of a cross section of an undeveloped SB-392 film. Illustrated here is the heterogeneous quality of this photographic emulsion.

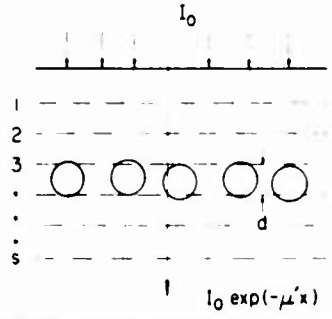


Fig. 15. Model for the calculation of the transmission of photons through a thickness x of heterogeneous emulsions that consist of s monolayer sections of thickness equal to an effective grain absorption thickness d and with a fraction V of AgBr grains and of $(1 - V)$ of gelatin.

that for passing through $(s - n)d$ thickness of gelatin. We shall write expressions for p_n and τ_n for the first few values of n in order to establish the general expression for $\Sigma\, p_n \tau_n$. Note that the area fraction occupied by the AgBr grains within this single layer is the same as the volume fraction V, and therefore the probability of encountering one or no AgBr grains for a single photon passing through this layer is V or $(1 - V)$, respectively. The expressions for p_n and τ_n are

$$n = 0: \quad p_0 = (1 - V)^s,$$
$$\tau_0 = \exp(-\mu_0 x),$$

$$n = 1: \quad p_1 = s(1 - V)^{s-1}V,$$
$$\tau_1 = \exp(-\mu_1 d)\exp[-\mu_0(x - d)]$$
$$= \exp(-\mu_0 x)\exp[-(\Delta\mu)d], \text{ where } \Delta\mu = (\mu_1 - \mu_0),$$

$$n = 2: \quad p_2 = [s(s - 1/2)](1 - V)^{s-2}(V)^2,$$
$$\tau_2 = \exp(-2\mu_1 d)\exp[-\mu_0(x - 2d)]$$
$$= \exp(-\mu_0 x)\exp(-2\Delta\mu d),$$

$$n = 3: \quad p_3 = [s(s - 1)(s - 2)/3!](1 - V)^{s-3}(V)^3,$$
$$\tau_3 = \exp(-3\mu_1 d)\exp[-\mu_0(x - 3d)]$$
$$= \exp(-\mu_0 x)\exp(-3\Delta\mu d).$$

It is evident, therefore, that

$$p_n = \frac{s!}{(s - n)!n!}(1 - V)^{s-n}V^n, \tag{A3}$$

$$\tau_n = \exp(-\mu_0 x)\exp(-n\Delta\mu d) \tag{A4}$$

and that

$$\tau = \exp(-\mu_0 x)\sum_0^s \frac{s!}{(s-n)!n!}(1-V)^{s-n}[V\exp(-\Delta\mu d)]^n. \tag{A5}$$

By recalling that the binomial equation may be written as

$$(A+B)^s = \sum_0^s \frac{s!}{(s-n)!n!}A^{s-n}B^n, \tag{A6}$$

we note that

$$\sum_0^s p_n = \sum_0^s \frac{s!}{(s-n)!n!}(1-V)^{s-n}(V)^n = 1 \tag{A7}$$

and that

$$\tau = \exp(-\mu_0 x)\{1 - V[1-\exp(-\Delta\mu d)]\}^s = \exp(-\mu' x). \tag{A8}$$

Finally, we may solve Eq. (A8) for μ', and, by letting $s = x/d$, we obtain

$$\mu' = \mu_0 - (1/d)\ln\{1 - V[1-\exp(-\Delta\mu d)]\}. \tag{A9}$$

This result is essentially the same expression for the heterogeneous absorption coefficient as that which has been applied by Brown *et al.*[2] and by Toor[5] in their photographic-film models.

In Fig. 8, we have, for the RAR 2497 film, compared the homogeneous linear absorption coefficient $\bar{\mu}$ and the heterogeneous linear absorption coefficient μ' for photon energies in the 100–10,000-eV region (using the atomic absorption data recently reported by Henke *et al.*[4]).

ACKNOWLEDGMENTS

We gratefully acknowledge the invaluable assistance in this program of Priscilla Piano and the helpful advice throughout this research of David Dixon of the Technical Photography Group, Lawrence Livermore National Laboratory, California, and his preparation of the SEM film studies. This program in low-energy x-ray physics and technology is supported by the U.S. Air Force Office of Scientific Research under grant no. 84-0001 and supplementally by the U.S. Department of Energy under contract no. DE-AS08-83DP40181.

REFERENCES

1. B. L. Henke, H. T. Yamada, and T. J. Tanaka, "Pulsed plasma source spectrometry in the 80–8000-eV x-ray region," Rev. Sci. Instrum. 54, 1311–1330 (1983).
2. D. B. Brown, J. W. Criss, and L. S. Birks, "Sensitivity of x-ray films. I. A model for sensitivity in the 1–100 keV region," J. Appl. Phys. 47, 3722–3731 (1976).
3. B. L. Henke, F. G. Fujiwara, M. A. Tester, C. H. Dittmore, and M. A. Palmer, "Low-energy x-ray response of photographic films. II. Experimental characterization," J. Opt. Soc. Am. B 1, 828–849 (1984).
4. B. L. Henke, P. Lee, T. J. Tanaka, R. L. Shimabukuro, and B. K. Fujikawa, "Low-energy x-ray interaction coefficients: photoabsorption, scattering, and reflection. E = 100–2000 eV, Z = 1–94," At. Data Nucl. Data Tables 27, 1–144 (1982).
5. A. Toor, Lawrence Livermore National Laboratory, Livermore, California 94550 (personal communication).

9. Low-energy x-ray response of photographic films. II. Experimental characterization

B. L. Henke, F. G. Fujiwara, and M. A. Tester

University of Hawaii, Honolulu, Hawaii 96822

C. H. Dittmore

Lawrence Livermore National Laboratory, Livermore, California 94550

M. A. Palmer

Sandia National Laboratory, Albuquerque, New Mexico 87185

Received February 27, 1984, accepted July 2, 1984

Optical density versus exposure data have been obtained at nine photon energies in the 100–2000-eV x-ray region for five spectroscopic films (Kodak films 101-07, SB-392, RAR 2492, RAR 2495, and RAR 2497). These data were determined operationally by a direct comparison of the peak absolute intensities of spectral lines, which were measured with a calibrated proportional counter, with the microdensitometer tracings of the corresponding photographically recorded spectral lines. Film-resolution limits were deduced from an analysis of contact microradiograms of linear zone plates constructed of gold bars. The relationship between the specular densities as measured here and the diffuse densities have been experimentally determined for the five films. Finally, experimental measurements of the optical density versus the angle of incidence of exposing radiation of constant intensity were obtained. These data, relating density to the x-ray intensity, its photon energy, and its angle of incidence, are shown to be fitted satisfactorily in the 100–10 000-eV region by the semiempirical mathematical model relations that were derived in Part I of this research [J. Opt. Soc. Am. B 1, 818–827 (1984)].

1. INTRODUCTION

In the research that is described here, we characterize photographic films for absolute spectrographic analysis, particularly in the low-energy x-ray photon-energy region of 100–2000 eV. Five films, which were chosen as being appropriate for low-energy x-ray spectroscopy because of their proven quality, vacuum compatibility, and range of sensitivity/resolutions, have been calibrated. These are Kodak's films 101-07 and SB-392 and RAR 2492, 2495, and 2497. The first four are currently available. The RAR 2497 film is no longer manufactured but has been included here because of its past and present extensive application at the AV National Laboratories. The 2497 film (and its predecessor, RAR 2490) has similar characteristics to those of the newer RAR 2492 and 2495. A comprehensive study of the RAR 2490 film has been reported by Benjamin *et al.*[1] An early paper on the calibration of the 101-type film for the low-energy x-ray region has been presented by Koppel,[2] who has also recently reported[3] some calibrations for the RAR 2492 and SB-5 film (which is the sheet-film version of the 35-mm SB-392 film that is characterized here). We would like also to refer the reader to another excellent paper, by Dozier *et al.*,[4] on film calibration for higher photon energies than those particularly addressed here. In Fig. 1 we present a comparison of the sensitivity versus photon-energy curves for the 101, SB-392, and RAR films as determined by the research described here.

In Section 2 we describe a method for the absolute sensitometric calibration of x-ray spectroscopic films and present graphs and tables for density versus normal-incidence exposure data at nine photon energies for the five film types. Also presented here are semiempirical equations derived from the mathematical models developed in Part I of this research[5] that introduce generally the dependence on the photon energy and on the angle of incidence of the exposing x radiation. In Section 3 we present a relatively simple definition and a method of measurement for spectroscopic film resolution and suggest resolution limits for the film types studied. In Section 4 we discuss the effect of batch-to-batch variation of film characteristics, concluding that each new batch should be calibrated at a few normalizing points for precise, absolute spectrometry. We present comparisons of our film calibrations with those reported from other laboratories for similar film types. In Appendix A we present data that relate the specular densities, as required for spectroscopic film calibration (and as measured directly in this research), to the diffuse density values that may be alternatively applied in comparing our data to other film characterizations. In Appendix B the film-processing procedures that have been followed are described. Finally, in Appendix C tables are presented for the five films of density-versus-exposure data calculated at regularly fine-spaced intervals in photon energy.

2. SENSITOMETRIC CALIBRATION OF X-RAY SPECTROSCOPIC FILMS

For quantitative low-energy x-ray spectroscopy, an accurate relationship must be established among the microdensity values (within slit widths of 20–100 μm), the corresponding exposures (in units presented here as photons per square

Reprinted from Journal of the Optical Society of America B, Vol. 1, p. 828, December 1984
Copyright © 1984 by the Optical Society of America and reprinted by permission of the copyright owner.

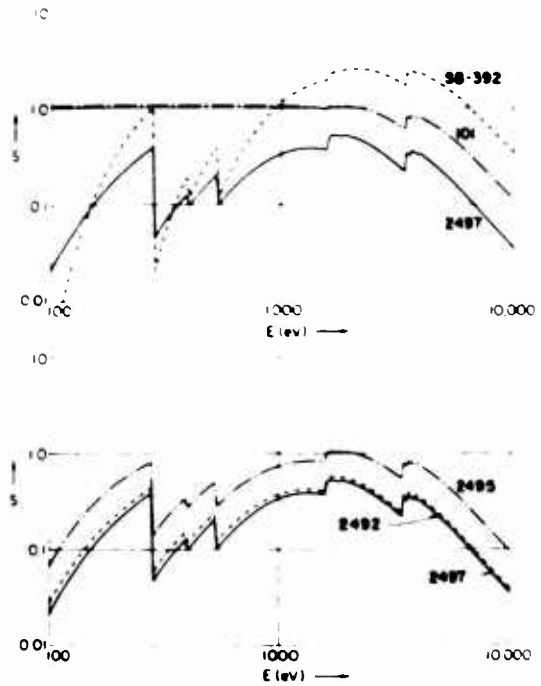


Fig. 1. Comparison of the sensitivities of the five investigated spectroscopic films for the 100–10,000-eV photon-energy region. Sensitivity is defined here as the reciprocal of the exposure I (photons per square micrometer) that is required to establish a specular density of 0.5. These curves were developed in this research.

micrometer), and the photon energy. Generally, this requires microdensitometer measurements using numerical apertures for the objective and the illumination lenses of about 0.1–0.25. For such densitometry, effectively all the absorbed and the scattered light is subtracted from the incident light beam to define the resulting transmitted beam. The measured ratio of the transmitted to the incident light τ then yields essentially the specular optical-density value D, which is defined by the relation

$$D = \log_{10}(1/\tau). \tag{1}$$

If all the light that is scattered in the forward direction is included in the measurement of the transmitted beam, the corresponding diffuse optical density that is calculated by using Eq. (1) has a somewhat smaller value. Often the diffuse densities are reported in the literature that characterizes a particular photographic material. For the five films studied here, the relationships between specular and diffuse densities have been experimentally determined and are presented in Appendix A. It should be emphasized that it is specular density that is directly measured in most analyses of photographically recorded spectra. All the optical densities that have been measured here are specular, as defined by nearly matched microdensitometer illumination and objective lens numerical apertures of 0.1. Occasionally, when fine spectroscopic detail requires the use of slits smaller than those used in this research, matched numerical apertures of 0.25 may be employed. With these apertures the optical densities that are measured will be somewhat smaller because more of the diffuse scattered light is accepted by the objective lens. We have also included in Appendix A measurements that permit a conversion between density values measured at 0.25 and those measured at our 0.1 numerical apertures.

An operational method has been developed for the specular microdensity calibration of spectroscopic films; the method is based on a direct comparison of the photographically recorded spectrum to the corresponding measured absolutely calibrated (photons per second per square micrometer) spectrum. As illustrated in Fig. 2, this is accomplished by

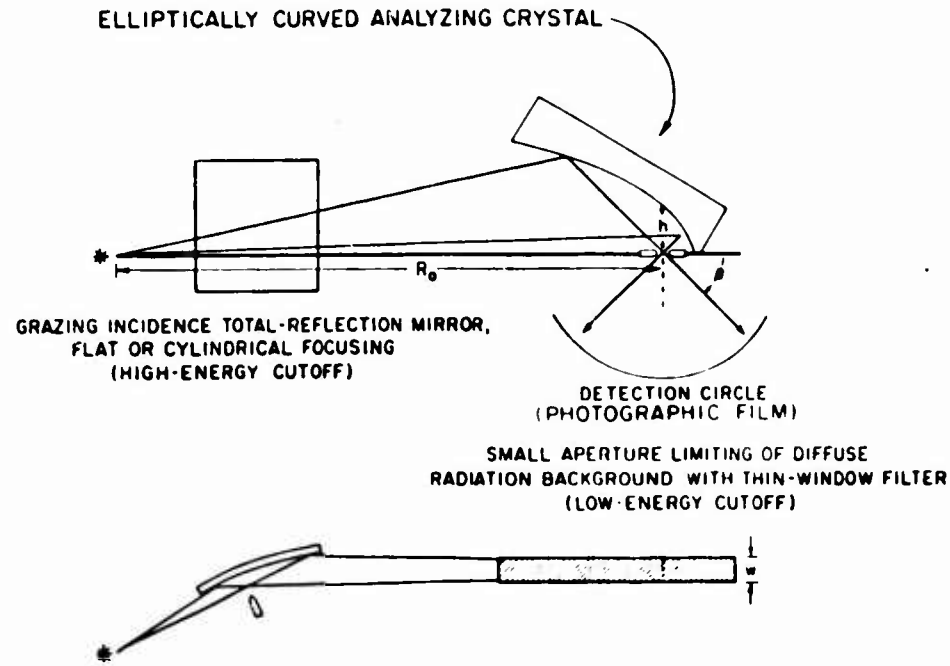


Fig. 2. The elliptical analyzer spectrograph that was used to generate normal-incidence line spectra in the 100–10,000-eV x-ray region. (An x-ray line source and the scatter aperture are located at the respective focal points for an elliptically curved cylindrical crystal analyzer.) A spectrum is recorded on a film located along the detection circle. A corresponding absolute intensity spectrum is measured by translating a flow proportional counter along the same circle. The specular density on a photographically recorded peak is related to the absolute intensity (photons per square micrometer) and is measured using matched microdensitometer and proportional counter slits of widths that are small compared with the spectral linewidth. (For the measurements described here, the mirror monochromator was not required.)

establishing along a normal-incidence detection circle a Bragg-reflected spectrum by means of an elliptically curved cylindrical crystal. A small-slit x-ray source and a scatter aperture are located at respective focal points for the given elliptical-analyzer profile. A detailed description of this elliptical-analyzer spectrograph, including a description of the crystals and the multilayers employed for establishing the normal-incidence detection of spectra in the 100–10,000-eV region, was recently presented in another paper.[6] Also described in Ref. 6 are the procedures by which the absolute spectral intensities are obtained using a calibrated, flow proportional counter that is scanned along the detection circle (using a goniometer with its axis through the focal point at the scatter aperture). The flow proportional counter is pressure tuned and calibrated for absolute photon counting by a method that was also described previously.[7] Peak intensities and corresponding microdensities are measured with matched microdensitometer and proportional-counter slit systems with slit widths that are set to be small compared with the instrumental spectral linewidths (~100 μm). Peak intensities and microdensities are compared on spectral lines that are recorded at a series of exposure times under constant and known x-ray spectral-line intensities.

Characteristic x radiations at nine photon energies in the 100–2000-eV region were obtained using demountable x-ray-tube anodes,[7] which provided broad-source large-angle illumination of the source slit. The anodes were of pure metals except for the graphited and the anodized aluminum anodes, which provided the characteristic C-Kα (277-eV) and the O-Kα (525-eV) radiations. The other characteristic photon energies were Be-Kα (109 eV), Mo-Mζ (193 eV), Cr-Lα (573 eV), Fe-Lα (705 eV), Cu-Lα (930 eV), Al-Kα (1487 eV), and Mo-Lα (2293 eV). Appropriate filters and x-ray-tube anode voltages were selected to minimize any high-order Bragg-reflected line or continuum background that might be associated with the measured spectral lines. An analysis of the proportional-counter pulse-height spectrum was applied to establish that any background remaining at a given spectral line was first-order diffracted and essentially of the same photon energy as that of the line itself. For this reason, peak intensities and microdensities did not require correction for extraneous x-ray background and were considered totally characteristic of the given spectral-line photon energy.

The measurement procedure was as follows: The absolute photons-per-second per-square-micrometer counting rates on the spectral lines were set by adjusting the x-ray-tube power to yield line intensities of the order of several thousand counts per second. The source was then monitored for constancy by moving the counter to the direction of zero angle, stopping the beam down in this position by means of a fine slit at the counter window to yield approximately the same counting-rate levels as those for the reflected lines. A film cassette was then moved into place with the film to be exposed along the same detection circle, and a multiple-exposure series was made using a spooled-film transport controlled through a flexible cable and a magnetic coupled feedthrough to outside the vacuum chamber. After each exposure, the diffracted line intensities were measured again, and, if necessary, a small drift correction for this intensity was made. Ten or more density-versus-exposure points were taken at each of the nine photon energies for each film. (It was necessary to spray a thin film of static-charge-eliminating solution on the back surface of the 101-07 film, which has no overcoat protection, in order to eliminate the static-discharge background exposure associated with transporting this type of film in vacuum.) Manufacturer-recommended film-processing procedures were followed, and these are described in Appendix B.

Repeated microdensitometer measurements were made using instruments with 0.1 numerical apertures for both the illumination and the transmission beam cones. One set was measured at the University of Hawaii on a microdensitometer with a 100-μm slit (Boller & Chivens Microphotometer, Model 14213). Other sets were measured at the Sandia National Laboratories and at the Lawrence Livermore National Laboratory using a 30-μm slit and integrating to the same total slit size as that of the first measurements. (The instruments used for these measurements were Photometric Data Systems Model 1010 microdensitometers.) We found no significant differences among these independent measurements of film densities.

These data were computer plotted as log D versus log I, D versus I, and D versus log I. Examples of these initial plots for the five films exposed to O-Kα (525 eV) are shown in Figs. 3–7. The onset region, plotted as D versus I, must allow a linear extrapolation to the origin, and this constitutes a check on the background subtraction that yielded these net densities from the measured gross densities. The correction to net

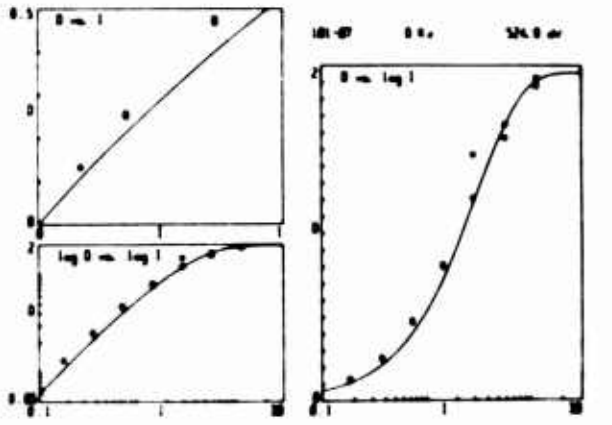


Fig. 3. The measured D-versus-I data obtained for the five films at nine photon energies and computer plotted as illustrated here for the 101-07 film at the O-Kα (525-eV) photon energy. The smooth curves were generated by the universal, semiempirical equation developed in this paper for this particular film.

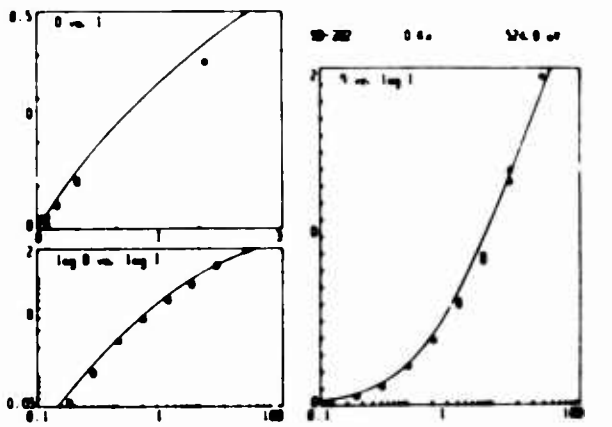


Fig. 4. Same as Fig. 3 for the SB-892 film.

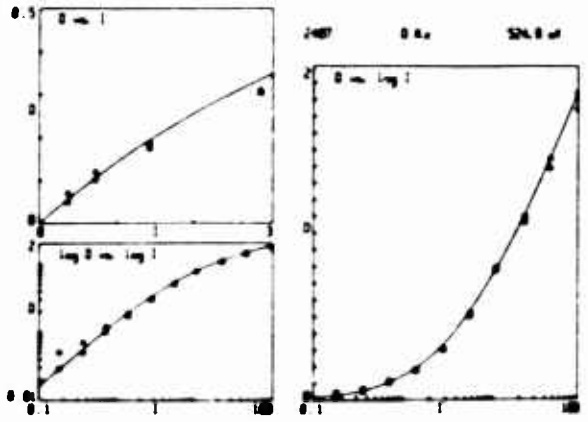


Fig. 5. Same as Fig. 3 for the RAR 2497 film.

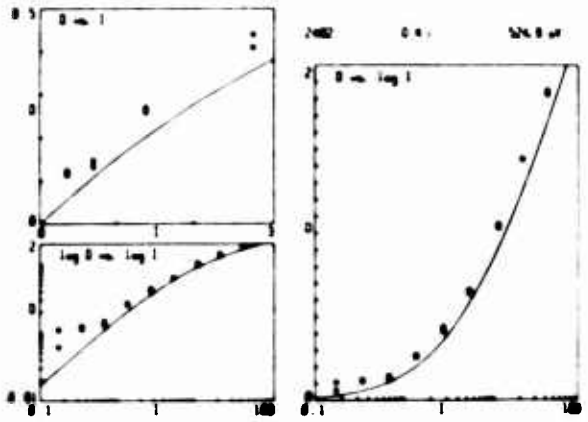


Fig. 6. Same as Fig. 3 for the RAR 2492 film.

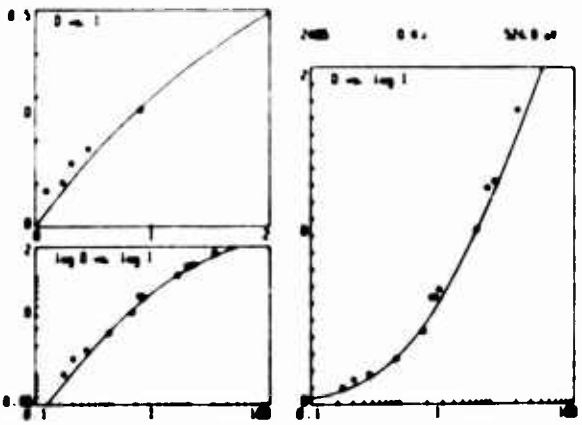


Fig. 7. Same as Fig. 3 for the RAR 2495 film.

densities involved canceling the transmission of an unexposed portion of film from the measured transmission so that the resulting transmission τ would be the result of only the effect of the exposed and developed grain density as defined by Eq. (1). Also plotted in Figs. 3–7 are the semiempirical model curves obtained as described below. As noted in Part I,[5] the averaged universal-model curves were derived from fitting many different film sample measurements at many different photon energies. Discrepancies with the experimental data on individual films from these universal-model predictions, particularly at the low-statistics low-exposure regions, may be the result mostly of a variation of the development conditions and of the absolute photon-intensity calibrations for the individual film measurements.

In Tables 1–5, we present for the five films the averaged density versus the normal-incidence exposure data for the nine photon energies in the 100–2000-eV region (also presented in Tables 10–14 in Appendix C at regularly spaced energy intervals in the extended 100–10,000-eV region). Listed in these tables are letters referring to the characteristic absorption-edge energies given in Table 6 for the silver-bromide and for the carbon, nitrogen, and oxygen constituents of the gelatin in the photographic emulsion. At these photon energies, significant discontinuities may occur in the film-sensitivity versus photon-energy curve. As may be noted from Fig. 1, the carbon, nitrogen, and oxygen edges are not in evidence for the 101-type film, which consists of essentially a monolayer of silver-bromide grains with no absorbing overcoat of gelatin (as is present for the emulsion-film types).

The significant systematic errors occurring in these calibrations were usually in the determination of the absolute photon intensities. Such errors were discovered by comparing plots of I versus E at constant density D for the five films. If calibration errors were made, the corresponding I point would be systematically off an average I-versus-E plot for all five films. (All films were measured at the same calibrated line intensities.) After correcting for these systematic errors, the residual statistical errors in the D-versus-I data were averaged out by least-squares fitting of the D-versus-I data to polynomials of the form

$$\log D = A + B \log I + C(\log I)^2.$$

The averaged density data were then plotted as universal curves (for an appropriate range of photon energies) by a procedure that was developed in Part I.[5] These curves, along with the definitions of the appropriate scaling factors that account for the dependence on photon energy E, are presented in Figs. 8–12. For the determination of these scaling factors [β_1, α, and β (defined in Figs. 8–12)] and of the linear absorption coefficients (μ_0 for gelatin, μ_1 for AgBr, and μ' for the heterogeneous emulsion), absorption data were calculated using data recently compiled by Henke *et al.*[6] The heterogeneous absorption coefficient was derived in Part I[5] to be

$$\mu' = \mu_0 - (1/d)\ln(1 - V[1 - \exp[-(\mu_1 - \mu_0)d]]). \quad (2)$$

This reduces to the linear absorption coefficient for a homogeneous system for which the AgBr grain size d approaches a small value, viz.,

$$\bar{\mu} = (1 - V)\mu_0 + V\mu_1. \quad (3)$$

A comparison of μ' and $\bar{\mu}$ for the heterogeneous and the homogeneous models of the RAR 2492 film is presented in Fig. 13.

The film-structure parameters, the grain size d, the effective surface-layer thicknesses d_0 and t_1, and the AgBr volume fraction V that appear in the scaling factors α, β, and β_1 were determined as described in Part I[5] by an iterative computer-plotting technique in the generation of the universal curves.

As a test of the validity of the semiempirical model equations that were derived in Part I,[5] the equations were fitted

Table 1. Exposure I (photons/μm^2) at Various Net Densities for Film 101-07

Absorption Edge	Photon Energy E (eV)	Net Density D (Specular, 0.1 × 0.1 nA)									Wavelength λ (Å)
		0.2	0.4	0.6	0.8	1.0	1.2	1.4	1.6	1.8	
A[a]											
	109	0.34	0.73	1.17	1.68	2.29	3.04	4.02	5.44	8.07	114.27
	193	0.34	0.73	1.17	1.68	2.29	3.04	4.02	5.44	8.07	64.37
	277	0.34	0.73	1.17	1.68	2.29	3.04	4.02	5.44	8.07	44.76
C[b]											
	525	0.34	0.73	1.17	1.68	2.29	3.04	4.02	5.44	8.07	23.62
	573	0.34	0.73	1.17	1.68	2.29	3.04	4.02	5.44	8.07	21.64
	705	0.34	0.73	1.17	1.68	2.29	3.04	4.02	5.44	8.07	17.59
	930	0.34	0.73	1.17	1.68	2.29	3.04	4.02	5.44	8.07	13.34
	1487	0.37	0.78	1.25	1.80	2.45	3.25	4.30	5.83	8.64	8.34
E[c]											
	2293	0.39	0.83	1.33	1.91	2.60	3.45	4.56	6.18	9.16	5.41

[a] Br M_4 edge
[b] N K, Ag $M_{4,5}$ edges
[c] Br $L_{3,2}$ edge

Table 2. Exposure I (photons/μm^2) at Various Net Densities for Film SB-392

Absorption Edge	Photon Energy E (eV)	Net Density D (Specular, 0.1 × 0.1 nA)[a]										Wavelength λ (Å)
		0.2	0.4	0.6	0.8	1.0	1.2	1.4	1.6	1.8	2.0	
A[b]												
	109	3.82 01	9.59 01	1.83 02	3.14 02	5.12 02	8.12 02	1.26 03	1.94 03	2.97 03	4.52 03	114.27
	193	9.83−01	2.34 00	4.22 00	6.82 00	1.04 01	1.54 01	2.23 01	3.18 01	4.49 01	6.31 01	64.37
	277	3.41−01	7.78−01	1.34 00	2.06 00	2.98 00	4.16 00	5.68 00	7.63 00	1.01 01	1.33 01	44.76
B[c]												
C[d]												
	525	8.06 −01	1.91 00	3.42 00	5.48 00	8.30 00	1.22 01	1.74 01	2.46 01	3.45 01	4.80 01	23.62
D[e]												
	573	1.83 00	4.43 00	8.13 00	1.34 01	2.09 01	3.15 01	4.67 01	6.82 01	9.88 01	1.42 02	21.64
	705	7.57 −01	1.79 00	3.19 00	5.10 00	7.71 00	1.13 01	1.61 01	2.27 01	3.17 01	4.39 01	17.59
	930	3.41 −01	7.76 −01	1.33 00	2.05 00	2.96 00	4.13 00	5.62 00	7.53 00	9.99 00	1.31 01	13.34
	1487	1.82 −01	3.97 −01	6.50 −01	9.49 −01	1.30 00	1.73 00	2.24 00	2.86 00	3.62 00	4.55 00	8.34
E[f]												
	2293	1.45 −01	3.12 −01	5.06 −01	7.33 −01	1.00 00	1.32 00	1.70 00	2.17 00	2.75 00	3.48 00	5.41

[a] In our notation in this table, a number followed by a space and another number indicates that the first number is to be multiplied by 10 raised to the power of the second number, e.g., 9.49 −01 means 9.49×10^{-1}.
[b] Br M_4 edge
[c] C K edge
[d] N K, Ag $M_{4,5}$ edges
[e] O K edge
[f] Br $L_{3,2}$ edge

to the universal plots of Figs. 8–12 and presented therein as the smooth curves. For the monolayer-type film (Kodak 101-07) the model equation is

$$D = a_1[1 - \exp(-b_1\beta_1 I)], \tag{4}$$

and, for the thick-emulsion film, the model equation is

$$\alpha D = a \ln(1 + b\beta I) \tag{5}$$

(Note that, to apply this relation, as in Figs. 8–12, we used D-versus-I data only for photon energies below 1500 eV, for which it could be assumed that the photons were essentially absorbed within the emulsion.)

In establishing these least-squares fits, the parameters a_1, b_1, a, and b were determined. In Table 7 these parameters, along with the empirical film structure parameters, are presented for the five films that have been characterized in this study.

Finally, the semiempirical equation that has been derived in Part I[5] for thin emulsions (of thicknesses T such that not all the incident photons are absorbed within the emulsion) becomes

$$\alpha D = a \ln \frac{1 + b\beta I}{1 + b\beta I \exp(-\mu' T/\sin\theta)}. \tag{6}$$

The fitting described above was on the D-versus-I data that were directly measured for normal-incidence intensities (for θ in the above equations set to 90°). Because for many spectroscopic applications the incident intensities on the photographic films are not at 90°, the θ dependence that has been included in these semiempirical equations is essential. In order to test the accuracy of this predicted θ dependence, we have measured for a given photon energy the D-versus-I data at a series of incidence angles. The method of measurement is illustrated in Fig. 14. A small line source of monochromatic radiation was generated by placing a thin wire (source of characteristic fluorescent line radiation) near the window of a demountable x-ray excitation source. The characteristic line radiation from this wire source was isolated

by using an appropriately filtered excitation radiation of energy only slightly higher than that excited. The source exposes a film that is wrapped under tension around a cylinder as shown in Fig. 14. The variable angle of incidence θ is related to the distance $r\phi$, as measured along the developed-film density pattern, by the relation

$$\theta = \tan^{-1}\left[\frac{\cos\phi + (r/R)}{|\sin\phi|}\right]. \quad (7)$$

The intensity I at a given position along the film is given by

$$I = I(90°)\frac{(R - r^2)}{R^2 + r^2 - 2Rr\cos\phi}. \quad (8)$$

The normal intensity $I(90°)$ is determined from the value of the optical density D, as measured at the center of the densitometer tracing, using the normal-incidence D-versus-I calibration curves. With these relations, D-versus-θ plots may be generated for constant I and for a given photon energy. Such plots were presented in Part I[5] for the 101-07 and the RAR 2497 films. Presented here in Fig. 15 is a D-versus-θ plot for the Kodak RAR 2492 film at the photon energy of Al-Kα (1487 eV). On all these plots we have also presented the D-versus-θ curves for constant incident intensity I, as predicted by the semiempirical relations given above. It may be noted that the agreement between the experimental data and the predictions of the model relations is quite satisfactory.

Table 3. Exposure I (photons/μm^2) at Various Net Densities for Film 2497

Absorption Edge	Photon Energy E (eV)	Net Density D (Specular, 0.1 × 0.1 nA)[a] 0.2	0.4	0.6	0.8	1.0	1.2	1.4	1.6	1.8	2.0	Wavelength λ (Å)
A[b]												
	109	7.45 00	2.11 01	4.61 01	9.17 01	1.75 02	3.28 02	6.08 02	1.12 03	2.06 03	3.77 03	114.27
	193	1.60 00	3.98 00	7.53 00	1.28 01	2.07 01	3.24 01	4.99 01	7.59 01	1.15 02	1.72 02	64.37
	277	8.48 −01	1.97 00	3.45 00	5.40 00	7.99 00	1.14 01	1.60 01	2.20 01	3.01 01	4.09 01	44.76
B[c]												
C[d]												
	525	1.48 00	3.64 00	6.77 00	1.13 01	1.80 01	2.76 01	4.17 01	6.22 01	9.19 01	1.35 02	23.62
D[e]												
	573	2.31 00	5.93 00	1.16 01	2.05 01	3.46 01	5.66 01	9.11 01	1.45 02	2.30 02	3.64 02	21.64
	705	1.51 00	3.68 00	6.80 00	1.13 01	1.78 01	2.70 01	4.04 01	5.97 01	8.73 01	1.27 02	17.59
	930	1.05 00	2.41 00	4.16 00	6.41 00	9.33 00	1.31 01	1.80 01	2.44 01	3.27 01	4.37 01	13.34
	1487	9.42 −01	2.04 00	3.34 00	4.87 00	6.71 00	8.94 00	1.17 01	1.51 01	1.95 01	2.54 01	8.34
E[f]												
	2293	8.59 −01	1.85 00	3.01 00	4.38 00	6.02 00	8.01 00	1.05 01	1.36 01	1.77 01	2.33 01	5.41

[a] In our notation in this table, a number followed by a space and another number indicates that the first number is to be multiplied by 10 raised to the power of the second number; e.g., 9.42 −01 means 9.42×10^{-1}.
[b] Br-M_4 edge.
[c] C-K edge
[d] N-K, Ag-$M_{4,5}$ edges
[e] O-K edge
[f] Br-$L_{3,2}$ edge

Table 4. Exposure I (photons/μm^2) at Various Net Densities for Film 2492

Absorption Edge	Photon Energy E (eV)	Net Density D (Specular, 0.1 × nA)[a] 0.2	0.4	0.6	0.8	1.0	1.2	1.4	1.6	1.8	2.0	Wavelength λ (Å)
A[b]												
	109	6.67 00	1.74 01	3.46 01	6.23 01	1.07 02	1.78 02	2.93 02	4.78 02	7.75 02	1.25 03	114.27
	193	1.47 00	3.48 00	6.22 00	9.98 00	1.51 01	2.21 01	3.17 01	4.48 01	6.28 01	8.73 01	64.37
	277	7.89 −01	1.77 00	2.99 00	4.51 00	6.41 00	8.77 00	1.17 01	1.54 01	2.00 01	2.57 01	44.76
B[c]												
C[d]												
	525	1.36 00	3.19 00	5.65 00	8.95 00	1.34 01	1.93 01	2.73 01	3.80 01	5.24 01	7.17 01	23.62
D[e]												
	573	2.11 00	5.11 00	9.38 00	1.55 01	2.41 01	3.65 01	5.41 01	7.92 01	1.15 02	1.66 02	21.64
	705	1.39 00	3.24 00	5.70 00	8.98 00	1.33 01	1.91 01	2.68 01	3.71 01	5.08 01	6.89 01	17.59
	930	9.85 −01	2.18 00	3.65 00	5.43 00	7.62 00	1.03 01	1.35 01	1.75 01	2.25 01	2.85 01	13.34
	1487	8.89 −01	1.89 00	3.03 00	4.32 00	5.81 00	7.51 00	9.49 00	1.18 01	1.45 01	1.78 01	8.34
E[f]												
	2293	8.13 −01	1.72 00	2.75 00	3.90 00	5.23 00	6.75 00	8.51 00	1.06 01	1.30 01	1.60 01	5.41

[a] In our notation in this table, a number followed by a space and another number indicates that the first number is multiplied by 10 raised to the power of the second number, e.g., 1.78 02 means 1.78×10^2.
[b] Br-M_4 edge
[c] C-K edge
[d] N-K, Ag-$M_{4,5}$ edges
[e] O-K edge.
[f] Br-$L_{3,2}$ edge

Table 5. Exposure I (photons/μm^2) at Various Net Densities for Film 2495

Absorption Edge	Photon Energy E (eV)	Net Density D (Specular, 0.1 × 0.1 nA)[a]										Wavelength λ (Å)
		0.2	0.4	0.6	0.8	1.0	1.2	1.4	1.6	1.8	2.0	
A[b]												
	109	2.73 00	7.14 00	1.43 01	2.59 01	4.46 01	7.50 01	1.24 02	2.04 02	3.33 02	5.41 02	114.27
	193	6.62 −01	1.60 00	2.92 00	4.79 00	7.42 00	1.11 01	1.64 01	2.38 01	3.43 01	4.92 01	64.37
	277	4.04 −01	9.34 −01	1.63 00	2.54 00	3.73 00	5.29 00	7.34 00	1.00 01	1.36 01	1.82 01	44.76
B[c]												
C[d]												
	525	6.22 −01	1.49 00	2.68 00	4.35 00	6.66 00	9.88 00	1.43 01	2.05 01	2.92 01	4.11 01	23.62
D[e]												
	573	9.08 −01	2.23 00	4.16 00	6.97 00	1.11 01	1.70 01	2.57 01	3.84 01	5.68 01	8.36 01	21.64
	705	6.32 −01	1.50 00	2.69 00	4.33 00	6.59 00	9.68 00	1.39 01	1.98 01	2.78 01	3.88 01	17.59
	930	4.80 −01	1.09 00	1.85 00	2.83 00	4.05 00	5.61 00	7.57 00	1.01 01	1.32 01	1.72 01	13.34
	1487	4.36 −01	9.34 −01	1.51 00	2.16 00	2.92 00	3.80 00	4.83 00	6.03 00	7.46 00	9.16 00	8.34
E[f]												
	2293	4.01 −01	8.52 −01	1.36 00	1.94 00	2.60 00	3.36 00	4.25 00	5.28 00	6.50 00	7.95 00	5.41

[a] In our notation in this table, a number followed by a space and another number indicates that the first number is to be multiplied by 10 raised to the power of the second number; e.g., 8.52 −01 means 8.52×10^{-1}.
[b] Br-M_4 edge.
[c] C K edge.
[d] N K, Ag-$M_{4,5}$ edges.
[e] O K edge.
[f] Br $L_{3,2}$ edge.

Table 6. Absorption Edges

	Edge	E (eV)
A	Br-M_4	71
B	C-K	284
C	N-K, Ag-$M_{4,5}$	398–402
D	O-K	532
E	Br-$L_{3,2}$	1553–1599
F	Ag-$L_{3,2}$	3351–3526

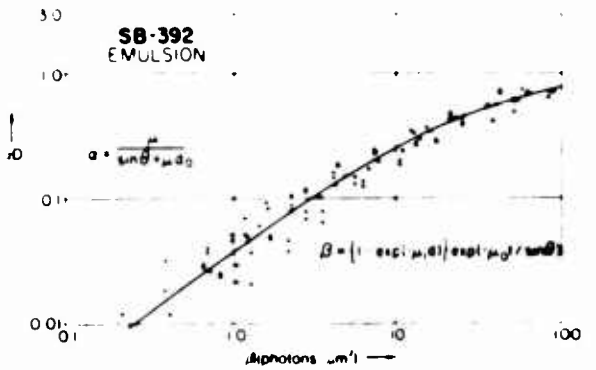


Fig. 8. Universal plot for the SB-392 film using the D versus I data measured at eight photon energies in the 100–1500 eV region and the energy-dependent scaling factors noted here, α and β. The smooth curve is a least-squares fit of the semiempirical Eq. (5).

3. DETERMINATION OF SPECTROSCOPIC FILM-RESOLUTION LIMITS

For the calibrations described above, the proportional counter and microdensitometer slits were set equal to 100 μm, which is small compared with the spectral linewidths generated by the low-energy x-ray spectrograph. (In a few instances, the x-ray source slit was broadened in order to ensure that the spectral linewidths did satisfy this criterion.) It was then assumed that the measured peak densities were precisely related to the corresponding absolute peak intensities through these D-versus-I calibrations not only for the measured lines but also for any that are broader. It is also important to know how narrow the line and/or how closely spaced adjacent lines

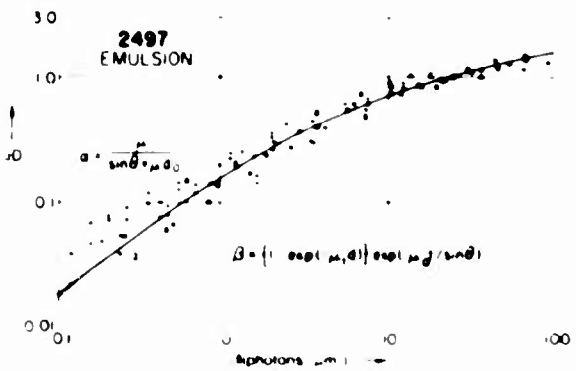


Fig. 9. Same as Fig. 8 for the RAR 2497 film.

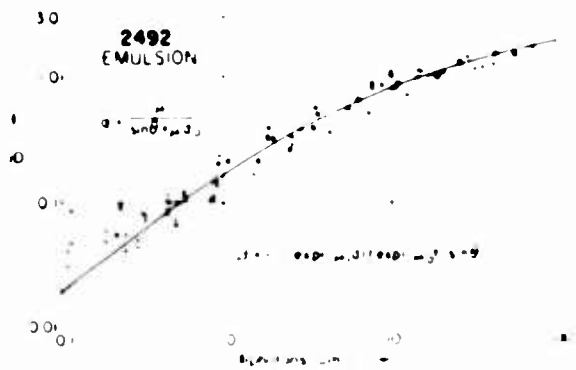


Fig. 10. Same as Fig. 8 for the RAR 2492 film.

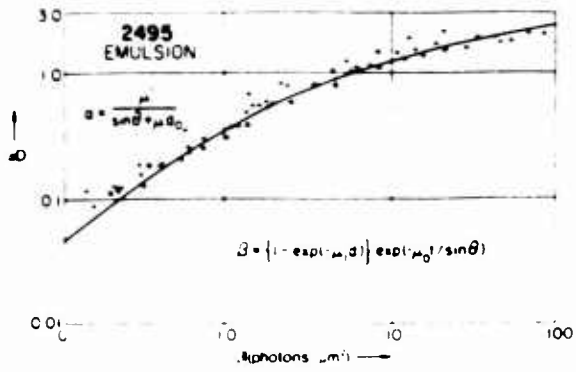


Fig. 11. Same as Fig. 8 for the RAR 2495 film.

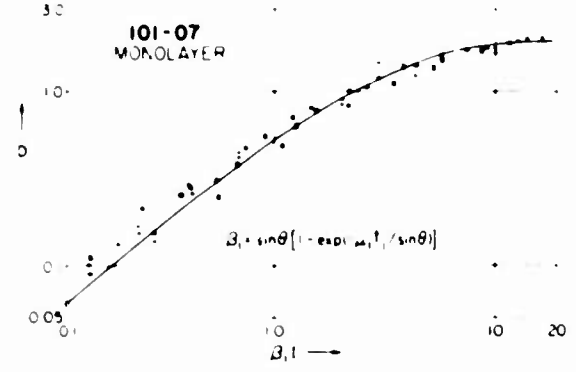


Fig. 12. Universal plot D versus $\beta_1 I$ for the 101-07 film in which the scaling factor β_1 noted here introduces the entire photon-energy dependence. D versus I data were used as measured at eight photon energies in the 100–1500-eV region. The smooth curve was obtained using the universal semiempirical Eq. (4).

may be before the effect of line spreading within the emulsion prevents an accurate determination of the peak intensity when using the D-versus-I calibrations that have been presented here.

A simple test has been applied for the spectroscopic film-resolution limits, it is based on an analysis of contact microradiograms, which are made using a linear zone plate of gold bars to simulate an appropriate range of spectral linewidths and spacings. The spacings between bars varied according to the Fresnel relation for the position of the bar edges of the zone plate

$$x = 100\sqrt{n}.$$

These microstructures were provided for this research by Ceglio *et al*[9] and were constructed by photolithographic techniques similar to those currently used in the microelectronics industry for the generation of integrated circuitry. A final electroplating procedure was applied to produce relatively thick gold-bar microstructures. The gold-bar structures, of about 8 μm in thickness, are essentially opaque to the low-energy x rays that were used to generate the contact microradiograms. The spacings and the openings between the bars $x_2 - x_1$ and $x_{100} - x_{99}$ for the original 100-line zone-plate mask were about 40 and 5 μm, respectively. After the final gold plating, the openings were accurately measured and found to be somewhat narrower (3–38-μm range). In Fig. 16 is shown a photomicrograph of a small section of the 2 mm ×

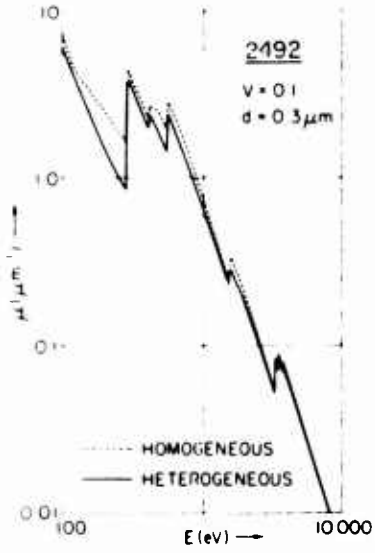


Fig. 13. Comparison of the heterogeneous linear absorption coefficient for the RAR 2492 film with the linear absorption coefficient for an amorphous system of the same volume fraction of AgBr. Note the appreciable difference in the low-energy x-ray region.

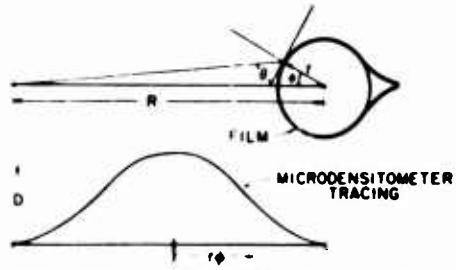


Fig. 14. Experimental method for the determination of the effect of the angle of incidence θ on exposure. The film, wrapped around a 2.5-cm (1-in) cylinder, is exposed by a filtered, fluorescent-line radiation source. The source is a thin wire placed near the window of an x-ray tube of effective excitation photon energy just sufficient to excite the desired characteristic fluorescent line from the wire source.

Table 7. Empirical Universal Equation Parameters

Film	t (μm)	d (μm)	d_0 (μm)	V	T (μm)	a (μm^{-1})	b (μm^2)
2497	0.3	0.3	0.6	0.1	7.0	0.414	0.454
2492	0.1	0.1	0.6	0.1	7.0	0.527	0.372
2495	0.3	0.3	0.6	0.2	7.0	0.528	0.926
SB 192	1.0	1.0	1.5	0.2	10.0	0.285	1.41
101-07		t_1 (μm) 2.0				a_1 1.957	b_1 (μm^2): 0.3128

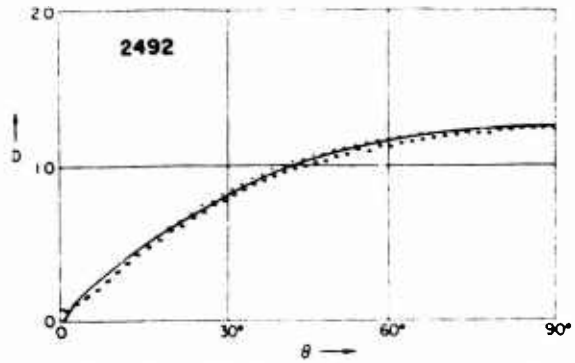


Fig. 15. Comparison of the D-versus-θ data (measured as illustrated in Fig. 14) for constant incident intensity I and energy Al-Kα (1487 eV) with that predicted by the universal semiempirical relation Eq. (6) for the RAR 2492 film.

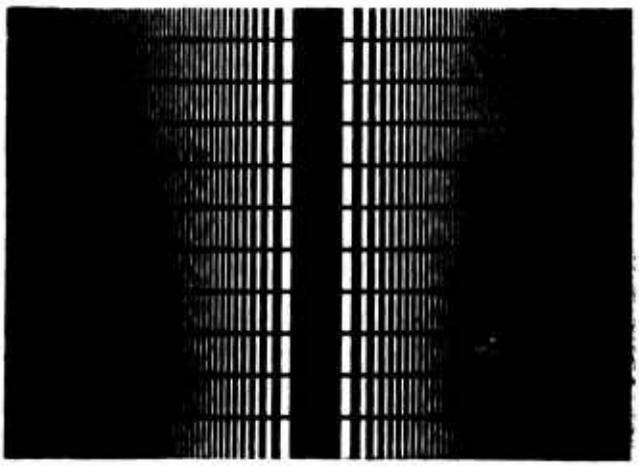


Fig. 16. Photomicrograph of a section of the linear zone plate that was applied to simulate exposures to spectral lines of varying width and spacing. The zone plate is formed by 8-μm-thick gold bars with openings that vary from 3 to 38 μm. The bars are essentially opaque to the x radiation that was used to generate the contact microradiograms [Mg-Kα (1254 eV)].

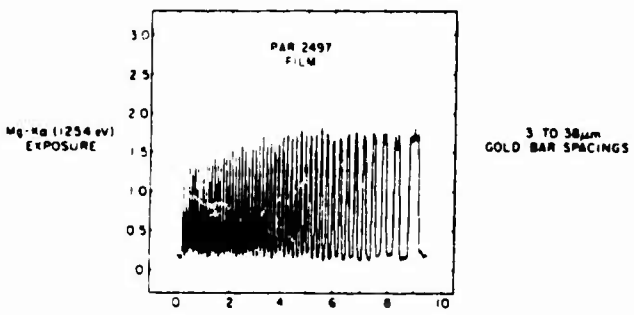


Fig. 17. Densitometer tracing (with a 2-μm microdensitometer slit) on a contact microradiogram of the linear zone plate using a uniform exposure of Mg-Kα (1254-eV) filtered fluorescent radiation of small effective source size on the RAR 2497 film. The onset of the reduction of the peak densities as the slit widths decrease indicates the spectroscopic film-resolution limit.

4 mm zone-plate structure. In Fig. 17 is shown a microdensitometer tracing on a contact microradiogram of this linear zone plate on RAR 2497 film with an exposure from a filtered fluorescent source of Mg-Kα (1254-eV) radiation excited by Al-Kα (1487-eV) anode radiation. A microdensitometer slit width of 2 μm was used. It may be noted that, as the openings in the zone plate became narrower, the peak densities decreased, and the densities within the regions obstructed by the gold bars increased as a result of the line spreading. The difference between these densities, $D_{max} - D_{min}$, should be a constant for linewidths above a defined spectroscopic film-resolution limit and equal to the net density as determined by the exposure I from the D-versus-I calibration. In Figs. 18–20 we present plots of the $D_{max} - D_{min}$ values versus linewidth for contact microradiograms on the three film types RAR 2497, 101-07, and SB-392. These have indicated spectroscopic film-resolution limits of approximately 5, 10, and 15 μm, respectively, at a density of about 1.5. Although this

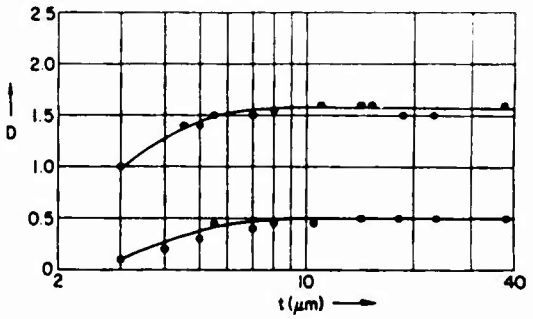


Fig. 18. Plots of net microdensity values $D_{max} - D_{min}$ versus zone-plate slit width t for two contact microradiograms on the RAR 2497 film. (Exposures described in Fig. 17.) The indicated spectroscopic film-resolution limit was about 5 μm.

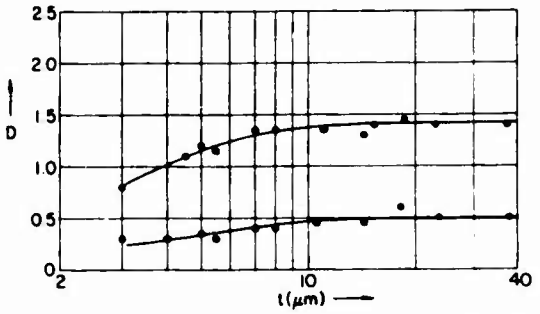


Fig. 19. Plots of $D_{max} - D_{min}$ versus zone-plate slit width t for two contact microradiograms on the 101-07 film. (Exposures described in Fig. 17.) The indicated spectroscopic film-resolution limit is about 10 μm.

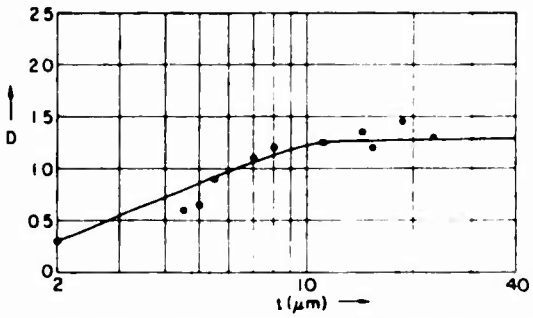


Fig. 20. Plot of $D_{max} - D_{min}$ versus zone-plate width t for a contact microradiograms on the SB-392 film. Exposures described in Fig. 17. The indicated spectroscopic film-resolution limit was about 15 μm.

operational criterion for spectroscopic resolution is not precise, it does establish that all the films that have been chosen here for low-energy x-ray spectroscopy can be applied to determine the absolute intensity distributions of typical spectral lines as generated by Bragg spectrographs in the 100–2000-eV region (widths > 20 μm).

4. ACCURACY OF FILM CALIBRATIONS: CONCLUSIONS

Absolute x-ray spectrometry demands an accurate knowledge of the D-versus-I relation continuously with photon energy in order to translate a microdensitometer record of a spectrum into an absolute intensity distribution versus photon energy. In order to minimize the considerable amount of effort that is usually involved in the experimental calibration of spectroscopic films for the low-energy x-ray region, the approach that has been adopted here is to apply semiempirical model equations, which introduce the effect of the photon energy through the accurately known energy dependence of the x-ray absorption coefficients that characterize the film response. If the manufacturer would make available the approximate values for the required model parameters, such as the average grain size, the emulsion and the overcoat thicknesses, and the volume fraction of AgBr, the semiempirical method presented in this paper would require the measurement of D versus I at only a few photon energies. Unfortunately, these data were not available, and it was necessary to make these measurements at an extended number of photon energies. Nevertheless, it has been demonstrated in this paper that (1) universal plots that fully account for the photon-energy dependence can be established and that (2) these plots can be precisely fitted by relatively simple, semiempirical equations involving only two adjustable parameters (a_1, b_1 or a, b). In Figs. 3–7, examples of experimental D-versus-I data are presented along with those predicted by the universal semiempirical equations that indicate the typical accuracy of the present calibrations.

In Part I[5] it was noted that these parameters have the following, approximate theoretical dependence on the film-structure parameters: for the monolayer film

$$a_1 \sim M_0 S \sim S/d^2, \quad b_1 \sim d^2,$$

and for the emulsion-type film

$$a \sim N_0 S \sim V(S/d^3), \quad b \sim d^2.$$

Here, M_0 is the number of monolayer AgBr grains per unit area, and N_0 is the number of AgBr grains per unit volume in the emulsion. V is the volume fraction of AgBr in the emulsion. S is an effective light-absorption cross section of the developed silver grain clusters, and d is an effective average diameter of the AgBr grain. The implications of these approximate proportionalities are that (1) the only effect of the development process on the sensitometric response is through the parameter a_1 or a by the growth of the cross section S and (2) the effect of grain size d is most sensitively reflected in the values of a_1, b_1 and a, b.

In a batch-to-batch variation of film parameters, we would expect that the volume fraction V would be reasonably constant but that the effective grain size could vary significantly. Such a small variation may affect the values of the scaling

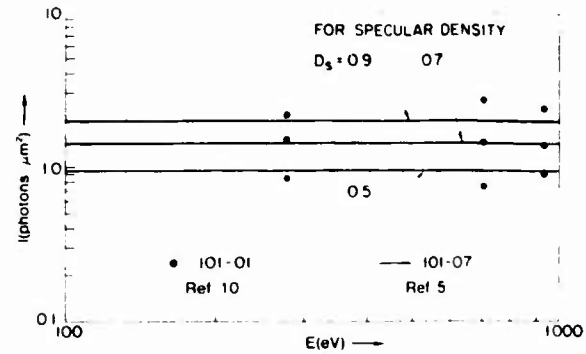


Fig. 21. Comparison of the intensities required to establish specular densities of 0.5, 0.7, and 0.9 as measured independently on the similar film types 101-01 and 101-07 for the 100–1000-eV photon-energy region.

factors (β_1, α, and β) only slightly but could cause relatively large changes in the empirical parameters, a_1, b_1 or a, b. It is therefore suggested here that, for precise film calibration, the following procedure be followed:

(1) For a given film type, the scaling factors should be established as described in this paper.

(2) For each new batch of film, a minimum set of D-versus-I data should be obtained that permits, with the preestablished scaling factors, the generation of the universal plots of αD versus βI (or D versus $B_1 I$ for the monolayer).

(3) Finally, a least-squares fitting of this universal plot then yields a new pair of fitting parameters, a_1, b_1 or a, b, that establish the universal, semiempirical equations $D = f(I, E, \theta)$ for the monolayer and the emulsion types of films.

To assist in the above procedure for the description of the five films that have been characterized here, we present in Appendix C tables of μ_0 for gelatin and μ_1 for AgBr; the scaling factors β_1, α, and β; and the universal functions relating D, I, and E (for the particular film batches studied in this research) at regularly spaced intervals in photon energy.

Finally, we would like to compare our film calibrations with those obtained independently on similar photographic materials as reported from other laboratories.

The Kodak 101-01 film has been calibrated for the 100–1000-eV x-ray region using three characteristic line series from copper, iron, and graphite targets that were excited by proton-beam bombardment using the ion accelerator (IONAC) at the Lawrence Livermore National Laboratory[10] and flow proportional-counter detectors. In Fig. 21, we present these experimental data for each photon energy as the number of photons required to establish a specular density of 0.5, 0.7, and 0.9. These densities correspond to the reported diffuse densities of 0.35, 0.50, and 0.65, which were determined using the diffuse-to-specular density calibration curves presented in Appendix A. Along with these experimental points are our semiempirical predicted curves (smooth) for the Kodak 101-07 film, which was studied in this paper. The principal difference between these film systems is that the 101-07 film is on a 4-mil ESTAR base and the 101-01 film is on a 5-mil acetate base.

The Kodak RAR 2490 film has been calibrated using filtered fluorescent x radiations excited in a low-energy x-ray calibration facility at the Los Alamos National Laboratory.

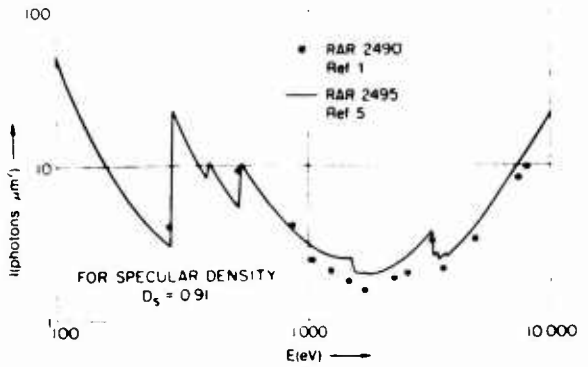


Fig. 22. Comparison of the intensities required to establish a specular density of 0.9 as measured independently on the similar film types RAR 2490 and RAR 2495 for the 100–10 000-eV photon-energy region.

Averaged data were reported for the 100–10,000-eV region for the exposure required to establish a diffuse density of 0.5. This corresponds to our specular density value of 0.9 as determined for a similar type emulsion, the Kodak RAR 2495. In Fig. 22, we present these data along with our semiempirical equation prediction for the RAR 2495 film. Although an absolute comparison is not possible here because two film types are involved, it should be noted that the model-prediction photon-energy dependence for $E > 2000$ eV for such similar systems seems to be satisfactorily verified.

APPENDIX A: SPECULAR-DENSITY VERSUS DIFFUSE-DENSITY CALIBRATIONS

The density measured and referred to in the body of this paper has been specular density D_s. Many laboratories use diffuse density D_d, and this appendix presents data to permit translation from one type of density to the other. The data presented here are in the form of plots of the ratio D_s/D_d versus D_d (Figs. 23–32). Similar types of plots have been presented by others[11] for different types of films, and there have been some theoretical and empirical treatments of the problem of relating specular to diffuse densities for different types of films.[12] The data presented here are directed specifically to the five types of films used and processed as described in Appendix B. The processing is important because of the dependence of these types of plots on the light-scattering cross section S, as discussed above.[13] The specular-density data were taken at two different matched numerical apertures (N.A.'s) for the optical system of the densitometer. One of these was the standard N.A. of 0.1. These data were used in Figs. 23–27, which give the D_s/D_d versus D_d plots for each of the five films used. In addition, in order to accomodate fine spectral lines, which necessitate increasing the optical apertures, data were also taken at the matched N.A.'s of 0.25. These N.A. = 0.25 data are shown in Figs. 28–32 for the five films used.

The densities were measured using the following setups:

(1) *Specular density* D_s. A Photometric Data Systems Model 1010 microdensitometer system equipped with a Hamamatsu R213 end-on photomultiplier and operating with matched objective and illumination optical systems at a N.A. of 0.1 was used. Readings were also taken at N.A. = 0.25. The effective objective aperture (i.e., scanned-sample dimensions) for N.A. = 0.1 was 0.286 mm × 4.416 mm; for N.A. = 0.25 it was 0.400 mm × 4.416 mm. A mean D_s was determined for this sample area.

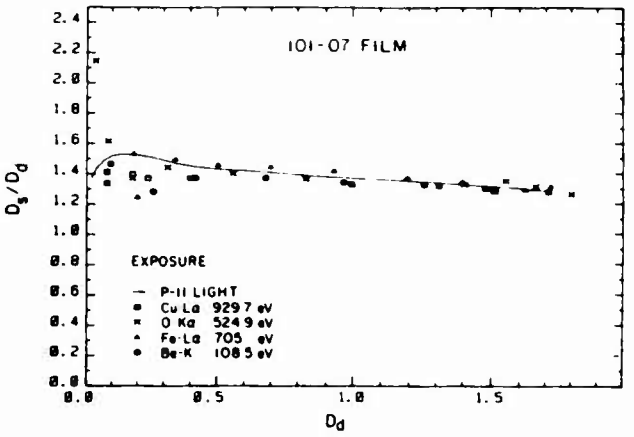


Fig. 23. Specular density measured with matched 0.1 numerical apertures.

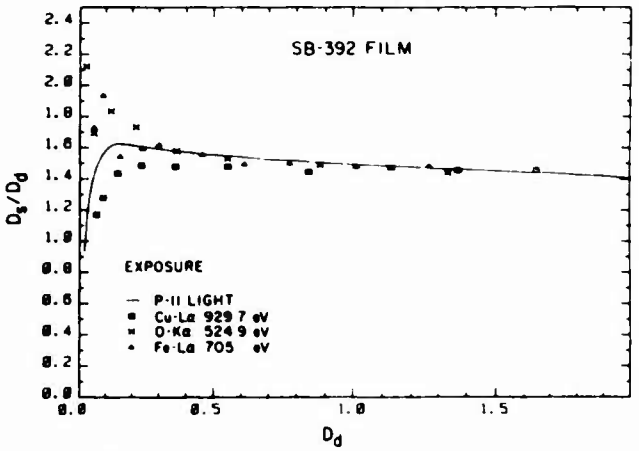


Fig. 24. Specular density measured with matched 0.1 numerical apertures.

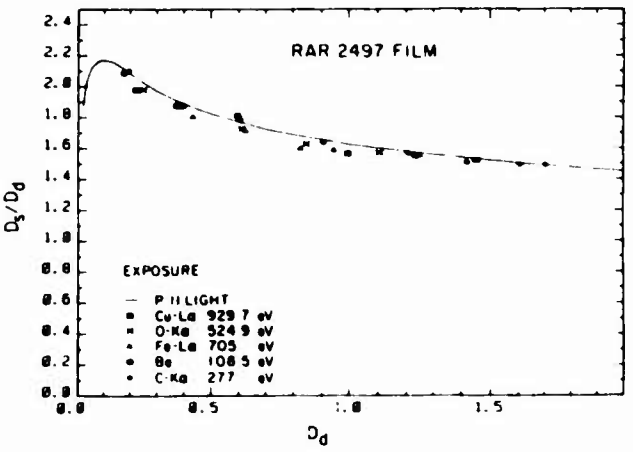


Fig. 25. Specular density measured with matched 0.1 numerical apertures.

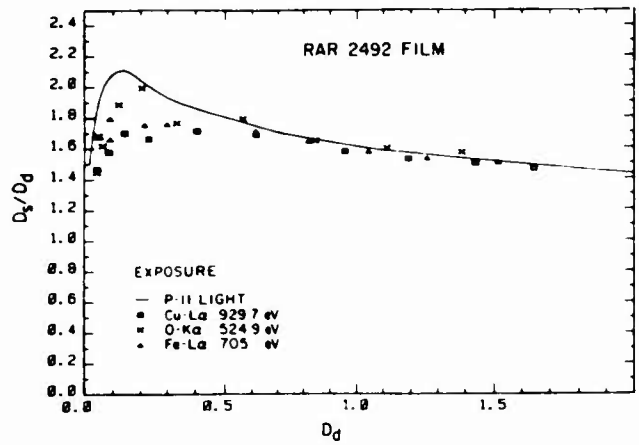


Fig. 26. Specular density measured with matched 0.1 numerical apertures.

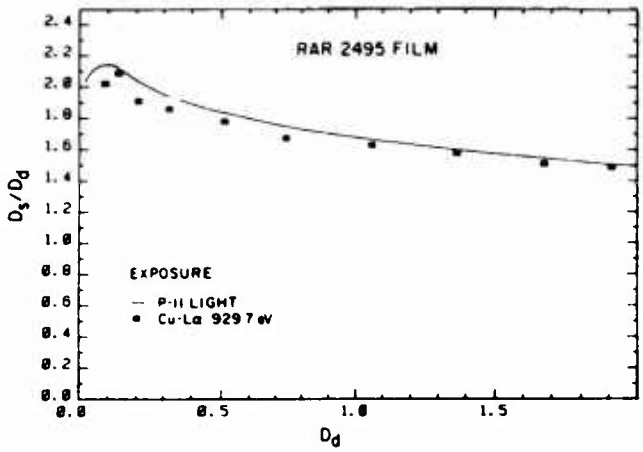


Fig. 27. Specular density measured with matched 0.1 numerical apertures.

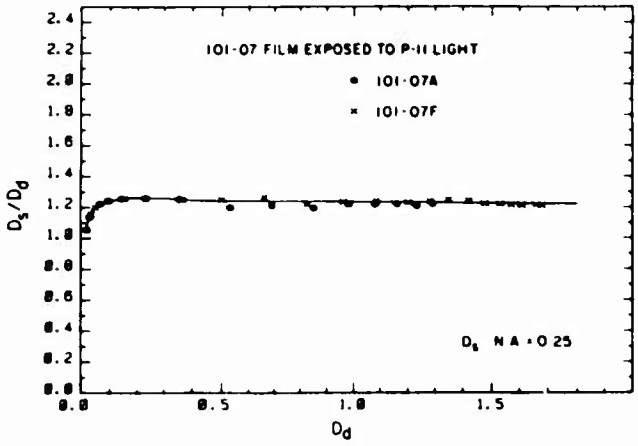


Fig. 28. Specular density measured with matched 0.25 numerical apertures.

(2) *Diffuse density* D_d (totally diffuse visual density type V 1-b, in conformity with ANSI Standard pH 2.19) A Westrex RA-1100-H integrating-sphere diffuse densitometer with a reading aperture of 0.356 mm × 4.420 mm was used.

The x-ray film measurements were on the same exposures used to obtain the film-calibration curves. Film-density samples from exposure to P-11 simulated phosphor light source were also measured. The curves in the plots are those fitted to the P-11 data, and the x-ray exposure data are plotted

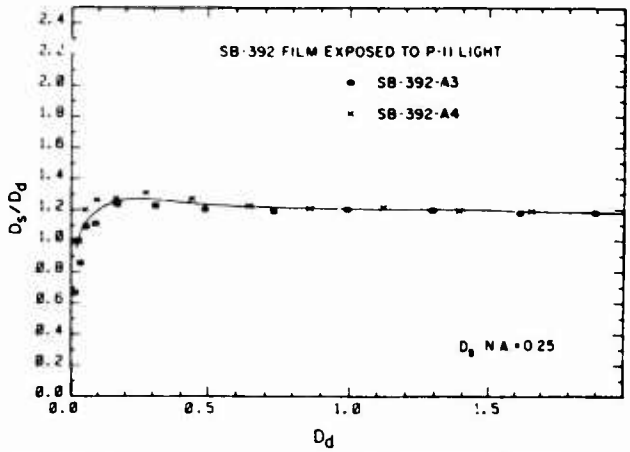


Fig. 29. Specular density measured with matched 0.25 numerical apertures.

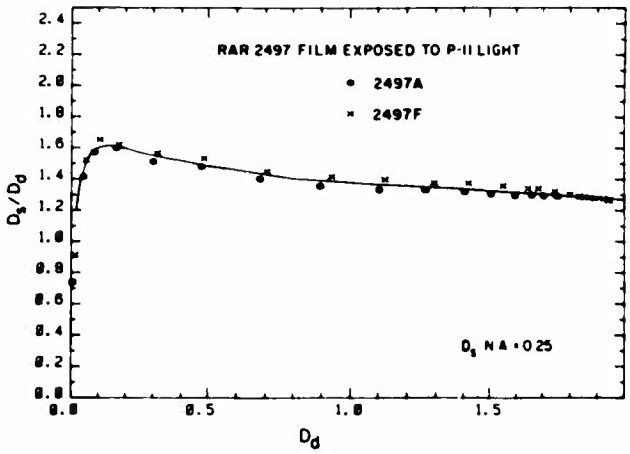


Fig. 30. Specular density measured with matched 0.25 numerical apertures.

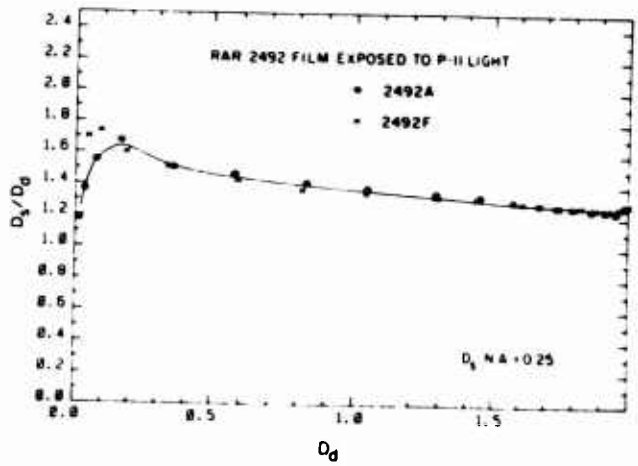


Fig. 31. Specular density measured with matched 0.25 numerical apertures.

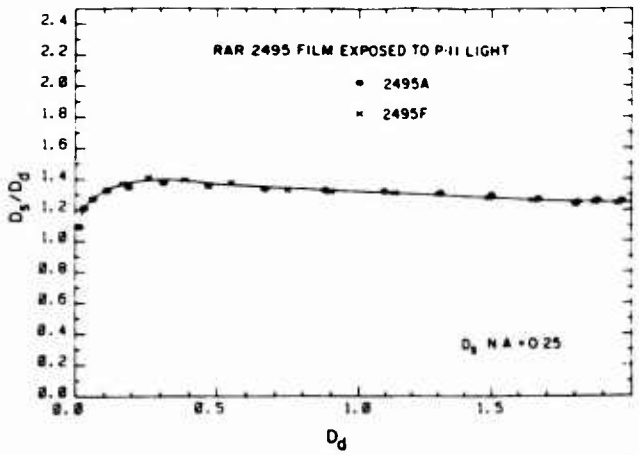


Fig. 32. Specular density measured with matched 0.25 numerical apertures.

as points for N.A. = 0.1. The plots for N.A. = 0.25 portray P-11 simulated phosphor data only. As this and other studies have shown,[14] however, these plots tend to be independent of the energy of the exposing soft x rays and similar to those for P-11 light.

APPENDIX B: FILM-HANDLING AND -DEVELOPMENT PROCEDURES

Kodak RAR 2492, 2495, and 2497 Films

These three films were handled and developed in the same manner with the exception that the RAR 2495 film required a Kodak Safelight Filter No. 2, whereas the RAR 2492 and 2497 films could be handled with either a No. 1 or a No. 2 filter. The exposed film was processed as follows in a developing tank at 68 ± 1°F:

(1) Presoak: 2 min in distilled water. (All five films used in this study were presoaked because of the varying times that the films were kept in vacuum.)
(2) Development: 6 min in Kodak Developer D-19 with constant agitation.
(3) Rinse: 30 sec in Kodak SB-5 Indicator Stop Bath with constant agitation.
(4) Fixing: 5 min in Kodak Rapid Fixer with constant agitation.
(5) Wash: At least 10 min in running water, then 30 sec in Kodak Photo-Flo 200 Solution.
(6) Drying: At room temperature in still air.

Kodak SB-392 (or SB-5)

The Kodak SB-392 film or the SB-5 film, the difference between the two being merely their format, was handled under Kodak Safelight Filter No. 1. Special care was taken not to bend the film too sharply, since doing so results in many minute cracks in the film. The processing of this film was as follows at 68 ± 1°F in a developing tank:

(1) Presoak: 2 min in distilled water.
(2) Development: 5 min in Kodak Liquid X-ray Developer or Kodak GBX Developer with constant agitation.
(3) Rinse: 30 sec in Kodak SB-5 Indicator Stop Bath with constant agitation.
(4) Fixing: 2 min in Kodak Rapid Fixer with constant agitation.
(5) Wash: 30 min in running water, then 30 sec in Photo-Flo 200 Solution.
(6) Drying: At room temperature in still air.

Kodak Special Film Type 101-07

Great care was taken in the handling of this film since the emulsion lacks a protective overcoat of gelatin and is easily marred. It was handled using Kodak Safelight Filter No. 1. It was necessary to spray the back of the film lightly with a commercially available brand of static guard just before loading the film into the camera. This prevents the occurrence of dark streaks on the developed film that result from static electricity. The processing of this film at 68 ± 1°F was as follows:

(1) Presoak: 2 min in distilled water.
(2) Development: 4 min in Kodak D-19 Developer diluted 1:1 with distilled water and constantly agitated.
(3) Rinse: 30 sec in Kodak SB-5 Indicator Stop Bath with constant agitation.
(4) Fixing: 2 min in Kodak Rapid Fixer with constant agitation.
(5) Wash: At least 7 min in running water followed by 30 sec in Kodak Photo-Flo 200 Solution.
(6) Drying: At room temperature in still air.

APPENDIX C: TABLES OF PARAMETERS APPLIED HERE FOR THE GENERATION OF FIVE SEMIEMPIRICAL, UNIVERSAL FILM-RESPONSE FUNCTIONS

Presented in Table 8 are the energy-dependent scaling factors β_1, α, and β that were applied to generate the universal photographic response functions for the five films studied in this research. [In Table 9 we have listed the calculated values for the linear absorption coefficients for gelatin —$C_8H_{16}O_5N_2$— (μ_0) and for AgBr (μ_1), which were used in the generation of the scaling factors.] With these factors, the universal plots, which are presented in Figs. 8–12, were obtained. These plots were then least-squares fitted to our semiempirical model equations to obtain the relatively sensitive pair parameters a_1, b_1 or a, b in order to establish the best-average characterizations (over photon energies in the 100–2000-eV region) for the investigated monolayer and emulsion-type films. (These parameters are listed in Table 7.) The averaged characterizations were presented above in Tables 1–5 as exposure I versus density D at the nine characteristic photon energies that were used for the D versus I calibrations. Presented in Tables 10–14 are the averaged film response characteristics predicted by the semiempirical relations for the extended photon-energy region of 100–10,000 eV as calculated at regularly spaced intervals in energy for the five films.

As was discussed in Section 4, the data presented here can be directly applied along with additional calibration data to new batches of these films to obtain corrected values of the fitting parameters a_1, b_1 or a, b.

Table 8. α (μm^{-1}), β, and β_1 Factors versus Photon Energy E (eV)

Absorption Edge	E (eV)	Film[a] 2492, 2497 α	2492, 2497 β	2495 α	2495 β	SB-392 α	SB-392 β	101-07 β_1
A[b]								
	75	1.44 00	4.76 −02	1.45 00	4.76 −02	6.26 −01	3.91 −05	1.000
	100	1.30 00	1.83 −01	1.32 00	1.83 −01	5.99 −01	3.51 −03	1.000
	125	1.16 00	3.46 −01	1.19 00	3.46 −01	5.64 −01	3.16 −02	1.000
	150	1.02 00	4.96 −01	1.07 00	4.96 −01	5.27 −01	1.00 −01	1.000
	175	8.99 −01	6.10 −01	9.72 −01	6.10 −01	4.89 −01	2.00 −01	1.000
	200	7.94 −01	6.95 −01	8.88 −01	6.95 −01	4.51 −01	3.10 −01	1.000
	225	7.06 −01	7.55 −01	8.19 −01	7.55 −01	4.16 −01	4.14 −01	1.000
	250	6.34 −01	7.98 −01	7.62 −01	7.98 −01	3.84 −01	5.05 −01	1.000
	275	5.76 −01	8.28 −01	7.17 −01	8.28 −01	3.56 −01	5.83 −01	1.000
B[c]								
	300	1.14 00	3.53 −01	1.18 00	3.53 −01	5.62 −01	3.54 −02	1.000
	325	1.08 00	4.17 −01	1.12 00	4.17 −01	5.44 −01	6.45 −02	1.000
	350	1.01 00	4.70 −01	1.06 00	4.70 −01	5.26 −01	1.02 −01	1.000
	375	9.52 −01	5.14 −01	1.01 00	5.14 −01	5.09 −01	1.46 −01	1.000
C[d]								
	425	9.44 −01	5.34 −01	1.00 00	5.34 −01	5.05 −01	1.54 −01	1.000
	450	9.03 −01	5.87 −01	9.72 −01	5.87 −01	4.91 −01	1.94 −01	1.000
	475	8.58 −01	6.22 −01	9.36 −01	6.22 −01	4.76 −01	2.36 −01	1.000
	500	8.15 −01	6.51 −01	9.00 −01	6.51 −01	4.61 −01	2.81 −01	1.000
D[e]								
	550	9.69 −01	5.16 −01	1.02 00	5.16 −01	5.13 −01	1.35 −01	1.000
	600	8.91 −01	5.70 −01	9.58 −01	5.70 −01	4.89 −01	2.00 −01	1.000
	650	8.20 −01	6.10 −01	8.97 −01	6.10 −01	4.65 −01	2.68 −01	1.000
	700	7.57 −01	6.37 −01	8.43 −01	6.37 −01	4.43 −01	3.35 −01	1.000
	750	6.96 −01	6.42 −01	7.88 −01	6.42 −01	4.21 −01	3.99 −01	1.000
	800	6.38 −01	6.37 −01	7.36 −01	6.37 −01	3.99 −01	4.59 −01	1.000
	850	5.86 −01	6.25 −01	6.87 −01	6.25 −01	3.79 −01	5.13 −01	1.000
	900	5.40 −01	6.06 −01	6.42 −01	6.06 −01	3.60 −01	5.58 −01	1.000
	950	4.97 −01	5.84 −01	6.00 −01	5.84 −01	3.43 −01	5.97 −01	0.999
	1000	4.57 −01	5.59 −01	5.60 −01	5.59 −01	3.26 −01	6.29 −01	0.999
	1050	4.21 −01	5.31 −01	5.23 −01	5.31 −01	3.11 −01	6.53 −01	0.998
	1100	3.88 −01	5.03 −01	4.88 −01	5.03 −01	2.96 −01	6.70 −01	0.996
	1150	3.58 −01	4.76 −01	4.55 −01	4.76 −01	2.82 −01	6.81 −01	0.992
	1200	3.31 −01	4.49 −01	4.25 −01	4.49 −01	2.69 −01	6.86 −01	0.988
	1250	3.06 −01	4.23 −01	3.98 −01	4.23 −01	2.56 −01	6.86 −01	0.982
	1300	2.84 −01	3.99 −01	3.72 −01	3.99 −01	2.44 −01	6.82 −01	0.975
	1350	2.63 −01	3.76 −01	3.48 −01	3.76 −01	2.33 −01	6.75 −01	0.966
	1400	2.44 −01	3.54 −01	3.26 −01	3.54 −01	2.22 −01	6.65 −01	0.955
	1450	2.27 −01	3.34 −01	3.06 −01	3.34 −01	2.12 −01	6.52 −01	0.943
	1500	2.12 −01	3.15 −01	2.87 −01	3.15 −01	2.02 −01	6.38 −01	0.929
E[f]								
	1800	1.98 −01	4.18 −01	3.04 −01	4.18 −01	1.90 −01	7.77 −01	0.976
	1900	1.81 −01	3.89 −01	2.82 −01	3.89 −01	1.80 −01	7.58 −01	0.966
	2000	1.63 −01	3.54 −01	2.56 −01	3.54 −01	1.70 −01	7.28 −01	0.949
	2100	1.46 −01	3.22 −01	2.33 −01	3.22 −01	1.59 −01	6.96 −01	0.929
	2200	1.32 −01	2.93 −01	2.13 −01	2.93 −01	1.49 −01	6.61 −01	0.905
	2300	1.20 −01	2.68 −01	1.94 −01	2.68 −01	1.40 −01	6.25 −01	0.878
	2400	1.09 −01	2.44 −01	1.78 −01	2.44 −01	1.31 −01	5.90 −01	0.849
	2500	9.92 −02	2.24 −01	1.63 −01	2.24 −01	1.23 −01	5.56 −01	0.818
	2600	9.06 −02	2.05 −01	1.50 −01	2.05 −01	1.15 −01	5.23 −01	0.786
	2700	8.29 −02	1.88 −01	1.38 −01	1.88 −01	1.08 −01	4.91 −01	0.754
	2800	7.60 −02	1.73 −01	1.27 −01	1.73 −01	1.01 −01	4.61 −01	0.721
	2900	6.98 −02	1.60 −01	1.17 −01	1.60 −01	9.49 −02	4.33 −01	0.689
	3000	6.43 −02	1.47 −01	1.08 −01	1.47 −01	8.91 −02	4.07 −01	0.657
	3100	5.93 −02	1.36 −01	1.00 −01	1.36 −01	8.36 −02	3.82 −01	0.626
	3200	5.49 −02	1.26 −01	9.30 −02	1.26 −01	7.85 −02	3.59 −01	0.596
	3300	5.08 −02	1.17 −01	8.64 −02	1.17 −01	7.38 −02	3.37 −01	0.567
F[g]								
	4000	6.32 −02	1.73 −01	1.16 −01	1.73 −01	9.13 −02	4.67 −01	0.720
	5000	3.71 −02	1.02 −01	6.92 −02	1.02 −01	5.98 −02	3.01 −01	0.513
	6000	2.33 −02	6.45 −02	4.40 −02	6.45 −02	4.01 −02	1.99 −01	0.359
	7000	1.56 −02	4.32 −02	2.95 −02	4.32 −02	2.77 −02	1.37 −01	0.255

continued overleaf

Table 8. Continued

Absorption Edge	E (eV)	Film[a] 2492, 2497 α	2492, 2497 β	2495 α	2495 β	SB-392 α	SB-392 β	101-07 β_1
	8000	1.09 −02	3.03 −02	2.07 −02	3.03 −02	1.98 −02	9.73 −02	0.185
	9000	7.89 −03	2.20 −02	1.51 −02	2.20 −02	1.46 −02	7.15 −02	0.138
	10000	5.91 −03	1.65 −02	1.13 −02	1.65 −02	1.11 −02	5.41 −02	0.105

[a] In our notation in this table, a number followed by a space and another number indicates that the first number is to be multiplied by 10 raised to the power of the second number; e.g., 1.27 −01 means 1.27×10^{-1}.
[b] Br-M_4 edge.
[c] C-K edge.
[d] N-K, Ag-$M_{4,5}$ edges.
[e] O-K edge.
[f] Br-$L_{3,2}$ edge.
[g] Ag-$L_{3,2}$ edge.

Table 9. Linear Absorption Coefficients[a]

Absorption Edge	E (eV)	μ_0 (μm^{-1})[b]	μ_1 (μm^{-1})[b]	λ (Å)
A[c]				
	75	1.01 01	4.63 01	165.19
	100	5.65 00	2.11 01	123.89
	125	3.45 00	1.22 01	99.11
	150	2.30 00	1.48 01	82.59
	175	1.61 00	1.46 01	70.79
	200	1.17 00	1.47 01	61.95
	225	8.83 −01	1.37 01	55.06
	250	6.82 −01	1.29 01	49.56
	275	5.40 −01	1.21 01	45.05
B[d]				
	300	3.34 00	1.09 01	41.30
	325	2.74 00	9.88 00	38.12
	350	2.28 00	9.00 00	35.40
	375	1.92 00	8.26 00	33.04
C[e]				
	425	1.87 00	9.10 00	29.15
	450	1.64 00	1.07 01	27.53
	475	1.44 00	1.06 01	26.08
	500	1.27 00	1.02 01	24.78
D[f]				
	550	2.00 00	9.42 00	22.53
	600	1.61 00	8.60 00	20.65
	650	1.32 00	7.84 00	19.06
	700	1.09 00	7.19 00	17.70
	750	9.17 −01	6.23 00	16.52
	800	7.74 −01	5.43 00	15.49
	850	6.59 −01	4.78 00	14.58
	900	5.68 −01	4.23 00	13.77
	950	4.93 −01	3.76 00	13.04
	1000	4.29 −01	3.36 00	12.39
	1050	3.76 −01	3.01 00	11.80
	1100	3.32 −01	2.71 00	11.26
	1150	2.94 −01	2.44 00	10.77
	1200	2.62 −01	2.22 00	10.32
	1250	2.34 −01	2.02 00	9.91
	1300	2.10 −01	1.84 00	9.53
	1350	1.89 −01	1.69 00	9.18
	1400	1.71 −01	1.55 00	8.85
	1450	1.55 −01	1.43 00	8.54
	1500	1.41 −01	1.33 00	8.26
E[g]	1800	8.44 −02	1.87 00	6.88
	1900	7.24 −02	1.69 00	6.52
	2000	6.25 −02	1.49 00	6.19
	2100	5.28 −02	1.32 00	5.90
	2200	4.62 −02	1.18 00	5.63
	2300	4.06 −02	1.05 00	5.39
	2400	3.59 −02	9.46 −01	5.16
	2500	3.19 −02	8.53 −01	4.96
	2600	2.85 −02	7.72 −01	4.77
	2700	2.55 −02	7.01 −01	4.59
	2800	2.29 −02	6.39 −01	4.42
	2900	2.07 −02	5.84 −01	4.27
	3000	1.87 −02	5.35 −01	4.13
	3100	1.70 −02	4.92 −01	4.00
	3200	1.55 −02	4.53 −01	3.87
	3300	1.41 −02	4.18 −01	3.75
F[h]				
	4000	7.94 −03	6.36 −01	3.10
	5000	4.01 −03	3.60 −01	2.48
	6000	2.28 −03	2.23 −01	2.06
	7000	1.41 −03	1.47 −01	1.77
	8000	9.27 −04	1.02 −01	1.55
	9000	6.38 −04	7.43 −02	1.38
	10000	4.55 −04	5.56 −02	1.24

[a] μ_0 (gelatin) for $\rho = 1.40$ g/cm^3; μ_1 (AgBr) for $\rho = 6.47$ g/cm^3. The notation $C_8H_{16}O_5N_2$ is for gelatin.
[b] In our notation in this table, a number followed by a space and another number indicates that the first number is to be multiplied by 10 raised to the power of the second number; e.g., 2.94 −01 means 2.94×10^{-1}.
[c] Br-M_4 edge.
[d] C-K edge.
[e] N-K, Ag-$M_{4,5}$ edges.
[f] O-K edge.
[g] Br-$L_{3,2}$ edge.
[h] Ag-$L_{3,2}$ edge.

Table 10. Exposure I (photons/μm^2) at Various Net Densities for Film 101-07

Absorption Edge	Photon Energy E (eV)	Net Density D (Specular, 0.1 × 0.1 nA) 0.2	0.4	0.6	0.8	1.0	1.2	1.4	1.6	1.8	Wavelength λ (Å)
A[a]											
	75	0.34	0.73	1.17	1.68	2.29	3.04	4.02	5.44	8.07	165.31
	150	0.34	0.73	1.17	1.68	2.29	3.04	4.02	5.44	8.07	82.65
	225	0.34	0.73	1.17	1.68	2.29	3.04	4.02	5.44	8.07	55.10
	300	0.34	0.73	1.17	1.68	2.29	3.04	4.02	5.44	8.07	41.33
	375	0.34	0.73	1.17	1.68	2.29	3.04	4.02	5.44	8.07	33.06
C[b]											
	475	0.34	0.73	1.17	1.68	2.29	3.04	4.02	5.44	8.07	26.10
	600	0.34	0.73	1.17	1.68	2.29	3.04	4.02	5.44	8.07	20.66
	750	0.34	0.73	1.17	1.68	2.29	3.04	4.02	5.44	8.07	16.53
	900	0.34	0.73	1.17	1.68	2.29	3.04	4.02	5.44	8.07	13.78
	950	0.34	0.73	1.17	1.68	2.29	3.04	4.02	5.44	8.07	13.05
	1000	0.35	0.73	1.17	1.68	2.29	3.04	4.02	5.45	8.08	12.40
	1050	0.35	0.73	1.17	1.68	2.29	3.04	4.03	5.45	8.09	11.81
	1100	0.35	0.73	1.18	1.69	2.30	3.05	4.04	5.46	8.10	11.27
	1150	0.35	0.74	1.18	1.69	2.30	3.06	4.05	5.48	8.13	10.78
	1200	0.35	0.74	1.18	1.70	2.31	3.07	4.07	5.50	8.16	10.33
	1250	0.35	0.74	1.19	1.71	2 33	3.09	4.09	5.54	8.21	9.92
	1300	0.35	0.75	1.20	1.72	2.35	3.11	4.12	5.58	8.27	9.54
	1350	0.36	0.76	1.21	1.74	2.37	3.14	4.16	5.63	8.35	9.18
	1400	0.36	0.77	1.23	1.76	2.39	3.18	4.21	5.69	8.44	8.86
	1450	0.37	0.78	1.24	1.78	2.42	3.22	4.26	5.77	8.55	8.55
	1500	0.37	0.79	1.26	1.81	2.46	3.27	4.32	5.85	8.68	8.27
E[c]											
	1800	0.35	0.75	1.20	1.72	2.34	3.11	4.12	5.57	8.26	6.89
	1900	0.36	0.76	1.21	1.74	2.37	3.14	4.16	5.63	8.35	6.53
	2000	0.36	0.77	1.23	1.77	2.41	3.20	4.23	5.73	8.50	6.20
	2100	0.37	0.79	1.26	1.81	2.46	3.27	4.32	5.86	8.68	5.90
	2200	0.38	0.81	1.29	1.86	2.53	3.35	4.44	6.01	8.91	5.64
	2300	0.39	0.83	1.33	1.91	2.60	3.46	4.57	6.19	9.18	5.39
	2400	0.41	0.86	1.38	1.98	2.69	3.58	4.73	6.41	9.50	5.17
	2500	0.42	0.89	1.43	2.05	2.79	3.71	4.91	6.65	9.86	4.96
	2600	0.44	0.93	1.49	2.14	2.91	3.86	5.11	6.92	10.26	4.77
	2700	0.46	0.97	1.55	2.23	3.03	4.03	5.33	7.22	10.70	4.59
	2800	0.48	1.01	1.62	2.33	3.17	4.21	5.57	7.54	11.18	4.43
	2900	0.50	1.06	1.70	2.44	3.32	4.41	5.83	7.90	11.71	4.28
	3000	0.52	1.11	1.78	2.56	3.48	4.62	6.12	8.28	12.28	4.13
	3100	0.55	1.17	1.87	2.68	3.65	4.85	6.42	8.69	12.89	4.00
	3200	0.58	1.23	1.96	2.82	3.84	5.10	6.74	9.13	13.54	3.87
	3300	0.61	1.29	2.06	2.96	4.03	5.36	7.09	9.60	14.23	3.76
F[d]											
	4000	0.48	1.02	1.63	2.33	3.18	4.22	5.58	7.56	11.21	3.10
	5000	0.67	1.42	2.28	3.28	4.46	5.92	7.83	10.60	15.72	2.48
	6000	0.96	2.03	3.26	4.68	6.37	8.45	11.18	15.14	22.45	2.07
	7000	1.35	2.87	4.59	6.59	8.97	11.91	15.75	21.33	31.63	1.77
	8000	1.86	3.94	6.32	9.07	12.34	16.39	21.68	29.35	43.53	1.55
	9000	2.50	5.30	8.48	12.17	16.57	22.00	29.10	39.40	58.43	1.38
	10000	3.27	6.94	11.12	15.96	21.73	28.85	38.17	51.68	76.63	1.24

[a] Br-M_4 edge.
[b] N-K, Ag-$M_{4,5}$ edges.
[c] Br-$L_{3,2}$ edge
[d] Ag-$L_{3,2}$ edge

Table 11. Exposure I (photons/μm^2) at Various Net Densities for Film SB-392

Absorption Edge	Photon Energy E (eV)	Net Density D (Specular, 0.1 × 0.1 nA)[a] 0.2	0.4	0.6	0.8	1.0	1.2	1.4	1.6	1.8	2.0	Wavelength λ (Å)
A[b]												
	75	1.00 04	2.56 04	4.98 04	8.73 04	1.46 05	2.36 05	3.76 05	5.94 05	9.32 05	1.46 06	165.31
	100	1.06 02	2.67 02	5.12 02	8.85 02	1.45 03	2.32 03	3.63 03	5.64 03	8.69 03	1.33 04	123.98
	125	1.09 01	2.71 01	5.12 01	8.71 01	1.40 02	2.19 02	3.37 02	5.11 02	7.71 02	1.16 03	99.18
	150	3.17 00	7.75 00	1.44 01	2.40 01	3.79 01	5.80 01	8.72 01	1.29 02	1.90 02	2.79 02	82.65
	175	1.45 00	3.49 00	6.37 00	1.04 01	1.61 01	2.42 01	3.55 01	5.15 01	7.41 01	1.06 02	70.85
	200	8.54 −01	2.03 00	3.63 00	5.84 00	8.87 00	1.30 01	1.87 01	2.66 01	3.73 01	5.20 01	61.99
	225	5.82 −01	1.36 00	2.41 00	3.80 00	5.68 00	8.18 00	1.15 01	1.60 01	2.20 01	3.01 01	55.10
	250	4.35 −01	1.00 00	1.75 00	2.73 00	4.00 00	5.68 00	7.87 00	1.07 01	1.45 01	1.94 01	49.59
	275	3.46 −01	7.91 −01	1.36 00	2.10 00	3.04 00	4.25 00	5.80 00	7.80 00	1.04 01	1.37 01	45.08
B[c]												
	300	9.70 00	2.41 01	4.54 01	7.71 01	1.24 02	1.94 02	2.97 02	4.50 02	6.77 02	1.01 03	41.33
	325	5.12 00	1.26 01	2.36 01	3.97 01	6.33 01	9.79 01	1.49 02	2.23 02	3.31 02	4.91 02	38.15
	350	3.11 00	7.61 00	1.41 01	2.35 01	3.72 01	5.69 01	8.54 01	1.27 02	1.86 02	2.73 02	35.42
	375	2.09 00	5.07 00	9.33 00	1.54 01	2.41 01	3.65 01	5.43 01	7.97 01	1.16 02	1.68 02	33.06
C[d]												
	425	1.96 00	4.75 00	8.74 00	1.44 01	2.25 01	3.41 01	5.05 01	7.40 01	1.07 02	1.55 02	29.17
	450	1.51 00	3.64 00	6.65 00	1.09 01	1.69 01	2.54 01	3.73 01	5.42 01	7.80 01	1.12 02	27.55
	475	1.19 00	2.86 00	5.18 00	8.43 00	1.30 01	1.93 01	2.82 01	4.05 01	5.78 01	8.19 01	26.10
	500	9.66 −01	2.30 00	4.15 00	6.70 00	1.02 01	1.51 01	2.18 01	3.11 01	4.39 01	6.17 01	24.80
D[e]												
	550	2.28 00	5.54 00	1.02 01	1.69 01	2.65 01	4.03 01	6.01 01	8.83 01	1.29 02	1.87 02	22.54
	600	1.46 00	3.51 00	6.40 00	1.05 01	1.62 01	2.43 01	3.57 01	5.18 01	7.45 01	1.06 02	20.66
	650	1.02 00	2.44 00	4.41 00	7.13 00	1.09 01	1.61 01	2.34 01	3.34 01	4.74 01	6.67 01	19.07
	700	7.73 −01	1.83 00	3.27 00	5.23 00	7.91 00	1.16 01	1.65 01	2.33 01	3.26 01	4.53 01	17.71
	750	6.12 −01	1.43 00	2.54 00	4.02 00	6.01 00	8.68 00	1.23 01	1.71 01	2.36 01	3.23 01	16.53
	800	5.01 −01	1.16 00	2.04 00	3.20 00	4.73 00	6.77 00	9.45 00	1.30 01	1.77 01	2.40 01	15.50
	850	4.22 −01	9.73 −01	1.69 00	2.63 00	3.85 00	5.45 00	7.53 00	1.02 01	1.38 01	1.84 01	14.59
	900	3.67 −01	8.39 −01	1.45 00	2.23 00	3.24 00	4.54 00	6.22 00	8.38 00	1.12 01	1.48 01	13.78
	950	3.24 −01	7.37 −01	1.26 00	1.93 00	2.78 00	3.87 00	5.25 00	7.02 00	9.27 00	1.21 01	13.05
	1000	2.92 −01	6.59 −01	1.12 00	1.70 00	2.43 00	3.36 00	4.52 00	5.99 00	7.85 00	1.02 01	12.40
	1050	2.66 −01	5.98 −01	1.01 00	1.53 00	2.17 00	2.97 00	3.98 00	5.23 00	6.80 00	8.78 00	11.81
	1100	2.46 −01	5.50 −01	9.25 −01	1.39 00	1.96 00	2.67 00	3.55 00	4.64 00	6.00 00	7.70 00	11.27
	1150	2.31 −01	5.12 −01	8.58 −01	1.28 00	1.80 00	2.44 00	3.22 00	4.19 00	5.39 00	6.88 00	10.78
	1200	2.18 −01	4.83 −01	8.04 −01	1.20 00	1.67 00	2.25 00	2.97 00	3.84 00	4.92 00	6.25 00	10.33
	1250	2.08 −01	4.59 −01	7.61 −01	1.13 00	1.57 00	2.11 00	2.76 00	3.56 00	4.55 00	5.76 00	9.92
	1300	2.00 −01	4.39 −01	7.26 −01	1.07 00	1.49 00	1.99 00	2.60 00	3.34 00	4.25 00	5.37 00	9.54
	1350	1.93 −01	4.24 −01	6.98 −01	1.03 00	1.42 00	1.90 00	2.47 00	3.17 00	4.02 00	5.07 00	9.18
	1400	1.88 −01	4.12 −01	6.77 −01	9.92 −01	1.37 00	1.82 00	2.37 00	3.03 00	3.84 00	4.84 00	8.86
	1450	1.84 −01	4.02 −01	6.59 −01	9.65 −01	1.33 00	1.76 00	2.29 00	2.92 00	3.70 00	4.66 00	8.55
	1500	1.82 −01	3.95 −01	6.46 −01	9.44 −01	1.30 00	1.72 00	2.23 00	2.84 00	3.59 00	4.52 00	8.27
E[f]												
	1800	1.42 −01	3.08 −01	5.03 −01	7.33 −01	1.01 00	1.33 00	1.72 00	2.19 00	2.77 00	3.49 00	6.89
	1900	1.40 −01	3.03 −01	4.94 −01	7.18 −01	9.84 −01	1.30 00	1.68 00	2.14 00	2.70 00	3.40 00	6.53
	2000	1.40 −01	3.02 −01	4.91 −01	7.1[illegible] −01	9.76 −01	1.29 00	1.66 00	2.12 00	2.68 00	3.38 00	6.20
	2100	1.40 −01	3.02 −01	4.90 −01	7.11 −01	9.72 −01	1.28 00	1.65 00	2.11 00	2.67 00	3.37 00	5.90
	2200	1.42 −01	3.05 −01	4.96 −01	7.19 −01	9.82 −01	1.29 00	1.67 00	2.13 00	2.69 00	3.41 00	5.64
	2300	1.44 −01	3.11 −01	5.04 −01	7.31 −01	9.98 −01	1.32 00	1.70 00	2.16 00	2.74 00	3.48 00	5.39
	2400	1.48 −01	3.18 −01	5.16 −01	7.47 −01	1.02 00	1.34 00	1.74 00	2.21 00	2.81 00	3.57 00	5.17
	2500	1.52 −01	3.27 −01	5.30 −01	7.67 −01	1.05 00	1.38 00	1.78 00	2.28 00	2.89 00	3.69 00	4.96
	2600	1.57 −01	3.37 −01	5.46 −01	7.91 −01	1.08 00	1.42 00	1.84 00	2.35 00	3.00 00	3.82 00	4.77
	2700	1.62 −01	3.49 −01	5.65 −01	8.18 −01	1.12 00	1.47 00	1.91 00	2.44 00	3.11 00	3.98 00	4.59
	2800	1.68 −01	3.62 −01	5.86 −01	8.48 −01	1.16 00	1.53 00	1.98 00	2.54 00	3.24 00	4.16 00	4.43
	2900	1.75 −01	3.76 −01	6.09 −01	8.82 −01	1.20 00	1.59 00	2.06 00	2.65 00	3.39 00	4.36 00	4.28
	3000	1.82 −01	3.92 −01	6.34 −01	9.18 −01	1.26 00	1.66 00	2.15 00	2.76 00	3.55 00	4.58 00	4.13
	3100	1.90 −01	4.08 −01	6.62 −01	9.58 −01	1.31 00	1.73 00	2.25 00	2.89 00	3.72 00	4.81 00	4.00
	3200	1.98 −01	4.26 −01	6.91 −01	1.00 00	1.37 00	1.81 00	2.35 00	3.03 00	3.91 00	5.06 00	3.87
	3300	2.07 −01	4.46 −01	7.22 −01	1.05 00	1.43 00	1.90 00	2.47 00	3.18 00	4.10 00	5.34 00	3.76
F[g]												
	4000	1.60 −01	3.44 −01	5.57 −01	8.07 −01	1.10 00	1.46 00	1.89 00	2.43 00	3.11 00	4.01 00	3.10
	5000	2.20 −01	4.74 −01	7.69 −01	1.12 00	1.53 00	2.03 00	2.65 00	3.43 00	4.45 00	5.83 00	2.48
	6000	3.10 −01	6.68 −01	1.09 00	1.58 00	2.17 00	2.89 00	3.79 00	4.94 00	6.46 00	8.58 00	2.07

Table 11. Continued

Absorption Edge	Photon Energy E (eV)	Net Density D (Specular, 0.1 × 0.1 nA)[a] 0.2	0.4	0.6	0.8	1.0	1.2	1.4	1.6	1.8	2.0	Wavelength λ (Å)
	7000	4.32 −01	9.32 −01	1.52 00	2.21 00	3.04 00	4.06 00	5.34 00	7.00 00	9.22 00	1.24 01	1.77
	8000	5.90 −01	1.27 00	2.07 00	3.03 00	4.17 00	5.59 00	7.37 00	9.68 00	1.28 01	1.73 01	1.55
	9000	7.88 −01	1.70 00	2.77 00	4.05 00	5.59 00	7.49 00	9.90 00	1.30 01	1.73 01	2.34 01	1.38
	10000	1.03 00	2.23 00	3.63 00	5.30 00	7.33 00	9.83 00	1.30 01	1.71 01	2.28 01	3.10 01	1.24

[a] In our notation in this table, a number followed by a space and another number indicates that the first number is to be multiplied by 10 to the power of the second number; e.g., 9.82 −01 means 9.82 × 10^{-1}.
[b] Br-M_4 edge
[c] C-K edge
[d] N-K, Ag-$M_{4,5}$ edges.
[e] O-K edge
[f] Br-$L_{3,2}$ edge
[g] Ag-$L_{3,2}$ edge

Table 12. Exposure I (photons/μm^2) at Various Net Densities for Film 2497

Absorption Edge	Photon Energy E (eV)	Net Density D (Specular, 0.1 × 0.1 nA)[a] 0.2	0.4	0.6	0.8	1.0	1.2	1.4	1.6	1.8	2.0	Wavelength λ (Å)
A[b]												
	75	4.65 01	1.40 02	3.26 02	7.00 02	1.45 03	2.95 03	5.97 03	1.20 04	2.41 04	4.84 04	165.31
	100	1.06 01	3.04 01	6.77 01	1.38 02	2.69 02	5.17 02	9.81 02	1.85 03	3.49 03	6.57 03	123.98
	125	4.77 00	1.31 01	2.77 01	5.32 01	9.79 01	1.76 02	3.13 02	5.51 02	9.69 02	1.70 03	99.18
	150	2.84 00	7.48 00	1.51 01	2.76 01	4.80 01	8.15 01	1.36 02	2.26 02	3.74 02	6.15 02	82.65
	175	1.97 00	5.00 00	9.69 00	1.69 01	2.81 01	4.53 01	7.20 01	1.13 02	1.77 02	2.75 02	70.85
	200	1.48 00	3.66 00	6.85 00	1.15 01	1.84 01	2.85 01	4.34 01	6.52 01	9.17 01	1.44 02	61.99
	225	1.19 00	2.86 00	5.21 00	8.52 00	1.32 01	1.98 01	2.90 01	4.20 01	6.04 01	8.63 01	55.10
	250	9.91 −01	2.34 00	4.17 00	6.67 00	1.01 01	1.47 01	2.10 01	2.96 01	4.13 01	5.74 01	49.59
	275	8.56 −01	1.99 00	3.49 00	5.48 00	8.11 00	1.16 01	1.63 01	2.24 01	3.07 01	4.18 01	45.08
B[c]												
	300	4.61 00	1.26 01	2.66 01	5.08 01	9.29 01	1.66 02	2.94 02	5.15 02	9.01 02	1.57 03	41.33
	325	3.61 00	9.69 00	1.99 01	3.72 01	6.62 01	1.15 02	1.97 02	3.36 02	5.69 02	9.61 02	38.15
	350	2.96 00	7.78 00	1.57 01	2.85 01	4.95 01	8.37 01	1.40 02	2.31 02	3.79 02	6.22 02	35.42
	375	2.50 00	6.46 00	1.27 01	2.27 01	3.84 01	6.34 01	1.03 02	1.66 02	2.65 02	4.22 02	33.06
C[d]												
	425	2.39 00	6.15 00	1.21 01	2.15 01	3.63 01	5.96 01	9.65 01	1.55 02	2.47 02	3.91 02	29.17
	450	2.05 00	5.23 00	1.01 01	1.78 01	2.95 01	4.77 01	7.59 01	1.19 02	1.87 02	2.91 02	27.55
	475	1.82 00	4.58 00	8.75 00	1.51 01	2.46 01	3.91 01	6.11 01	9.43 01	1.45 02	2.21 02	26.10
	500	1.63 00	4.06 00	7.65 00	1.30 01	2.09 01	3.26 01	5.00 01	7.58 01	1.14 02	1.71 02	24.80
D[e]												
	550	2.55 00	6.62 00	1.31 01	2.35 01	4.01 01	6.66 01	1.09 02	1.76 02	2.84 02	4.57 02	22.54
	600	2.08 00	5.28 00	1.02 01	1.78 01	2.95 01	4.74 01	7.50 01	1.18 02	1.83 02	2.84 02	20.66
	650	1.76 00	4.37 00	8.26 00	1.40 01	2.26 01	3.54 01	5.44 01	8.26 01	1.25 02	1.87 02	19.07
	700	1.53 00	3.73 00	6.90 00	1.15 01	1.81 01	2.76 01	4.13 01	6.11 01	8.97 01	1.31 02	17.71
	750	1.37 00	3.29 00	5.98 00	9.74 00	1.50 01	2.24 01	3.27 01	4.72 01	6.76 01	9.62 01	16.53
	800	1.25 00	2.95 00	5.28 00	8.44 00	1.28 01	1.86 01	2.67 01	3.77 01	5.27 01	7.34 01	15.50
	850	1.16 00	2.69 00	4.74 00	7.46 00	1.11 01	1.59 01	2.24 01	3.10 01	4.26 01	5.81 01	14.59
	900	1.09 00	2.50 00	4.35 00	6.75 00	9.89 00	1.40 01	1.94 01	2.64 01	3.58 01	4.81 01	13.78
	950	1.03 00	2.35 00	4.04 00	6.20 00	8.97 00	1.25 01	1.71 01	2.31 01	3.09 01	4.11 01	13.05
	1000	9.90 −01	2.23 00	3.80 00	5.77 00	8.27 00	1.14 01	1.55 01	2.06 01	2.73 01	3.60 01	12.40
	1050	9.59 −01	2.15 00	3.62 00	5.45 00	7.74 00	1.06 01	1.42 01	1.8801	2.47 01	3.24 01	11.81
	1100	9.36 −01	2.08 00	3.48 00	5.21 00	7.35 00	1.00 01	1.33 01	1.75 01	2.29 01	2.98 01	11.27
	1150	9.20 −01	2.03 00	3.39 00	5.04 00	7.06 00	9.56 00	1.27 01	1.66 01	2.16 01	2.80 01	10.78
	1200	9.10 −01	2.00 00	3.32 00	4.91 00	6.86 00	9.25 00	1.22 01	1.59 01	2.06 01	2.67 01	10.33
	1250	9.06 −01	1.99 00	3.28 00	4.84 00	6.72 00	9.03 00	1.19 01	1.55 01	2.00 01	2.59 01	9.92
	1300	9.06 −01	1.98 00	3.26 00	4.79 00	6.64 00	8.90 00	1.17 01	1.52 01	1.96 01	2.54 01	9.54
	1350	9.11 −01	1.98 00	3.26 00	4.78 00	6.61 00	8.84 00	1.16 01	1.50 01	1.94 01	2.51 01	9.18
	1400	9.19 −01	2.00 00	3.27 00	4.79 00	6.62 00	8.83 00	1.16 01	1.50 01	1.93 01	2.50 01	8.86
	1450	9.31 −01	2.02 00	3.30 00	4.83 00	6.66 00	8.88 00	1.16 01	1.50 01	1.94 01	2.52 01	8.55
	1500	9.46 −01	2.05 00	3.35 00	4.89 00	6.73 00	8.97 00	1.17 01	1.52 01	1.96 01	2.54 01	8.27
E[f]												
	1800	6.87 −01	1.49 00	2.43 00	3.54 00	4.87 00	6.48 00	8.47 00	1.10 01	1.42 01	1.84 01	6.89
	1900	7.03 −01	1.52 00	2.48 00	3.61 00	4.96 00	6.61 00	8.63 00	1.12 01	1.44 01	1.88 01	6.53

continued overleaf

Table 12. Continued

Absorption Edge	Photon Energy E (eV)	Net Density D (Specular, 0.1 × 0.1 nA)[a] 0.2	0.4	0.6	0.8	1.0	1.2	1.4	1.6	1.8	2.0	Wavelength λ (Å)
	2000	7.35 −01	1.59 00	2.59 00	3.76 00	5.17 00	6.88 00	8.99 00	1.16 01	1.51 01	1.97 01	6.20
	2100	7.69 −01	1.66 00	2.70 00	3.93 00	5.40 00	7.18 00	9.38 00	1.22 01	1.58 01	2.07 01	5.90
	2200	8.12 −01	1.75 00	2.85 00	4.14 00	5.69 00	7.57 00	9.90 00	1.28 01	1.67 01	2.19 01	5.64
	2300	8.60 −01	1.85 00	3.01 00	4.39 00	6.02 00	8.02 00	1.05 01	1.36 01	1.77 01	2.33 01	5.39
	2400	9.13 −01	1.97 00	3.20 00	4.65 00	6.39 00	8.51 00	1.11 01	1.45 01	1.89 01	2.49 01	5.17
	2500	9.70 −01	2.09 00	3.40 00	4.95 00	6.80 00	9.05 00	1.19 01	1.54 01	2.01 01	2.66 01	4.96
	2600	1.03 00	2.23 00	3.62 00	5.27 00	7.24 00	9.64 00	1.26 01	1.65 01	2.15 01	2.84 01	4.77
	2700	1.10 00	2.37 00	3.86 00	5.61 00	7.71 00	1.03 01	1.35 01	1.76 01	2.30 01	3.05 01	4.59
	2800	1.17 00	2.53 00	4.11 00	5.98 00	8.22 00	1.10 01	1.44 01	1.88 01	2.46 01	3.26 01	4.43
	2900	1.25 00	2.69 00	4.38 00	6.38 00	8.77 00	1.17 01	1.54 01	2.00 01	2.63 01	3.49 01	4.28
	3000	1.33 00	2.87 00	4.67 00	6.80 00	9.35 00	1.25 01	1.64 01	2.14 01	2.81 01	3.74 01	4.13
	3100	1.42 00	3.06 00	4.98 00	7.25 00	9.97 00	1.33 01	1.75 01	2.28 01	3.00 01	4.00 01	4.00
	3200	1.51 00	3.26 00	5.30 00	7.72 00	1.06 01	1.42 01	1.86 01	2.44 01	3.20 01	4.28 01	3.87
	3300	1.61 00	3.47 00	5.64 00	8.22 00	1.13 01	1.51 01	1.99 01	2.60 01	3.42 01	4.57 01	3.76
F[d]												
	4000	1.13 00	2.44 00	3.96 00	5.77 00	7.93 00	1.06 01	1.39 01	1.82 01	2.38 01	3.18 01	3.10
	5000	1.78 00	3.83 00	6.24 00	9.09 00	1.25 01	1.68 01	2.21 01	2.89 01	3.81 01	5.12 01	2.48
	6000	2.71 00	5.84 00	9.51 00	1.39 01	1.91 01	2.56 01	3.38 01	4.44 01	5.87 01	7.91 01	2.07
	7000	3.96 00	8.54 00	1.39 01	2.03 01	2.80 01	3.75 01	4.95 01	6.51 01	8.63 01	1.17 02	1.77
	8000	5.57 00	1.20 01	1.96 01	2.86 01	3.95 01	5.29 01	6.99 01	9.20 01	1.22 02	1.65 02	1.55
	9000	7.58 00	1.64 01	2.67 01	3.90 01	5.38 01	7.21 01	9.53 01	1.26 02	1.67 02	2.26 02	1.38
	10000	1.00 01	2.17 01	3.54 01	5.16 01	7.13 01	9.56 01	1.26 02	1.66 02	2.21 02	3.00 02	1.24

[a] In our notation in this table, a number followed by a space and another number indicates that the first number is to be multiplied by 10 raised to the power of the second number; e.g., 9.13 −01 means 9.13×10^{-1}.
[b] Br-M_4 edge.
[c] C-K edge.
[d] N-K, Ag-$M_{4,5}$ edges.
[e] O-K edge.
[f] Br-$L_{3,2}$ edge.
[g] Ag-$L_{3,2}$ edge.

Table 13. Exposure I (photons/μm²) at Various Net Densities for Film 2492

Absorption Edge	Photon Energy E (eV)	Net Density D (Specular, 0.1 × 0.1 nA)[a] 0.2	0.4	0.6	0.8	1.0	1.2	1.4	1.6	1.8	2.0	Wavelength λ (Å)
A[b]												
	75	4.11 01	1.12 02	2.35 02	4.46 02	8.11 02	1.44 03	2.53 03	4.41 03	7.65 03	1.32 04	165.31
	100	9.42 00	2.49 01	5.03 01	9.19 01	1.60 02	2.72 02	4.56 02	7.58 02	1.25 03	2.06 03	123.98
	125	4.29 00	1.10 01	2.13 01	3.73 01	6.22 01	1.01 02	1.61 02	2.53 02	3.97 02	6.20 02	99.18
	150	2.57 00	6.36 00	1.20 01	2.02 01	3.23 01	5.02 01	7.66 01	1.15 02	1.73 02	2.57 02	82.65
	175	1.80 00	4.32 00	7.88 00	1.29 01	1.99 01	2.98 01	4.37 01	6.33 01	9.08 01	1.30 02	70.85
	200	1.36 00	3.21 00	5.70 00	9.06 00	1.36 01	1.98 01	2.81 01	3.93 01	5.45 01	7.51 01	61.99
	225	1.10 00	2.53 00	4.41 00	6.87 00	1.01 01	1.43 01	1.98 01	2.70 01	3.64 01	4.87 01	55.10
	250	9.20 −01	2.09 00	3.58 00	5.48 00	7.90 00	1.10 01	1.49 01	1.99 01	2.63 01	3.44 01	49.59
	275	7.97 −01	1.79 00	3.03 00	4.57 00	6.49 00	8.90 00	1.19 01	1.56 01	2.03 01	2.62 01	45.08
B[c]												
	300	4.15 00	1.06 01	2.05 01	3.57 01	5.93 01	9.58 01	1.52 02	2.39 02	3.73 02	5.80 02	41.33
	325	3.27 00	8.18 00	1.56 01	2.67 01	4.35 01	6.87 01	1.07 02	1.64 02	2.50 02	3.80 02	38.15
	350	2.68 00	6.63 00	1.24 01	2.09 01	3.34 01	5.18 01	7.88 01	1.18 02	1.77 02	2.62 02	35.42
	375	2.28 00	5.55 00	1.02 01	1.70 01	2.66 01	4.05 01	6.04 01	8.90 01	1.30 02	1.89 02	33.06
C[d]												
	425	2.17 00	5.29 00	9.74 00	1.61 01	2.52 01	3.83 01	5.69 01	8.36 01	1.22 02	1.77 02	29.17
	450	1.88 00	4.52 00	8.24 00	1.35 01	2.09 01	3.13 01	4.59 01	6.66 01	9.57 01	1.37 02	27.55
	475	1.67 00	3.98 00	7.18 00	1.16 01	1.77 01	2.63 01	3.80 01	5.44 01	7.70 01	1.08 02	26.10
	500	1.50 00	3.54 00	6.33 00	1.01 01	1.53 01	2.23 01	3.20 01	4.50 01	6.29 01	8.72 01	24.80
D[e]												
	550	2.32 00	5.67 00	1.05 01	1.75 01	2.76 01	4.22 01	6.32 01	9.36 01	1.38 02	2.01 02	22.54
	600	1.90 00	4.57 00	8.32 00	1.36 01	2.09 01	3.13 01	4.58 01	6.61 01	9.46 01	1.35 02	20.66
	650	1.61 00	3.82 00	6.83 00	1.09 01	1.65 01	2.42 01	3.47 01	4.89 01	6.84 01	9.51 01	19.07
	700	1.41 00	3.28 00	5.78 00	9.12 00	1.36 01	1.95 01	2.74 01	3.79 01	5.19 01	7.06 01	17.71
	750	1.27 00	2.92 00	5.07 00	7.87 00	1.15 01	1.63 01	2.25 01	3.05 01	4.11 01	5.48 01	16.53
	800	1.16 00	2.64 00	4.53 00	6.93 00	1.00 01	1.39 01	1.89 01	2.53 01	3.34 01	4.38 01	15.50

Table 13. Continued

Absorption Edge	Photon Energy E (eV)	Net Density D (Specular, 0.1 × 0.1 nA)[a] 0.2	0.4	0.6	0.8	1.0	1.2	1.4	1.6	1.8	2.0	Wavelength λ (Å)
	850	1.08 00	2.42 00	4.11 00	6.21 00	8.85 00	1.21 01	1.63 01	2.15 01	2.80 01	3.62 01	14.59
	900	1.01 00	2.26 00	3.80 00	5.69 00	8.01 00	1.09 01	1.44 01	1.88 01	2.42 01	3.09 01	13.78
	950	9.66 −01	2.14 00	3.55 00	5.28 00	7.37 00	9.91 00	1.30 01	1.68 01	2.14 01	2.71 01	13.05
	1000	9.27 −01	2.04 00	3.36 00	4.95 00	6.86 00	9.15 00	1.19 01	1.53 01	1.93 01	2.42 01	12.40
	1050	8.99 −01	1.96 00	3.22 00	4.71 00	6.49 00	8.59 00	1.11 01	1.41 01	1.78 01	2.21 01	11.81
	1100	8.79 −01	1.91 00	3.11 00	4.53 00	6.20 00	8.17 00	1.05 01	1.33 01	1.66 01	2.06 01	11.27
	1150	8.65 −01	1.87 00	3.04 00	4.40 00	6.00 00	7.87 00	1.01 01	1.27 01	1.58 01	1.95 01	10.78
	1200	8.57 −01	1.85 00	2.99 00	4.31 00	5.85 00	7.65 00	9.76 00	1.22 01	1.52 01	1.87 01	10.33
	1250	8.54 −01	1.83 00	2.96 00	4.26 00	5.76 00	7.51 00	9.56 00	1.20 01	1.48 01	1.82 01	9.92
	1300	8.55 −01	1.83 00	2.95 00	4.23 00	5.71 00	7.43 00	9.43 00	1.18 01	1.45 01	1.79 01	9.54
	1350	8.59 −01	1.84 00	2.95 00	4.23 00	5.69 00	7.39 00	9.37 00	1.17 01	1.44 01	1.77 01	9.18
	1400	8.67 −01	1.85 00	2.97 00	4.25 00	5.71 00	7.40 00	9.37 00	1.17 01	1.44 01	1.76 01	8.86
	1450	8.79 −01	1.87 00	3.00 00	4.28 00	5.76 00	7.45 00	9.42 00	1.17 01	1.45 01	1.77 01	8.55
	1500	8.94 −01	1.90 00	3.04 00	4.34 00	5.83 00	7.54 00	9.53 00	1.18 01	1.46 01	1.79 01	8.27
E[f]												
	1800	6.49 −01	1.38 00	2.21 00	3.15 00	4.22 00	5.45 00	6.89 00	8.56 00	1.05 01	1.29 01	6.89
	1900	6.64 −01	1.41 00	2.25 00	3.21 00	4.30 00	5.56 00	7.02 00	8.72 00	1.07 01	1.32 01	6.53
	2000	6.95 −01	1.47 00	2.35 00	3.35 00	4.49 00	5.80 00	7.31 00	9.09 00	1.12 01	1.37 01	6.20
	2100	7.27 −01	1.54 00	2.46 00	3.50 00	4.69 00	6.05 00	7.63 00	9.48 00	1.17 01	1.43 01	5.90
	2200	7.68 −01	1.63 00	2.60 00	3.69 00	4.94 00	6.38 00	8.05 00	1.00 01	1.23 01	1.51 01	5.64
	2300	8.13 −01	1.72 00	2.75 00	3.91 00	5.23 00	6.75 00	8.52 00	1.06 01	1.31 01	1.60 01	5.39
	2400	8.63 −01	1.83 00	2.91 00	4.15 00	5.55 00	7.16 00	9.04 00	1.12 01	1.39 01	1.70 01	5.17
	2500	9.18 −01	1.94 00	3.10 00	4.41 00	5.90 00	7.62 00	9.61 00	1.20 01	1.48 01	1.81 01	4.96
	2600	9.77 −01	2.07 00	3.30 00	4.69 00	6.28 00	8.11 00	1.02 01	1.27 01	1.57 01	1.94 01	4.77
	2700	1.04 00	2.20 00	3.51 00	5.00 00	6.69 00	8.64 00	1.09 01	1.36 01	1.68 01	2.07 01	4.59
	2800	1.11 00	2.35 00	3.74 00	5.33 00	7.13 00	9.21 00	1.16 01	1.45 01	1.79 01	2.21 01	4.43
	2900	1.18 00	2.50 00	3.99 00	5.68 00	7.60 00	9.82 00	1.24 01	1.55 01	1.91 01	2.36 01	4.28
	3000	1.26 00	2.67 00	4.25 00	6.05 00	8.11 00	1.05 01	1.32 01	1.65 01	2.04 01	2.52 01	4.13
	3100	1.34 00	2.84 00	4.53 00	6.45 00	8.64 00	1.12 01	1.41 01	1.76 01	2.18 01	2.69 01	4.00
	3200	1.43 00	3.03 00	4.83 00	6.87 00	9.20 00	1.19 01	1.50 01	1.88 01	2.32 01	2.87 01	3.87
	3300	1.52 00	3.22 00	5.14 00	7.31 00	9.80 00	1.27 01	1.60 01	2.00 01	2.47 01	3.05 01	3.76
F[g]												
	4000	1.07 00	2.26 00	3.61 00	5.13 00	6.88 00	8.89 00	1.12 01	1.40 01	1.73 01	2.14 01	3.10
	5000	1.68 00	3.56 00	5.68 00	8.09 00	1.08 01	1.40 01	1.78 01	2.22 01	2.75 01	3.40 01	2.48
	6000	2.56 00	5.42 00	8.65 00	1.23 01	1.65 01	2.14 01	2.71 01	3.39 01	4.21 01	5.21 01	2.07
	7000	3.74 00	7.93 00	1.27 01	1.80 01	2.42 01	3.13 01	3.97 01	4.97 01	6.17 01	7.65 01	1.77
	8000	5.26 00	1.12 01	1.78 01	2.54 01	3.41 01	4.42 01	5.60 01	7.00 01	8.70 01	1.08 02	1.55
	9000	7.17 00	1.52 01	2.43 01	3.46 01	4.65 01	6.02 01	7.63 01	9.55 01	1.19 02	1.47 02	1.38
	10000	9.50 00	2.01 01	3.22 01	4.58 01	6.15 01	7.97 01	1.01 02	1.27 02	1.57 02	1.95 02	1.24

[a] In our notation in this table, a number followed by a space and another number indicates that the first number is to be multiplied by 10 raised to the power of the second number; e.g., 7.27 −01 means 7.27×10^{-1}.

[b] Br-M_4 edge.

[c] C-K edge.

[d] N-K, Ag-$M_{4,5}$ edge

[e] O-K edge

[f] Br-$L_{3,2}$ edge

[g] Ag-$L_{3,2}$ edge

Table 14. Exposure I (photons/μm^2) at Various Net Densities for Film 2495

Absorption Edge	Photon Energy E (eV)	Net Density D (specular, 0.1 × 0.1 nA)[a]										Wavelength λ (Å)
		0.2	0.4	0.6	0.8	1.0	1.2	1.4	1.6	1.8	2.0	
A[b]												
	75	1.65 01	4.51 01	9.46 01	1.80 02	3.28 02	5.84 02	1.03 03	1.79 03	3.11 03	5.40 03	165.31
	100	3.83 00	1.02 01	2.06 01	3.78 01	6.62 01	1.13 02	1.90 02	3.18 02	5.28 02	8.76 02	123.98
	125	1.78 00	4.56 00	8.93 00	1.58 01	2.65 01	4.34 01	6.98 01	1.11 02	1.76 02	2.78 02	99.18
	150	1.09 00	2.74 00	5.20 00	8.91 00	1.45 01	2.28 01	3.54 01	5.43 01	8.26 01	1.25 02	82.65
	175	7.89 −01	1.93 00	3.58 00	5.96 00	9.40 00	1.44 01	2.16 01	3.20 01	4.70 01	6.87 01	70.85
	200	6.21 −01	1.49 00	2.71 00	4.41 00	6.80 00	1.01 01	1.48 01	2.14 01	3.05 01	4.34 01	61.99
	225	5.20 −01	1.23 00	2.20 00	3.52 00	5.31 00	7.77 00	1.11 01	1.57 01	2.19 01	3.04 01	55.10
	250	4.53 −01	1.06 00	1.87 00	2.94 00	4.38 00	6.30 00	8.87 00	1.23 01	1.69 01	2.30 01	49.59
	275	4.07 −01	9.42 −01	1.64 00	2.56 00	3.77 00	5.35 00	7.43 00	1.02 01	1.37 01	1.85 01	45.08
B[c]												
	300	1.72 00	4.40 00	8.58 00	1.51 01	2.53 01	4.13 01	6.62 01	1.05 02	1.66 02	2.61 02	41.33
	325	1.36 00	3.45 00	6.63 00	1.15 01	1.89 01	3.02 01	4.75 01	7.39 01	1.14 02	1.76 02	38.15
	350	1.13 00	2.83 00	5.36 00	9.15 00	1.48 01	2.33 01	3.59 01	5.48 01	8.30 01	1.25 02	35.42
	375	9.75 −01	2.40 00	4.49 00	7.56 00	1.20 01	1.86 01	2.82 01	4.23 01	6.29 01	9.31 01	33.06
C[d]												
	425	9.35 −01	2.30 00	4.30 00	7.22 00	1.15 01	1.77 01	2.69 01	4.02 01	5.98 01	8.83 01	29.17
	450	8.19 −01	2.00 00	3.72 00	6.19 00	9.76 00	1.49 01	2.24 01	3.32 01	4.88 01	7.13 01	27.55
	475	7.38 −01	1.79 00	3.29 00	5.43 00	8.48 00	1.28 01	1.90 01	2.78 01	4.04 01	5.84 01	26.10
	500	6.74 −01	1.62 00	2.95 00	4.83 00	7.46 00	1.12 01	1.64 01	2.37 01	3.40 01	4.85 01	24.80
D[e]	550	9.92 −01	2.45 00	4.61 00	7.78 00	1.25 01	1.94 01	2.95 01	4.45 01	6.66 01	9.92 01	22.54
	600	8.29 −01	2.02 00	3.73 00	6.20 00	9.74 00	1.48 01	2.21 01	3.27 01	4.78 01	6.95 01	20.66
	650	7.71 −01	1.72 00	3.14 00	5.13 00	7.92 00	1.18 01	1.74 01	2.51 01	3.60 01	5.13 01	19.07
	700	6.38 −01	1.52 00	2.72 00	4.39 00	6.68 00	9.83 00	1.42 01	2.01 01	2.83 01	3.97 01	17.71
	750	5.85 −01	1.37 00	2.44 00	3.87 00	5.80 00	8.41 00	1.19 01	1.67 01	2.30 01	3.16 01	16.53
	800	5.45 −01	1.27 00	2.22 00	3.48 00	5.14 00	7.34 00	1.02 01	1.41 01	1.92 01	2.59 01	15.50
	850	5.14 −01	1.18 00	2.05 00	3.17 00	4.63 00	6.52 00	8.97 00	1.22 01	1.63 01	2.17 01	14.59
	900	4.91 −01	1.12 00	1.92 00	2.94 00	4.24 00	5.90 00	8.03 00	1.07 01	1.42 01	1.87 01	13.78
	950	4.73 −01	1.07 00	1.81 00	2.75 00	3.93 00	5.42 00	7.29 00	9.64 00	1.26 01	1.63 01	13.05
	1000	4.59 −01	1.03 00	1.73 00	2.60 00	3.68 00	5.02 00	6.69 00	8.76 00	1.13 01	1.45 01	12.40
	1050	4.48 −01	9.95 −01	1.66 00	2.48 00	3.49 00	4.71 00	6.22 00	8.07 00	1.04 01	1.32 01	11.81
	1100	4.40 −01	9.71 −01	1.61 00	2.39 00	3.33 00	4.47 00	5.85 00	7.53 00	9.58 00	1.21 01	11.27
	1150	4.34 −01	9.52 −01	1.57 00	2.31 00	3.20 00	4.27 00	5.56 00	7.11 00	8.98 00	1.13 01	10.78
	1200	4.30 −01	9.39 −01	1.54 00	2.26 00	3.11 00	4.12 00	5.33 00	6.78 00	8.52 00	1.08 01	10.33
	1250	4.28 −01	9.30 −01	1.52 00	2.21 00	3.04 00	4.01 00	5.16 00	6.53 00	8.17 00	1.01 01	9.92
	1300	4.27 −01	9.24 −01	1.51 00	2.18 00	2.98 00	3.92 00	5.03 00	6.34 00	7.90 00	9.77 00	9.54
	1350	4.28 −01	9.23 −01	1.50 00	2.17 00	2.95 00	3.86 00	4.93 00	6.20 00	7.70 00	9.50 00	9.18
	1400	4.30 −01	9.24 −01	1.50 00	2.16 00	2.92 00	3.82 00	4.87 00	6.11 00	7.57 00	9.32 00	8.86
	1450	4.33 −01	9.29 −01	1.50 00	2.16 00	2.92 00	3.80 00	4.84 00	6.05 00	7.49 00	9.20 00	8.55
	1500	4.37 −01	9.37 −01	1.51 00	2.17 00	2.93 00	3.80 00	4.83 00	6.03 00	7.45 00	9.15 00	8.27
E[f]												
	1800	3.44 −01	7.39 −01	1.19 00	1.72 00	2.32 00	3.02 00	3.84 00	4.81 00	5.95 00	7.31 00	6.89
	1900	3.49 −01	7.47 −01	1.20 00	1.72 00	2.33 00	3.03 00	3.84 00	4.79 00	5.92 00	7.26 00	6.53
	2000	3.59 −01	7.67 −01	1.23 00	1.76 00	2.37 00	3.08 00	3.90 00	4.86 00	5.99 00	7.34 00	6.20
	2100	3.70 −01	7.88 −01	1.26 00	1.80 00	2.43 00	3.14 00	3.97 00	4.94 00	6.09 00	7.46 00	5.90
	2200	3.84 −01	8.18 −01	1.31 00	1.87 00	2.51 00	3.24 00	4.09 00	5.09 00	6.27 00	7.67 00	5.64
	2300	4.01 −01	8.52 −01	1.36 00	1.94 00	2.60 00	3.36 00	4.24 00	5.28 00	6.49 00	7.95 00	5.39
	2400	4.19 −01	8.90 −01	1.42 00	2.02 00	2.71 00	3.50 00	4.42 00	5.49 00	6.76 00	8.28 00	5.17
	2500	4.40 −01	9.33 −01	1.49 00	2.12 00	2.84 00	3.66 00	4.62 00	5.74 00	7.07 00	8.66 00	4.96
	2600	4.62 −01	9.80 −01	1.56 00	2.22 00	2.98 00	3.84 00	4.85 00	6.02 00	7.42 00	9.09 00	4.77
	2700	4.87 −01	1.03 00	1.64 00	2.34 00	3.13 00	4.04 00	5.10 00	6.33 00	7.80 00	9.56 00	4.59
	2800	5.13 −01	1.09 00	1.73 00	2.46 00	3.30 00	4.26 00	5.37 00	6.67 00	8.22 00	1.01 01	4.43
	2900	5.41 −01	1.15 00	1.83 00	2.60 00	3.48 00	4.49 00	5.66 00	7.04 00	8.67 00	1.06 01	4.28
	3000	5.71 −01	1.21 00	1.93 00	2.74 00	3.67 00	4.74 00	5.98 00	7.43 00	9.16 00	1.13 01	4.13
	3100	6.04 −01	1.28 00	2.04 00	2.90 00	3.88 00	5.01 00	6.32 00	7.86 00	9.69 00	1.19 01	4.00
	3200	6.38 −01	1.35 00	2.15 00	3.06 00	4.10 00	5.29 00	6.67 00	8.30 00	1.02 01	1.26 01	3.87
	3300	6.74 −01	1.43 00	2.27 00	3.23 00	4.33 00	5.59 00	7.06 00	8.78 00	1.08 01	1.33 01	3.76

Table 14. Continued

Absorption Edge	Photon Energy E (eV)	Net Density D (specular, 0.1 × 0.1 nA)[a] 0.2	0.4	0.6	0.8	1.0	1.2	1.4	1.6	1.8	2.0	Wavelength λ (Å)
F[e]												
	4000	4.97 −01	1.05 00	1.68 00	2.39 00	3.19 00	4.12 00	5.20 00	6.46 00	7.96 00	9.78 00	3.10
	5000	7.37 −01	1.56 00	2.49 00	3.54 00	4.74 00	6.12 00	7.73 00	9.63 00	1.19 01	1.47 01	2.48
	6000	1.09 00	2.30 00	3.67 00	5.22 00	7.00 00	9.05 00	1.14 01	1.43 01	1.77 01	2.18 01	2.07
	7000	1.56 00	3.30 00	5.27 00	7.50 00	1.01 01	1.30 01	1.65 01	2.06 01	2.55 01	3.15 01	1.77
	8000	2.17 00	4.59 00	7.33 00	1.04 01	1.40 01	1.81 01	2.29 01	2.87 01	3.56 01	4.41 01	1.55
	9000	2.93 00	6.21 00	9.91 00	1.41 01	1.89 01	2.45 01	3.11 01	3.88 01	4.82 01	5.98 01	1.38
	10000	3.86 00	8.18 00	1.31 01	1.86 01	2.50 01	3.23 01	4.10 01	5.13 01	6.37 01	7.90 01	1.24

[a] In our notation in this table, a number followed by a space and another number indicates that the first number is to be multiplied by 10 raised to the power of the second number, e.g., 3.84 −01 means 3.84 × 10^{-1}.
[b] Br M_{α} edge
[c] C K edge
[d] N K, Ag $M_{\alpha,\beta}$ edges
[e] O K edge
[f] Br $L_{\beta 2}$ edge
[g] Ag L_{γ_1} edge

ACKNOWLEDGMENTS

We gratefully acknowledge the invaluable assistance in this program of Priscilla Piano. Our thanks also to Robert Anwyl of Eastman-Kodak Company, Rochester, New York, for his help in the initial planning of this study and to Al Widman of the Sandia National Laboratory for his help in the microdensitometer measurements. This program in low-energy x ray physics and technology is supported by the U.S. Air Force Office of Scientific Research under grant no. 84-0001 and supplementally by the U.S. Department of Energy under contract no. DE-AS08-83DP40181.

REFERENCES

1. R. F. Benjamin, P. B. Lyons, and R. H. Day, "X-ray calibration of RAR 2490 film for application to laser plasma experiments," Appl. Opt. **16**, 393–397 (1977).
2. L. N. Koppel, "Sub kilovolt x-ray calibration of photographic film," in *Advances in X-Ray Analysis*, W. L. Pickels, C. S. Barrett, J. Newkirk, and C. O. Ruud, eds. (Plenum, New York, 1975), Vol. 18, pp. 146–153.
3. L. N. Koppel, "X ray calibration of film types SB-5 and RAR 2492 in the 1.5–8 keV region," ARACOR Document No. TR-112-08-02 (Advanced Research and Applications Corp., Sunnyvale, Calif., March 1982).
4. C. M. Dozier, D. B. Brown, L. S. Birks, P. B. Lyons, and R. F. Benjamin, "Sensitivity of x-ray film. II. Kodak NO SCREEN film in the 1–100 keV region," J. Appl. Phys. **47**, 3732–3739 (1976).
5. B. L. Henke, S. L. Kwok, J. Y. Uejio, H. T. Yamada, and G. C. Young, "Low-energy x ray response of photographic films. I. Mathematical models," J. Opt. Soc. Am. B **1**, 818–827 (1984).
6. B. L. Henke, H. T. Yamada, and T. J. Tanaka, "Pulsed plasma source spectrometry in the 80–8000 eV x-ray region," Rev. Sci. Instrum. **54**, 1311–1330 (1983).
7. B. L. Henke and M. A. Tester, "Techniques of low-energy x-ray spectroscopy (0.1 to 2 keV region)," in *Advances in X-Ray Analysis*, W. L. Pickels, C. S. Barrett, J. Newkirk, and C. O. Rudd, eds. (Plenum, New York, 1975), Vol. 18, pp. 76–106.
8. B. L. Henke, P. Lee, T. J. Tanaka, R. L. Shimabukuro, and B. K. Fujikawa, "Low-energy x-ray interaction coefficients: photoabsorption, scattering, and reflection. E = 100–2000 eV, Z = 1–94," At. Data Nucl. Data Tables **27**(1), 1–144 (1982).
9. Linear zone plates kindly loaned to us by N. Ceglio's group, Lawrence Livermore National Laboratory, Livermore, California 94550.
10. R. Ernst, Lawrence Livermore National Laboratory, Livermore, California 94550 (personal communication).
11. B. H. Carroll, G. C. Higgins and T. H. James, *Introduction to Photographic Theory, The Silver Halide Process* (Wiley, New York, 1980), pp. 19–27; C. E. K. Mees and T. H. James, eds., *The Theory of the Photographic Process*, 3rd ed. (Macmillan, New York, 1966); J. G. Streiffert, "Callier Q of various motion picture emulsions," J. Soc. Motion Pict. Eng. **49**, 506–522 (1947); C. Tuttle, "The relation between diffuse and specular density," J. Opt. Soc. Am. **12**, 559–565 (1926).
12. J. P. Stoering and A. Toor, "X-ray calibration of Kodak NO SCREEN, Type-AA and Type-M in the 1–4.5 keV region," UCID 16775 (Lawrence Livermore National Laboratory; Livermore, Calif., 1975); D. B. Brown, J. W. Criss and L. S. Birks, "Sensitivity of x-ray films. I. A model for sensitivity in the 1–100 keV region," J. Appl. Phys. **47**, 3722–3731 (1976).
13. J. G. Streiffert, "Callier Q of various motion picture emulsions," J. Soc. Motion Pict. Eng. **49**, 506–522 (1947).
14. C. E. K. Mees and T. H. James, eds., *The Theory of the Photographic Process*, 3rd ed. (Macmillan, New York, 1966), pp. 190–191.

Reprinted from Journal of the Optical Society of America B, Vol. 3, page 1540, November 1986
Copyright © 1986 by the Optical Society of America and reprinted by permission of the copyright owner.

10

High-energy x-ray response of photographic films: models and measurement

B. L. Henke and J. Y. Uejio

Lawrence Berkeley Laboratory, University of California, Berkeley, California 94720

G. F. Stone and C. H. Dittmore

Lawrence Livermore National Laboratory, Livermore, California 94550

F. G. Fujiwara

University of Hawaii, Honolulu, Hawaii 96822

Received May 12, 1986; accepted June 23, 1986

A detailed characterization has been established for the new, high-sensitivity double-emulsion Kodak Direct Exposure Film (DEF). The experimental data base consisted of density-versus-exposure measurements that were duplicated at several laboratories for x radiations in the 1000–10,000-eV region. The absorption and geometric properties of the film were determined, which, along with the density-exposure data, permitted the application of a relatively simple analytical model description for the optical density, D, as a function of the intensity, I (photons/μm^2), the photon energy, E (eV), and the angle of incidence, θ, of the exposing radiation. A detailed table is presented for the I values corresponding to optical densities in the 0.2–2.0 range and to photon energies, E (eV), in the 1000–10,000-eV region. Experimentally derived conversion relations have been obtained that allow the density values to be expressed as either diffuse or specular. Also presented here is a similar characterization of the complementary, single-emulsion x-ray film, Kodak SB-5 (or 392). For the 1000–10,000-eV region this x-ray film is appreciably less sensitive but has higher resolution.

1. INTRODUCTION

There is a considerable need at this time for absolute, high-sensitivity, position-sensitive x-ray detection for imaging and for spectroscopic analysis in the higher-x-ray photon-energy region of 1000–10,000 eV. An important example of such a need is that for the absolute x-ray diagnostics of high-temperature plasmas that are involved in fusion energy and x-ray laser research. For many such applications, position-sensitive x-ray detection with photographic films can be exceptionally simple and effective.[1]

In companion works[2,3] we recently reported the development of effective two-parameter analytical equations for the optical density, D, that is generated in thick and thin single-emulsion films by x radiation in the 100–1000-eV region. These equations are functions of the exposure, I (photons/μm^2), the photon energy, E (eV), and the angle of incidence, θ. We have applied these model relations to obtain detailed characterizations for the response of the Kodak films that are currently used for position-sensitive detection in the low-energy x-ray region, viz., Kodak 101, RAR 2492, 2495, and 2497, and SB-392. In the present work, we extend this analytical modeling to obtain the detailed response characteristics of the double-emulsion films and specifically of the Kodak Direct Exposure Film (DEF), which has been designed for high sensitivity at the higher photon energies (1000–10,000 eV) as compared to that of its predecessor, the Kodak No-Screen double-emulsion film, which is no longer manufactured. We have also extended by a similar procedure the characterization of the complementary, single-emulsion x-ray film, the Kodak SB-5 (or 392) for this higher-photon-energy region.

2. ANALYTICAL MODELS FOR PHOTOGRAPHIC FILM RESPONSE

In Ref. 2 we developed a phenomenological model for the photographic response of thick emulsions that implicitly expresses the photon-energy dependence through the linear absorption coefficients for the x-ray absorption within a supercoat, for the heterogeneous absorption within the emulsion, and for the absorption within a AgBr film grain. This model led to a "universal" function, ϕ, for the density, D, as a function of exposure, I, defined as

$$\alpha D = \phi(\beta I), \tag{1}$$

where α and β are the photon-energy-dependent factors given by

$$\alpha = \mu'/\sin\theta \tag{2}$$

and

$$\beta = [1 - \exp(-\mu_1 d)]\exp(-\mu_0 t_0/\sin\theta). \tag{3}$$

Note that in Ref. 2, α was defined as $(\sin\theta/\mu' + d_0)^{-1}$, where d_0 is a measure of the thickness of the first layer of AgBr grains that may be the primary absorption layer for the low photon energies (<1000 eV). This parameter, d_0, can be neglected for the higher photon energies of interest here.

These "universalizing" factors, α and β, are expressed in

0740-3224/86/111540-11$02.00 © 1986 Optical Society of America

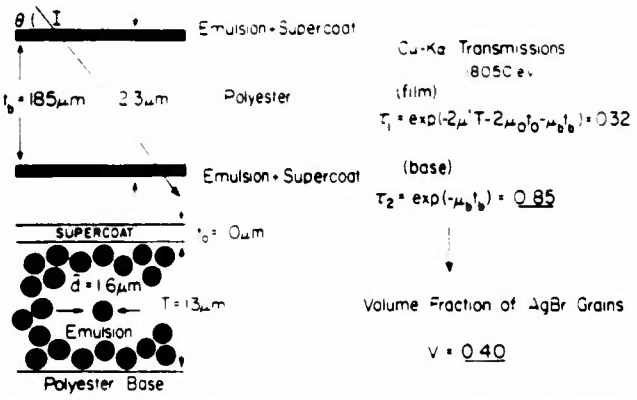


Fig. 1. Properties of the double-emulsion film, DEF. The micrometered total thickness and the transmission for Cu–Kα (8050 eV) of the film and of the polyester base yield the indicated values of the emulsion and base thicknesses, T and t_b, and of the volume fraction of the AgBr grains, V. (For the base transmission measurements, the emulsions are dissolved away by using a bleach solution.) The estimate of the film grain size, d, is obtained from SEM film cross-section photos as shown in Fig. 2. The supercoat thickness, t_0, is sensitively determined by model equation fitting of the low-energy x-ray exposure data.

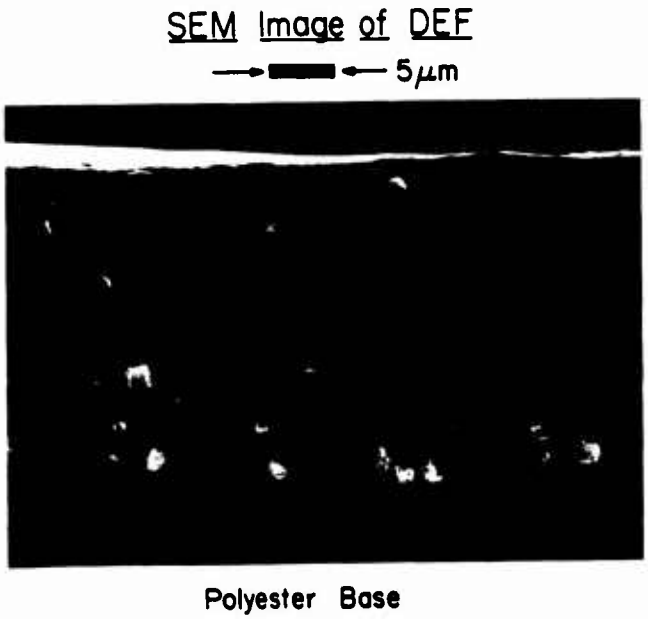


Fig. 2. Cross section of a DEF emulsion, imaged by a SEM. Sample sections were obtained by breaking liquid-nitrogen-frozen pieces of film. The average grain size was estimated from such photos by the measurement of the outermost embedded grains.

terms of the energy-dependent linear absorption coefficients, μ_0, μ_1, and μ', for, respectively, the supercoat, the film grain material (AgBr), and the heterogeneous emulsion of these grains within gelatin. The geometric parameters that have been chosen here to define an emulsion are the supercoat thickness, t_0, the emulsion thickness, T, and the effective film grain thickness, d. The angle of incidence, θ, of the exposing radiation is measured from the film plane.

An example of the predicted universal curve, $aD = \phi(bI)$, will be presented below using measured density-versus-exposure (D–I) data for the DEF film. It was also predicted and demonstrated (see Refs. 2 and 3) that this universal curve may be efficiently fitted by a two-parameter equation for the *thick (completely absorbing) emulsion response*, viz.,

$$aD = a \ln(1 + b\beta I). \tag{4}$$

The parameters a and b may be determined by least-squares fitting of the experimentally determined and universally plotted data.

For the corresponding response of a thin (incompletely absorbing) emulsion of thickness, T, we must subtract from the optical density, D, given by Eq. (4) for the infinitely thick emulsion, the contribution to the density that is generated within the layers below a depth, T [where the exposing intensity at the emulsion's top surface has been reduced by the factor $\exp(-\mu' T/\sin\theta)$]. This consideration leads immediately to the simple modification of Eq. (4) for the *thin-emulsion response*, viz.,

$$aD = a \ln\left[\frac{1 + b\beta I}{1 + b\beta I \exp(-\mu' T/\sin\theta)}\right]. \tag{5}$$

We now extend this model description for the double-emulsion film. In Figs. 1 and 2 we describe the properties of a double-emulsion film (presented here for the new DEF film). For such a film with photon energies above about 4000 eV, a significant amount of additional optical density will be generated within the second emulsion. This second thin emulsion section will contribute a density that may be predicted by an expression like that described by the model relation (5) for a thin emulsion but with two simple modifications: We replace in Eq. (5) the term for the supercoat transmission, $\exp(-\mu_0 t_0/\sin\theta)$ (in the β factor) by $\exp(-\mu_b t_b/\sin\theta)$, with μ_b and t_b the linear absorption coefficient and the thickness of the polyester base, and we replace the incident intensity, I, by its reduced value at the top surface of the polyester base, $I\exp(-\mu_0 t_0 - \mu' T)$. In terms of our originally defined value of β given in Eq. (3), the additional density, ΔD, within the second emulsion may then be deduced directly from Eq. (5) to be

$$a\Delta D = a \ln\left\{\frac{1 + b\beta I \exp[(-\mu_b t_b - \mu' T)/\sin\theta]}{1 + b\beta I \exp[(-\mu_b t_b - 2\mu' T)/\sin\theta]}\right\}. \tag{6}$$

In Ref. 2 we have discussed the justification for a linear addition of the optical density contributions of successive layers when the total optical density is within the usual range of density measurements. With the same assumption, we then add the ΔD density given by Eq. (6) to that of the upper thin-emulsion contribution given by (5) to obtain the expression for the *double-emulsion response*, viz.,

$$aD = a \ln\left(\left\{\frac{1 + b\beta I}{1 + b\beta I \exp[(-\mu' T)/\sin\theta]}\right\} \times \left\{\frac{1 + b\beta I \exp[(-\mu_b t_b - \mu' T)/\sin\theta]}{1 + b\beta I \exp[(-\mu_b t_b - 2\mu' T)/\sin\theta]}\right\}\right). \tag{7}$$

It should be noted that the fitting parameters a and b, appearing in Eqs. (4)–(7) for the thick, thin, and double-emulsion films, are those initially suggested for the universal curve fitting and thus for the thick-emulsion, low-energy-photon-absorption regime. The same values of a and b then reappear, as described above, in the subsequently developed expressions for the thin and double-emulsion, higher-energy-photon-absorption regime, with the important assump-

tion that these parameters will be independent of photon energy. For the photon energies in the 100–10,000-eV region this assumption is considered to be a good one because (1) these photon energies are sufficiently high to ensure that a film grain is rendered developable by a single-photon absorption and (2) these photon energies are sufficiently low to ensure that any additional excitation of grains by high-energy photoelectrons is negligible.

3. CHARACTERIZATION OF THE KODAK DIRECT EXPOSURE FILM

We would like to develop here a detailed characterization of the Kodak DEF double-emulsion film by using the model relations presented above and experimental (D versus I) data that have been obtained independently at four laboratories for the 1000–10,000-eV region. In all these investigations, the films were processed with conventional x-ray developers for microdensitometric applications. These studies may be described as follows:

(1) Phillips and Phillips[4]; Cu-Kα (8050 eV); developed with agitation in GBX for 3 min at 68°F and densitometered with an Optronics-1000 using matched influx and efflux optics of 0.25 N.A.,

(2) Rockett *et al.*[5]; Cu-Lα (930 eV), Al-Kα (1490 eV), Si-Kα (1740 eV), Ti-Kα, β (4510–4930 eV), and Co-Kα (6930 eV); developed with agitation in Kodak Industrex for 5 min at 68°F and densitometered with a Macbeth transmission densitometer, TD-404 (diffuse density), and

(3) Henke *et al.*, this work; Cu-Lα (930 eV), Al-Kα (1490 eV), and Cu-Kα (8050 eV); developed with agitation in Kodak Rapid X-Ray (RXR) for 6 min at 72°F and densitometered with a PDS microdensitometer using matched influx and efflux optics of 0.1 N.A.

All exposure data were for normal-incidence radiation ($\sin\theta = 1$). For these measurements it is important to have highly monochromatized exposing radiation of accurately known intensity. The Phillips and Phillips[4] Cu-Kα radiation, from a copper anode, was Ni foil filtered, focused by a double mirror reflection, and Bragg diffracted from a polyethylene sample. The characteristic line radiations of Rockett *et al.*[5] from x-ray tube anodes were filtered, and the background continuum radiation was estimated by pulse-height analysis with their flow-proportional and solid-state x-ray detectors. In this work we have applied the characteristic x-ray line radiations from a demountable anode source; the line radiations are then filtered and Bragg reflected onto a normal-incidence detection circle of an elliptically curved crystal analyzer spectrograph[3,6] (see Fig. 3). An intensity spectrum is obtained by scanning an absolutely calibrated flow-proportional counter along this detection cycle. Photographic spectra are then obtained for a series of different exposures of the 35-mm film that is transported along the same detection circle. Microdensitometry is performed with an effective slit of dimensions that match those of the proportional counterslit window and of width smaller than that of the diffraction line spectrum widths. At the monoenergetic Bragg diffraction line peaks, the net optical densities, D, in the photographic spectra are related to the corresponding intensity peaks, I (photons/square micrometer), in the intensity spectra. (This "operational" procedure for film calibration was designed to correspond precisely to the actual procedure, in reverse, for obtaining absolute measurements of intensities from photographic spectra.)

A. Normalizing Independent Density-Versus-Exposure Data Sets

In our combining of the DEF calibration data from the independent laboratory measurements described above, we consider that batch-to-batch variations and any other variations that result from using different (but conventional) x-ray film development procedures can be assumed to be small compared with the variations resulting from density and intensity measurement errors. All density values are for *net* density, i.e., that above the unexposed developed film background density. We ensure that this background correction has been precisely accomplished by requiring that a linear plot of D versus I for the lower densities does indeed extrapolate to the 0–0 origin.

Before combining these data for fitting by our model relations, we converted the D–I data of Phillips and Phillips[4] to an equivalent 5-min development result by using their D versus time-of-development curves (a small correction). We then converted all the D–I data of Refs. 4 and 5 to the specular density values at 0.1 N.A. for the influx and efflux microdensitometer optics. This is a straightforward conversion procedure because the factors, D_s/D_d (net specular density/net diffuse density), needed for this conversion are slowly varying functions of diffuse density, D_d, and are independent of the photon energy.[3] We have measured the D_s/D_d versus D_d curves, which are shown in Fig. 4, for D_s at 0.1

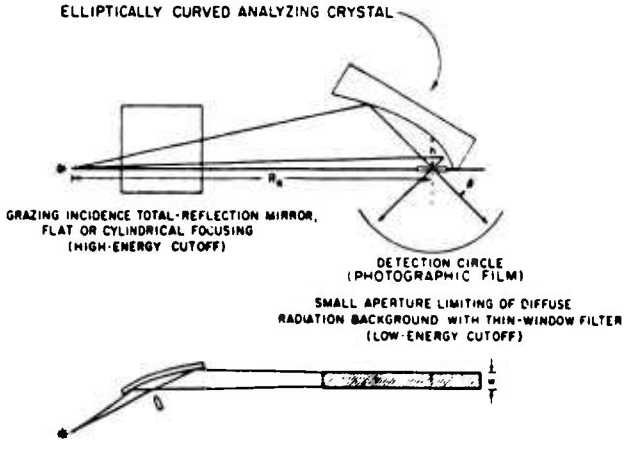


Fig. 3. Method for obtaining monoenergetic, characteristic line exposures, normally incident to a detection circle of an elliptical analyzer spectrograph. An intensity spectrum is obtained by scanning an absolutely calibrated-flow proportional counter along this detection circle. Photographic spectra are obtained by a series of exposures of film transported along the same circle. Microdensitometry is with a slit of effectively the same dimensions as that of the proportional counter slit window and of width that is small as compared to the instrumental broadened diffraction line width. The density-exposure data are taken from corresponding photographic density and absolute intensity peaks (photons/square micrometer), operationally similar, but in reverse, to the procedure for the determination of an absolute intensity of spectral lines from a calibrated photographic film spectrum.

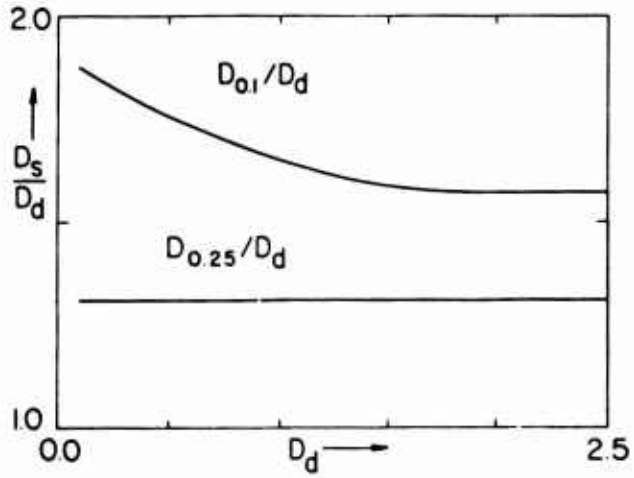


Fig. 4. Plots of experimentally measured conversion ratios, D_s/D_d (net specular density/net diffuse density), versus diffuse D_d for specular density measurements with matched influx–efflux optics at 0.1 and 0.25 N.A. and for total diffuse density. (These ratios are essentially independent of photon energy and are for the conventional, x-ray film development.) These experimental curves yield the conversion Eqs. (8) and (9) that have been applied here to normalize the data sets of Refs. 4 and 5.

and 0.25 N.A. [using the PDS and the Macbeth (double-diffuse) densitometers].

By fitting these D_s/D_d data, we obtain the required conversion equations

$$D_{0.1}/D_d = 1.9 - 0.35\,D_d + 0.092\,D_d^2 \qquad (8)$$

and

$$D_{0.25}/D_d = 1.31,$$

which yield

$$D_{0.1}/D_{0.25} = 1.5 - 0.20\,D_{0.25} + 0.041\,D_{0.25}^2. \qquad (9)$$

B. Fitting the Model Equations

The linear absorption coefficients, μ_0, μ_1, μ', and μ_b for an assumed gelatin supercoat ($C_8H_{16}O_5N_2$, $\rho = 1.40$ g/cm^3), for AgBr, for the heterogeneous emulsion, and for the polyester base ($C_5H_4O_2$, $\rho = 1.40$ g/cm^3), respectively, were determined as described in the companion Refs. 2 and 3, using photoabsorption data compiled by Henke *et al.*[7]

Note that we have been unable to obtain from the manufacturer of the DEF the chemical formula for its special supercoat material, and we assume here that its linear ab-

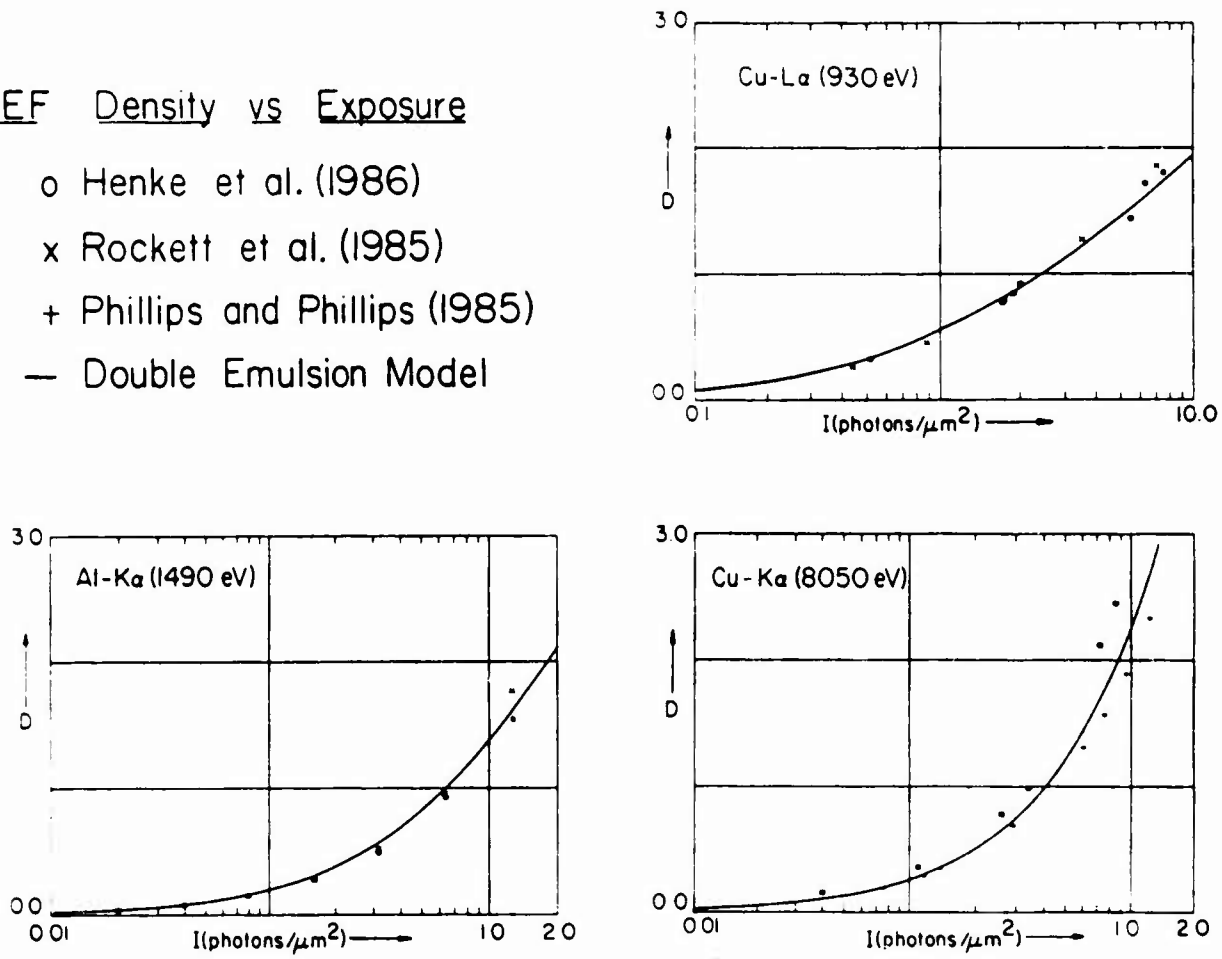


Fig. 5. The density-exposure data chosen here for the model equation fitting, consisting of independent duplicated measurements of several laboratories at the representative photon energies, Cu-Lα (930 ev), Al-Kα (1490 eV), and Cu-Kα (8050 eV). Also plotted here are the predicted D–I curves obtained by fitting the analytical model Eq. (7) to these data. Optical densities are net densities (above nonexposed developed background density) as would be measured by microdensitometry using matched influx-efflux optics of 0.1 N.A.

sorption coefficient is essentially proportional to that for gelatin and that, for example, a difference in mass density can be accommodated in our choice of an effective value for the supercoat thickness, t_0, determined by a precise fitting of the measured lower photon energy data. Similarly, the geometric specifications for the DEF are not available, and we have therefore developed the following procedure for their determination:

The total DEF thickness was carefully micrometered to yield a value of about 213 μm. We then measured the x-ray transmission of the base-plus-emulsion, choosing an x-ray wavelength that is transmitting in the 20–40% range and that has a negligible absorption within the thin supercoat. This transmission is given as τ_1 in Fig. 1. The emulsion is then dissolved away from the polyester base by soaking for about 10 min in a 1:1 dilution of a common bleach solution (5% aqueous solution of sodium hypochlorite, by weight). The transmission, defined in Fig. 1 as τ_2 for the remaining polyester base, is then measured. We have chosen the Cu–Kα (8050-eV) line radiation for these transmission measurements, derived from a Cu anode, filtered and Bragg reflected with a pentaerythritol (PET) crystal analyzer. The values for τ_1 and τ_2 are presented in Fig. 1 for the DEF and were 0.32 and 0.85, respectively. These results, along with those for the film thickness, yielded the values of 13 and 185 μm for the emulsion and polyester base thicknesses and a volume fraction, V, of the AgBr grains equal to 0.40. The general relations for this determination of the emulsion and base thicknesses follow from the transmission equations in Fig. 1 and are

$$T = (1/\mu')\ln\sqrt{\tau_2/\tau_1} \tag{10}$$

and

$$t_b = (1/\mu_b)\ln(1/\tau_2), \tag{11}$$

in which μ', the linear heterogeneous emulsion absorption coefficient, contains the dependence on the volume fraction, V (see Ref. 2).

The film grain size was estimated from averaged measurements of the outermost imbedded grains imaged in scanning electron microscope (SEM) micrographs of the DEF cross section. The SEM photos were obtained by Dixon,[8] using small DEF sections obtained by breaking liquid-nitrogen-frozen pieces of the DEF. An example of one of these micrographs is shown in Fig. 2. As will be demonstrated, our model Eq. (7) requires only an estimate of the effective grain size. We have determined from the SEM photos that the average grain size, d, is about 1.6 μm. It is not feasible to

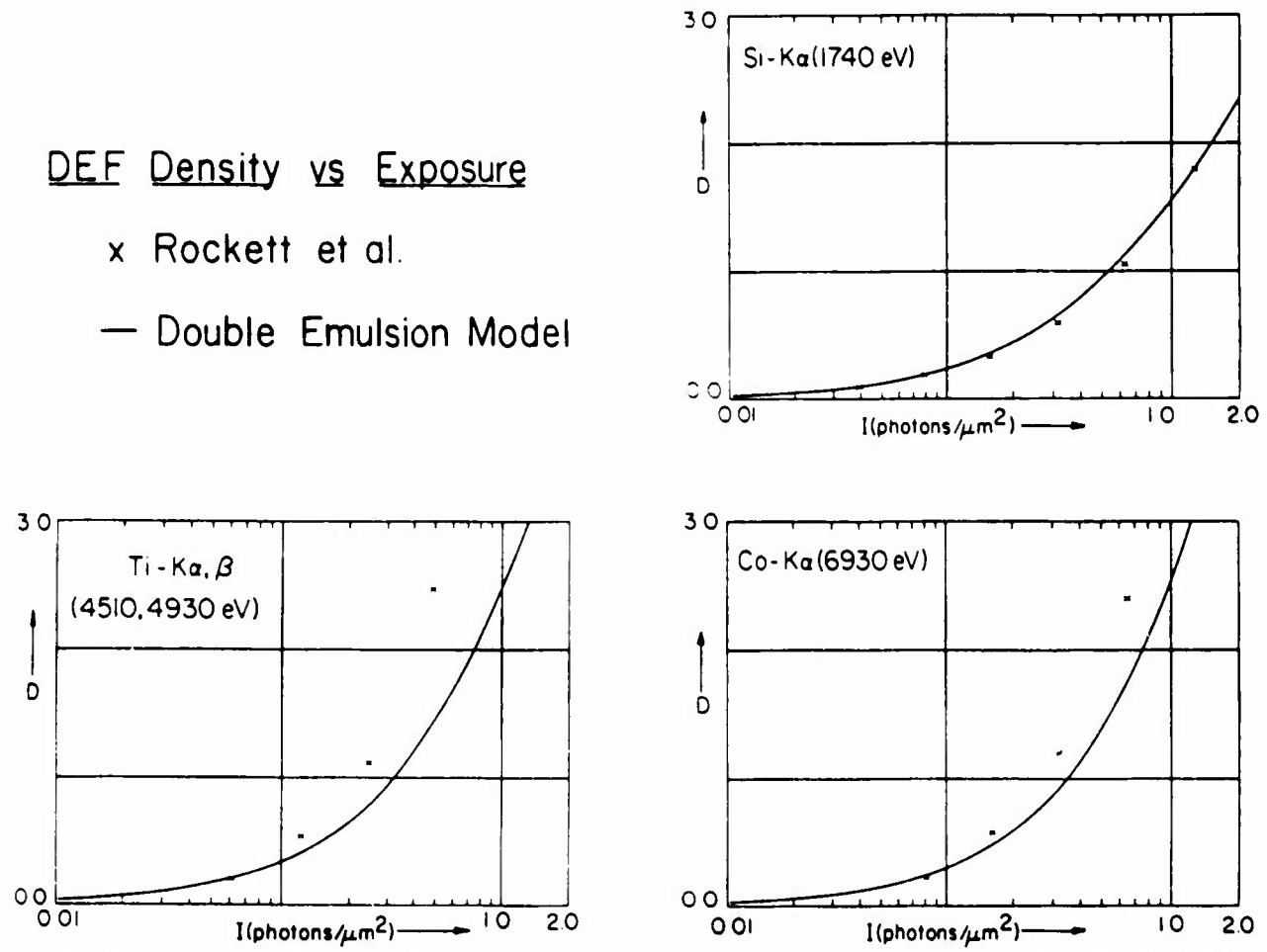


Fig. 6. Applying the model Eq. (7) determined by the data sets shown in Fig. 5 to predict D–I curves for additional but unduplicated D–I data at photon energies, Si-Kα (1740 eV), Ti-Kα, β (4510, 4930 eV), and Co–Kα (6930 eV). The prediction for the photon energy at 1740 eV is excellent. It is suggested here that the high-density values shown here for measurements with Ti-Kα and Co–Kα radiations are excessively high because the films were also exposed to the appreciably higher continuum radiation that cannot be completely filtered out at the higher photon energies and that was not completely included in the detector "window." [A Si (Li) solid-state detector was used only for these two radiations.] See Ref. 5.

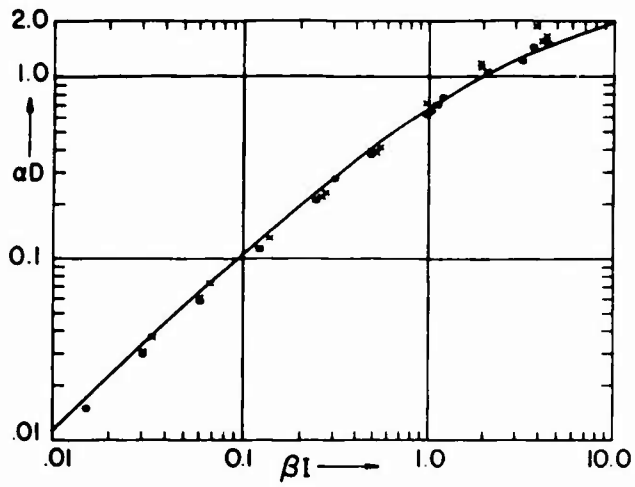


Fig. 7. Demonstration of the universality of the plot of the αD versus βI data for the x radiations that are completely absorbed within the first emulsion, Cu-Lα (930 eV), Al-Kα (1490 eV), and Si-Kα (1740 eV) [for the data of Rockett *et al.* (×) and Henke *et al.* (●) shown in Figs. 4 and 5]. Also plotted here is the model Eq. (4) using parameters derived by fitting data at both the high and the low energies.

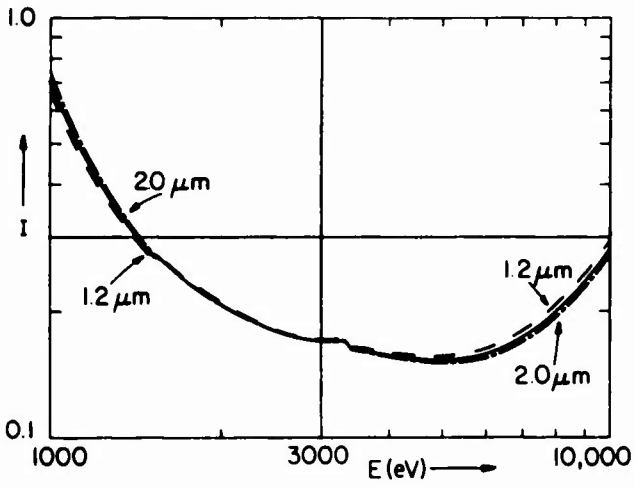


Fig. 8. Plotted here for the DEF is the intensity, I (photons/square micrometer), that is required to generate a specular density, $D_{0.1}$ = 0.5, versus photon energy, E (electron volts), using the best fit model curve [Eq. (7)] for the data sets shown in Fig. 5 and the parameters listed in Fig. 1 with the AgBr grain size at 1.6 μm and also at the varied values of 1.2 and 2.0 μm in order to illustrate the insensitivity of Eq. (7) to the film grain size. (The fitting parameter, b, effectively compensates for a variation in d.)

determine an accurate value of the supercoat thickness, t_0, from these SEM photos. We therefore establish this value along with those of the fitting parameters, a and b, by a least-squares best fitting of the model Eq. (7) to the D–I data sets. Fitting only the duplicated data sets that are plotted in Fig. 5 (from four laboratories), we obtain the following values for the DEF film:

$$a = 0.680\ \mu m^{-1}, \qquad b = 1.69\ \mu m^{2}, \qquad t_0 = 1.0\ \mu m.$$

Our determinations of the geometric parameters that are needed in the model Eq. (7) are in excellent agreement with those that have been independently determined by Rockett *et al.*[5] on another DEF batch.

In Fig. 6 we present our model D–I curves along with the unduplicated experimental data of Rockett *et al.*[5] for Si-Kα (1740 eV), Ti-Kα, β (4510 eV, 4930 eV), and Co-Kα (6930 eV), which were not included in the data base (presented in Fig. 5) chosen for our fitting of Eq. (7). Our prediction of their D–I curve for 1740 eV is excellent. We do not agree, however, with their D–I measurements at the higher photon energies, 4510/4930 eV and 6930 eV. Only for these energies have they replaced their proportional gas counter detector by a Si(Li) solid-state detector. A possible explanation for their higher-density values at these higher photon energies is that the film exposure included that for the higher continuum background associated with these energies (not eliminated in their filtered, direct source radiation and that may not have been completely included in their solid-state detector "window"). Our rejection of these two data sets in our fitting of Eq. (7) seems to be strongly justified by the very satisfactory, simultaneous fitting of the lower-energy data along with that for the highest photon energy, 8050 eV (obtained by Phillips and Phillips[4] and by this work).

To demonstrate the "universality" of this model description for the DEF we present in Fig. 7 the universal plot, $\alpha D = \phi(\beta I)$, using only the D–I data sets for the x radiations that are essentially completely absorbed within the first emulsion, viz., Cu-Lα (930 eV), Al-Kα (1490 eV), and Si-Kα (1740 eV). Also plotted in Fig. 7 is the model fit curve for a thick emulsion [Eq. (4)] using the geometric parameters and values of a and b as presented above for the overall fit of Eq. (7) for the DEF at both the low and the high photon energies.

It was noted earlier that the grain size, d, chosen here to be 1.6 μm, was not amenable to direct, accurate evaluation but, nevertheless, was not required to be known accurately in our model Eq. (7). The fitting parameter, b, can compensate for a variation in d [from Eq. (3) we note that $b\beta \approx b\mu_1 d$ for the higher photon energy dependence on d in the model equations]. To illustrate this insensitivity we plot in Fig. 8 the intensity I (photons/square micrometer) that is required to generate an optical specular density, $D_{0.1}$, of 0.5, as a function of the photon energy, E (electron volts), using the "best-choice parameters" determined above (and listed in Fig. 1),

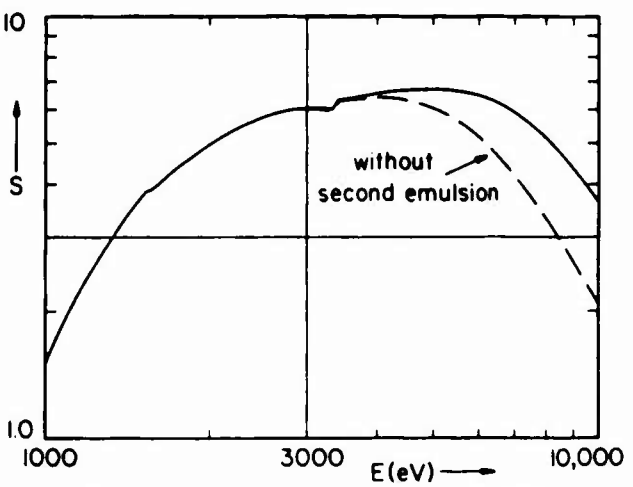


Fig. 9. The sensitivity, S, for the DEF in the 1000–10,000-eV region. S is defined here as the *reciprocal* of the intensity that is required to generate an optical density, $D_{0.1}$ = 0.5. Also shown is the calculated sensitivity, S, for the first emulsion only in DEF in order to illustrate the significant improvement in the DEF sensitivity for photon energies higher than about 4000 eV.

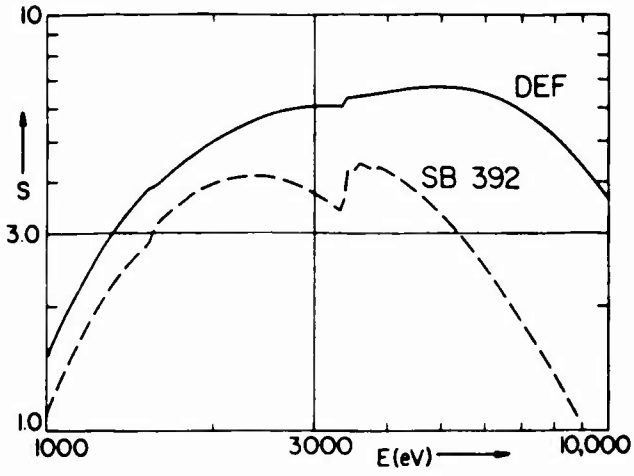


Fig. 10. The sensitivity, S, is plotted here for an optical density, $D_{0.1} = 0.5$, and for the 1000–10,000-eV region for DEF and compared with that sensitivity for the single-emulsion film Kodak SB-392 (as characterized in Section 4).

along with similar best-fit intensity curves with the grain size parameter, d, varied from the chosen value 1.6 μm to the values 1.2 and 2.0 μm.

C. Expressing the Detailed Photographic Response of the Direct Exposure Film

In Fig. 9 we present the sensitivity of the DEF for the 1000–10,000-eV region, defined here as the *reciprocal* of that intensity (photons/square micrometer) that is required to generate an optical density, $D_{0.1}$, of 0.5. Also shown here is the same sensitivity curve calculated for the first emulsion only (effect of second emulsion removed) in order to illustrate for which photon energies there is a significant improvement resulting from having the double emulsion. In Fig. 10 we present this DEF sensitivity curve for the 1000–10,000-eV photon-energy region and compare it with that for the single-emulsion x-ray film Kodak SB-392 (characterized for this high-energy region as described in Section 4).

In Table 1 we present for Kodak DEF a detailed tabulation, using the fitted model Eq. (7), for the normal-incidence

Table 1. Exposure I (photons/μm^2) versus Net Optical Density $D_{0.1}$ and Photon Energy E (eV) for the Kodak DEF

Photon Energy	Net Density D (Specular, 0.1 × 0.1 N.A.)										Wavelength
E (eV)	0.2	0.4	0.6	0.8	1.0	1.2	1.4	1.6	1.8	2.0	λ(A)
1000	2.24-01	5.03-01	8.50-01	1.28 00	1.82 00	2.49 00	3.32 00	4.36 00	5.65 00	7.26 00	12.40
1050	1.96-01	4.36-01	7.29-01	1.09 00	1.53 00	2.07 00	2.73 00	3.54 00	4.54 00	5.75 00	11.81
1100	1.74-01	3.84-01	6.38-01	9.44-01	1.31 00	1.76 00	2.30 00	2.95 00	3.74 00	4.69 00	11.27
1150	1.57-01	3.44-01	5.67-01	8.33-01	1.15 00	1.53 00	1.98 00	2.52 00	3.17 00	3.94 00	10.78
1200	1.43-01	3.12-01	5.11-01	7.46-01	1.02 00	1.35 00	1.74 00	2.20 00	2.73 00	3.37 00	10.33
1250	1.32-01	2.86-01	4.66-01	6.76-01	9.22-01	1.21 00	1.55 00	1.94 00	2.40 00	2.94 00	9.92
1300	1.22-01	2.64-01	4.29-01	6.19-01	8.40-01	1.10 00	1.39 00	1.74 00	2.14 00	2.60 00	9.54
1350	1.14-01	2.46-01	3.98-01	5.72-01	7.72-01	1.00 00	1.27 00	1.57 00	1.92 00	2.33 00	9.18
1400	1.08-01	2.31-01	3.72-01	5.33-01	7.16-01	9.25-01	1.17 00	1.44 00	1.75 00	2.11 00	8.86
1450	1.02-01	2.19-01	3.50-01	5.00-01	6.69-01	8.61-01	1.08 00	1.33 00	1.61 00	1.93 00	8.55
1500	9.76-02	2.08-01	3.32-01	4.71-01	6.29-01	8.07-01	1.01 00	1.23 00	1.49 00	1.78 00	8.27
Absorption Edges: Br-$L_{3,2}$ (1533–1599 eV)											
1800	8.10-02	1.72-01	2.73-01	3.87-01	5.15-01	6.58-01	8.19-01	9.99-01	1.20 00	1.43 00	6.89
1900	7.73-02	1.64-01	2.60-01	3.67-01	4.86-01	6.19-01	7.68-01	9.34-01	1.12 00	1.33 00	6.53
2000	7.42-02	1.57-01	2.48-01	3.49-01	4.61-01	5.86-01	7.24-01	8.78-01	1.05 00	1.24 00	6.20
2100	7.17-02	1.51-01	2.38-01	3.34-01	4.40-01	5.58-01	6.87-01	8.30-01	9.89-01	1.16 00	5.90
2200	6.96-02	1.46-01	2.30-01	3.22-01	4.23-01	5.34-01	6.56-01	7.90-01	9.38-01	1.10 00	5.64
2300	6.78-02	1.42-01	2.23-01	3.11-01	4.08-01	5.14-01	6.30-01	7.57-01	8.96-01	1.05 00	5.39
2400	6.64-02	1.39-01	2.17-01	3.03-01	3.96-01	4.97-01	6.08-01	7.28-01	8.60-01	1.00 00	5.17
2500	6.52-02	1.36-01	2.12-01	2.95-01	3.85-01	4.83-01	5.89-01	7.05-01	8.30-01	9.67-01	4.96
2600	6.44-02	1.34-01	2.09-01	2.90-01	3.77-01	4.72-01	5.74-01	6.85-01	8.06-01	9.36-01	4.77
2700	6.37-02	1.32-01	2.06-01	2.85-01	3.71-01	4.63-01	5.62-01	6.70-01	7.86-01	9.12-01	4.59
2800	6.33-02	1.31-01	2.04-01	2.82-01	3.66-01	4.56-01	5.53-01	6.57-01	7.70-01	8.92-01	4.43
2900	6.30-02	1.30-01	2.02-01	2.79-01	3.62-01	4.51-01	5.46-01	6.48-01	7.58-01	8.76-01	4.28
3000	6.29-02	1.30-01	2.02-01	2.78-01	3.60-01	4.47-01	5.41-01	6.41-01	7.48-01	8.64-01	4.13
3100	6.30-02	1.30-01	2.01-01	2.77-01	3.58-01	4.45-01	5.37-01	6.36-01	7.41-01	8.54-01	4.00
3200	6.32-02	1.30-01	2.01-01	2.77-01	3.58-01	4.43-01	5.35-01	6.32-01	7.36-01	8.48-01	3.87
3300	6.35-02	1.31-01	2.02-01	2.78-01	3.58-01	4.43-01	5.34-01	6.30-01	7.33-01	8.43-01	3.76
Absorption Edges: Ag-$L_{3,2}$ (3351–3526 eV)											
4000	5.81-02	1.20-01	1.86-01	2.56-01	3.32-01	4.12-01	4.98-01	5.90-01	6.89-01	7.94-01	3.10
5000	5.76-02	1.18-01	1.81-01	2.47-01	3.16-01	3.89-01	4.65-01	5.45-01	6.29-01	7.17-01	2.48
6000	6.01-02	1.22-01	1.87-01	2.54-01	3.23-01	3.94-01	4.69-01	5.46-01	6.25-01	7.08-01	2.07
7000	6.63-02	1.35-01	2.05-01	2.77-01	3.52-01	4.28-01	5.07-01	5.89-01	6.73-01	7.60-01	1.77
8000	7.64-02	1.55-01	2.35-01	3.18-01	4.03-01	4.90-01	5.79-01	6.71-01	7.66-01	8.63-01	1.55
9000	9.04-02	1.83-01	2.78-01	3.75-01	4.75-01	5.78-01	6.83-01	7.91-01	9.01-01	1.02 00	1.38
10000	1.08-01	2.19-01	3.33-01	4.49-01	5.69-01	6.91-01	8.16-01	9.45-01	1.08 00	1.21 00	1.24

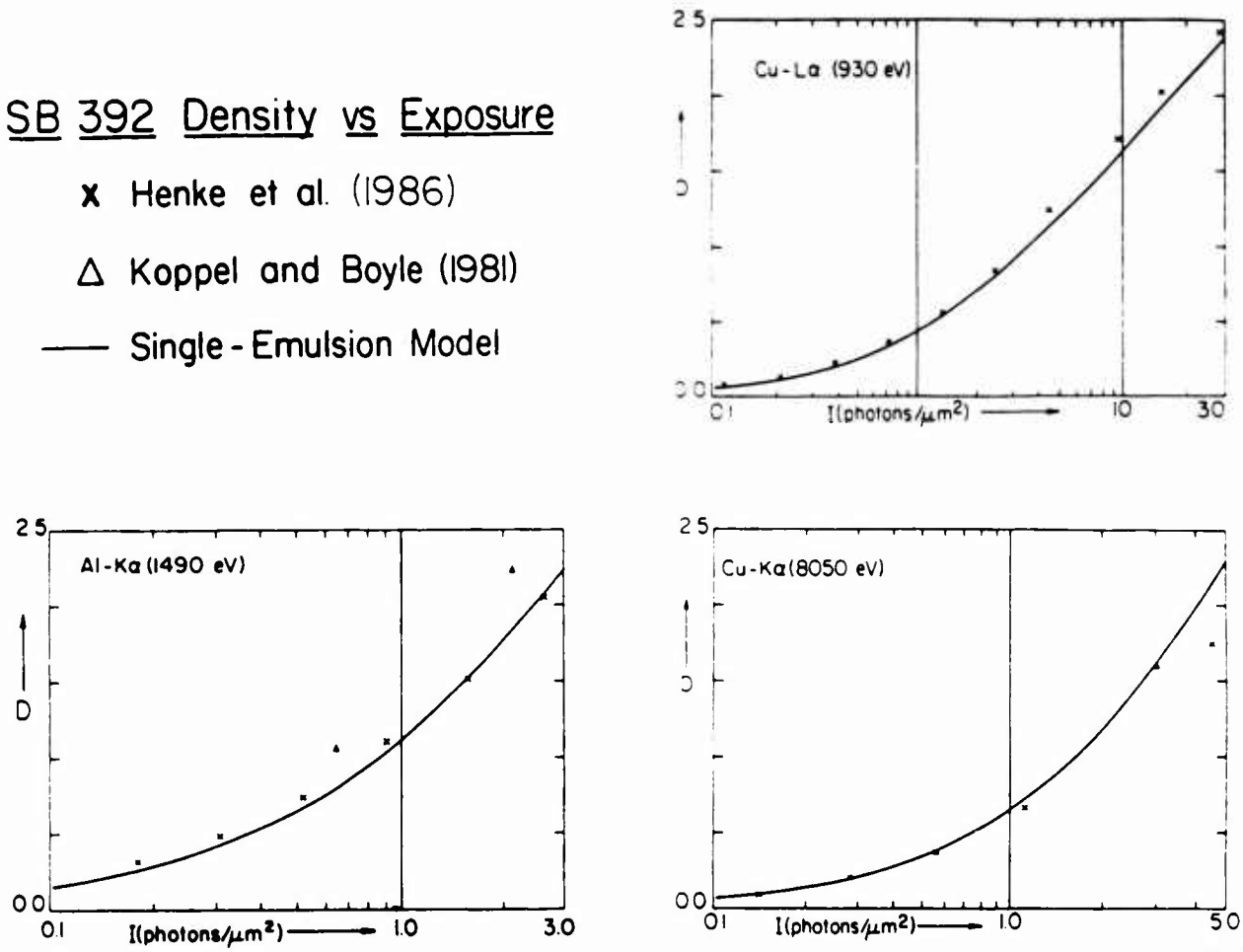


Fig. 11. The density-exposure data chosen here for the model equation fitting for SB-392 film at the representative photon energies, Cu-Lα (930 eV), Al-Kα (1490 eV), and Cu-K (8050 eV). Also plotted here are the predicted D–I curves obtained by fitting the analytical model Eq. (5) to these total data. Optical densities are net densities (above unexposed, developed background density) as would be measured by using microdensitometry with matched influx–efflux optics of 0.1 N.A.

intensity I (photons/square micrometer) that corresponds to a given specular optical density, $D_{0.1}$ (microdensitometered at matched 0.1-N.A. optics) in the 0.2–2.0 range and at a given photon energy, E (electron volts), in the 1000–10,000-eV region. Corresponding values of diffuse optical densities and those microdensitometered at matched 0.25-N.A. optics for Table 1 can be obtained by using the conversion relations (8) and (9).

4. CHARACTERIZATION OF THE KODAK SB-392

For optimized measurements with position-sensitive photographic detection, higher resolution may be more important than higher sensitivity. Then the alternative single-emulsion x-ray film, Kodak SB-5 or SB-392 film, should be considered. (SB-5 and SB-392 differ only in format, i.e., sheet or 35 mm, respectively.) In Ref. 3 we presented a characterization of the SB-392 specifically for the low-energy x-ray region as based on D–I data at only these energies. To estimate the relative response of this film at the higher photon energies (>1000 eV) we then simply extrapolated into the next energy decade the low-energy results by using our model relations. We now present a more accurate characterization of the SB-392 for the high photon energies (1000–10,000 eV) by using a D–I experimental data base representative only of this energy region and by applying the improved procedures for the parameterization of the model description, as has been described in detail in Section 3 for the characterization of the complementary Kodak DEF.

Using the same calibration procedure as described above for the present work, we have added D–I data for the Cu-Kα (8050-eV) x radiation to the previously measured data presented in Ref. 3 for the photon energies Cu-Lα (930 eV) and Al-Kα (1490 eV). These data are presented in Fig. 11 along with the predicted curves by using the analytical single-emulsion model Eq. (5) that is based on a parameterization determined as follows:

The emulsion-plus-base thickness of the SB-392 was micrometered to be 196 μm. Using PET-crystal-monochromatized Cu-Kα radiation, the transmission for two layers of the film, τ_F, and of two layers of the base, τ_b (with the emulsion removed), were measured to be 0.461 and 0.725, respectively. These transmissions are related to the emulsion and base thicknesses, T and t_b, as follows:

$$T = \frac{1}{\mu'} \ln\left(\frac{\tau_b}{\tau_F}\right)^{1/2}, \tag{12}$$

Table 2. Exposure I (photons/μm^2) versus Net Optical Density $D_{0.1}$ and Photon Energy E (eV) for the Kodak SB-392

Photon Energy	Net Density D (Specular, 0.1 × 0.1 N.A.)										Wavelength
E (eV)	0.2	0.4	0.6	0.8	1.0	1.2	1.4	1.6	1.8	2.0	λ(A)
1000	3.03-01	6.87-01	1.17 00	1.79 00	2.56 00	3.55 00	4.79 00	6.37 00	8.37 00	1.09 01	12.40
1050	2.63-01	5.90-01	9.94-01	1.49 00	2.12 00	2.89 00	3.84 00	5.03 00	6.50 00	8.34 00	11.81
1100	2.33-01	5.16-01	8.60-01	1.28 00	1.79 00	2.41 00	3.17 00	4.10 00	5.23 00	6.61 00	11.27
1150	2.09-01	4.59-01	7.59-01	1.12 00	1.55 00	2.07 00	2.69 00	3.44 00	4.34 00	5.43 00	10.78
1200	1.96-01	4.15-01	6.81-01	9.96-01	1.37 00	1.81 00	2.33 00	2.96 00	3.70 00	4.58 00	10.33
1250	1.75-01	3.80-01	6.20-01	9.00-01	1.23 00	1.61 00	2.06 00	2.59 00	3.22 00	3.95 00	9.92
1300	1.63-01	3.52-01	5.70-01	8.23-01	1.12 00	1.46 00	1.85 00	2.31 00	2.85 00	3.48 00	9.54
1350	1.53-01	3.29-01	5.30-01	7.61-01	1.03 00	1.33 00	1.69 00	2.09 00	2.56 00	3.11 00	9 18
1400	1.45-01	3.10-01	4.98-01	7.12-01	9.56-01	1.23 00	1.55 00	1.92 00	2.34 00	2.82 00	8.86
1450	1.38-01	2.95-01	4.71-01	6.71-01	8.98-01	1.16 00	1.45 00	1.78 00	2.16 00	2.60 00	8.55
1500	1.33-01	2.82-01	4.50-01	6.38-01	8.51-01	1.09 00	1.36 00	1.67 00	2.02 00	2.42 00	8.27
Absorption Edges: Br-$L_{3,2}$ (1533-1599 eV)											
1800	1.01-01	2.13-01	3.39-01	4.79-01	6.36-01	8.12-01	1.01 00	1.23 00	1.48 00	1.77 00	6.89
1900	9.67-02	2.04-01	3.23-01	4.56-01	6.03-01	7.68-01	9.53-01	1.16 00	1.39 00	1.65 00	6.53
2000	9.41-02	1.98-01	3.13-01	4.40-01	5.80-01	7.37-01	9.11-01	1.11 00	1.32 00	1.57 00	6.20
2100	9.23-02	1.94-01	3.05-01	4.28-01	5.64-01	7.15-01	8.81-01	1.07 00	1.27 00	1.51 00	5.90
2200	9.13-02	1.91-01	3.01-01	4.21-01	5.54-01	6.99-01	8.61-01	1.04 00	1.24 00	1.46 00	5.64
2300	9.09-02	1.90-01	2.98-01	4.17-01	5.47-01	6.91-01	8.48-01	1.02 00	1.22 00	1.43 00	5.39
2400	9.11-02	1.90-01	2.98-01	4.16-01	5.45-01	6.87-01	8.43-01	1.01 00	1.20 00	1.42 00	5.17
2500	9.18-02	1.91-01	3.00-01	4.18-01	5.46-01	6.88-01	8.42-01	1.01 00	1.20 00	1.41 00	4.96
2600	9.29-02	1.94-01	3.03-01	4.21-01	5.51-01	6.92-01	8.47-01	1.02 00	1.20 00	1.41 00	4.77
2700	9.45-02	1.97-01	3.07-01	4.27-01	5.58-01	7.00-01	8.56-01	1.03 00	1.22 00	1.42 00	4.59
2800	9.64-02	2.00-01	3.13-01	4.35-01	5.68-01	7.12-01	8.70-01	1.04 00	1.23 00	1.44 00	4.43
2900	9.87-02	2.05-01	3.20-01	4.44-01	5.79-01	7.27-01	8.87-01	1.06 00	1.26 00	1.47 00	4.28
3000	1.01-01	2.10-01	3.28-01	4.55-01	5.94-01	7.44-01	9.08-01	1.09 00	1.28 00	1.50 00	4.13
3100	1.04-01	2.17-01	3.37-01	4.68-01	6.10-01	7.64-01	9.31-01	1.11 00	1.32 00	1.54 00	4.00
3200	1.08-01	2.23-01	3.48-01	4.82-01	6.28-01	7.86-01	9.58-01	1.15 00	1.35 00	1.58 00	3.87
3300	1.11-01	2.30-01	3.59-01	4.98-01	6.48-01	8.11-01	9.88-01	1.18 00	1.39 00	1.63 00	3.76
Absorption Edges: Ag-$L_{3,2}$ (3351-3526 eV)											
4000	8.94-02	1.86-01	2.90-01	4.02-01	5.24-01	6.57-01	8.01-01	9.60-01	1.13 00	1.33 00	3.10
5000	1.14-01	2.37-01	3.69-01	5.10-01	6.64-01	8.30-01	1.01 00	1.21 00	1.42 00	1.66 00	2.48
6000	1.53-01	3.18-01	4.94-01	6.84-01	8.88-01	1.11 00	1.35 00	1.61 00	1.90 00	2.21 00	2.07
7000	2.08-01	4.30-01	6.69-01	9.25-01	1.20 00	1.50 00	1.83 00	2.18 00	2.56 00	2.99 00	1.77
8000	2.79-01	5.77-01	8.97-01	1.24 00	1.61 00	2.01 00	2.45 00	2.92 00	3.43 00	4.00 00	1.55
9000	3.68-01	7.62-01	1.18 00	1.64 00	2.13 00	2.65 00	3.23 00	3.85 00	4.53 00	5.28 00	1.38
10000	4.77-01	9.87-01	1.53 00	2.12 00	2.76 00	3.44 00	4.18 00	4.99 00	5.87 00	6.84 00	1.24

$$t_b = \frac{1}{\mu_b} \ln\left(\frac{1}{\tau_b}\right)^{1/2}. \tag{13}$$

Applying these equations for the two layers of the film and of the base, the single-emulsion thickness, T; base thickness, t_b; and the volume fraction of the AgBr grains, V, were determined to be 11.3 μm, 183.8 μm, and 0.20, respectively. (It is interesting to note that these values were determined by model fitting alone of the low-photon-energy data in Ref. 2 to be, for T and V, 10 μm and 0.2.) With these parameters, the model relation for the single-emulsion film [Eq. (5)] was least-squares fitted to the data sets presented in Fig. 11 to yield the following values of fitting parameters, a and b, and of the supercoat thickness, t_0:

$$a = 0.545\ \mu m^{-1}, \qquad b = 1.39\ \mu m^{-2}, \qquad t_0 = 1.0\ \mu m.$$

In Ref. 3 we reported the measured ratios, D_s/D_d (net specular density/net diffuse density), for the specular densities, $D_{0.1}$ and $D_{0.25}$ (measured with microdensitometer influx and efflux matched optics at N.A. values of 0.1 and 0.25). These measurements yield the conversion equations for SB-392

$$D_{0.1}/D_d = 1.6 - 0.10\,D_d,$$

$$D_{0.25}/D_d = 1.2, \tag{14}$$

and

$$D_{0.1}/D_{0.25} = 1.3 - 0.07\,D_{0.25}. \tag{15}$$

Using Eqs. (14), we have converted the diffuse-density, D–I data on SB-5 by Koppel and Boyle[9] and present these also in Fig. 11. (Their development procedure was 5 min in RXR at 68° with agitation as compared with our procedure at 6 min in RXR at 72° with agitation.)

Using the analytical Eq. (5) thus determined for the SB-392 film, we presented in Fig. 10 its sensitivity, S, in comparison with that for DEF, and in Table 2 we present the normal-incidence intensity, I (photons/square micrometers), that generates the specular density $D_{0.1}$ in the 0.2-

2.0 range and at the photon energy E (electron volts) in the 1000–10,000-eV region.

Finally it is important to note that for the single-emulsion film at medium or low exposures of significantly high-photon-energy x radiation, the D–I relation becomes simply

$$D = c\mu_1 I, \tag{16}$$

with the energy dependence given completely as that for the absorption coefficient, μ_1, of AgBr and with the dependence on the film grain size (before development) and the silver cluster grain size (after development) along with the T and V parameters disappearing within a single fitting parameter, c, that is independent of the angle of incidence, θ. This result may be readily derived by expanding the model Eq. (5) for the high-energy limit for which $\mu_1 d$, $\mu_0 t_0$, and $\mu' T$ are small compared with unity. For the Kodak SB-392 film exposed with medium or low intensities of photon energies around 10,000 eV, the D–I relation may be well approximated by the characteristic equation

$$D_{01} = 7.3\,\mu_1(\mu\text{m}^{-1})I(\text{photons}/\mu\text{m}^2), \tag{17}$$

where μ_1 is the linear absorption coefficient of AgBr for a particular photon energy (see μ_1-versus-E table in Ref. 3).

5. SUMMARY

In this work we have presented detailed characterizations of the new, high-sensitivity double-emulsion Kodak DEF and the less sensitive but higher-resolution single-emulsion Kodak SB-392 film for microdensitometric applications in the high-energy x-ray region. These characterizations were shown not to be strongly affected by the normal variations (several laboratories evaluated) resulting from the choice of a conventional x-ray development procedures and from batch-to-batch differences. The accuracy of our averaging characterizations was limited mostly by the experimental errors of the D–I measurements. The magnitude of these errors and the accuracy of our characterizations may be estimated by the comparison of the D–I data from the several laboratories as plotted against our model curves in Figs. 5 and 11.

The three significant figures expressed in Tables 1 and 2 for the exposure I (photons/square micrometer) are, of course, indicative not of the absolute accuracy of these averaged characterizations but rather of relative precision. The absolute accuracy can be evaluated and perhaps improved by fitting our average characterizations to a few experimental D–I film calibrations made on a particular film batch and with a given laboratory's measurement procedure.

The model relations that have been developed in this paper and in companion works[2,3] for the response of x-ray films and presented here in Eqs. (4)–(7) are relatively simple analytical relations amenable to small-computer generation of absolute spectral intensities. These model descriptions are based on two- or three-parameter fitting of a few D–I experimental data sets that are representative of the photon-energy region of application. A simple procedure has been established for the determination of the basic geometric parameters of the x-ray film that are required for these model analytical descriptions.

The θ dependence of our model Eqs. (4)–(7) has been experimentally verified for incidence angles greater than about 10 deg (see Ref. 3). The same parameters that have been used to calculate the film characterizations presented in Tables 1 and 2 for normal incidence can be applied in these model equations to calculate the film response for smaller angles of incidence between 10 and 90 deg.

In Appendix A we summarize a recommended film-handling and -processing procedure that will produce the DEF and SB-392 characteristics described in this work.

APPENDIX A: FILM-HANDLING AND -DEVELOPMENT PROCEDURES

Kodak Type DEF (DEF-392)

The Kodak DEF or DEF-392 (the difference being the sheet-film or 35-mm format) should be handled under Kodak Safelight Filter no. GBX-2 with a 15-W bulb, no closer than 1 m from the film. This practice should be followed during processing as well. Special care should be taken not to bend the film too sharply, since doing so will result in many minute cracks in the emulsion. Fresh processing solutions should be used whenever possible; this is especially true for the developer because it will deteriorate when in an open tray or processing tank. The processing of the film is as follows, with all solutions, including the wash water, at 68°F in either a developing tank for roll film or a tray for sheet film:

1. Development: 5 min in Kodak GBX developer with gentle but continuous agitation.
2. Rinse: 30 sec in Kodak Indicator stop bath with gentle but constant agitation.
3. Fixing: 6 min in Kodak Rapid Fixer or GBX fixer with constant agitation.
4. Wash: 30 min in running water then 30 sec in Kodak Photo-Flo 200 working solution.
5. Drying: At room temperature in still air, or at elevated temperatures not over 100°F in moving air.

In drying the film at elevated temperatures, care should be taken not to allow the relative humidity at the film to drop below 50%, as this can cause excessive shrinkage of the emulsion and a possible distortion of the image. The use of Photo-Flo wetting agent will help promote uniform drying of the film by either method, with a minimum of drying artifacts and water spots.

Kodak Type SB-5 (SB-392)

Recommended film handling and development procedure is that described above for Kodak DEF.

ACKNOWLEDGMENTS

The authors gratefully acknowlege the important assistance in this work of Debra Nanod, Ron Tackaberry, and Jonathan Kerner and the helpful suggestions of W. C. Phillips, G. N. Phillips, Jr., and P. D. Rockett. The program on Low-Energy X-Ray Physics and Technology at the University of California's Lawrence Berkeley Laboratory (LBL) is supported by a grant from the U.S. Air Force Office of Scientific Research (AFOSR no. 84-0001) and supported supplementally by contracts with the U.S. Department of Energy

(SAN#CID#9501, Task 1) through the Los Alamos National Laboratory and the Lawrence Livermore National Laboratory and (no. DE-AC03-76SF00098) through LBL.

REFERENCES AND NOTES

1. B. L. Henke and P. A. Jaanimagi, "Two-channel, elliptical analyzer spectrograph for absolute, time-resolving time-integrating spectrometry of pulsed x-ray sources in the 100–10,000 eV region," Rev. Sci. Instrum. **56**, 1537–1552 (1985).
2. B. L. Henke, S. L. Kwok, J. Y. Uejio, H. T. Yamada, and G. C. Young, "Low-energy x-ray response of photographic films. I. Mathematical models," J. Opt. Soc. Am. B **1**, 818–827 (1984).
3. B. L. Henke, F. G. Fujiwara, M. A. Tester, C. H. Dittmore, and M. A. Palmer, "Low-energy x-ray response of photographic films. II. Experimental characterization," J. Opt. Soc. Am. B **1**, 828–849 (1984).
4. W. C. Phillips and G. N. Phillips, Jr., "Two new x-ray films: conditions for optimum development and calibration of response," J. Appl. Cryst. **18**, 3–7 (1985).
5. P. D. Rockett, C. R. Bird, C. J. Hailey, D. Su livan, D. B. Brown, and P. G. Burkhalter, "X-ray calibration of Kodak direct exposure film," Appl. Opt. **24**, 2536–2542 (1985).
6. B. L. Henke, H. T. Yamada, and T. J. Tanaka, "Pulsed plasma source spectrometry in the 80–8000-eV x-ray region," Rev. Sci. Instrum. **54**, 1311–1330 (1983).
7. B. L. Henke, P. Lee, T. J. Tanaka, R. L. Shimabukuro, and B. K. Fujikawa, "Low-energy x-ray interaction coefficients: photoabsorption, scattering, and reflection. E = 100–2000 eV, Z = 1 to 94," At. Data Nucl. Data Tables **27**, 1–44 (1982).
8. The SEM film studies were kindly provided by David D. Dixon of the Technical Photography Group, Lawrence Livermore National Laboratory.
9. L. N. Koppel and M. J. Boyle, "X-ray calibration of film types SB-5 and RAR 2492 in the 1.5–8-keV region," Document No. FR-81-112-Sec. IV (Advanced Research and Applications Corp., Sunnyvale, Calif., 1981).

11. TECHNICAL NOTES: THE CHARACTERIZATION OF X-RAY PHOTOCATHODES

The absolute efficiency for the conversion of x-ray photons to photoemitted electrons and the statistics governing the number of electrons per photon-induced "bunch" need to to characterized for the development of absolute spectrometry particularly for the time-resolving x-ray diodes and streak cameras.

When an x-ray photon is absorbed within a photocathode the resulting primary electrons (photo-and Auger electrons) proceed to generate a much greater number of low energy secondaries (electron hole-pairs). Generally, the average penetration depth of the photons is very large compared to the average escape depth, λ_s, of the "random walking" secondaries within the photoemitter. This "sea" of secondaries has an energy distribution just inside the vacuum-photocathode interface which is determined by the electronic band structure of the material. Because of the relatively large depth through which these secondaries are formed, the energy distribution at the surface becomes independent of the exciting photon energy, E. In addition, the fraction of these secondaries that can escape through the surface and their emitted energy distribution are determined only by the surface work function or electron affinity and are also independent of the exciting photon energy. The quantum yield, Y, (emitted electrons per normally incident photon), however, is strongly dependent upon the photon energy, E, and we find that it is proportional to $E\mu(E)$ where $\mu(E)$ is the mass absorption coefficient of the photocathode. These results have been explained by a phenomenological model and verified experimentally in our previous work. In Fig. 1 the general argument for this energy dependence is given, based upon the reason that since the shape of the energy distribution curves (EDC's) are independent of the photon energy, E, it follows that the yield, Y, should then essentially be proportional to the energy that is deposited within the escape depth, λ_s, viz. $E\mu(E)\rho\lambda_s$. It is noted that Y is also simply proportional to the average imaginary component, f_2, of the atomic scattering factors of the material. Therefore, for pure element photocathodes, their energy dependence is essentially that of our f_2 plots for the 94 elements (ADNDT, Vol. 27).

In Fig. 2 are presented the quantum yield curves as we have measured them for gold and high density cesium iodide, along with the $E\mu(E)$ curves (arbitrary scale) which verify this energy dependence.

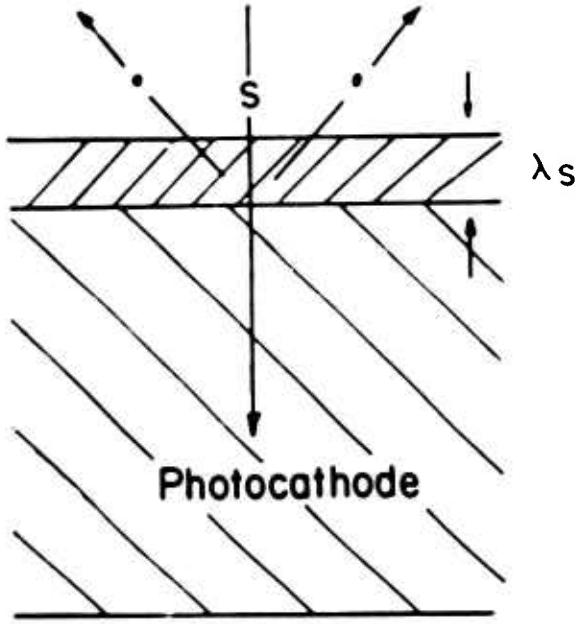
We are also measuring the number of "electron bunches" per photon via the counts measured per photon using microchannel plate pulse-counting. These photon counting efficiencies for the high and low density cesium iodide are shown in Fig. 4. The photocathodes were generated by high vacuum evaporation and by evaporation under about 15 Torr of Ar, respectively. The ratio of the quantum yield, Y, to this

photon counting efficiency gives us the average number of electrons per bunch which is an important parameter in time-resolving statistics.

We are currently investigating the photoemission characteristics of solid Xe and Ar for which the escape depths are orders of magnitude larger than those of the conventionally applied photocathode. As predicted, these photocathodes have considerably higher yields at the higher photon energies. For example, in our preliminary measurements, we obtain for both Xe and Ar at 1254 eV about 45 emitted electrons per photon, which is twenty times the value for CsI and one thousand times that for gold at this energy. The escape depths of the solid rare gases are no longer small compared to the photon absorption depths for lower energy photons and, consequently, we must expect a falling off from the $E\mu(E)$ dependence according to the model described in Fig. 2 in the low energy region.

Figure 1. **Photocathode Response, Y_s**

(Y_s = Emitted Secondary Electrons per Incident Photon)



$$Y_s \sim E\mu(E)\rho\lambda_s$$

$$\boxed{Y_s = Kf_2(E)}$$

E - photon energy

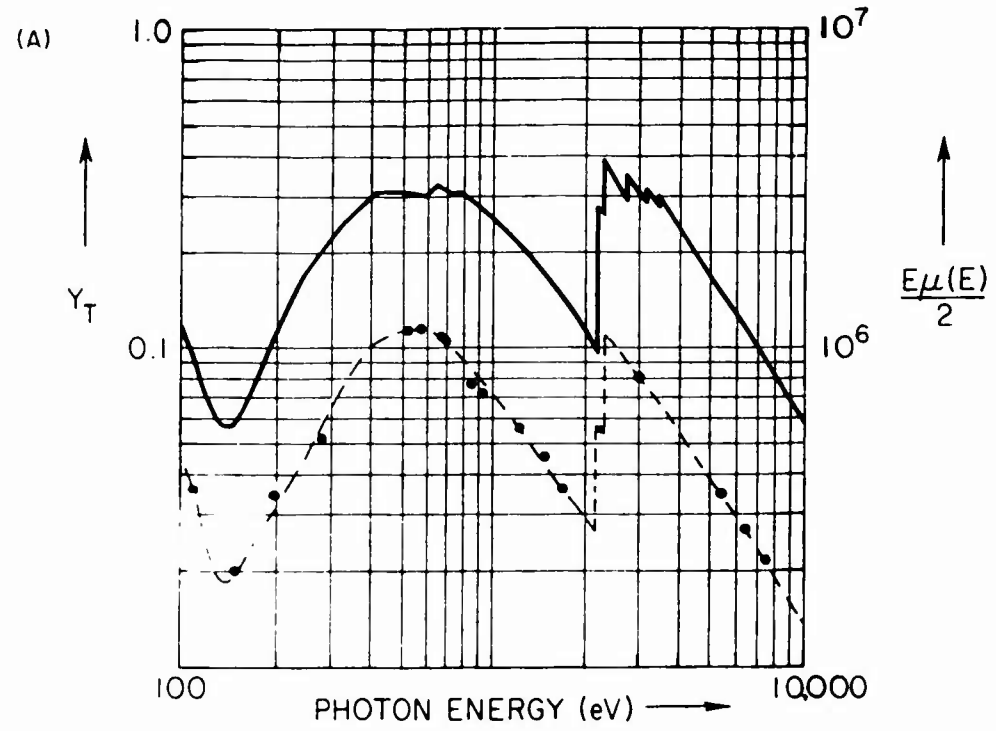
$\mu(E)\rho$ - linear x-ray absorption coef.

λ_s - secondary electron escape depth

K - material constant

XBL 867-2664

Figure 2. **Thick Gold Photocathode**



Thick Cesium Iodide Photocathode

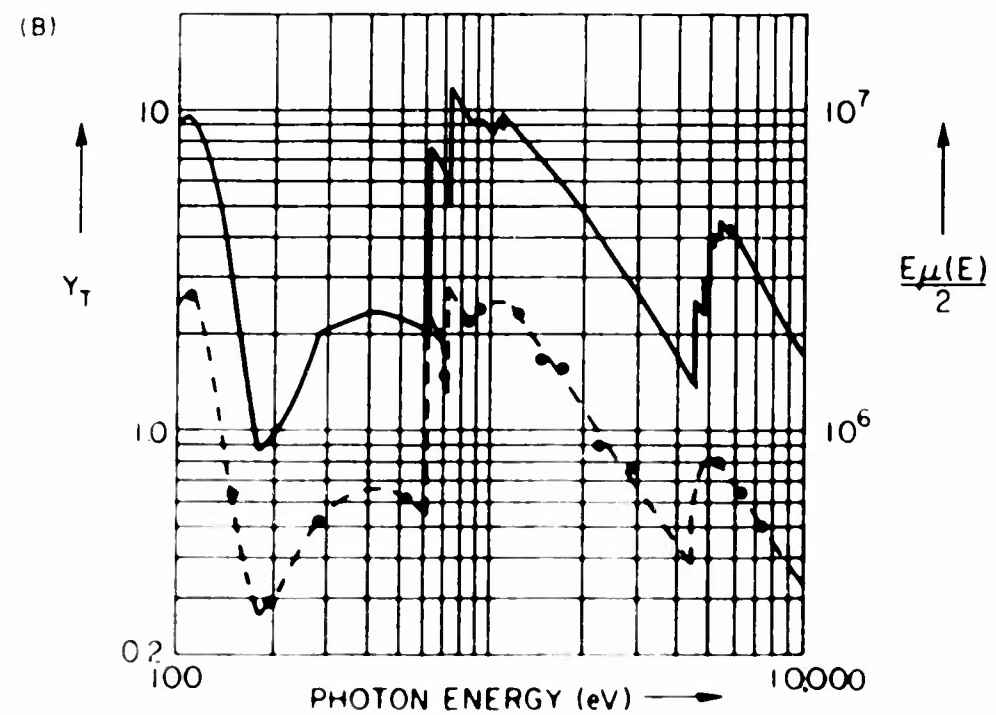
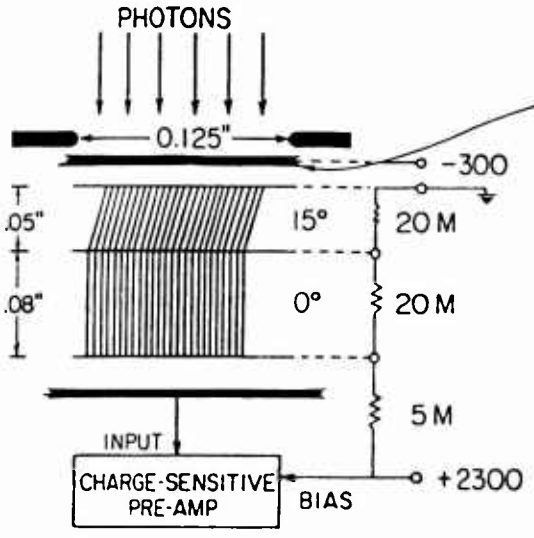


Figure 3. **Photon Counting Efficiency**

(for high and low density CsI)

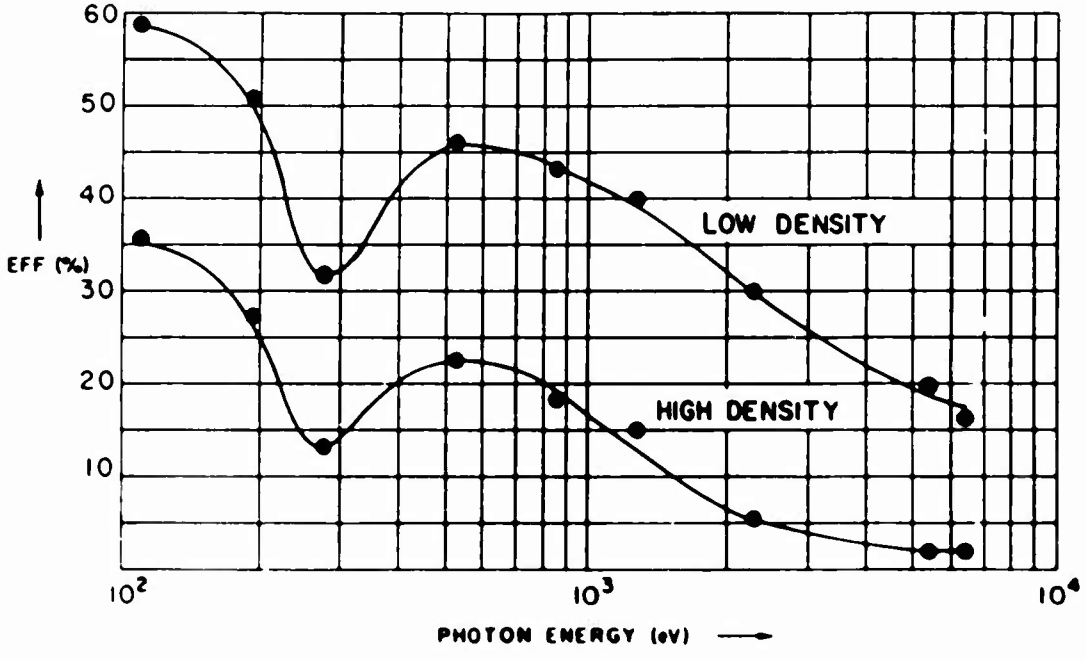


MICROCHANNEL PLATES

PORE DIAMETER -- 35μ

CENTER-TO-CENTER -- 45μ

LENGTH-TO-DIAM. RATIOS -- 35 AND 54

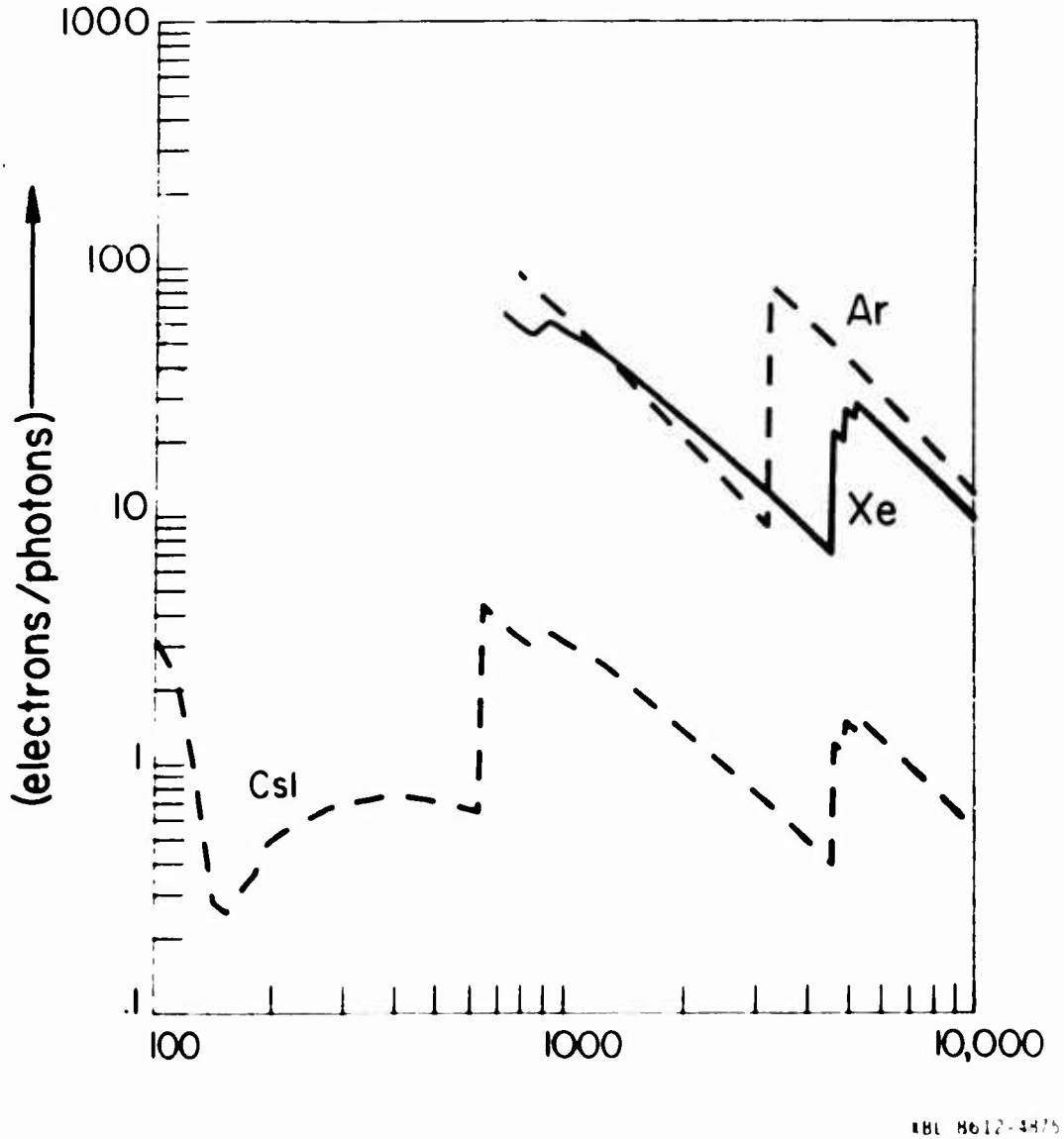


XBL 867-2661

Figure 4.

Quantum Yield, Y, vs Photon Energy, E, for Solid Ar and Xe "Super" Photocathodes Compared to Thick CsI

Preliminary Results - Henke et al (1986)



XBL 8612-3875

12. TECHNICAL NOTES: LOW-ENERGY FLUORESCENT X-RAY SPECTROSCOPY FOR MATERIALS ANALYSIS

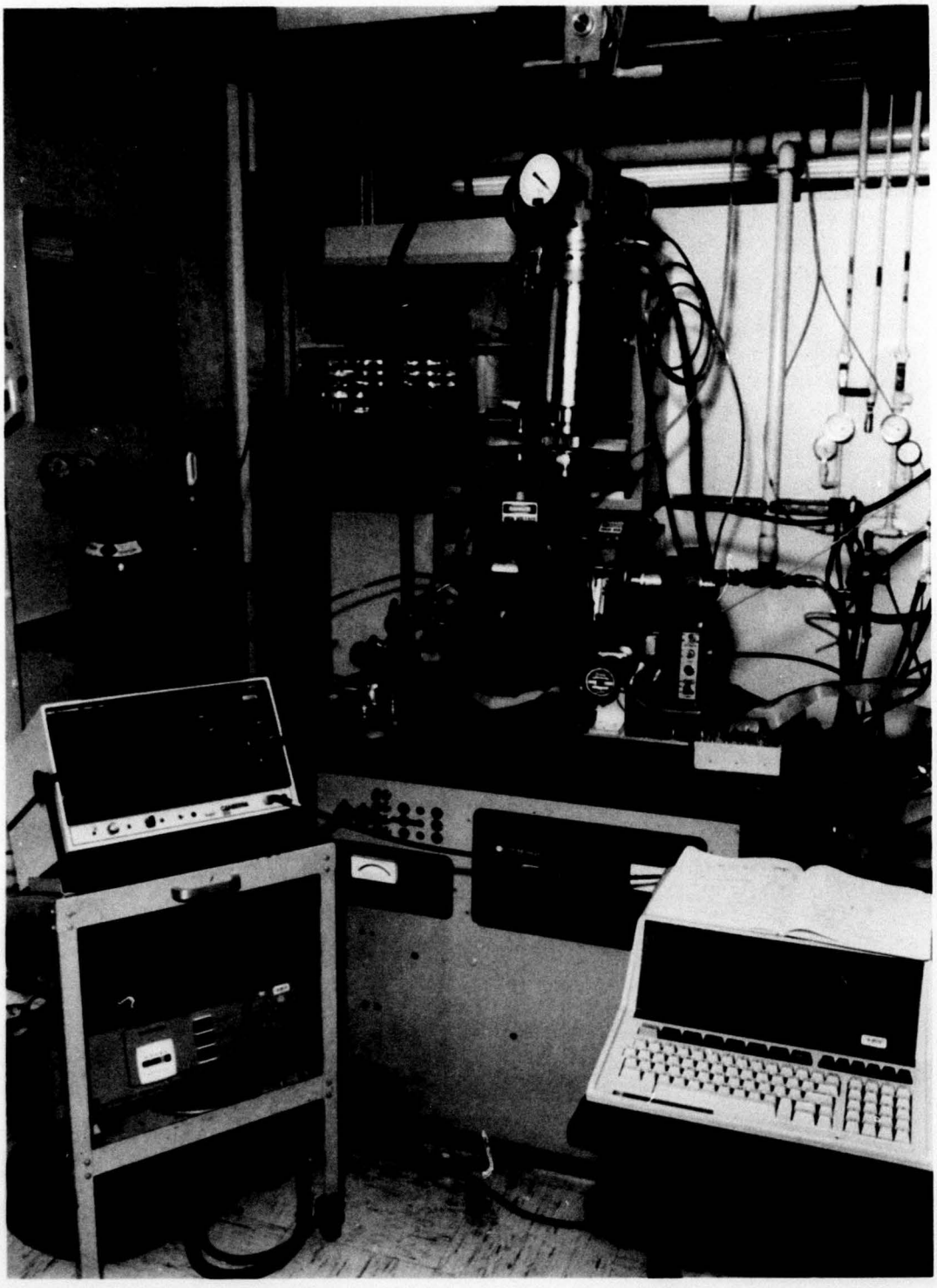
The low energy fluorescent x-ray spectra of molecules and solids are rich in spectral bands that are the result of radiative transitions from the outermost electronic levels to the photoionized core "holes" of the first sharp inner levels. Consequently, these spectra can be energy "maps" of the symmetries and densities of states of the chemical-and-solid state state-sensitive outer electron levels. The band energy structure and shifts become more pronounced and resolvable in the low energy spectra because there are larger effects relative to the low energy region of measurement.

Through many years in this laboratory we have developed a very efficient type of low energy spectroscopy based upon using a cosely coupled high powered de-mountable characteristic line excitation x-ray source, a large-area fluorescent sample, flat crystal/multilayer anlayzers with Soller-slit collimination and pressure-tuned pulse-height discriminating flow proportional counter detection step-scanned data colleciton is by on-line computer programming.

Generally, it is important to selectively excite the desired core states by choosing a characteristic excitation source line of higher energy that is very close to the photoionization energy. In this way, the spectral series that is measured is well defined and unwanted background radiation is eliminated. After the excitation source is chosen, its filter window, that of the counter, the crystal/multilayer analyzer and the counter gas and pressure are carefully chosen in order to optimize the efficiency-and-resolution of the measurement.

Shown here is our vacuum spectrograph as currently set up for the measurement of the band spectra of solid rare gases and of the new "high temperature" superconductor materials.

High Efficiency X-Ray Spectrograph
for the
100-10,000 eV Region



Shown here is a helium refrigerator system that allows the fluorescent sample temperature to be controlled down to about 15 degrees Kelvin. A shroud, held at a temperature lower than that of the sample, provides effective cryo-pumping at the sample surface. This system is currently being applied for the measurement of the band spectra of solid Xe and Ar and for the "high temperature" superconductors (e.g. Cu-Ba-Y-O).

13 Temporal dependence of the mass-ablation rate in uv-laser-irradiated spherical targets

P. A. Jaanimagi,* J. Delettrez, B. L. Henke,* and M. C. Richardson
Laboratory for Laser Energetics, University of Rochester, 250 East River Road, Rochester, New York 14623-1299
(Received 6 January 1986)

In this paper we present new measurements of thermal transport in spherical geometry using time-resolved x-ray spectroscopy. We determine the time dependence of the mass-ablation rate by following the progress of the ablation surface through thin layers of material embedded at various depths below the surface of the target. These measurements, made with 6 and 12 uv (351 nm) beams from the OMEGA laser system of the Laboratory for Laser Energetics of the University of Rochester, are compared to previous thermal transport data and to detailed hydrodynamic code simulations. We find agreement with code results for the scaling of the mass-ablation rate with absorbed intensity, but measure larger absolute values than predicted. This finding is interpreted as being the result of irradiation nonuniformities on target. The sharp decrease in the mass-ablation rate after the peak of the laser pulse predicted in simulations is consistent with experimental observations.

I. INTRODUCTION

Thermal transport in spherical targets uniformly irradiated with multiple, nanosecond-duration laser beams has been a topic of much theoretical[1] and experimental interest.[2–6] An understanding of thermal transport processes in laser fusion plasmas is important in that they impact directly on laser-induced ablation processes which drive the implosion of direct-drive laser fusion targets. The direct measurement of the transport of thermal energy from the absorption region to the ablation surface is not possible. However, the mass-ablation rate $\dot{m}$ (g/cm^{2}s) which is dependent on the thermal transport can be measured through a variety of diagnostics, such as plasma velocity and x-ray spectroscopic techniques. In effect, $\dot{m}$ is a measure of the depth of material penetrated by the heat front during the laser pulse.

There is a growing body of experimental measurements of $\dot{m}$, some of which appears to suggest that the transport of thermal energy is inhibited. Computer simulations of these experiments place an upper limit on the heat flux q,[7] such that $q=\min(q_{\rm cl}, fq_{\rm fs})$, where $q_{\rm cl}$ is the classical value, $q_{\rm fs}$ is the free-streaming limit and f is referred to as the flux limiter. Experiments in spherical geometry have inferred various levels of flux inhibition. For $\lambda=1.05\ \mu$m laser irradiation[2–5] values range from as low as $f=0.06$ to fluxes in excess of the free-streaming limit. In Ref. 4, a low-temperature foot on the heat front was postulated which cannot be explained with a simple flux-limited inhibition model. At $\lambda=0.53\ \mu$m, a flux limiter of $f>0.1$ has been inferred.[2] In experiments at $\lambda=0.35\ \mu$m, markedly different values of $\dot{m}$ and of its scaling with absorbed intensity I_A were estimated depending on whether they were inferred from charge-collector or time-integrated x-ray spectroscopy measurements.[6]

This broad range of inferred flux limiters from apparently similar experiments is difficult to reconcile. The inconsistency could be due to differences in experimental parameters such as laser pulse shape and irradiation geometry and uniformity. Other factors such as the shorter scale lengths on smaller targets and the onset of resonant absorption at higher intensities will also affect thermal transport. Further, important consideration must be given to the influence of time-dependent effects.

In this paper we discuss the time dependence of the mass-ablation rate and its scaling with absorbed intensity. In Sec. II we present simulations of the mass-ablation rate, emphasizing its time dependence during the laser pulse. This is followed in Sec. III with our experimental results from time-resolved x-ray spectroscopy.

II. COMPUTER SIMULATIONS OF THE MASS-ABLATION RATE

Simulations of the interaction of intense 351-nm laser radiation with spherical targets were made with the one-dimensional Lagrangian code LILAC.[8] In the simulations a 2.5 TW peak power, 600-ps [full width at half maximum (FWHM)] Gaussian laser pulse was tangentially focused on 404-μm-diam targets, producing an average incident intensity of $I_0=5\times10^{14}$ W/cm^2. The hydrocode simulations include ray tracing using the azimuthally averaged laser spatial profile, radiation transport with local thermodynamic equilibrium (LTE) opacities and heat flux as the harmonic mean of $q_{\rm cl}$ and $fq_{\rm fs}$. Simulations were run for a variety of flux limiters ranging from $f=0.02$ to 0.4. From these code calculations we can obtain the instantaneous mass-ablation rate during a single laser pulse as a function of the instantaneous absorbed intensity as referenced to the original target diameter. The case for a flux limiter of $f=0.1$ is illustrated in Fig. 1 for a solid glass sphere and a 6-μm-thick glass shell target. The mass-ablation rate was determined by following the progress of the 500-eV isotherm as referenced to the original Lagrangian frame:

$$\dot{m}=\rho\Delta r/\Delta\tau\ , \tag{1}$$

where ρ is the material density, and Δr is the thickness of material progressively heated to 500 eV in a time $\Delta\tau$. The 500-eV isotherm was chosen as a characteristic tempera-

 ©1986 The American Physical Society

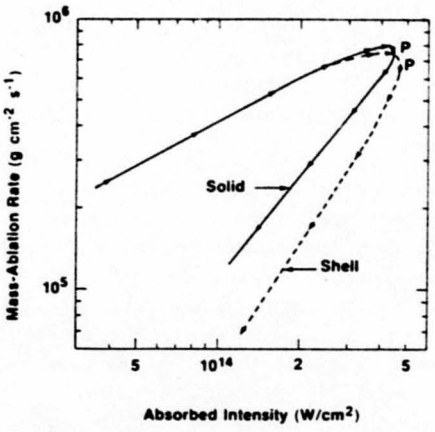


FIG. 1. LILAC simulation for the instantaneous mass-ablation rate [from Eq. (1)] vs the instantaneous absorbed intensity during a single laser pulse, $I_0=5\times10^{14}$ W/cm^2, $f=0.1$ on 404-μm-diam glass targets; solid target (——), 6-μm wall shell target (— — —). Arrows mark 100-ps time intervals starting at 200 ps code time and P denotes the peak of the laser pulse at 773 ps.

ture for Si line emission in the 2.0–2.5 keV range which was used as a diagnostic in the experiments described later. $\dot{m}(t)$ derived from the 300-eV or 1-keV isotherms is essentially the same as for the 500-eV isotherm, with peak values occurring marginally earlier and later in time, respectively. This is characteristic of the steep classical heat front in the overdense material.

The noteworthy features of the curves in Fig. 1 are (i) that $\dot{m}$ does not have the same scaling with absorbed intensity (I_A) on the rising and falling edges of the laser pulse and (ii) that the peak value of $\dot{m}$ is achieved prior to the peak values of both the incident and absorbed intensities. These features are even more pronounced for the case of an imploding glass shell target as compared to the solid target. A similar dependence of $\dot{m}$ on I_A was observed in simulations with other flux limiters as well as for targets of different diameters and different Z.

In a general sense, an empirical mathematical relationship between $\dot{m}$ and I_0 is valuable for understanding thermal transport, and would aid laser fusion target design. However, our efforts to use the simulations to generate scaling laws of the form $\dot{m}\propto I_A^x R_A^y$ (as in Ref. 1), where R_A is the radius of the 500-eV isotherm, have been successful only for individual cases and then only for imploding-shell targets. On solid glass spheres the excursion of R_A during the laser pulse may range up to 30% of the initial target radius, but it cannot account for the observed decrease in $\dot{m}$. Larger excursions are observed for higher intensity laser pulses (5×10^{15} W/cm^2) and for smaller (200 μm) diameter targets.

At $\lambda=351$ mn the predominant absorption mechanism is inverse bremsstrahlung in the subcritical region, and we can define an energy deposition radius R_D as the weighted average absorption radius. Typically R_D lies between the critical and quarter-critical density radii, but inside the peak temperature ($\nabla T=0$) surface. Defining $\Delta R=R_D-R_A$ as the separation between the energy deposition and ablation surfaces, we find the scaling laws for glass targets:

$$\dot{m}\propto I_A^{0.5}R_A^{1.4}\Delta R^{-0.06} \quad \text{for } f=0.02\,,$$

$$\dot{m}\propto I_A^{0.65}R_A^{1.3}\Delta R^{-0.3} \quad \text{for } f=0.04\,,$$

and

$$\dot{m}\propto I_A^{1.0}R_A^{1.0}\Delta R^{-0.73} \quad \text{for } f=0.4\,.$$

The scaling at $f=0.1$ is similar to that at $f=0.4$. The magnitude of ΔR is partially dependent on the size and constituents of the target. For moving-shell targets ΔR increases monotonically throughout the laser pulse, but for solid spheres ΔR is approximately constant after the peak of the laser pulse. We also note that ΔR is proportional to the density scale length L_D at R_D, and perhaps L_D is a more meaningful parameter for the scaling laws, as it affects energy deposition in the corona directly. Another factor which contributes to decreasing $\dot{m}$ is the fact that the fraction of the absorbed energy deposited outside the $\nabla T=0$ surface increases during the laser pulse.

As suggested in Ref. 1, laser energy absorption by inverse bremsstrahlung leads to reduced $\dot{m}$ and reduced ablation pressure compared to an energy dump at critical density. More of the laser energy is dissipated at subcritical densities, flowing more directly into blow-off kinetic energy. With respect to the above scaling laws, inverse bremsstrahlung implies a larger ΔR since R_D is greater than the critical-density radius. From Ref. 1 we note that the ablation pressure has a much weaker scaling with radius than $\dot{m}$ does, and our simulations do show that the pressure at the 500-eV isotherm scales with I_A on both the leading and trailing edges of the pulse for the solid targets.

In light of the above simulations, care must be taken when plotting $\dot{m}$ obtained from time-resolved x-ray spectroscopy versus absorbed intensity. Using a pulse-averaged I_A will result in an underestimate in the value of $\dot{m}(I_A)$. To avoid such problems the time-varying values of $\dot{m}$ should be plotted versus the instantaneous value of I_A.

III. EXPERIMENTS

The primary diagnostic for our mass-ablation rate measurements was time-resolved x-ray spectroscopy.[9,10] The experiments were carried out using 6 and 12 uv ($\lambda=351$ nm) beams of the OMEGA laser system of the Laboratory for Laser Energetics at the University of Rochester at incident irradiances of $I_0=(1-4)\times10^{14}$ W/cm^2. The laser pulse had a Gaussian temporal profile with a pulsewidth of 600–750 ps FWHM. Two types of targets were used in these studies. One set consisted of empty glass microballoons ($\sim$230 μm diameter) with a 1.0-μm-thick wall. These shells were coated with parylene (CH) (1.0–8.0 μm thick) and then overcoated with a 150-Å layer of Au to provide an initial x-ray time marker. The Au layer thickness was increased to 300 Å for the 12-beam target shots. The second set of targets

were solid glass spheres ($\sim 200\ \mu$m diameter) coated with three layers: 1.5 μm CH, 0.05 μm Al, and 1.5 μm CH.[11]

An elliptically curved pentaerythritol (PET) crystal analyzer was used to disperse the x-ray spectrum (1.7–2.7 keV range) onto the slit of the x-ray streak camera. Spectral and temporal resolutions were $E/\Delta E \sim 600$ and 15 ps, respectively. Representative perspective plots of the x-ray intensity from streak records for 6- and 12-beam shots on the imploding targets are presented in Fig. 2 showing the Au M-band emission and the Si line emission. The time of occurrence of the implosion can be deduced from the peak in the x-ray continuum emission. This x-ray burst is characteristic of the higher temperatures and densities achieved during the stagnation of the glass shell and lasts ~ 150 ps. The mass-ablation rate through the CH layers of known thickness was measured from the time delay between the start of the Au or Al line emission to the onset of the Si emission from the glass substrate. In all of the target shots where $\dot{m}$ could be measured, the CH layer ablated during the rising edge of laser pulse. Thicker CH layers (6–8 μm) did not appear to burn through for intensities $< 3\times 10^{14}$ W/cm^2.

In order to construct a meaningful plot of $\dot{m}$ versus I_A, we require knowledge of the absorbed laser intensity during the CH burnthrough time of interest. Since we could not measure directly the absorption fraction as a function of time nor relate the x-ray emission to the incident laser pulse, $I_A(t)$ was inferred from careful comparisons of the streak data with the LILAC code simulations. We assumed that, if the overall predicted absorption of the laser energy agreed with the experimental measurement, then the code could be relied upon to predict the instantaneous absorbed laser intensity during the pulse. A flux limiter of $f=0.04$ was required to match the absorbed fractions. We also assumed that the hydrodynamic implosion time predicted by the code for the shell targets was correct. Then, by matching the predicted and experimental implosion times we are able to relate the x-ray emission on the streak record to the incident laser pulse. The accuracy of equating the implosion times was checked by calculating the predicted absorbed laser energy up to a time corresponding to the onset of the Au emission as measured on the streak record. The calculated absorbed laser energy was in the range 3.0 to 5.5 J, Fig. 3, and corresponds to a time window of ~ 80 ps. Conservatively, this implies a 100-ps accuracy in our timing fiducial technique. By including a ± 50-ps jitter in the streak record timing we obtain a timing fiducial with 150-ps accuracy for the solid sphere targets.

In Fig. 4 we present the scaling of the measured mass-

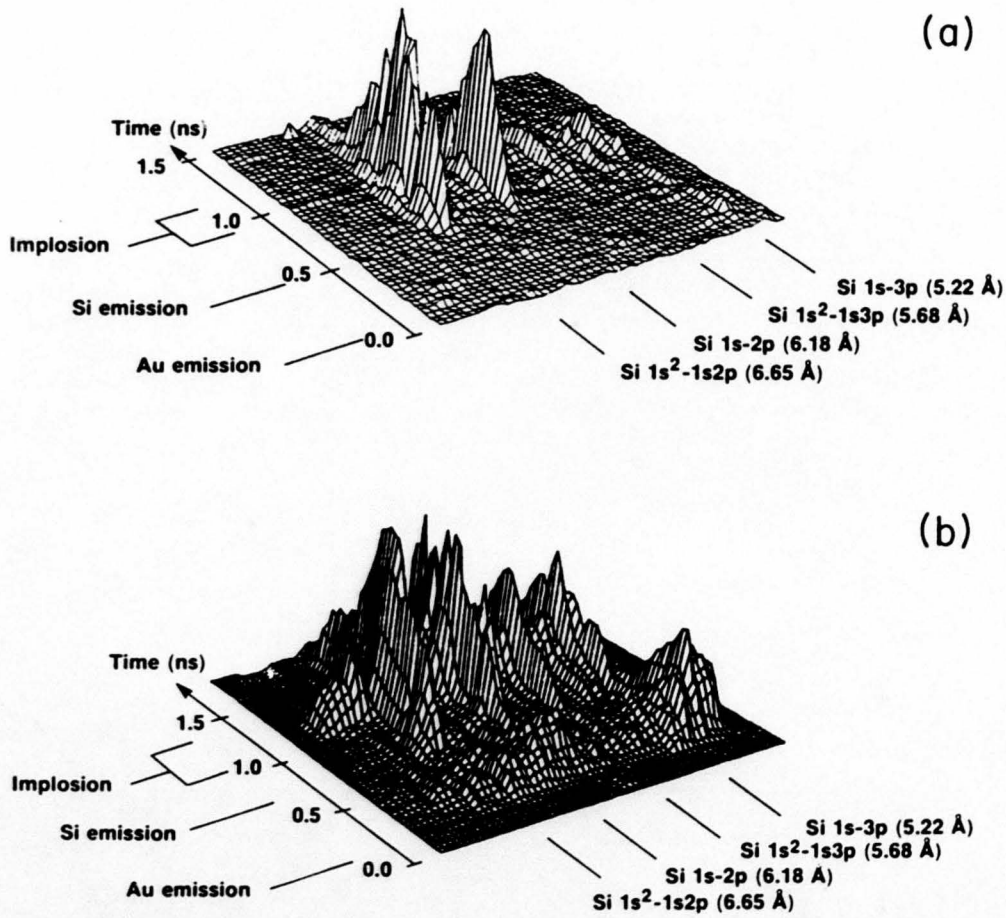


FIG. 2. Perspective plots of the x-ray intensity as recorded by the streak camera. Correction for the spectrometer response function would increase the intensity on the long-wavelength side by 40%. (a) 150 Å Au on 4 μm CH on 1.0-μm glass shell target. Diameter is 229 μm at $I_0=2.8\times 10^{14}$ W/cm^2 with six-beam irradiation. (b) 300 Å Au on 3 μm CH on 1.0-μm glass shell target. Diameter is 289 μm at $I_0=4.2\times 10^{14}$ W/cm^2 with 12-beam irradiation.

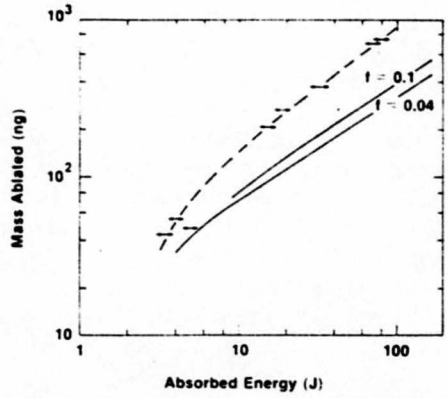


FIG. 3. Ablated mass vs absorbed energy during a single laser pulse for six-beam irradiation of multilayer targets. Solid lines are LILAC simulations for the mass outside the 500-eV isotherm. For the experimental data the total mass outside the glass substrate is assumed to have been ablated. Data points at ~4 J absorbed energy are for the ablation of the outer Au layer only.

ablation rate as a function of the average absorbed laser intensity during the CH burnthrough interval; I_A is derived from the simulations as outlined above. We also include data for $\dot{m}$ for the outer CH layer on the solid targets where I_A is derived using 3 J of absorbed energy for time zero. The time-resolved six-beam data is in excellent agreement with the time-integrated measurements at $I_A = 7.5 \times 10^{13}$ W/cm^2, which was measured for a similar target diameter (Ref. 6). The scaling of $\dot{m}$ with I_A for six-beam irradiation and $I_A \lesssim 10^{14}$ W/cm^2 is in reasonable agreement with code predictions although the magnitude of $\dot{m}$ is ~2 times higher than that predicted for uninhibited transport ($f = 0.4$). The scaling of $\dot{m}$ with I_A derived from the time-integrated x-ray spectroscopy of Ref. 6 is much weaker than that reported here.

A possible cause for the discrepancy between the measured and calculated values of $\dot{m}$ could be the known variances in the intensity distribution across the surface of the target.[12,13] These have been estimated using a three-dimensional superposition code which combines the equivalent target plane intensity distribution of each beam and computes a spherical-harmonic mode decomposition of the intensity distribution on the target surface.[14] An initial assessment of the irradiation uniformity with six uv (351-nm) beams of OMEGA indicates an overall rms nonuniformity of ~50% in the lowest 30 l modes.[12] Alternatively this can be stated as a few percent of the laser energy is absorbed at an intensity greater than three times the average intensity.[15] Further characterization of the irradiation nonuniformities is obtained from x-ray pinhole pictures of solid high-Z (Au) targets irradiated with six beams, which show large-scale intensity variations across the target surface.[16] Time-resolved imaging of the x-ray emission from these targets has also confirmed the existence of discrete hot spots.[16] Given the amount of energy in the hot spots and the sensitivity of our diagnostic (Au emission is detected at the 2% of the total absorbed energy level from Fig. 3), the value of $\dot{m}$ obtained using time-resolved spectroscopy should be characteristic of the absorbed intensity in the hot spots. A shift of our experimental points in Fig. 4 by a factor of 3 in I_A results in reasonable agreement with code predictions for $f = 0.1$. Under the assumption that the laser energy distribution on target is the same for the approximately constant diameter targets used in these studies, the measured scaling of $\dot{m}$ with I_A should be valid. Similarly the discrepancy between the measured and calculated values of the amount of mass ablated during the laser pulse in Fig. 3 can be attributed to the burnthrough of only small areas of the CH coating corresponding to the hot spots in the irradiation pattern.

With 12-beam irradiation the illumination uniformity should be improved and the effects of hot spots on the burnthrough should be commensurately less. Experimentally we do observe a significant decrease in the magnitude of $\dot{m}(I_A)$ (see Fig. 4). Further evidence for the decrease in $\dot{m}$ with the more uniform 12-beam irradiation are the "burnthrough" curves presented in Fig. 5, as measured by the time-integrating channel of the x-ray spec-

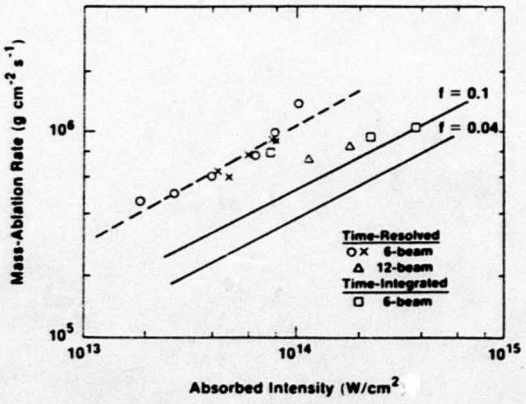


FIG. 4. Mass-ablation rate versus absorbed intensity at $\lambda = 0.351$ μm. Compilation from this study (— — —), time-integrated measurements from Ref. 6, and LILAC simulations at $f = 0.1$ and 0.04 for the rising edge of the pulse.

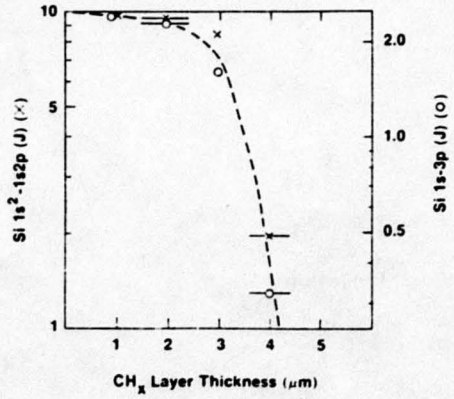


FIG. 5. "Burnthrough" curves for CH and Au/CH on glass targets with 12-beam irradiation at $I_0 = 4.0 \times 10^{14}$ W/cm^2 for the Si He$_\alpha$ (x) and Si H$_\beta$ (0) x-ray resonance lines.

trometer.[10] Here we plot the absolute energy in the Si^{+12} $1s^2$-$1s2p$ and Si^{+13} $1s$-$3p$ lines as a function of CH overcoat thickness. The 300-Å Au layer on two of the targets was assumed to have an areal mass density equivalent to 0.5 μm of CH, although the effective thickness of the Au layer is greater than this due to radiation cooling in the higher-Z material. The projected burnthrough thickness of ≤ 5 μm of CH is much less than the 9 μm of CH interpolated at $I_0 = 3 \times 10^{14}$ W/cm^2 from the six-beam data (Ref. 6). This difference cannot be accounted for strictly by the difference in burnthrough depth between shells and solids, nor by the presence of the thin Au layer on the outside of the targets used in these experiments. Although we have not investigated a very large range of absorbed intensities with 12-beam irradiation, it is our contention that the scaling of $\dot{m}$ with I_A would be the same as for the time-resolved six-beam data.

Although we do not have any direct measurements of the mass-ablation rate on the trailing edge of the laser pulse, we do not observe any Si line emission on the streak records for the six-beam shots on targets with 6- and 8-μm-thick overcoats of CH. This is consistent with the predicted decrease in $\dot{m}$ starting before the peak of the laser pulse as illustrated in Fig. 1. Using the timing fiducial method outlined above we estimate that the onset of the Si line emission for a target with a 4-μm CH overcoat occurs ~ 50 ps before the peak of the laser pulse. If there had been a symmetric scaling of $\dot{m}$ with I_A on the leading and trailing edges of the pulse, surely we would have observed the Si line emission from the targets with the thicker CH coatings. In addition, if we extrapolate the experimental data in Fig. 3 to the mass of these CH layers, the absorbed laser energy on these target shots was sufficient to produce some Si line emission.

Consideration must also be given to the probability of lateral thermal smoothing of the hot spots in the intensity distribution on the target which appear to dominate the burnthrough and $\dot{m}$ measurements with six-beam irradiation. The amount of smoothing depends on the fractional separation distance $\Delta R/R_0$, where R_0 is the target radius.[17,18] For the imploding targets used in this study, the value of $\Delta R/R_0$ is ~ 0.2 at the peak of the laser pulse. A value of ~ 0.3 is predicted at the peak of the laser pulse for the 90-μm-diam targets irradiated at 10^{15} W/cm^2 in Ref. 6. It is suggested that the lower scaling of $\dot{m}$ with I_A in Ref. 6 is the result of thermal smoothing. This smoothing decreases the magnitude of $\dot{m}$ to a level more characteristic of the average intensity on target.

IV. CONCLUSION

The measurement of the mass-ablation rate in spherical geometry with short-wavelength lasers in influenced significantly by time-dependent effects during the laser pulse.[19] The transport of thermal energy and therefore $\dot{m}$ is affected by the increasing separation between the energy deposition and ablation surfaces. Irradiation nonuniformities also have a significant effect on x-ray spectroscopic measurements of the mass-ablation rate since the burnthrough seems to be dominated by hot spots. Our experimental measurements of $\dot{m}$ are in agreement with code predictions for the scaling of $\dot{m}$ with I_A on the rising edge of the laser pulse as shown in Fig. 4; only indirect evidence is presented for lower values of $\dot{m}$ on the trailing edge of the laser pulse.

ACKNOWLEDGMENTS

We acknowledge useful discussions with Dr. R. Epstein, Dr. L. Goldman, Dr. A. Hauer, Dr. R. L. McCrory, Dr. J. M. Soures, Dr. S. Skupsky, and Dr. B. Yaakobi and the technical support of Dr. S. A. Letzring, G. Gregory, and the OMEGA operations group. This work was supported by the U. S. Department of Energy Office of Inertial Fusion under Agreements No. DE-A508-82DP40175 and No. DE-FC08-85DP40200 and by the Laser Fusion Feasibility Project at the Laboratory for Laser Energetics which has the following sponsors: Empire State Electric Energy Research Corporation, General Electric Company, New York State Energy Research and Development Authority, Northeast Utilities Service Company, Ontario Hydro, Southern California Edison Company, The Standard Oil Company, and the University of Rochester.

---

*Permanent address: Lawrence Berkeley Laboratory, University of California, 1 Cyclotron Road, Berkeley, CA 94720.

[1]C. E. Max, C. F. McKee, and W. C. Mead, Phys. Fluids 23, 1620 (1980).

[2]T. J. Goldsack, J. D. Kilkenny, B. J. MacGowan, P. F. Cunningham, C. L. S. Lewis, M. H. Key, and P. T. Rumsby, Phys. Fluids 25, 1634 (1982).

[3]J. A. Tarvin, W. B. Fechner, J. T. Larsen, P. D. Rockett, and D. C. Slater, Phys. Rev. Lett. 51, 1355 (1983).

[4]B. Yaakobi, J. Delettrez, L. M. Goldman, R. L. McCrory, R. Marjoribanks, M. C. Richardson, D. Shvarts, S. Skupsky, J. M. Soures, C. Verdon, D. M. Villeneuve, T. Boehly, R. Hutchinson, and S. Letzring, Phys. Fluids 27, 516 (1984).

[5]A. Hauer, W. C. Mead, O. Willi, J. D. Kilkenny, D. K. Bradley, S. D. Tabatabaei, and C. Hooker, Phys. Rev. Lett. 53, 2563 (1984).

[6]B. Yaakobi, O. Barnouin, J. Delettrez, L. M. Goldman, R. Marjoribanks, R. L. McCrory, M. C. Richardson, and J. M. Soures, J. Appl. Phys. 57, 4354 (1985).

[7]R. C. Malone, R. L. McCrory, and R. L. Morse, Phys. Rev. Lett. 34, 721 (1975).

[8]For descriptions of earlier versions of LILAC, see E. B. Goldman, Laboratory for Laser Energetics Report No. 16 (unpublished); J. Delettrez and E. B. Goldman, Laboratory for Laser Energetics Report No. 36 (unpublished).

[9]B. L. Henke, H. T. Yamada, and T. J. Tanaka, Rev. Sci. Instrum. 54, 1311 (1983).

[10]B. L. Henke and P. A. Jaanimagi, Rev. Sci. Instrum 56, 1537 (1985).

[11]The CH/Al/CH solid-sphere targets were supplied as part of a collaborative effort on thermal transport with Los Alamos National Laboratory (LANL).

[12]M. C. Richardson, S. Skupsky, J. M. Soures, W. Lampeter, S. Tomer, R. Hutchison, M. Dunn, and W. Beich, Conference on Lasers and Electro-optics, 1984, Technical Digest (unpublished).

[13]Laboratory for Laser Energetics, Quarterly Report No. 23, 1985 (unpublished).

[14]M. C. Richardson, S. Skupsky, J. Kelly, L. Iwan, R. Hutchison, R. Peck, R. L. McCrory, and J. M. Soures, Proc. SPIE 380, 473 (1983).

[15]S. Skupsky (private communication).

[16]S. A. Letzring, M. C. Richardson, P. D. Goldstone, G. Gregory, and G. Eden, Bull. Am. Phys. Soc. 29, 1318 (1984).

[17]S. E. Bodner, J. Fusion Energy 1, 221 (1981).

[18]S. Skupsky, R. L. McCrory, R. S. Craxton, J. Delettrez, R. Epstein, K. Lee, and C. Verdon, in *Laser Interaction and Related Plasma Phenomena*, edited by H. Hora and G. H. Miley (Plenum, New York, 1984), Vol. 6, p. 751.

[19]The authors thank W. C. Mead of LANL for bringing to our attention a figure which he presented at the 1984 Annual Meeting of the Division of Plasma Physics, Bull. Am. Phys. Soc. 29, 1380 (1984), which indicated a rollover in $\dot{m}$ in simulations of experiments with Gaussian-shaped pulses at $\lambda = 1\ \mu$m.

14. TECHNICAL NOTES: A SEMI-EMPIRICAL DESCRIPTION OF THE LOW-ENERGY X-RAY INTERACTIONS WITH CONDENSED MATTER - PHOTOABSORPTION, SCATTERING, SPECULAR AND BRAGG REFLECTION

For x-rays of photon energies in the 100-10,000 eV region (but not near the absorption edge energy) we have demonstrated that accurate calculations for absorption and scattering within condensed matter can be made based upon the atomic scattering factors ($=f_1 + if_2$) for the atoms comprising the systems (e.g. for the photon energy response of filters, mirrors, multilayers and crystals).

The atomic scattering factors are derived using the Kramers-Kronig relations and the available experimental photoabsorption data (and by interpolating these data using normalized theoretical, Hartree-Slater segments).

The calculational approach of describing x-ray interactiors within condensed matter as scattering by a system of atoms seems to complement well that of the boundary value, E&M solutions e.g. for multilayer characterization based upon the optical constants of the materials. Our analytical descriptions often have the advantages, however, of computational simplicity, speed and flexibility. Presented here is a brief outline of this approach.

To illustrate our atomic scattering description of a phot interaction within condensed matter we consider the reflection-absorption-scattering of an x-ray beam incident at angle upon a slab consisting of N layers of atoms or of unit cells of scattering factor, $f_1 + if_2$, or unit cell structure factor, $F_1 + iF_2$, respectively. Following the method of Darwin we write the equations relating the total downward amplitudes and upward amplitudes that must obtain for any two successive layers within the slab and which dynamically are the sums of the amplitudes of all possible multiple reflections and transmissions. The resuting difference equations are presented in Fig. 1.

In (4) we have derived a modification of the Darwin-Prins solution of these equations (for the case of an ideal, infinitely thick multilayer system) giving the reflected and transmitted beams for a finite number of layers. The resulting reflected amplitude for small grazing angles of incidence accurately corresponds to the E&M Fresnel Eq. prediction when the refractive index unit decrements, δ and β, are related to the average atomic scattering factor, $f_1 + if_2$, as noted in Fig. 2. For large angle reflection from a periodic multilayer, we obtain the Bragg reflected amplitude equation as a function of the Darwin-Prins infinite crystal reflected ratio, S_0/T_0, and of an analytic parameter, x, that is also simply defined in terms of the atomic scattering factors. This modified Darwin-Prins (MDP) result is also given in Fig. 2. The result predicts exactly that obtained by optical

E&M (OEM) solution when the layers are described by their optical constants, δ and β, using relations as those noted in Fig. 2.

In Fig. 3 we present the prediction of our MDP (4) result for the transmitted beam for normal incidence and through a uniform slab of atoms of atomic photoabsorption cross-section, μ_a, in order to obtain the relation between the atomic scattering and the photoabsorption cross section. We find that the only effect of the real part of the atomic scattering factor, f_1, is to establish the phase of the transmitted amplitude and we obtain the important relation between the imaginary part, f_2, and the atomic photoabsorption cross section, μ_a, that is presented in Fig. 3.

In establishing our atomic scattering tables we obtain the f_2 values from the experimental transmission measurements of absorption using uniform foil systems. It is important to note that if the absorbers are not uniform, the transmitted intensity is a function of both f_1 and f_2 and it is not possible to deduce f_2 by a transmission measurement as suggested in Fig. 3.

We determine the f_1 atomic scattering factors for zero-angle scattering by the Kramers-Kronig relations that may be written as shown in Fig. 4 and are also defined in terms of our compiled and interpolated absorption cross sections, μ_a. For large angle scattering, we must take into account the phase differences of the electronic scattering from different regions of the atomic electron distribution, i.e. we must make a form-factor correction to our tabulated f_1 values. We have shown that this can be simply and accurately accomplished as suggested in Fig. 5

An important test of the accuracy of this relatively simple semi-empirical approach for obtaining the atomic scattering factors is presented in Figs. 6 through 9. Here we compare our values of f_1 determined semi-empirically using the Kramers-Kronig model and measured photoabsorption cross sections (using neon gas and solid carbon films absorbers) to f_1 values determined by the nearly exact S-matrix theory (by expensive, large computer calculation). These are given for both 0° and 90° scattering angles.

Finally it is important to point out that our atomic absorption and scattering cross sections cannot be expected to lead to accurate descriptions of absorption, scattering and reflection by condensed matter using semi-empirical approach outlined above if the atoms within the condensed matter are not scattering "atomic-like". Generally, this atomic-like character is preserved within condensed matter except for photon energies below about 100 eV or photon energies very close to absorption thresholds for which chemical or solid state effects become significant. Examples of comparisons of atomic vs condensed matter photoabsorption at the lower energies are shown in Figs. 10.

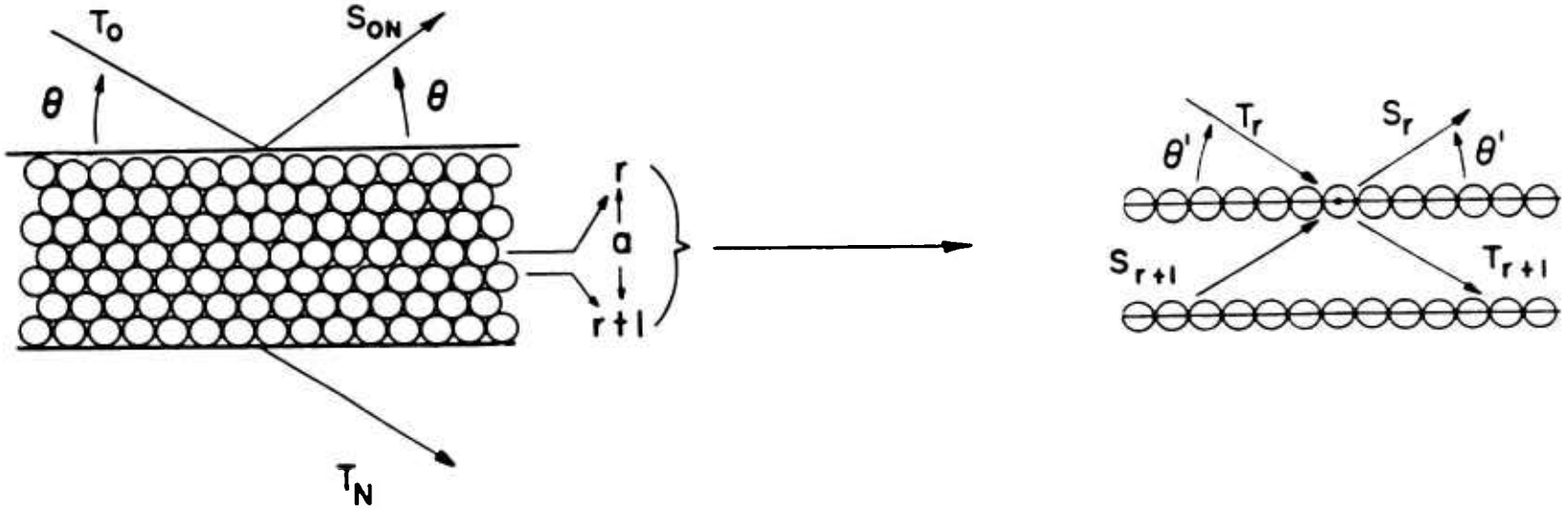
It has been five years since we have developed our absorption and scattering cross section tables (Vol. 27 of ADNDT-1982) and we are now

revising these as based upon additional measured absorption coefficients of the past five years. We are comparing our present absorption files to the current measured data base and to the best available theory. Examples of such comparisons are shown in Figs. 11 and 12.

We will continue to make available to the scientific community the fine-spaced versions of our absorption and scattering factor tables on convenient floppy disks. Descriptions of their formats are attached here.

Figure 1. **Dynamical Reflection and Transmission**

T_r and S_r are <u>total</u> downward and upward amplitudes at the r^{th} layer of a large slab



Difference Equations

$$S_r = -is\,T_r + (1-i\sigma)e^{id}\,S_{r+1}$$

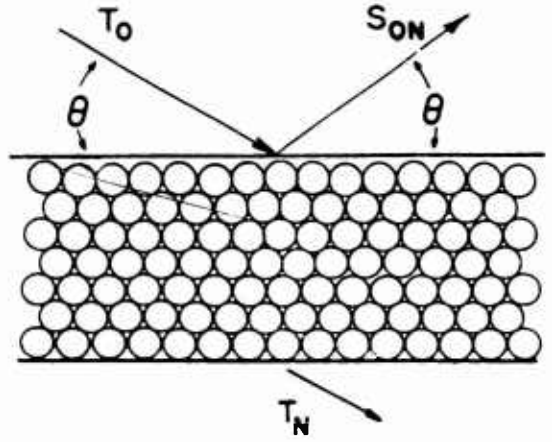
$$T_{r+1} = (1-i\sigma)e^{id}\,T_r - ise^{2id}\,S_{r+1}$$

XBL 872-624

Figure 2. **Dynamical Reflection**

for

N layers of m unit cells/unit area



For small angles

S_{0N}/T_0 reduces to Fresnel Eq. with

$$\delta = \frac{r_0\lambda^2}{2\pi} n_A \bar{f}_1 \qquad \beta = \frac{r_0\lambda^2}{2\pi} n_A \bar{f}_2$$

For large angle periodic-plane diffraction:

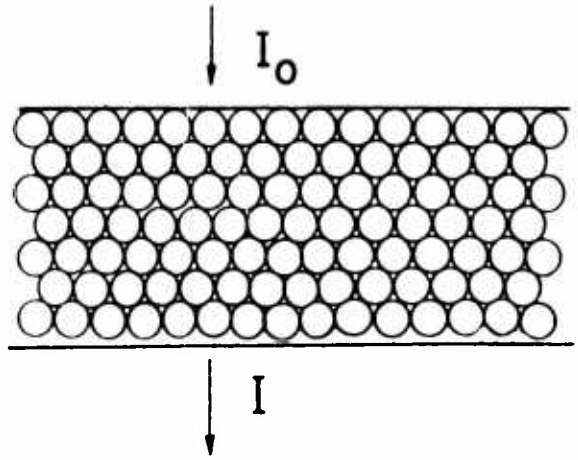
$$S_N/T_0 = \frac{S_0}{T_0} \frac{1-x^{2N}}{1-(S_0/T_0)^2 x^{2N}}$$

where S_0/T_0 is Darwin - Prins for $N = \infty$
and $x = f(m, \theta, F_1, F_2)$

Figure 3. **Dynamical Transmission**

through

N layers of m atoms/unit area of photoabsorption cross - section, μ_a



Model

$$I/I_o = \exp[-2Nmr_o\lambda f_2]$$

Experiment

$$I/I_o = \exp[-Nm\mu_a]$$

Relating $f_2 = \mu_a/(2r_o\lambda)$

XBL 872-621

Figure 4.

Semi - Empirical, Kramers - Kronig, f_1

$$f = \Sigma z_q g_q + C \int_0^{\infty} \frac{\epsilon^2 \mu_a(\epsilon) d\epsilon}{E^2 - \epsilon^2}$$

Short wavelength limit

Anomalous effects

$C = (\pi r_0 hc)^{-1}$

For long wavelength and/or small angle

$$\Sigma z_q g_q = Z$$

yielding the angle - independent, f_1

$$f_1 = Z + C \int_{E_1}^{E_2} \frac{\epsilon^2 \mu_a(\epsilon) d\epsilon}{E^2 - \epsilon^2}$$

XBL 872-619

Figure 5.

Short Wavelength, Large Angle Scattering

$$\Sigma z_q g_q = f_0 = \int_0^\infty U(r) \frac{\sin \mu r}{\mu r} d_r \text{ with } \mu = \frac{4\pi \sin\theta}{\lambda}$$

where f_0 = the form factor = $Z - \Delta f_0$

Then the atomic scattering factor, f, becomes

$$\boxed{f = (f_1 - \Delta f_0) + i f_2}$$

XBL 872-620

Figure 6.

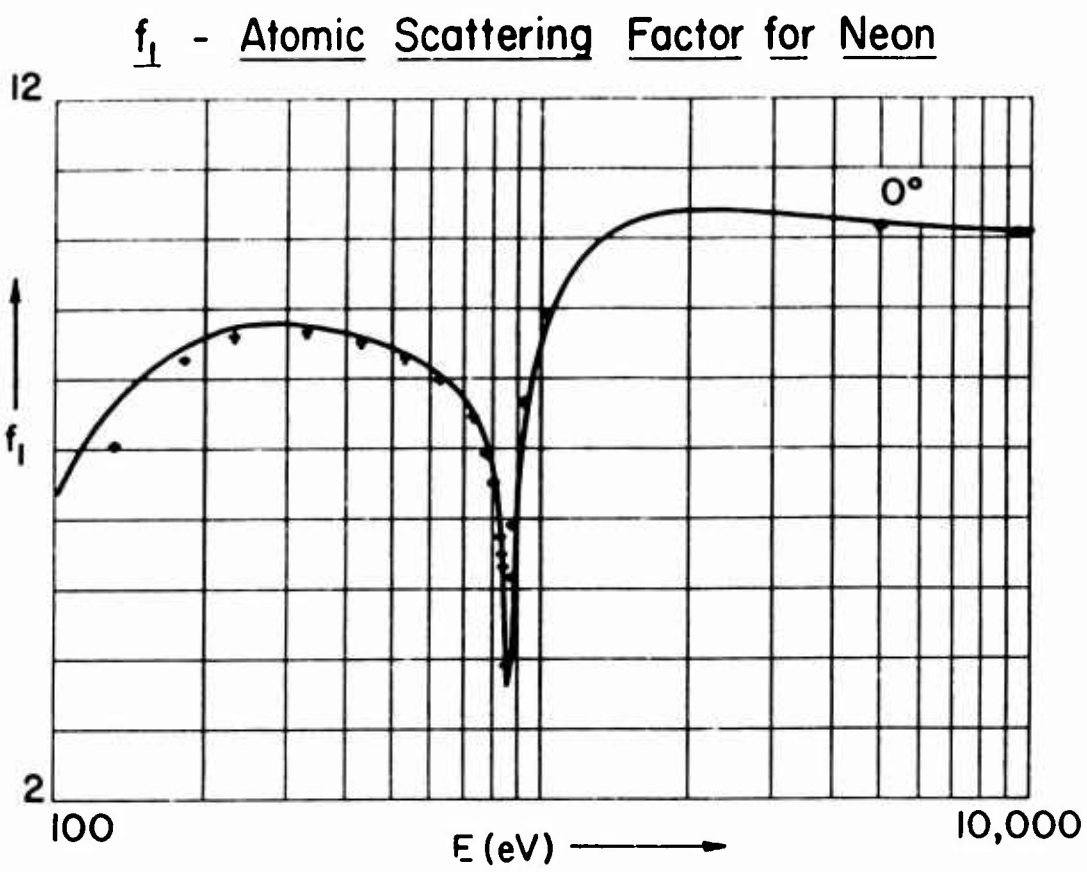

f1 - Atomic Scattering Factor for Neon
12
2
f1
0°
100
E (eV)
10,000
—— Henke et al.
(Kramers - Kronig)
♦ Kissel Parker Pratt
(S - Matrix Theory)
Binding energy set at empirical K-edge
XBL 872-480

Figure 7.

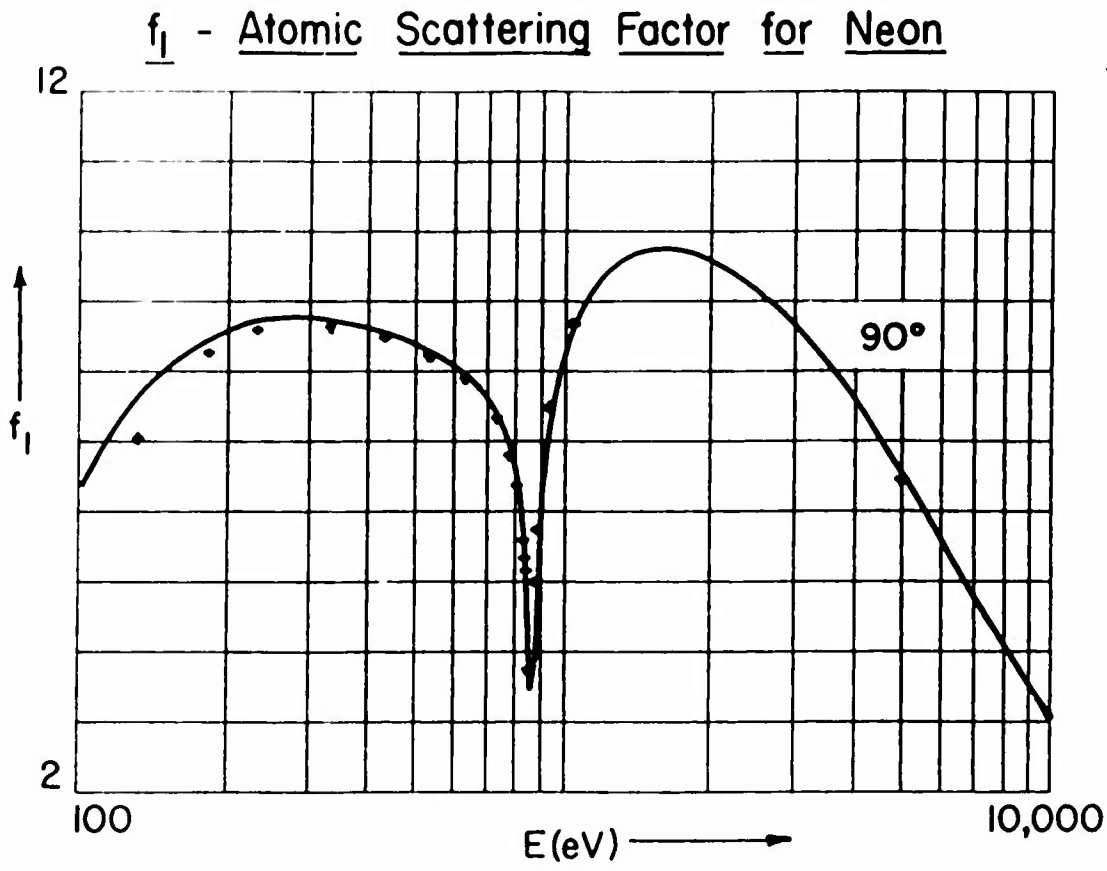
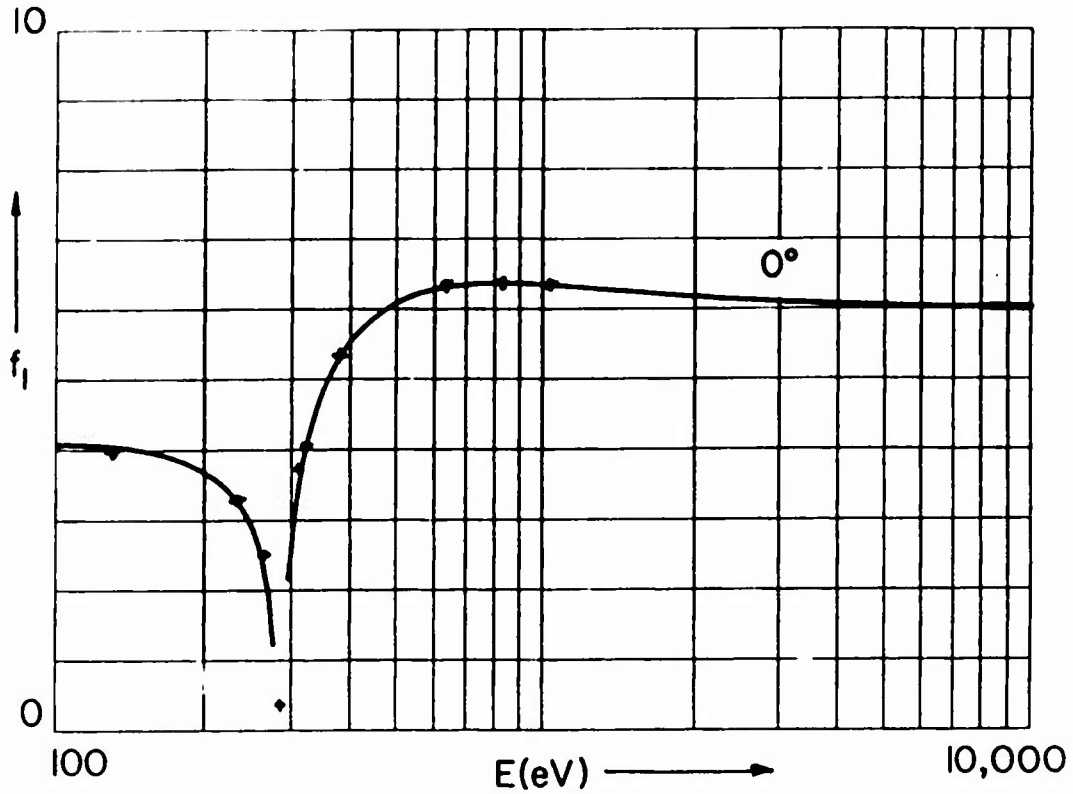

f1 - Atomic Scattering Factor for Neon
12
2
f1
90°
100
10,000
E(eV)
Henke et al.
(Kramers - Kronig)
Kissel Parker Pratt
(S - Matrix Theory)
Binding energy set at empirical K - edge
XBL 872-479

Figure 8.

f_1 - Atomic Scattering Factor for Carbon



—— Henke et al. (Kramers - Kronig)

♦ Kissel Parker Pratt (S - Matrix Theory)

Binding energy set at empirical K-edge

XBL 872-477

Figure 9.

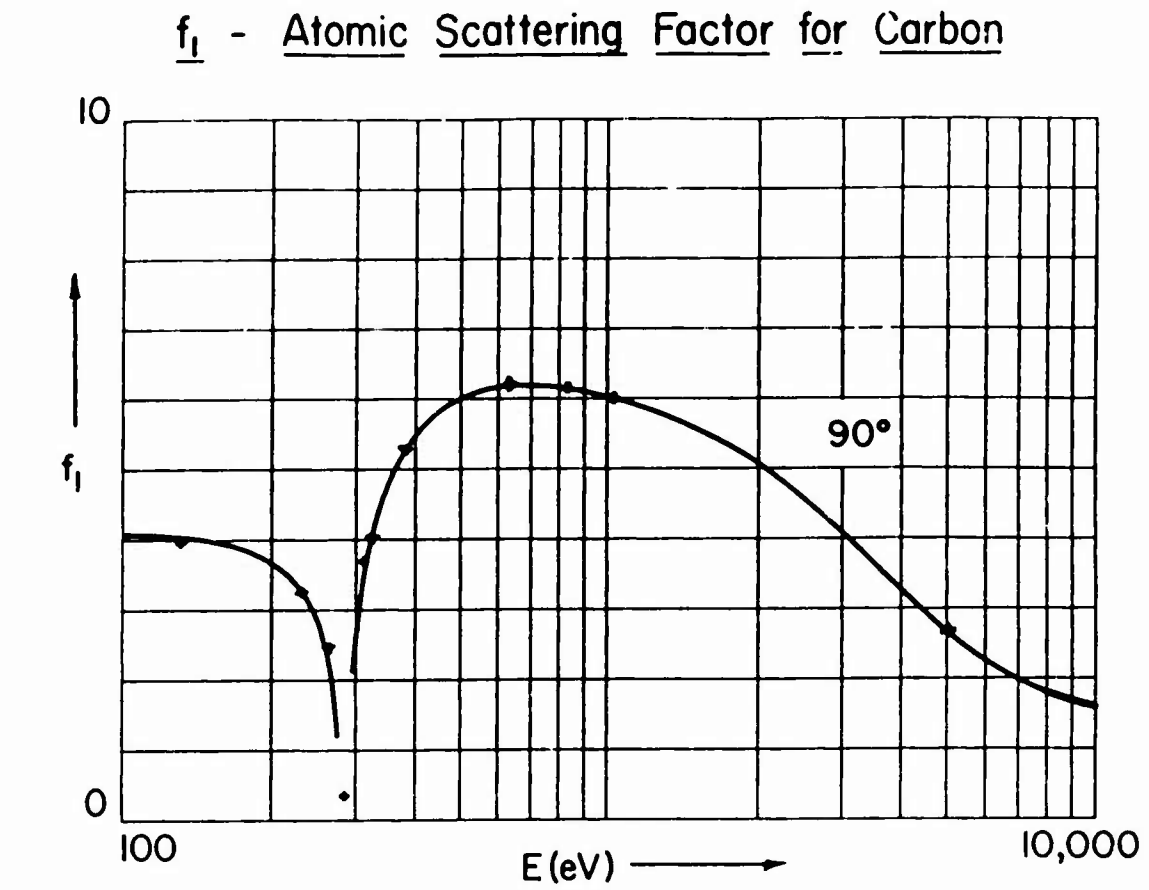
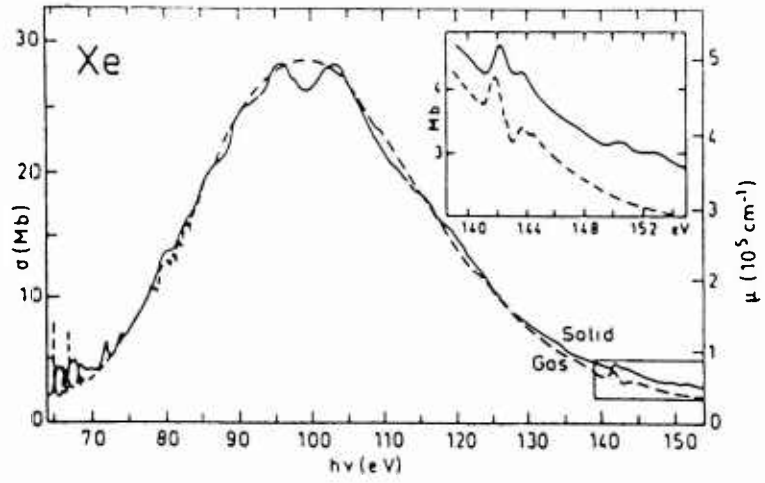
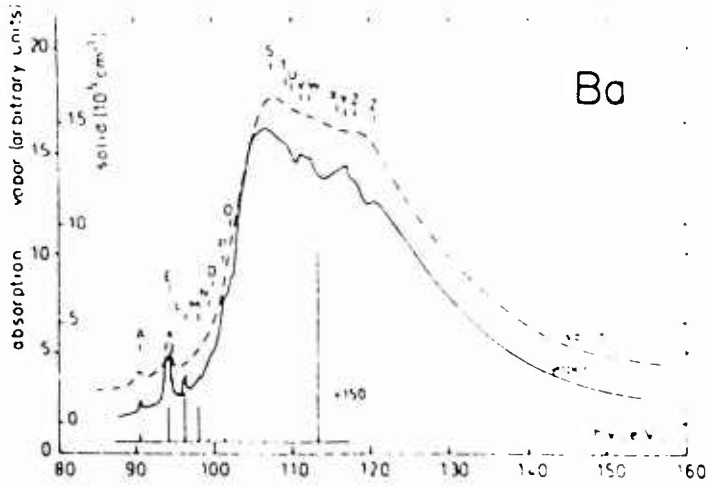

f1 - Atomic Scattering Factor for Carbon
10
0
f1
90°
100
E(eV)
10,000
Henke et al.
(Kramers - Kronig)
Kissel Parker Pratt
(S - Matrix Theory)
Binding energy set at empirical K - edge
XBL 872-476

Figure 10.

Atomic vs Condensed Matter Photoabsorption





——Haensel et al. (1969)

------ Ederer (1964)

Rabe et al. (1974)

Figure 11.

NBS Comparisons of μ-Values for Gold
(NBSIR 80-3431-1986 Saloman and Hubbell)

Exp. Points - NBS Measured Data Base

——— Theoretical (Hartree-Slater) - Scofield (1973, 1986)

---- Semi-Empirical - Henke et al. (1982)

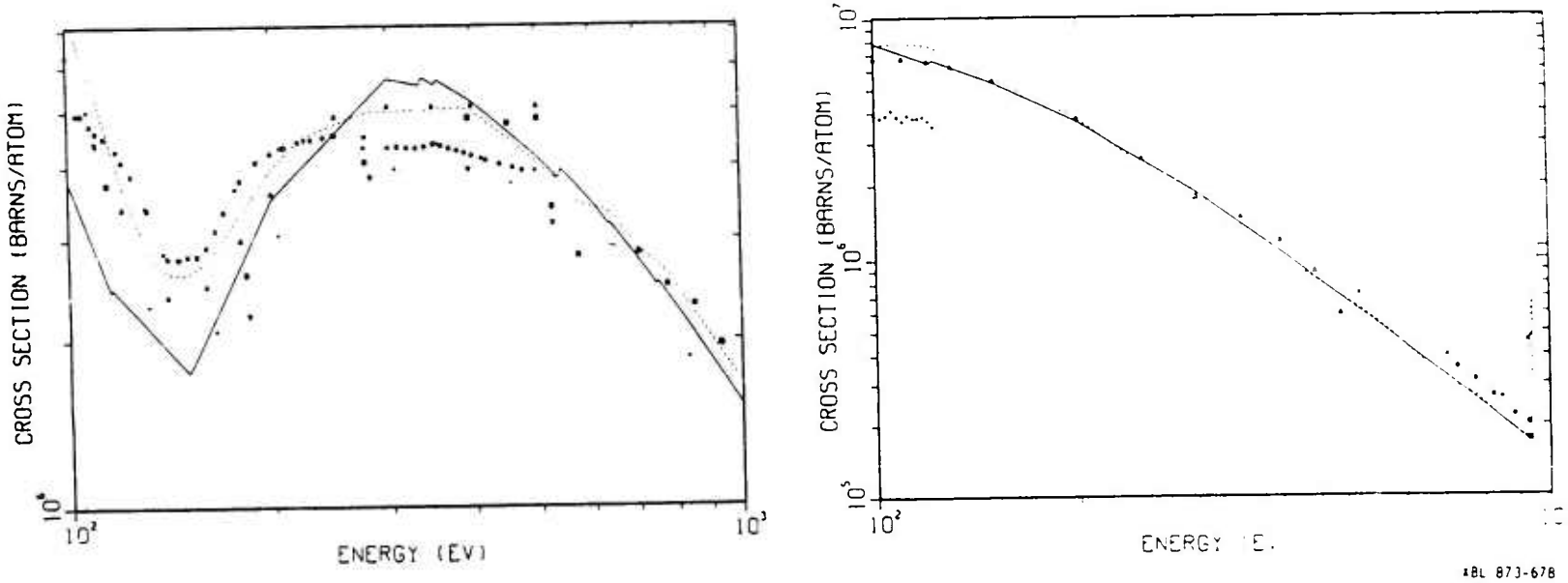


Figure 12.

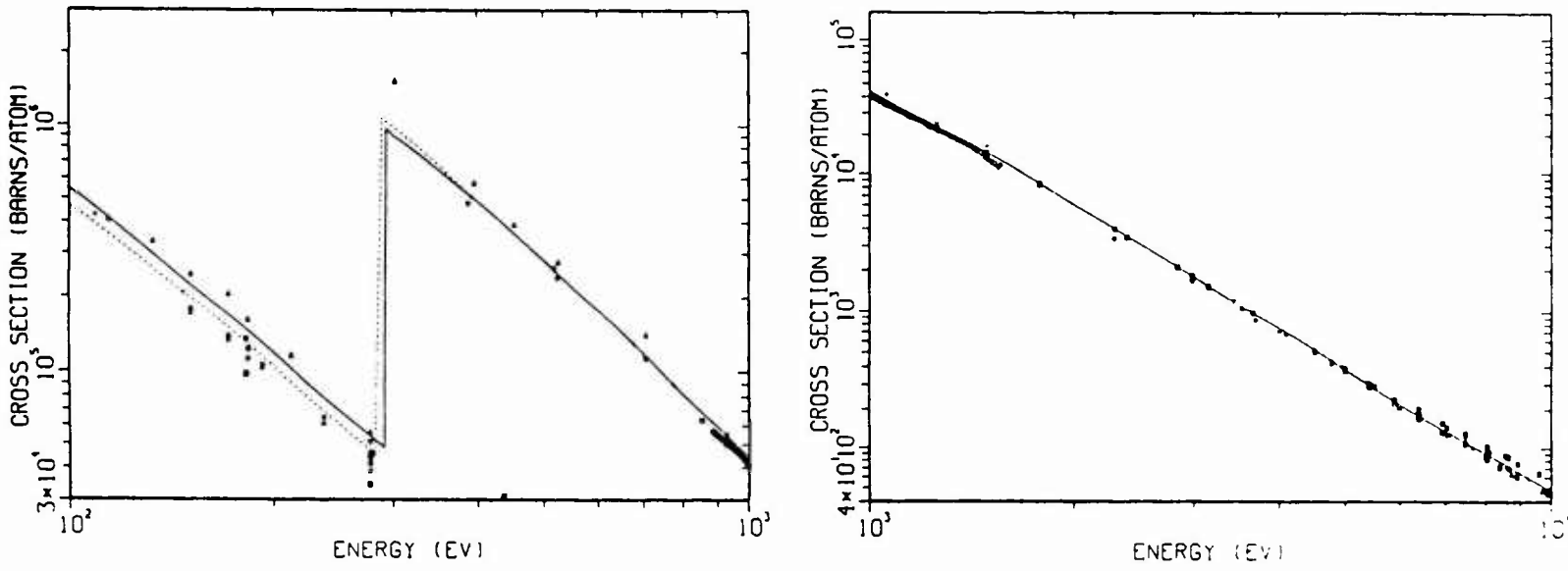
NBS Comparisons of μ-Values for Carbon

(NBSIR 80-3431-1986 Saloman and Hubbell)

Exp. Points - NBS Measured Data Base

——— Theoretical (Hartree-Slater) - Scofield (1973, 1986)

----- Semi - Empirical - Henke et al. (1982)



XBL 873-677

The Atomic Scattering Factor, f1+i*f2, for 94 Elements and for the 100 to 10,000 eV Photon Energy Region (*)

B. L. Henke, H. T. Yamada, and J. Y. Uejio

Center For X-Ray Optics, Lawrence Berkeley Laboratory

In a recent work (1), a "state of the art" evaluation and fitting of the best available experimental and theoretical photoabsorption cross sections has been presented for the 30 to 10,000 eV region. Using the quantum dispersion relations, the atomic scattering factors were uniquely determined from the photoabsorption cross section data for the low-energy x-rays. In Ref. 1, the original data were given at fifty laboratory wavelengths along with compilation references and a description of the fitting procedures. Presented here are the f1 and f2 values which have been interpolated at regular intervals. The tables of the f1 value have been extended from 2 keV to 10 keV by Auerbach et al. (2) who have applied the numerical integration procedures and the higher energy photoabsorption compilation as described in ref. 1. For these shorter wavelengths, it is very important to use the atomic form factor correction, as desribed below.

As discussed recently by Henke (3,4), the f1 and f2 parameters may be applied to calculate the low-energy x-ray interactions--absorption, scattering, specular and Bragg reflection.

The corresponding value for the photoabsorption cross section is related to f2 by E*mu(E)=K*f2. (The data file contains K values.) For E*mu(E) in eV-barns/atom units, K is equal to 6.987E+07 for all atoms.

For the shorter wavelengths and for the larger angles of scattering, the accuracy of these atomic scattering factors might be improved by the inclusion of two small correction terms for relativistic and charge distribution effects. Such corrections can become of relative importance when the magnitude of the scattering factor has been appreciably reduced by anomalous dispersion. As is discussed in Refs. 1 and 3, the modified scattering factor becomes simply

f = f1 - delta f sub r - delta f0 + i*f2,

where the relativistic correction, delta f sub r, is equal to (5/3)*ABS(E(tot))/(m*c**2), which has been tabulated by Cromer and Liberman (5) for Z=3 to Z=98; and the charge distribution correction, delta f0 is equal to (Z - f0), where f0 is the atomic form factor which recently has been tabulated as a function of (sin(theta)/lambda) by Hubbell and Overbo (6). (note that theta(Hubbell) = 2*theta(Henke).) For (sin(theta)/lambda) less than or equal to .05 A**-1, f0 is approximately equal to Z, and for (sin(theta)/lambda) approximately equal to 0.1 A**-1, f0 is approximately 0.9*Z for most elements. An estimate of the value for the relativistic correction, delta f sub r, may be given by (1,3)

delta f sub r=5/3*(E(tot)/m*c**2)
-2.19E-06*Z**3 + 1.03E-04*Z**2

The data are presented here at 285 values of photon energy, E (eV). The scattering factor data are stored as REAL*4 values in an unformatted FORTRAN direct access file called "F12C.DAT" which contains 570 records, each 95 double words (one double word is 4 bytes) long. If data for the element with atomic number Z is desired, then the first ninety-five f1 values are located

in record 6Z+1, the second ninety-five are located in record 6Z+2, and the remaining ninety five are located in record 6Z+3; f2 data are similarly found in records 6Z+4, 6Z+5, and 6Z+6. The energies associated with the f1 and f2 values are located in the first three records of the file (stored as REAL*4 values).

The following useful quantities are contained in a second direct access file "INDEX.DAT":

1. atomic number of element (INTEGER*2)
2. chemical symbol of element (INTEGER*2)
3. atomic weight (REAL*4)
4. K (energy*mu/f2 in eV*cm**2/gram) (REAL*4)
5. mu(barns/atom)/mu(cm**2/gram) (REAL*4)

Where the record number is the same as the atomic number.

The data is divided between records in such an unusual fashion because certain file transfer utilities place a limit on the record size. For an RT-11 system or if the file transfer routine permits records that are 2280 bytes long, the file may be treated as 95 records that are all 570 double words long. In this case, the energies are found in record 1; for atomic number Z, the f1 values are found in record Z+1, followed by the f2 values. found in record 2*Z+1.

The file "F12SUB.FOR" contains two subroutines that the user may find useful. The file "F12RT.FOR" contains the same subroutines as "F12SUB.FOR", but in a format that more convenient for RT-11 system (see the preceeding paragraph). "INTRAC.FOR" contains a program that will print a table of f1 and f2 values for a given element. For more details, see the program listings.

The RSX-11 and VMS operating systems require input files to be in the FILES-11 format. Hence it is necessary to convert the files on the library data floppy disk to this format as they are read in on a RX02 floppy disk device. The file transfer utility FLX is used. This utility is described at length in the RSX-11 and VAX/VMS reference manuals so only the appropriate commands will be described here. After starting FLX you will be prompted for a command with the letters FLX>. For the example it is assumed that the floppy is mounted on device DY1: and the files will be read in onto the user's disk. After allocating and mounting the disk use the following commands: FLX>DY1:/RT/LI> This will list the files on the disk. Except for F12C.DAT, and INDEX.DAT all files are formatted ASCII. Let NAME.TXT be a sample ASCII file name, then each ASCII file is read in with the command: FLX>=DY1:NAME.TXT/RT. The data library file is read in with the the command: FLX>=DY1:F12C.DAT/RT/IM:380. (Note the decimal point in 380. Absolutely mandatory). Similarly, FLX>=DY1:INDEX.DAT/RT/IM:16. will read "INDEX.DAT".

Please note: These photoabsorption data and the associated derived (Kramers-Kronig) atomic scattering factors are for free neutral atoms. Nevertheless, for photon interactions at energies sufficiently outside the absorption threshold regions, condensed matter can be modeled as a collection of free atoms and these atomic data may be applied to predict condensed matter absorption and scattering. In the threshold regions, however, these processes may be strongly affected, for example, by the chemical or solid state and their description must then be by direct experimental measurement upon specific systems (typically using synchrotron radiation sources). Accordingly, we have been able to accurately fit experimentally measured, low energy x-ray small angle reflection from optically smooth surfaces of many materials using the Fresnel relation and optical constants derived from these free atom scattering factors-- except at photon energies near thresholds.

Finally, we remind the user that these tables are based upon "state of the art" compilations of experimental/theoretical photoabsorption data (to 1982). To improve their accuracy, considerably more experimental photoabsorption data is needed. The authors would like to strongly urge all user groups who can carry out photoabsorption measurements to devote some of their effort to meet this important need.

(*) The data on this disk are taken from the Monterey Conference Proceedings appendix (see references 3 and 4); however, the f1-f2 data as originally presented in the Monterey Conference Proceedings have been re-evaluated and some small improvements in the fittings have been included here in the photon energy region below about 300 eV for 26 elements as based, in part, upon newly acquired photoabsorption data. The data are identical with the data in the report "On the Prediction and Application of Low Energy X-ray Interactions" (unpublished).

(1) "Low Energy X-Ray Interaction Coefficients: Photoabsorption, Scattering and Reflection," B. L. Henke, P. Lee, T. J. Tanaka, R. L. Shimabukuro and B. K. Fujikawa, Atomic Data and Nuclear Data Tables Vol. 27, (1982).

(2) The calculations for f1 have been extended into the 2000-10,1000 eV region at the Lawrence Livermore National Laboratory--see UCRL Report No. 91230 by J. M. Auerbach and K. G. Tirsell.

(3) "Low Energy X-Ray Interactions: Photoionization, Scattering, Specular and Bragg Reflection," B. L. Henke, AIP Conference Proceedings No. 75, Low Energy X-Ray Diagnostics-1981, Monterey (American Institute of Physics, New York, 1981).

(4) "Low Energy X-ray Spectroscopy with Crystals and Multilayers," B. L. Henke, AIP Conference Proceedings No. 75, Low Energy X-Ray Diagnostics-1981, Monterey (American Institute of Physics, New York, 1981).

(5) D. T. Cromer and D. Liberman, J. Chem. Phys. 53, 1891 (1970).

(6) J. H. Hubbell and I. Overbo, J. Phys. Chem. Ref. Data 8, 69 (1979).

An Eight-inch, Flexible, Data Disk for the Mass Absorption Coefficients of 94 Elements for the 30 to 10,000 eV Photon Energy Region

B. L. Henke, H. T. Yamada, and J. Y. Uejio

Center for X-ray Optics
Lawrence Berkeley Laboratory
Berkeley, California 94720

These data are presented at 288 uniformly spaced values of photon energy, E(eV), in three logarithmically spaced regions: 40 points between 30 and 100 eV (E1); 124 points between 100 and 2,000 eV (E2); and 124 points between 2,000 and 10,000 eV (E3). [1] The energy intervals are calculated using the following formulae:

```
E1=INT(30*10^(N*LOG10(100/30)/40)
E2=INT(100*10^(N*LOG10(2000/100)/124)
E3=INT(2000*10^(N*LOG10(10000/2000)/124)
```

Where N is the index for the point number.

The mass absorption coefficients are stored as REAL*4 values in an unformatted FORTRAN direct access file called "EMU.DAT" which contains 97 records, each 288 double words (4 bytes) long. (In BASIC, the file is dimensioned (96,287).) The element names are located in the first record, the atomic weights in the second record, the energies in the third record, and the mass absorption coefficients for the 94 elements in records four thru 97.

Also on the disk are two sample FORTRAN programs ELENMU.FOR and MOLEMU.FOR and cheir executable *.SAV versions. ELENMU.FOR lists the energy and mass absorption coefficients for an element. MOLEMU.FOR creates a new file or lists an existing file of mass absorption coefficients for a given molecule. The created file contains 2 records each 288 double words long. Further descriptions of these programs can be found in their respective listings.

NOTE: The FORTRAN programs ELENMU.FOR and MOLEMU.FOR are written in FORTRAN IV for the PDP-11 system.

Please note: These photoabsorption data and the associated derived (Kramers-Kronig) atomic scattering factors are for free neutral atoms. Nevertheless, for photon interactions at energies sufficiently outside the absorption threshold regions, condensed matter can be modeled as a collection of free atoms and these atomic data may be applied to predict condensed matter absorption and scattering. In the threshold regions, however, these processes may be strongly affected, for example, by the chemical or solid state and their description must then be by direct experimental measurement upon specific systems (typically using synchrotron radiation sources). Accordingly, we have been able to accurately fit

experimentally measured, low energy x-ray small angle reflection from optically smooth surfaces of many materials using the Fresnel relation and optical constants derived from these free atom scattering factors--except at photon energies near thresholds.

Finally, we remind the user that these tables are based upon "state of the art" compilations of experimental/theoretical photoabsorption data (to 1982). To improve their accuracy, considerably more experimental photoabsorption data is needed. The authors would like to strongly urge all user groups who can carry out photoabsorption measurements to devote some of their effort to meet this important need.

---

[1] This finely spaced data is equivalent to that found in "Low-Energy X-Ray Interaction Coefficients: Photo-Absorption, Scattering, and Reflection", B. L. Henke, F. Lee, T. J. Tanaka, R. L. Shimabukuro and B. K. Fujikawa, Atomic Data and Nuclear Data Tables, Vol. 27 (January 1982).

APPENDIX 3

LISTING OF REPORTS AND PUBLICATIONS FOR THIS PROGRAM ON LOW ENERGY X-RAY PHYSICS AND TECHNOLOGY

Appendix 3

RESEARCH PUBLICATION BY B.L. HENKE
AND CO-WORKERS ON THIS RESEARCH PROGRAM

1. "Low Angle X-Ray Diffraction with Long Wavelengths," Phys. Rev. 89, 1300 (March 15, 1953).

2. "Diffraction of Long Wavelengths X-Rays," Special Technical Report No. 24, Office of Naval Research; Special Technical Report No. 3, 1-104, Atomic Energy Commission (June 1953).

3. "Submicroscopic Structure Determination by Long Wavelength X-Ray Diffraction," J. Appl. Phys. 26, (1955) (w/ Jesse W. M. DuMond), 903-917.

4. "Slide Rule for Radiographic Analysis," Rev. Sci. Instr. 27, (1956) (w/ Bruno Lundberg), 1043-1045.

5. "Conditions for Optimum Visual and Photometric 'Contrast' in Microradiograms," X-Ray Microscopy and Microradiography (Academic Press, New York, 1957) (w/ B. Lundberg and A. Engstrom), 240-248.

6 a. "Monochromatic Sources of Ultrasoft X-Radiations for Quantitative Microradiographic Analysis," X-Ray Microscopy and Microradiography (Academic Press, New York, 1957), 71-88.

and

b. "High Resolution Contact Microradiography with Ultrasoft Polychromatic X-Rays," X-Ray Microscopy and Microradiography (Academic Press, New York, 1957) (w/ A. Engstrom, R. C. Greulich and B. Lundberg) 218-233.

7. "Semiempirical Determination of Mass Absorption Coefficients for the 5 to 50 Angstrom X-Ray Region," J. Appl. Phys. 28 (1957) (w/ R. White and B. Lundberg), 98-105.

8. "Ultrasoft X-Ray Physics and Applications," Summary Technical Report No. 1, AFOSR TN-57-436, ASTIA Document No. AD 136 426, 1-15.

9. "High Resolution Microradiography," Technical Report No. 2, AFOSR TN-58-803, 1-64.

10. "Ultrasoft X-Ray Interaction Coefficients," Technical Report No. 3, AFOSR TN-59-895, August 1959.

11. "X-Ray Microscopy," Technical Report No. 4, AFOSR AF 49 (638)-394, File No. 1-1-20 and The Encyclopedia of Microscopy, George L. Clark, Ed. (Reinhold Publishing, New York, 1961), Vol. 4.

12. "Measurement in the 10 to 100 Angstrom X-Ray Region," Advances in X-Ray Analysis (Plenum, New York, 1961), Vol. 4, 244-279.

13. "Microanalysis with Ultrasoft X-Radiations," Technical Report No. 6, AFOSR AF 49(638)-394, 1961.

14. "Ultrasoft X-Ray Analysis of Micron Systems," Norelco Reporter IV, 82, 1-16, (1957).

15. "Ultrasoft X-Ray Interaction Coefficients," Proceedings, 2nd International Symposium on X-Ray Microscopy and Microanalysis (Elsevier Publishing, Netherlands, 1960) (w/ Jack C. Miller).

16. a. "Projection X-Ray Microscopy at Pomona College," Norelco Reporter, VII, 137 (1960).

    b. "Isolation of Selected Elements with an Electron Microscope," Norelco Reporter, VII (1961).

17. "Microstructure, Mass and Chemical Analysis with 8 to 44 Angstrom X-Radiation," Proceedings, 7th Annual Conference on Industrial Applications of X-Ray Analysis, 117-155, University of Denver, 1958.

18. "Microanalysis with Ultrasoft X-Radiations," Advances in X-Ray Analysis, (Plenum, New York, 1962), Vol. 5, 285-305.

19. "Small Energy Losses of Electrons in Solids; Design of a Low Energy Electron Spectrometer," (informal notes, 1960, i-xviii) (w/ Charles Greenhall).

20. "Production, Detection and Application of Ultrasoft X-Rays," X-Ray Optics and X-Ray Microanalysis (Academic, New York, 1963).

21. "Sodium and Magnesium Fluorescence Analysis--Part I: Method: Advances in X-Ray Analysis (Plenum, New York, 1963), Vol. 6, 361-376.

22. "Surface Analysis by Soft X-Ray Excitation of Auger and Photoelectrons," (technical notes, 1963, 1-4) (w/ J. Merritt).

23. "X-Ray Fluorescence Analysis for Sodium, Fluorine, Oxygen, Nitrogen, Carbon and Boron," Advances in X-Ray Analysis (Plenum, New York, 1964), Vol. 7, 460-488.

24. "Oxygen Determinations in Silicates and Total Major Elemental Analysis of Rocks by Soft X-Ray Spectrometry," Analyt. Chem. 37 (1965) (w/ A. K. Baird), 727-729.

25. "Some Notes on Ultrasoft X-Ray Fluorescence Analysis--10 to 100 Angstrom Region," Advances in X-Ray Analysis (Plenum, New York, 1965), Vol. 8, 269-284.

26. "Spectroscopy in the 15 to 150 Angstrom Ultrasoft X-Ray Region," 4th International Symposium on X-Ray Microscopy and X-Ray Microanalysis, Orsay, France, Optique des Rays X et Microanalyse, R. Castaing, P. Deschamps and J. Philibert, Eds. (Editions Scientifiques Hermann, Paris, 1966), 440-453.

27. "Valence Electron Band Analysis by Ultrasoft X-Ray Fluorescence Spectroscopy," J. Appl. Phys. 37, 922, (1966) (w/ Eric N. Smith), 1-2.

28. "Application of Multilayer Analyzers to 15 to 150 Angstrom Fluorescence Spectroscopy for Chemical and Valence Band Analysis," Advances in X-Ray Analysis (Plenum, New York, 1966), Vol. 9, 430-440.

29. "Design Notes on an Intermediate Resolution Experiment for the Measurement of the Ultrasoft X-Radiations of the Solar Corona," Technical Report No. 7, 1-413, AFOSR 66-2446 (September 1966).

30. "X-Ray Absorption in the 2 to 200 A Region," Technical Report, AFOSR 67-1254 (June 1967), (w/ R. L. Elgin, R. E. Lent and R. B. Ledingham).

31. "Techniques of Low Energy X-Ray and Electron Physics--50 to 1000 eV Region," Proceedings of the 2nd Symposium of Low Energy X- and Gamma Ray Sources and Applications, 522-556, Austin, Texas, March 1967.

32. "Techniques of Low Energy X-Ray and Electron Physics--50 to 1000 eV Region," Norelco Reporter, XIV, No. 3-4, (1967) (w/ R. L. Elgin, R. E. Lent and R. B. Ledingham).

33. "X-Ray Absorption in the 2 to 200 A Region," Norelco Reporter, XIV, No. 3-4, 75-83, (1967).

34. "Some Recent Work in Low Energy X-Ray and Electron Analysis," Advances in X-Ray Analysis (Plenum, New York, 1969), Vol. 12, (w/ R. E. Lent), 480-495.

35. "An Introduction to Low Energy X-Ray and Electron Analysis," Advances in X-Ray Analysis (Plenum, New York, 1970), Vol. 13, 1-25.

36. "X-Ray Absorption Tables for the 2 to 200 A Region," Advances in X-Ray Analysis (Plenum, New York, 1970), Vol. 13, 639-665.

37. Advances in X-Ray Analysis, Vol. 13, a special volume on low energy x-ray and electron analysis, edited by Burton L. Henke, John B. Newkirk and Gavin R. Mallett (Plenum, New York, 1970).

38. "Measurement of Primary Electron Interaction Coefficients (500 to 1500 eV Region," Colloque International du C.N.R.S., Processus Electroniques Simples et Multiples du Domaine X et X-UV (Paris, September 1970), Le Journal de Physique, Colloque C4, Suppl. 10, Vol. 32, October 1971, 115-123.

39. "Surface Characterization by Low Energy Photoelectron Spectroscopy," Proceedings of the 6th International Congress on X-Ray Optics and Microanalysis (Osaka, Japan, September 1971), 367-384.

40. "The Measurement of Inner Shell Ionization Cross Sections for the 100- 1000 eV Region as Involved with X-Ray Electron Interactions within Solids," Proceedings of International Conference on Inner Shell Ionization Phenomena (Atlanta, Georgia, April 1972), 1-75, published as Inner Shell Ionization Phenomena and Future Applications, edited by R. W. Fink et al. (Technical Information Division of the U.S. Atomic Energy Commission, Oak Ridge, Tennessee, 1973).

41. "Ultrasoft X-Ray Reflection, Refraction and the Production of Photo-electrons (100-1000 eV Region)," Proceedings of Spring Meeting of the American Physical Society (Washington, D.C., April 1972), published in Bulletin of the American Physical Society.

42. "The Measurement of Low Energy Electron and X-Ray Interaction Coefficients for Solids," Proceedings of the 7th National Conference of the Electron Probe Analysis Society of America (San Francisco, July 1972).

43. "Ultrasoft X-Ray Reflection, Refraction and Production of Photo-electrons (100-1000 eV Region)," Physical Review A6, 94-104 (1972).

44. "Electron Interactions within Solids--Electron Spectroscopy" and "Light Element Analysis" Proceedings of the U.S.-Japan Seminar on Fundamentals of Scanning Electron Microscopy (Osaka, Japan, November-December 1972).

45. "Low Energy X-Ray and Electron Absorption within Solids (100-1500 eV Region)," Interim Report, AFOSR 72-2174 (August 1973) (w/ Eric S. Ebisu), 1-65.

46. "Low Energy X-Ray and Electron Absorption within Solids (100-1500 eV Region)," Advances in X-Ray Analysis (Plenum, New York, 1974), Vol. 17, 150-213 (w/ Eric S. Ebisu).

47. "Ultrasoft X-Ray Bragg and Specular Reflection: The Effects of Anomalous Dispersion," Interim Report, AFOSR 72-2174 (August 1974) (w/ Rupert C. C. Perera and Ronald H. Ono).

48. "Demountable Ultrasoft X-Ray Source," (informal notes, August 1974).

49. "Techniques of Low Energy X-Ray Spectroscopy (0.1 to 2 keV Region)," Advances in X-Ray Analysis (Plenum, New York, 1975) (w/ Murray A. Tester), 76-106.

50. "Techniques of Low Energy X-Ray Spectroscopy (0.1 to 2 keV Region)," Interim Report, AFOSR 75-2762 (November 1974) (w/ Murray A. Tester).

51. "Valence Band Spectroscopy in the Ultrasoft X-Ray Region (50 to 100 A), Advances in X-Ray Analysis (Kendall/Hunt, Dubuque, 1976), Vol. 19 (w/ Kazuo Taniguchi), 627-640.

52. "Parameters for the Calculation of X-Ray Absorption Coefficients for H (1) through Ge (32) in the 100-1500 eV Region," Advances in X-Ray Analysis (Kendall/Hunt, Dubuque, 1976), Vol. 19 (w/ Mark L. Schattenburg), 749-767.

53. "Quantitative Low Energy X-Ray Spectroscopy (50-100 A Region)," J. Appl., Phys. 47 (1976) (w/ Kazuo Taniguchi), 1027-1037.

54. "Sulfur $L_{II,III}$ Emission Spectra and Molecular Orbital Studies of Sulfur Compounds," J. Chem. Phys. 64 (1976) (w/ Kazuo Taniguchi), 3021-3035.

55. "X-Ray Calibration Sources for the 100-1000 eV Region," Proceedings of the 1976 ERDA Symposium of X- and Gamma-Ray Sources and Applications (University of Michigan, Ann Arbor, May 1976), 36-39.

56. "Secondary Electron Energy Distributions for Gold as Excited by C-K (277 eV) and Al-K (1487 eV) X-Rays," Appl. Phys. Lett. 29 (1976) (w/ J. A. Smith and D. T. Attwood), 539-541.

57. "0.1 to 10 keV X-Ray-Induced Electron Emissions from Solids--Models and Secondary Electron Measurements," J. Appl. Phys. Lett. 29 (1976) (w/ J. A. Smith and D. T. Attwood), 1852-1866.

58. "High Efficiency Low-Energy X-Ray Spectroscopy in the 100-500 eV Region," J. Appl. Phys. 49 (1978) (w/ R. C. C. Perera, E. M. Gullikson and M. L. Schattenburg), 480-494.

59. Cl-$L_{II,III}$ Fluorescent X-Ray Spectra Measurement and Analysis for the Molecular Orbital Structure of ClO_4, ClO_3 and ClO_2," J. Chem. Phys.68, (1978) (w/ R. C. C. Perera and D. S. Urch), 3692-3704.

60. "Some Recent Studies in Low Energy X-Ray Physics," Proceedings of the 8th International Conference on X-Ray Optics and Microanalysis (Boston, August 1977).

61. "Models and Measurement for the Response of Dielectric X-Ray Photocathodes," Scientific Reports, AFOSR 75-2762-F and DOE (04-3)235-PA15, March 1978.

62. "Low Energy X-Ray Emission Spectroscopy in the 100-500 eV Region: Molecular Orbital Interpretation," (Ph.D. Thesis by R. C. C. Perera) Special Scientific Report, AFOSR 75-2762-F, May 1978.

63. "The Secondary Electron Emission Photocathode Characteristics for Time Resolved X-Ray Spectroscopy," Proceedings of the International Conference on X-Ray and XUV Spectroscopy (Sendai, Japan, August 1978); Jap. J. Appl. Phys. 17, 477-482; Suppl. 17-2, p. 23 (1978) (w/ K. Premaratne).

64. "C-K and Cl-L Emission Spectra and Molecular Orbital Analysis of CCl_4" Proceedings of the International Conference on X-Ray and XUV Spectroscopy (Sendai Japan, August 1978); Jap. J. Appl. Phys. 17, 112-115; Suppl. 17-2, (1978) (w/ R. C. C. Perera).

65. "A Soft X-Ray Spectrometer for the Study of Plutonium and Plutonium-Based Materials," X-Ray Spectrometry 7 (1978) (w/ P. L. Wallace, W. L. Haugen and E. M. Gullikson), 160-163.

66. "Soft X-Ray Induced Secondary Electron Emission from Semiconductors and Insulators: Models and Measurements," Phys. Rev. B19, (1979) (w/ J. Liesegang and S. D. Smith), 3004-3021.

67. "Low Energy X-Ray Emission Spectra and Molecular Orbital Analysis of CH_4, CCl_4 and $CHCl_3$," J. Chem. Phys. 70, (1979) (w/ R. C. C. Perera), 5398-5406.

68. "The Characterization of Photocathodes for Application to Time-Resolved X-Ray Spectroscopy," Technical Progress Report, AFOSR 79-0027 and DOE DE-AS03-76SF00235, April 1979.

69. "Multilayer X-Ray Spectrometry in the 20-80 A Region: A Molecular Orbital Analysis of CO & CO_2 in the Gas and Solid States," X-Ray Spectrometry 9, (1980) (w/ R. C. C. Perera), 81-89.

70. "X-Ray Spectroscopy in the 100-1000 eV Region," Nucl. Instrum. Methods 177, (1980), 161-171.

71. "Evaluation of High Efficiency CsI and CuI Photocathodes for Soft X-Ray Diagnostics," Appl. Opt. 19, (w/ E. B. Saloman and J. A. Pearlman), 749-753.

72. "The Characterization of X-Ray Photocathodes in the 0.1-10 keV Photon Energy Region," J. Appl. Phys. (March 1981) (w/ J. P. Knauer and K. Premaratne), 1509-1520.

73. "Low Energy X-Ray Interactions: Photoionization, Scattering, Specular and Bragg Reflection," AIP Conference Proceedings No. 75 on Low Energy X-Ray Diagnostics, Monterey, California (American Institute of Physics, New York, 1981), 146-155, D. T. Attwood and B. L. Henke, Editors.

74. "Low Energy X-Ray Spectroscopy with Crystals and Multilayers," AIP Conference Proceedings No. 75 on Low Energy X-Ray Diagnostics, Monterey, California (American Institute of Physics, New York, 1981), 85-100, D. T. Attwood and B. L. Henke, Editors.

75. "Appendix: The Atomic Scattering Factor, f + if, for 94 Elements and for the 100 to 2000 eV Photon Energy Region," AIP Conference Proceedings No. 75 on Low Energy X-Ray Diagnostics, Monterey, California (American Institute of Physics, New York, 1981) D. T. Attwood and B. L. Henke, Editors (w/ P. Lee, T. J. Tanaka, R. L. Shimabukuro and B. K. Fujikawa).

76. "X-Ray Diffraction in Multilayers," Opt. Commun. 37, Vol. 34, No. 3, 159-164 (1981), (P. Lee).

77. "Low-Energy X-Ray Interaction Coefficients: Photoabsorption, Scattering and Reflection," Atomic Data and Nuclear Data Tables 27, No. 1, (1982) (w/ P. Lee, T. J. Tanaka, R. L. Shimabukuro and B. K. Fujikawa), 1-143.

78. "The Stability of Cesium Iodide X-Ray Photocathodes," Nucl. Instrum. Methods 207, (1983) (w/ K. Premaratne and E. R. Dietz), 465-467.

79. "Pulsed Plasma Source Spectrometry in the 80-8000 eV X-Ray Region," Rev. Sci. Instrum. 54, (1983) (w/ H. T. Yamada and T. J. Tanaka), 1311-1330.

80. "Low-Energy X-Ray Response of Photographic Films: Part I. Mathematical Models," J. Opt. Soc. America (Dec. 1984) (w/ S. L. Kwok, J. Y. Uejio, H. T. Yamada and G. C. Young), 1-29.

81. "Low-Energy X-Ray Response of Photographic Films: Part II. Experimental Characterization," J. Opt. Soc. America (Dec. 1984) (w/ F. G. Fujiwara, M. A. Tester, C. H. Dittmore and M. A. Palmer), 1-29.

82. "Photon Counting Efficiency with High and Low Density CsI Photocathodes in the 100-10,000 eV Region," (w/ K. S. Tan and P. Y. Maeda), in preparation.

83. "X-Ray Diagnostics of Laser Plasmas with a Calibrated Elliptical Analyzer Spectrograph," Doctoral Thesis, University of Hawaii, Tina J. Tanaka, May 1983, 1-124.

84. "A Two-Channel, Elliptical Analyzer Spectrograph for Absolute Time-Resolving/Time-Integrating Spectrometry of Pulsed X-Ray Sources in the 100-10,000 eV Region," Rev. Sci. Instrum., (Aug. 1985) (w/Paul A. Jaanimagi).

85. "Large Aperture Picosecond X-Ray Streak Camera," (w/ P. A. Jaanimagi), submitted to Rev. Sci. Instrum.

86. "Numerical Solution of Poisson's Equation," (w/ P.A. Jaanimagi), submitted to J. Comput. Physics, Nov. 1984.

87. "The Characterization of Multilayer Analyzers - Models and Measurements," (w/ J.Y. Uejio, H.T. Yamada, and R.E. Tackaberry) Proceedings of Society of Photo-Optical Instrumentation Engineers (SPIE) 29th Annual International Symposium on Optical and Electro-Optical Engineering, San Diego (August 1985).

88. "An Absolutely Calibrated Time-Resolving X-Ray Spectrometer," (w/ P.A. Jaanimagi) Proceedings of Society of Photo-Optical Instrumentation Engineers (SPIE) 29th Annual International Symposium on Optical and Electro-Optical Engineering, San Diego, August 1985.

89. "Characterization of Multilayer X-Ray Analyzers - Models and Measurements," (w/ J.Y. Uejio, H.T. Yamada, and R.E. Tackaberry) Opt. Engin., Vol 25, No. 8 (August 1986), 937-947.

90./91. "Reflectivity Characteristics of Multilayers and Crystal

Analyzers for the 100-10,000 eV X-Ray Region - Theory and Experiment," (w/ H.T. Yamada, J.A. Kerner, J.C. Davis, and A.L. Oren) To be published.

92. "Reflectivity Characteristics of Low-Energy X-Ray Mirror Monochromators," (w/ F. G. Fujiwara, R. E. Tackaberry and D. Kania) to be published.

93. "High Energy X-Ray Response of Photographic Films. Models and Measurements," (w/J.Y. Uejio, G.F. Stone, C.H. Dittmore, F.G. Fujiwara) J. Opt. Soc. (August 1986), 818-827.

94. "Design and Characterization for Absolute X-Ray Spectrometry in the 100-10,000 eV Region," Proc. of the 11th International Conference on X-Ray Optics and Microanalysis, University of Western Ontario Press, 1987.

95. "Temporal Dependence of the Mass-Ablation Rate in UV-Laser-Irradiated Spherical Targets," P.A. Jaanimagi (w/J. Delettrez, B.L. Henke, and M.C. Richardson), Phys. Rev. A, Vol. 34, No. 2, (August 1986) 1322-1327.

96. "Time-Resolved X-Ray Diagnostics for High Density Plasma Physics Studies," (w/ M.C. Richardson, G.G. Gregory, R.L. Keck, S.A. Letzring, R.S. Marjoribanks, F.J. Marshall, G. Pien, J.S. Wark, B. Yaakobi, P.D. Goldstone, A. Hauer, G.S. Stradling, F. Ameduri, and P.A. Jaanimagi), Laser Interaction and Related Plasma Phenomena, Vol. 7 (1986), Plenum Publishing Corp., 179-211.

97. "Effect of Laser Illumination Nonuniformity on the Analysis of Time-Resolved X-Ray Measurements in U.V. Spherical Transport Experiments," (w/ P.A. Jaanimagi, J. Delettrez, R. Epstein, and M.C. Richardson) LBL-22935, submitted for publication.

APPENDIX 4

CITATIONS OF PUBLICATIONS ON THIS PROGRAM BY B.L. HENKE, ET AL. AS LISTED IN THE SCIENCE CITATION INDEX INSTITUTE FOR SCIENTIFIC INFORMATION, INC. (PHILADELPHIA, PENNSYLVANIA) 1980 TO EARLY 1987

B. L. Henke

1980

60 ADV XRAY ANAL 2
PARESSA DJ ULTRAMICROS 5 367 00
73 THESIS TH ILMENAU
HOFMANN C FORTSCHR PH 27 545 79
** ADV XRAY ANAL 17 136
SPILLER E NUCL INSTR 177 107 00
** ADV XRAY ANAL 17 188
POLMAR W J NUCL MAT 85-6 485 79
** UNPUBLISHED
HENKE BL NUCL INSTR 177 161 00
PEREIRA NCC X-RAY SPECT 9 81 00
67 ADV XRAY ANAL 3 285
CORALLO DM J PHYS E 13 623 00
64 ADVANCES XRAY ANALYS 7 460
HASHMOTAY H THIN SOL FI 68 21 00
NEUMAN RD J COLL I SC 76 266 00
MYY CW THIN SOL FI 68 101 00
VOGEL C J CHIM PHYS 76 909 79
64 ADV XRAY ANAL 8 269
HOPKINS F BKO 15378 B 17 995 00
65 ADVAN XRAY ANAL 8 269
VOGEL C J CHIM PHYS 76 903 79
" " " 76 909 79
65 ADV XRAY ANAL 9 430
KOSUCH N J ELEC SPEC 20 11 00
66 ADVAN XRAY ANAL 9 430
VOGEL C J CHIM PHYS 76 903 79
" " " 76 909 79
66 J APPL PHYSIOLOGY 37 922
YAMIGUCHI K BKO 12707 23 193 00
67 NORELCO REPORTER 14
KENNEDY AJ IEEE NUCL S 26 4605 79
67 NORELCO REPORTER 14 112
SIMNA BK J PHYS D 13 1253 00
" PHYS FLUIDS 23 1704 00
THRANE EV J ATM TER P 41 1047 79
67 11234 NOR REP
BONNET JJ J PHYS B L 13 L187 00
67 14 NOR REP 112
BRUNNER K NUCL INSTR 173 357 00
68 ADV XRAY ANAL 13 439
RAPPERT HF APPL PHYS 21 151 00
68 J CHEM PHYSICS 68 3642
BARBER M J CHEM S F2 76 443 00
69 ADV XRAY ANAL 12 480
BARBUS DM PHYS REV B 22 4632 00
MAEDA K SPECT ACT B 35 561 00
69 ADV XRAY ANAL 13 439
BABU L REV SO PHYS 25 653 00
70 ADVANCES XRAY ANALYS 13 439
KAWATSURA K NUCL INSTR 170 469 00
SMILES E PHYS REV B 22 5618 00
YAKZHENKS VG J ELEC SPEC 4 14 173 00
ZEISS GD NONLEC PHYS 20 1066 00
70 ADV XRAY ANAL 13 457
WAGNER CD J ELEC SPEC 20 83 00
71 ADV XRAY ANAL 27 150
CAMPBELL AB THIN SOL FI 64 445 79
71 J PHYSICS C 4 319
AUGUSTYNJ BKO 11164 B 13 291 79
71 J PHYS PARIS C 32 119
ADAMS A PHYS REV B 22 4256 00
BASCHENAGNA J ELEC SPEC 21 393 00
72 PHYSICAL REVIEW A 6 04
" " J PHYS CH S 41 1167 00
72 PHYSICAL REVIEW A 6 04
AUGUSTYNJ BKO 11164 B 13 291 79
BREMER J " L 37 360 00
" J PHYS C 13 2225 00
" " L 13 L249 00
GALDING BK BIOMATERIAL 1 163 00
SJAUNAR J J ELEC SPEC 19 393 00
74 ADV XRAY ANALYSIS 17 150
CAMPBELLAB J APPL PHYS 51 383 00
FLAGGERIS GC APPL PHYS L 36 93 00
" " J VAC SCI T 10 1015 79
GALLOWAY KF J ELCHEM SO 126 2245 79
HEINLOTZ RE J COLL I SC 75 108 00
BABU L REV SO PHYS 25 653 00
LAMP H O MINERAL 103 389 00
SMILES E PHYS REV B 22 5612 00
SJAUNAR J J ELEC SPEC 19 393 00
YAMUMA S BUNSEKI KAG 29 513 00
74 ADV XRAY ANAL 18 76
BHAGAVAT VA IEEE J Q EL 16 603 00
75 ADV XRAY ANAL 18
ANDERMANN G NUCL INSTR 177 137 00
GUPTA PD J APPL PHYS 51 1073 00
HENKE BL NUCL INSTR 177 161 00
75 ADV XRAY ANAL 18 76
ANDERMANN G REV SCI INS 51 814 00
BARBUS DM PHYS REV B 22 4032 00
HEINLOTZ RE J COLL I SC 75 108 00
LEWIS M ASTROPH ASTR 37 313 00
MCELROY DL ASTROPHYS J 241 409 00
PEREIRA NCC X-RAY SPECT 9 81 00
76 ADV XRAY ANAL 18 76
YAMIGUCHI K BKO 12707 23 193 00
76 ADV XRAY ANAL 19
ZUTAVERN FJ NUCL INSTR 172 351 00
76 ADV XRAY ANAL 19 249
SUBZ J BKO 14756 1400 339 00
76 J APPL PHYSICS 47 1827
GUPTA PD J APPL PHYS 51 1073 00
HAGUE CF REV SCI INS 51 621 00
HENKE BL NUCL INSTR 177 161 00
KOSUCH N J ELEC SPEC 20 11 00
YAMIGUCHI K BKO 12707 23 193 00
WILMER G PHYS ST S-A A 50 E 7 00
76 J APPL PHYSICS 47 1829
PEREIRA NCC X-RAY SPECT 9 81 00
77 J APPL PHYSICS 48 1852
DEBOSTELMU IEEE NUCL S 24 4978 79
HENKE BL NUCL INSTR 177 161 00
77 8TH INT C XRAY OPT M
ANDERMANN G REV SCI INS 51 814 00
78 ADS INT C XRAY ION S
HANE HC J APPL PHYS 51 2242 00
78 ADS P INT C XRAY ION
78 JAP J APPL PHYS S 17 23
HENKE BL NUCL INSTR 177 161 00
78 J APPL PHYSICS 49 488
BRUNO BO J APPL PHYS 51 2540 00
HAYCOCK DE J CHEM S F2 75 1697 79
HENKE BL NUCL INSTR 177 161 00
MACDONALD A ANALYT CHEM B 52 0100 00
PEREIRA NCC X-RAY SPECT 9 81 00

78 J CHEM PHYSICS 68 3697
FUJIWARA F SPECT LETT 13 211 00
HENKE BL NUCL INSTR 177 161 00
PEREIRA NCC X-RAY SPECT 9 81 00
TANIGUCHI K BKO 12707 23 193 00
TOBBELL JA NUCLEAR CHEM 19 3328 00
78 P INT C XRAY XUV SPE
GRADLEY DJ PHI T ROY A 290 281 00
79 PHYSICAL REVIEW B 19
DEBOSTELMU IEEE NUCL S 26 4978 79
79 PHYSICAL REVIEW B 19 3004
GRUNDER M J APPL PHYS 51 5396 00
HENKE BL NUCL INSTR 177 161 00
WILLS RA PHYS REV B 22 581 00
SALOMAN EB APPL OPTICS 19 749 00

1981

80 J CHROMATOGR 187 109
MAGNUSSON J CHROMAT 211 237 00
WAHLUND KG " 218 671 81
** U HAWAII INTERIM REP
WIZUI J PHYS REV L 47 .000 81
** UNPUBLISHED
LEE P OPT COMMUN 37 159 81
59 J APPL PHYS 26 823
MEARS J ADV COLL IN B 14 173 81
57 J APPL PHYS 28 98
HEROUX L BKO 20006 1981 239 81
64 ADVANCES XRAY ANALYS 7 460
BARBUS DM X-RAY SPECT 10 46 81
CAMPBELL DE AM CERAM S 60 640 81
64 ADV XRAY ANAL 8 269
HUIZENGA H REV SCI INS 52 673 81
66 ADV XRAY ANAL 9 430
YUMATOV VD J STRUCT CH 21 503 00
69 ADV XRAY ANAL 12 480
BARBUS DM X-RAY SPECT 10 46 81
69 ADV XRAY ANAL 13 1
DILES A BKO 20006 B 4 277 81
" J POL SC PC 19 1319 81
RATNER BD J COLL I SC 83 630 81
70 ADVANCES XRAY ANALYS 13 439
COSTA JL THROMB RES 22 399 81
MCCORMELE RA APPL PHYS A 26 261 81
POPIL R J APPL PHYS 52 5046 81
WITTELS RD BKO 16522 B 1 1 00
71 J PHYS C SOLID STATE 4 115
DILES A BKO 20006 B 4 277 81
HUMPER B J ELEC SPEC B 23 103 81
RATNER BD J COLL I SC 83 630 81
72 NORELCO REPORTER 28
SZAJMAN J J ELEC SPEC 23 83 81
72 P INT C INNER SHELL
CHAUDHARI SN APPL SP REV B 16 187 00
72 PHYS REV A 6 04
CHADWICK D J ELEC SPEC 24 181 81
CHAUDHARI SN APPL SP REV B 16 187 00
FOX R PHYS C GLAS 22 32 81
PAYOTEE PW SURF INT AN B 3 186 81
PLOLAT M SURF SCI 105 116 81
RODERTS WW BKO 16008 B 20 59 00
VULLI M SURF INT AN B 3 67 81
74 ADV XRAY ANALYSIS 17 150
ALAHWAL BA J PHYS F 11 1303 81
DAY BW J APPL PHYS 52 6965 81
FOX R PHYS C GLAS 22 32 81
JHANWAR BL CAN J PHYS 59 105 81
KAINOLA L APPL OPTICS L 20 1249 81
TARUMA S SPECT ACT B 36 757 81
VASILIEV VI DAN SSSR 255 963 00
VILISOV VA J ANAL CHEM 35 909 00
WITTELS RD BKO 16522 B 1 1 00
74 ADV XRAY ANAL 18 76
HEROUX L BKO 20006 1981 239 81
SPILLER E APPL PHYS L 37 1048 00
75 ADV XRAY ANAL 18
HENKE BL J APPL PHYS 52 1509 81
75 ADV XRAY ANAL 18 76
STOEDING JP REV SCI INS 52 825 81
UNDERWOOD JH APPL OPTICS 20 3027 81
76 APPL PHYS LETT 39 339
GROB M APPL OPTICS 20 1550 81
76 J APPL PHYS 45 1827
JONES BC SOIL SCI SO 45 810 81
77 J APPL PHYS 48 1852
DAY BW J APPL PHYS 52 6965 81
HENKE BL " 52 1509 81
OKUTANI T JPN J A PHY 20 1435 81
POLACE F REV SCI INS 52 207 81
WOLCOTT JD NUCL TECH L 52 130 81
78 JAP J APPL PHYS 517 17 23
HENKE BL J APPL PHYS 52 1509 81
78 J APPL PHYS 49 430
ULMER K Z PHYS B 43 109 81
78 J APPL PHYS 49 488
JONES BC SOIL SCI SO 45 810 81
78 P INT C XRAY XUV SPE
HENKE BL J APPL PHYS 52 1509 81
79 8 ADV PHYS SOC 24 1098
STRADLING RA APPL PHYS L 37 782 00
79 PHYS REV B 20 3004
DIANCONI A APPL SURF S 6 392 00
HENKE BL J APPL PHYS 52 1509 81
STRADLING RA APPL PHYS L 37 782 00

1982

66 ADV XRAY ANAL 7 460
SOLEM JC SCIENCE 218 229 82
80 J CHROMATOGR 187 109
WESTERLUD A ACT PHARM S M 19 78 82
** MONTEREY P 85
** MONTEREY P 146
ATTWOOD DT AP CONF PR 1982 254 82
** UNPUB ATOMIC DATA RU
BERLAND M P SOC PHOTO 315 156 81
80 J APPL PHYS 53 903
FRANKEL RD METH ENZYM A 88 278 82
80 J APPL PHYS 28 98
BASOV NG KVAN ELEKTR B 9 1535 82
KORLUKOV VV " M 9 1711 82
82 ADV XRAY ANAL 5 288
KOLESCHO AW NUCL INSTRU L 198 477 81

63 ADV XRAY ANAL 6
GANSCHOW O J VAC SCI T 21 845 82
63 ADV XRAY ANAL 6 363
ARAI T JPN J A P 1 21 1347 82
64 ADVANCES XRAY ANALYS 7 460
ARAI T JPN J A P 1 21 1347 82
NAGEL DJ NUCL INSTRU 195 63 82
" P SOC PHOTO 315 110 81
66 ADV XRAY ANAL 8
GANSCHOW O J VAC SCI T 21 845 82
67 NORELCO REP 14 75
ARAI T JPN J A P 1 21 1347 82
67 NORELCO REP 14 112
JHANWAR BL CHEM PHYS 67 185 82
69 ADV XRAY ANAL 12 480
ARAI T JPN J A P 1 21 1347 82
69 ADV XRAY ANAL 13 1
JENKINS R ADV X-RAY R 25 200 82
70 ADV XRAY ANAL 13 439
MAZING MA INSTR EXP R 24 1301 81
73 J PHYS C SOLID STATE 4 115
HOULE VA ULTRAMICROS 7 371 82
73 J PHYS PARIS C 4 155
WANG PS J HAZARD M 5 297 82
72 ADV XRAY ANAL 13 439
TAWARA H PHYS REV A 26 154 82
72 PHYS REV A 6 04
AMORE JM PHYS REV B 25 5671 82
ARAI T JPN J A P 1 21 1347 82
FRASER GW NUCL INSTRU 195 523 82
PUOLAT M ANALUSIS 10 8 82
RIFE JC P SOC PHOTO 315 103 81
74 ADV XRAY ANALYSIS 17 150
ARAI T JPN J A P 1 21 1347 82
DELRUE JP THIN SOL FI 87 73 82
HAMADA M BUNSEKI KAG 31 T 61 82
KOZLENKO AI MIKROCH ACT 2 158 82
ROCKETT PD PHYS FLUIDS 25 1286 82
SANDBORG AO SCAN ELEC M 1981 63 81
75 ADV XRAY ANAL 18
GERSTEN M J APPL PHYS 53 1297 82
GALFRICH JV ADV X-RAY R 25 355 82
75 ADV XRAY ANAL 18 76
ARAI T JPN J A P 1 21 1347 82
ROCKETT PD PHYS FLUIDS 25 1286 82
75 ADV XRAY ANAL 18 87
GALFRICH JV APPL SPECTR 36 58 82
76 ADV XRAY ANAL 19 249
ARAI T JPN J A P 1 21 1347 82
BURKERT W ASTRON ASTR 115 187 82
MCKENZIE DL J ATM TER P 44 499 82
76 APPL PHYS LETT 39 339
ATTWOOD DT AP CONF PR 1982 254 82
CAZAUX J APPL SURF S 10 124 82
77 J APPL PHYS 48 1852
ATTWOOD DT AP CONF PR 1982 254 82
HASSELKA D SURF SCI L 119 L388 82
78 J APPL PHYS 49 488
BERLAND M P SOC PHOTO 316 160 81
DVALL KG J PHYS B 15 203 82
" " 15 1811 82
GERSTEN M J APPL PHYS 53 1297 82
NORDGREN J PHYS SCR 25 382 82
78 J CHEM PHYS 68 3692
TOPOL IA IAN SSS FIZ 46 770 82
79 PHYS REV B 19 3004
ATTWOOD DT AP CONF PR 1982 254 82
80 NUCL INSTRUM METHODS 177 187
ROSENBLU AE APPL PHYS L 40 466 82
81 AM J PHYS 49 340
GAPONOV SV IAN SSS FIZ 46 1543 82
81 J APPL PHYS 52 1509
ATTWOOD DT AP CONF PR 1982 254 82
PROHASKA R APPL PHYS L 40 283 82
SOLEM JC SCIENCE 218 229 82
WANG CL REV SCI INS 53 582 82
81 LOW ENERGY XRAY DIAG 85
NAGEL DJ P SOC PHOTO 315 110 81
81 P TOPICAL C LOW ENER
LEE P OPT COMMUN 42 195 82
NAGEL DJ P SOC PHOTO R 279 88 81
RIFE JC " 315 103 81
81 P TOPICAL C LOW ENER 85
NAGEL DJ NUCL INSTRU 195 63 82
82 ATOMIC NUCLEAR DATA 27
GAPONOV SV IAN SSS FIZ 46 1543 82
RIFE JC P SOC PHOTO 315 103 81
ROSENBLU AE APPL PHYS L 40 466 82
82 ATOMIC DATA NUCLEAR 27 1
ATTWOOD DT AP CONF PR 1982 254 82

1983

** COMMUNICATION
STRADLIN GL IEEE J Q EL 19 604 83
** UNPUB
** UNPUB CHARACTERIZATI
HENKE BL REV SCI INS 54 1311 83
57 J APPL PHYS 28 98
BIEBER M NUCL INSTRU 208 281 83
59 AFOSR TR-8305 TECHN
BIEBER M J VAC SCI B 1 1271 83
" " NUCL INSTRU 208 281 83
64 ADVANCES XRAY ANALYS 7 460
KOBAYASHI NUCL INSTRU 204 525 83
66 J APPL PHYS 37 922
MAZALOV LN J STRUCT CH R 24 276 81
67 NORELCO REPORTER 14 112
ALAVERDO VI OPT SPEKTRO N 53 1113 82
MCCAMMON D ASTROPHYS J 268 107 83
70 ADVANCES XRAY ANALYS 13 439
BARSTOW MA J OPT SOC L 73 1220 83
MORITA S JPN J A P 1 22 1763 83
73 J PHYS C SOLID STATE 4 115
ASHLEY JC J ELEC SPEC 26 177 82
73 6TH P INT C XRAY OPT 367
UEZUMI M JPN J A P 1 22 808 83
73 APPL PHYS LETT 39 348
GAPONOV SV NUCL INSTRU 208 227 83
73 PHYS REV A 6 04
ABBATI I PHYS REV L 50 1780 83
ARAI T ADV X-RAY R 26 473 83
CITRIN PH PHYS REV B 27 3160 83
FILATOVA EO FIZ TVERD T 25 1280 83
FRASER GW NUCL INSTRU 206 251 83
LILJEQUI D J PHYS D 16 1567 83
ROSEN G PHYS REV B 28 3031 83
74 ADV XRAY ANAL 17
KAUFFMAN RL IEEE J Q EL 19 616 83

74 ADV XRAY ANALYSIS 17 150
ARAI T ADV X-RAY A 26 423 83
FILATOVA EO FIZ TVERD T 25 1780 83
SMIRNOV VN " N 25 887 83
STRADLIN GL IEEE J O EL 19 804 83
TANAKA S MIKROCH ACT 1 298 83
74 ADV XRAY ANAL 17 187
BAKOV S J MATER SCI 18 623 82
VALEEV KA ZH TEKH FIZ N 53 563 83
75 ADV XRAY ANAL 18
NISHIBORI H PHYS FLUIDS 26 1888 83
75 ADV XRAY ANAL 18 76
GAZARI M J APPL PHYS 54 112 83
HENKE BL REV SCI INS 54 1311 83
76 ADV XRAY ANAL 19 709
ARAI T ADV X-RAY A 26 423 83
SUZUKI IH NUCL INSTRU L 211 565 83
76 APPL PHYS LETT 29 539
JAANIMAG PA REV SCI INS 54 1095 83
MEZHEVIC AN RADIOTEK EL 28 1407 83
76 J APPL PHYS 47 1027
BONNET JJ PHYS LETT A 86 13 83
HENKE BL REV SCI INS 54 1311 83
TURNER NH J VAC SCI A M 1 1229 83
77 J APPL PHYS 48 1852
FRASER GW NUCL INSTRU 206 251 83
JAANIMAG PA REV SCI INS 54 1095 83
KALISKA R J APPL PHYS 54 4295 83
KAUFFMAN RL IEEE J O EL 19 616 83
MARLOWE RS OPT COMMUN 44 113 82
MEZHEVIC AN RADIOTEK EL 28 1407 83
NAKAMURA M J APPL PHYS 54 3141 83
PREMARAT K NUCL INSTRU 207 465 83
SIEGMUND OH ACS SYMP S R 1983 253 83
STRADLIN GL IEEE J O EL 19 804 83
TAYLOR RC REV SCI INS 54 171 83
78 JAP J APPL PHYS S172 17 23
PREMARAT K NUCL INSTRU 207 466 83
78 JPN J APPL PHYS 17 477
JAANIMAG PA REV SCI INS 54 1095 83
78 J APPL PHYS 49 680
HENKE BL REV SCI INS 54 1311 83
MACDOWELL AA J PHYS E 16 487 83
78 J CHEM PHYS 68 3692
HONDRATE AV THEOR CHIM 64 31 83
79 PHYS REV B 19 3884
ELANGO M PHYS ST S-B 114 487 82
FRASER GW NUCL INSTRU 208 751 83
" " 208 266 83
JAANIMAG PA REV SCI INS 54 1088 83
PREMARAT K NUCL INSTRU 207 466 83
SIEGMUND OH ACS SYMP S R 1983 253 83
STRADLIN GL IEEE J O EL 19 804 83
80 NUCL INSTRUM METHODS 177 161
HENKE BL REV SCI INS 54 1311 83
KOMAROV FF RAD EFF LET 76 110 83
83 AIP C P 75 88
BILDERBA DH NUCL INSTRU 208 251 83
DAY R " 208 246 83
HENKE BL REV SCI INS 54 1311 83
NIEMANN B P SOC PHOTO 388 7 83
83 AIP C P 75 146
BILDERBA DH NUCL INSTRU 208 251 83
HENKE BL REV SCI INS 54 1311 83
83 AIP C P 75 340
MORRISON R ASTROPHYS J 270 110 83
83 J APPL PHYS 52 1509
CEGLIO NM APPL OPTICS 22 316 83
FRASER GW NUCL INSTRU 208 251 83
" " 208 266 83
" " 208 445 83
KALISKA R J APPL PHYS 54 4298 83
KAUFFMAN RL IEEE J O EL 19 616 83
LETZRING SA J APPL PHYS 54 6300 83
POLACK F NUCL INSTRU 208 373 83
PREMARAT K 207 466 83
SIEGMUND OH ACS SYMP S R 1983 253 83
STRADLIN GL IEEE J O EL 19 804 83
TAYLOR RC REV SCI INS 54 171 83
83 P SPIE 346 336
SIEGMUND OH ACS SYMP S R 1983 253 83
83 SPIE J 336 146
TAYLOR RC REV SCI INS 54 171 83
83 AT DATA NUCL DATA TA 27
ESTEVA JM J PHYS B L 16 L263 83
GAPONOV SV NUCL INSTRU 208 227 83
HENKE BL REV SCI INS 54 1311 83
MARGRET R APPL OPTICS L 22 17 83
83 AT DATA NUCL DATA TA 27 1
CEGLIO NM J VAC SCI B 1 1206 83
DAY R NUCL INSTRU 208 245 83
GAVRILA M AP CONF PR R 1982 357 82
MORRISON R ASTROPHYS J 270 119 83
WANG MS PHYS REV A N 28 3115 83
83 AT DATA NUCL DATA TA 27 3
JONES KW PHYS LETT A 87 377 83
83 ATOMIC NUCLEAR DATA 27
LEE P APPL OPTICS 22 1941 83

1984

** UNPUB
COWAN PL NUCL INST A 222 46 84
** UNPUB J APPL PHYS
KAUFFMAN RL P SOC PHOTO 427 84 83
56 J APPL PHYS 26 983
FORSYTH JM REV SCI INS 55 1235 84
57 J APPL PHYS 28 1
POUCHOU JL RECH AEROSP 167 84
57 J APPL PHYS 28 98
BORUKHOV VV KVAN ELEKTR 11 1364 84
60 ADV XRAY ANAL 6 244
GRUDSKY AY OPT SPEKTRO 57 880 84
63 XRAY OPTICS XRAY MIC 157
SAMSON JAR NUCL INST A 222 215 84
66 J APPL PHYS 57 922
TANIGUCH K B CHEM S J 57 909 84
67 BIBRECLO REP 14 79
COWAN PL NUCL INST A 222 46 84
67 BIBRECLO REPRINTER 14 112
KOSAREV EL OPT SPEKTRO 56 843 84
VILA E AN QUIM B 80 208 84
67 9 BIBR REP
POUCHOU JL RECH AEROSP 167 84
69 ADV XRAY ANAL 12 480
TANIGUCH K B CHEM S J 57 921 84
70 ADV XRAY ANAL 13 1
PANDEY MO APPL SPECTR N 38 80 84
70 ADVANCES XRAY ANALYS 13 459
GOTURA A J PHYS JPN 53 1881 84
PAGNI O APPL OPTICS 23 762 84
YAGNIK MK I J RAD SP 12 208 83
YAMAGUSHI Y APPL OPTICS 23 888 84
72 PHYS REV A 6 94
GOWDY S JPN J A P 2 23 L 15 84
WERTHEIM GK P SOC PHOTO 447 47 84
73 ADV XRAY ANAL 13 1
GILBERG E P SOC PHOTO 447 68 84
73 PHYS REV A 6 96
ANDREEVA MA PHYS ST S-B 175 481 84

74 ADV XRAY ANALYSIS 17 150
BORDOVSKII O J PHYSIQUE 45 9 84
KUHNE M OPTICS LETT 9 16 84
LAVRENTE YG IND LAB R 48 806 83
LOVE G J PHYSIQUE 45 21 84
POUCHOU JL RECH AEROSP 167 84
SEMPE B P SOC PHOTO 393 295 83
SMIRNOV VN OPT SPEKTRO 57 266 84
75 ADV XRAY ANAL 18 28
CONTARDI L SCAN ELEC M 1984 577 84
75 ADV XRAY ANAL 18 76
AGREN H CHEM PHYS 83 63 84
ANDERMAN G ANALYT CHEM 56 1711 84
EDELSTEIJ APPL OPTICS L 23 3267 84
HODGE WL REV SCI INS 55 16 84
JITSCHIN W J PHYS E 17 137 84
ROCKETT PD AP CONF PR 171 84
SMITH GC NUCL INST A 222 230 84
TANIGUCH K B CHEM S J 57 909 84
" " 57 921 84
" JPN J A P 1 23 358 84
76 APPL PHYS LETT 29 539
PROCTOR A APPL SPECTR 38 505 84
76 J APPL PHYS 47 1017
TANIGUCH K JPN J A P 1 23 358 84
76 J APPL PHYS 47 1027
TANIGUCH K B CHEM S J 57 909 84
" " 57 921 84
77 J APPL PHYS 48 1852
CHEVORIN VK RADIOTEK EL 29 2210 84
77 APPL PHYS 48 1852
POLACK F J PHYSIQUE 45 73 84
78 J APPL PHYS 45 480
PENA F GEODERMA 33 283 84
78 J APPL PHYS 49 680
BLAKE RL ASTROPHYS J 282 784 84
TANIGUCH K B CHEM S J 57 909 84
78 J CHEM PHYS 68 3692
PEREIRA RCC J CHEM PHYS 81 3275 84
YUMATOV VD J STRUCT CH 24 676 83
79 PHYS REV B 19
DYMCHENKO AA P SOC PHOTO 427 78 83
79 PHYS REV B 19 3884
CAZAUX J SCAN ELEC M 1984 1193 84
FRASER GW NUCL INST A 224 272 84
STOHR J PHYS REV B 30 5571 84
80 NUCL INSTRUM METHODS 177 161
BOOLCHI S SOL ST COMM 49 11 84
NAGEL DJ REV SCI INS N 54 1797 83
83 AT DATA NUCL DAT MAY
CHAMPELL JM NUCL INST A 221 150 84
83 AIP C LOW ENERGY XRA 75
WILLINGA R NUCL INST A 221 1 84
83 AIP C P 75 88
GAPONOV SV ZH TEKH FIZ 54 747 84
JORDENSE B REV SCI INS 55 35 84
LEPETRE Y OPTICS LETT 9 433 84
83 AIP P 75 324
SPILLER E AIP CONF PR 312 84
83 AIP C P 75 340
GAPONOV SV ZH TEKH FIZ 54 747 84
HAELBICH RP P SOC PHOTO 448 83 84
HUNTER WR APPL OPTICS 23 793 84
VLADIMIR Y P SOC PHOTO 448 25 84
83 AIP C P 75 379
TATCHYN R PHYS REV L 53 1284 84
83 J APPL PHYS 52 1389
BRAUN W P SOC PHOTO 447 117 84
KAUFFMAN RL AIP CONF PR 330 84
" P SOC PHOTO 427 88 83
KINOSHIT K " 427 36 83
PRICE RH IEEE NUCL S 31 804 84
SAMSON JAR NUCL INST A 222 215 84
SOLEM JC OPT ENG 23 783 84
83 LOW ENERGY XRAY DIAG 88
NAGEL DJ REV SCI INS N 54 1797 83
83 P TOPICAL C LOW ENER
LEE P P SOC PHOTO 444 73 84
83 1983 AIP C P LOW EN 346
PERKINS RT ACT CRYST A 40 817 84
83 1983 AIP C P LOW EN 340
VINOGRAD AV ZH TEKH FIZ 54 1756 84
83 ATOMIC DATA NUCLEAR 27
BARBEE TW AIP CONF PR 53 84
BARTLETT RJ OPT ENG 23 667 84
" P SOC PHOTO 447 23 84
BRUUN MP NUCL INST A L 218 603 84
GOLUB L APPL OPTICS 23 3629 84
KAMA DR AIP CONF PR 207 84
PIANETTA P P SOC PHOTO 448 80 84
STERN RA " 445 347 84
83 AT DATA NUCL DATA TA 27 1
ANDERMAN G ANALYT CHEM 56 1711 84
ATTWOOD DT AIP CONF PR 284 84
BRODSKY SM J RAD NUCL 83 155 84
BROWN JD J PHYSIQUE 45 809 84
COWAN PL NUCL INST A 222 46 84
CREAGH D PHYS LETT A 103 52 84
DHEZ P AIP CONF PR 188 84
" J PHYSIQUE 45 66 84
GAPONOV SV ZH TEKH FIZ 54 747 84
OSPOMER A RECHERCHE 15 1120 84
HALL G NUCL INST A 220 356 84
KAMBARA T J PHYS B 17 1589 84
KAMA DR APPL PHYS L 44 1058 84
" NUCL INST A 222 270 84
KUHNE M OPTICS LETT 9 16 84
MAGEE NH ASTROPHYS J 283 264 84
MARENKOV OS J PHYSIQUE 45 51 84
MARSHALL AT J MICROSC O 134 113 84
NAGEL DJ REV SCI INS N 54 1797 83
PARKER JC PHYS REV A 29 162 84
UNDERWOOD JH PHYS TODAY 37 44 84
VIDAL B APPL OPTICS 23 1784 84
WILLICH P J PHYSIQUE 45 621 84
83 ATOMIC DATA NUCLEAR 27 22
PIANETTA P NUCL INST A 222 356 84
83 AT DATA NUCL DATA TA 27 339
BARTLETT RJ NUCL INST A 222 95 84
83 ATOMIC DATA NUCLEAR 27 329
CONTARDI L SCAN ELEC M 1984 577 84

1985

56 J APPL PHYS 26 983
TANG MY J POL SC PP 22 2215 84
60 ADV XRAY ANAL 6 244
GRUDSKY AY OPT SPEKTRO 57 880 84
74 ADV XRAY ANALYSIS 17 150
MILLER NC J APPL PHYS 57 512 85
75 ADV XRAY ANAL 18 76
HENKE BL J OPT SOC B 1 828 84
78 J APPL PHYS 49 480
PENA F GEODERMA 33 283 84
79 PHYS REV B 19 3884
GERMER R Z KRISTALL M 167 142 84
81 AIP C P 75 146
CERRINA F J VAC SCI B 3 277 85
82 AT DATA NUCL DATA TA 27 1
HAMILTON AJ ASTROPHYS J 297 282 84
HENKE BL J OPT SOC B 1 818 84
" " 1 828 84
SCHATTEN MK J VAC SCI B 3 272 85

83 REV SCI INSTRUM 54 1311
HENKE BL J OPT SOC B 1 818 84
" " 1 828 84
84 J OPT SOC AM B 1 818
HENKE BL J OPT SOC B 1 828 84
84 J OPT SOC AM B 1 828
HENKE BL J OPT SOC B 1 818 84
** COMMUNICATION
KIRZ J REV SCI INS R 56 1 85
56 J APPL PHYS 26 983
FRANKEL RD BIOPHYS J 47 387 85
60 ADV XRAY ANAL 4 244
LABOV S APPL OPTICS 24 578 85
63 ENCY MICROSCOPY
KIRZ J REV SCI INS R 56 1 85
63 XRAY OPTICS XRAY MIC 157
LABOV S APPL OPTICS 24 578 85
72 PHYS REV A 6 94
SALVAI F J PHYS D 18 299 85
73 ADV XRAY ANALYSIS 17 150
BLOOMFIE DJ X-RAY SPECT 14 8 85
75 ADV XRAY ANAL 18 76
MUDELFUD A APPL OPTICS 24 788 85
78 J APPL PHYS 49 480
BONNET JJ J PHYS B L 18 L 23 85
83 AIP C P 75 88
BARBEE TW APPL OPTICS 24 863 85
BONNET JJ J PHYS B L 18 L 23 85
83 AIP C P 75 340
VINOGRAD AV ZH TEKH FIZ 55 244 85
83 J APPL PHYS 52 1509
FRASER GW NUCL INST A 228 532 85
83 LOW ENERGY XRAY DIAG
84 LOW ENERGY XRAY DIAG 146
KIRZ J REV SCI INS R 56 1 85
83 P TOPICAL C LOW ENER 85
LEE P OPT ENG 24 197 85
82 ATOMIC NUCLEAR DATA 27
BARBEE TW APPL OPTICS 24 863 85
LEE P OPT ENG 24 197 85
82 AT DATA NUCL DATA TA 27 1
KIRZ J REV SCI INS R 56 1 85
LABOV S APPL OPTICS 24 578 85
SAMSON JAR PHYS REV A 31 1470 85
SUZUKI IH NUCL INST A 228 2C1 84
WANG JU ATOM DATA N 32 1 85
82 ATOMIC DATA 27 3
ZHEVAGO NK OAN SSSR 280 347 85
70 PHYS REV A 6 94
HECHT HH J ELEC SPEC 36 211 85
72 PHYS REV A 6 94
FADLEY CS PROG SURF S R 16 275 84
72 PHYS REV A 64 360
FILATOVA EO FIZ TVERD T 27 881 85
75 ADV XRAY ANAL 18
78 J APPL PHYS 49 480
MANN JA LANGMUIR 1 10 85
78 J CHEM PHYS 68 3692
YUMATOV VD J STRUCT CH 25 545 84
81 AIP C P 75 146
81 AIP C P 75 340
ASCHENBA B REP PR PHYS R 48 579 85
82 ATOMIC NUCLEAR DATA 27
BARBEE TW SUPERLATT M 1 311 85
82 AT DATA NUCL DATA TA 27 1
ASCHENBA B REP PR PHYS R 48 579 85
GAPONOV SV P SOC PHOTO 473 298 84
" ZH TEKH FIZ 55 575 85
KUMAR A CAN J PHYS 63 417 85
" MOLEC PHYS 54 823 85
WILLICH P X-RAY SPECT 14 84 85
84 ADV XRAY ANAL 17 158
FUJIMO N TETSU HAGAN M 70 1041 84
75 ADV XRAY ANAL 18 76
HETTRICH MC APPL OPTICS 24 1737 85
YANG BR NUCL INST A 236 419 85
76 ADV XRAY ANAL 19 190
LEONOV YS ZH TEKH FIZ N 55 1184 85
78 J CHEM PHYS 68 3692
YUMATOV VD J STRUCT CH 25 721 84
81 J APPL PHYS 52 1509
WANG CA P SOC PHOTC 491 82 85
" REV SCI INS 56 835 85
YANG BR NUCL INST A 236 419 85
81 P AIP C LOW ENERGY X 146
SESHAC S REV SCI INS 56 1160 85
81 P SOC PHOTOOPT INSTR 316
HETTRICH MC APPL OPTICS 24 1737 85
82 ATOMIC DATA NUCLEAR
SEWELL DA J PHYS D 18 1269 85
82 ATOM DATA NUCL DATA 27
BRUUN MP SURF SCI 154 621 85
HETTRICH MC APPL OPTICS 24 1737 85
SEWELL DA J PHYS D 18 1233 85
" " 18 1245 85
82 AT DATA NUCL DATA TA 27 1
CREAGH D AUST J PHYS 38 371 85
YARE T JPN J A P 2 24 L439 85
83 REV SCI INSTRUM 54 1311
DANIELS RR J VAC SCI A M 3 976 85
84 J OPT SOC AM B 1 818
84 J OPT SOC AM B 1 828
HETTRICH MC APPL OPTICS 24 1737 85
** UNPUB MULTILAYER A 2
** UNPUB REFLECTIVITY C
HENKE BL REV SCI INS 56 1537 85
57 J APPL PHYS 28 98
LAVERNE JA J PHYS CHEM 89 4219 85
72 PHYS REV A 6 94
BUSSING TD J VAC SCI A 3 1973 85
PANG L AM J PHYS 53 665 85
75 ADV XRAY ANAL 18
KUHNE M J PHYS E R 18 637 85
75 ADV XRAY ANAL 18 76
WERNER U J PHYS B 18 3111 85
79 PHYS REV B 19
DYMCHENKO AA ADV ELECTR 64 53? 85
79 PHYS REV B 19 3884
LOWRANCE A ADV ELECTR 64 55? 85
" " 64 54? 85
81 AIP C P 75 85
HENKE BL REV SCI INS 56 153? 85
83 J APPL PHYS 52 1509
DHEZ E NUCL INST A 230 359 85
HENKE BL REV SCI INS 56 153? 85
SHE YZ ADV ELECTR 64 54? 85
82 ATOMIC DATA NUCLEAR 27
HENKE BL REV SCI INS 56 1537 85
PIANETTA P P SOC PHOTO 537 69 85
PANG L AM J PHYS 53 665 85
SELLA C THIN SOL FI 125 367 85
82 AT DATA NUCL DATA TA 27 1
AKIMOV VN OPT SPEKTRO 58 342 85
DHEZ P J MICROSC O 134 267 85
HERRING CA J EL MICR T 2 471 85
JOHNSON AL J PHYS CHEM 89 4071 85
KUMAR A CAN J CHEM 63 1616 85
LAUNSPAC J P SOC PHOTO 491 683 85
MCDANIEL EW ATOM DATA N R 33 1 85
83 REV SCI INSTRUM 54 1311
HENKE BL REV SCI INS 56 1537 85
84 J OPT SOC AM B 1 818
HENKE BL REV SCI INS 56 1537 85
ROCKETT PD APPL OPTICS 24 2538 85
84 J OPT SOC AM B 1 828
HENKE BL REV SCI INS 56 1537 85
ROCKETT PD APPL OPTICS 24 2538 85
85 AMS P INT SOC OPT EN
HENKE BL REV SCI INS 56 1537 85

1986

61 ADV XRAY ANAL 4 244
MATSUMOTO Y TETSU HAGAN 71 1983 85
66 ADV XRAY ANAL 8 269
BANKS LS SPECT ACT B R 40 1181 85
70 ADV XRAY ANAL 13 639
MATSUMOTO Y TETSU HAGAN 71 1983 85
72 PHYS REV A 6 96
POWELL CJ SURF INT AN 7 263 85
74 ADV XRAY ANALYSIS 17 150
BAO X SURF SCI 163 444 85
MATSUMOTO Y TETSU HAGAN 71 1983 85
THOMAS LE ULTRAMICROS 18 173 85
75 ADV XRAY ANAL 18 76
76 ADV XRAY ANAL 19 249
MATSUMOTO Y TETSU HAGAN 71 1983 85
81 AIP C P 75 340
GALOSKY AY OPT SPEKTRO 59 1266 85
81 LOW ENERGY XRAY DIAG 340
MORAR JF PHYS REV B 33 1346 86
82 AT DATA NUCL DATA TA 27 1
CHOU SY J VAC SCI B 3 1587 85
MOCHALKIN I PHYS REV A 33 525 86
SUZUKI H APPL OPTICS 24 4434 85
WENDIN G PHYS SCR 32 298 85
82 AT DATA NUCL DATA TA 27 110
WATANABE M APPL OPTICS 24 4208 85
10 ADVANCES XRAY ANALYS 13 639
LOCHNER JC NUCL INST A 242 382 86
72 PHYS REV A 6 96
DELPENNIO J ELEC SPEC N 37 389 86
YOON C J NON CRYST R 79 217 86
75 ADV XRAY ANA 17 213
BRUNNER G ISOTOPENPRA 22 12 86
77 J APPL PHYS 48 1852
OSSOH I SCAN ELEC M 1985 1441 85
78 J CHEM PHYS 68 3692
KOSTIKOV GP V LENIN FIZ 42 86
81 AIP C P 340
BEESE L BIOPHYS J 49 259 86
81 LOW ENERGY XRAY DIAG 146
MALCHE CW ASTROPHYS J 302 371 86
SCHATTEN K " 301 759 86
82 AT DATA NUCL DATA TA 27 1
HOUDY P PHIL J RES 40 375 86
SCHATTEN KH ASTROPHYS J 301 759 86
SIVKOV VN OPT SPEKTRO 60 318 86
SUZUKI H JPN J A P I 25 130 86
VAHEDI KM PHYS REV A 33 2367 86
XU YM NATURE 318 652 86
82 ATOMIC DATA 27 3
ZHEVAGO NA FIZ TVERD T 28 130 86
84 J OPT SOC AM B 1 818
BROWN WA ASTROPHYS J 301 981 86
ELTON RC PHYS REV A N 33 2817 86
84 J OPT SOC AM B 1 828
ELTON RC PHYS REV A N 33 2817 86
RICHARDS MC " " " 44 86
85 REV SCI INSTRUM 56 1537
RICHARDS MC PHYS REV A " 44 86
70 ADVANCES XRAY ANALYS 13 639
BICHSEL H PHYS REV A N 33 3567 86
74 ADV XRAY ANALYSIS 17 150
BASTIN GF X-RAY SPECT 15 135 86
" " " 15 143 86
GOODRICH GA GEOCH COS A 50 861 86
75 ADV XRAY ANAL 18 76
78 J APPL PHYS 49 480
FLEURY A NUCL INST B 14 353 86
78 J CHEM PHYS 68 3692
PEREIRA RCC J CHEM PHYS 84 4228 86
VALLANKA J J PHYS C 19 " 86
80 NUCL INSTRUM METHODS 177 161
81 AIP C P 75 85
FLEURY A NUCL INST B 14 353 86
81 AIP C P 75 340
GAPONOV SV ZH TEKH FIZ 56 881 86
82 AT DATA NUCL DATA TA 27 1
BASTIN GF SCANNING 8 45 86
" X-RAY SPECT 15 135 86
" " 15 143 86
BICHSEL H PHYS REV A N 33 3567 86
KADIN AM SCRIP METAL 20 443 86
KRAUSE MO PHYS REV A 33 3146 86
MCGUIRE EJ " N 33 3577 86
PETRE R ASTROPHYS J 304 356 86
SAMSON JAR PHYS REV L 56 2080 86
83 REV SCI INSTRUM 54 1311
POQUERUS A OPT COMMUN 58 108 86
TALLENTS GJ AUST J PHYS 38 253 86
85 P SPIE 563 201
KADIN AM SCRIP METAL 20 443 86

HENKE B

82 AT DATA NUCL DATA TA 27 2
RARBACK H NUCL INST A 244 150 86

HENKE BL

79 ADV XRAY ANAL 18 76
YANO BN NUCL INST A 246 523 86
77 J APPL PHYS 48 1852
KOWALSKI MP APPL OPTICS 25 2440 86
78 J APPL PHYS 49 3
GLUSKER ES NUCL INST A 246 384 86
79 PHYS REV B 19 3884
KOWALSKI MP APPL OPTICS 25 2440 86
81 J APPL PHYS 52 1509
DIETZ E NUCL INST A 246 362 86
GULLIKSON EM PHYS REV L 57 378 86
JARK W NUCL INST A 246 320 86
KOWALSKI MP APPL OPTICS 25 2440 86
MACDOWELL AA NUCL INST A 246 131 86
PETERSEN H " 246 280 86
YANO BN " 246 523 86
81 LOW ENERGY XRAY DIAG 340
ME KS NUCL INST A 246 688 86
82 AT DATA NUCL DATA TA 27
PIANETTA P NUCL INST A 246 364 86
82 AT DATA NUCL DATA TA 27 1
JARK W NUCL INST A 246 320 86
KANE PP PHYS REPORT R 140 75 86
KOSMAS MF APPL SURF S 29 468 86
MAEZAWA H NUCL INST A 246 68 86
BAGER B J VAC SCI A 4 6611 86
TAKACS PZ NUCL INST A 246 287 86
82 AT DATA NUCL DATA TA 27 71
GERARD P Z PHYS D 2 173 86
83 REV SCI INSTRUM 54 1311
85 ADV XRAY ANAL 8 268
NICOLOSI JA OPT ENG 25 864 86
86 AIP C P 75 85
86 AIP C P 75 146
HENKE BL OPT ENG 25 837 86
72 PHYS REV A 6 96
ANNAIX " J ELEC SPEC 40 353 86
GURMAN SJ PHIL MAG B L 54 L45 86
KHALON MV FIZ TVERD T N 28 2460 86
THURNLEY TR J PHYS C L 19 L563 86
73 ADV XRAY ANALYSIS 17 150
RYCHLY R SBORNIKY R 30 287 86
74 ADV XRAY ANAL 17 187
ALEKSANDROV SOV MICROEL 15 42 86
75 ADV XRAY ANAL 18 76
HENKE BL OPT ENG 25 837 86
76 J APPL PHYS 47 1807
NAUMOVSKAYA I PHYS REV B 34 3710 86
77 J APPL PHYS 48 1852
WANG CL REV SCI INS 57 1740 86
78 J APPL PHYS 49 480
HENKE BL OPT ENG 25 837 86
80 NUCL INSTRUM METHODS 177 161
MEDA N REV SCI INS 57 2480 86
81 AIP C P 75 85
BARBEE TW OPT ENG 25 888 86
81 AIP C P 75 146
BARBEE TW OPT ENG 25 888 86
NICOLOSI JA " 25 864 86
SPILLER E " 25 864 86
81 AIP C P 75 340
SPILLER E OPT ENG 25 864 86
81 J APPL PHYS 52 1509
DWIGHT DW SURF INT AN N 8 76 86
JAANIMAGI PA REV SCI INS 57 2180 86
82 ATOMIC DATA NUCLEAR 27
BARBEE TW OPT ENG 25 888 86
HENKE BL " 25 837 86
82 AT DATA NUCL DATA TA 27 1
METTRICK MC APPL OPTICS 25 3208 86
KORNBLUM HN REV SCI INS 57 2179 86
MAEZAWA H APPL OPTICS 25 3200 86
MEEKINS JF " 25 2767 86
82 ATOMIC DATA NUCLEAR 27 22
EDMANN K LASER PART 4 521 86
83 REV SCI INSTRUM 54 1311
HENKE BL OPT ENG 25 837 86
84 J OPT SOC AM B 1 818
GERASSIM M REV SCI INS 57 2049 86
METTRICK MC APPL OPTICS 25 3208 86
MEDA N REV SCI INS 57 2480 86
84 J OPT SOC AM B 1 828
EDMANN K APPL PHYS L 49 377 86
" LASER PART 4 521 86
GERASSIM M REV SCI INS 57 2049 86
METTRICK MC APPL OPTICS 25 3208 86
85 P SPIE 563 201
NICOLOSI JA OPT ENG 25 864 86
85 REV SCI INSTRUM 56 1537
HENKE BL OPT ENG 25 837 86
JAANIMAGI PA REV SCI INS 57 2180 86
84 J OPTICAL SOC AM B 1 829
TREMES J J PHYSIQUE 47 308 86

HENKE BL

66 ADV XRAY ANAL 9 340
HUANG TC X-RAY SPECT 15 245 86
74 ADV XRAY ANALYSIS 17 150
POUCHOU JL J MICROSC S 11 229 86
76 J APPL PHYS 47 1827
HUANG TC X-RAY SPECT 15 245 86
77 J APPL PHYS 48 1852
PAN G NUCL INST B 18 101 86
78 J APPL PHYS 49 480
MACDOWELL AA REV SCI INS 57 2067 86
79 PHYS REV B 19 3004
AUSMEES A PHYS ST S-B 137 495 86
WALKUP RE PHYS REV L 57 2227 86
81 AIP C P MONTEREY 75
VANBRUG H APPL PHYS L 49 914 86
81 AIP C P 75 85
PROCOPI M APPL OPTICS 25 3640 86
81 J APPL PHYS 52 1509
AUSMEES A PHYS ST S-B 37 495 86
MACDOWELL AA REV SCI INS 57 2067 86
82 ATOMIC DATA NUCLEAR 27
DHEZ P J PHYSIQUE 47 287 86
82 AT DATA NUCL DATA TA 27 1
AKHSAKHALADZE PISMA ZH T 12 1081 86
BASTIN GF J MICROSC S 11 215 86
BUSTAMANTE C PHOTOCHEM P 44 331 86
HENKE BL J OPT SOC B 3 1540 86
JARK W OPT COMMUN 60 201 86
LITZMAN O ACT CRYST A 42 552 86
PROCOPI M APPL OPTICS 25 3640 86
POUCHOU JL J MICROSC S 11 229 86
VANBRUG H APPL PHYS L 49 914 86
83 REV SCI INSTRUM 54 1311
HENKE BL J OPT SOC B 3 1540 86
SCHUMACHER U NUCL INST A 251 584 86
84 J OPT SOC AM B 1 818
84 J OPT SOC AM B 1 828
HENKE BL J OPT SOC B 3 1540 86
85 REV SCI INSTRUM 56 1537
BURKHALTER PG J PHYSIQUE 47 247 86
HENKE BL J OPT SOC B 3 1540 86
85 XRAY DATA BOOKLET 2
JASOLEK G J CRYST GR 78 105 86

1987

78 ADV XRAY ANAL
BOBASHEV SV PISMA ZH T 12 1539 86
76 APPL PHYS LETT 29 539
BOUABELLA A THIN SOL FI 149 51 86
81 AIP C P 75 85
BRUUN MP NUCL INST A 253 136 86
81 J APPL PHYS 52 "
BOBASHEV SV PISMA ZH T 12 1539 86
83 J APPL PHYS 53 1509
SIEGMUND OH J OPT SOC A 3 2138 86
82 AT DATA NUCL DATA TA 27
KAPLAN AE J OPT SOC A M 3 P 70 86
84 J OPT SOC AM B 1 828
ZIGLER A PHYS REV A 36 2800 87

APPENDIX 5

CURRICULUM VITAE OF PRINCIPAL INVESTIGATOR

CURRICULUM VITAE

ERIC M. GULLIKSON

[redacted]

EDUCATION:	Ph.D. Physics, 1984 University of California, San Diego
	B.S. Physics, Highest Honors, 1977 University of Hawaii

PROFESSIONAL POSITIONS:

May 1987 to Present	Staff Scientist Lawrence Berkeley Laboratory
Dec. 1984 to May 1987	Post Doctoral Position AT&T Bell Laboratories
Sept. 1978 to Dec. 1984	Research Assistant, Department of Physics University of California, San Diego
Sept. 1977 to June 1978	Teaching Assistant, Department of Physics University of California, San Diego
June 1977 to Sept. 1977	Research Associate Lawrence Livermore National Laboatory
June 1975 to June 1977	Research Assistant, Department of Physics University of Hawaii

FIELDS OF STUDY:

Low energy x-ray physics
Positron interactions in condensed matter
ESR and magnetization studies in spin glasses

[redacted]

Research Publications by E.M. Gullikson

(1) B. L. Henke, R. C. C. Perera, E. M. Gullikson, and M. L. Schattenburg. High-Efficiency Low-Energy X-ray Spectroscopy in the 100-500 eV Region. *J. Appl. Phys.* **49,** 480 (1978).

(2) P. L. Wallace, W. L. Haugen, E. M. Gullikson, and B. L Henke. A Soft X-ray Spectrometer for the Study of Plutonium and Plutonium-based Materials. *X-ray Spectrometry* **7,** 160 (1978).

(3) S. Schultz, E. M. Gullikson, D. R. Fredkin, and M. Tovar. Simultaneous ESR and Magnetization Measurements Characterizing the Spin-Glass State. *Phys. Rev. Lett.* **45,** 1508 (1980).

(4) S. Schultz, E. M. Gullikson, D. R. Fredkin, and M. Tovar. Characterization of the Spin-Glass State via ESR. *Proceedings of Bariloche 80, Condensed Matter Workshop,* 15-20 Dec. 1980, pp. 296-306.

(5) S. Schultz, E. M. Gullikson, D. R. Fredkin, and M. Tovar. Simultaneous ESR and Magnetization Measurements Characterizing the Spin-Glass State. Proceedings of the 26th Annual Conference on Magnetism and Magnetic Materials, Dallas, Texas; 11-14 Nov. 1980. *J. Appl. Phys.* **52,** 1776 (1981).

(6) E. M. Gullikson, S. Schultz, and D. R. Fredkin. ESR Determination of the Anisotropy Energy in the Spin-Glass CuMn. Abstract KF 16, APS Meeting in Phoenix, Arizona; 16-20 Mar. 1981. *Bull. Am. Phys. Soc.* **26,** 440 (1981).

(7) E. M. Gullikson, and S. Schultz. Calorimetric Determination of the Magnetization in a Spin-Glass. *Phys. Rev. Lett.* **49,** 238 (1982).

(8) E. M. Gullikson, S. Schultz, and D. R. Fredkin. The Frequency Dependence of the Anisotropy Energy in the Spin-Glass CuMn. Abstract KL 6, APS Meeting in Dallas, Texas; 8-12 Mar. 1982. *Bull. Am. Phys. Soc.* **27,** 383 (1982).

(9) E. M. Gullikson, D. R. Fredkin, and S. Schultz. Experimental Demonstration of the Existence and Subsequent Breakdown of Triad Dynamics in the Spin-Glass CuMn. *Phys. Rev. Lett.* **50,** 537 (1983).

(10) E. M. Gullikson, S. Schultz, and D. R. Fredkin. Observation of Triad Dynamics in the Spin-Glass CuMn. Abstract HP 2, APS Meeting in Los Angeles, CA; 21-25 Mar. 1983. *Bull. Am. Phys. Soc.* **28,** 468 (1983).

(11) S. Schultz and E. M. Gullikson. Measurement of Static Magnetization using Electron Spin Resonance. *Rev. Sci. Instrum.* **54,** 1383 (1983).

(12) E. M. Gullikson, R. Dalichaouch and S. Schultz. Direct Observation of the Triad Longitudinal Mode in a Spin-Glass. *Phys. Rev. B* **32,** 507 (1985).

(13) E. M. Gullikson, A. P. Mills, Jr., W. S. Crane, and B. L. Brown. Absence of Energy Loss in Positron Emission from Metal Surfaces. *Phys. Rev. B* **32,** 5484 (1985).

(14) A. P. Mills, Jr., E. M. Gullikson, L. Pfeiffer, and W. S. Rockward. Mobility of Positrons in Polyethylene. *Phys. Rev. B* **33,** 7799 (1986).

(15) P. J. Schultz, E. M. Gullikson, and A. P. Mills, Jr. Transmitted Positron Reemission from a thin Single-Crystal Ni(100) Foil. *Phys. Rev. B* **34,** 442 (1986).

(16) E. M. Gullikson, and A. P. Mills, Jr. Positron Dynamics in Rare Gas Solids. *Phys. Rev. Lett.* **57,** 376 (1986).

(17) A. P. Mills, Jr., and E. M. Gullikson. Solid Ne Moderator for Producing Slow Positrons. *Appl. Phys. Lett.* **49,** 1121 (1986).

(18) E. M. Gullikson. Interaction of Positrons with Rare Gas Solids. Invited Paper QO1, APS Meeting in New York, NY; 16-20 Mar. 1987. *Bull. Am. Phys. Soc.* **32,** 898 (1987).

(19) E. M. Gullikson and A. P. Mills, Jr. Positron Deformation Potential and the Temperature Dependence of the Electron and Positron Work Functions. *accepted for publication in Phys. Rev. B.*

(20) E. M. Gullikson. Hot Electron Diffusion Length in Rare Gas Solid Photocathodes. *in preparation.*